Extra-terrestrial Organics: Organic matter in meteorites and martian analogues

Áine Clare O'Brien

Submitted in fulfilment of the requirements for the degree of

Doctor of Philosophy

School of Geographical and Earth Sciences

College of Science and Engineering

October 2022

Abstract

Astrobiology and the assessment of planetary habitability centres on the detection of organic matter as all known biological lifeforms on Earth are carbon-based. To understand how life began, and where else it may be found in the Solar System, requires knowledge of the origins of the building blocks of life (organic molecules).

Mars is the most likely planet in our Solar System to host either extant or extinct life, thus the characterisation of its organics is key to improving our understanding of its habitability. Detecting organics has been a priority of Mars missions since the Viking era in the 1970s. There are two broad theories for the source of organic matter found both on Mars by rovers and in martian meteorites: martian carbon is exogenous, deposited on Mars from impacts of carbon-rich material, such as carbonaceous chondrites, or indigenous, originating from the reduced martian mantle.

This thesis seeks to characterise the organic matter in martian meteorites, Mars analogues, carbonaceous chondrites, and ureilites, to determine the likely origin of martian organic material, and improve our understanding of the formation and processing of organics in the Solar System. In addition, by evaluating the protocols and techniques used to detect organic matter, this research demonstrates effective analytical workflows to maximise the scientific return from valuable planetary samples in anticipation of Mars Sample Return.

This project has demonstrated that CHONPS, life's building blocks, and available on Mars through the detection of sulfur, nitrogen, and oxygen-bearing organic molecules in small samples of martian meteorites, and orthophosphate in Nakhla. Despite these compounds being formed through abiotic processes, this demonstrates that Mars has some of the key essentials for life to form.

Macromolecular carbon (MMC) inclusions detected in the shergottites Tissint, NWA 8159, and SaU 008 are likely indigenous to Mars. Similarities between the STXM XANES peaks in NWA 8159 and previously published data from ALH 84001 demonstrate that abiotic synthesis of carbon has continued on Mars for at least two billion years.

Raman and STXM XANES data from Tissint and the ureilites Goalpara and Hajmah (a) demonstrate the sensitivity of meteoritic organic matter to thermal processing, both on

planetary bodies and during laboratory analysis.

Results from the analysis of the bulk organic content of the nakhlites Lafayette and Nakhla, as well as CM chondrites, using liquid chromatography mass spectrometry (LC-MS) indicate the presence of a mixture of extra-terrestrial organic compounds in these meteorites. Organic sulfonates detected in Lafayette and Nakhla are consistent with sulfur-bearing compounds detected at Gale Crater on Mars by Curiosity's SAM instrument, as well as in Tissint, Nakhla, and NWA 1950 using time of flight secondary ion mass spectrometry. Numerous fatty acids detected with LC-MS in Nakhla and Lafayette show that Fischer-Tropsch-Type synthesis of organic matter probably occurred on planetary bodies.

Results from the LC-MS analyses of Nakhla and Lafayette also reveal the presence of likely organic contaminants from the fall environments of these meteorites. Several plant-derived metabolites were detected in Lafayette, helping to constrain the fall scenario of this meteorite. The detectable presence of organic contaminants in small masses (< 40 mg) of martian meteorites which fell ~a century ago demonstrates the importance of careful curation of extra-terrestrial samples to minimise the ingress of terrestrial compounds. Results from LC-MS analysis of the Winchcombe meteorite also show the urgency of collecting environmental control samples from the fall sites of meteorites, when possible, to distinguish between organics indigenous to the sample, and terrestrial contaminants. LC-MS analysis of martian analogues stored in polyethylene sample bags also show evidence of plastic contamination during storage, illustrating the importance of comprehensive curation records, and the avoidance of any hydrocarbon-based storage for extra-terrestrial samples.

The protocols used in this project demonstrate the effectiveness of a correlative in-situ workflow when studying organics in thin sections of extra-terrestrial samples, starting with optical microscopy and Raman spectroscopy to identify macromolecular carbon, and finally analysing functional groups at the nanoscale with STXM XANES. Non-destructive microscopy at the mm/μm scale reveals the context of organic material whilst nanoscale analyses with whilst STXM XANES show molecular details of organics, whilst only destroying ~tens of microns of precious samples. LC-MS is highly effective at non-targeted analysis of the bulk organic content of igneous materials. The extraction protocol developed in this project captures a wide range of metabolite classes in all four meteorites studies, as well as the martian analogues.

Acknowledgements

Much of the work of this thesis was carried out during the COVID pandemic. As a result of this, the scope and objectives of this project changed due to access to laboratory and computational facilities.

Thank you to all my colleagues and friends who supported me through my PhD, some of whom are named below.

Thank you to my supervisors Lydia Hallis and Martin Lee for their support and encouragement throughout my PhD, and for all the opportunities you gave me all over the world. Thanks to Lydia for always knowing the right things to say, and helping shape an awesome project. Thanks to Martin for the instantaneous comprehensive feedback on all my work, and of course all the caterpillar cakes. I am so lucky to have the guidance and support of you both.

Thanks to the additional mentors I've gained along the way who I could not have got this far without. To Andrew Steele, thanks for the patience, the thanksgiving dinners, and the pearls of wisdom during long hours in D.C. and Diamond. To Douglas Morrison, for the many Zooms in lockdown and for bringing an astrophysicist's knowledge of biochemistry up to a passable level, whilst having fun along the way. To Luke Daly for the insane hours on the FIB, trips all around the world (including the obligatory airport bubbles), the meteorite hunts, and the pep talks. To Annemarie Pickersgill for all the adventures, the many lockdown coffees, and thesis melodrama support and above all helping me realise I would make it here. To Malcolm MacDonald for opening as many doors to me in the space world as opportunities to have cynical rants about it, too. To Clement Regnault for the LC-MS wizardry, responding to my endless questions (and gifs) on Teams, and helping us put together a paper I couldn't be more excited about during lockdown. To Ashley King, for helping me wade through STXM data at visits to the NHM, for so much fireball excitement, and for providing excellent Taco Cat content. To Sheila Kanani, my mentor at Space School aged 16 and still to this day the person I aspire to be in every way. To Natasha Stephen, for being a total hero to work with when meteorite searching, and in EDI. To Jane MacArthur, my 'PhD Fairy Godmother', for always being there with answers and advice, especially in teaching me how to say no when it was the last thing I wanted to hear.

Thanks to the Angus Mitchell Award Scholarship fund for the PhD stipend for giving me the opportunity to do my PhD. Thanks to additional funding for lab work, conference trips, and knowledge exchange visits from the RAS, Geological Society of London, SAGES, U of G Graduate School Mobility Fund, GES Research Enabling Fund, and STFC for the Diamond beamtime, as well as Winchcombe funding analysis.

Thanks to the amazing people I've been able to work alongside in the planets team at GES. Thanks especially to Sammy Griffin, my 'PhD sister', thanks for never tiring of my questions, for being cheerful always, and being enthusiastic about absolutely every adventure, no matter how difficult it might be for you to feed yourself along the way! To Enrica Bonato, my 'big PhD sister' for the NHM coffees, for the STXM support, but above all for being one of the most positive supportive friends anyone could ask for. To Cameron Floyd, thanks for being such a dependable source of fun, or at least always being keen to vent about the trials and tribulations of doing a PhD in a pandemic, and thanks for always saying yes to my wild outreach ideas all over Scotland. To Pierre-Etienne Martin, thanks for the positivity, enthusiasm, and covering the world in post-its. To Arola Moreras Marti, thanks for being such a source of support during my last few months and helping me believe I would finish at some of the darkest moments when I never believed I would.

Thanks to the many friends and colleagues in GES for the incredible fun and support I've had these last few years. To Ellen MacDonald, the best PhD flatmate anyone could ask for, thanks for putting up with my habits, and dealing with living in a 2 bed house with 3 people in lockdown. Above all, thanks for being my absolute stalwart pal to vent equally about thesis writing, as about millennial life. Thanks to Jenny Mallon (and Reef the dog) for being an absolutely inspirational scientist, unbelievably supportive pal, and for understanding so many of life's challenges like no one else. Thanks to Rory Porteous for bending over backwards to help me out, be it by driving across the country or just with memes and hugs when I needed it most. Thanks to Charlie Young for being an absolute queen in every way, making time for me wherever you are in the world, and always being up for adventures. Thanks to Charlie Rex, for somehow always keeping positive, despite literal houses burning down during a pandemic, and for being one of the most kind-hearted people I've ever known. Thanks to Charlotte Slaymark, for always making time to make the world a better place, and without whom I am certain GES would crumble.

Thanks to colleagues I have been lucky enough to meet and work with around the UK and the world and learn from: Cari Corrigan, Gavin Blackburn, Phil Whitfield, Katie Joy,

Philippa Ascough, Alastair Tait, Marissa Tremblay, Caroline Smith, Jaime Toney, Ali Salik, Eleanor MacKay, and Liane Benning.

Thanks to my friends across the globe whose PhDs came a little before mine, for putting up with the endless questions of ‘is this normal at this stage?’: Rosie Johnson, Katie Raymer, Ciara McGrath, Anna Henschel, Tom Albrow-Owen, Heidi Budd-Thiemann, JJ Hoste, Fredola, Tim Hewlett, and Helena Bates.

Thanks to my fellow planetary and space science PhD cohort in the UK for the camaraderie, particularly in the last couple of years when it has been so tough for us all. Thanks to Sara Motaghian, for being an amazing person to work with on Roving with Rosalind, for being an absolutely tireless advocate for space, and for making me want to be a better person every day. To Megan Maunder: I couldn’t have asked for a better person to have worked with for the RAS ECN, thanks for the endless encouragement, and for making me look forward to Monday morning Teams meetings. To Marina Barcenilla for cheering us all up in lockdown with the Aromatom gifts, and for always boosting me up when I never knew I needed it. To Divya Persaud, from whom I have learned so much about Mars and how to make the world a better place.

Thanks to my chief pals who especially helped me cope through the darkest days of the lockdowns, be it through zoom quizzes, memes, pictures of pets, or just a call to remember fonder times, or to provide a distraction from the loss of loved ones. To Bryony Waugh, may we never tire of enthusing over frogs, thanks for somehow always knowing exactly what is going on inside my brain, and how to make me cry with laughter seconds after I’m crying real tears. To Jenny Hay, Sindy Rajput, and Natasha Venchard (the Dream Team) we’ve come a long way from fighting over peppermint creams in primary school, thanks for seeing me through it all. To Anjali Joseph, for everything from the DMCs, to the photos of puppies. To Eleanor Hughes, for providing the most wonderful escape to Edinburgh whenever I need a piece of home in Scotland. To Joseph Dudley for everything from judging interior design and data visualisation, to helping me with every job application and iteration of my CV, as well as almost every meltdown I’ve ever had. To Stephen Rich, for all the awful puns, for letting me bother you endlessly, and for always being able to provide the perfect distraction. To Catherine Ryan for all the games of spot the cat, for the times you’ve helped me when I’ve been down; I’m looking forward to all the animal and child content we share for the rest of our lives.

Thank you to my family for everything. To the Glasgow O'Briens, the side of my family I am so lucky to have had on the doorstep throughout my PhD. To Ailidh, for everything from rescuing me when I got hit by a taxi, to watching trash tv with me, to chatting nonsense about our mad little family. To Jenny and Gordy, and Matthew and Kirsty, for being the best support network in the west end (featuring Vinnie, Rosie, and Tina the pups of course). To my aunties Phil and Tricia, for always being folk I can call when I need someone on the doorstep, even if it's just for a cup of tea and a biscuit or three. To my uncles John and David, I'll never know how my dad would have felt seeing me living in his old stomping ground getting a PhD; but having his brothers around has made me feel that bit closer to him since he passed. Thank you for keeping my father alive in his memory and helping me as much as you have your own daughters.

To Rob Garner, for dropping everything 'and coming to try out living with me' in March 2020 when we had no idea what was in store. Thank you for picking me up on every down day, for the cooking, for putting up with my nonsense, for all the sacrifices you made for your career. Here's to the next five years. To my brother, for all the times I've announced with no notice I am coming home, for looking after grandma all these years, for coping on your own at some of the most difficult times, and for putting up with me and mum around at some of the most difficult times, too. Thank you for being the most thoughtful, kind-hearted brother I could ask for. To my mother, thank you for keeping it together when we've had absolutely everything thrown at us in the last few years, and still having so much to give to others. It wasn't exactly easy being on the other side of the world from one another for two years, and I'll never forget how you managed to join zoom quizzes at 4am in Australia just so you could catch up with us all, and obviously still win half the time. Thank you for making me the person I am today.

Finally, thanks to my dad who never lived to see me graduate from my undergraduate degree, but who I miss every day. Here's to you, Greg. Love, Dottrh x

Author's Declaration

I declare that this dissertation is the result of my own work and has not been submitted for any other degree at the University of Glasgow or any other institution.

Áine Clare O'Brien

Table of contents

List of figures

List of tables

List of acronyms

ALH	Allan Hills (in this thesis refers to ALH 84001 meteorite)
AMASE	Arctic Mars Analog Svalbard Expedition
BECS	Biomarkers for Environmental and Climate Science (lab at the University of Glasgow)
BVC	Bockfjorden Volcanic Complex, Svalbard
CC	Carbonaceous chondrite
DCM	Dicholoromethane
DON	Deoxynivalenol
FIB	Focused ion beam
FHB	Fusarium head blight
GC-MS	Gas chromatography mass spectrometry
GES	School of Geographical and Earth Sciences, University of Glasgow
HILIC-MS	Hydrophilic interaction chromatography mass spectrometry
HMDB	Human metabolome database
HPLC	High performance liquid chromatography
HyPy	Hydrogen pyrolysis
KEGG	Kyoto Encyclopedia of Genes and Genomes
LC-MS	Liquid chromatography mass spectrometry
MMC	Macromolecular carbon
MOMA	Mars organic molecule analyser
MSR	Mars Sample Return
NC	non-carbonaceous chondrite
NWA	Northwest Africa
OM	Organic matter
PCA	Principal component analysis
PTFE	Polytetrafluoroethylene
SaU	Sayh al Uhaymir
SEM	Scanning electron microscopy
SHERLOC	Scanning habitable environments with Raman and Luminescenes for Organics and Chemicals
STXM XANES	Scanning transmission X-ray microscopy X-ray analysis near edge structures
SUERC	Scottish Universities Environmental Research Centre
TGO	Trace Gas Orbiter
UKFAll	UK Fireball Alliance
U of G	University of Glasgow

1 Introduction

Aims

If we are to assess the habitability of Mars, and ultimately detect life, we must understand the structure of abiotic martian organics, so that we may distinguish them from any possible future martian biota detection. The work of this thesis seeks to aid our understanding of abiotic extra-terrestrial carbon through the identification and characterisation of organic content in meteorites and martian analogues.

Objectives

Specifically, the work of this thesis will:

- Use in-situ techniques Raman spectroscopy and scanning transmision X-ray microscropy to detect macromolecular carbon in martian meteorites, ureilites, and Mars analogues from Svalbard;
- Use bulk analysis techniques (liquid chromtagrophy mass spectrometry and hydrogen pyrolysis followed by gas chromatography mass spectrometry) to analyse the complete organic content of martian meteorites, and martian analogues;
- Evaluate the efficacy and similarity of the analogue material to martian meteorites, in terms of their organic bearing material;
- Evaluate and improve upon analytical protocols for analysing organics in readiness for Mars Sample Return;
- Investigate possible organic contaminants in martian meteorites.

Thesis Content Overview

The research in this thesis is divided between five main chapters: 2 (Background), 3 (Samples), 4 (In-Situ Techniques), 5 (Bulk Results: LC-MS), 6 (Bulk Results: HyPy), 7 (Discussion) and 8 (Conclusions). Description of the primary techniques carried out in this project are detailed in their corresponding technique sections, with additional details given in Appendix 1. Supplementary information from the martian LC-MS and HyPy GC-MS

experiments is given in Appendix 1. The results from all experiments carried out are evaluated in the discussion chapter, including recommendations of future work in this area. Finally, the conclusions outline the main inferences which can be drawn from the in-situ and bulk analyses.

Presentations of this work

Conference Abstracts

This work has been presented at the following conferences:

Oral Presentations

- National Astronomers Meeting, Online 2021
- Lunar and Planetary Science Conference, Online 2021
- Royal Astronomical Society Martian Biosignatures Specialist Discussion Meeting, Online 2021
- British Planetary Science Conference, Oxford 2020
- Lunar and Planetary Science Conference, Houston, 2019
- Meteoritical Society, Moscow, 2018

Poster Presentations

- European Molecular Geobiology Workshop, Heidelberg 2018
- UK Planetary Forum, 2017

Journal Publications

Work from this thesis is included in the following manuscripts:

O'Brien, Á. C., Hallis, L. J., Regnault, C., Morrison, D., Blackburn, G., Steele, A., ... & Lee, M. (2022). Using Organic Contaminants to Constrain the Terrestrial Journey of the Martian Meteorite Lafayette. *Astrobiology* (this manuscript is primarily contained in parts of chapters 2, 5 and 6)

A. C. O'Brien et al. (2022) The Winchcombe Meteorite: One year on, Astronomy and Geophysics DOI: 10.1093/astrogeo/atac009 (my contribution to this publication is

primarily included in Appendix 2)

A. Steele et al (2022) Organic Synthesis associated with serpentinization and carbonation on early Mars, *Science*, DOI: 10.1126/science.abg7905 (my contribution to this publication is primarily included in chapters 2, 3 and 5 of this thesis)

A. J. King et al (accepted) (~13th co-author, 92 co-authors)The Winchcombe Meteorite, a Unique and Pristine Witness from the Outer Solar System, Science (my contribution to this manuscript is primarily contained in appendix 2).

L. Daly et al (2020) Exploring Mars at the nanoscale: Applications of transmission electron microscopy and atom probe tomography in planetary exploration *IOP Conference Series: Materials Science and Engineering*, DOI: 10.1088/1757-899X/891/1/012008 (my contribution to this publication is primarily included in chapter 4 of this thesis)

2 Background

Meteorites and the formation of the Solar System

Meteorites provide a crucial insight into other worlds we have not visited, where spacecraft have not been and/or returned samples from. They also provide a cost-free way of sampling extra-terrestrial bodies. They can give us a snapshot of the solar system billions of years ago at its earliest stages, before the current disk of planets, asteroids, comets, and meteoroids began orbiting our star. Although astronomical observations allow us to see other planetary systems at varying stages in their formation, and these inform our models of the solar system's evolution, it is the constituents of meteorites that give us the most precise components for the timeline of events. For example, our best estimate of the age of our Solar System comes from calcium and aluminium rich inclusions (CAIs) found inside chondritic meteorites. These are irregularly shaped sub-mm sized grains that occur in many types of chondrites and formed at high temperatures (>1800 K) very near to the sun early in its history (Grady et al. 2014). They have been dated using uranium-lead isotope ratios

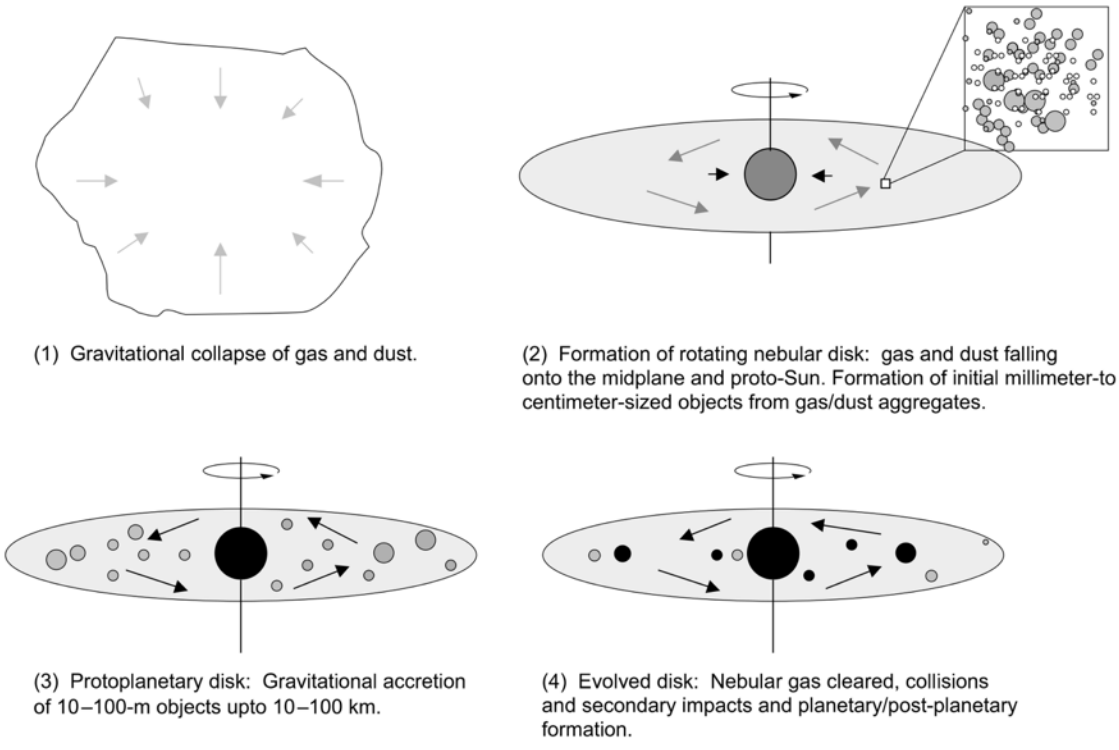

Figure 1 Schematic diagram of the formation of the early Solar System. Image credit: R. H. Nichols in MESS II (2006)

to determine that our home star system is 4.5672 ± 0.0005 billion years (Ga) old (Amelin et al. 2002).The initial formation of the early solar system is outlined in Figure 1.

The primary phase was a collapse under gravity of a cloud of gas and dust, to form a much more stable solar nebular disk rotating about the Sun before hydrogen fusion began in its core. At this stage, the largest bodies were no more than ~1cm in size. Subsequently, as the protoplanetary disk began to evolve, accretion continued under gravity and rocky bodies with m-km sizes began to form, the nebular gas then cleared, and impacts between larger bodies began.

The timings of the formation and initial processes of the major solar system bodies which occurred in the first 200 million years is shown in Figure 2, adapted from Grady et al (2013). From this we can see that the primitive achondrites were some of the first bodies to form in the Solar System. One such example are the ureilites, which accreted 1.6 Ma after the Solar System formed (Budde et al. 2015). These ultramafic meteorites come from a partially differentiated parent body that never fully evolved into a planet. This accretion age reflects their partially differentiated nature too, as they formed ~1 Myr after the iron

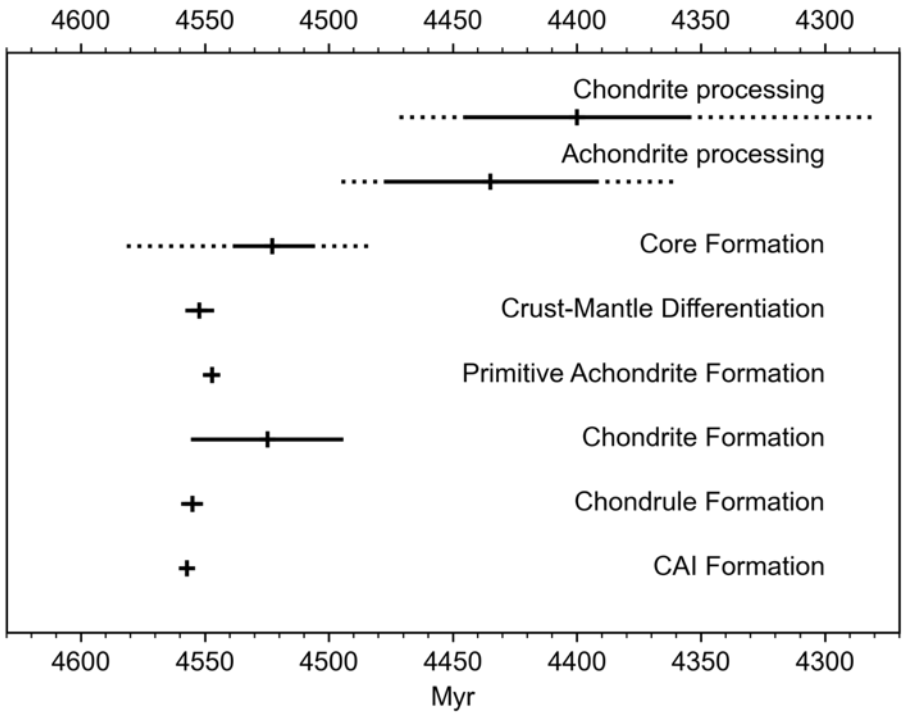

Figure 2 Initial timeline of planetary/meteoritical component formation adapted from Grady et al. (2013)

meteorite parent bodies (which were differentiated) but ~0.5 Myr before the

undifferentiated parent bodies of the chondrites (Budde et al. 2015).

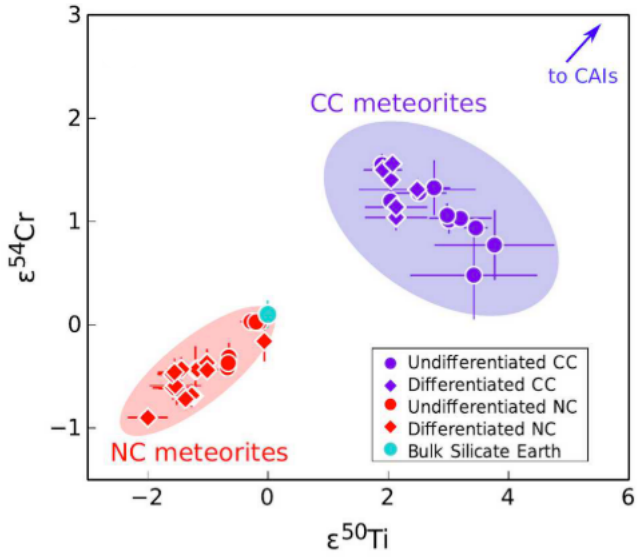

Figure 3 Cr^{54} – Ti50 plot which shows the two distinct fields of CC and NC meteorites which formed in different regions concurrently in the Solar System. Adapted from Burkhadt (2021).

There is a measured isotopic dichotomy between the carbonaceous and non-carbonaceous meteorites (CC and NC, respectively), which indicates that the parent bodies of these two main groups of meteorites formed in different parts of the protoplanetary disk (see Figure 4), with Jupiter forming in between acting as a barrier (Warren 2011). This concept, first

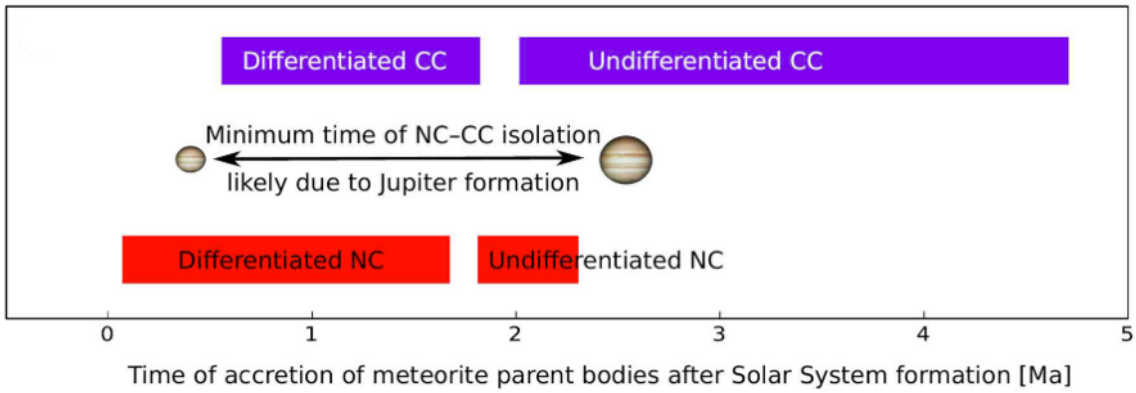

Figure 4 Schematic timeline showing the coexistence of NC and CCs in time, in relation to the formation of Jupiter. Schematic displays the dichotomy of these two groups of meteorites, separated by Jupiter, with the minimum time they must have been isolated, according to Raymond and Izidoro (2017). Image adapted from Burkhadt (2021).

suggested by Warren (2011) comes from measured O, Ti, and Cr isotopic anomalies (see Figure 3) which can only be explained by the model outlined in Figure 4 (particularly after analysis of NC and CC iron meteorites constraining the temporal aspect, Kruijer et al. 2017). In this model, Jupiter's core must have reached ~20 M_{Earth} by the time the Solar

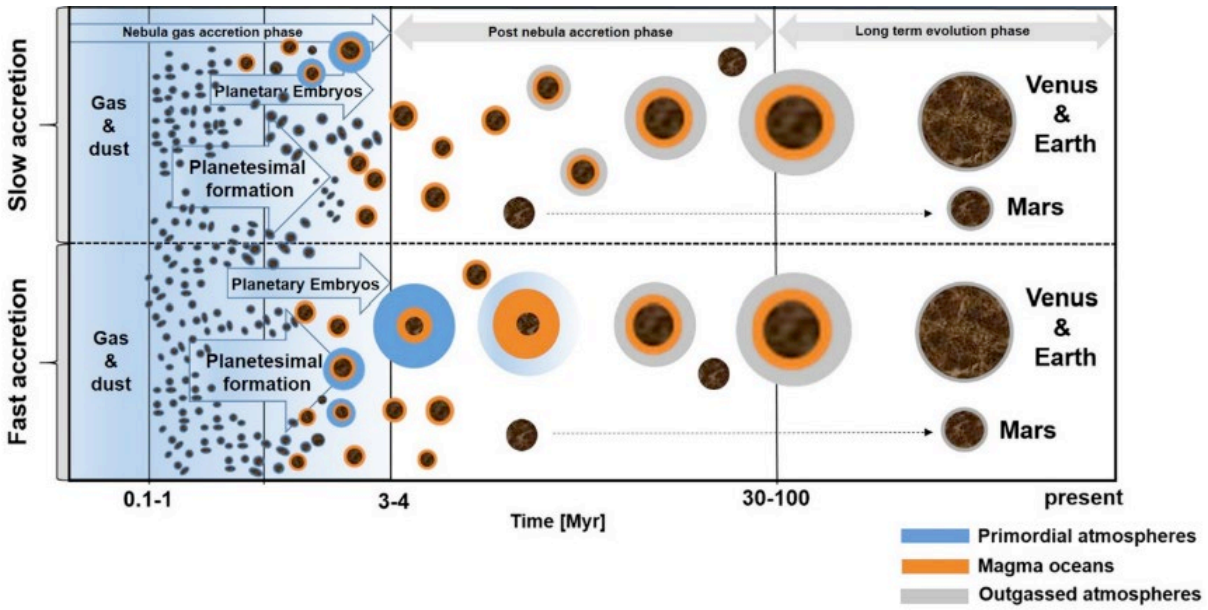

Figure 5 Outline of the two main proposed formation scenarios for Mars, Venus and Earth: slow accretion and fast accretion, over time, adapted from Lammer et al. (2020).

System was 1 Myr old, forming a barrier between the NC and CC material. The model then shows that once Jupiter's mass reached ~50 M_{Earth} it scattered the outer planetesimals, such as the CCs, inward, during its phase of rapid gas accretion (Raymond and Izidoro 2017), causing mixing and ultimately the formation of the asteroid belt. This NC and CC dichotomy led to a new suggested classification scheme for meteorites (Figure 4), whereby the first level of distinction between meteorites is their NC/CC status, as opposed to the standard chondrite/achondrite division (Warren 2011).

The initial formation of the terrestrial planets can be split into four main phases: 1) dust settling, 2) planetesimal formation 3) planetary embryo formation and 4) accretion of protoplanets to form terrestrial planets via giant impacts (Lammer et al. 2020). These processes are displayed in Figure 5, showing two possible scenarios depending on the speed of planetary accretion. Looking at the top model, the 'slow accretion scenario' in Figure 5; this is the case where the bulk of the accretion of the terrestrial planets occurs mostly following dissipation of the protoplanetary nebula after ~3.3-4.5 Myr (Lammer et al. 2020). The bottom model displays the 'fast accretion scenario' that occurs earlier and more quickly, so protoplanets begin with primordial atmospheres (displayed as blue envelopes) captured from the protoplanetary nebula, which is subsequently lost as they go onto become more massive.

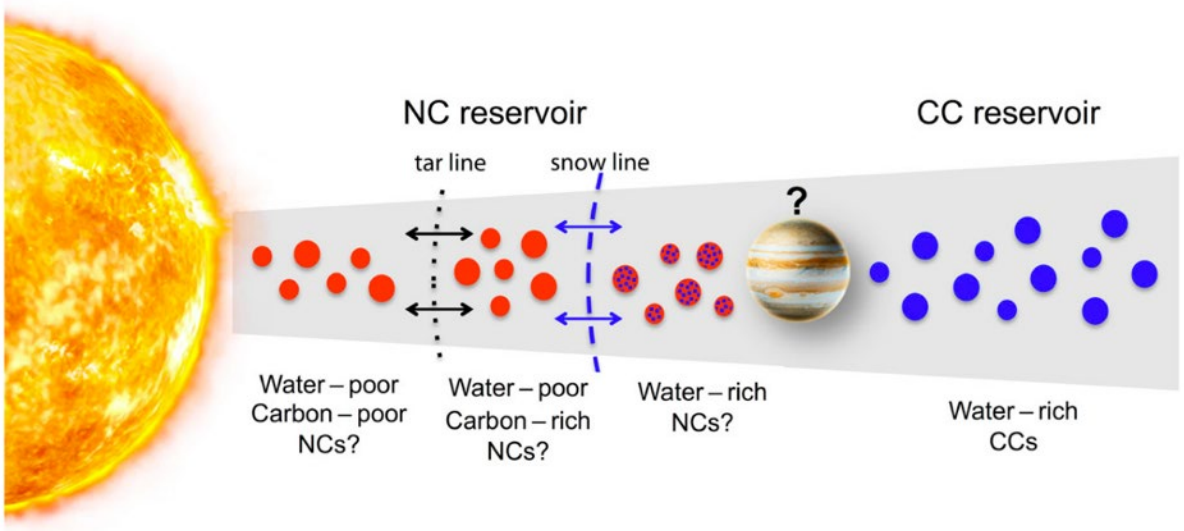

Figure 6 Schematic diagram of distribution of chondrites in protoplanetary disk. Non-carbonaceous meteorites (NCs) accreted separately from carbonaceous chondrites (CCs) which then migrated inward. The CCs are believed to have formed beyond the snow line, separated from the NCs by the proto-Jupiter. Image credit: Bermingham et al (2020). Image not to scale.

This thesis explores the organic content of meteorites from Mars, the ureilite parent body (ureilites), and CM2 chondrites, as well as from terrestrial analogues of Mars. This approach gives snapshots of carbon from planetary bodies at a variety of stages of evolution in the Solar System, as well as helping to evaluate whether meteorites such as ureilites and CM2 chondrites could have been the source of martian organic material. Understanding the origin of extra-terrestrial organics is crucial to our understanding of planetary astrobiology and habitability since all terrestrial life forms are carbon-based.

Historical Background of Mars

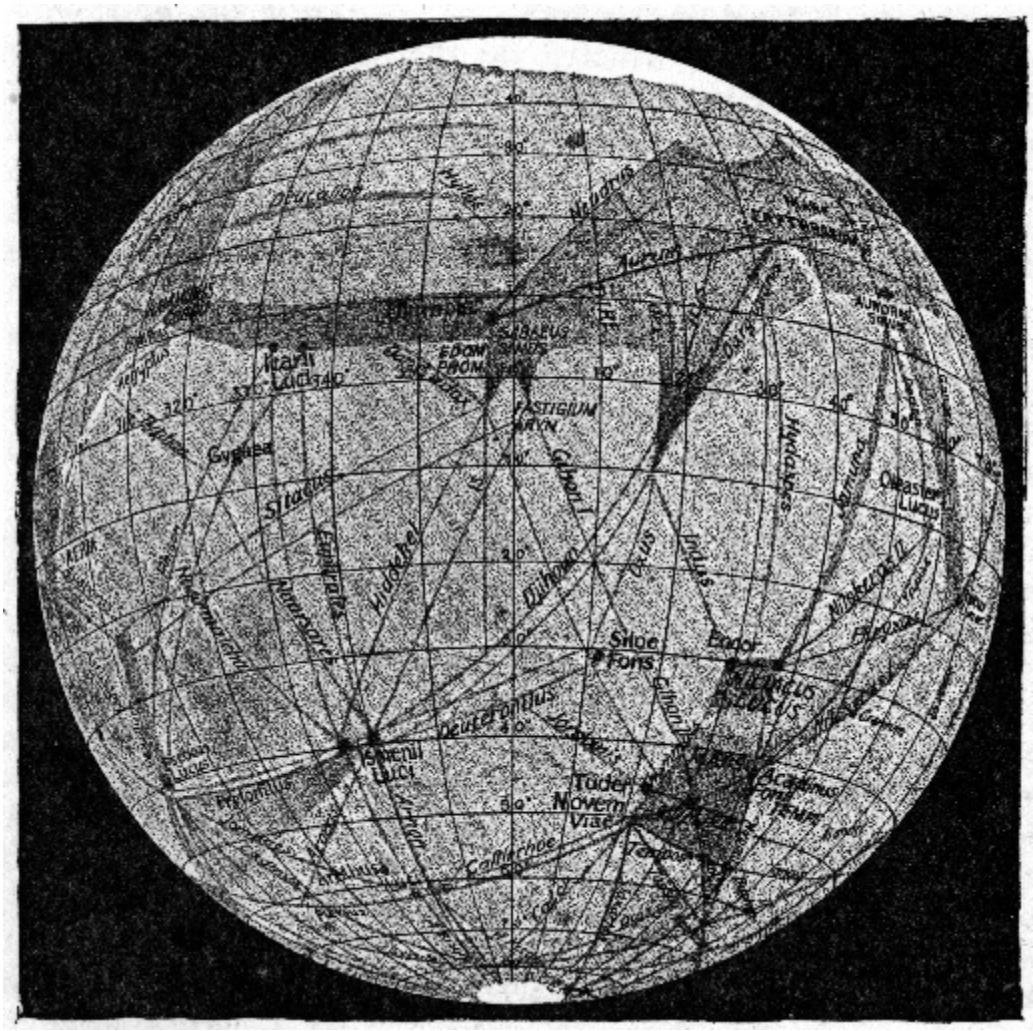

Figure 7 Percival Lowell's 'canals' on Mars, thought to be evidence for intelligent life. Image credit: NASA

Humanity has been fascinated by Mars for centuries, with the potential for life on the red planet being discussed since before even the Canali observed by Schiaperelli were interpreted as signs of ancient life by Percival Lowell in the 1890s (Figure 7).

Mars does not have networks of waterways on its surface and is a dry, cold and harsh environment, yet potentially it still harbours the evidence for past or even extant life (Westall et al. 2015).

Mars is a smaller and older planet than Earth and lost its dipole magnetic field as the planet has cooled (Carr and Head 2010). This means it has a much thinner atmosphere, because without a magnetosphere to protect it much of its atmospheric components were stripped by the solar wind. Mars did, however have a magnetic field earlier in its history, whereby

its magnetic moment peaked at ~ 0.2 M_{Earth} during its first 250 Myr (Dehant *et al.*, 2007).

Mars formed quickly and early in the solar system's history, whereby accretion and differentiation occurred within tens of Myr after the solar system was formed (Lee and Halliday 1997; Brandon et al. 2000), and by 4 Gyr ago, 70% of its crust had formed (Carr and Head 2010). There are little to no surviving pre-Noachian era surfaces and modelling this period (~4.5 Gyr-4.1 Gyr ago) renders very wide uncertainties, since we do not know the volatile content of Mars at this stage (Carr and Head 2010). What we do know, however, is that in this early period, Mars was affected by many impact events generating large (> 500 km) craters, such events would have vaporised any surface water, and increased surface temperatures by hundreds of K (Carr and Head 2010).

The Martian surface through time

Mars has a wide variety of geological and geomorphological features, which suggest it had a much warmer and wetter past. For example, evidence of ancient dendritic river channels, outflow channels, and lakebeds are all visible on the martian surface (Ramirez, 2017). This evidence for widespread presence of water in the Noachian and Hesperian eras (see Figure 10) means that surface temperatures must have been higher. This might be unexpected, given that the solar luminosity at this stage of Solar System evolution was ~ 80 % lower (Wordsworth *et al.*, 2017), and stellar luminosity, L, is related to temperature, T, according to the Stefan Boltzmann Law:

$$L = 4\pi R^2 \sigma T^4$$

meaning that solar warming of the red planet was significantly lower in its past than it is today.

However, atmospheric modelling has suggested that a greenhouse gas effect, caused primarily by CO_2, CH_4 and H_2 would have led to sufficient surface heating, for a long enough period to allow surface water cycling and the production of the features discussed above (Wordsworth et al., 2017). This model is supported by the presence of an ancient magnetosphere to protect such an atmosphere, as mentioned above. Wordsworth et al. (2017) suggest that a transient source of methane would reinforce the greenhouse effect, whereby the ice surrounding methane clathrate melts under variational heating (e.g., due to volcanic activity or impacts), and releases the encapsulated methane. Wordsworth et al. (2017) suggest that H_2 and CH_4 were also released through aqueous alteration in the martian crust. Therefore, interplay between water and organics may have been crucial for making ancient Mars more habitable than it is currently.

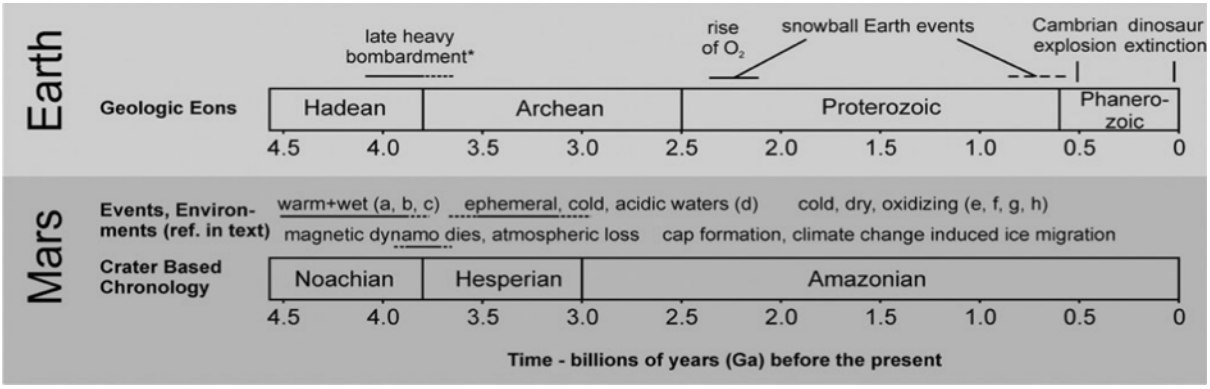

Figure 8 Geological timeline of Mars, compared to Earth. Adapted from Domagal-Goldman et al., 2016.

Figure 8 shows the geological timeline on Mars, aligned with a simplified version of Earth's, adapted from Domagal-Goldman et al (2016). This timeline gives an astrobiological perspective of the geological activity on Mars, and shows the warm wet era in the Noachian, the loss of its magnetic dipole, and gradual loss of its surface water, and atmosphere. We can therefore see that the optimum period for life to have developed and survived on the martian surface was in the Noachian or early Hesperian.

Below is a brief overview of the dominant geology of the main eras on Mars.

The Noachian

Noachian surfaces are the oldest on Mars, and there is only one meteorite from this era - ALH 84001, a carbonate bearing cumulate orthopyroxenite. The breccia NWA 7034 does contain zircons dated at 4.4 Gyr (Bouvier et al. 2018; Udry et al. 2020), but the meteorite

was not lithified until much later. There were three main geological processes that dominated the Noachian: impact cratering, water-rock interactions, and volcanism (Carr and Head 2010). An outline of each of these and key observable features is given below.

Impact Cratering

Mars was most heavily impacted during the Noachian, roughly in line with the hypothesised era of the late heavy bombardment (Bottke and Norman 2017), and the frequency of impacts reduced significantly ~3.5 Gyr ago. There are 98 craters on Mars with diameters > 150 km almost entirely attributed to the early-mid Noachian (see Figure 9). The northern half, sometimes referred to as the Borealis basin, of Mars lies much lower than its southern uplands. This division is often known as the crustal dichotomy, and the formation of it is debated. One explanation is that a very large impact during the Late Heavy Bombardment generated the basin, making it the largest impact structure in the solar system (Carr and Head 2010). Many of the Noachian craters are significantly more eroded than their early Hesperian counterparts that formed only a few million years later; this difference is attributed to the presence of water during this era (Carr and Head 2010).

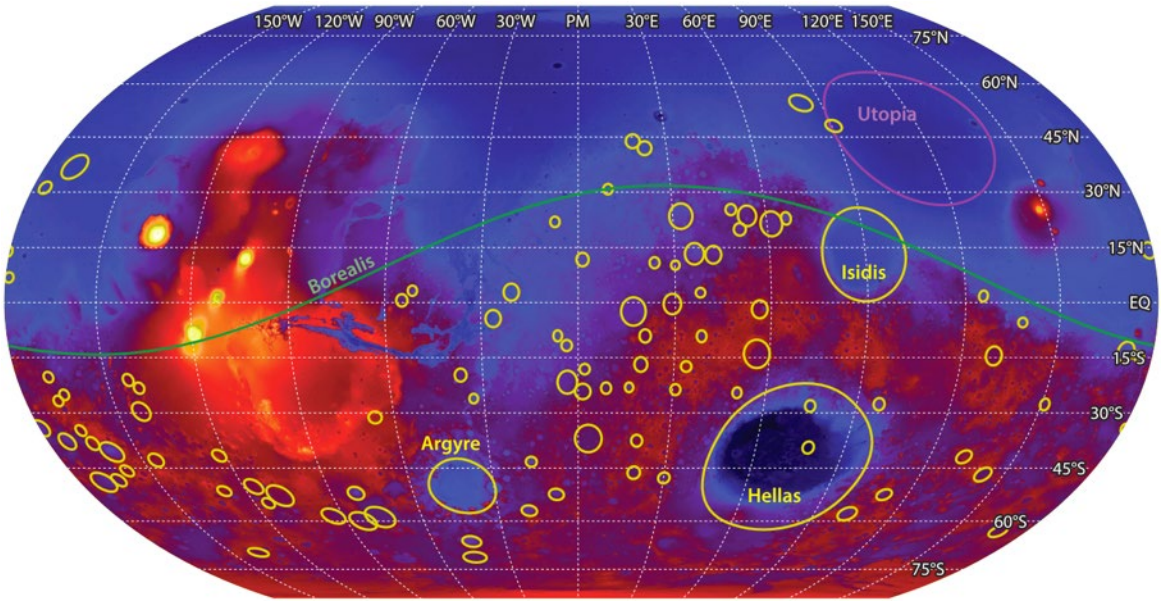

Figure 9 Map of martian impact craters with diameters greater than 150 km. Most are dated to early/mid Noachian epoch. Image credit: Bottke and Norman (2017).

Water-Rock Interactions

Many Noachian surfaces, particularly those found between ~60°S and ~20°N have extensive clay deposits (Ehlmann et al. 2011). These clay deposits are phyllosilicates - the product of the aqueous alteration of basalts - thus evidence for the presence of extensive

ancient water. It is for this reason that the ExoMars Rosalind Franklin rover (mission currently delayed to at least 2028) is planned to visit such a clay rich Noachian region, Oxia Planum (see Figure 27) (Quantin-Nataf et al. 2021). The Perseverance rover is currently exploring a late Noachian/early Hesperian region on Mars, Jezero Crater, which is both clay-rich and carbonate-rich (Horgan et al. 2020). Toward the end of the Noachian there was less alteration, leaving some primary minerals from this era exposed and suggesting that the warm wet beginnings of this epoch gave way to a colder dryer later Noachian (Carr and Head 2010).

In addition to mineralogical alteration of the crust, water played a major role in forming valleys on Mars in the Noachian. Figure 10 shows a global map of the valleys, with those in red dating back to the Noachian, those in purple to the Hesperian and those in blue to the Amazonian (Hynek et al. 2010). The vast swathes of red compared to isolated regions of blue and purple clearly demonstrate the scale at which such interactions dominated in this era compared to subsequent periods on Mars.

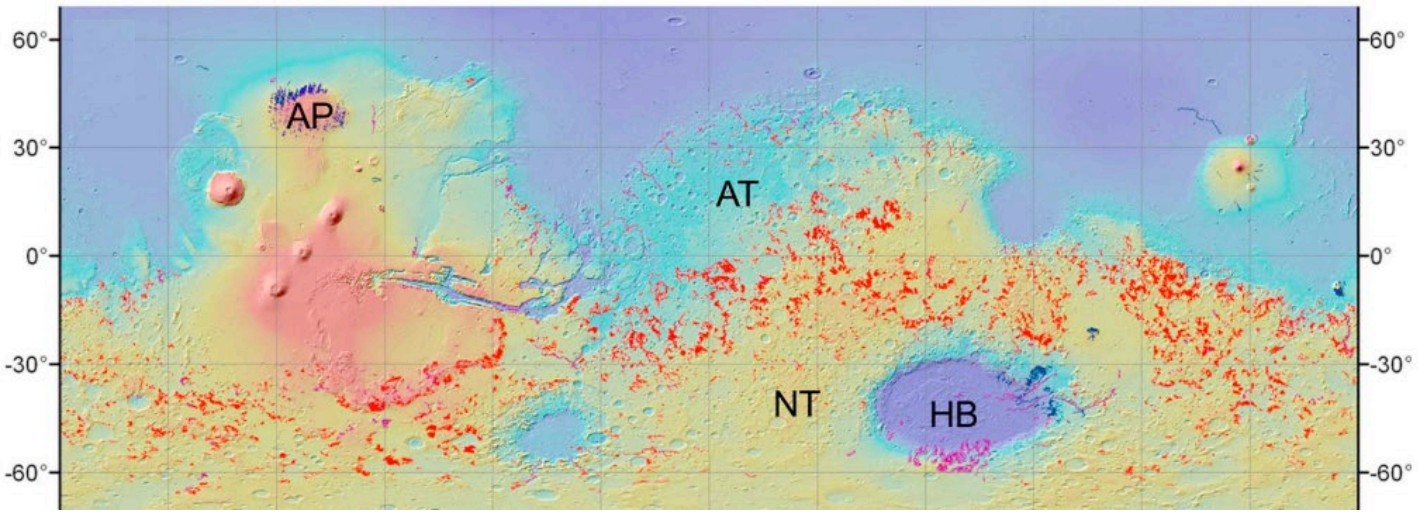

Figure 10 Global map of Mars overlain with valley networks. Those in red date back to Noachian, those in purple to the Hesperian, and those in blue to the Amazonian. This demonstrates how widespread water on Mars was during the Noachian epoch. Adapted from Hynek et al (2010)

Volcanism

Volcanism was highly active during the Noachian, with the bulk of this activity concentrated at the Tharsis region, a volcanic bulge that is the largest volcano-tectonic centre on Mars (Bouley et al. 2016). The presence/exchange of energy associated with Tharsis itself was enough to cause the position of the equator to change through a polar reorientation, or true polar wander (TPW), (see Figure 11) (Bouley et al. 2016). Tharsis is also the source location for the only martian meteorites whose origin has been determined, the depleted Shergottites, whose source has been constrained to the Tooting and 09-00015

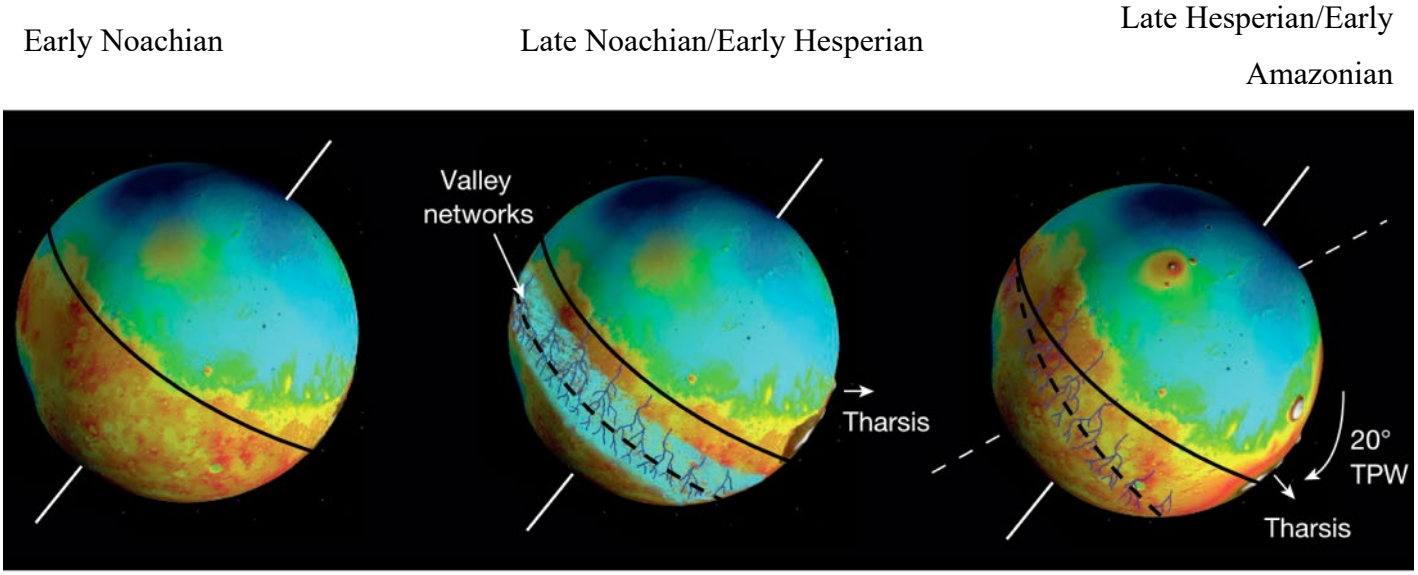

Figure 11 Effect of the Tharsis volcanic region on the reorientation of Mars. Adapted from Bouley et al. (2016).

craters in this region (though they are not Noachian rocks) (Lagain et al. 2021).

The Hesperian

The Hesperian era (from ~3.7 Gyr ago to ~3 Gyr ago) was similar to the Noachian in that it was dominated by volcanism and water-rock interactions, although the frequency of cratering in this period is reduced compared to its predecessor (Carr and Head 2010).

The primary result of volcanic action in this era was the formation of plains in both hemispheres (Salvatore et al. 2010). One such landscape, which is the namesake of the era is Hesperia Planum, a broad volcanic plain which has visibly fewer impact craters than its surrounding Noachian regions (Figure 12). Another key feature of Hesperian volcanism is that the pyroxene from this era is enriched in calcium compared to that of the Noachian,

forming a clear transition known as the LCP/HCP (low calcium pyroxene/high calcium

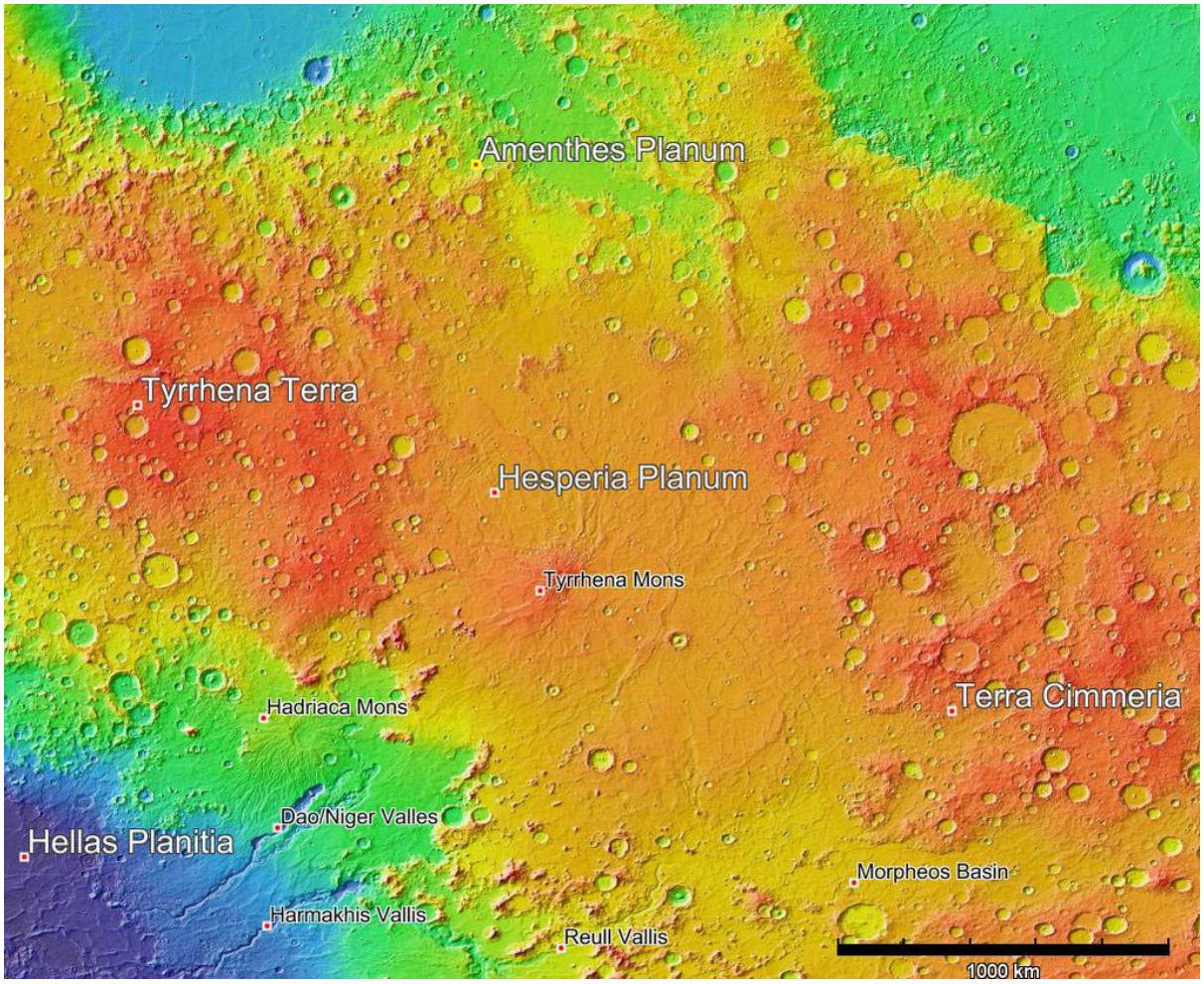

Figure 12 Mars Orbiter Laser Altimeter relief map of Hesperia Planum, the namesake region for the Hesperian epoch, a volcanic plain on Mars with notably fewer impact craters than the two Noachian regions either side (Terra Cimmeria and Tyrrhena Terra). Image credit: NASA/ASU.

pyroxene) suggested to be due to changes in mantle temperatures and/or pressures at the Noachian/Hesperian boundary (Baratoux et al. 2013).

The water-rock interactions of the Hesperian differ to the Noachian, in that little erosion occurred, and little-to-no aqueous alteration forming of clays took place. The era was dominated by the deposition of sulphates (Ehlmann and Edwards 2014). Another key feature of this period was the formation of large outflow channels, although there is debate as to whether all of these were formed by liquid water or lava (Carr and Head 2010). Characteristic of the Hesperian was also the formation of canyons, including Vallis Marineris, the tectonic landform that dominates the centre of many views of Mars (see Figure 13).

There are no known martian meteorites that crystallised during the Hesperian (Udry et al.

2020) (see Figure 34).

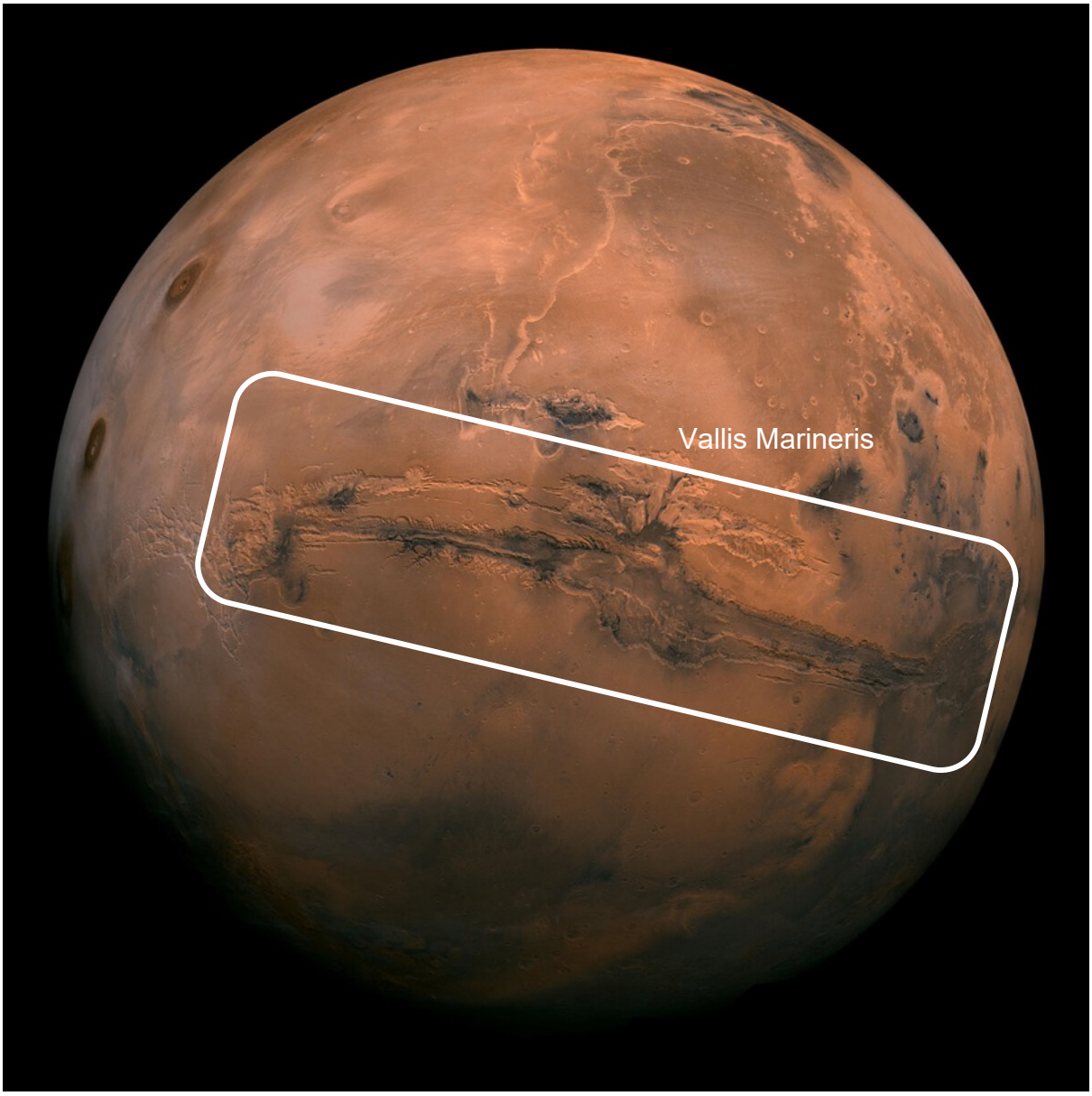

Figure 13 Mosaic of the Vallis Marineris hemisphere of Mars as would be seen from space. Adapted from: NASA/JPL-Caltech

The Amazonian

The Amazonian era extends from ~3 Gyr ago to the present-day on Mars, but despite it being the longest geological era, the martian surface has undergone the least amount of change in this time. Volcanic, erosion, and alteration processes are all at a much smaller/more localised scale and more intermittent in the Amazonian, whilst the dominating geomorphological agent in this period is ice (Carr and Head 2010). For example, glacial landforms are observed throughout Amazonian surfaces, most now frozen to the martian surface. However, a late-Amazonian esker is observed at a mid-latitude, showing basal melting and therefore the presence of a heat source at its base (Butcher et al.

2017).

Most martian meteorites originate from the Amazonian era, with all three of the main classes (Shergottites, Nakhlites, and Chassignites) having crystallisation ages within this period (Udry et al. 2020).

Mission Science

There has been several historical mission successes relevant to this project, and below is an overview of the most significant step changes in martian exploration relevant to our understanding of astrobiology and martian organics.

Viking Landers

The first major milestone in both the robotic exploration of the surface of Mars and, specifically in the search for martian organic molecules came with the NASA Viking mission in the 1970s (see Figure 14). A key mission goal for these landers was to search for organic molecules in the martian regolith at the landing sites, determine the structure of the material, and if possible identify whether biotic or abiotic processes synthesised the molecules (Biemann *et al.*, 1977). The Viking landers were equipped with a GC-MS to detect organic molecules with a 12-200 Dalton mass range and a ppb detection limit (Anderson *et al.*, 1972). Both Viking 1 and 2 detected chlorinated hydrocarbons at 0.04-40 ppb which were attributed to terrestrial contamination at the time (Biemann *et al.*, 1977). This finding has since been revisited, now that perchlorates, and thiophenes have been detected on Mars (see below).

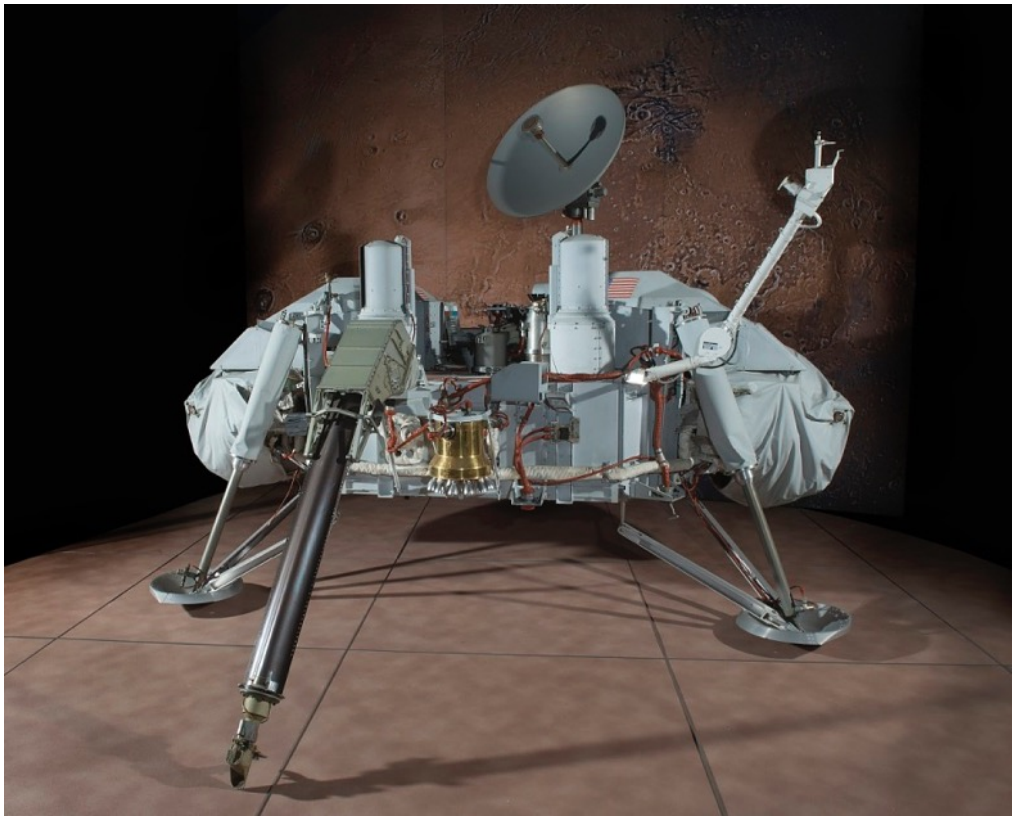

Figure 14 Viking lander test vehicle (full scale model built for testing on Earth). The Viking missions were the first generation of NASA missions with the aim of searching for organic molecules on Mars. Image credit: Smithsonian Air and Space Museum

Phoenix Lander

In May 2008 NASA's Phoenix lander touched down at 68 ºN to study the martian polar climate and evaluate the habitability of polar soil. During this five-month mission, the lander's scoop exposed water ice under the topsoil at the landing site, which sublimed over the subsequent four sols, proving water ice availability on Mars (See Figure 15). This scoop also collected surface soil which was then analysed using the Wet Chemistry Lab onboard, which crucially found evidence for the presence of perchlorate salts in the sample. This discovery allowed scientists to revisit the results of the Viking mission, since evidence with analogue samples found that perchlorate salts reacted with organics during pyrolysis to produce the same chlorinated hydrocarbons as were detected by Viking 1 and 2 (Glavin *et al.*, 2013).

Figure 15 Exposure of sub-surface of water ice by the NASA Phoenix lander on Mars after removing surface soil. Ice sublimed over subsequent 4 sols. Image credit: NASA

Curiosity

The Curiosity rover landed on Mars in 2012 and continues to operate. The Sample Analysis at Mars (SAM) instrument has made several significant discoveries crucial to our understanding of martian carbon. The highlights of these findings are outlined below.

Seasonal methane variability

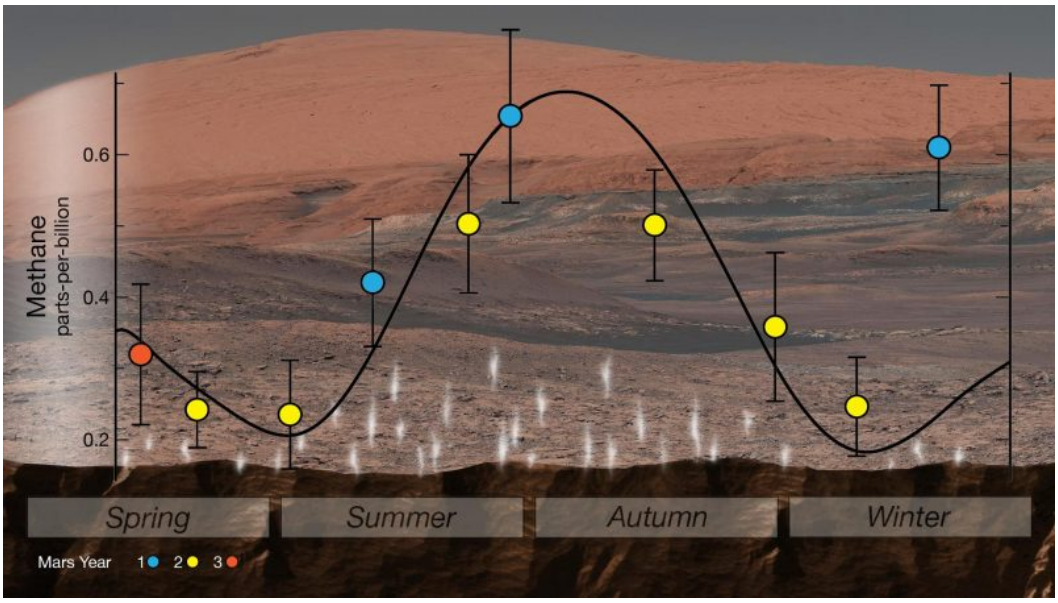

Figure 16 Plot of the measured methane concentration at Gale Crater over the martian seasons during Curiosity's first three years on Mars. Plot shows Methane abundance varies from 0.2 ppb in Winter to >0.6 ppb in Summer. Image credit: NASA JPL.

In-situ measurements of methane have been carried out by the SAM instrument at Gale Crater throughout its mission history. Methane is a critical biomarker since on Earth it is produced primarily through biotic processes (Formisano *et al.*, 2004), however abiotic processes such as serpentinization of olivine or pyroxene on Mars have also been suggested as formation mechanisms (Chassefière and Leblanc, 2011). Central to determining the possible source mechanism is detection of the compound both temporally and spatially. Curiosity carried out a five year study of the concentration of methane in Gale Crater and showed that methane varies consistently with the planet's seasons (see Figure 16) (Webster *et al.*, 2018). This is despite methane being stable in the martian atmosphere for ~300 years, meaning that processes producing/releasing methane must be in line with these seasons (Webster *et al.*, 2018).

Sulfonated organic compounds

The GC-MS onboard the SAM instrument successfully detected sulfonated organic compounds at Gale Crater (see Figure 17) such as methanethiol, dimethylsulfide, thiophene, 2-methylthiophene, and 3-methylthiophene preserved in 3 billion year old mudstone (Eigenbrode *et al.*, 2018). This was a significant moment as it was the first time organics had been detected in situ on Mars which weren't chlorinated organics such as those detected originally by the Viking landers (Biemann *et al.*, 1977). ToFSIMS (Time of flight secondary ion mass spectrometry) analyses also showed that organic material in martian meteorites are consistent with those detected by Curiosity (Steele *et al.*, 2018).

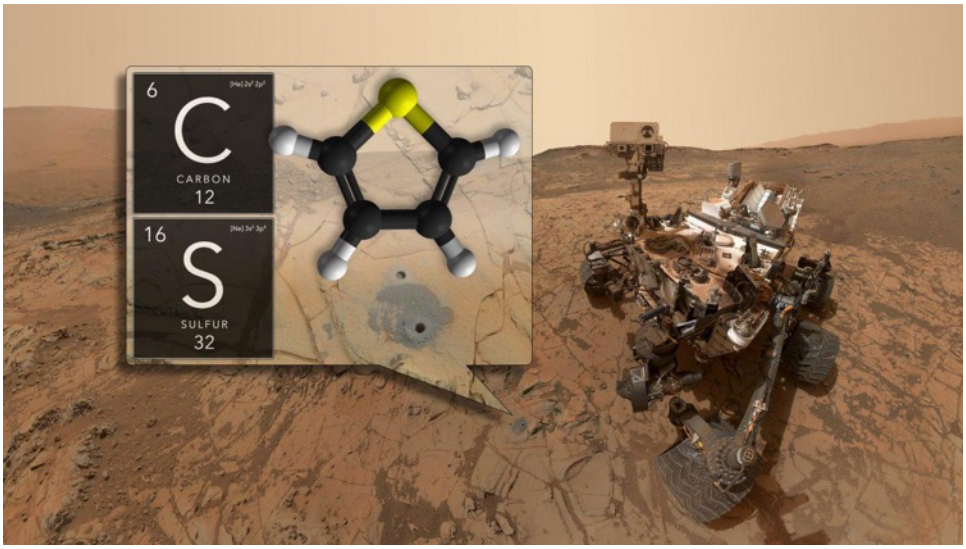

Figure 17 Self-portrait photo taken by Curiosity at Gale Crater, with superimposed graphic of thiophene molecule detected by the SAM instrument (Eigenbrode et al, 2018). Image credit: NASA JPL

Organics with varying C-13 isotope ratios

The SAM instrument collected 24 powdered samples from a range of stratigraphic regions on Gale Crater and measured their C-13 isotope ($^{13}C/^{12}C$) ratios. These $\delta^{13}C$ values ranged from -137 ± 8 ‰ to +22 ± 10 ‰ (House *et al.*, 2022). Many of these ratios were significantly depleted compared to the atmospheric $\delta^{13}C$ measurements carried out by SAM, which returned a $\delta^{13}C$ enrichment of +46‰ (Webster *et al.*, 2013). House et al (2022) suggest that the martian atmosphere had a much lower $\delta^{13}C$ value at the time the analysed sediments were deposited compared to the present day. This lower $\delta^{13}C$ value is consistent with that of the reduced organic species in martian meteoritical organics – 19.8 ± 4.3 ‰ – (Grady et al., 2004; Steele *et al.*, 2012).

Perseverance

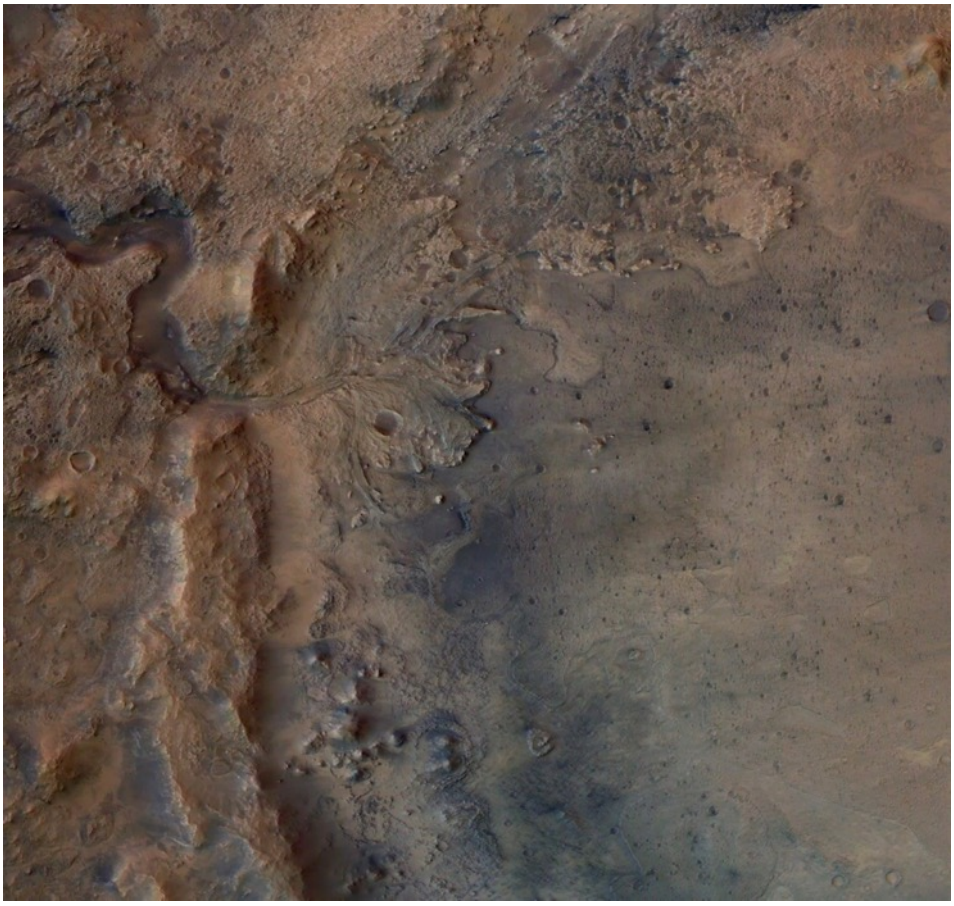

Figure 18 Jezero Crater, the Perseverance rover's landing site. Image credit: ESA/DLR/FU-Berlin

The Perseverance rover landed on Mars in 2021. It is an upgraded version of the Curiosity rover with much of the same exterior design features but with instruments onboard that mark new milestones in martian scientific exploration. The mission has four science goals:

A. Explore an astrobiologically relevant ancient environment on Mars to decipher its geological processes and history, including the assessment of past habitability.

B. Assess the biosignature preservation potential within the selected geological environment and search for potential biosignatures.

C. Demonstrate significant technical progress towards the future return of scientifically selected, well-documented samples to Earth.

D. Provide an opportunity for contributed Human Exploration and Operations Mission Directorate or Space Technology Program participation, compatible with the science payload and within the mission's payload capacity.(Williford *et al.*, 2018)

This mission also marks the start of the Mars Sample Return campaign, as Perseverance is caching samples ready to be collected by ESA's Sample Fetch Rover, and brought back to Earth. Perseverance landed at Jezero Crater on 18th February 2021. This ancient river delta was chosen for its potential to preserve biosignatures (see Figure 18).

The key instrumentation onboard Perseverance for this project are outlined below.

SHERLOC is a deep UV Raman system located at the end of Perseverance's robotic arm. SHERLOC is primed for the detection of organic materials and is the first Raman spectrometer on the red planet (Abbey et al. 2017). With a system capable of detecting Raman and native fluorescence, without structurally altering the molecules therein,

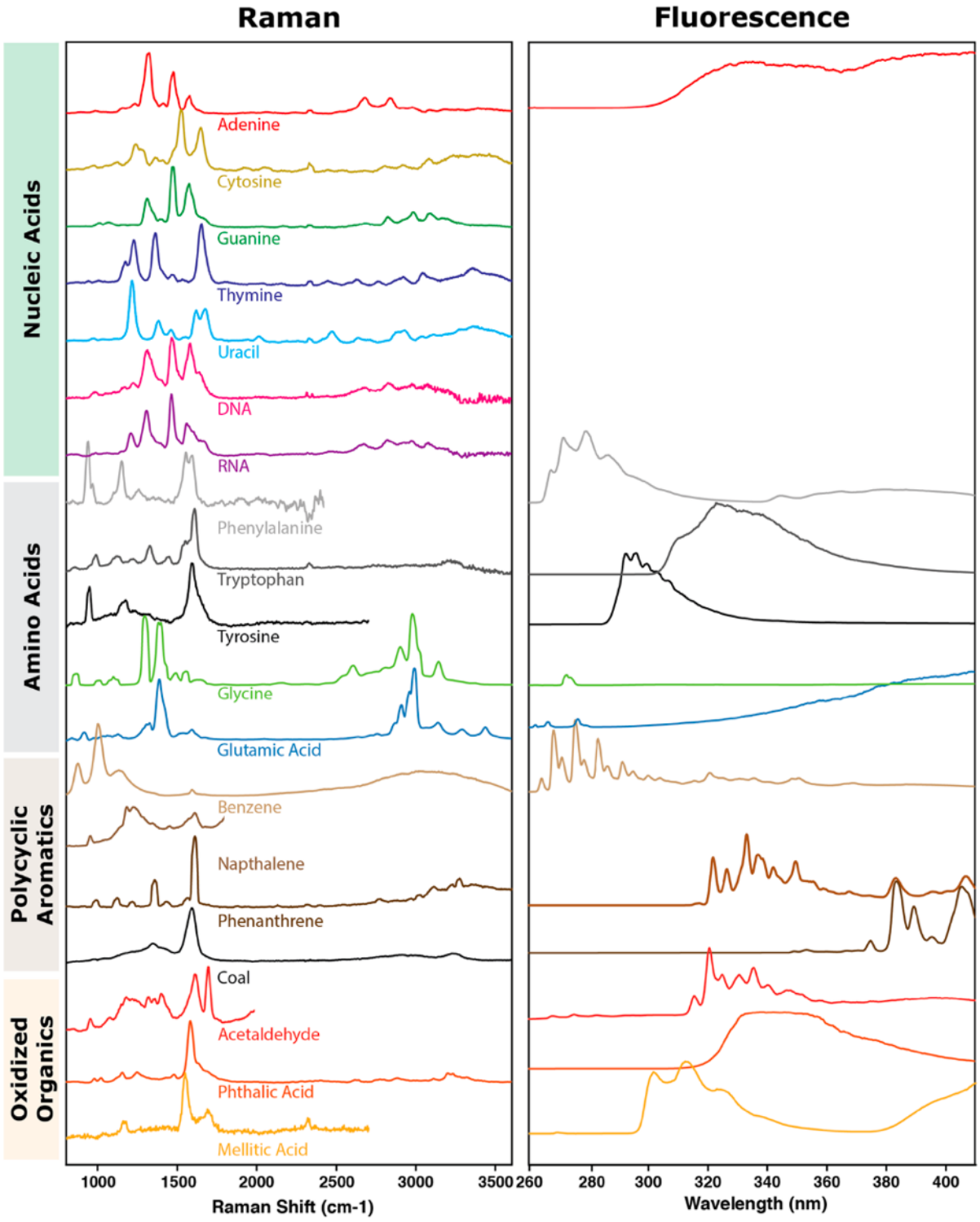

Figure 19 Examples of deep UV Raman and native fluorescence spectra of organic molecules by the SHERLOC instrument. Data attained by the SHERLOC prototype instrument, MOBIUS. Image credit: Bhartia et al. (2021).

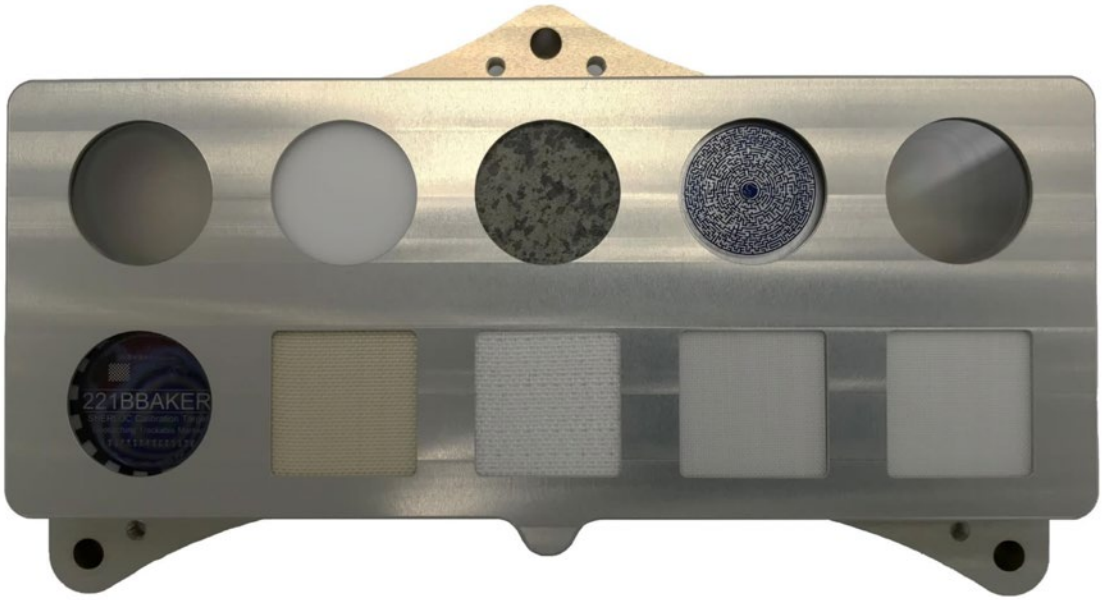

Figure 20 SHERLOC Calibration Target. Top row, from left: aluminium gallium nitride on sapphire; a quartz diffuser; a slice of Martian meteorite SaU008; a maze for testing laser intensity; a separate aluminium gallium nitride on sapphire with different properties. Image credit: NASA

SHERLOC is primed for characterisation of potential biosignatures (see Figure 19). In order to do this most effectively, the instrument carries onboard calibration targets, including a piece of Mars returning to its home planet: the martian meteorite SaU 008 (see Figure 20). SaU 008 was used to prove the instrument was capable of detecting martian organics, and resolving heterogeneity within individual organic bearing regions (see Figure 21). The calibration target (Figure 20) now acts to ensure accuracy of the instrument's measurements on Mars, as it starts each new sol, and was chosen for its mineralogy and strength (Graff *et al.*, 2019).

In this project, a thin section of SaU 008 was studied using confocal Raman imaging spectroscopy (CRIS) and scanning transmission X-ray microscopy X-ray analyses near edge structures (STXM-XANES) to characterise the organics therein. This work therefore provides additional baseline data for the Perseverance mission, and associated goals in the detection of martian organics in understanding this key martian sample.

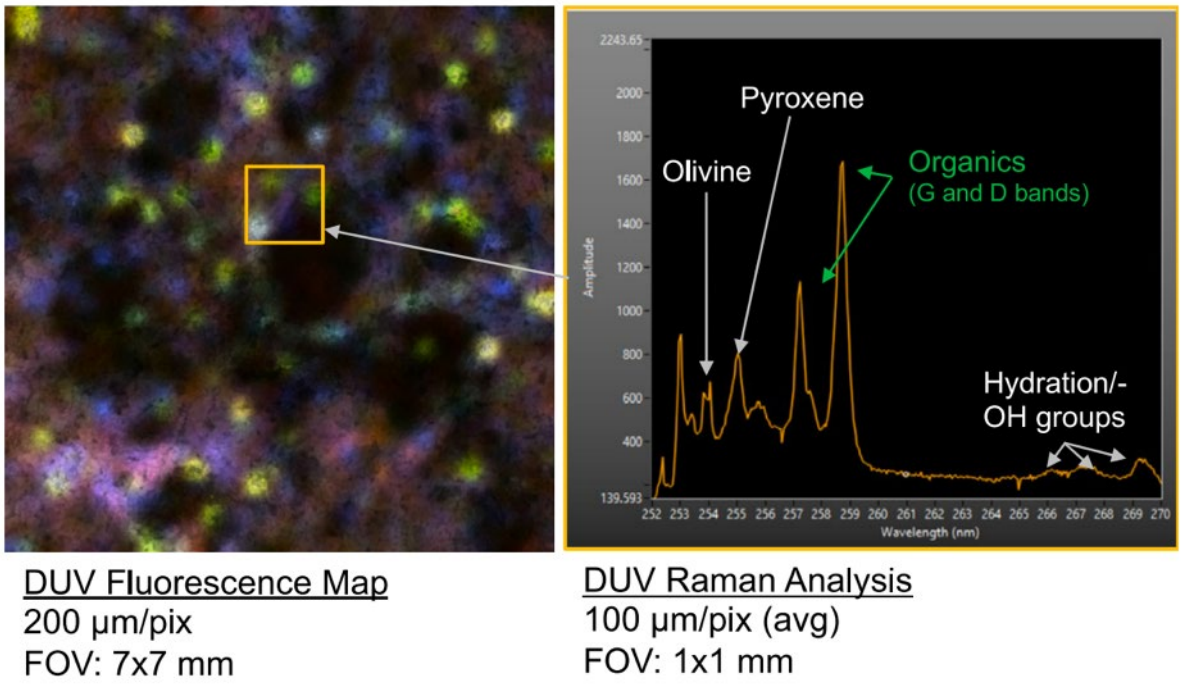

Figure 21 Deep UV analyses of the SaU 008 slice onboard Perseverance studied with SHERLOC demonstrating capability to spatially resolve organic material. Image credit: Graff et al (2019)

ExoMars

The ESA ROSCOSMOS ExoMars mission consists of two main components: a satellite, the Trace Gas Orbiter (TGO) (see Figure 22), and the Rosalind Franklin rover. The overall ExoMars mission's aim is to search for signs of life/habitability on Mars. TGO launched in March 2016, and began taking measurements in April 2018, with its primary aim to characterise the composition of trace gases in the martian atmosphere. TGO's scientific

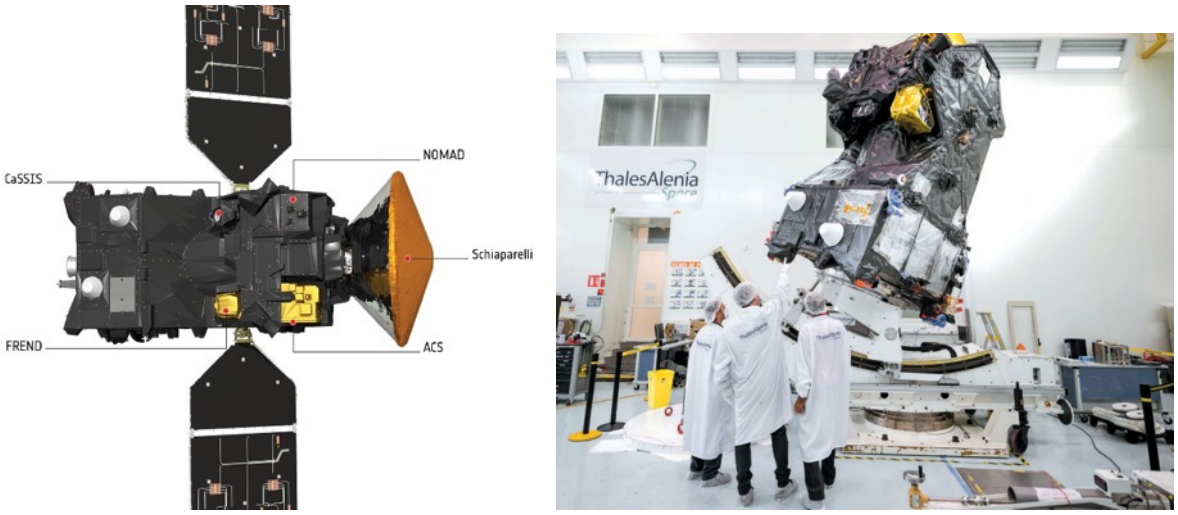

Figure 22 A - schematic diagram of the ESA ROSCOSMOS Trace Gas Orbiter. Its primary scientific payload instruments, along with the test lander, Schiaparelli, are indicated. B – Trace Gas Orbiter during manufacture. Image credits: ESA

payloads were built to detect gases relevant to habitability such as ozone, methane, and water vapour, which collectively make up less than 1% of the martian atmosphere (Gaind, 2018).

TGO Payloads:

NOMAD (**N**adir and **O**ccultation for **MA**rs **D**iscovery)

NOMAD consists of two infrared and one ultraviolet spectrometers capable of detecting

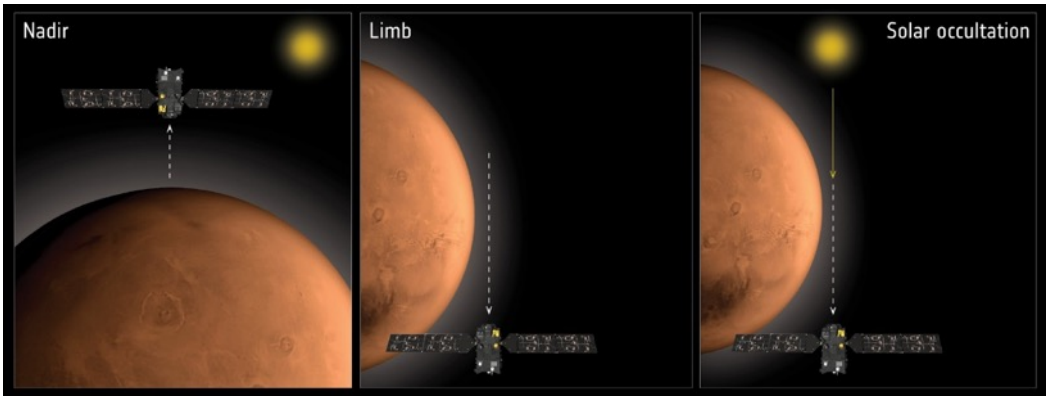

Figure 24 Orientation of TGO with respect to the Sun at different stages of its orbit. At solar occultation, the maximum amount of atmosphere can be probed by NOMAD, as sunlight passes directly through the martian atmosphere. At Nadir, reflected sunlight can by analysed. Image credit: ESA

atmospheric components to an unprecedented detail (Bellucci et al., 2019). By observing the martian atmosphere at varying geometries with the sun (see Figure 24) it detects absorption of trace gases such as methane and their associated latitudes. Bellucci et al. (2019) also showed that it can be used to give valuable dust storm and ice cap data, furthering our understanding of martian meteorological systems.

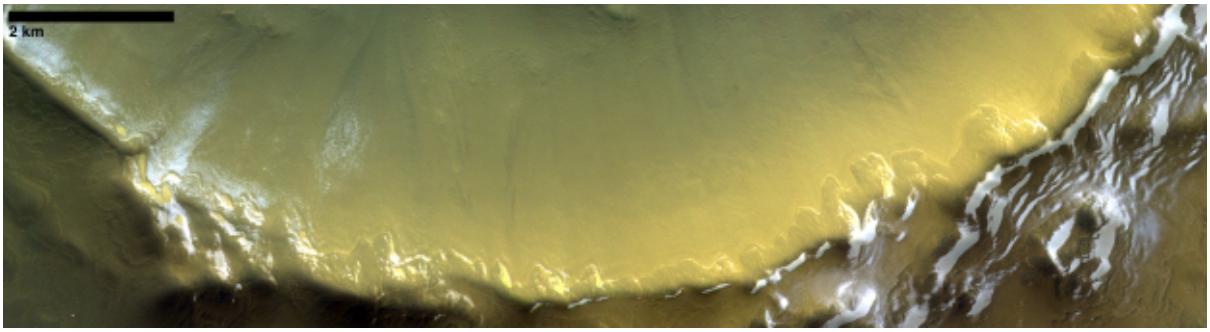

Figure 23 Permanent ice deposit on martian crater at 192.99°E/70.4°N. Image taken by CASSIS on 29th October 2019. Mapping of seasonal water ice presence in craters is of particular importance due to the long-lasting heating effects of impacts, and therefore the increased habitability of impact craters with water ice presence (Osinski et al., 2013).

CASSIS (Colour and Stereo Surface Imaging System)

CASSIS is a high-resolution camera, imaging areas from multiple points in orbit, to generate 3D maps (see Figure 25). CASSIS is an astrobiologically relevant instrument since CASSIS data have been used to map seasonal variation in water ice in craters (see Figure 23) and any detected spikes of methane can be cross-referenced with surface images, so that possible sources may be found.

Since arriving into orbit, the TGO mission may have triggered more questions than it has answered concerning organics on Mars. Despite seasonal methane levels being detected by multiple other previous instruments and missions (e.g. (Mumma *et al.*, 2009; Webster *et al.*, 2018) neither the ACS or the NOMAD instruments on TGO detected any methane in its initial orbital period in Spring 2018, see Figure 26 (Korablev *et al.*, 2019). Some of

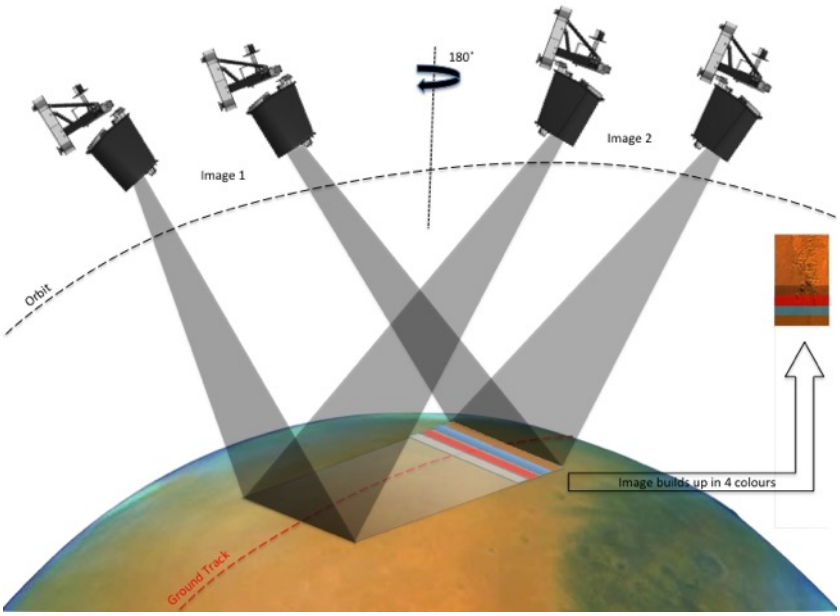

Figure 25 Schematic of TGO's CASSIS payload, a high resolution 3D imaging system. Image credit: University of Bern

these measurements were synchronised by date and region with Curiosity (i.e., the orbiter was above Gale Crater at the time) and correlated with a positive detection of methane by Curiosity; a suggestion has therefore been made that any methane generating/loss systems are local on Mars.

More recent measurements made by Curiosity suggest that a diurnal atmospheric dilution mechanism may explain the discrepancy between Curiosity and TGO's detections of methane. Daytime measurements by the SAM instrument give concentrations of methane during the martian day at 0.05 ± 0.22 ppbv whilst night time levels were measured at 0.52

± 0.10 ppbv (Webster *et al.*, 2021) at the same region in the same season. TGO requires sunlight for its CH_4 measurements and therefore any detections that took place needed to be in the daytime. In contrast, SAM's instruments normally carried out their methane detections in the martian night, to benefit from the extra power available whilst other equipment was not being used. Once additional CH_4 daytime detections had been made, clearly lower than their night time equivalent, Webster et al (2021) suggested that a

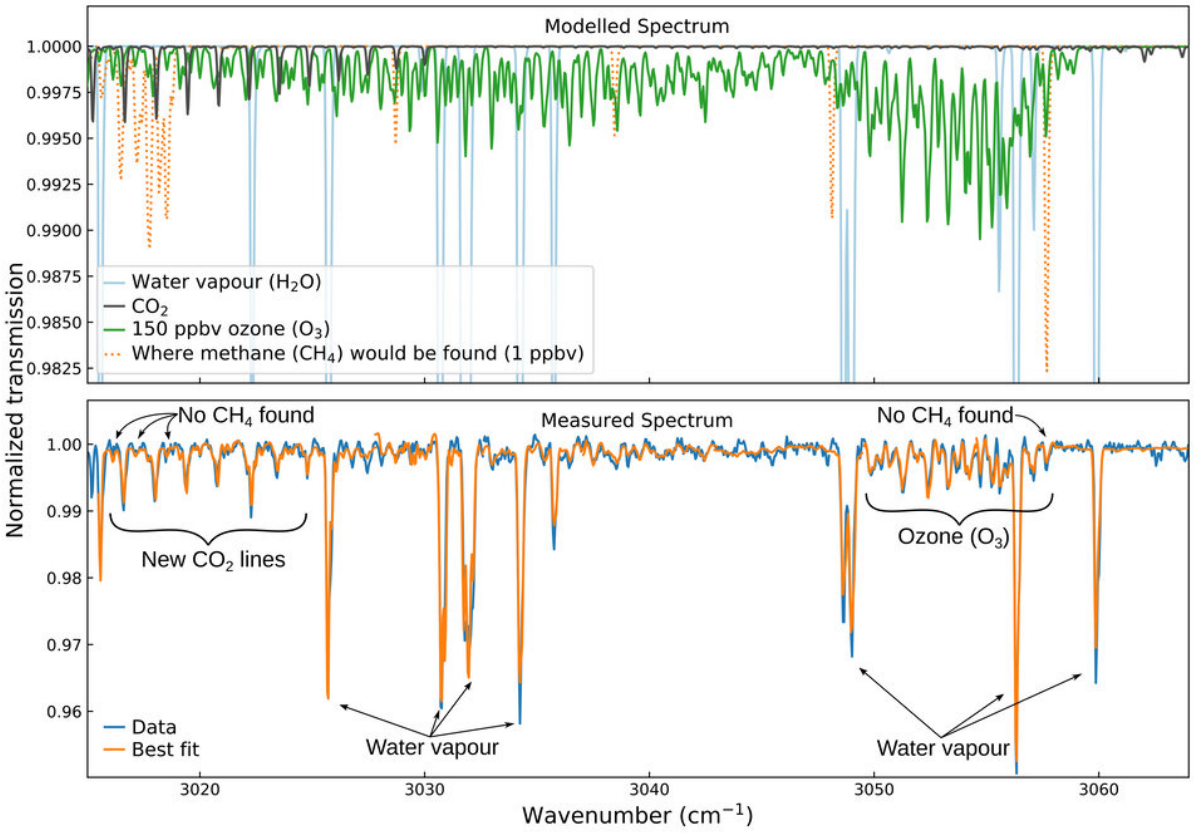

Figure 26 Spectral signatures of gases detected by ESA's Trace Gas Orbiter (TGO) ACS instrument. ACS was primed for methane detection but no methane was found (orange dots indicate where methane spectrum would be observed). Further work by NASA JPL indicates diurnal variation may be reason for nondetection of methane by TGO. Image credit: ESA.

daytime atmospheric dilution takes place, explaining the non-detection by TGO.

Rosalind Franklin Rover

TGO's partner spacecraft, the Rosalind Franklin rover, mission delayed to 2028, will be heading toward its landing site Oxia Planum, an ancient martian delta (see Figure 27). The rover will search for evidence of extant and extinct life through its instrument suite (Figure 30). Oxia Planum is a clay-rich region, thought to date back to the Noachian period, according to crater counting calculations in the area (Loizeau *et al.*, 2007). It was chosen thanks to the region's age (~4 Ga) and the likelihood of any possible biosignatures to be preserved in the clay-rich features accessible by the rover (Quantin-Nataf et al., 2021).

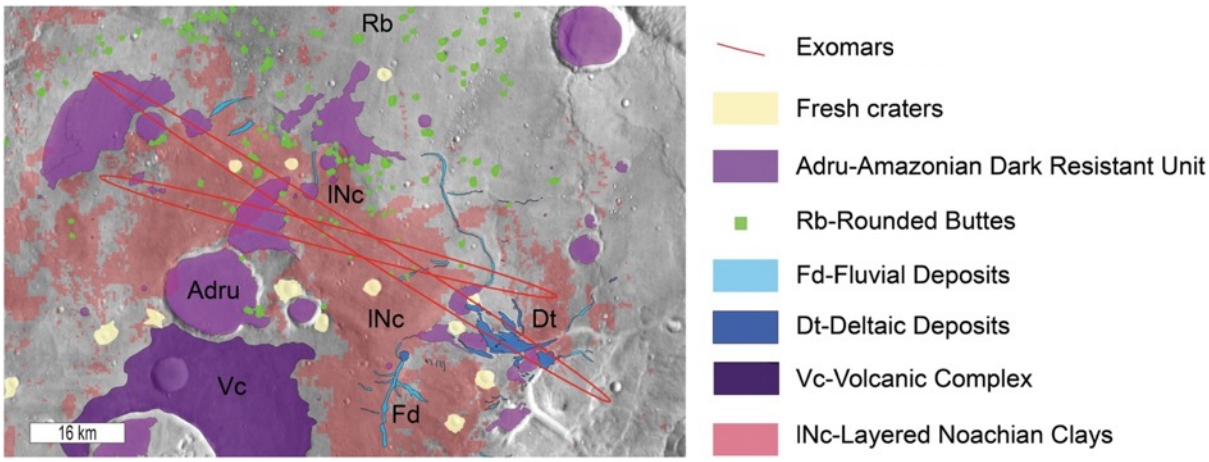

Figure 27 Overlay map of the main geological units at Oxia Planum, the ExoMars Rosalind Franklin rover landing site. Image credit: Quantin-Nataf et al (2021)

A geological map of the planned landing ellipse at Oxia Planum is shown in Figure 27, adapted from Quantin-Nataf et al (2021). We can see the dominating Noachian clays in the area in light pink. The suggested geological history and formation mechanism for Oxia Planum is then shown in Figure 28, through which we can see the water rich Noachian environment, with some water content remaining in the region until the Hesperian, and possibly the Amazonian (Quantin-Nataf et al. 2021). The longevity of water presence in the region heightens the possibility of possible biosignature presence.

The rover will be equipped with a 2-metre drill to study sedimentary samples from much farther below the surface than has ever been achieved before. This is a key component of the ExoMars mission, and has far-reaching implications for martian organic geochemistry since this depth is thought to provide sufficient protection for organic molecules from cosmic and solar radiation to shield them from ionisation, fragmentation and oxidation (Goetz *et al.*, 2016).

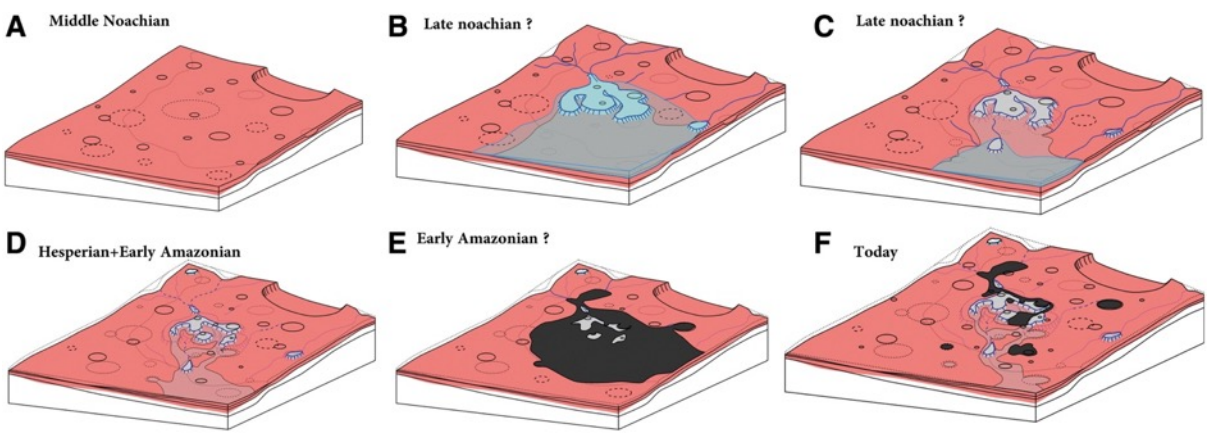

Figure 28 Geological history of Oxia Planum, the ExoMars landing site on Mars. Image credit: Quantin-Nataf et al (2021)

Below is a summary of the instruments onboard that are most relevant to this project:

Raman Laser Spectrometer (RLS)

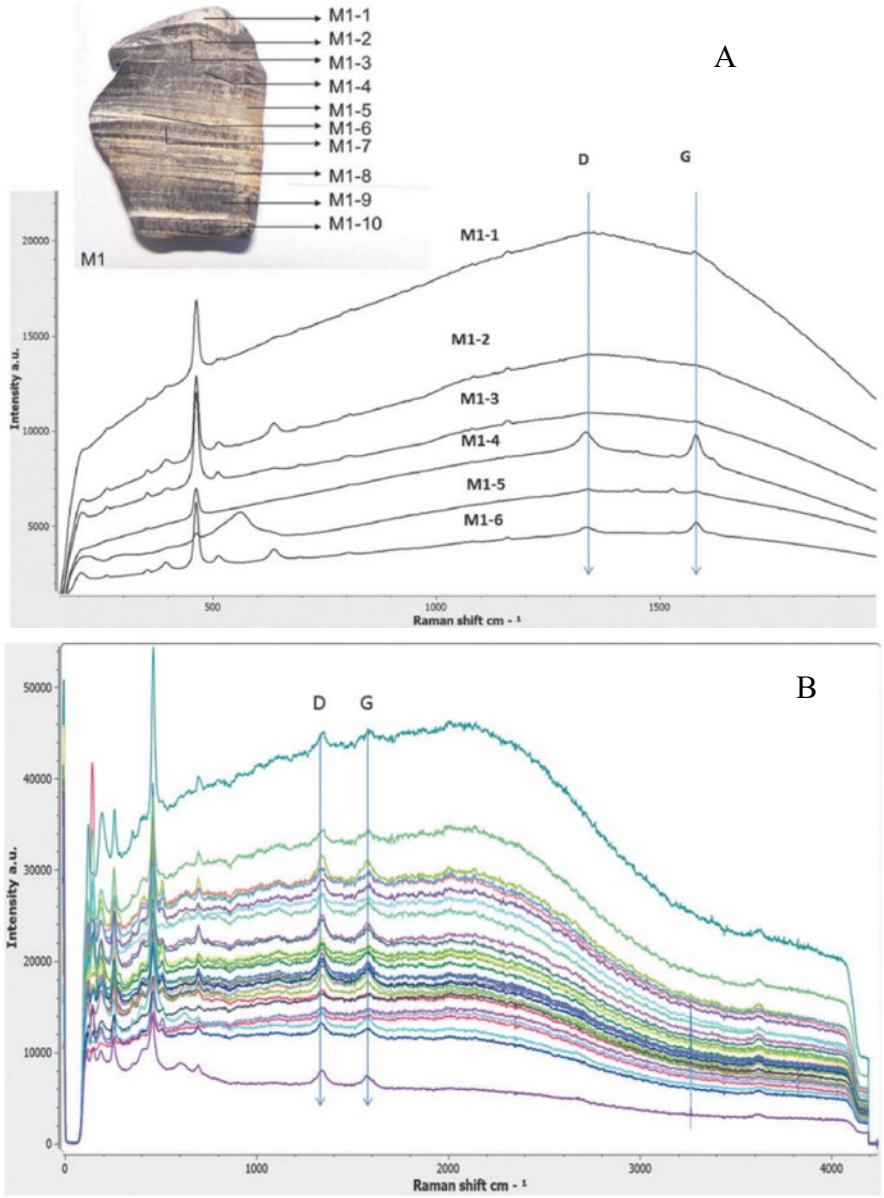

Figure 29 A – RLS line scan of sample shown, with characteristic D and G peaks visible at lines M1-6 and M1-4. B – RLS line scan of crushed sample, showing D and G peaks throughout. Figure adapted from Rull et al. (2017).

RLS is a spectroscopy suite that will allow the rover to identify minerals and organic matter in samples (Rull *et al.*, 2017). RLS will analyse crushed samples, meaning that small-scale contextual information will be lost in the search for organic matter. This effect can be observed in Figure 29 whereby the organic matter signature (characteristic D and G peaks) is seen throughout the crushed sample, compared with the RLS scan pre-crushing, where the D and G peaks can only be observed for lines M1-4 and M1-6. These data

suggest it is important to perform parallel confocal Raman spectroscopy on martian meteoritic organics (e.g. Steele et al. (2012)) so as to determine their contextual information, which cannot be obtained from rover Raman analyses. As martian meteorites are igneous samples, we ought to still carry out this work on sedimentary material on Mars, due to their biosignature preservation potential, as outlined above. Carrying out Raman analyses on meteoritic samples allows us to compare with those that RLS will acquire; any similarities can then be found, to give further insight as to the source of martian organic matter. If meteoritic OM is similar to that found by RLS on Mars, it aids the argument of Steele et al. (2012) that martian macromolecular carbon is magmatic in origin.

MOMA (Mars Organic Molecule Analyser)

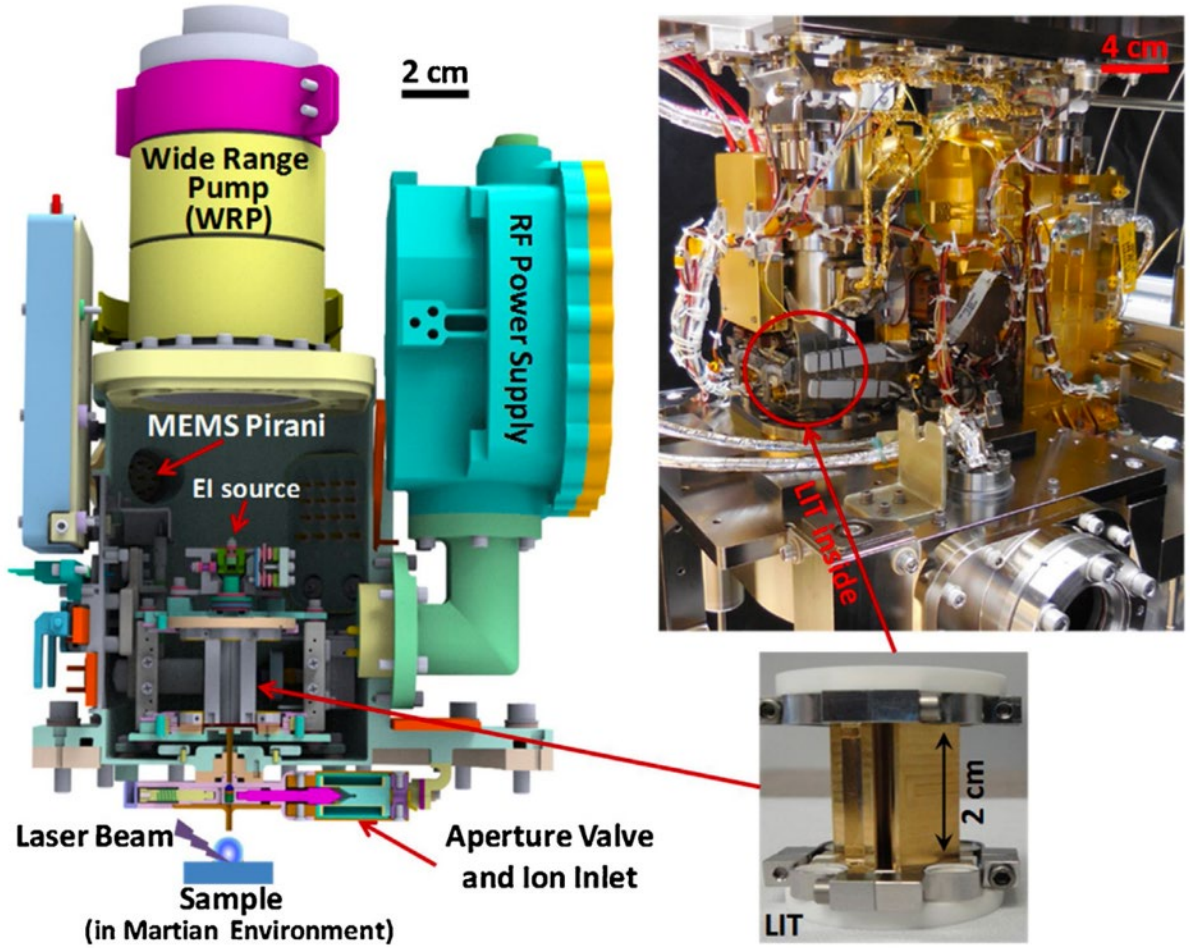

Figure 30 Set up of the MOMA instrument suite onboard the Rosalind Franklin rover. Adapted from Li et al. (2017)

MOMA is an instrument suite dedicated to the detection and characterisation of organic and inorganic samples found at Oxia Planum by the Rosalind Franklin rover. MOMA consists of an ion trap that can perform both pyrolysis gas chromatography mass spectrometry (pyr-GCMS) and laser desorption ionisation mass spectrometry (LD MS). The set up (shown in Figure 30) allows for the analyses of both volatile and refractory

organic material (Goesmann *et al.*, 2015), with volatilisation required for chromatographic separation achieved either through pyrolysis heating or UV laser pulses. This will be the first time LD MS has been carried out in space (Li *et al.*, 2017). This is of particular importance in the field of martian organic geochemistry since LD MS instrument testing suggests that perchlorate presence does not cause oxidation during volatilisation and thus reduces the oxidative impact reported in Glavin et al. (2013) during pyrolysis in the SAM instrument on board Curiosity. In this study, we performed GC-MS experiments on martian meteorites, analogues, and simulants, using both solvent extracted and hydrogen pyrolyzed samples. The aim was to study both volatile and refractory organic material much like the MOMA team is planning to achieve.

This work of this thesis informs mission science such as that of NOMAD, RLS and MOMA, through the detection and characterisation of organic matter in martian meteorites. Combining measurements and data from the high-resolution techniques used in this thesis with in-situ data from Mars will provide greater insight into the martian carbon cycle, and thus martian habitability.

Mars Sample Return

The Perseverance rover/Mars 2020 mission has initiated the campaign to collect pristine martian specimens and bring them back to Earth (see Figure 32). The first sample from Jezero crater was sealed in a titanium tube on 1st September 2021. This pencil-sized core was hermetically sealed and will not be opened until it is within a receiving facility on Earth (see Figure 31) (NASA JPL, 2021). Mars Sample Return marks a step change technologically and scientifically in space exploration. For example, the engineering feat of sending spacecraft to Mars that will then be able to ascend and leave the planet, rendezvous with an orbiter and return to Earth. In addition, strict planetary protection requirements are needed for the samples (see Figure 31). The scientific rationale for such

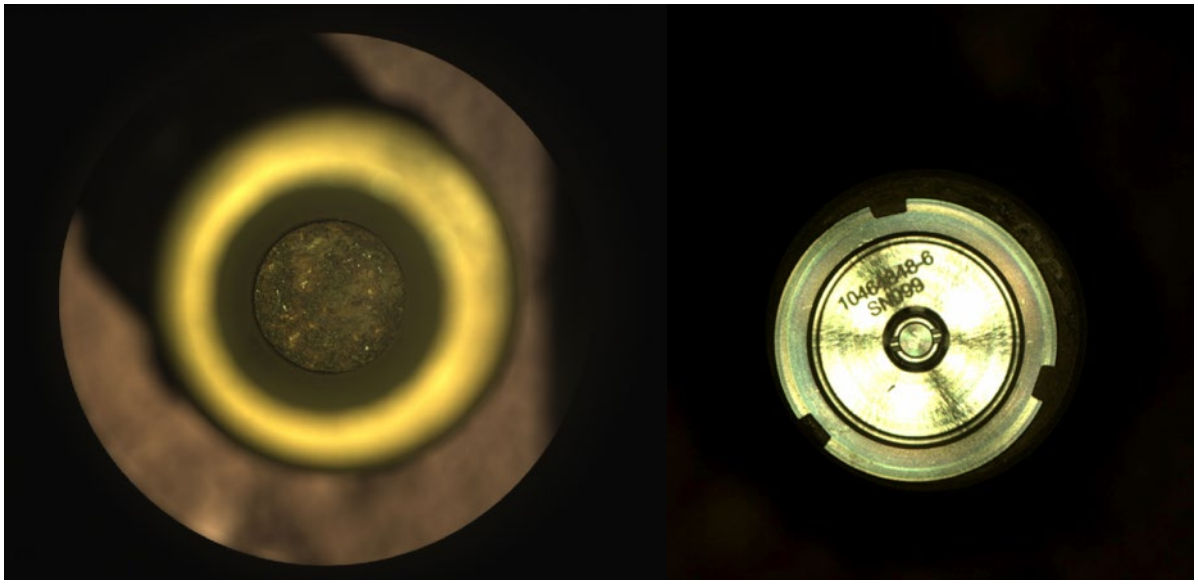

Figure 31 The first martian core collected by Perseverance at Jezero Crater before and after it was hermetically sealed, this will be returned to Earth in the 2030s as part of the joint NASA-ESA Mars Sample Return campaign.

an ambitious mission is reason is enough to take on such an endeavour, as these returned specimens will be pristine, abundant, and representative of a much broader range of rock types than is represented by martian meteorites (Grady, 2020; IMOST, 2018).

MSR also provides the additional advantage compared to meteoritical studies, as the geological context of the sampling sites is known. At the time of writing, only one classification of martian meteorite, the depleted Shergottites, have a likely source location, narrowed down to two craters in one volcanic province: Tharsis (Lagain et al. 2021). This link was achieved through algorithmic analysis of remote sensing data of martian craters. Hopefully similar algorithms will be applied to identify the provenance of other martian meteorites in the future, but it does not compare to having fully characterised sample sites on Mars, and indeed sites chosen specifically for their scientific interest, rather than being

ejected by impact and serendipitously landing and being found on Earth (Cockell et al. 2019).

Advances in nanoscale analytical techniques on Earth mean that returned specimens from Mars will be preserved for decades whilst ensuring significant scientific return on investment. For example, electron microscopy techniques can provide huge amounts of mineralogical and petrological information from mm-sized samples (Grady 2020). Developments in techniques such as atom probe tomography have shown the significant scientific output that can be obtained from nano-scale samples returned from previous space missions, such as Hayabusa (Daly et al., 2021). Such technology cannot be placed onboard robotic or orbital spacecraft, and thus returned samples would be required for their application.

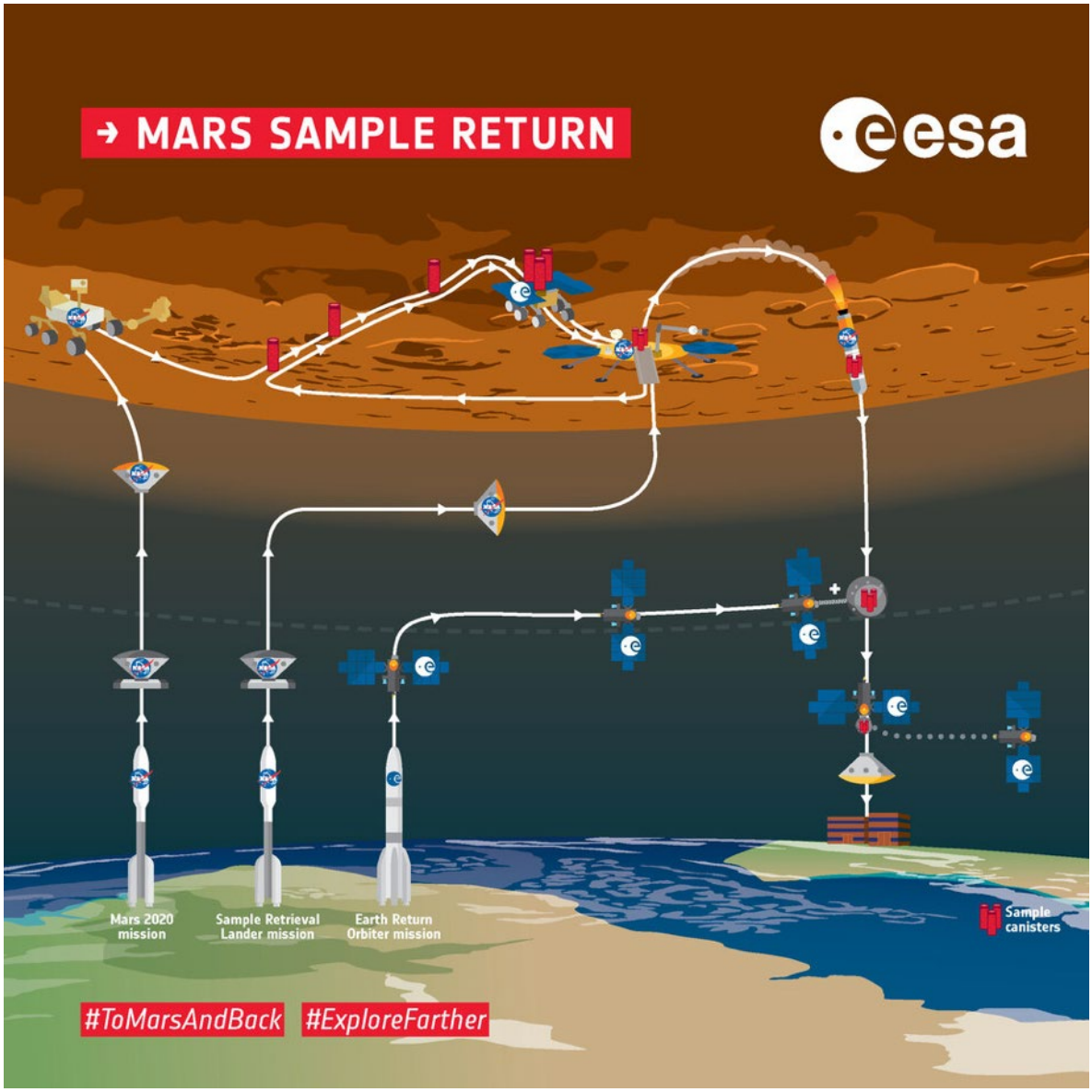

Figure 32 Schematic diagram illustrating the steps required for Mars Sample Return to take place. The first step, the Mars 2020 mission sees the Perseverance rover caching martian core samples, ready for the ESA/Airbus sample fetch rover to collect them. This rover then deposits these samples at a NASA launch site on Mars, for a space craft to rendezvous with an orbiter to then return to Earth. Image credit: ESA

Martian Meteorites

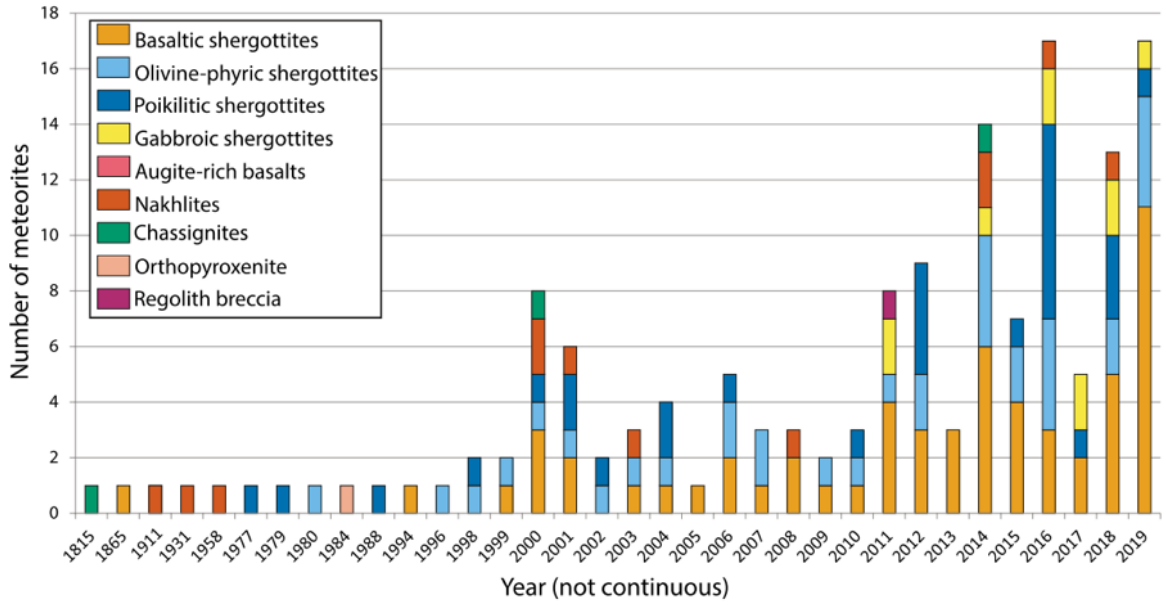

Figure 33 Number of martian meteorites identified per year, according to classification. Image credit: Udry et al. (2020)

The martian meteorites were first identified as originating from Mars when noble gas ratios in trapped gas pockets within EETA 79001 matched the composition of the martian atmosphere as analysed by the Viking landers (Becker and Pepin 1984). The first recorded fall of what later became the martian meteorite group was the Chassigny meteorite in October 1815 (Mason et al. 1976). The timeline in Figure 33 shows the years in which martian meteorites were recovered, grouped by classification (Udry et al. 2020). There are currently 177 known martian meteorites (301 stones when treating paired stones individually). The largest individual stone is the recently discovered Taoudenni 002, a gabbroic shergottite find from Mali with a mass of 14.510 kg (Meteoritical Bulletin, 2021).

There are three main groups of martian meteorites: Shergottites, Nakhlites and Chassignites, and nine distinct classifications (Righter, 2017):

- Nakhlite;
- Chassignite;
- Brecciated Shergottite;
- Diabasic Shergottite;
- Fine grained Shergottite;
- Gabbroic Shergottite;
- Olivine-phyrric Shergottite;

- Orthopyroxeneite;
- Poikilitic Shergottite.

All the martian meteorites are igneous rocks, bar NWA 7034, a breccia (Agee et al. 2013; MacArthur et al. 2019), however these ~177 samples still provide the only martian samples available to study on Earth. As discussed above, we only know the likely source location on Mars of the depleted Shergottites (Lagain et al. 2021), a group that is comprised mostly of the olivine-phyrric Shergottites, due to their depleted rare earth elements. The vast majority of the martian meteorites crystallised in the Amazonian, meaning this is the most sampled era on Mars, (see Figure 34) (Udry et al. 2020).

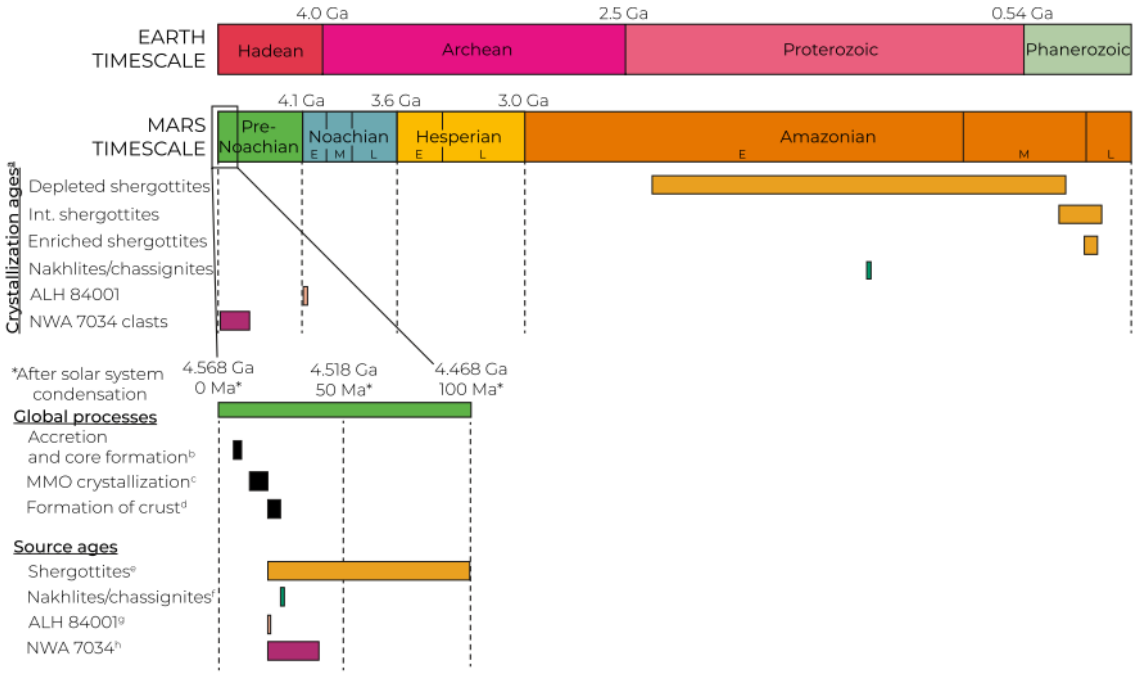

Figure 34 Martian geological timeline, compared to Earth's including the formation of the martian meteorites. Taken from Udry et al (2020).

Organics in Meteorites

Extra-terrestrial Organic Nomenclature

Several terms exist in meteoritics for the study of extra-terrestrial organic material and their main sub-classes, and their meaning. Meteorites are known to contain both insoluble and soluble organic matter (e.g. Hayatsu et al. 1977; Alexander et al. 2007; Hilts et al. 2014). However, the terminology for this, and the exact meaning of the sub-classes differs. The solvent soluble organic material (SOM) may be referred to as free organic matter (Sephton 2013), or be sub-divided into labile (in this case referring to amino acids or

macromolecules affected by heat/water) and volatile. The insoluble component refers to kerogen-like refractory macromolecular material that is solid at 275 K, and unaffected by heat and water (Sephton, 2013). It is important to clarify the nature of the organics studied and the phrasing used to avoid any ambiguity or confusion since terms such as volatile, refractory and labile have different meanings depending on context (Chan et al. 2020). These divisions and classes, with examples are summarised in Figure 35, based on the terminology used by Chan et al (2020). This project focuses primarily on the IOM found in martian meteorites in the in-situ analyses, whilst bulk analyses investigate the solvent-soluble material using liquid chromatography mass spectrometry, with an additional attempt to extract the macromolecular component using hydrogen pyrolysis.

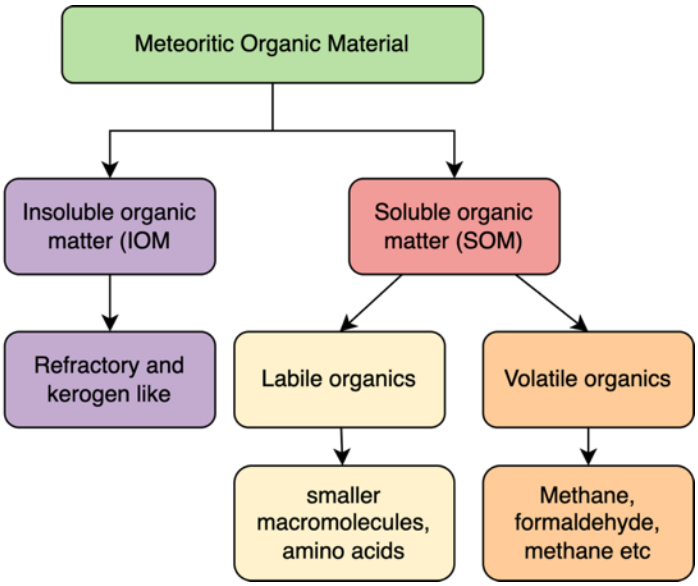

Figure 35 Overview of organic material found in meteorite, interplanetary dust particles, and comets, based on designations as given in Chan et al. (2020). Main breakdown of insoluble and soluble organics is given, with brief description/examples

Organics in Martian Meteorites

Due to the presence of highly oxidising perchlorates, it is difficult to find organic material in situ on Mars (e.g. Glavin et al. 2013; Sephton et al. 2014; Royle et al. 2018). Thus we ought to be focusing on characterising and determining the origin of martian carbon in meteorites. In addition, given the imminent return of specimens via Mars Sample Return, it is crucial that we have a proven optimised process for detecting and analysing martian organics. Given the limited volume of material that will be available, the best way to do this is through work on analogue samples and martian meteorites. Complex organic molecules have been found in the form of Macromolecular carbon (MMC) inclusions in magmatic minerals of multiple martian meteorites, both in falls and finds (Steele et al., 2012). Much of this organic material consists of polycyclic aromatic hydrocarbons; these are of particular significance since such compounds are key reactants in the synthesis of amino acids (Shock & Schulte, 1990).

These inclusions have been found by Steele et al (2012) below the surface of thin sections. They have not been found near fractures or cracks, and as they are prolific in both meteoritic falls and finds the material is not thought to be terrestrial in origin (Steele et al., 2016). Such material displays characteristic features in its Raman spectra: the disordered D peak, at ~ 1350 cm-1 and the graphitic G peak at ~ 1590 cm-1 (Steele et al., 2016). The narrower the G peak, the more ordered the material.

The origin of martian organic matter is also debated, in part because there are several forms found in the different classes of meteorites, but there is also discussion as to whether the material is indigenous to Mars or exogenous. This debate is summarised in Figure 36 in the context of the N-rich organics found in ALH 84001 (Koike et al. 2020). The main theories and key studies are then outlined below.

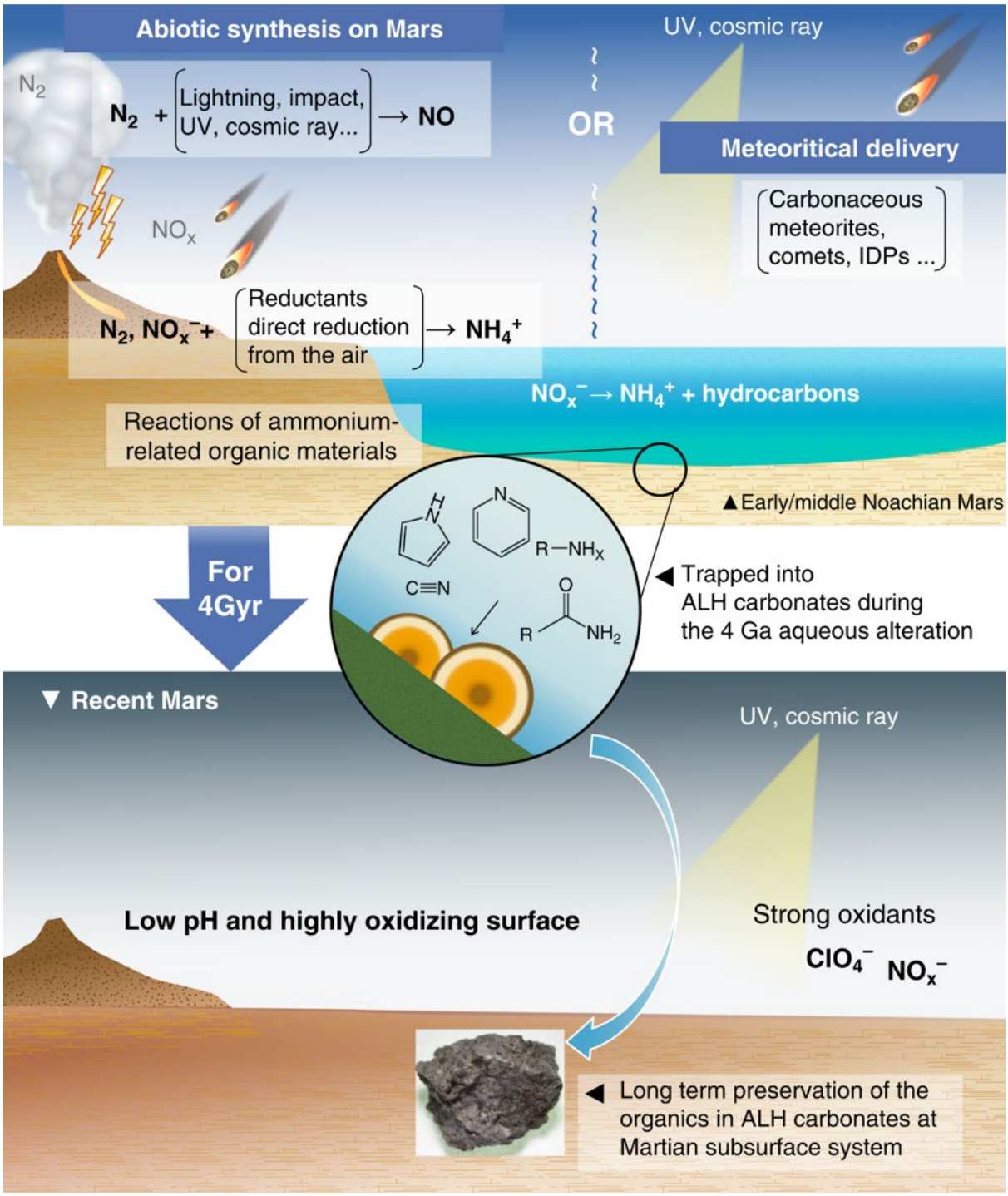

Figure 36 Two main theories put forward for formation of N-bearing organic material in ALH 840001, either material is indigenous to Mars, from a reducing environment enough to reduce nitrogen, or the material was deposited on Mars by comets, carbonaceous chondrites, or interplanetary dust particles. Image credit: Koike et al (2020)

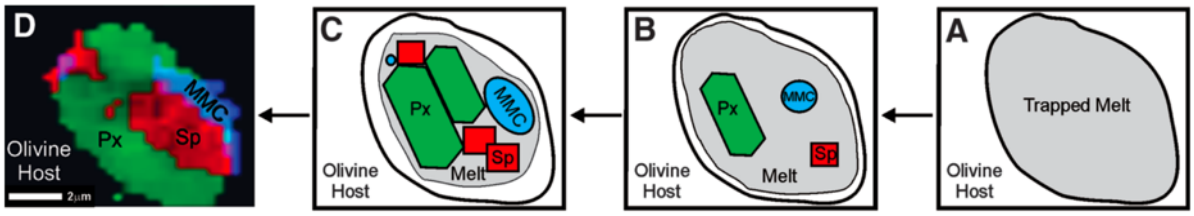

Figure 37 Formation sequence proposed by Steele et al (2012) of MMC bearing inclusion during ascent, cooling and crystallisation..

In this theory, the MMC is indigenous to Mars, originating from a reduced martian mantle, having been detected by confocal Raman imaging spectroscopy (CRIS) (Steele et al., 2012). The crystallisation scenario of these inclusions is shown in Figure 37, an example whereby a carbon-rich melt rises, cools and crystallises within an olivine host. All MMC bearing minerals are igneous, and therefore Steele et al. (2012) argue that organic material was formed through igneous processes in the mantle. Further analyses of martian MMC compared to mission data have shown that is consistent with the organics detected by Curiosity's SAM instrument (Eigenbrode et al. 2018; Steele et al. 2018). Since MMC inclusions have been found with consistent features in relatively young (800 Myr, for Tissint) and in the oldest (4 Gyr, for ALH 84001) meteorites, this suggests that the associated abiotic organic synthesis mechanism has occurred throughout Mars' history (Steele et al. 2022).

Organics deposited on Mars through impact

In this theory, the MMC is exogenous to Mars, deposited upon its surface by meteorites, such as carbonaceous chondrites, comets, or interplanetary dust particles (Becker et al., 1999). Becker et al. (1999) argue that the conditions early in martian history were too oxidizing for complex organic molecules to be synthesized and sustained at the surface. Assuming the incident material has ~2% wt. C (matching that of the CM chondrites) then using the estimated present day meteoritic influx of 5.9 x 10^7 kg/yr (Flynn and McKay, 1990) we find that ~1.2 x 10^6 kg/yr of organic carbon should be deposited on the martian surface, providing a significant influx of carbonaceous material.

Furthermore, flash pyrolysis– gas chromatography–isotope ratio mass spectrometry was carried out on samples of Nakhla to study its refractory organic material; C-13 isotope measurements carried out in this study showed the material is similar to that of carbonaceous chondrites, suggesting a chondritic origin (Sephton *et al.*, 2002). However, if

such carbonaceous chondritic material provided the building blocks for Mars to form, one might expect to see similar $\delta^{13}C$ measurements from martian magmatic carbon in any case, since C-13 ratios are unaffected by mantle heating.

Biotic origin for martian organics

In this theory, the MMC is biogenic (Lin et al., 2014). Lin et al. (2014) found carbonaceous material in Tissint and suggest that it has a biotic origin. They infer that the material's likely provenance is biological from the inclusions' low δ13C values (> δ13C= -33.1 ‰) relative to martian atmospheric CO2 levels. However, this theory is not widely accepted.

Additional Detection techniques for martian meteoritic organics

Gas chromatography-mass spectrometry (GC-MS) has also been used to detect organics in martian meteorites. Through this technique, similarities in the high molecular weight OM in Nakhla and EET A79001 were found, whilst measurements of carbon isotope data in Nakhla suggested that this material is similar to the organic component present in carbonaceous chondrites (Sephton et al., 2002).

Liquid chromatography time of flight mass spectrometry (LC ToF MS) has also been used to search for soluble organic matter in bulk samples of martian meteorites (e.g. Bada *et al.*, 1998; Callahan *et al.*, 2013). Callahan et al (2013) powdered samples of Roberts Massif 04262 and extracted the soluble OM via acid hydrolysis which was then derivatised to target nucleobases and amino acids to further target and amplify the signal for these molecules. The result of this work was the positive detection of ~25 amino acids in RBT 04262 above detection limits, at levels between <1 and 70 ppb. Callahan et al. (2013) subsequently carried out successful compound specific carbon 13 measurements of amino acids in three additional acid hydrolysed extracted samples of RBT 04262. Through this they measured the $\delta^{13}C$ of the β-Alanine and ε-ACA amino acids in the meteorite to be -24‰ ± 6‰, and -27‰ ± 5‰, respectively. The former is consistent with the average $\delta^{13}C$ value of -19.8‰ ± 4.3‰ in Tissint calculated by Steele et al. (2012), suggesting a possible martian amino acid, although it is within the range for some terrestrial biota, and therefore a martian origin cannot be verified.

The separation of terrestrial and indigenous martian organic compounds during bulk-rock

analysis of martian meteorites continues to be a significant problem in meteoritical science. In-situ hydrogen (D/H) isotopic analyses (e.g., via NanoSIMS) enables this separation (Steele *et al.*, 2018), since Mars is significantly deuterium enriched compared to Earth (e.g., Hallis, 2017). Compound specific D/H analyses using bulk techniques have yet to be achieved for martian organic molecules. Techniques such as GC-IRMS have the capabilities to measure the D/H ratio of known organic molecules in a sample, if their abundance is high enough. However, due to the low abundances of organic compounds in martian samples (~ppb) up to 1 kg of sample would be required for successful compound specific GC-IRMS analyses (Callahan *et al.*, 2014).

3 Samples

This chapter introduces the samples studied in this project. Firstly, the petrological and mineralogical information of meteorites studied is outlined, as well as any details known about the fall. The second half of this chapter outlines the justifications for the samples chosen for organic geochemical analyses, putting these specimens into context of the experiments carried out on them in this project.

Samples Overview

Table 1 Summary of samples studied during PhD project. Basic descriptions (classification, fall/find, and sample source) are given for each specimen, alongside the techniques used to characterise their organic content.

Sample Name	Description and Source	Analysis carried out
Lafayette	Martian meteorite. Nakhlite find. Chip from Natural History Museum (NHM).	Chip crushed at Durham University, and solvent-soluble material dissolved then analysed using LCMS and GCMS. Hydrogen pyrolysis + subsequent GCMS carried out
Nakhla	Martian meteorite. Nakhla fall. Chip from NHM, thin section prepared at U of G Sample number BM.1913,25	Chip crushed and solvent-soluble material dissolved then analysed using LCMS and GCMS. Hydrogen pyrolysis + GCMS carried out
NWA 8159	Martian meteorite. Augite rich Shergottite. Meteoritic find. Chip from SUERC, thin section prepared at U of G.	Optical microscopy, confocal Raman imaging spectroscopy, SEM, FIB-SEM, STXM-XANES
SaU 008	Martian meteorite. Chip from SUERC prepared into thin section at U of G	Optical microscopy, confocal Raman imaging spectroscopy, SEM, FIB-SEM, STXM-XANES
Tissint	Martian meteorite, fall. 2 thin sections, one thin section prepared at U of G and one from NHM.	Optical microscopy, confocal Raman imaging spectroscopy, SEM, FIB-SEM, STXM-XANES
Yamato 749	Martian meteorite. Chip from NIPR Japan prepared into thin section at U of G	Optical microscopy, confocal Raman imaging spectroscopy
Yamato 593	Martian meteorite. Chip from NIPR Japan prepared into thin section at U of G	Optical microscopy, confocal Raman imaging spectroscopy

Hajmah (a)	Ureilite. Thin section acquired from NHM	Optical Microscopy, SEM, FIB-SEM, STXM XANES
Goalpara	Ureilite. Thin section acquired from NHM.	Optical Microscopy, SEM, FIB-SEM, STXM XANES
JSC Mars 1	Martian regolith simulant from NASA, sample acquired from Dr. Andrew Steele, Carnegie Planets.	Provided powdered, solvent-soluble material dissolved then analysed using LCMS and GCMS. Hydrogen pyrolysis + subsequent GCMS carried out
Sverrefjellett	Martian meteorite analogue from Svalbard. Sample acquired from Dr. Andrew Steele, Carnegie Planets.	Chip crushed and solvent-soluble material dissolved then analysed using LCMS and GCMS. Hydrogen pyrolysis and subsequent GCMS carried out
Sigjurdfjellet	Martian meteorite analogue from Svalbard. Sample acquired from Dr. Andrew Steele, Carnegie Planets.	Chip crushed and solvent-soluble material dissolved then analysed using LCMS and GCMS. Hydrogen pyrolysis + subsequent GCMS carried out

Samples analysed in this study

A range of planetary samples and analogues were studied. They have been selected for their relevance to improving our understanding of martian organics and/or the organic content of the early solar system, and detection techniques in readiness for Mars Sample Return. Below is a geological introduction to each sample, whilst justifications for studying them with these techniques to improve our understanding of martian organics and astrobiology are given at the end of this chapter.

Martian samples

Tissint

Figure 38 Photograph of a fragment of the Tissint meteorite being held. Its dark fusion crust is clearly visible. Image credit: Natural History Museum, London

The Tissint meteorite fell in Morocco on 18th July 2011 and was the fifth martian meteorite observed to fall. It is a depleted picritic shergottite (an olivine rich martian basalt) (Chennaoui Aoudjehane et al. 2012). The mineralogical composition is: fine grained light grey pyroxene groundmass (50 vol%), olivine macrocrysts and microphenocrysts (16%), maskelynite (18 ± 2 %), oxides (Ti-poor chromite, ilmenite, titanomagnetite) make up < 1 % (Chennaoui Aoudjehane et al 2012). Tissint is heavily shocked, such that all its plagioclase has been converted to maskelynite and its peak pressure was calculated to be 25 GPa (Baziotis et al. 2013). Hosted in both the maskelynite and pyroxene are olivine macrocrysts, some of which themselves bear melt pockets and inclusions (Chennaoui Aoudjehane et al. 2012). The stone is ~600 My old, whilst its cosmic ray exposure age, based on ^{10}B dating suggests it was ejected from the martian surface 1.1 My ago (Righter, 2017). The stone has a dark shiny fusion crust, as can be seen in Figure 38. Over 12 kg of Tissint has been found, meaning that plenty of this unweathered meteorite is available for analysis (Righter, 2017).

Lafayette

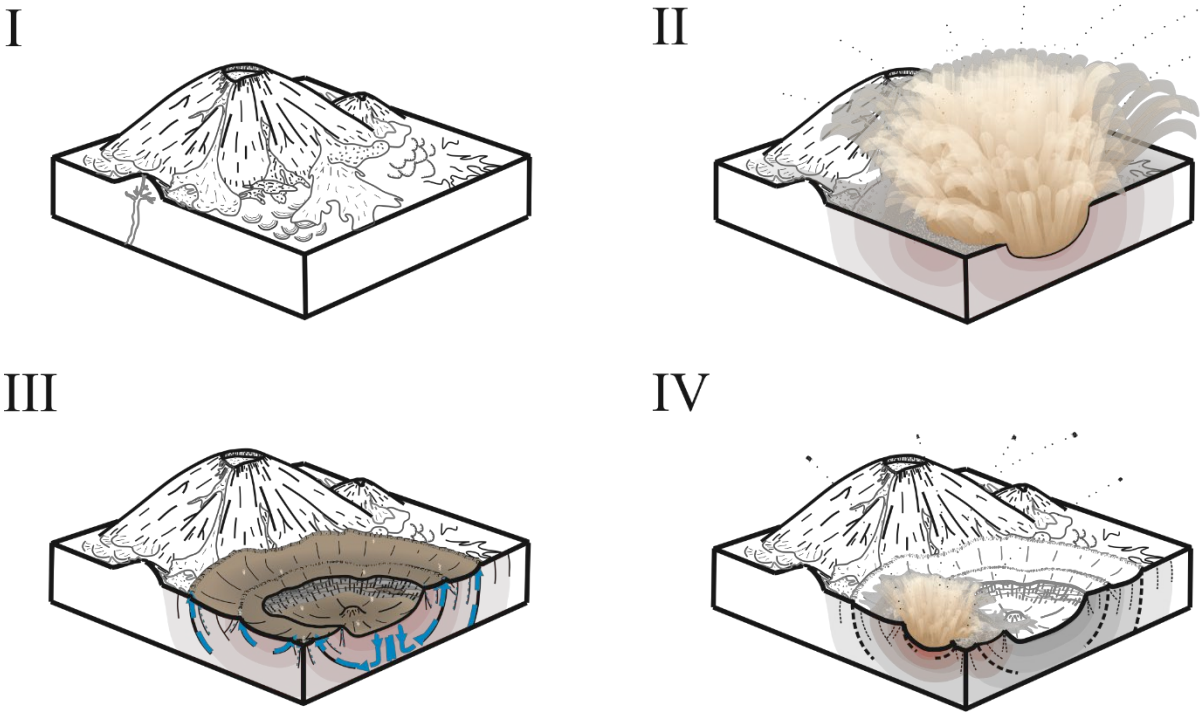

Figure 39 Process which formed the Nakhlites according to Daly et al (2019). Initial impact (II) on an ancient martian lava flow (I) caused sufficient heating to instigate a hydrothermal system (III), followed by a subsequent impact which ejected some of the material in the area. Image credit: Griffin (2021).

Lafayette is a nakhlite meteorite, a group of mafic pyroxene-rich martian meteorites thought to be originate from a series of lava flows (Cohen et al. 2017a). Its modal mineralogy (vol. %) is: 75.5% augite, 12.8% olivine, 6.8% mesostasis, 3.6% iddingsite and 1.3% orthopyroxene (Daly et al. 2019). The volcanic content of the nakhlite launch site is in the schematic diagram in Figure 39 (Griffin 2021) which displays an overview of the findings of Daly et al (2019). This work, investigating alteration and shock effects in the nakhlites, states that the alteration the nakhlites experienced (as evidenced by the iddingsite veins therein), was caused by impact induced hydrothermal circulation, whilst a second impact then ejected the meteorites from the host volcanic region (Daly et al. 2019).

Lafayette is a find that was first identified as a meteorite in the collections of Purdue University by O. C. Farrington in 1931 (Nininger 1935). Its pristine fusion crust with its atmospheric entry markings suggest it could not have been exposed to the elements long before recovery and curation (see Figure 40). Its history prior to being found in the Purdue collections is unconfirmed.

Figure 40 Photograph of the main mass of the Lafayette meteorite. View is of the pristine fusion crust with visible markings during atmospheric entry. Image credit: Smithsonian Institute of Washington.

SaU 008

Sayh al Uhaymir 008 (SaU 008) is part of a paired collection of ~10 kg of ~ 9 stones found in a strewn field in Oman (Meyer, 2012). The mineralogical composition is 48% pyroxene, 25% olivine, and 15% maskelynite (Zipfel 2000). The stones contain large olivine phenocrysts within pyroxene and maskelynite (Zipfel 2000). Despite being terrestrial finds these stones have experienced minimal terrestrial weathering when compared to similar martian stones from desert environments. The SaU 008/005 pairs are texturally, mineralogically and chemically similarly to DaG 476/489 (Zipfel 2000) but with significantly less terrestrial weathering. Such weathering features include low temperature alteration (and no evidence of martian alteration) (Gnos et al. 2002). The SaU stones are also heavily shocked, with the SaU 094 meteorite peak shock pressure experienced calculated by Gnos et al (2002) to be 45 GPa using refractive indices of the maskelynite. The maskelynite does however appear to be heterogeneous within SaU 005 (Papike et al. 2009).

The shock pressures evident and the strength of the sample, as well as its large mass, made SaU 008 the ideal meteorite to serve as a calibration target for the Mars 2020 Perseverance

Rover's SHERLOC (Scanning Habitable Environments for Organics and Chemicals) instrument (see mission science section above for details).

Nakhla

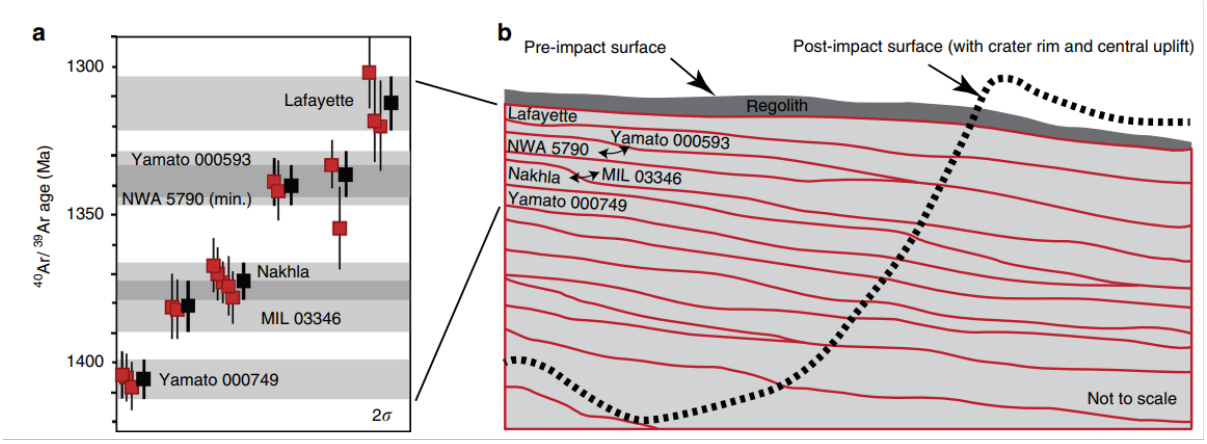

Figure 41 B Inferred stratigraphy for series of lava flows for the Nakhlite meteorites, as suggested by Cohen et al. based on Ar-Ar dating shown in A. Image credit: Cohen et al (2017)

The Nakhla meteorite fell in Egypt on 28th June 1911, comprising approximately a dozen stones over a strewn field of ~4.5 square km (Meyer, 2012). It is the namesake of the Nakhlite group of meteorites. Nakhla has a crystallisation age of 1383 ± 7 Ma (Cohen et al. 2017a), (see Figure 41), and a cosmic ray exposure age of 12.28 ± 0.73 Ma (Korochantseva et al., 2011). Its composition (by volume) is: 79.4% pyroxene (predominantly augite), 9.5% olivine, 11.1% mesostasis and 1% alteration products – mostly found in olivine grains - (Needham et al. 2013). Many of its olivine and augite grains contain magmatic melt inclusions. The peak shock pressure experienced by the stone was calculated to be 20 GPa (Greshake 1998). Ar-Ar dating by Cohen et al (2017) suggests that the nakhlites were formed in at least four distinct lava flows, with Nakhla being part of the second (see Figure 41).

NWA 8159

Northwest Africa 8159 (NWA 8159) was purchased from a Moroccan meteorite dealer and classified in 2013 (Herd et al. 2017a). It is an augite rich shergottite with a crystallisation age of 2.37 ± 0.25 Ga (Herd et al. 2017a) and so from the early Amazonian, a period in Mars' geological history with very few samples (see Figure 42) (Váci and Agee 2020). NWA 8159's composition (modal %) is: ~48% augite, ~37% plagioclase, ~5% olivine, ~5% magnetite, 0.5% maghemite, 1% orthopyroxene (Herd et al. 2017). It is depleted in

LREE, similar to Tissint and the other depleted shergottites, however its bulk composition and oxygen fugacity sets it apart from all other martian meteorites, such that it sits apart in

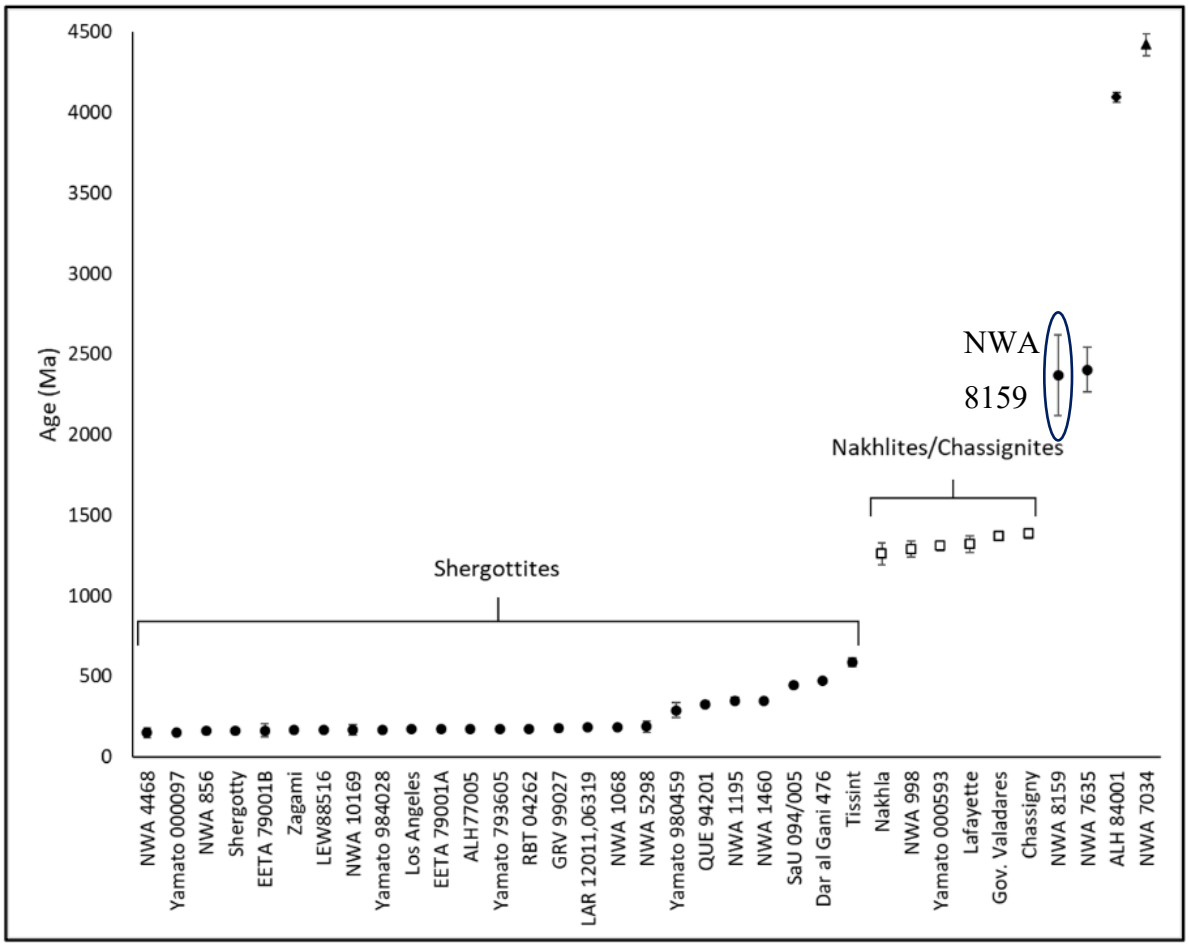

Figure 42 The crystallisation ages of selected martian meteorites, demonstrating that NWA 8159 represents period in the early Amazonian with relatively few samples. Adapted from Vaci et al. (2020)

its own category (Herd et al. 2017a). The stone has undergone significant terrestrial weathering, as evidenced by Figure 43, with no in tact fusion crust (Herd et al. 2017a). The meteorite experienced lower shock pressures than other shergottites, with its peak shock estimated at 16-18 GPa, leading to the suggestion it was from the edge of the ejection zone of the shergottites (Sharp et al. 2019).

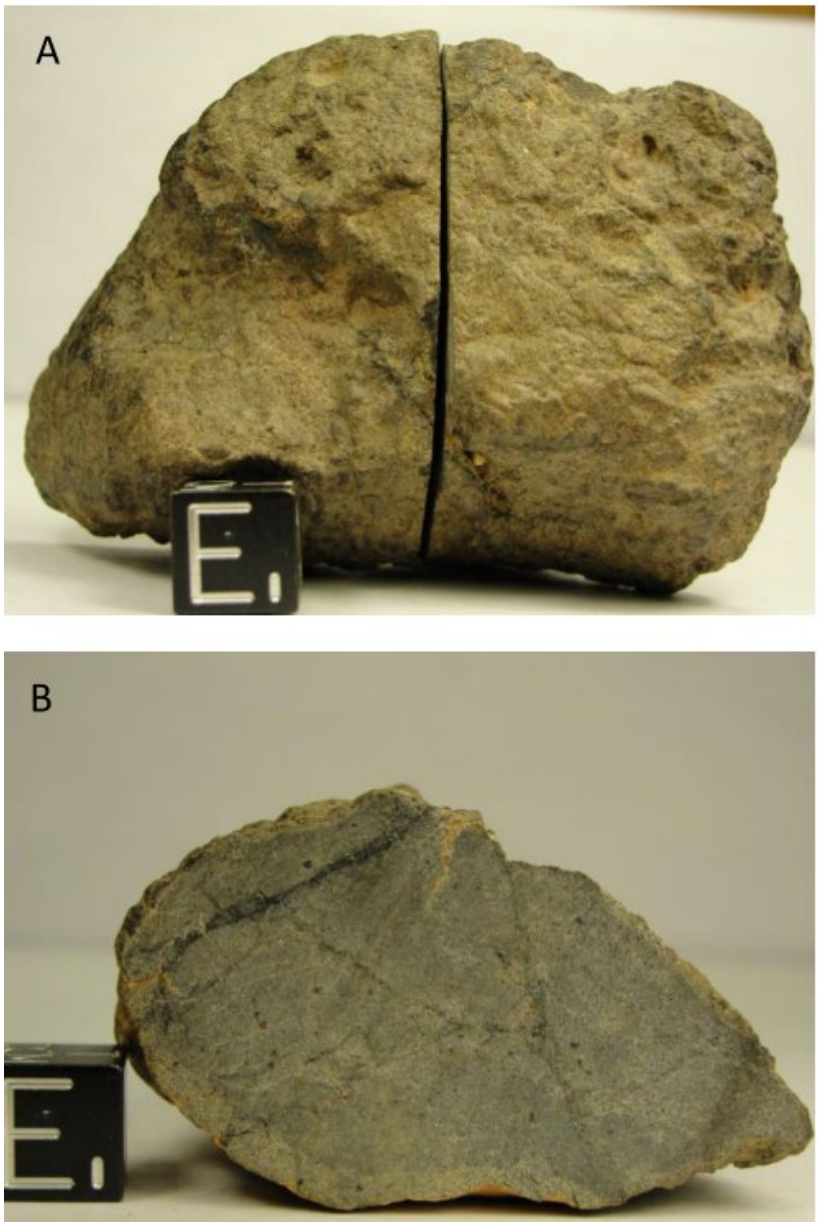

Figure 43 Main mass of NWA 8159, scale cube = 1 cm. No fusion crust remains, and significant terrestrial weathering features are visible to the naked eye. Image credit: Herd et al. (2017)

Yamato 000593 and 000749

Yamato 000593 and 000749 (Y 000593 and Y 000749) are part of a paired set of meteorites collected by the 41st Antarctic Research Expedition in 2000 (Imae et al. 2005). They are paired cumulate clinopyroxenites and from the nakhlite group of martian meteorites. They are identified as paired since they have matching mineralogical textures and compositions (Mikouchi and Kurihara 2008). Their paired status is, however, contested, as their crystallisation ages, as measured by Ar-Ar dating, suggest they are distinct from one another (Cohen et al. 2017a). The crystallisation age of Y 000593 was calculated through this technique to be 1343 ± 8 Ma, whilst that of Y 000749 was

calculated to be 1415 ± 8 Ma (see Figure 41) (Cohen et al. 2017a). They have a cosmic ray exposure of 11-12 Ma (Meyer, 2012). Their composition was calculated through petrography by Imae et al (2005) which gives their average modal composition by volume as: pyroxene phenocrysts 77%, olivine phenocrysts 12%, titanomagnetite microphenocrysts 1%, and mesostasis 10%.

Ureilites

The ureilites are the second largest group of achondritic meteorites. They are a carbon- and olivine-rich group of ultramafic meteorites originating from a differentiated planetesimal from the inner solar system (Goodrich 1992; Barrat et al. 2017; Rai et al. 2020). This planetesimal did not survive long enough to become a planet, however it accreted sufficient mass such that core formation and partial melting began (Rai et al. 2020).

The meteorites themselves are subdivided into the unbrecciated and the polymict breccias; with most ureilites falling into the former group (Goodrich 1992). Despite this mix of unbrecciated and brecciated samples, they have identical compositions, and thus have been shown to originate from the same asteroid, the ureilite parent body (UPB) (Downes et al. 2008). Rai et al (2020) used statistical modelling, constrained by measurements such as oxygen isotope ratios in ureilites, to build up a history of the UPB. Their model suggests that the UPB must have accreted in the same region of the solar system as the MgO rich and FeO rich chondrules, as such material is the only precursor material that fits their model to generate the observed bulk characteristics of ureilites today (Rai et al. 2020). A schematic diagram of the history of the UPB from their model is shown in Figure 44.

The ureilites contain ~ 1-7 wt% carbon (Goodrich et al. 2013). This carbon is predominantly graphitic; however, diamonds have been found as well as its hexagonal polymorph lonsdaleite, in many of the more shocked ureilites too (Ross et al. 2011; Nakamuta and Toh 2013; Lorenz et al. 2019). The formation mechanism/origin of ureilitic diamonds has been contested for over sixty years, despite ureilitic diamonds first being located over a century ago (Kunz 1888; Lipschutz 1964; Goodrich et al. 2021). There are three main theories for the formation for diamonds in the ureilites:

1. Static pressure in a larger UPB

On Earth, natural diamonds are formed >160 km below the surface when graphite stabilizes under intense pressure (Goodrich et al. 2021); this led to the belief that such a

similar high static pressure mechanism must have converted ureilitic graphite into diamond (Urey 1956). For this to take place, a parent body at least the size of Mars would be required (Nabiei et al. 2018).

2. Impact shock pressures on the UPB

Studies of nanodiamonds in three ureilites showed that they appeared to have preferential crystallographic orientation, suggesting that the UPB was impacted, and associated shock pressures converted the graphite into diamond (Lipschutz 1964). Recent work supports this, whereby large diamonds (> 100 μm) were found to coexist with nanodiamonds (the nanodiamonds being those which support the shock formation theory), thus suggesting that impact shock could generate larger diamonds in ureilites, too (Nestola et al. 2020).

3. Chemical vapour deposition in the solar nebula

This theory for diamond formation suggests that ureilitic diamonds were formed before the UPB accretion. Impurities such as noble gases have been found hosted inside diamonds in the ureilites, and the shock formation scenario cannot account for this, since graphite does not host the material (Fukunaga et al. 1988). Fukunaga et al (1988) showed that diamonds could be created through condensation of a mixture of hydrogen, methane, and argon. More recent work supports this hypothesis and suggests that not all ureilite diamonds could be formed either through impact or static pressures; heterogeneous impurities in large diamonds found in Almaha Sitta led to the suggestion its diamonds were formed through chemical vapour deposition (Miyahara et al. 2015).

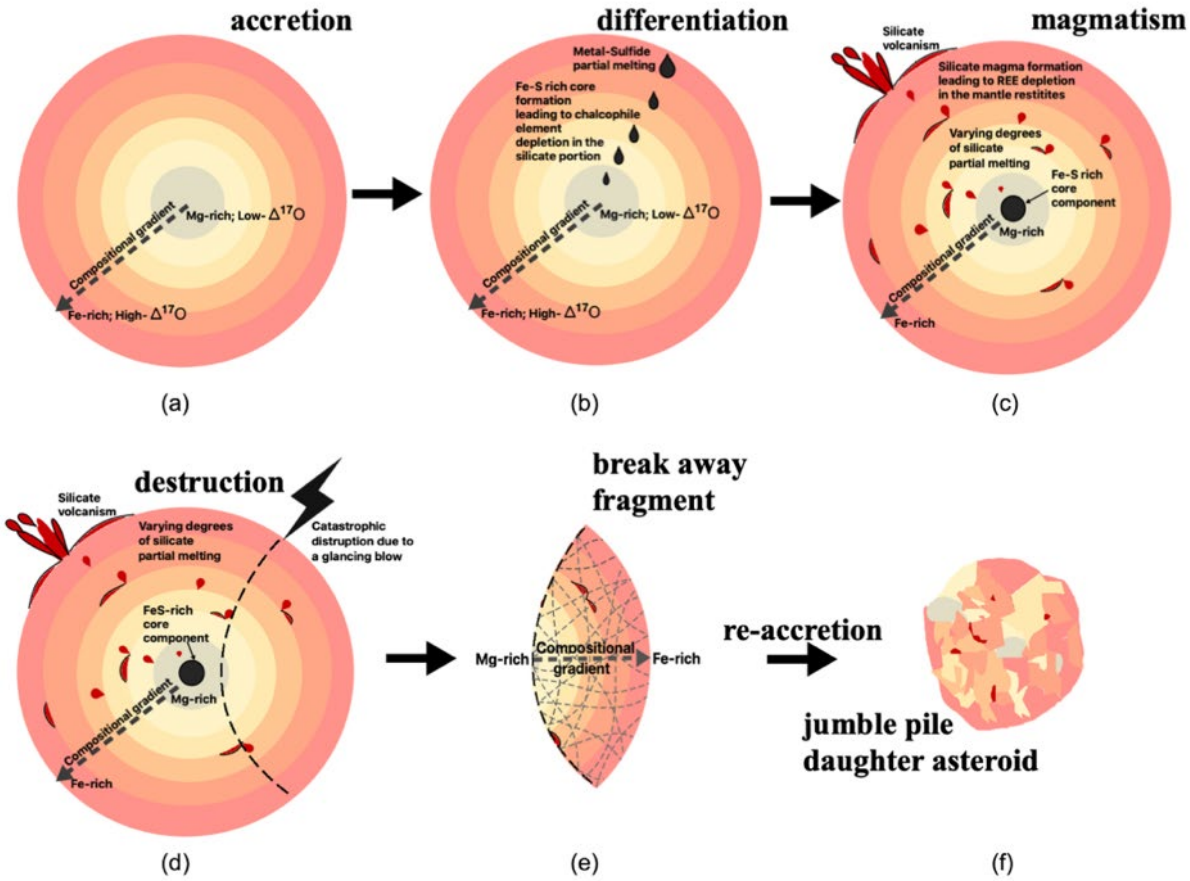

Figure 44 The history of the ureilite parent body (UPB) according to Rai et al (2020). The UPB is formed in a MgO and FeO chondrule rich zone of the early inner solar system, during accretion (a). Differentiation then begins with partial melting occurring (b), followed by a magmatic phase (c) which is affected by impact (d), causing ejection (e) and ultimately a daughter asteroid (f).

This project focuses on the detection and characterisation of martian organic material, and of course the ureilites are not martian in origin. However, the mechanism of volatile delivery (including organics) to the terrestrial planets in the early Solar System is debated (e.g., delivery after or during planetary accretion). Therefore, studying fragments from the interior of the carbon-rich ureilite parent body (UPB), which was formed and differentiated during the early Solar System, provides further insights into volatile delivery to rocky planetary bodies (Barrat et al. 2017). In addition, it provides an additional perspective to the formation of organics early in the Solar System, since the parent body was partly evolved, rather than totally primitive, such as the chondrites (Grady et al. 2014).

In this study, two ureilites were analysed with STXM-XANES to gain information about the carbon-rich regions of these rocks. An overview of these two meteorites is given below.

Goalpara

Goalpara was found in Northeast India in 1868 (Saikia et al. 2017). It has a cosmic ray exposure age of 28.9 Ma (Leya and Stephenson 2019). Goalpara was studied to generate the original theory of impact formed diamonds mentioned above, whereby impact pressures converted graphite to diamond (Lipschutz 1964). Goalpara was also one of the first ureilite samples where lonsdaleite (the suggested hexagonal polymorph of diamond) was located (Hanneman et al. 1967). It is a heavily shocked meteorite, with 78.6 % olivine, and 4.4 % pigeonite (Goodrich 1992; Berkley 2006).

Hajmah (a)

Hajmah (a) is an unbrecciated ureilite found as part of three meteorites in the desert in Oman whilst prospecting for oil pre-1958 (Bevan 2006). It is one of only five ureilites with a cosmic ray exposure age of less than 2 Ma, with a CRE of 1.4 Ma (Leya and Stephenson 2019). It is also a highly shocked meteorite, and has 84.5% olivine content and 9% pigeonite (Goodrich 1992; Berkley 2006)

Mars Analogues and Simulants

Mars analogues were used in this study as a comparison to the meteorite samples to evaluate their efficacy as analogues for martian meteorite material. Analogues provide the opportunity to evaluate the protocols and methods used, without running the risk of wasting precious extra-terrestrial samples. In addition, experiments requiring larger sample masses can be carried out on analogue specimens, where sufficient martian material is not available. If analogues are particularly effective (ie similar to their extra-terrestrial counterpart) they provide an excellent insight into extra-terrestrial processes at minimal expense.

All analogues and simulants were provided by Dr Andrew Steele of Carnegie Planets, Washington D.C. An overview of the two samples is given below, with further detail outlined in the ‘justification of samples’ section below.

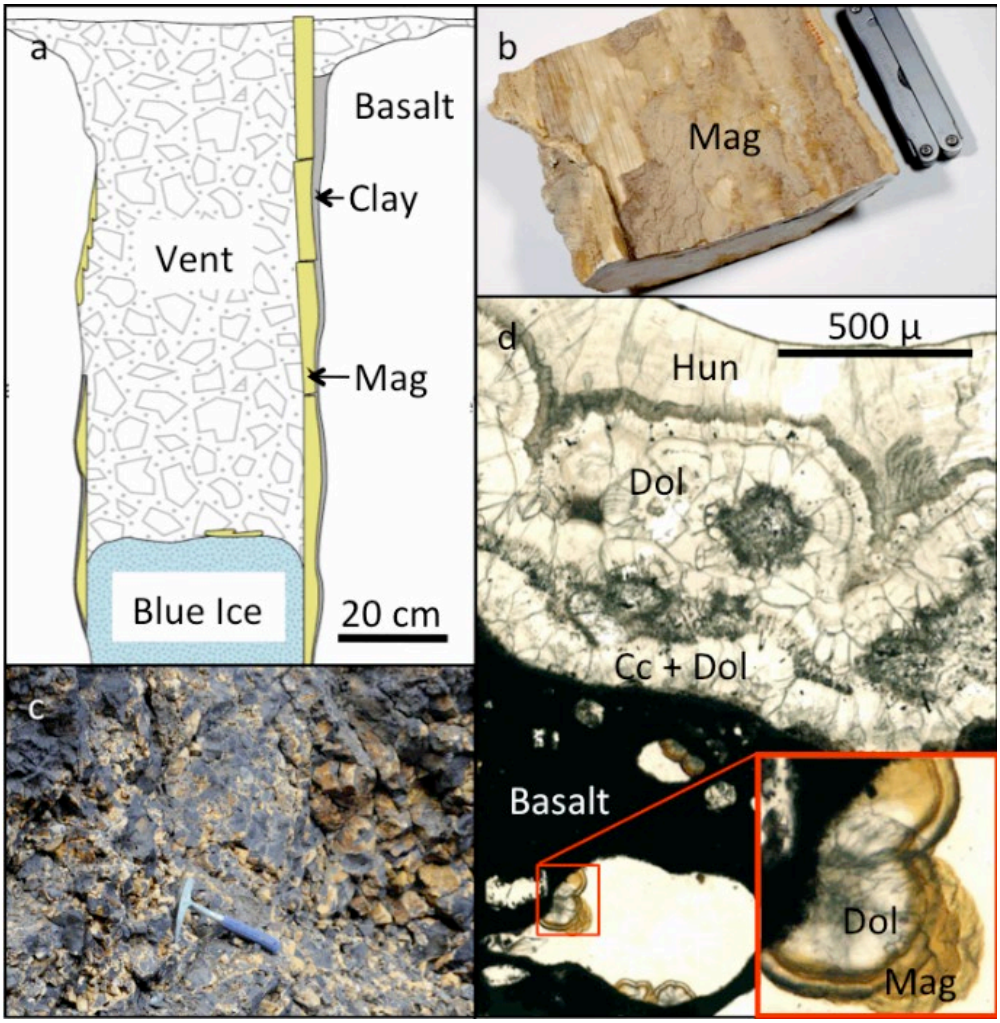

Figure 45 a) Cross section of the Sverrefjellet vent where the BVC samples originate from. The vent is lined with magnesite b) and set in clay, which protrudes into ice. c) A carbonate basalt breccia at the site d) plane polarised thin section image of the carbonate globules in a sample from the area shown in c). Image credit: Amundsen et al. (2011)

Ultramafic spinel lherzolite xenoliths from Svalbard were used as martian analogues in both the bulk analysis work and our STXM XANES work. Svalbard is used as a Mars analogue field site as it has an average temperature of -6 °C, and annual rainfall of 210 mm (Siljeström et al. 2014). These samples, from the Bockfjorden volcanic complex (BVC) formed 1 Myr ago and contain MMC-bearing carbonate globules analogous to those found in ALH 840001 (Steele et al. 2007) (see Figure 45).

JSC Mars 1

JSC Mars 1 is a martian regolith simulant developed by NASA Johnson Space Centre. Derived from Pu'u Nene, in the saddle region between Mauna Kea and Mauna Loa in

Hawai'i at 2140 m elevation, the simulant is a palogentic tephra (weathered mafic basaltic glass product) (Morris et al. 1993; Allen et al. 1998). The upper age for the region is ~ 66 ka(Morris et al. 1993). The material was developed as a martian simulant because visible and near infra-red (VIS/NIR) spectroscopic analysis indicate that it is similar to the martian regolith (Allen et al. 1998).

Samples – Martian Meteorites

Below are the justifications for why these martian samples were studied using these techniques, in search of organic matter.

Lafayette

Lafayette is a relatively visibly pristine martian meteorite with an unknown terrestrial history. The stone was chosen for this study because of its limited terrestrial weathering features, meaning potential likelihood of detecting indigenous martian organic matter (OM). Additionally, identifying terrestrial OM contaminants within Lafayette may help constrain the meteorite's currently unconfirmed fall history. Nininger (1935) reported that an unidentified Purdue University student was fishing in a pond in Tippecanoe County at an unknown date when the 'stone which resembled a corn pone' fell into the mud nearby. The student retrieved the stone and kept it at his home before donating it to Purdue University. Initially the meteorite was curated within Purdue's geological collection, as the fusion crust re-entry flow markings (see Figure 40) were mistaken for terrestrial quaternary glacial striations. It was not until 1931 that O.C. Farrington identified Lafayette as a meteorite (Nininger, 1935). Nininger suggests that the meteorite had not been resting for long on the terrestrial surface before it was picked up, since its fusion crust remained largely intact, with minimal weathering features (Nininger, 1935). Regrettably, Farrington passed away before publishing his paper on the meteorite, and his notes were never found, meaning the fall scenario remains unconfirmed.

Lafayette is now classified as a member of the martian nakhlite meteorite group. The nakhlites, which are hypothesised to originate from a single ejecta crater on Mars due to their ejection ages of 11 Ma (Treiman, 2005), represent a series of basaltic igneous rocks encompassing at least four different magmatic events from a related parental melt that span at least ~1.4 to 1.3 Ga ago (Cohen *et al.*, 2017). Aqueous alteration from martian fluids, a notable feature across the group, was dated at ~633 ± 23 Ma within Lafayette (Borg and Drake, 2005). Of the nakhlites, Lafayette contains the most evidence of martian aqueous alteration, identified as veins of 'iddingsite' within olivine phenocrysts and matrix regions (Bunch and Reid, 1975). The relationship between shock deformation features and fluid alteration veins within several nakhlite samples, including Lafayette, has led to the current hypothesis of impact-induced hydrothermal activity as the driving mechanism behind alteration (Daly et al., 2019).

In this work, a chip of Lafayette was used, which was crushed, and then dissolved in the solvents hexane, dichloromethane, and methanol to carry out non-targeted metabolomics using liquid chromatography mass spectrometry (LC-MS).

Tissint

Tissint was the fifth martian meteorite fall (a meteorite observed on its fall to Earth and collected soon thereafter); it fell in Morocco in 2011 and is a depleted shergottite meteorite (Chennaoui Aoudjehane et al., 2012). This sample was chosen for this study as it is a relatively recent fall collected soon after its atmospheric entry, and as it fell in a dry desert environment, with little, but well characterised organic contamination from its fall locality (Summons et al., 2014).

Previous studies of organic content in Tissint include the detection of thiophenes, similar to those found by Curiosity, following pyrolysis-GC-MS, a similar process to that of the Sample Analysis on Mars (SAM) instrument onboard the rover (Jaramillo et al., 2019). Additional similarities have been found between Gale Crater's OM and that hosted inside Tissint (Steele et al. 2018). Confocal Raman imaging spectroscopy (CRIS), coupled with transmission electron microscopy (TEM), and scanning transmission x-ray microscopy (STXM) analyses found evidence of brine interacting with CO_2 to enable its reduction into macromolecular carbon, alongside the presence of perchlorate salts, which have also been found on Mars (Kounaves et al., 2014; Steele et al., 2018). Studying Tissint is therefore an excellent analogue for Mars Sample Return samples due to the minimal contamination, and the similar features to those detected by Curiosity at Gale Crater.

In this project, two thin sections of Tissint were used for in-situ analyses. One (Tissint A) was prepared using the gold coating technique outlined below, and one was not, as it had been prepared earlier, and provided by the NHM (Tissint B) and thus served as a comparison sample. Prior to this work, an MSc student at SUERC and U of G undertook a pilot study to evaluate bulk techniques to analyse the OM in the Tissint meteorite. This project in part serves as a follow on to her work, and as a result it is appropriate to use the same sample for a comparative in-situ study.

SaU 008

Sayh al Uhaymir (SaU) 008 was found in Oman in 1999 and is thought to be paired with SaU 005, and several other small fragments found later in 2001, across a ~2km strewn field (Yu & Gee, 2005, Meyer, 2012). The meteorite has minimal terrestrial weathering features, and a total of 9923 g was found with its primary paired stone, SaU 005 (Yu & Gee, 2005). The minimal terrestrial weathering and large amount available was the primary initial reason to study this meteorite for organic matter.

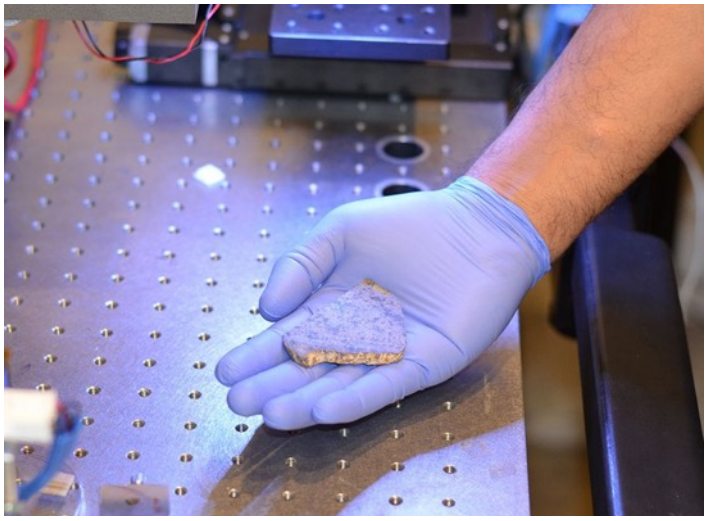

Figure 46 The small slice of SaU 008 martian meteorite that has gone home to Mars. This serves as a calibration target for SHERLOC onboard Perseverance, aiding its search for organic molecules at Jezero Crater. Image credit: NASA Jet Propulsion Laboratory

This stone was chosen as a calibration target onboard the Perseverance rover to return it to Mars in 2021 (NASA Jet Propulsion Laboratory, 2018). The SHERLOC (Scanning Habitable environments with Raman and Luminescence for Organics and Chemicals) instrument uses a small slice of SaU 008 (see Figure 46) to calibrate the laser each time it analyses its targets on Mars.

In this project we study a thin section of SaU 008 using Raman spectroscopy, the same technique employed by the SHERLOC instrument. It is thus important to characterise the organic matter in this important specimen as fully as possible, to provide a comparison dataset for the Perseverance mission's analyses on Mars.

Nakhla

Nakhla was observed to fall as a shower of total mass ~ 10 kg in Egypt in 1911, over an area spanning ~ 4.5 km diameter (Meyer, 2008). In this project a chip of Nakhla was crushed and the organic matter therein studied using LC-MS and GC-MS, as part of our

protocol development. The stone was studied because it was a fall with in-tact fusion crust, and therefore has less terrestrial contamination than other martian samples, because of the availability of the material and because organic matter has been detected in samples of Nakhla using similar bulk techniques in the past, suggesting a high chance of success.

Solvent extracted samples of Nakhla were studied using flash pyrolysis GC-MS to successfully detect high molecular weight organic material (Sephton et al., 2002) - see Figure 47. These were thought not to be due to terrestrial contamination, since it has been suggested the organic contamination content is low molecular weight material resulting

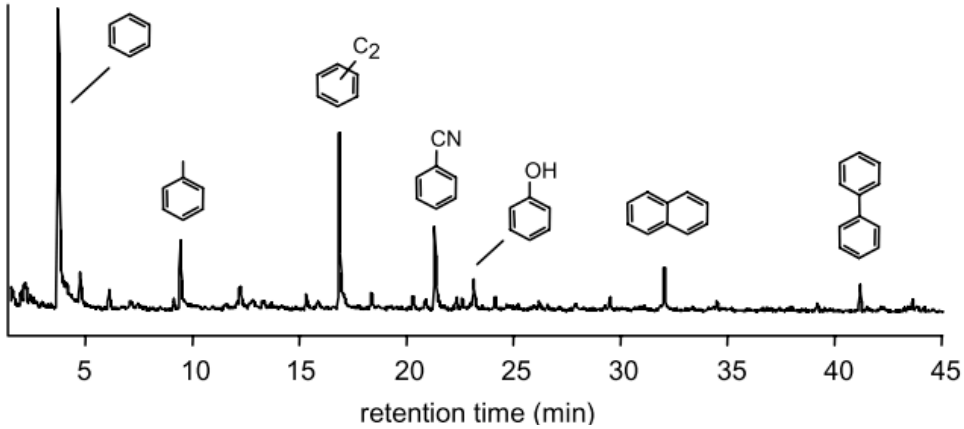

Figure 47 Ion chromatogram displaying high molecular weight organic fragments detected in solvent extract of Nakhla analysed using flash pyrolysis GC-MS, adapted from Sephton et al (2002)

from the agricultural region surrounding the Nile river delta upon which the meteorite fell (Glavin et al., 1999). This contamination characterisation was carried out via high performance liquid chromatography analysis of hot water extracts of the sample, and a number of amino acids with a terrestrial enantiomeric ratio were detected, strongly suggesting a rapid ingress of biogenic matter to the sample when the meteorite landed on Earth (Glavin et al., 1999). Contamination of this stone has been further investigated through a four year time-series study investigating microbial presence in Nakhla, whereby scanning electron microscopy and epifluorescence microscopy were used to identify DNA and fungal contaminants and their dynamics over time (Toporski & Steele, 2007). This study showed how, despite sterile storage and laboratory conditions, contamination of extra-terrestrial samples is inevitable, and demonstrated how crucial rapid studying of martian specimens will be once Mars Sample Return takes place.

The number of reports of organic material found in Nakhla (additional studies include e.g. Jull et al., 2000; Steele et al., 2018), both *in-situ* and bulk studies, made this sample ideal for an evaluation of our bulk technique development. It was expected that organic matter

would be detected in the sample thanks to the number of studies carried out, with a good chance of detecting likely indigenous martian high molecular weight material, if our protocols were effective.

Northwest Africa 8159

Northwest Africa 8159 (NWA 8159) is an augite rich Shergottite purchased by a Moroccan meteorite hunter and sent for identification in 2013 (Herd et al., 2017). The meteorite has no in-tact fusion crust, and a 3 mm thick outer weathering band, with visible weathering

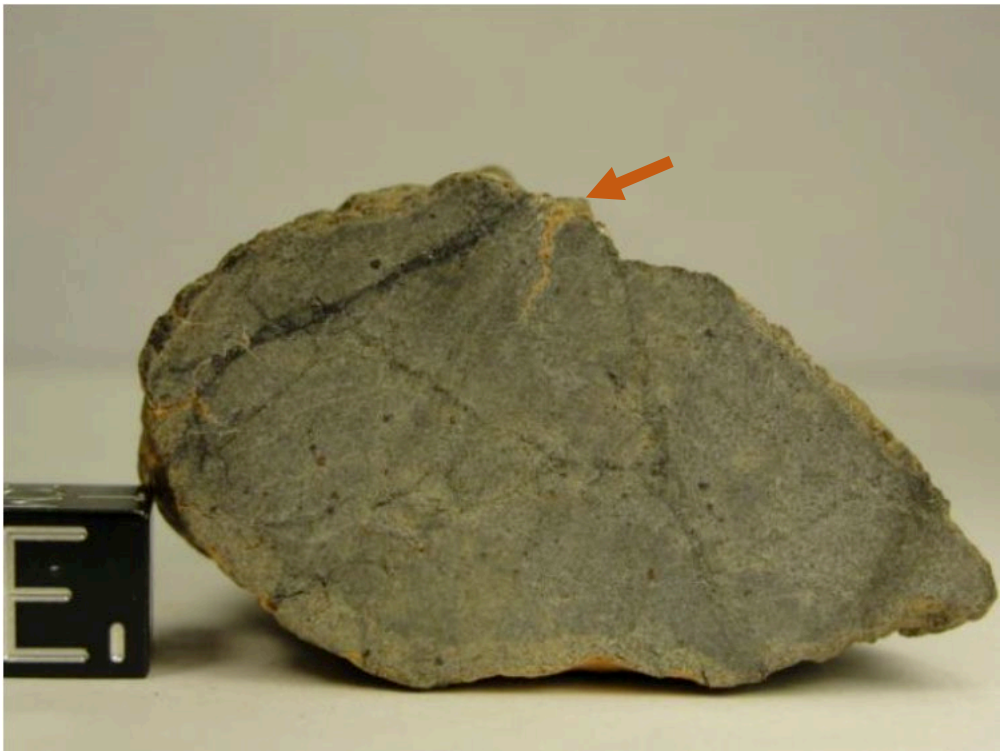

Figure 48 Slice of the NWA 8159 meteorite with a likely terrestrial weathering vein indicated by arrow, and dark melt veins visible. Scale cube = 1 cm. Image adapted from Agee et al. (2014).

veins that 0.5 cm deep as can be seen in Figure 48 (Herd et al., 2017). This lack of fusion crust, and extensive weathering features would normally be a reason to disregard the sample, when searching for martian organic molecules. However, NWA 8159 appears to be a unique martian meteorite originating from a unique martian mantle source (Herd et al., 2017). Since the primary theory for the formation of martian macromolecular carbon is reduction in the martian mantle (Steele et al., 2012), locating likely indigenous MMC in this meteorite may sample martian organics from an as yet un-sampled source.

Yamato 000593 and 000749

Yamato 000593 and 000749 (Y000593 and Y000749) are paired Antarctic meteorites found in the 2000-2001 season, which are also paired with Y000802 (Meyer, 2012).

Y000593 was the largest of the stones, at 13.7 kg, with Y000749 weighing 1.28 kg and Y000802 22 g. Y000593 was found with about 60% of its fusion crust in-tact, with one side significantly better preserved than the other, probably due to Antarctic surface weathering (Meyer, 2012).

Organics have been studied in Y000593 through TEM-EDS, EELS and NanoSIMS, leading to a differing hypothesis to their formation and source of that of Steele et al. (2012), as organic matter was found associated around the margins of olivine's alteration product iddingsite, rather than as inclusions in the mineral (McLoughlin et al., 2019). The authors argue that if the organic matter was magmatic in origin, it would be hosted throughout the magmatic grains, rather than around the edges of the alteration veins of iddingsite (see Figure 49). A previous study also found organic material associated with iddingsite in Yam 000593, and suggested these may be biogenic in origin, due to their spherical appearance (White et al., 2014).

McLoughlin et al. (2019) propose that Yam 000593's organics are exogenous, rather than indigenous – ie were deposited on the surface of Mars through impact, and were then incorporated through hydrothermal circulation as a result of the impact heating and alteration. This is consistent with recent electron backscatter diffraction work showing that the nakhlites were impacted once before the impact that ejected them, and that this impact's hydrothermal circulation caused the secondary alteration observed in the nakhlites (Daly et al., 2019). Studying organics in this stone, and its primary pair (Yam000749), using *in-situ* techniques will help understand if McLoughlin et al.'s hypothesis holds true for both the Yamato paired stones.

Small chips (~1 mm) of Yam 000593 and Yam 000749 were gold coated and mounted as thin sections as outlined below and studied using Raman spectroscopy.

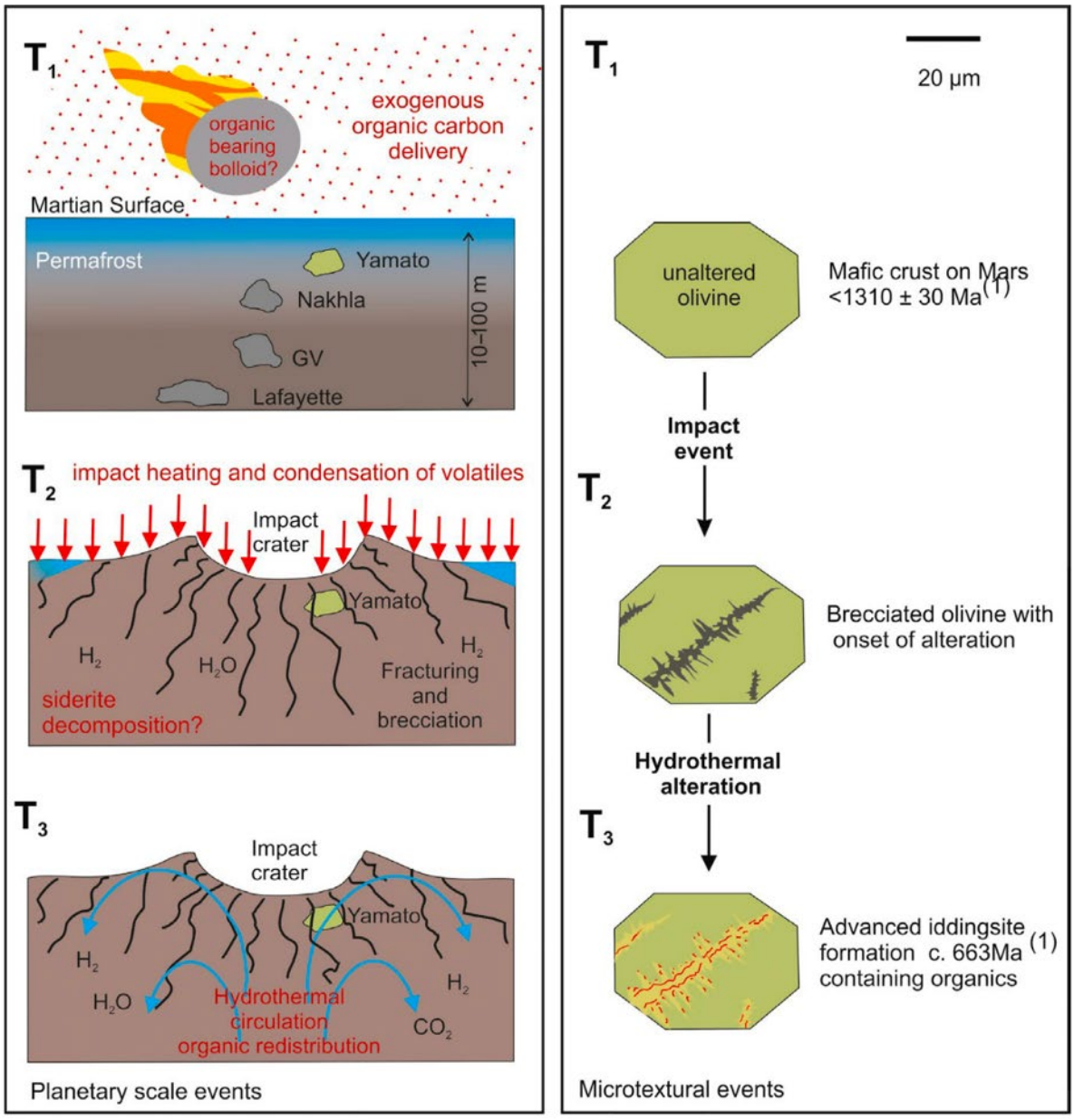

Figure 49 Formation scenario of organics in Yamato 000593 meteorite as outlined by McLoughlin et al. (2019), whereby organics are delivered to the surface of Mars through e.g. carbon-rich meteorite or asteroid impact. The impact then causes hydrothermal circulation, melting martian permafrost and incorporating the organics from the impact into Lafayette, with the hydrothermal circulation causing sufficient alteration for iddingsite to form.

Samples - Ureilites

This project's primarily aim was to study martian meteorites to characterise their organic content, to determine the best techniques to do this in preparation for Mars Sample Return, as well as add to our understanding of the possible formation/origin scenarios of martian carbon. One of the possible origin scenarios as summarised by Steele et al (2016) is that martian carbon is exogenous, deposited on Mars during influx/impacts of other smaller solar system bodies, such as comets and meteorites, with the surface. To investigate this scenario, we studied two carbon-rich ureilite meteorites, using STXM-XANES at Diamond

Light Source, a technique we also used with martian samples, so that comparisons that could be made to assess whether they could be a potential source of martian carbon.

Ureilites themselves are known to be relatively carbon-rich, which contains carbon in the form of a mixture of graphite, diamond, as well as solvent soluble organics. Ureilites are thought to originate from a partially melted asteroid which is known as the Ureilite Parent Body (UPB) (Goodrich et al., 2004). Similar to martian carbon, the formation scenario of some of the ureilite's organic content, specifically its diamond, and diamond's polymorph lonsdaelite, is debated, with the main theories as to their formation being:

1) Shock pressures due to a solar system body impacting the UPB
2) Chemical vapour deposition in the solar nebula
3) Consistently high pressures inside the UPB (Nabiei et al., 2018).

We could therefore also add to the dataset of ureilitic carbon and its structures, contexts and add evidence toward its possible formation scenarios.

Glavin et al. (2010) studied the solvent soluble content of the ureilite breccia Almaha Sitta and found evidence for indigenous amino acids. Hot water extracts were performed and analysed using LC-FD/ToF-MS and found a range of amino acids with a 1:1 (racemic) enantiomeric ratio, suggesting they were not terrestrial in origin (since most biological processes are homochiral and favour left-handed amino acids) (Glavin et al., 2010).

An overview of these two samples is given below.

Goalpara

Goalpara is a heavily shocked ureilite which fell in India in. It has a cosmic ray exposure age of 20.1 ± 1.2 Ma. Previous studies have located diamonds in samples of Goalpara (E.g. Urey 1956), and, due to the heavily shocked nature of the stone, have thus supported the theory that ureilite diamonds were formed due to UPB shock. More recently, TEM, Raman spectroscopy, and X-ray powder diffraction has been carried out to locate, isolate and characterise graphite, diamond and lonsdaleite in thin sections of Goalpara, to determine crystallographic structure of the minerals (Nakamuta & Toh, 2013). The authors suggest that the graphite in Goalpara crystallised with the igneous minerals in the asteroid, whilst the diamond and lonsdaelite are themselves formed from slices of that graphite, suggesting a shock formation scenario.

Goalpara was also used studied more recently still, and the results of which further support the shock formation scenario for ureilitic diamonds (Nakamuta et al., 2016). The authors found diamonds associated with graphite in low and high shock ureilites (including Goalpara), and through EBSD analyses found that the crystallographic orientations of diamonds and graphite in Y-8448 (a low shock ureilite) were the same as those in Goalpara. In the low shock ureilites, diamond exists as fine grains of the order of ~1 μm in size. Whilst in the highly shocked ureilites, diamond forms in two morphologies, with grains ~ 1 μm, and additional larger grains ~10 μm in size. They suggest that in low shock ureilites, diamond is formed at low pressures (<10 GPa) and requires an iron metal catalyst; whilst in high shock ureilites, diamonds formed both spontaneously at high pressures (<12 GPa) as well as under catalysis reactions, as in the low shock ureilites (Nakamuta et al., 2016).

Hajmah (a)

Hajmah (a) was found in Oman pre 1958 and is an unbrecciated ureilite. It has also experienced less shock than Goalpara (Grady et al. 1985). It was important to study two contrasting samples in terms of shock, since one of the shock impactor theories for diamond formation on the UPB suggests that the level of shock influenced the size and nature of diamonds produced (Nakamuta et al., 2016). Ideally, we would have studied a fall sample, for a more direct comparison and a more pristine sample, however a fall was not available from the NHM collections.

Samples – Mars Analogues

Analogues of martian samples were required for our bulk analysis work, to test the limits of the experiment – as we were unsure if the martian samples were carbon-rich enough for the detection limits of LC-MS and GC-MS, and to practise extraction protocols. The Mars analogues were both provided by Dr A. Steele of the Carnegie Institute of Washington, and the justification for their use is outlined below.

Bockfjorden Volcanic Complex -Sigurdfjellet and Sverrefjellet

Due to Svalbard's climatic and geological properties being closely resembling that of Mars (low temperatures, arctic desert, steep rocky slopes), it was the site of multiple analogue Mars missions to test mission payloads, such as that of Curiosity and ExoMars, as part of AMASE (Arctic Mars Analog Svalbard Expedition) (Amundsen et al., 2011). Igneous

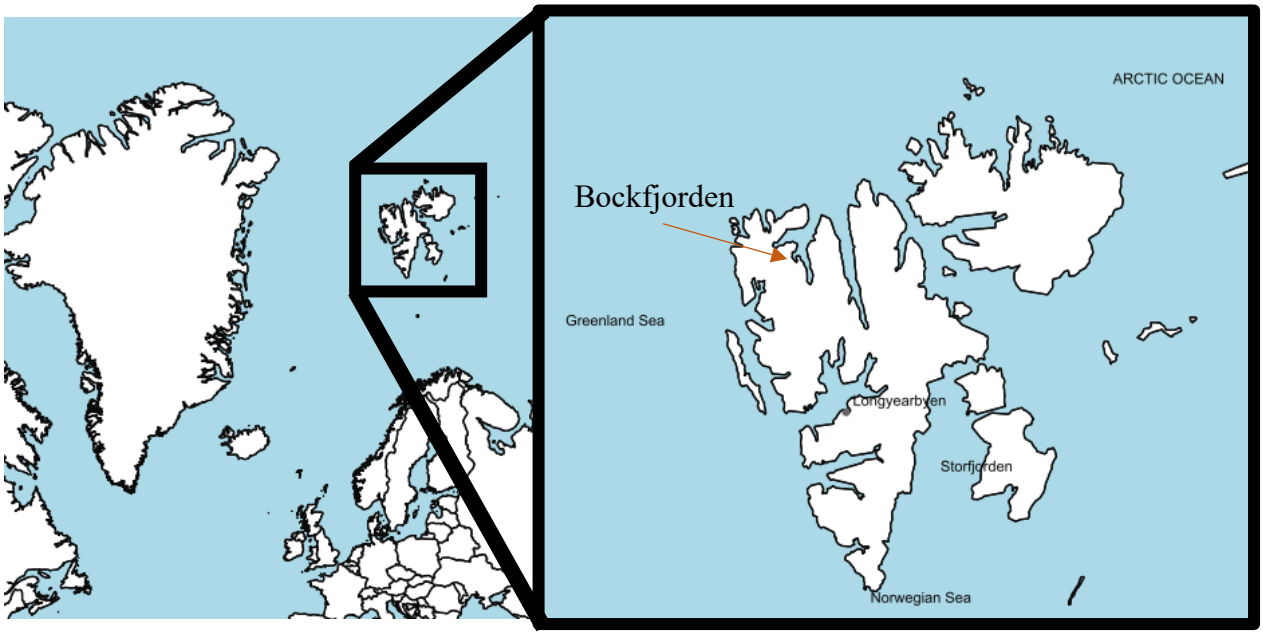

Figure 50 The location of Bockfjorden Volcanic Complex where the Sverrefjellet and Sigjurdfjelle volcanoes are located, from which the AMASE mission sampled, in order to collect Mars analogues, as a result of the macromolecular carbon ringed carbonate inclusions similar to those found in the martian meteorite ALH 84001.

samples collected during these annual expeditions were used as analogues for martian meteorites as they have been found to contain organic-bearing carbonates that closely resemble those found in ALH 84001 (Steele et al., 2007). These xenolith samples originate from the Bockfjorden Volcanic Complex (BVC) (see Figure 50), from theSigurdfjellet and Sverrefjellet volcanoes, which erupted under the island's ice sheet ~ 1 Ma ago (Amundsen et al., 2011). We used BVC samples for bulk analyses in our LC-MS and GC-MS studies, given the similarity between the organic content in BVC samples and martian samples. These samples have similar MMC contents to ALH 84001 with an analogous proposed

abiotic igneous formation scenario, too (Steele et al. 2007). These were therefore used in this study to evaluate how similar their content was when studied with LC-MS and GC-MS, as martian meteorite analogues.

JSC Mars 1

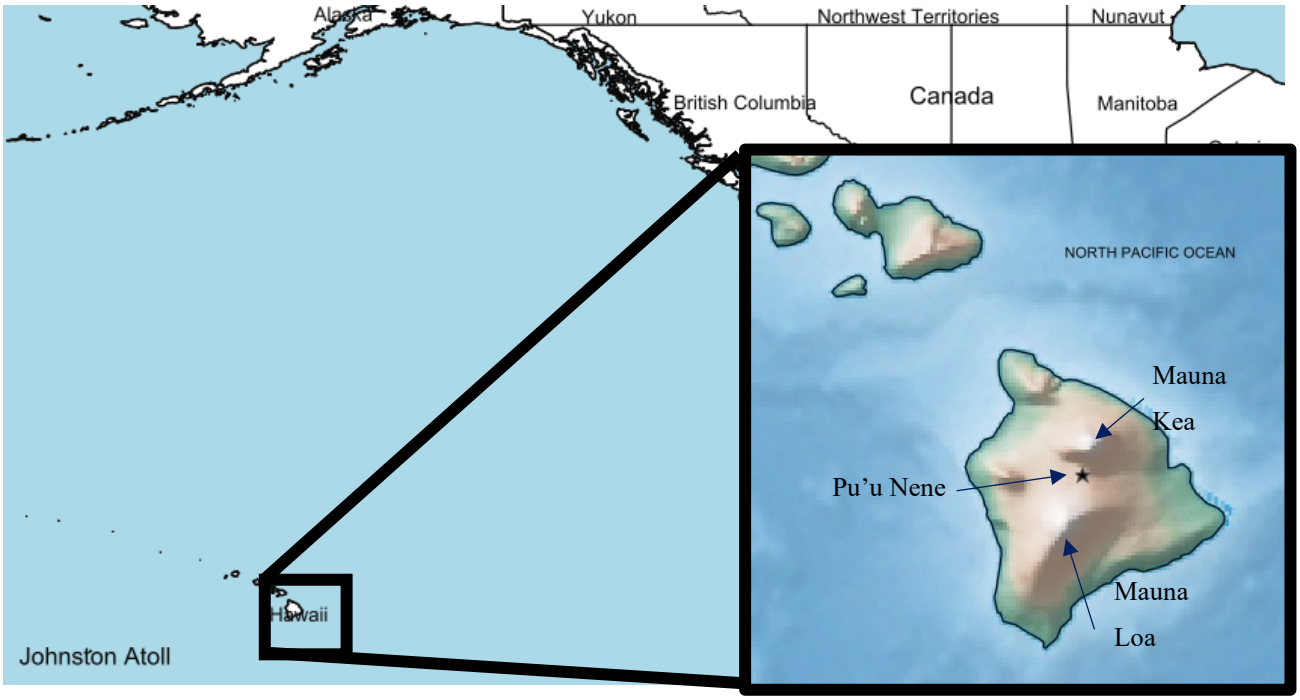

Figure 51 The location of the sample site, Pu'u Nene, in the volcanic 'saddle region' between Mauna Loa and Mauna Kea on Hawai'i from which martian simulant JSC Mars 1 was collected by NASA Johnson Space Centre.

JSC Mars 1 is a martian regolith analogue developed by NASA Johnson Space Centre, using volcanic ash from Hawai'i (Allen et al., 1998). It was collected from Pu'u Nene volcano, which lies in the saddle region between Mauna Loa and Mauna Kea (see Figure 51) Hawai'i's two largest volcanoes. The Pu'u Nene material is a palogenitic tephra, glassy volcanic ash which was altered at low temperatures. The material was chosen as martian simulant material due to its spectral similarity to martian regolith, as well as the availability/abundance of the ash (Allen et al., 1998).

This material was chosen to be used in our bulk analysis study as it has been previously used in a liquid chromatography experiment, specifically high-performance liquid chromatography (HPLC) to study the organic content (Garry et al., 2006). This previous study successfully detected the presence of amino acids in the material (see Figure 52), thus we could use this as a comparison to our extraction and liquid chromatography protocols and evaluate their efficacy as martian meteorite analogues. In addition, the large volume of material available (compared to martian meteorite samples) allowed us to run additional samples of JSC Mars 1 in the HyPy GC-MS study, to assess the effects of

solvent extraction on the results of HyPy (see Chapter 6 for further details).

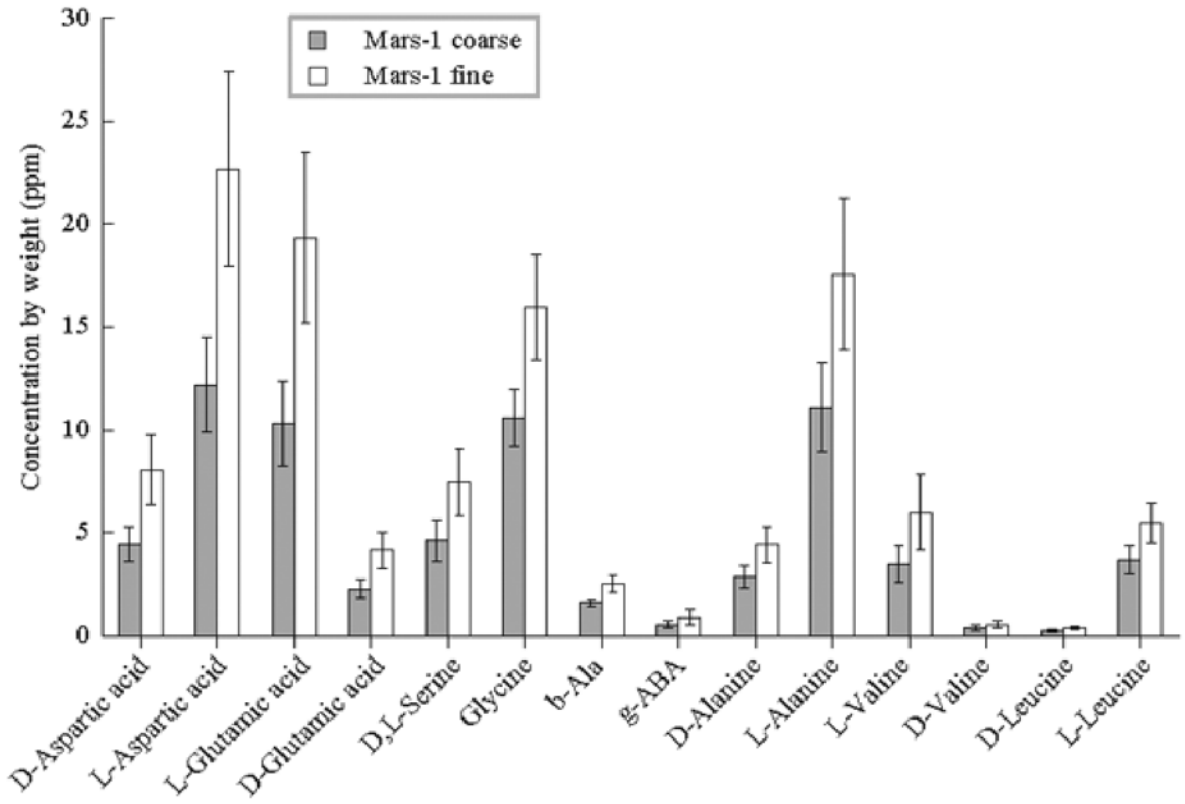

Figure 52 The distribution of amino acids detected via HPLC by Garry et al. (2005) in extracts of JSC Mars 1, in both coarse grained and fine grained samples of the material

4
In-Situ Techniques

In-Situ Methods Summary

A correlative approach was taken to *in-situ* analyses. For most thin section samples this started with optical microscopy and ended with STXM-XANES. An overview of the procedure followed is given below in Figure 53, outlining the techniques applied to meteorites and analogues studied with each technique.

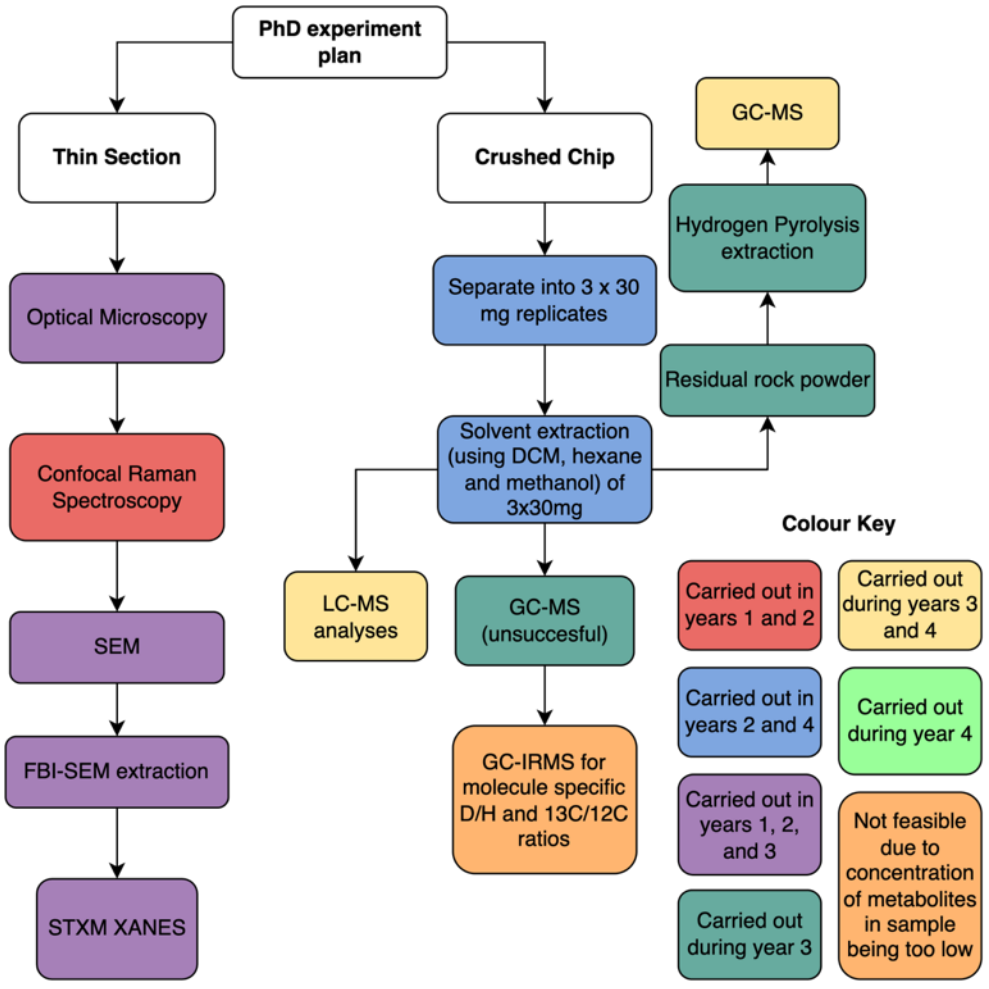

Figure 53 Summary of the experimental techniques carried out during PhD, with approximate timings of each activity given via colour coding. Activities split by year carried out. One planned activity was not possible due to concentration of molecules in extract not being high enough for the detection limits of the instrument.

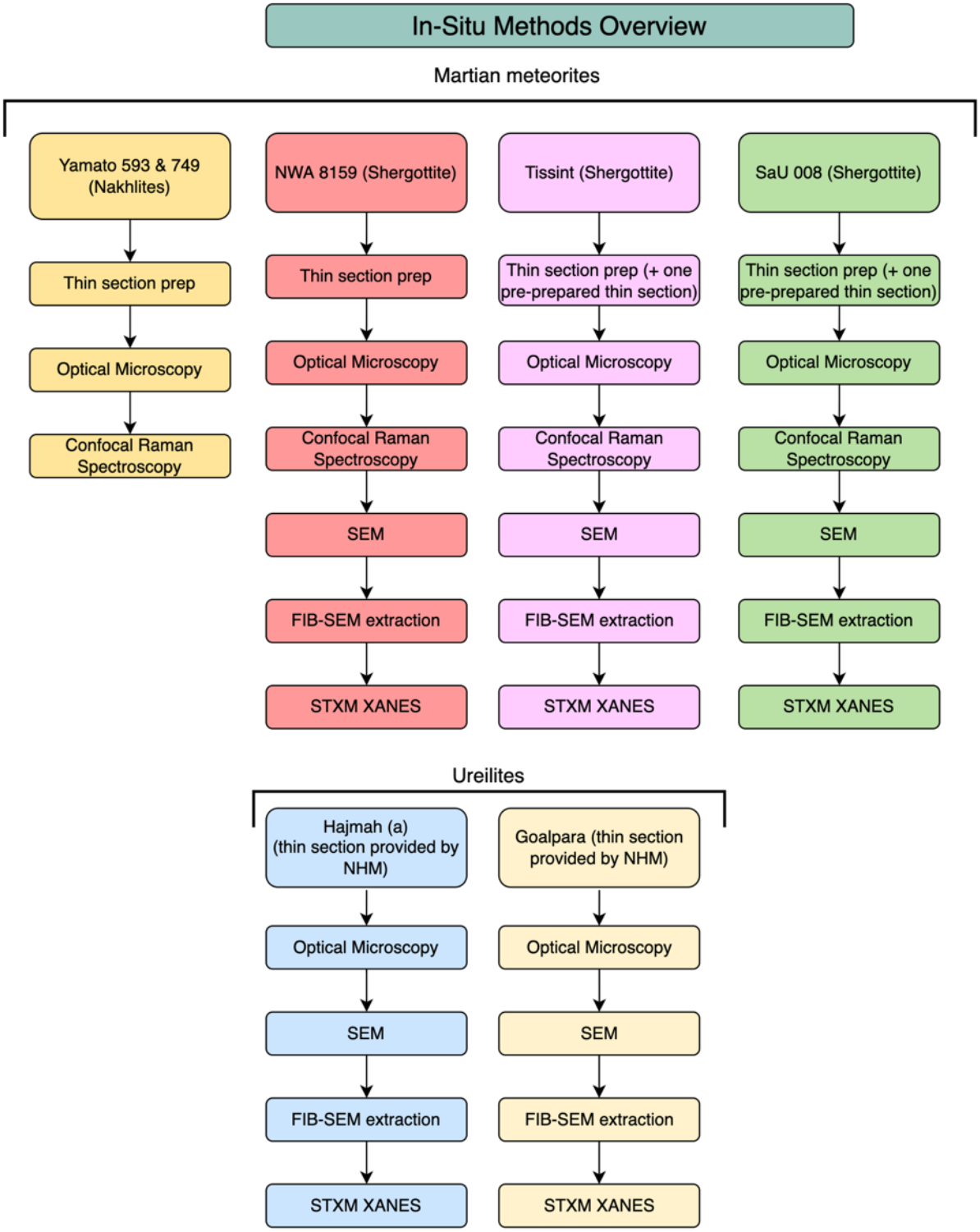

Figure 54 Overview of the in-situ techniques used on the samples studied in this project.

The samples studied with in-situ techniques are shown in Figure 54.

The overall aim of the methods was to analyse the structure of meteoritical organic matter, and to evaluate the techniques used to inform future Mars Sample Return analyses.

Introduction to Analytical Techniques

Raman Spectroscopy

Raman spectroscopy allows us to detect presence of minerals. When monochromatic light is incident upon a material, most of the light collides elastically with the material. The light is scattered without a change in its wavelength (Rayleigh scattering). This happens because the dipole moment induced by the beam is the same frequency as the beam. A small number of inelastic collisions with vibrating functional groups cause the light beam to undergo a wavelength shift, due to a change in energy of the functional group (Raman scattering, see Figure 55). A spectrometer detects this shift in frequency, this is then plotted as wavenumber, ω, against intensity of the signal, where wavenumber is described by

$$\omega = \frac{\nu_s - \nu_0}{c}.$$

Where ν_m is the frequency of the scattered radiation and ν_0 the incident radiation frequency. Each peak in a Raman spectrum corresponds to a particular vibrational mode of a functional group. This allows us to detect minerals as different minerals demonstrate characteristic wavenumbers. Furthermore, this process is (largely) non-destructive, and

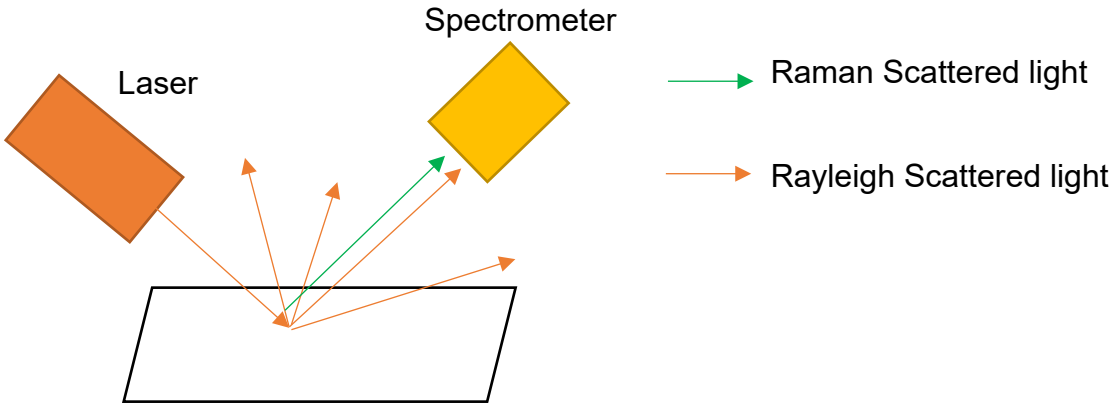

Figure 55 A schematic diagram of a Raman spectrometer is displayed. Monochromatic light, such as a laser beam is directed at a sample. Most of the scattered light does not undergo a frequency shift; this process is known as Rayleigh scattering. A small amount of light is shifted in frequency, due to an induced dipole moment whose energy matches that of a vibrational mode.

was therefore chosen for this project as organic compounds can be detected, without the removal of material (Steele et al. 2020). This technique was chosen for this project as it has previously been used to show presence of organics in martian meteorites and is also onboard the most recent generation of Mars rovers, such as Perseverance, specifically for

organics detection (Steele et al. 2012; Hollis et al. 2021).

In this project, a WiTec confocal Raman spectrometer with a 532 nm laser was used at the Carnegie Planets laboratory, Washington DC.

STXM XANES

Scanning transmission X-ray miscroscopy (STXM) X-ray Absorption Near Edge Structure (XANES) analysis is used for the detection of functional groups as its spectra give information about an atom's locality (inter-atomic distance, chemical bonding and site symmetry) (Bianconi, 1980). This gives us crystallographic information. The method involves incident X-rays onto a sample. There are several resultant forms of radiation as a result of this, these are summarised below in Table 2.

Table 2 The forms of radiation emitted when X-rays are incident upon a sample during XANES are outlined. All information adapted from (Norman, 1986)

Radiation Type	Description
Transmitted X-rays	Incident X-rays are transmitted without a change in energy.
Auger Electrons	Outer electron receives enough energy to eject it from its atom.
Scattering	Thomson – X-ray photon scattered by an electron due to an elastic collision. Energy of photon and electron does not change Compton – X-ray photon scattered by an electron due to an inelastic collision. Kinetic energy of photon decreases.
Fluorescence	X-ray photon is absorbed by low energy level electron causing it excite to a higher energy level; intermediary electron de-excites to fill vacancy left behind, emitting photon of energy equal to the difference between the initial and final energy levels.
Photoelectron	X-ray photon is absorbed by core energy level electron and causes ionisation. Electron is ejected from atom.

As outlined in Table 2 X-ray fluorescence occurs when the incident photon is absorbed by electrons, these electrons are excited to a higher energy level, leaving behind vacancies (holes). Other electrons then de-excite into these holes, emitting photons of energy characteristic to that atom. This is known as the X-ray fluorescence process and is outlined in Figure 57.

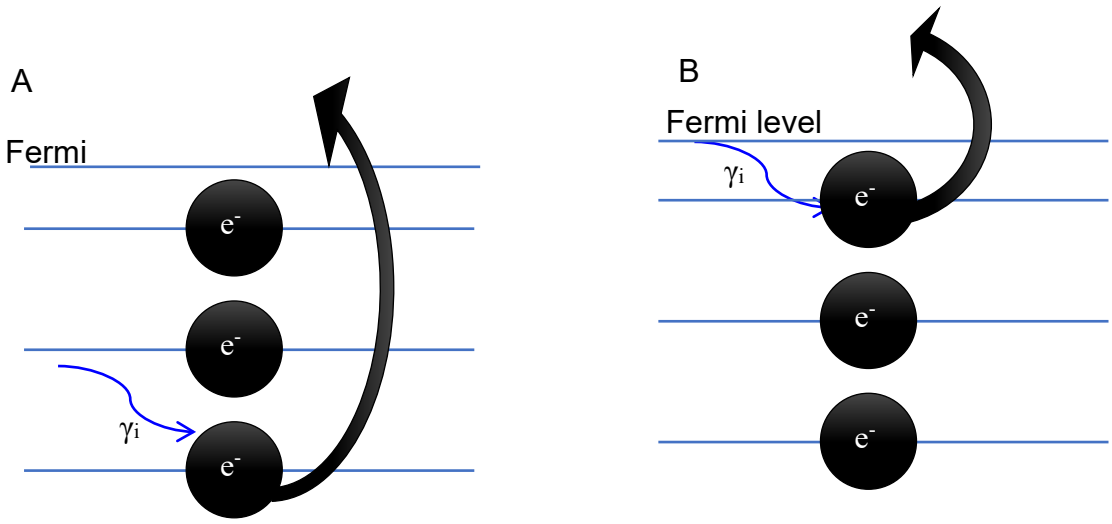

Figure 56 A. The process of photoelectron emission is displayed, whereby a core electron absorbs an incident photon (γ_i), which has an energy greater than the difference between its current state and the Fermi level, causing ionisation. B. The process of Auger electron emission is displayed, whereby an outer electron absorbs an incident photon (γ_i), which has an energy greater than the difference between its current state and the Fermi level causing ionisation.

The process of photoelectron emission is outlined in Table 2 and displayed in Figure 56. Since the possible electron transitions are discrete (and unique to the element) only certain energy absorptions are observed. This means that for a broad spectrum of incident energy, no absorption spectra are observed until the energy is reached of the lowest energy transition. Once this energy is reached, a large jump in the amount of energy absorbed (known as the linear absorption coefficient) is observed. This is known as the edge.

The wave front associated with the photoelectron is sensitive to its locality, meaning that it can be backscattered by nearby atoms. This backscattering causes a phase shift of the

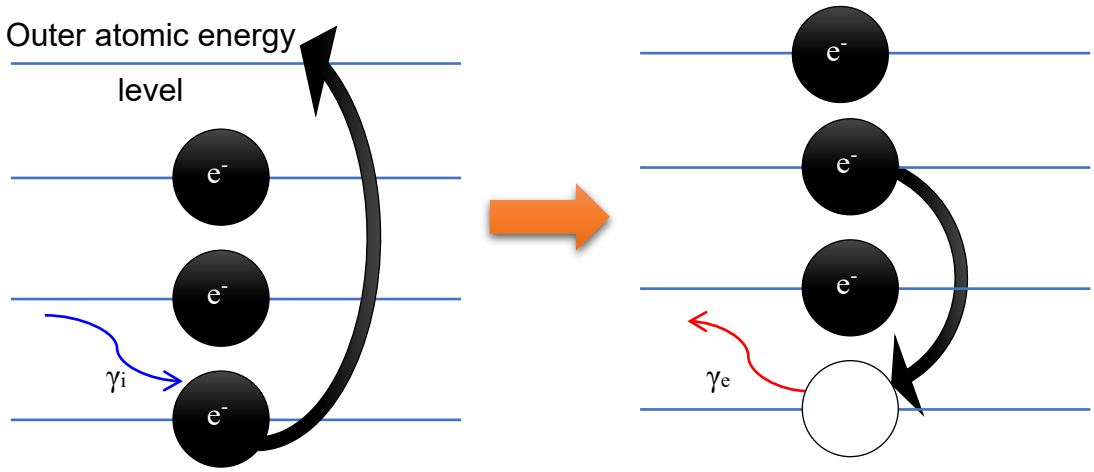

Figure 57 The process of X-ray fluorescence is displayed. An electron absorbs an incident X-ray photon, γ_i, moves to a higher energy state, leaving behind a hole. Another electron then moves to this hole, emitting a photon, γ_e of energy equal to the difference between its initial and final states

wave, thus wave superposition takes place, causing cancellation and reinforcement. The result of this is a perturbation of the spectra which tells us about the atomic locality (Norman, 1986).

Different organic functional groups excite with different energies on the K edge, allowing for such groups to be identified in carbon-based material (Alexander et al. 2017) STXM XANES therefore gives us nanoscale resolution structural information about the materials analysed, whilst retaining the mineralogical context within which these structures exist. This technique has previously been used to study extra-terrestrial organics in carbonaceous chondrites, as well as martian meteorites, and therefore using this technique in this study provided a comparison for the organic structures detected (Alexander et al. 2017; Steele et al. 2018). The STXM instrument at beamline io8 at Diamond Light Source Synchrotron was used for this project, as the X-ray source produces a continuous range of X-rays at a large range of energies, providing nanoscale resolution and the possibility of e.g. carbon, nitrogen, oxygen, and iron K edge analyses (although only carbon and nitrogen were investigated in this project).

Methods

Initial Thin Section Preparation

The primary goal of this project is to locate, extract and analyse organic material in martian meteorites so a key consideration during the manufacture of thin-sections was minimizing the risk of terrestrial contamination. The resin used for sample preparation is epoxy, an organic resin, thus it was deemed important to reduce the ingress of the resin into the meteorite chips. By coating the chips in gold-palladium, and compressing the samples less than usual (the thin sections were not placed under the mechanical press at the final stage to avoid the epoxy glue being sucked under) it was hoped that this would minimise this contamination. The procedure used for this initial thin section preparation is shown in Figure 58.

However, some epoxy was found to have ingressed into these samples (e.g Figure 67). In

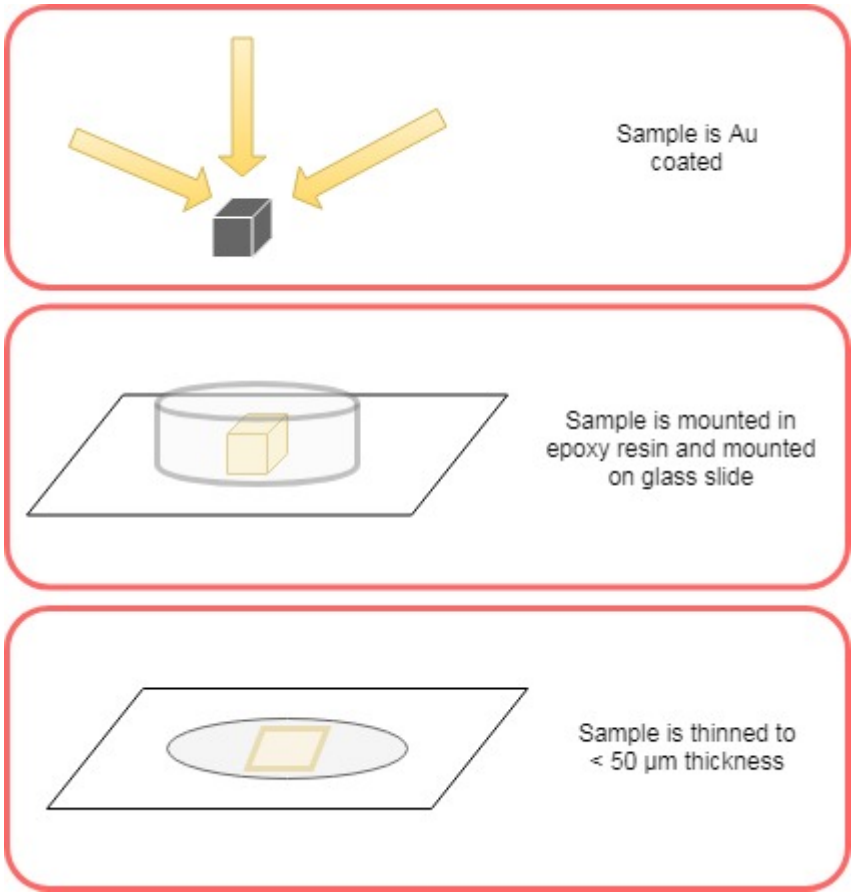

Figure 58 The procedure developed for thin section preparation of meteorite samples is displayed. Samples were coated using gold-palladium, to stop absorption of epoxy into the meteorite chip and thus helping prevent sample contamination.

addition, these thin sections have degraded in quality somewhat, with areas of risen/bubbled resin (see Figure 59), probably due to the missing additional compression

step. These risen areas caused problems during Raman analysis due to the inconsistent height of the sample. It is thought that this has occurred as we chose not to do the final compression step on these samples to the glass when setting them, again to avoid epoxy contamination. Thanks to the announcement in June 2018 of the detection of complex organics by the SAM instrument onboard Curiosity (Eigenbrode et al., 2018) and their similarity to their meteorite counterparts (Steele et al., 2018) the need to prove that these organic compounds are not terrestrial contaminants is reduced somewhat. It is therefore concluded that due to the premature degradation of these thin sections, this technique is not worthwhile.

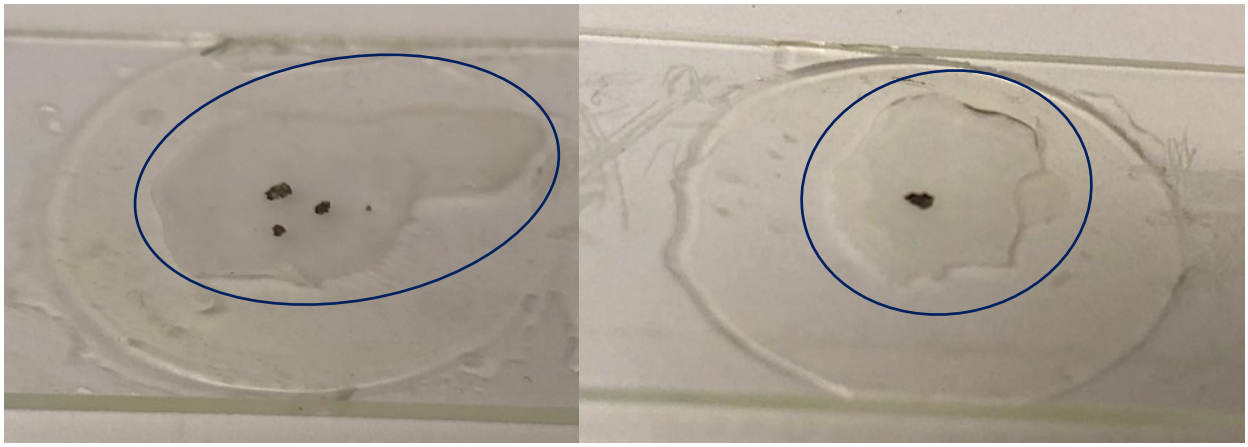

Figure 59 Thin sections of gold coated martian meteorites, SaU 008 and Y000593 prepared as outlined in Figure 58 are displayed. Regions of raised epoxy resin surrounding the chips are highlighted in dark blue.

Optical Microscopy

Potential carbon-rich regions were identified using optical microscopy at the University of Glasgow. As outlined in Steele et al., 2012, martian MMC is found as thin films enveloping dark oxide inclusions of ~10-50 μm in diameter in igneous minerals. They often appear as sprays of small particles with a diffuse or fuzzy appearance. Dozens of potential sites were located and imaged in transmitted (plane polarised light) and reflected light using optical microscopy to then be scanned using Raman spectroscopy. Care was taken to ensure sites of interest were hosted below the surface of the thin section (therefore not exposed to terestrial contamination), whilst not being so deep as they could be reached

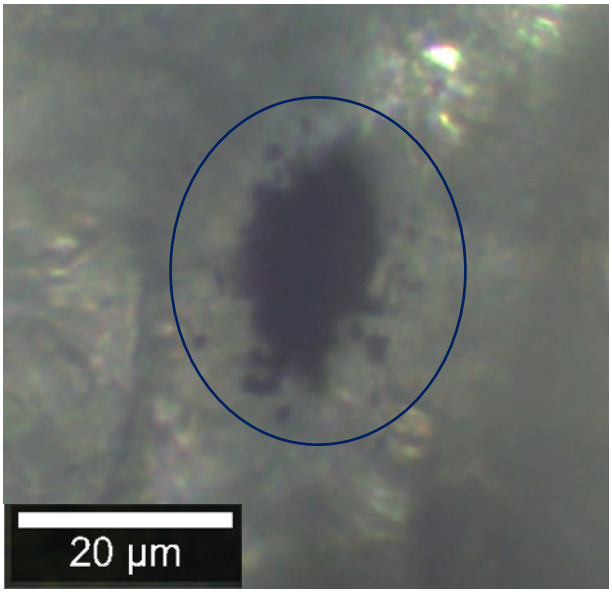

Figure 60 MMC-bearing region surrounding an oxide inclusion hosted in maskelynite in the Tissint meteorite. Sample imaged in plane polarized light and later analysed using Raman spectroscopy. MMC found to envelope some of the outer 'sprays' of oxide surrounding the central larger oxide inclusion (circled in blue)

by a focused ion beam (ideally enclosed 1-10 μm below the surface). Images were taken at all magnifications so that inclusions could be found easily when using Raman and Focused Ion Beam Scanning Electron Microscopy (FIB-SEM)

CRIS (Confocal Raman imaging spectroscopy)

In order to locate MMC-rich regions in thin sections of martian meteorites, a WiTec confocal Raman and imaging spectroscope (CRIS) was used at the Carnegie Planets Laboratory, Washington D.C. for two one-week trips to the USA in 2017 and 2018. Organic compounds exhibit distinct D and G band Raman shifts at ~ 1350 cm^{-1} and ~ 1580 cm^{-1} allowing for largely non-destructive detection and mapping of MMC (Gomez-Lazaro et al. 2017). Raman spectroscopy also gives crucial contextual information, with igneous minerals such as pyroxene having characteristic Raman shifts, meaning that MMC inclusions can be mapped in their known host minerals. This informs the possible formation scenarios for the material. In addition, thin section epoxy resin has a distinct Raman shift at ~ 3000 cm^{-1} allowing for mapping of any epoxy contamination due to thin section preparation.

The MMC inclusions being studied are small and are observed as thin envelopes surrounding oxide inclusions in igneous minerals (Steele et al., 2012). The MMC is therefore highly localized, meaning that a high precision (depth confocality ~ 300 nm) Raman instrument was required to map the material accurately. This accurate mapping was required so that a focused ion beam (FIB) could then be used to extract the 100 nm thick FIB lamellae of MMC (see below). This CRIS instrument also allowed for analysis at depth whereby a region up to ~ 30 µm below the thin section surface could be scanned with precision. MMC inclusions which were hosted below, and were not exposed to, the thin section surface could be characterised in full.

A 532 nm laser was used, integration time and scan speed varied for each scan, depending on time available and size of the region of interest. Inclusions of interest were located using optical microscopy, their depth was recorded and the Raman laser then focused on this region. Single depth area CRIS scans were then performed, focusing at the depth with most of the inclusion in the focal plane. Following this, if a large area of MMC was found, then, time permitting, a depth scan (area maps at ~ 1.5 µm intervals travelling down through the section) was performed, generating a rough 3-dimensional map of MMC in the inclusion. This was carried out to determine the optimal depth for FIB milling. Once scans were obtained, the data sets were reduced by removing the effects of cosmic rays (observed as tall thin spikes in spectra) and background noise, using WiTec's Project 5

software. Maps were then generated showing distribution of MMC and its host minerals. Regions were chosen for further analysis using STXM-XANES, and therefore requiring FIB-SEM extraction according to the criteria:

- Contamination risk: MMC inclusions that were away from cracks and were below the thin section surface were prioritised. This was to minimise the risk of terrestrial organic contamination through the cracks/from being exposed at the surface.
- FIB-SEM extraction feasibility: milling deeper than 10 µm below the surface using a FIB-SEM is difficult and hugely time consuming. Inclusions that were at ~ 5 µm depth were ideal as this minimised sample destruction, whilst ensuring the inclusions were below the surface and therefore lower risk of terrestrial contamination

FIB-SEM (Focused ion beam scanning electron microscopy)

Below is an outline of the process followed to extract electron transparent lamellae from thin sections, in order to analyse with STXM XANES. A gallium ion FEI FIB SEM was used in the U of G Physics department. Images are all secondary electron images, with scale bars shown.

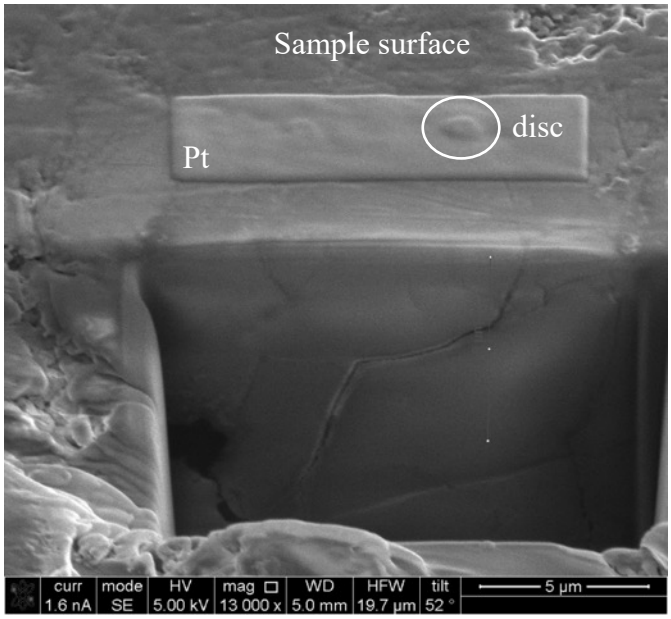

1. Platinum is deposited on surface above region of interest. A heightened disc of platinum is deposited over topographical area thought to be above the inclusion. A trench is then milled at a distance and depth far beyond where the inclusion is expected to be found, using the ion beam at high energy.

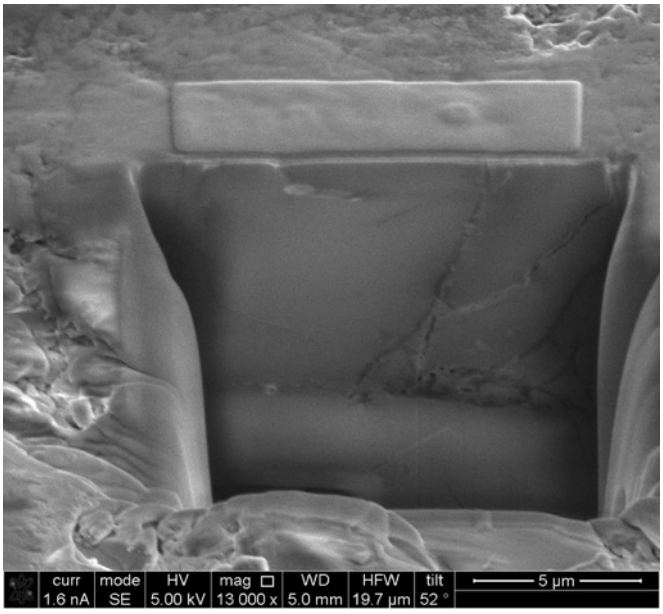

2. Trench is milled towards the region of interest, at increasingly lower energies, to prevent damage to the likely MMC-containing region.

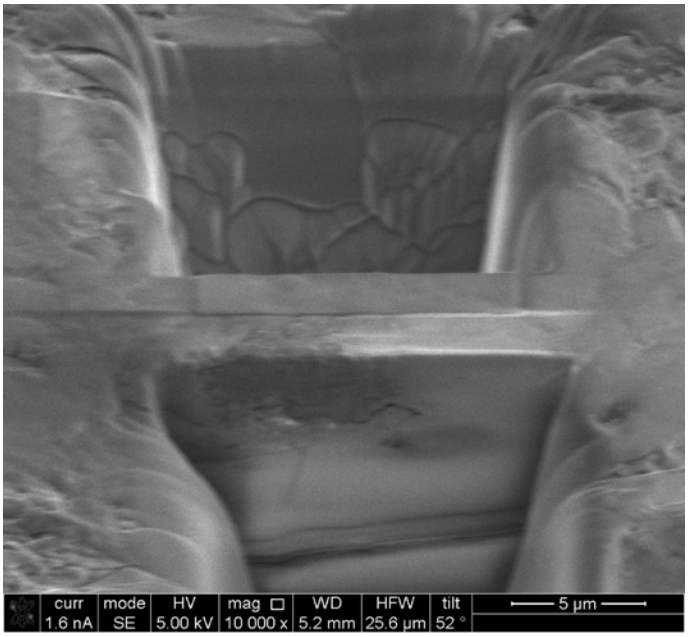

3. Once possible region of interest is identified from one side, milling proceeds from the other.

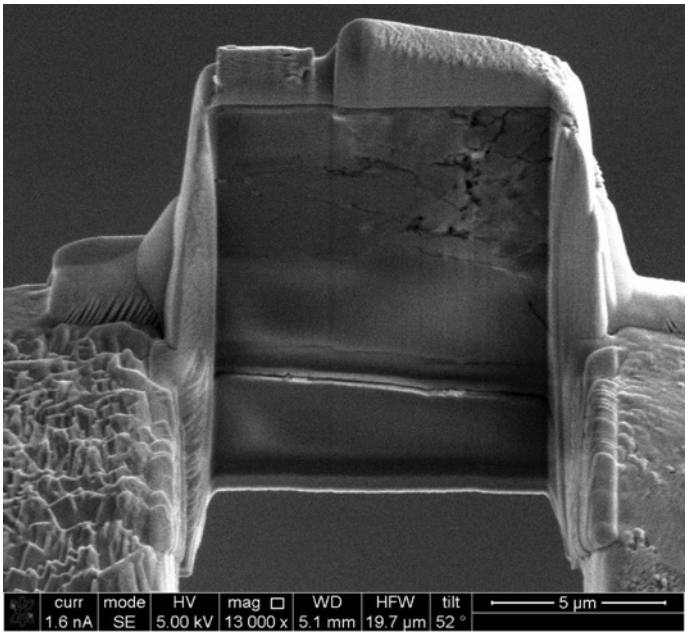

4. Region of interest is extracted from the host mineral and attached to a copper grid.

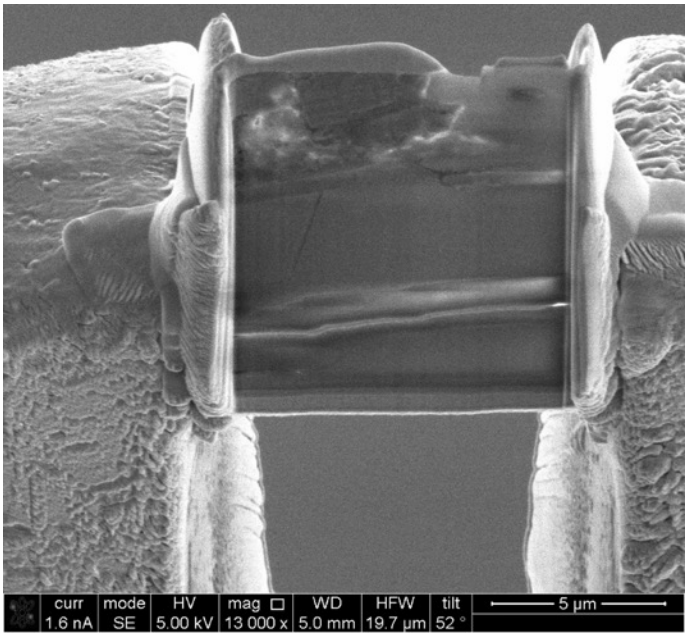

5. Sample is thinned to ~100 nm thickness (thickness required for electron transparency, and STXM XANES)

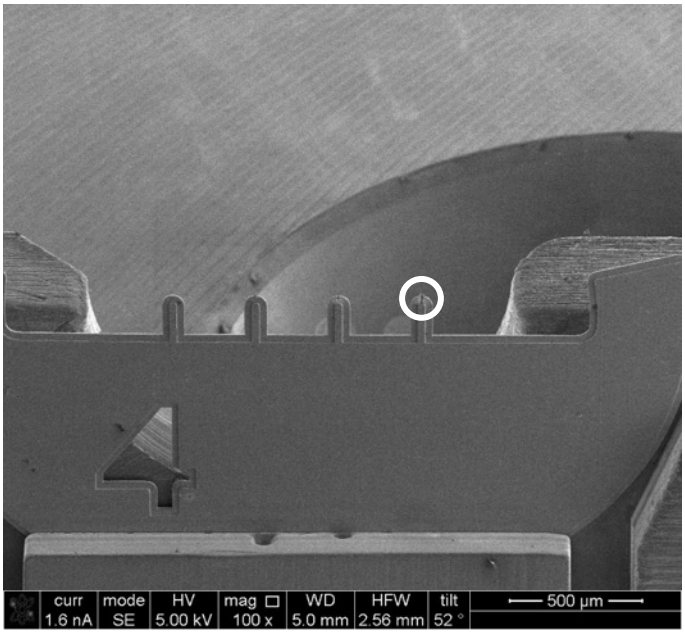

6. Location on TEM grid noted for future analyses

STXM-XANES

Raman Spectroscopy confirms presence of organic materials and allows us to identify the minerals they are hosted in but tells us fewer details about the structure of the organic matter. After extraction using FIB-SEM, as outlined above, samples were analysed at the Diamond Light Source I08 Scanning Tunnelling X-ray Microscope X-Ray absorption near edge structures (STXM-XANES) facility in Oxfordshire, an instrument capable of scanning samples between 250 and 4200 eV. STXM-XANES uses the characteristic absorption of X-rays by different bonding environments at specific wavelengths to allow nanoscale 2D mapping of functional groups in electron-transparent samples. Diamond Light Source is an STFC synchrotron which releases X-rays at a wide range of wavelengths which are harnessed by beamline instrumentation. In this project, we focused on the carbon K edge (at ~284.2 eV), the nitrogen K edge (409.9eV), and spectral features of interest close to the K edge using this technique. In total, three trips to Diamond Light Source were made to analyse samples from 2018-2019.

Each sample was first scanned for carbon presence. The carbon K edge lies at ~ 284.2 eV, samples were therefore analysed between 273 eV and 320 eV. 1 eV intervals were used between 273 eV and 280 and between 300 and 320 eV, 0.1 eV intervals were used between 280 and 300 eV, as this is where most functional groups lie, so more detailed spectra are required in this region. To calibrate each individual scan, a ‘sample free’ I0 region was required, therefore care was taken to ensure each scan included a space beyond the sample to acquire a calibration spectrum.

Time allowing, where a high concentration of carbon (ie strong carbon K edge signal) was found, a scan for nitrogen was then carried out, to allow for further detail of the molecular make up to be determined. The nitrogen K edge jump lies at ~ 409.9 eV, thus samples were analysed between 380 eV and 430 eV, again with smaller intervals used between 400 and 420 eV.

Due to the unstable nature of the synchrotron beam, at any visit the beamline may be lost at any time, meaning that not all samples prepared for each trip could be analysed. In addition, FIB lamellae are prone to loss from the TEM grids they are fixed to. A summary of lamellae prepared, and samples subsequently successfully analysed is given in Table 4.

Some sample drift occurs during STXM scans, it is therefore necessary to align the sample spectra during data processing. This means that the location of a given feature does not appear to change as the sample is observed at different wavelengths. This ensures that the spectrum of a location is accurate, and not a mix of different neighbouring locations at different wavelengths. During the first and second visit to DLS, scans were aligned using Mantis, open-source X-ray analysis software, whose alignment function is limited due to software bugs. At the third visit to DLS, however, scans were performed using aXis 2000, X-ray analysis software hosted in IDL, which allowed for more accurate alignment and therefore smoother spectra were acquired. Unfortunately, we were unable to use aXis 2000 for previous datasets as access to IDL is costly and could not be obtained.

Calibration due to additional beam current was also required for the full dataset from each beamtime session. This was carried out through the analysis of a known mineral or compound, with a narrow k-edge peak distinct from any others in that wavelength region, such as carbonate minerals (~290 eV) and then compared to its known value. This correction varied with each visit from ~ ±1.0-1.3 eV.

SEM (Scanning electron microscopy)

To simplify FIB lamellae extraction, backscatter and secondary electron scans of samples were carried out using the scanning election microscope at U of G, generating images at higher magnification than those from optical microscopy, and matching the imaging (SE and BSE) style of the FIB-SEM. For most samples, this was carried out after CRIS

analysis, to obtain high magnification images of regions of interest, to make them easier to locate in the FIB-SEM.

For one set of samples, however, CRIS analysis could not be carried out, due to timings of visits to Carnegie Planets and Diamond. Surface carbon mapping was carried out using SEM EDX instead of CRIS mapping. These samples were ureilite thin sections from the Natural History of London. Ureilites are known to be relatively carbon-rich (e.g. Day et al., 2017), and therefore there was reduced concern regarding verification of whether or not organics in the sample were due to terrestrial contamination. This meant that surface EDX mapping of carbon using an SEM was sufficient to locate such regions.

In-Situ Results

The in-situ results comprise primarily of data from confocal Raman imaging spectroscopy analyses (CRIS) and scanning transmission X-ray microscopy X-ray analyses near edge structures (STXM XANES). Where CRIS was not possible (on ureilite samples) X-ray energy dispersive spectroscopy (EDS) was carried out on a scanning electron microscope (SEM) to locate carbon rich areas. This section contains examples of such results from all samples studied using techniques. Not all maps are displayed, either because carbon was not detected, or there would be numerous similar maps and spectra for the same sample, not adding anything meaningful to the overall dataset. CRIS data is shown first, then SEM EDS, then STXM XANES.

CRIS Results

The aim of the confocal Raman imaging spectroscopy (CRIS) was to locate MMC rich regions in martian meteorite thin sections, below the thin section surface and away from cracks, to minimise the risk of detecting terrestrial contamination, as opposed to indigenous organic material. CRIS was used to locate MMC, so FIB-SEM could be used to extract the MMC-rich regions as electron transparent lamellae to be characterised with STXM-XANES.

After potential MMC-rich sites had been identified using optical microscopy, these were examined using CRIS at the Carnegie Planets Laboratory on two occasions in 2017 and 2018. Sites of interest (either with MMC presence or other significant components) are detailed below, grouped by their meteorite type. Some samples were found to have multiple inclusions of MMC, where no additional information of interest was found (e.g., sites with different minerals, epoxy/calcite contamination etc) a representative selection of their spectra and mineral maps are shown for brevity.

Some thin sections were created, but no MMC was found, either due to time constraints (in total only ~two weeks were spent at the Carnegie Laboratory) meaning that the samples could not be studied in detail, or as all inclusions studied had no MMC presence. An overview of the MMC detected, and in which samples is shown in Table 3.

Table 3 Overview of thin sections studied with confocal Raman imaging spectroscopy

Meteorite Name	No. of thin sections created/studied	MMC Detected	Notes
Tissint	2	Yes	One gold chip coated thin section (Tissint A); one thin section prepared using standard methods provided by NHM (Tissint B)
SaU 008	1	Yes	Gold coated chip thin section
Yamato 000749	1	Yes*	Gold coated chip thin section *MMC detected only in a single point, not in an area scan
Yamato 000593	1	No	Gold coated chip thin section
NWA 8159	1	Yes	Gold coated thin section

Tissint

Two thin sections of Tissint (Tissint A and Tissint B) were successfully studied during two visits to the Carnegie Planets Laboratory. During the first visit a thin section that was prepared with gold (see methods chapter) was studied, in the second visit, a thin section prepared using standard techniques, loaned by the Natural History Museum of London was used (Tissint B). A total of 16 scans were carried out over the two visits, and in seven of these MMC was successfully detected. MMC inclusions were found within igneous minerals such as maskelynite, augite, and pyroxene. In some cases, the position of the G band was found to vary within individual inclusions on a sub-micron scale (see Figure 63). As well as the complex refractory organic MMC, labile carbon was detected, whereby when the Raman laser was fixed on an individual location, D and G peaks began to form over time (see Figure 66), suggesting a range of organic content in the sample. Most areas analysed (irrespective of whether the thin sections had been prepared with gold or not prior to thin section preparation) were found to have epoxy in the same regions as the MMC. Such regions are shown in the maps.

Figure 61 shows an overlay map of an MMC rich region in Tissint, with the Raman map showing the MMC rich region overlaying the transmitted light image of the thin section. The Raman map shows only the MMC and no other minerals. The MMC inclusion shown in Figure 61is characteristic of the inclusions found throughout this study, with the MMC enveloping an oxide inclusion such as hematite. This overlay image was created with the

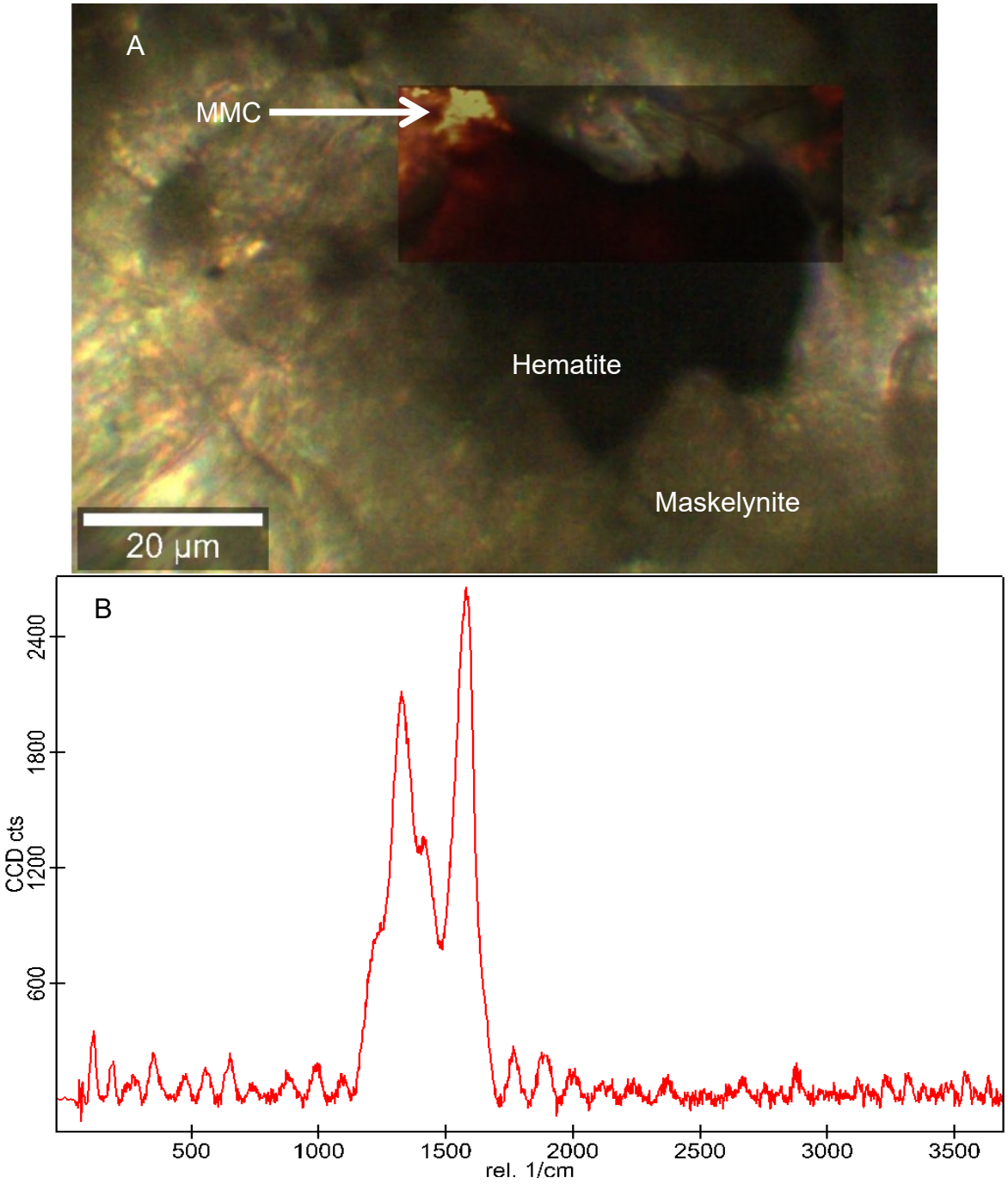

Figure 61 a) An optical microscope image of Tissint A, showing an MMC-rich area associated with a haematite inclusion within an area of maskelynite. The overlay image is a Raman spectroscopy map, showing the MMC-rich region in yellow and orange – brightness represents intensity. The optical image was produced using the WiTech Confocal imaging microscope, housed at Carnegie Planets. b) The average MMC spectrum for the MMC region shown in a) - as determined by WiTech Project 5 Software.

WiTec Project 5Plus software only available on site at Carnegie Planets, and as a result is the only such figure created. Also displayed in Figure 61 is the average spectrum of the MMC in the map, as calculated by the Project 5Plus software. The D and G bands are clearly visible, with no epoxy feature at 2880-3100 cm^{-1}.

The same region is then shown in more detail in maps in Figure 62 and Figure 63.

Figure 62 shows that this MMC rich region contains thin section epoxy in the same locality scanned. This was from a thin section which had been gold coated prior to thin section creation. The figure shows the MMC hosted in maskelynite and augite, and spectrally distinct from the epoxy. Also shown is the spectrum of the epoxy, which is associated with the augite, rather than the organic material. No epoxy peaks were found associated with MMC peaks.

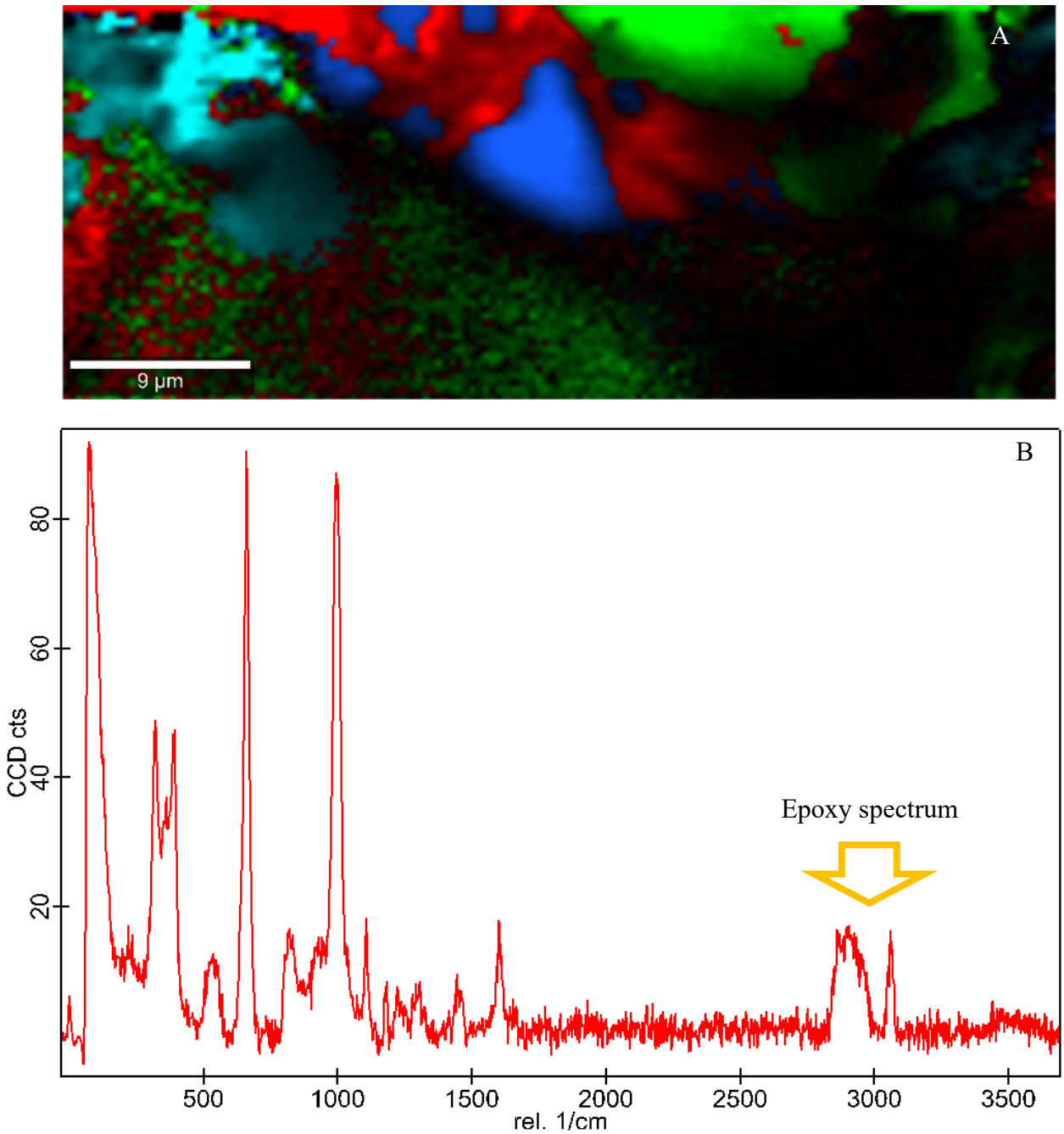

Figure 62 A displays MMC bearing region in Tissint A showing MMC is distinct from epoxy resin used to manufacture thin section. MMC is shown in light blue, epoxy in red, maskelynite in green and augite in dark blue B shows epoxy spectrum associated with augite spectrum demonstrating epoxy resin is associated with some augite in the region, not the MMC.

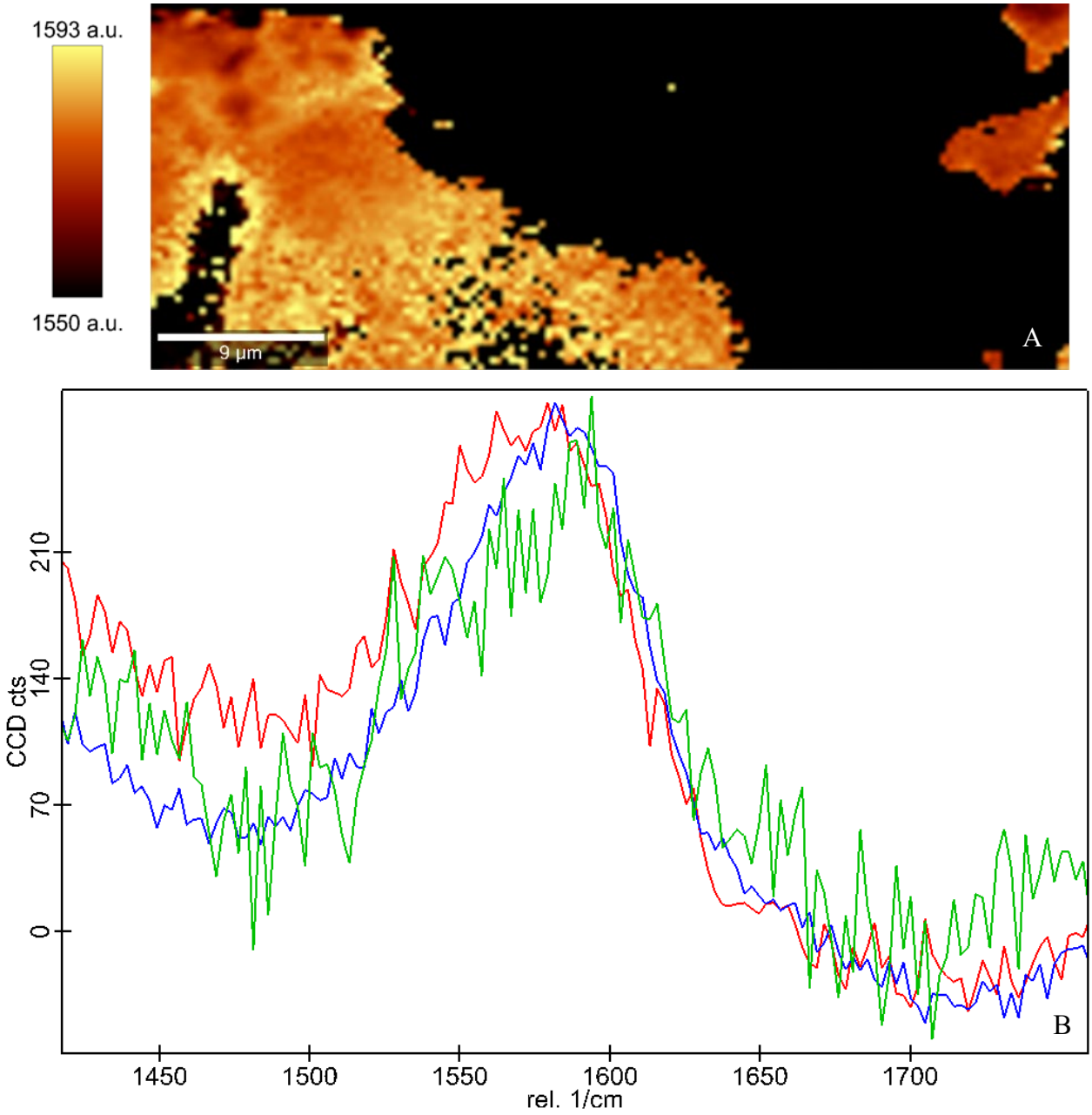

Figure 63 A Raman map of G peak centre position variation observed in MMC rich region in Tissint (same regions displayed in Figure 61and Figure 62. B displays representative peaks showing variable distribution of the G band in the inclusion.

Figure 63A maps the same region as in Figure 62 but displays the variation of the centre of the G band in the MMC. Examples of the corresponding spectra for the G bands from the sample are then shown in Figure 63B, showing that the nature of the macromolecular material varies over a micron scale in this region. This ability to map G band variation is a feature only available in WiTech Project 5+ and therefore such a figure was only created for this sample.

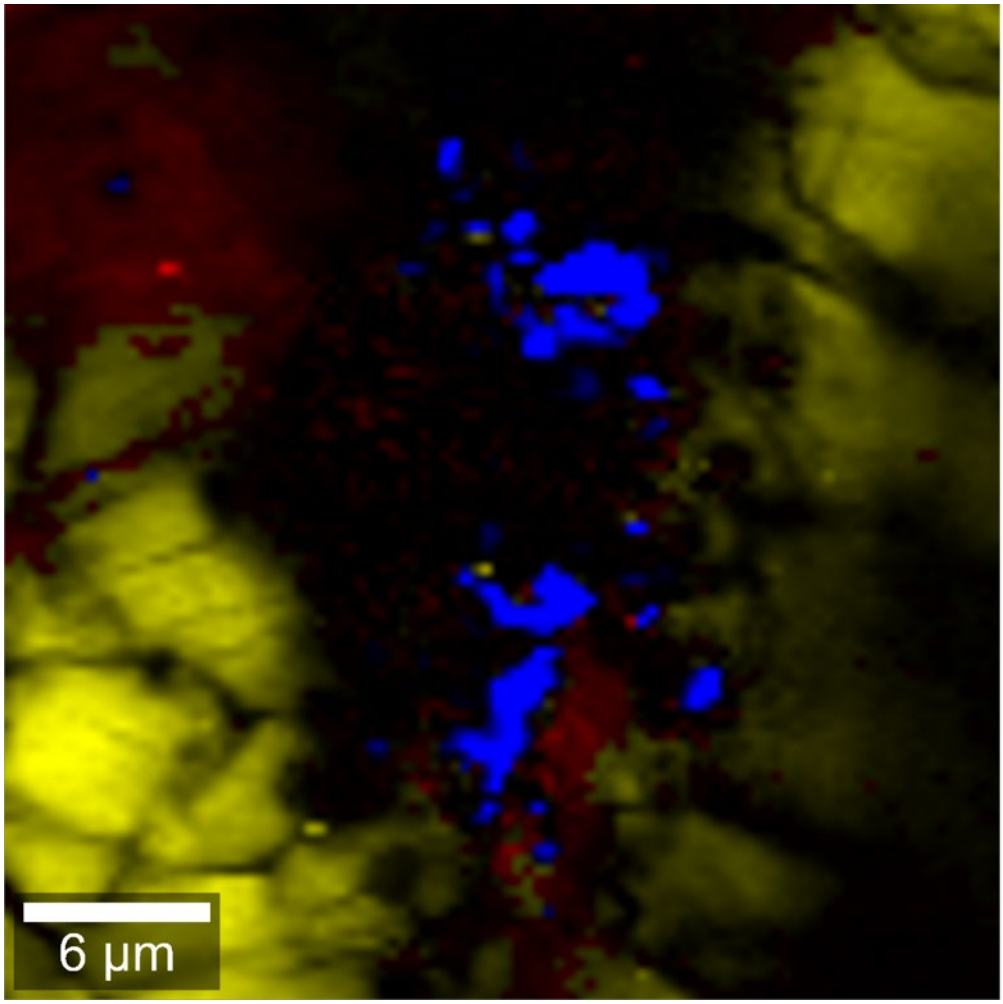

Figure 64 MMC bearing region in Tissint B, showing MMC associated with spinel. MMC is displayed in blue and spinel in yellow. Epoxy resin bearing regions are shown in red, showing most MMC is clear of the epoxy resin.

Figure 64 shows another MMC bearing region in Tissint where epoxy is hosted in the same area scanned with CRIS. This scan was from the second thin section that was on loan from the Natural History Museum. This MMC inclusion is hosted in spinel and the epoxy is closely associated and in some cases in the same regions as the MMC. This region was therefore not chosen for FIB extraction.

Figure 65 and Figure 66 show the detection of likely labile carbon in the thin section Tissint B on loan from the Natural History Museum. MMC was found hosted in pyroxene, with significant epoxy in the region (see Figure 65). During the scan it was noticed that some MMC peaks were only beginning to appear at the end of the integration times, suggesting the laser was interacting with the material. After the scan was complete, the laser was focused on the spot indicated by the crosshairs for 48 seconds (see Figure 65) and the D and G bands began to form over time, suggesting initial labile carbon presence forming macromolecular carbon with heating due to the laser beam (Figure 66).

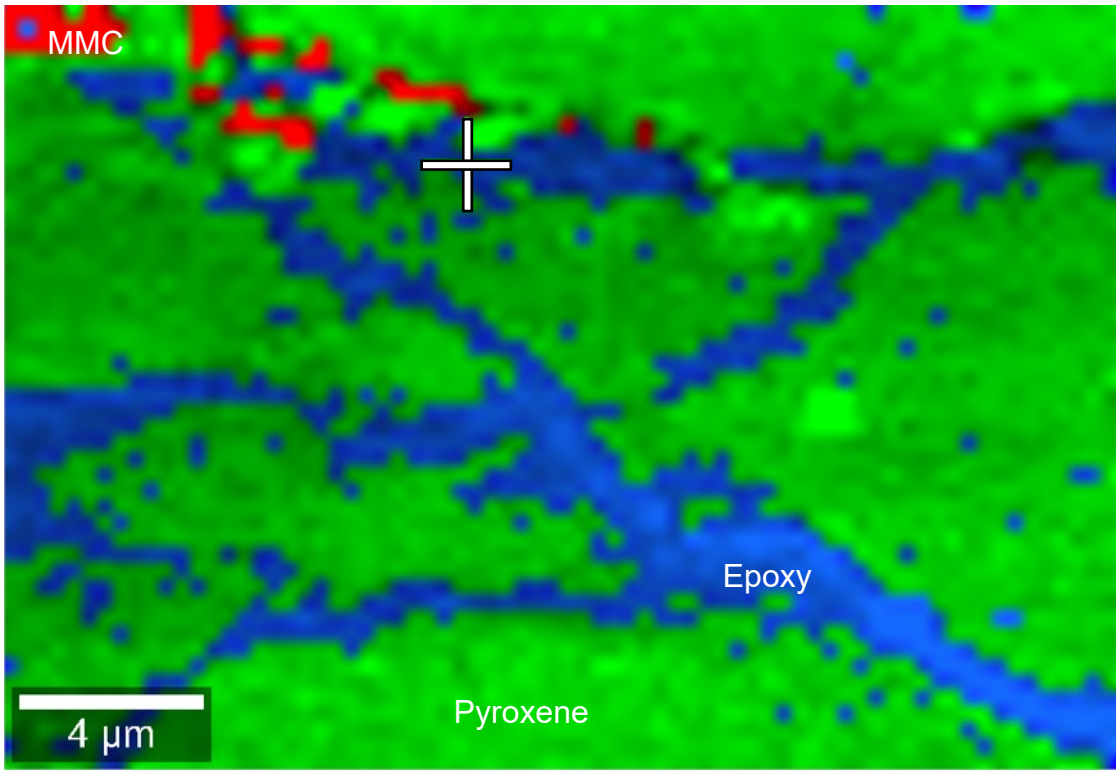

Figure 65 MMC Bearing region in Tissint B which was found to contain labile organic carbon. Cross hairs mark region where single spot scan was carried out for 48 seconds and MMC appeared under laser heating (see Figure 66)

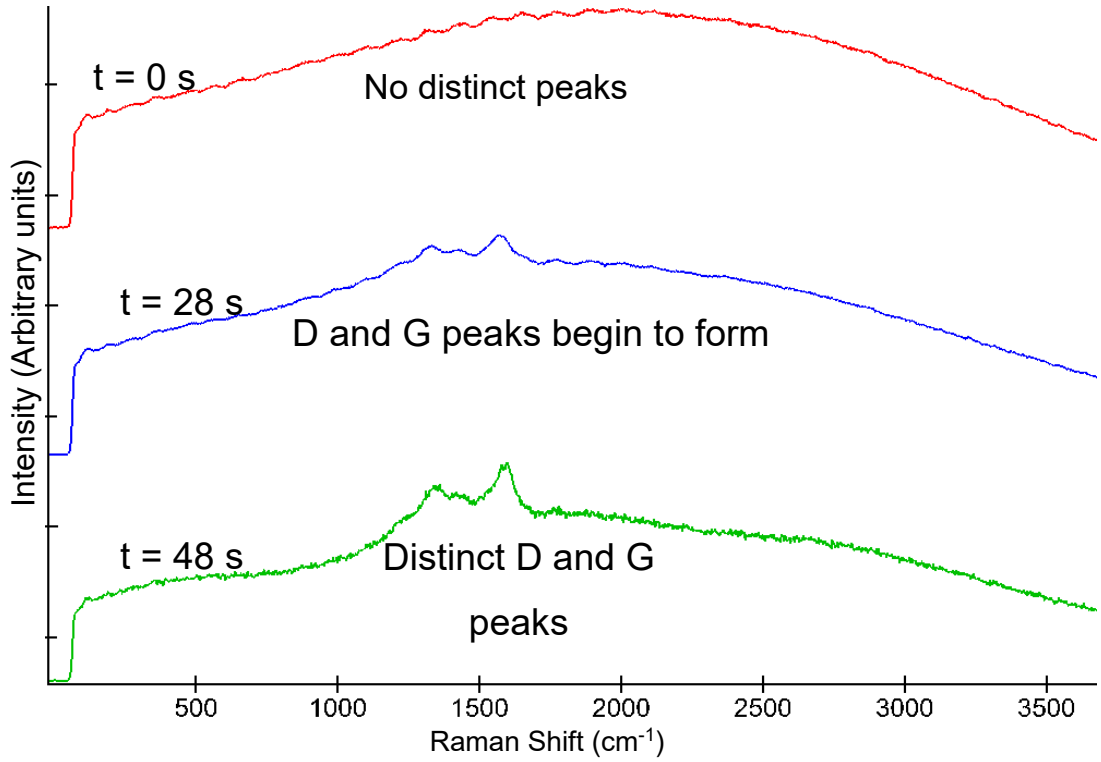

Figure 66 Extract of time series Raman spectra of labile organic material in Tissint B. The Raman laser was focused on the marked region in Figure 65, 1 µm below the thin section surface. 20 successive spectra were acquired over a 48 second period. Initially, only resonance effects were observed in the spectra, with D and G peaks forming under laser heating, indicating increasing maturation of the organics with time. No epoxy peaks are present.

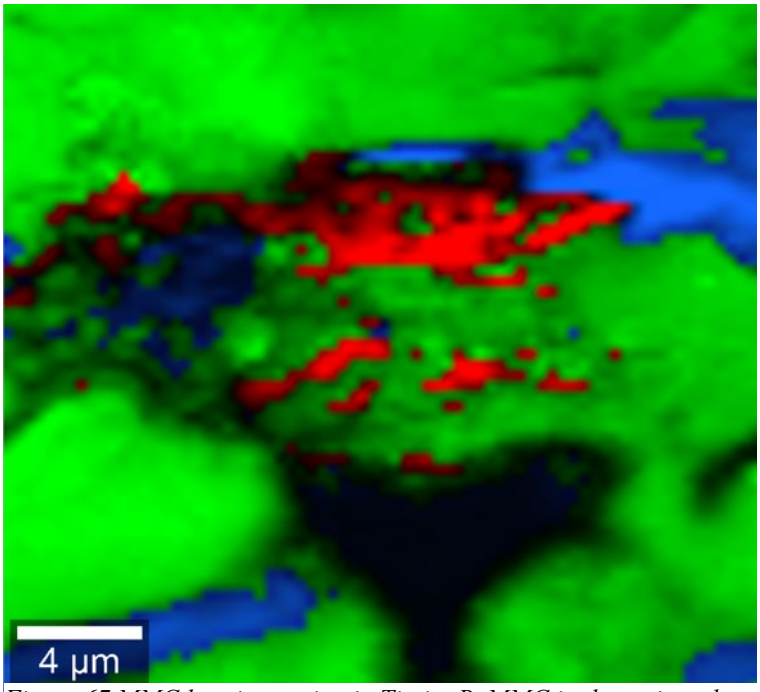

Figure 67 MMC bearing region in Tissint B. MMC is shown in red, pyroxene is shown in green, epoxy resin is shown in blue.

Figure 67 and Figure 68 show two further MMC bearing regions in the thin section Tissint B, on loan from the NHM. Firstly, in Figure 67, the MMC was found hosted in pyroxene, with epoxy nearby, but again with no epoxy peaks associated with the MMC (ie observed in the MMC spectra). Secondly, in Figure 68 the MMC was found hosted in augite, with epoxy also found distinct from its MMC inclusions.

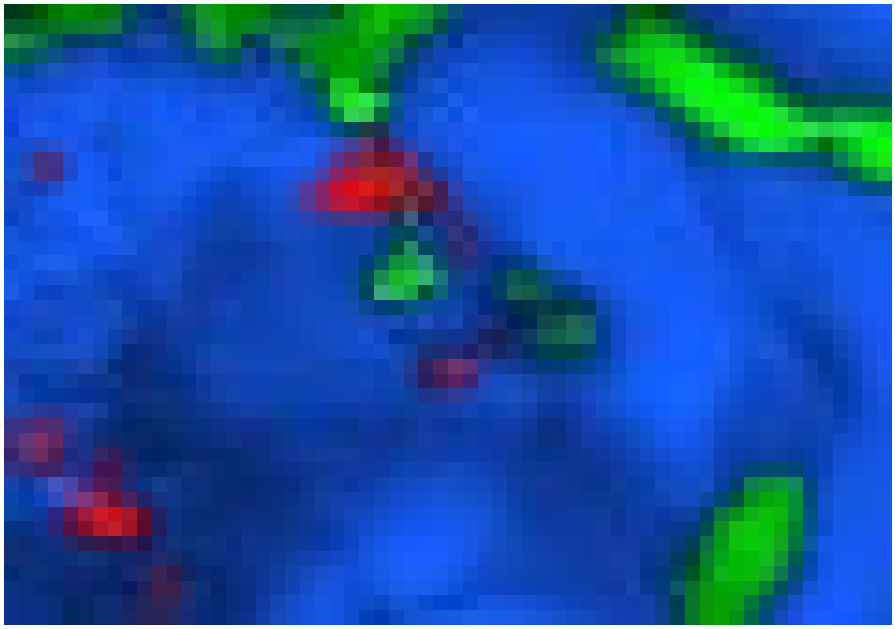

Figure 68 MMC bearing region in Tissint B. MMC shown in green, augite in blue, epoxy is shown in green. Blue augite red MMC green epoxy

One thin section of NWA 8159, prepared with a gold coated chip, was studied with CRIS during the first visit to the Carnegie Planets Laboratory. Nine regions of the thin section were scanned. MMC was successfully detected hosted in augite, close to, but not in direct association with calcite (Figure 69). Four inclusions of MMC were found in this calcite bearing region, each with differing G band centre position (see Figure 70). Whilst searching for MMC, a region of elemental sulfur was also detected (see Figure 71). The sulfur was found associated with hematite and hosted in augite.

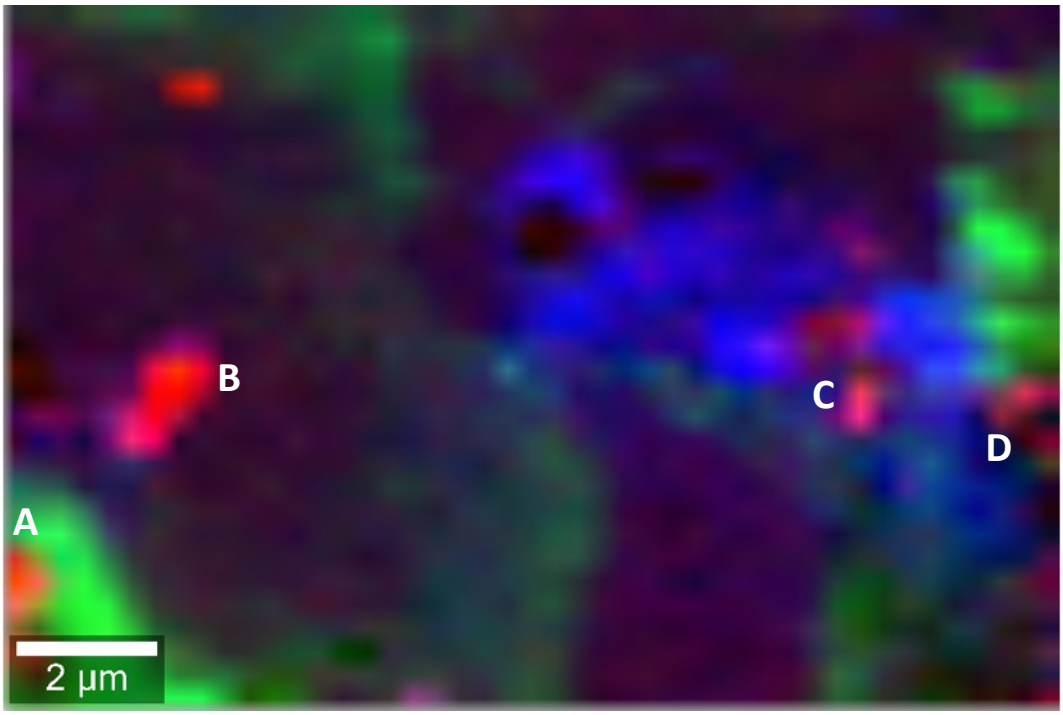

Figure 69 Distribution of MMC in NWA 8159. MMC inclusions shown in red, calcite shown in green, augite shown in blue. Spectra coresponding to the inclusions shown in Figure 70

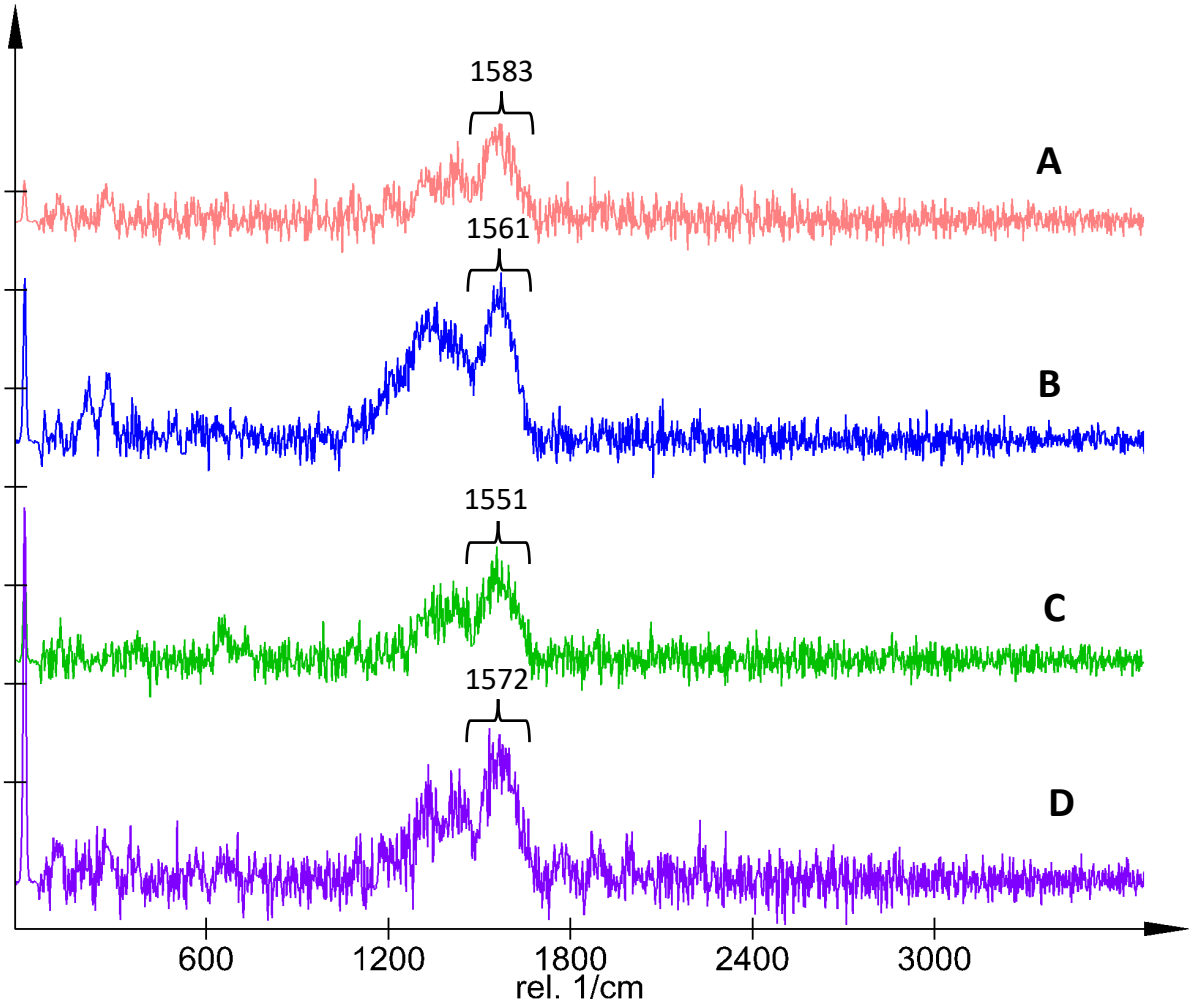

Figure 70 Raman spectra corresponding to the MMC inclusions in NWA 8159, displayed in Figure 69. Demonstrates the variation in G band position and how ordered the organic material is in a small (< 20μm) region.

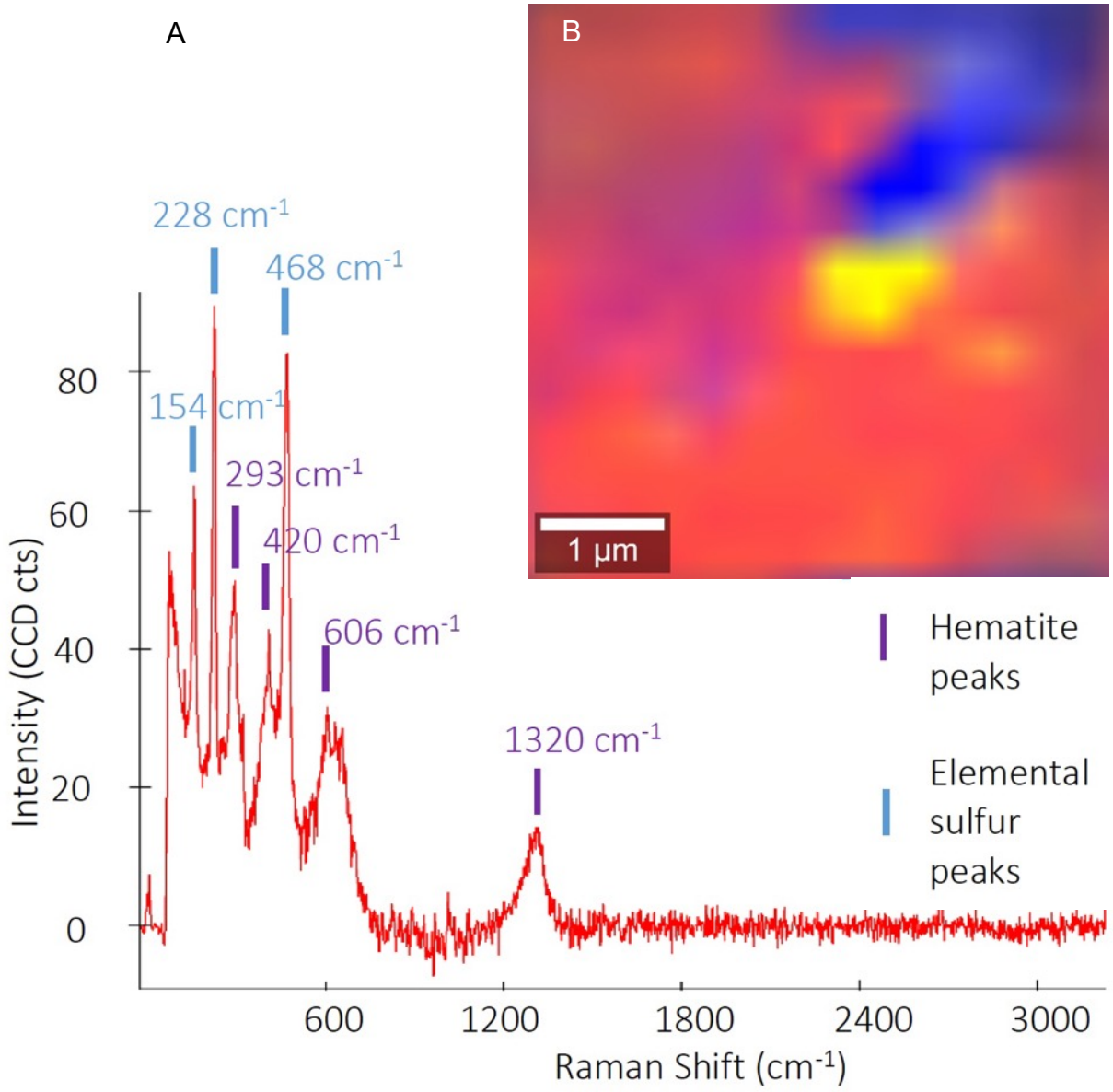

Figure 71 A The Raman spectrum of the elemental sulfur inclusion found in NWA 8159 is displayed in red, showing its association with hematite (hematite and sulfur peaks are highlighted). B Map of inclusion is shown, with elemental sulfur in yellow, augite in blue, and hematite in red.

SaU 008

One thin section of SaU 008 was studied with CRIS during two visits to the Carnegie Planets Laboratory. Three scans were carried out during the first visit, and four scans during the second visit. One region of MMC was found. A depth scan was carried out over

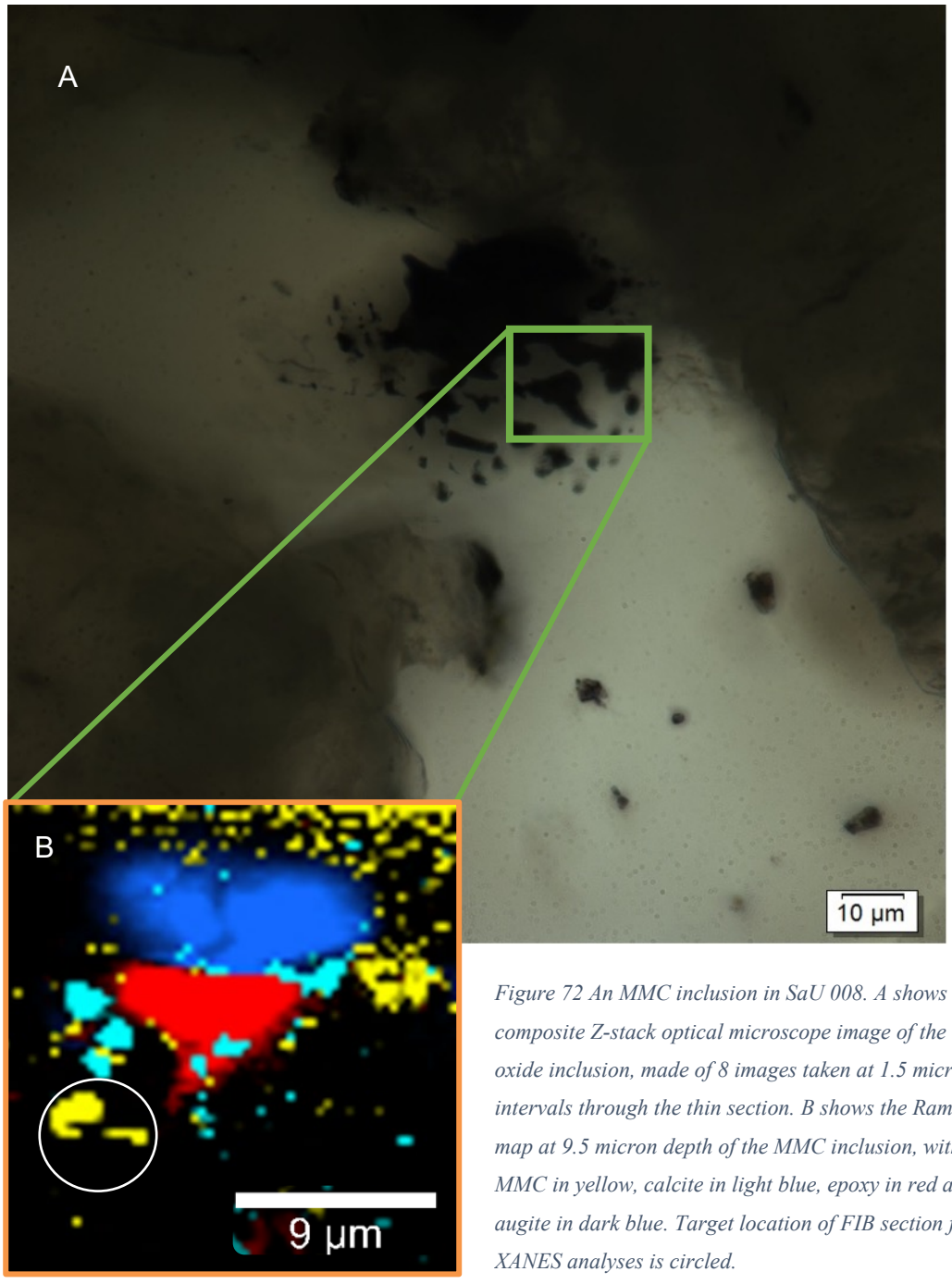

Figure 72 An MMC inclusion in SaU 008. A shows a composite Z-stack optical microscope image of the oxide inclusion, made of 8 images taken at 1.5 micron intervals through the thin section. B shows the Raman map at 9.5 micron depth of the MMC inclusion, with MMC in yellow, calcite in light blue, epoxy in red and augite in dark blue. Target location of FIB section for XANES analyses is circled.

this region (Figure 72), whereby the area was analysed with CRIS at 1.5 micron increments

between 6.5 and 11 microns below the thin section surface, after an initial positive detection of MMC had taken place (see Figure 73). Some MMC in this region in SaU 008 was found to be in association with calcite (see Figure 74). The region chosen for STXM XANES is circled, this was a region without calcite peaks. No MMC was found in SaU 008 during the second visit to Carnegie. This MMC absence could be explained by the thin section having been carbon coated for SEM imaging and FIB extraction, then polished, but some carbon coat remained (see Figure 75 for carbon coat remnants detected during the second visit). The carbon coat creates a dominating signal at high intensities, which would likely prevent the identification of any further MMC-bearing regions.

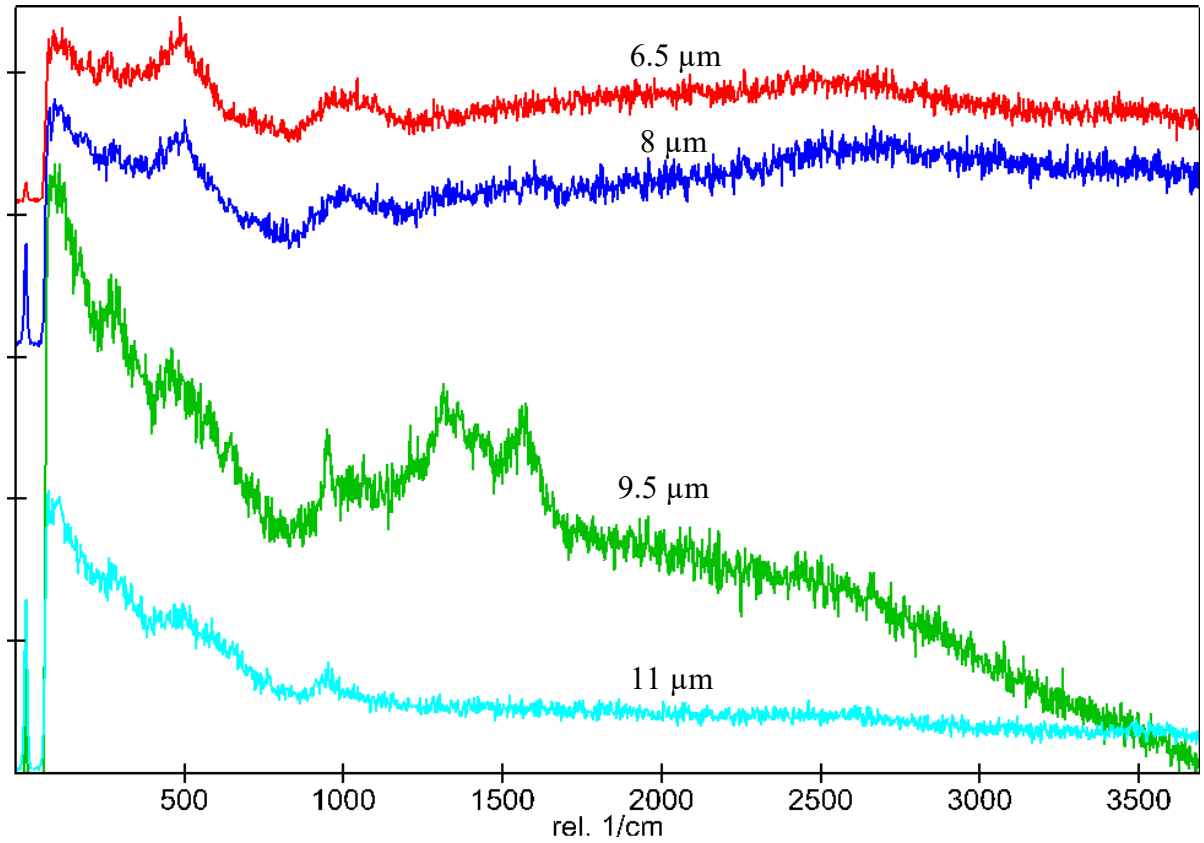

Figure 73 Depth profile Raman spectra of MMC in SaU 0008, region shown in Figure 72, D and G bands only visible at 9.5 µm depth showing how localised the inclusion is, aiding FIB extraction procedure

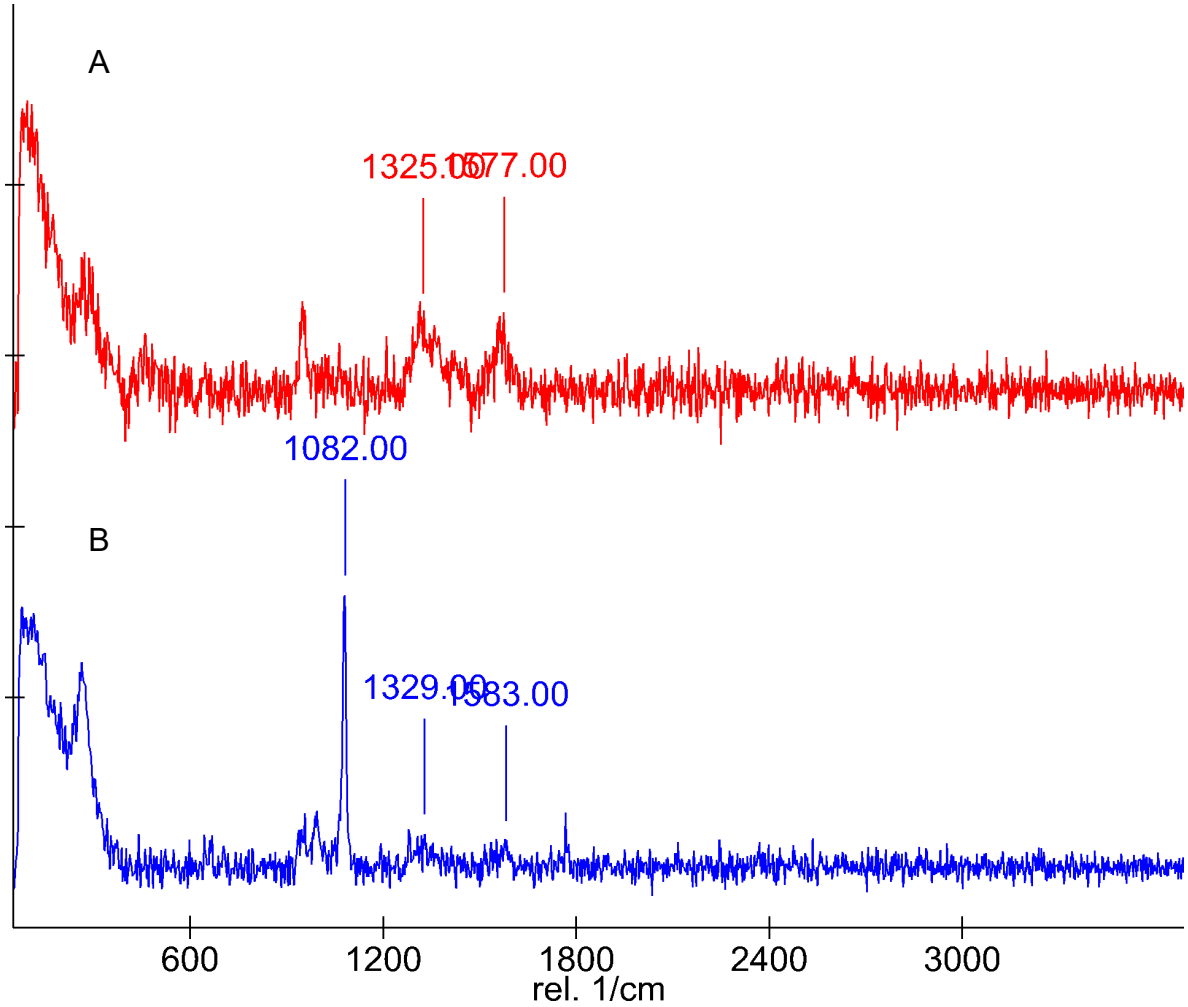

Figure 74 MMC peaks in SaU 008 in depth profile region shown in Figure 72 a) without calcite association, b) less clear MMC bands with calcite peak at 1082 cm^{-1}. Calcite presence indicates that some MMC in SaU 008 is contaminated with likely terrestrial weathering features.

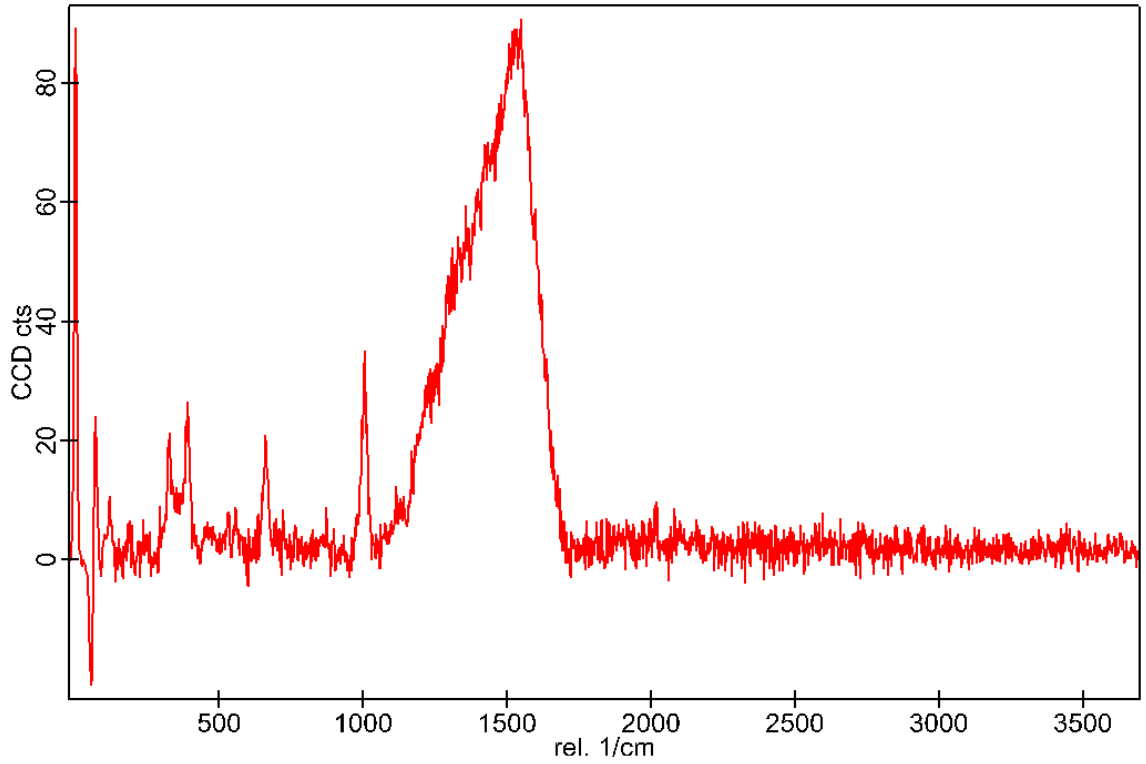

Figure 75 Example Raman spectrum of carbon coat found across SaU 008 thin section on second visit to Carnegie Planets. This thin section had been used for FIB-SEM extraction, then re-polished to re-analyse, but this broad carbon peak dominating the D and G band area suggests that either the polishing was insufficient, or this thin sections cannot be reused for CRIS MMC detection after carbon coating.

Yamato 593 & 749

Two Yamato thin sections were taken to the Carnegie Planets laboratory during one visit, Y 000593 and 000749. One MMC spectrum was found in Y 000749. This region did not appear to contain MMC during the first CRIS scan, however a subsequent single spot scan with a higher retention time successfully detected MMC presence (see Figure 76) Three other scans were carried out on Y 000749 with no MMC detected. Only one region in Y000593 was scanned and no MMC was detected.

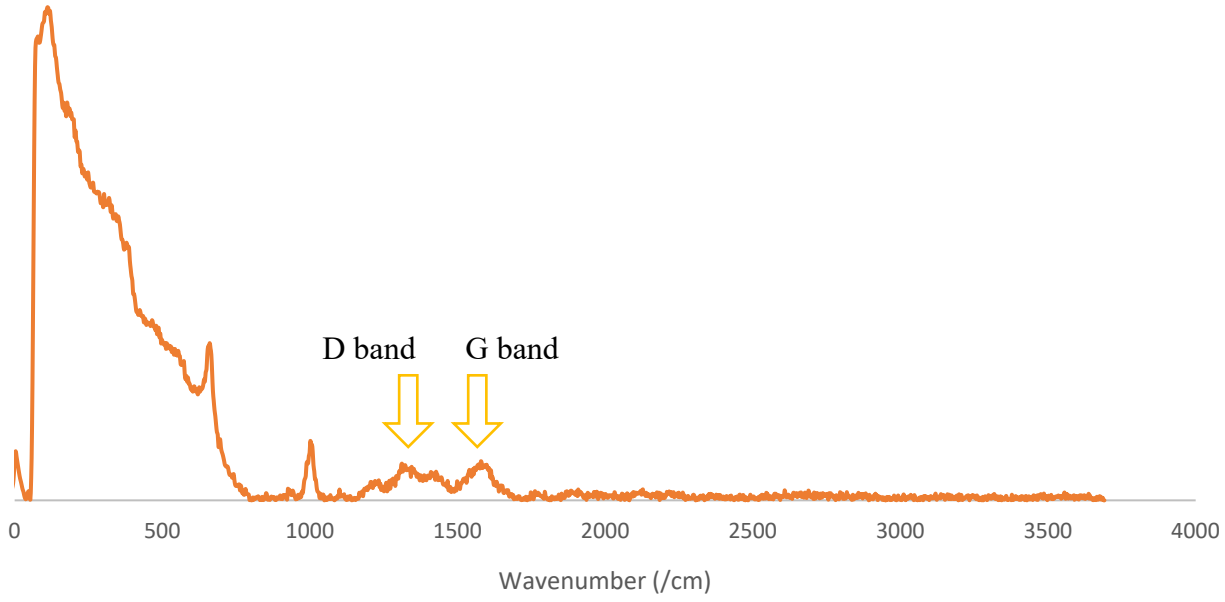

Figure 76 Single spectrum of MMC found associated with pyroxene in Yamato 749. Small D and G bands can be seen. No MMC was found from areas mapped with CRIS scans but a single spectrum scan with a longer integration time of a site of interest in final scan – this is the spectrum shown.

SEM Results

Scanning electron microscopy (SEM) was used in both secondary electron (SE) and backscatter electron (BSE) mode to image the surfaces of thin sections after carbon-rich regions in martian meteorites had been located with MMC using CRIS. This was to aid the location of MMC sites when creating FIB lamellae since FIB-SEM extraction observes the surface of the sample in the first instance, whilst MMC inclusions were extracted from the interior of the thin sections.

Ureilites

SEM was also used to locate carbon-rich regions in ureilite thin sections of Goalpara and Hajmah (a). In this case, EDX was used to detect high intensity regions of carbon (regions that were higher than the carbon coat on the sample). This is because these two ureilite

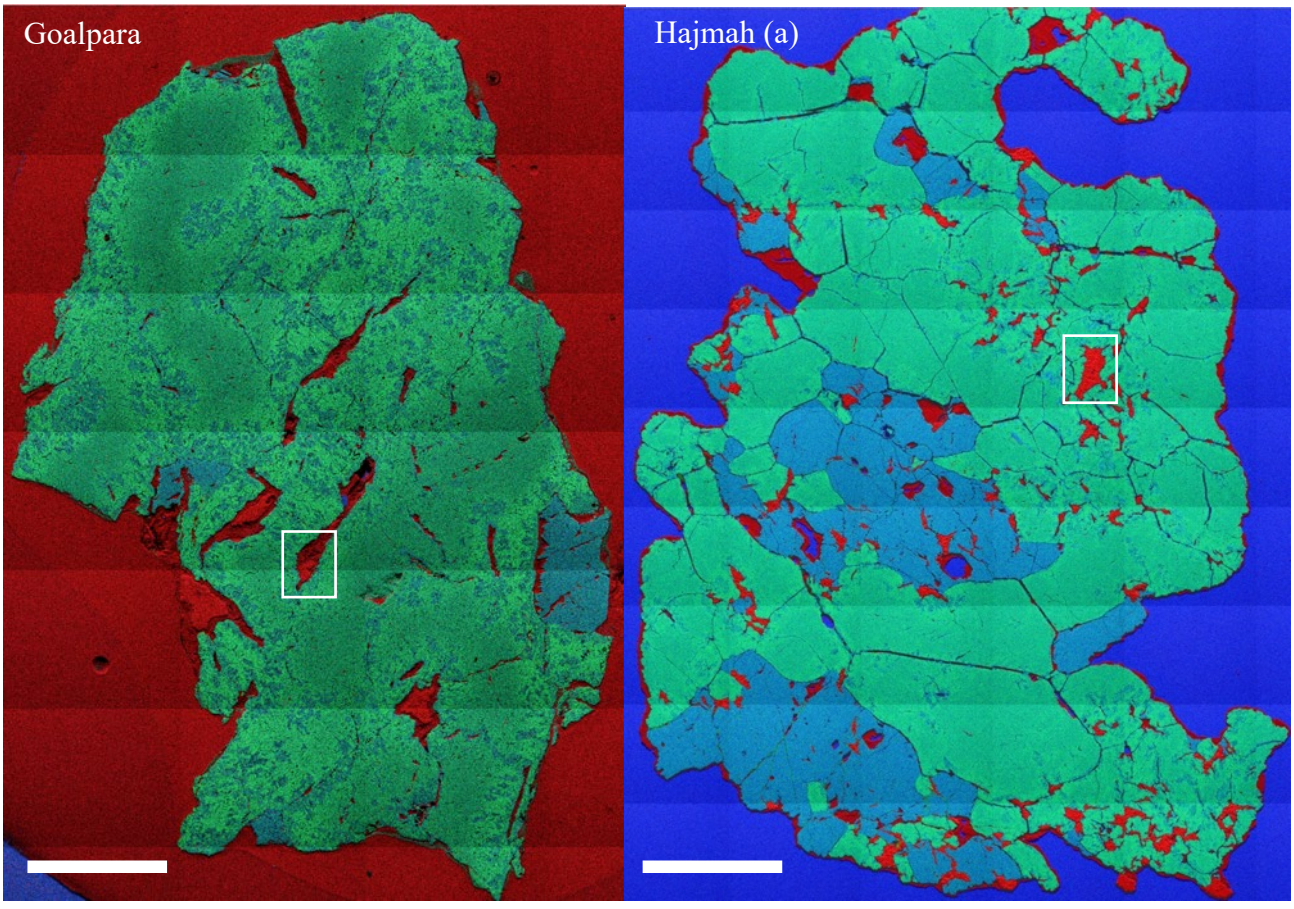

Figure 77 EDS images of the two ureilite samples Goalpara and Hajmah (a). Red represents carbon, green magnesium and blue silicon. White boxes indicate where FIB lamellae were extracted. Scale bars represent 1 mm. Background colours are different due to priority ordering of red, green and blue during figure creation.

samples were loaned from the NHM without access to perform CRIS before scheduled Diamond beam time. The EDX maps are shown in Figure 77, these scans were performed

without elemental standards.

The region of Goalpara that was extracted with FIB-SEM in the first instance is shown in a more detailed EDS image in Figure 78.

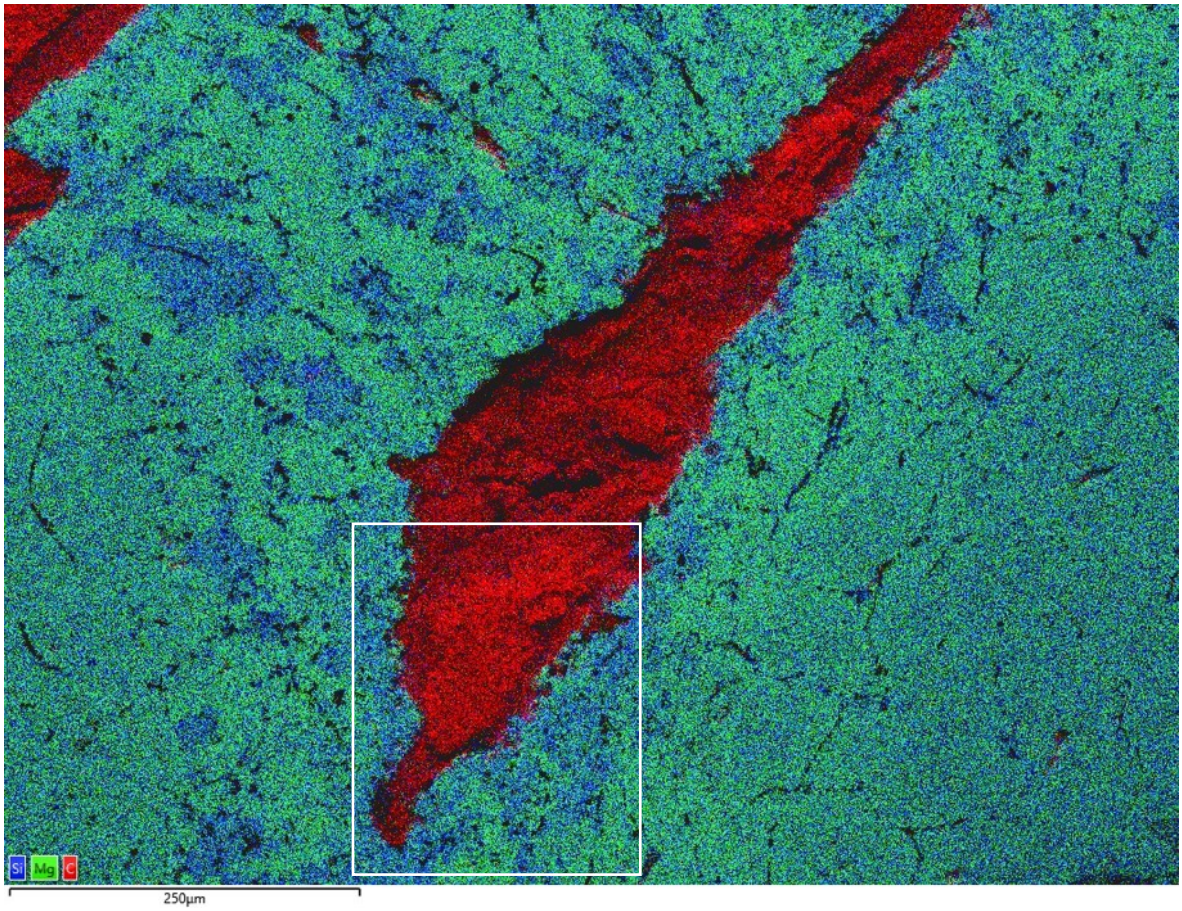

Figure 78 EDS Scan Region of interest in Goalpara where FIB-SEM extraction took place for STXM-XANES analyses. Carbon is shown in red, magnesium in green, and silicon in blue.

STXM XANES

STXM XANES was carried out during three separate trips to Diamond Light Source. The first, in May 2018, the second in September 2019, and third, in December 2019. The carbon K edge peak energies and their corresponding electron transitions used to identify peak features are shown in Table 4. A summary of samples prepared for STXM XANES analyses, and which subsequent analyses were successful is shown in Table 5.

Table 4 Relevant STXM XANES transitions and their corresponding functional groups used to identify features in the spectra in this project (Cody et al., 2008; Brandes et al., 2010; Pao et al., 2010; Kebukawa et al., 2014; Alexander et al., 2017).

Energy (eV)	Transition	Functional group
284.8-285.2	1s-p*	Aromatic
286.5	1s-p*	Ketone
286.9	1s-p*	Nitrile
287.2	1s-p*	Enol
287.2	1s-p*	Phenol
288.4-288.7	1s-p*	Carboxyl
288.6	1s-s*	Diamond
289.5	1s-3p/s	Alcohol
290.1	1s-p*	Calcite
292.0	1s-s*	Graphite

Table 5 Overview of meteorites studied with STXM XANES, both successfully and unsuccessfully, in this project.

Meteorite ID	Number of FIB Lamellae Created	Number of Lamellae studied with STXM XANES	Carbon detected successfully?	Notes
Tissint A	2	1	Yes	One sample lost as was placed on TEM grid at an unstable angle
SaU 008	4	3	No	One sample was lost in transit, it was the sample most likely to contain MMC
NWA 8159	2	1	Yes	One lamella was never thinned, it was an extraction of the elemental sulfur, TEM was planned but never carried out due to instrument down-time and subsequent lockdown
Hajmah (a)	2	1	No	
Goalpara	3	2	Yes	
Sigurdfjelle	1	1	Yes	

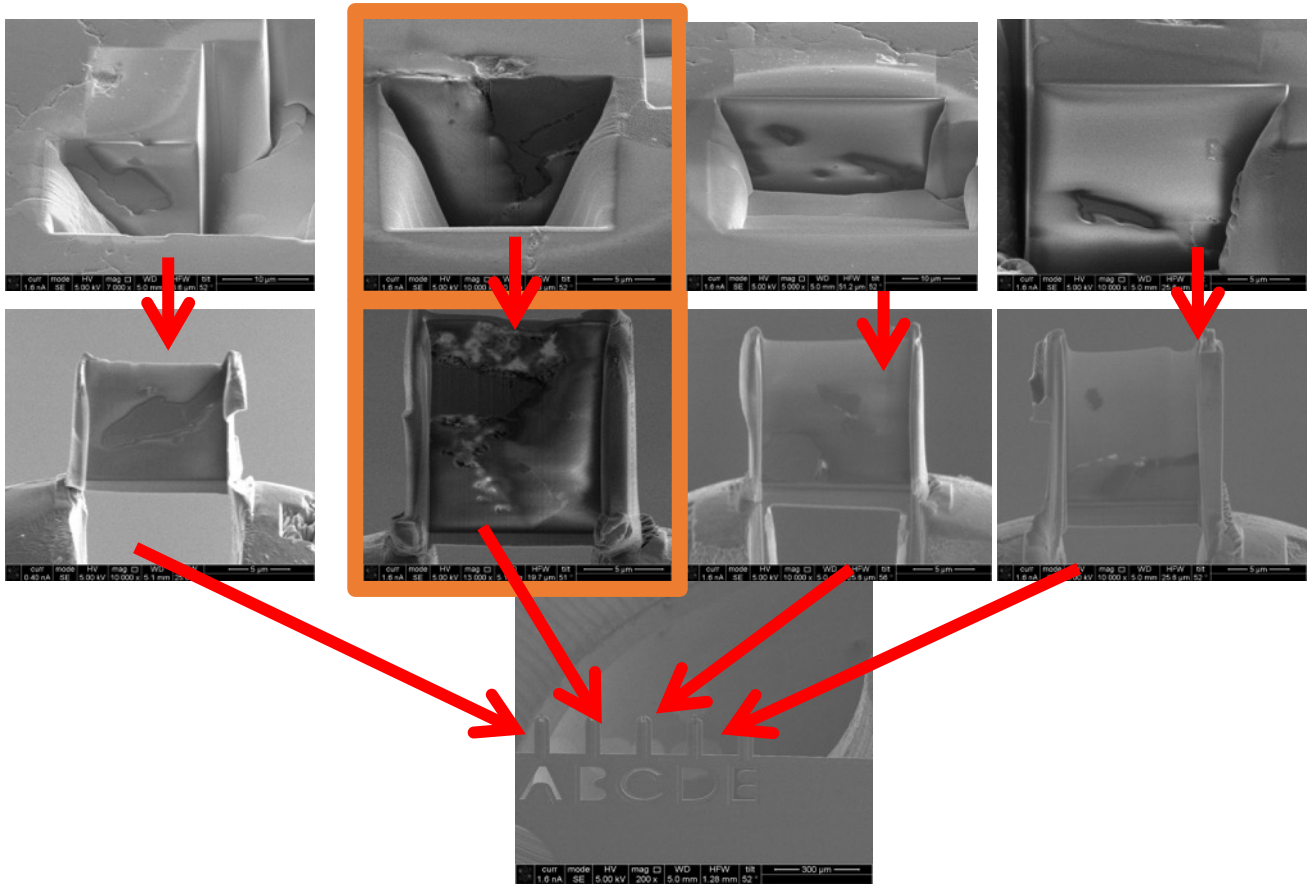

Figure 79 Secondary electron images of the FIB Lamellae extracted from SaU 008. Extract regions are shown (top row), followed by thinned lamellae (middle row), and finally the location on the TEM grid (bottom image). The sample highlighted in the red box is the sample lost in transit prior to STXM XANES.

Six lamellae were created in preparation for the first visit to the Diamond Light Source to perform XANES. One extracted from Tissint, one from NWA 8159, and four from SaU 008. Four were extracted from SaU 008 since a depth profile had been carried out using CRIS, showing that MMC was localised to one small region amongst oxides covering a large area, so it was hoped that by extracting multiple FIB sections, there would be a greater chance of detecting MMC.

One FIB lamella of Tissint was taken to Diamond Light Source during the first visit and scanned at its carbon K edge and nitrogen K edge. The FIB lamella is shown in Figure 80, with the region scanned indicated by a yellow box, and the carbon K edge spectrum is shown in Figure 81, its nitrogen K edge spectrum shown in Figure 82. One FIB lamella of NWA 8159 was also taken to Diamond Light Source during that first visit, this FIB section is shown in Figure 80, with the region scanned indicated by a yellow box, and its carbon K edge spectrum and map is shown in Figure 83.

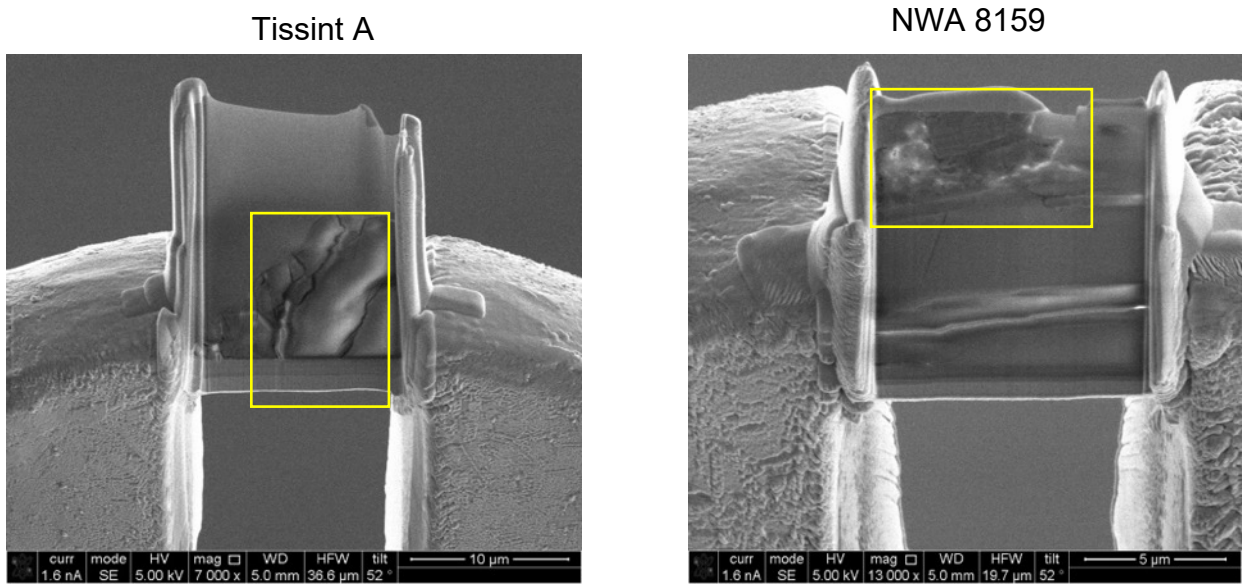

Figure 80 Secondary electron images of FIB lamellae extracted from Tissint A and NWA 8159 and studied with STXM XANES. Yellow box regions denote areas scanned with STXM XANES.

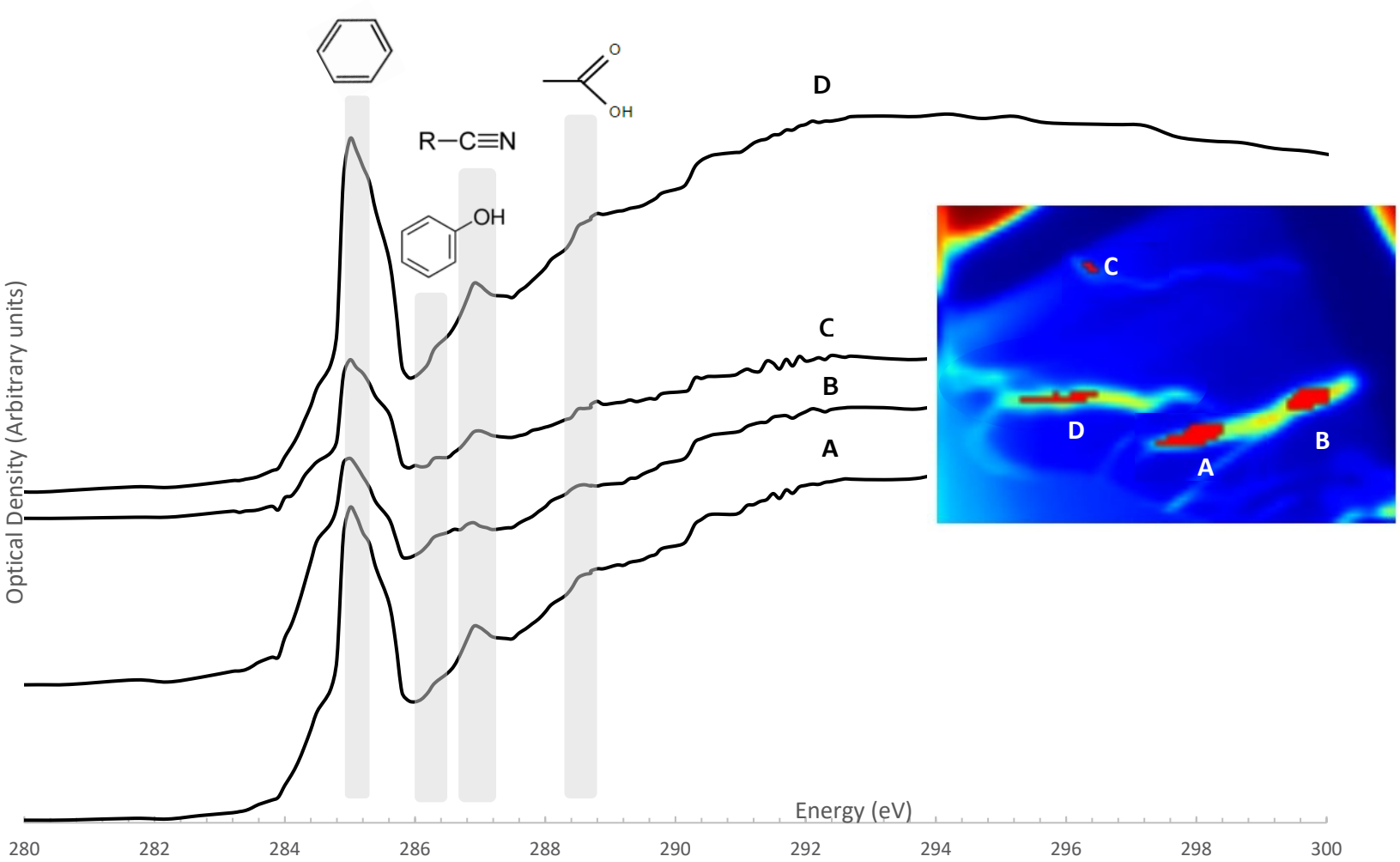

Figure 81 Averaged carbon K edge spectra from regions A-D in intensity scan of Tissint FIB section, subsection of FIB lamella in Figure 80. Aromatic, phenol, nitrile, and carboxyl features are indicated.

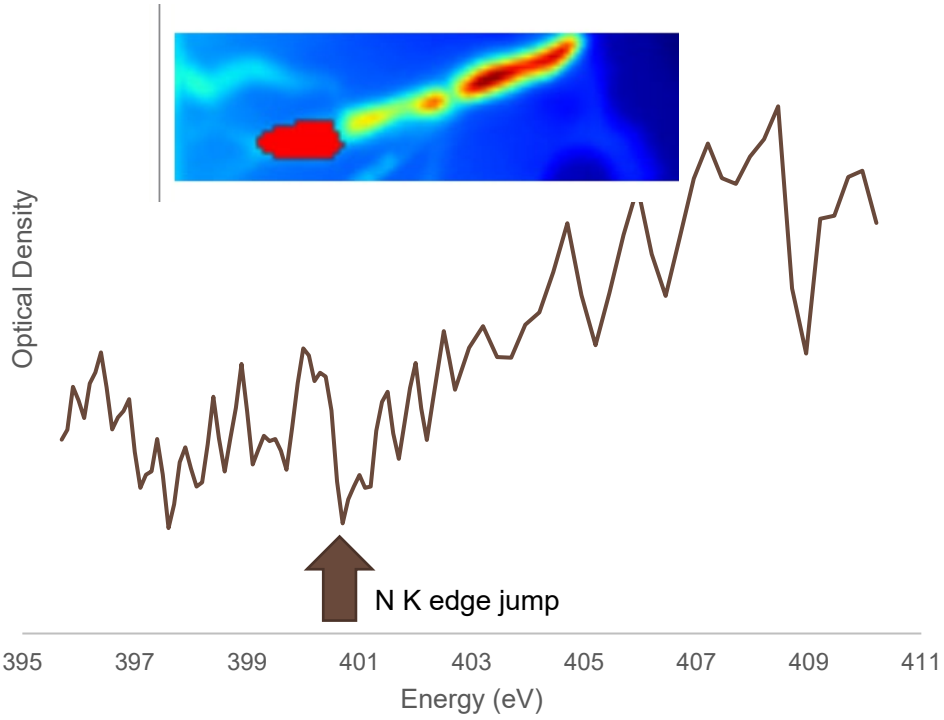

Figure 82 Average Nitrogen K edge STXM XANES spectrum in Tissint for area in red polygon. Edge jump for nitrogen is indicated.

The Tissint A FIB lamella analysed with STXM XANES was found to contain three main MMC rich regions, as shown by Figure 81. These are three vein like regions with A-B, C and D being representative regions where averaged spectra were created used Mantis, an open-source software for X-ray STXM data. After alignment in Mantis, then calibration using the carbonate peak found in NWA 8159 (see below), spectra were plotted using MS Excel and features were identified as shown in Figure 81. Each spectrum has a well-defined aromatic peak at ~285.2 eV, followed by a weak enol/phenol feature at 287.2 eV (taken to be phenol, given the presence of aromatic rings, although an enolic structure cannot be ruled out). A distinct nitrile functional group feature is then observed at 286.9 eV - which is consistent with the nitrogen K edge jump observed in Figure 82 for this sample -. Finally, a carboxyl feature is observed at 288.6 eV.

A nitrogen K edge scan was carried out in the A-B region, since the carbon K edge peak intensity was high enough, this was a good possible region for nitrogen detection. The nitrogen K edge scan is shown in Figure 82 the spectrum represents the area highlighted in the map. Although the edge jump at ~400 eV is discernible, there is too much noise to discern any other peaks in the spectrum.

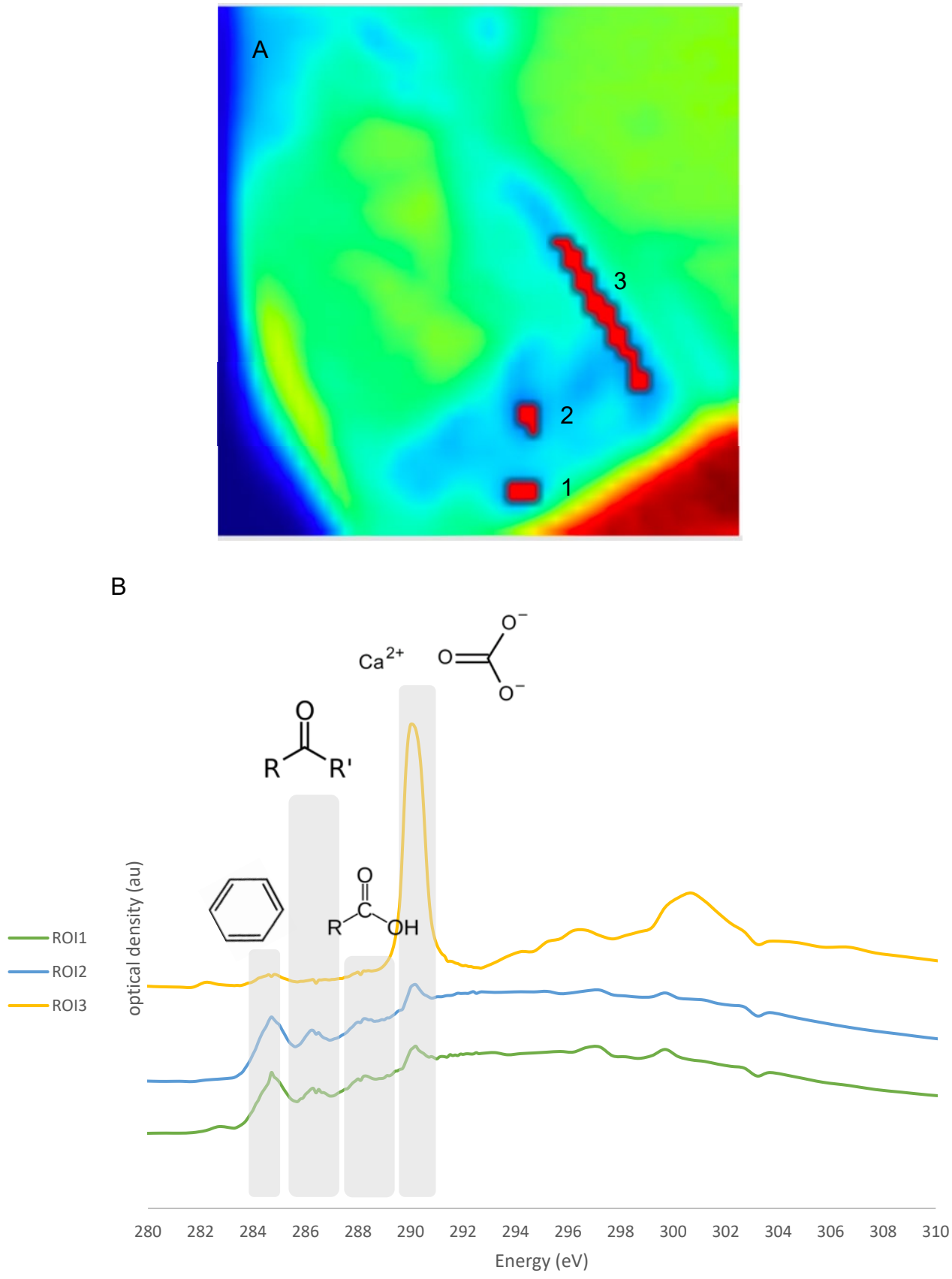

Figure 83 a) A carbon K edge optical density map of the scanned region of NWA 8159 displayed in Figure 80. Specific regions of interest with high carbon abundance are indicated. b) Spectra corresponding to those C-rich regions of interest are shown, with aromatic, ketone, carboxyl, and calcite energies indicated.

One FIB lamella from NWA 8159 was studied using STXM XANES at the carbon K edge only, during the first visit to Diamond Light Source. The optical density map of the region scanned is shown in Figure 83A, with corresponding spectra for three regions of interest displayed in Figure 83B. These regions of interest show a variation in MMC content depending on calcite peak intensity. ROI 1 contains a high intensity peak of calcite (calcium carbonate) at 290.1 eV, and a minor aromatic peak. ROIs 2 and 3 have much more distinct aromatic carbon peaks, as well as ketone peaks.

SaU 008 was analysed during the first visit to the Diamond Light Source. Four FIB lamellae were created and placed on a TEM grid as shown in Figure 79. Unfortunately, one lamella perished during transit to Diamond, and was the most likely carbon bearing candidate amongst the lamellae since its features most strongly resemble that of Tissint. This sample is shown in Figure 79 highlighted by a red box. No carbon was found in the three lamellae that survived, thus their spectra are not shown here.

Ureilites

Five ureilite FIB lamellae were created, for two visits Diamond Light Source beamline I08 in late 2019 (September and December). One of these (Goalpara) was analysed with STXM XANES in September 2019 and two additional (one Goalpara and Hajmah (a)) in December 2019, during an invited additional visit with collaborators Dr Andrew Steele and Dr Liane Benning. The five lamellae created are summarised, with the IDs used for the study in Table 6.

Table 6 Summary of ureilite FIB lamellae created and subsequently analysed in this study

Lamella ID	**Description**	**Studied with STXM?**
G-1	Goalpara FIB lamella	Yes – Sept 2019, C detected & N edge jump
G-2	Goalpara FIB lamella	Yes – Dec 2019, C detected
G-3	Goalpara FIB lamella	No
H-1	Hajmah (a) FIB lamella	Yes Dec 2019, C detected
H-2	Hajmah (a) FIB lamella	No

Carbon was successfully detected in G-1, G-2, and H-1. SEM images of these three FIB lamellae analysed are shown in Figure 84 and Figure 85, taken after the sections had been thinned, with the areas in the yellow box showing the regions scanned with STXM, firstly at the carbon K edge, and in the case of the first Goalpara sample, also at the nitrogen K edge. Figure 86 shows a comparison of the average representative carbon K edge spectra for the Hajmah (a) and second Goalpara samples, allowing basic comparisons to be made. The remaining figures show detailed information from the STXM scans with spectra from individual regions of interest in the lamellae. Aromatic carbon was found throughout as well as graphitic carbon, but no nanodiamonds, despite them being detectable by STXM XANES, and fairly common features in ureilites (Nakamuta and Toh, 2013; Kebukawa et al., 2014). All spectra were calibrated using calcium carbonate which has a defined peak of

~290.1 eV (Brandes et al., 2010).

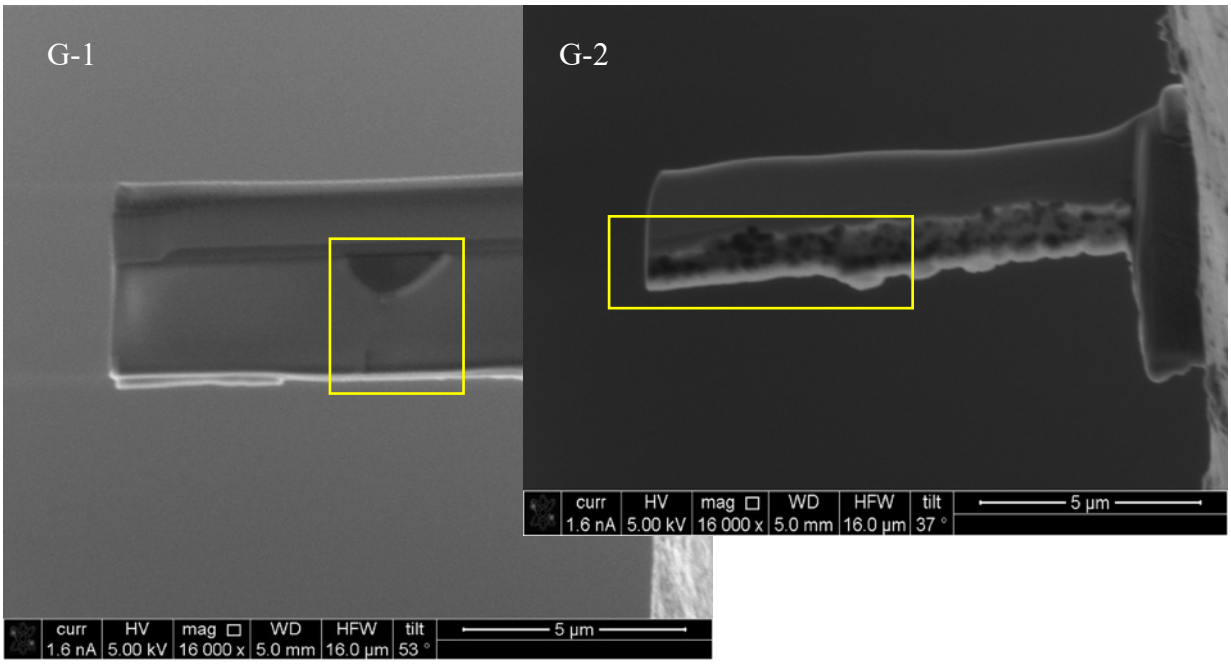

Figure 84 Goalpara FIB lamella G-1 scanned with STXM XANES at Diamond Light Source. Lamella G-1 was studied during a visit in September 2019, and lamella G-2 during December 2019. Yellow boxes indicate regions scanned with XANES.

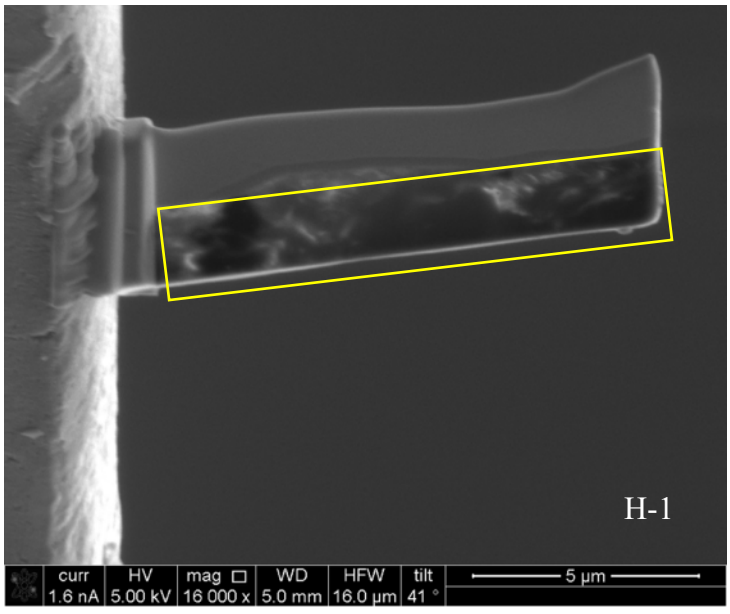

Figure 85 Hajmah (a) FIB lamella H-1 scanned with STXM XANES at Diamond Light Source in December 2019. Yellow box indicates region scanned with XANES.

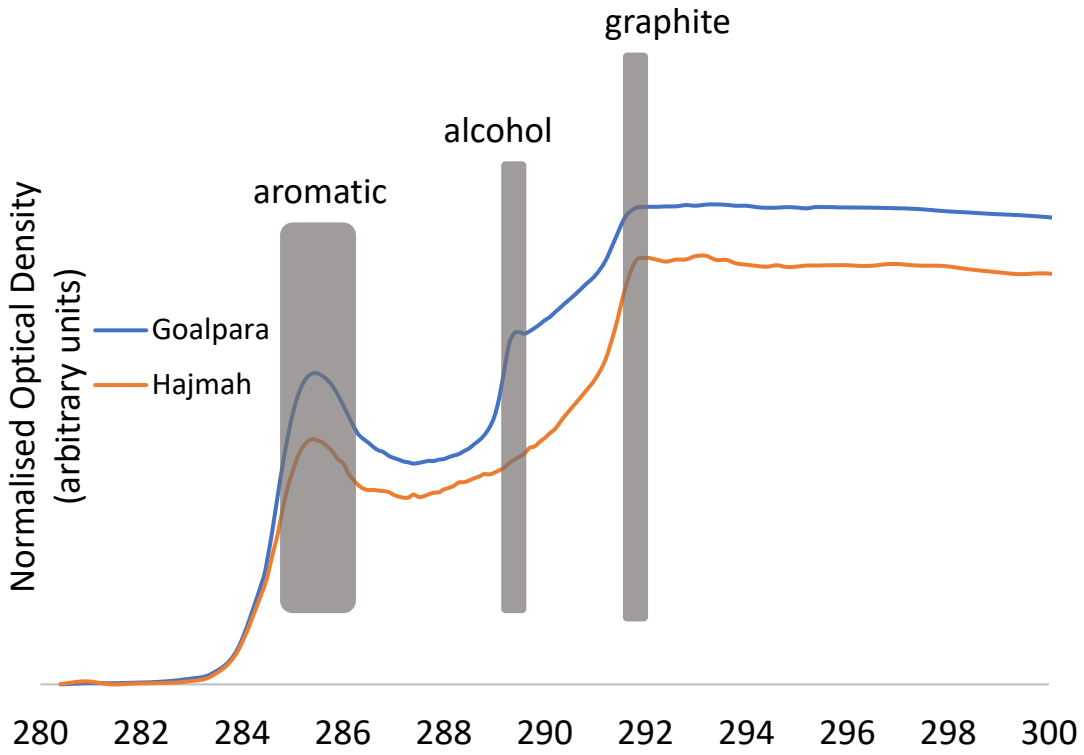

Figure 86 Comparison of average carbon K edge spectra in G-2 and H-1, representing the two ureilites studied. Aromatic, alcohol, and graphite peaks are shown.

During the second visit to the Diamond Light Source in September 2019, one FIB lamella of Goalpara was analysed with STXM XANES (G-1 in Figure 84). Both carbon and nitrogen K edge scans were carried out on this sample. In the first region of interest, aromatic carbon was detected. A nitrogen K edge scan was also carried out in this region of G-1, and an edge jump consistent with nitrogen associated with this organic material was observed (see Figure 87) (Leinweber et al. 2007). The N XANES and C XANES spectra for both are too noisy to discern any other peaks for this region in the FIB lamella. Lower down in the FIB lamella (G-1), aromatic carbon was also detected, but no nitrogen edge jump was detected in association with this region (see Figure 88).

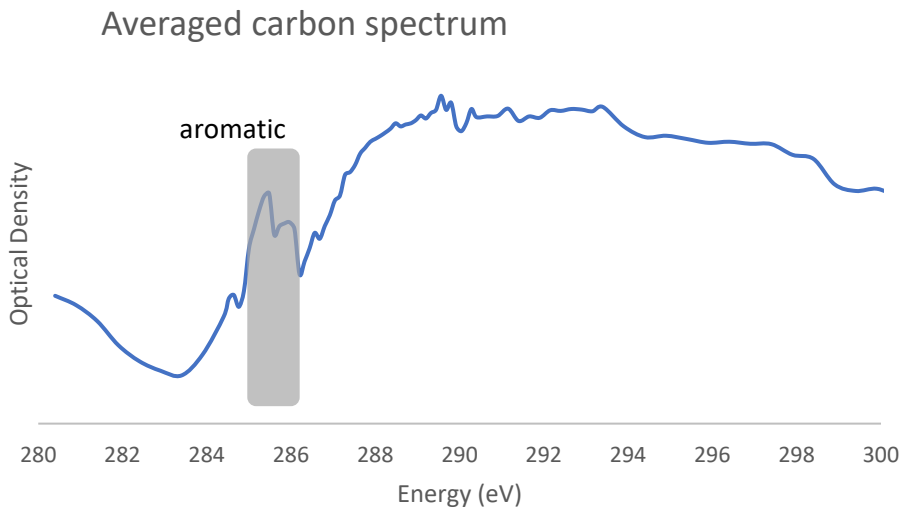

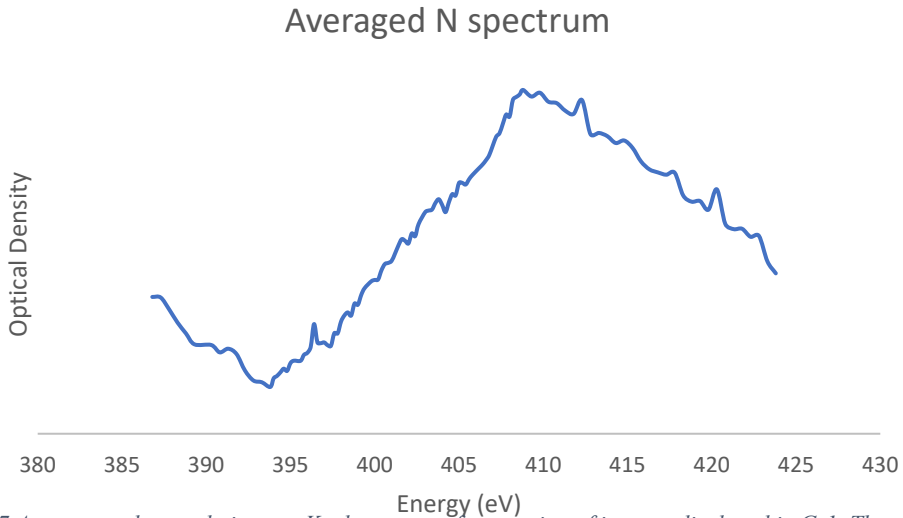

Figure 87 Average carbon and nitrogen K edge spectra from region of interest displayed in G-1. The aromatic energy is shown in the carbon K edge spectrum, whilst all other features are likely artefacts/noise. The edge jump in the nitrogen spectrum is discernible, with all other features likely noise.

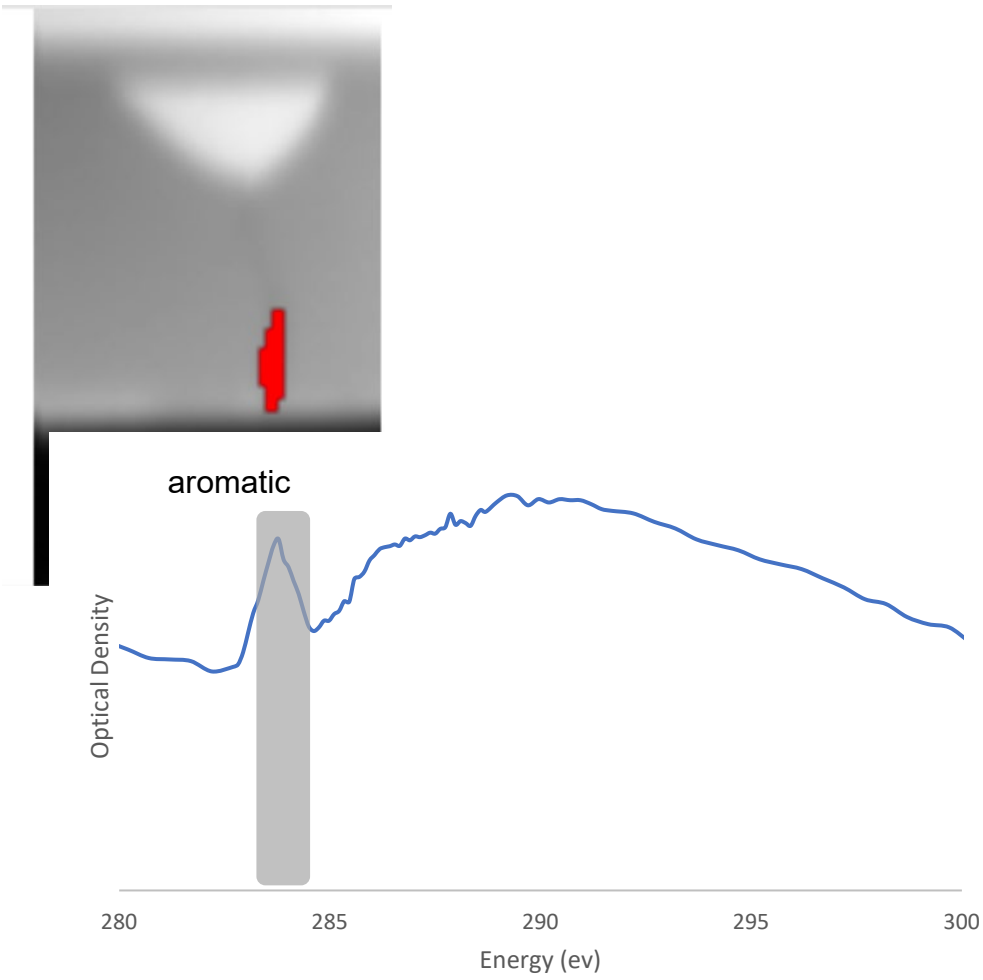

Figure 88 The average carbon K edge in the region highlighted in G-1.

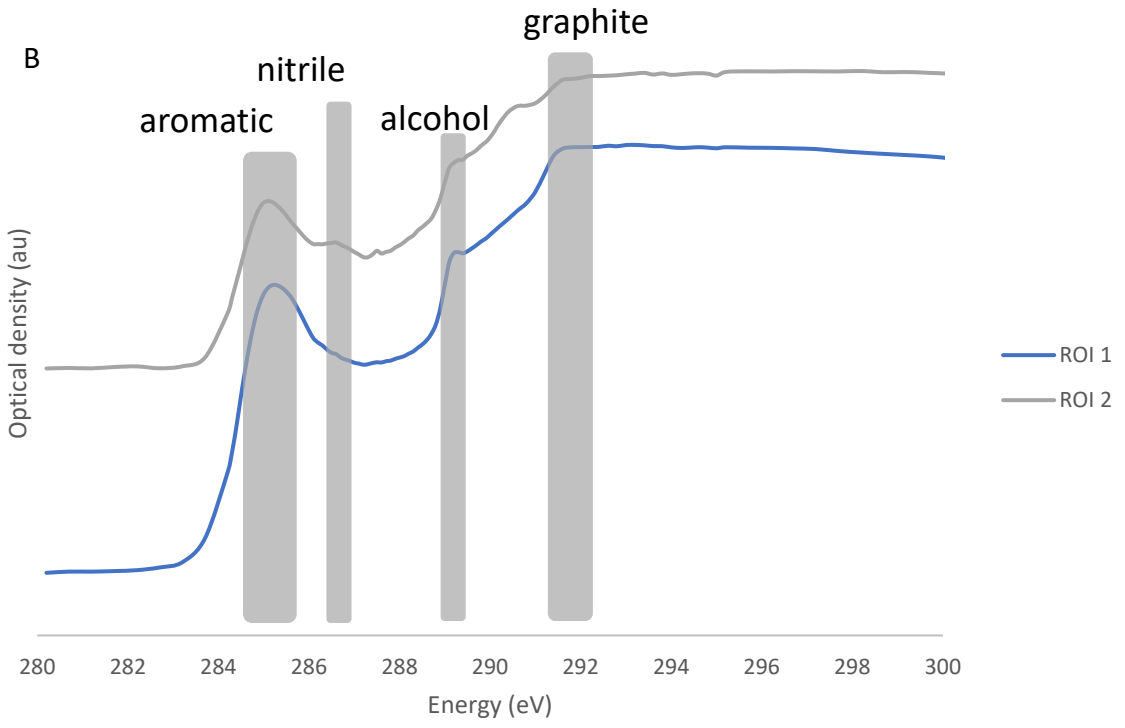

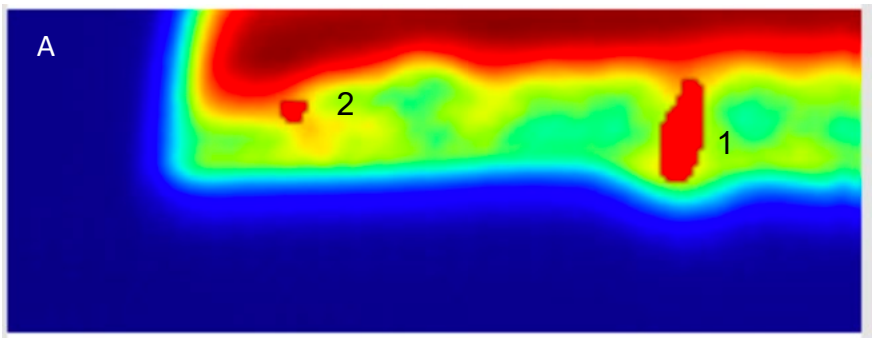

Figure 89. The average carbon K edge in G-2. Two regions of interest are highlighted in the optical density map (a), and their corresponding spectra are shown in (b), where aromatic, nitrile, alcohol, and graphite energies are highlighted.

During the third visit to Diamond Light Source, in December 2019, one additional FIB section of Goalpara (G-2) was scanned at the carbon K edge. The optical density area scan and the corresponding average spectra from two regions of interest are shown in Figure 89. Region of interest 1 contains aromatic carbon, an alcohol functional group, and graphite, whilst the second region of interest has the same functional groups, with an additional nitrile group. This trip was at the invitation of collaborators Andrew Steele and Liane Benning, thus additional nitrogen scans could not be carried out, though given the small nitrile feature, it is expected a small nitrogen edge jump would be observed in this region.

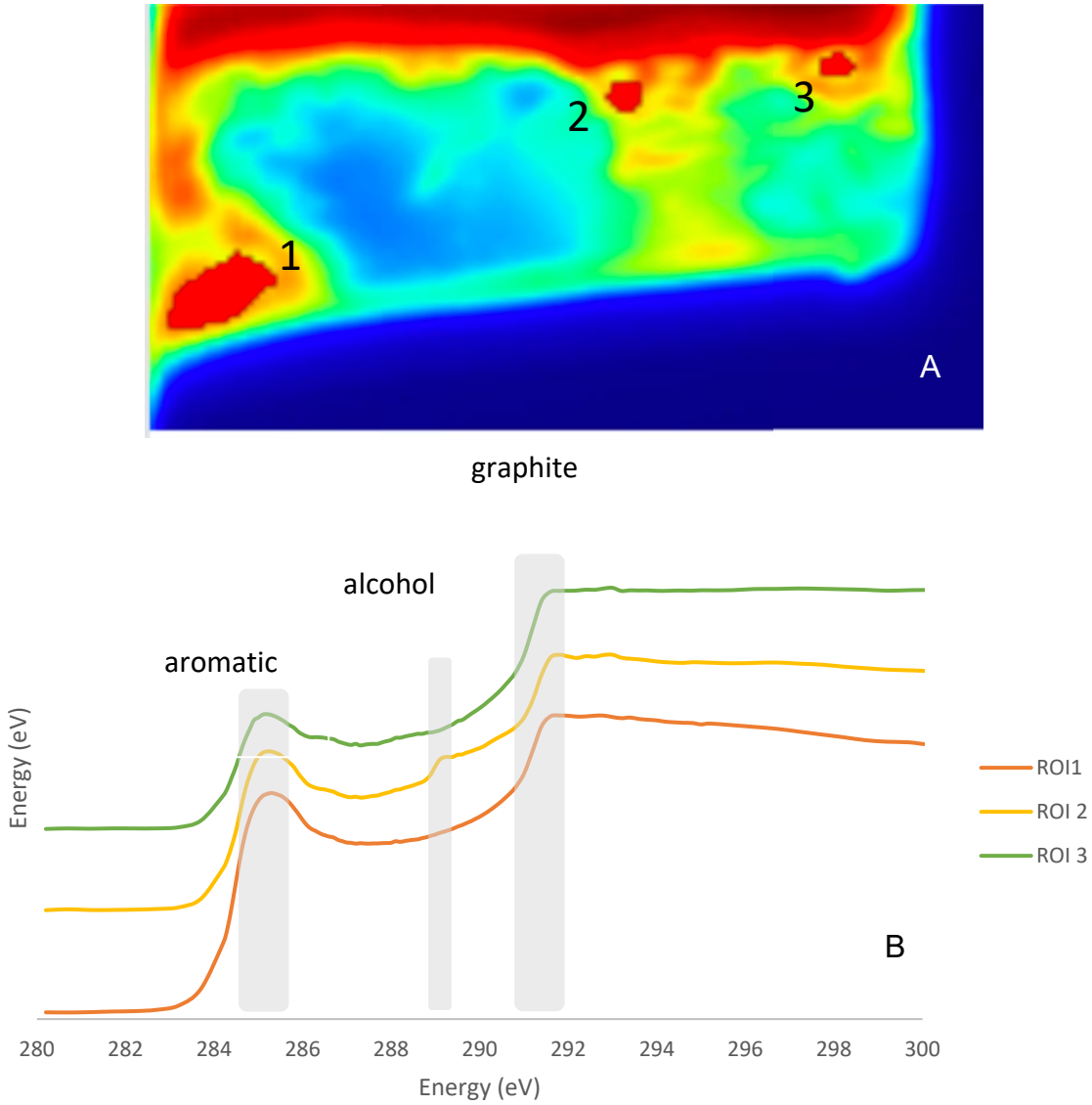

Figure 90 Hajmah (a) STXM XANES carbon K edge scan of H-1 region in yellow box shown in Figure 85. Optical density map is shown with three regions of interest indicated, and their averaged carbon spectra shown. Spectral features are highlighted.

One FIB lamella of Hajmah (a) (H-1) was scanned at the carbon K edge during the third visit to Diamond Light Source. The optical density area scan is shown in Figure 90 with three regions of interest (ROI) highlighted, and their corresponding spectra shown. The spectra from ROIs 1 and 3 show the same aromatic and graphitic features, with ROI 2 containing an additional alcohol functional group, on top of the aromatic and graphitic energies.

Three FIB lamella from the BVC samples were created, two from theSigurdfjellet site and one from the Sverrefjellet site (BVC1-3, see Table 7).

Table 7 Summary of BVC Mars analogue FIB lamellae studied at the Diamond Light Source in 2019.

Lamella ID	**Description**	**Studied with STXM?**
BVC-1	FIB lamella fromSigurdfjellet	Yes, in Sept 2019. Carbon detected
BVC-2	FIB lamella fromSigurdfjellet	No, due to beamline disruption
BVC-3	FIB lamella from Sverrefjellet	No, due to beamline disruption

These FIB sections were brought to the second visit to Diamond in September 2019. Unfortunately, during this four-day trip approximately 50% of the time there were faults with the beamline meaning STXM could not be carried out, and so only one of the three lamellae was scanned at the C K edge. This was aSigurdfjellet sample and is shown in Figure 91. No prior CRIS/EDS was required as the carbonate globules are clearly visible in BSE during FIB-SEM (see introduction). A whole area carbon K edge scan was carried out (Figure 92) followed by a smaller area scan with smaller pixel sizes (Figure 94). This latter region is shown by the yellow box, and the corresponding C K edge spectrum is shown below. Also shown is the calcium carbonate peak used to calibrate the measurements for this visit (Figure 93).

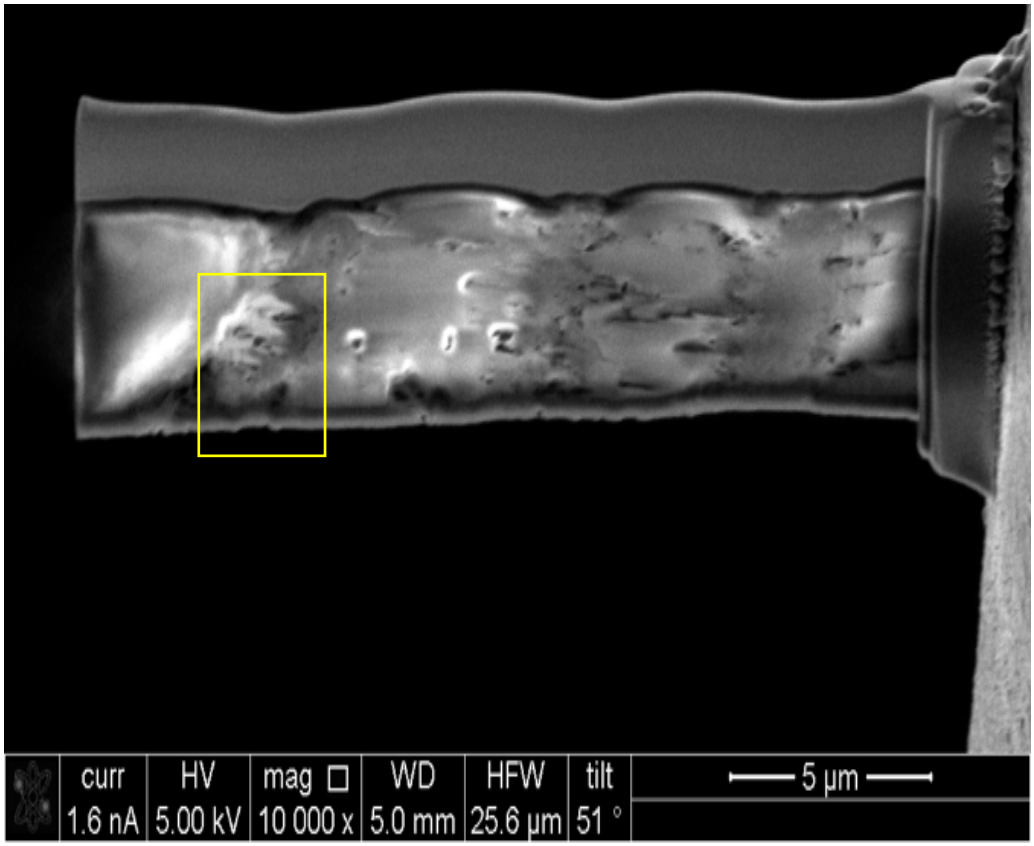

Figure 91 FIB lamella BVC-1 extracted fromSigurdfjellet thin section, martian analogue. The whole lamella was scanned with STXM XANES, followed by a higher resolution (smaller pixel size) scan of the region in the yellow box).

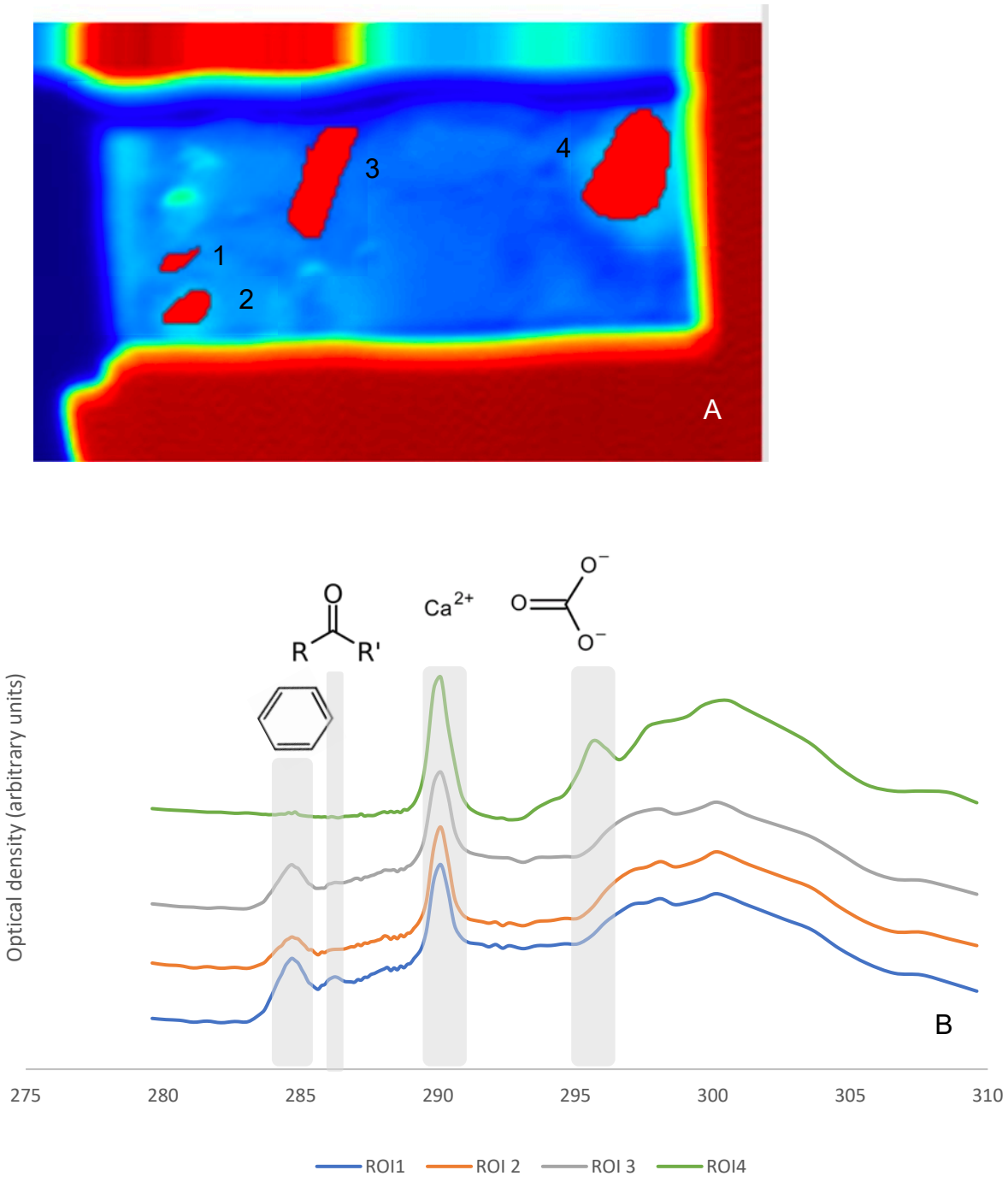

Figure 92 Average carbon K edge spectrum inSigurdfjellet FIB lamellae BVC-1. Four regions of interest are indicated (a) with their spectra (b) showing aromatic, ketone and calcite energies (including the secondary calcite energy at 295.2 eV) .

The optical density carbon K edge scan for the full FIB lamella of BVC-1 (Figure 92) shows calcite is present in all regions of interest, whilst only the outer edges of the carbonate globule (ROIs 1-3) show features of MMC, ie aromatic carbon, with the spectrum of ROI 1 also containing a ketone peak. The central carbonate globule has such a high concentration of calcite that its spectrum shows a secondary calcite peak at 295.2 eV,

in addition to its primary peak at 290.1 eV (Brandes et al., 2010). The organic bearing outer edge of the globule was scanned at a higher resolution (ie smaller pixel size) following the initial large area map. This map (Figure 94) shows a region with a very clearly defined aromatic and ketone peak, and no calcite presence, suggesting localised regions of MMC are present which are not associated with calcite.

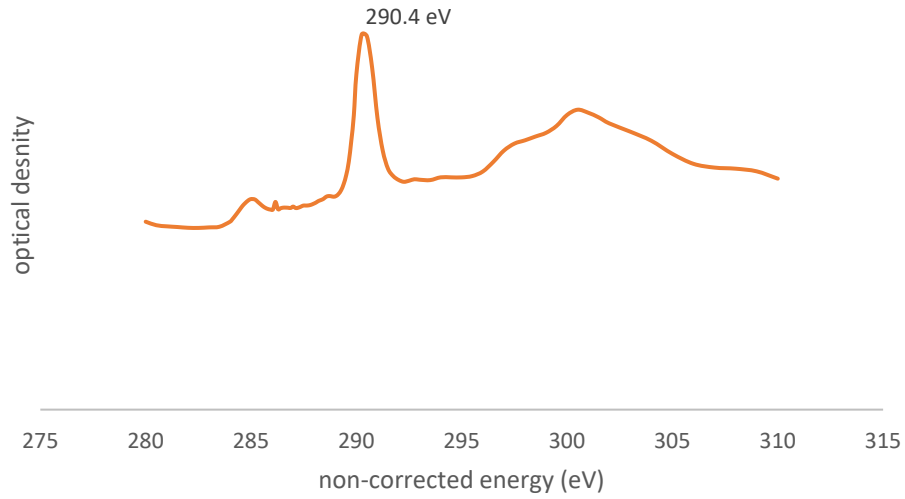

Figure 93 The spectrum of the calcium carbonate peak used to calibrate the energies during the second visit to Diamond Light Source. The measured value of the energy of the peak was 290.4 eV, at this known calcite grain, whist this energy is known to be 290.1 eV (Brandes et al, 2010).

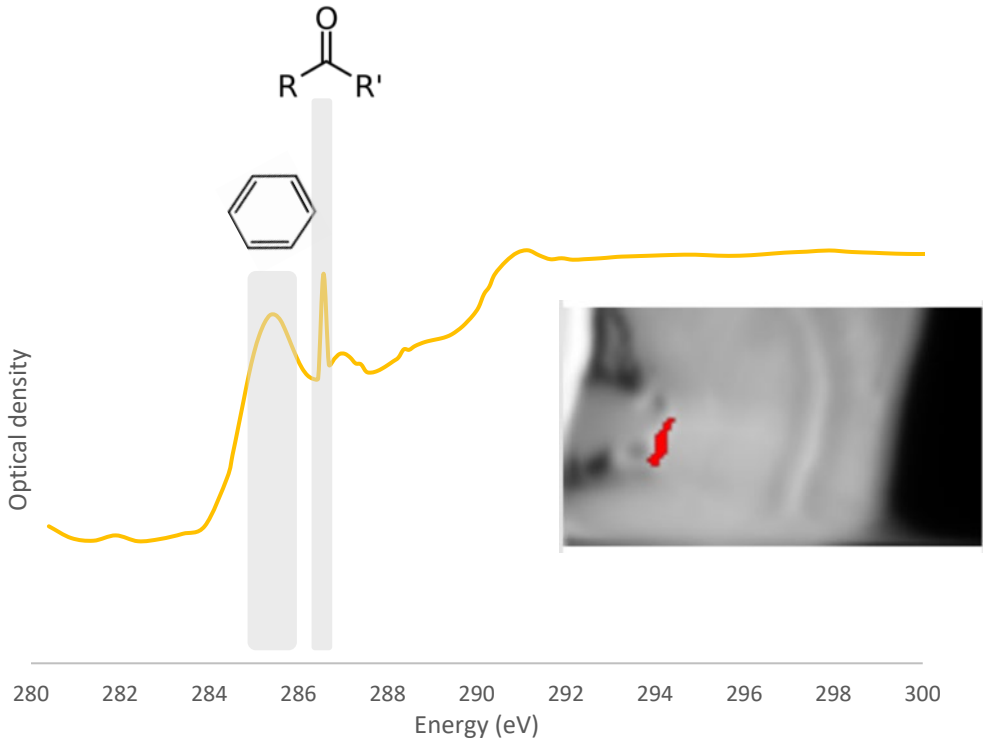

Figure 94 Carbon K edge optical density scan and corresponding spectrum for highlighted region inSigurdfjellet FIB lamella BVC-1. Aromatic and ketone energies are indicated.

Summary of Key In-Situ Findings

- The CRIS and STXM XANES analyses of martian meteorites and analogues was successful in detecting MMC in thin sections and FIB lamellae
- MMC of likely martian origin was detected in NWA 8159 and Tissint using CRIS and STXM XANES, although its proximity to calcite in NWA 8159 may suggest it has been altered since primary formation on Mars
- MMC was detected in SaU 008 using Raman spectroscopy, unfortunately sample loss occurred prior to STXM XANES analyses
- Organic carbon was detected in Goalpara and Hajmah (a), since these are ureilites in which diamonds have been previously detected, this is indicative of heterogeneous heating on the Ureilite Parent Body
- CRIS analyses of organics in Tissint indicates that labile carbon is present, as MMC forms over time, suggesting that martian carbon is sensitive to Raman laser heating
- The likely detection of indigenous MMC in meteorites spanning billions of years on Mars suggests that abiotic organic synthesis occurred on Mars from the Noachian to the Amazonian
- These results suggest that both CRIS and STXM XANES are useful methods for analysis of organics in specimens afters Mars Sample Return, however sample loss is possible after FIB extraction, and Raman itself alters the structures of organics.

5
Bulk Techniques: LC-MS

LC-MS Overview

Bulk analysis of the carbon content of meteorite and analogue chips was carried out U of G and SUERC to evaluate extraction protocols and the chromotographic mass spectrometry techniques available on campus when applied to martian meteorite samples. Bulk analyses involve dissolving the organic content in a crushed sample using solvents, separating the components in the sample using chromatography, then measuring their m/z ratio using a mass spectrometer (Seyler et al., 2020). This can be as part of a targeted or non-targeted study, depending on whether standards are used. We did not know what organic content to expect to find, and thus a non-targeted study was chosen.

Bulk techniques allow for all the organics content in a sample to be analysed at once, rather than studying individual inclusions, as in *in-situ* studies. The benefits of knowing the geological context of the organic matter are lost, so this study was in part to evaluate how much detail could be learned about the structure of organics, in a given amount of time, compared to the restricted time available in doing STXM-XANES studies, which identifies functional groups, but not overall molecular structure.

An overview of the samples studied with bulk techniques, and the procedures used with them is given in Figure 95.

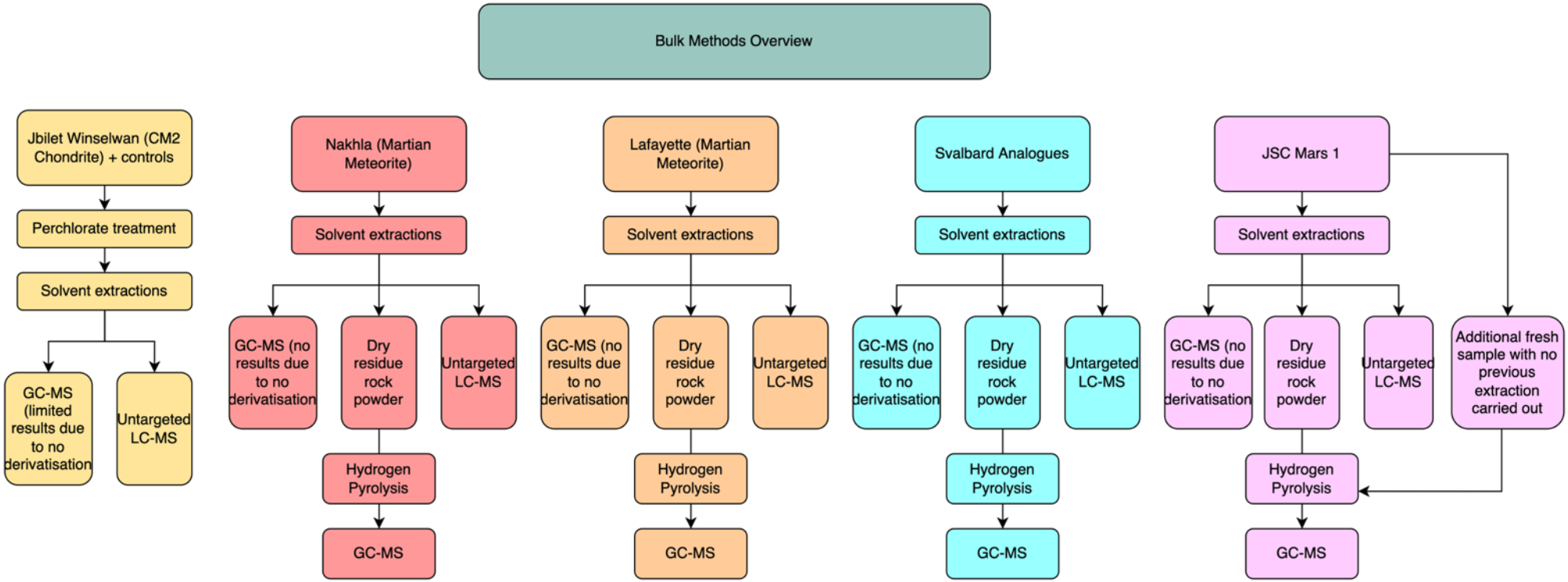

Figure 95 An overview of methods used for bulk experiments to analyse the organic content in martian meteorite, martian analogues and simulants, as well as Jbilet Winselwan (project in collaboration with Dr Alastair Tait). The details of the Jbilet Winselwan experiment are given in the appendix.

Principles of Analytical Techniques

LC-MS

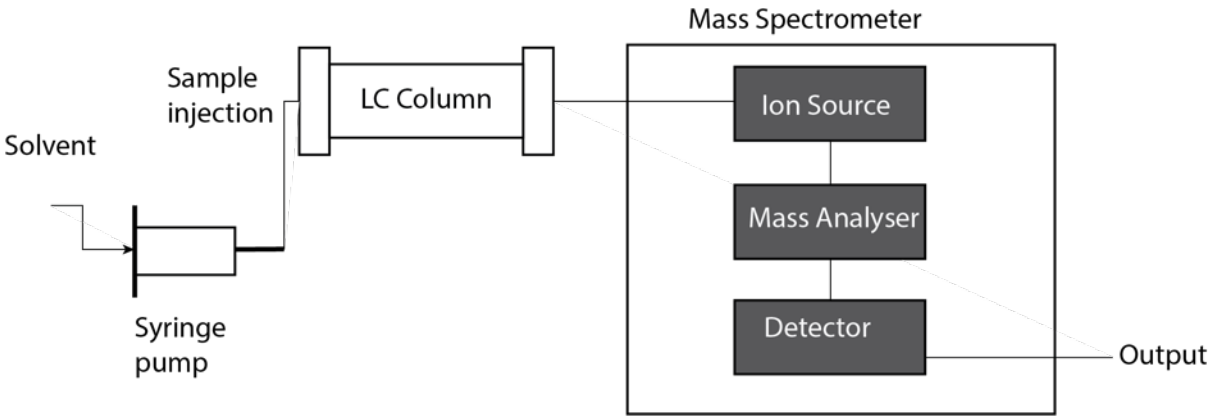

Figure 96 Schematic outline of basic LC-MS set up

Liquid chromatography mass spectrometry (LC-MS) allows for the detection of moderately polar to polar compounds in solution. A schematic overview of the process is shown in Figure 96. Upon injection, the solution is separated into its substituent components as it passes through the column. Compounds are dispersed based on their affinity to the solvent (polar mobile phase) which moves them through the column versus the stationary phase, solid materials in the column. A compound with a greater affinity to the stationary phase will take the longest to travel through the column (known as retention time) (Pitt 2009; Seyler et al. 2020). Electron spray ionisation then occurs of the aqueous/solvent solution, and after the solution passes through a mass analyser, the set-up is capable of detecting compounds with a difference of 10,000 times in abundance (Seyler et al. 2020). LC-MS is primed for the detection of non-volatile and thermally unstable materials (Simkus et al. 2019). The technique also allows for molecular fragmentation detection, meaning that further details of a compound can be gleaned as it fragments.

In this project, the mass spectrometer used was a Thermo Scientific Orbitrap QExactive. This model is a quadrupole mass spectrometer with a sub ppm mass accuracy. This set up was chosen for this experiment due to its sensitivity and high-resolution mass accuracy. This was a non-targeted approach to LC-MS, and therefore the maximum achievable resolution and sensitivity was desired with such precious martian samples.

LC-MS had previously been used on martian samples such as Nakhla (Glavin et al. 1999), and a non-targeted metabolomics approach to LC-MS has also been recommended for astrobiological meteoritics analyses (Seyler et al. 2020).

Methods

Solvent Extraction

In the first bulk analysis experiment, organic solvents were used to extract solvent soluble organic matter from Lafayette and Nakhla (martian meteorites), Sigjurdfjelle and Sverrefjellet (martian analogue xenoliths from Svalbard) and JSC Mars 1 (a NASA martian simulant) to perform untargeted metabolomics. Figure 97 outlines the extraction procedure carried out on meteorites, blanks, simulants, and analogues in order to extract organic molecules from the samples to be analysed using bulk mass spectrometry techniques. Table 8 summarises the sample and blank names as referenced in the results. Hexane, dichloromethane, and methanol were used as the solvents as they have a wide range of polarities and thus would dissolve a wide range of molecular polarities, as this was an untargeted study, we wanted to capture as broad a spectrum of metabolites as possible.

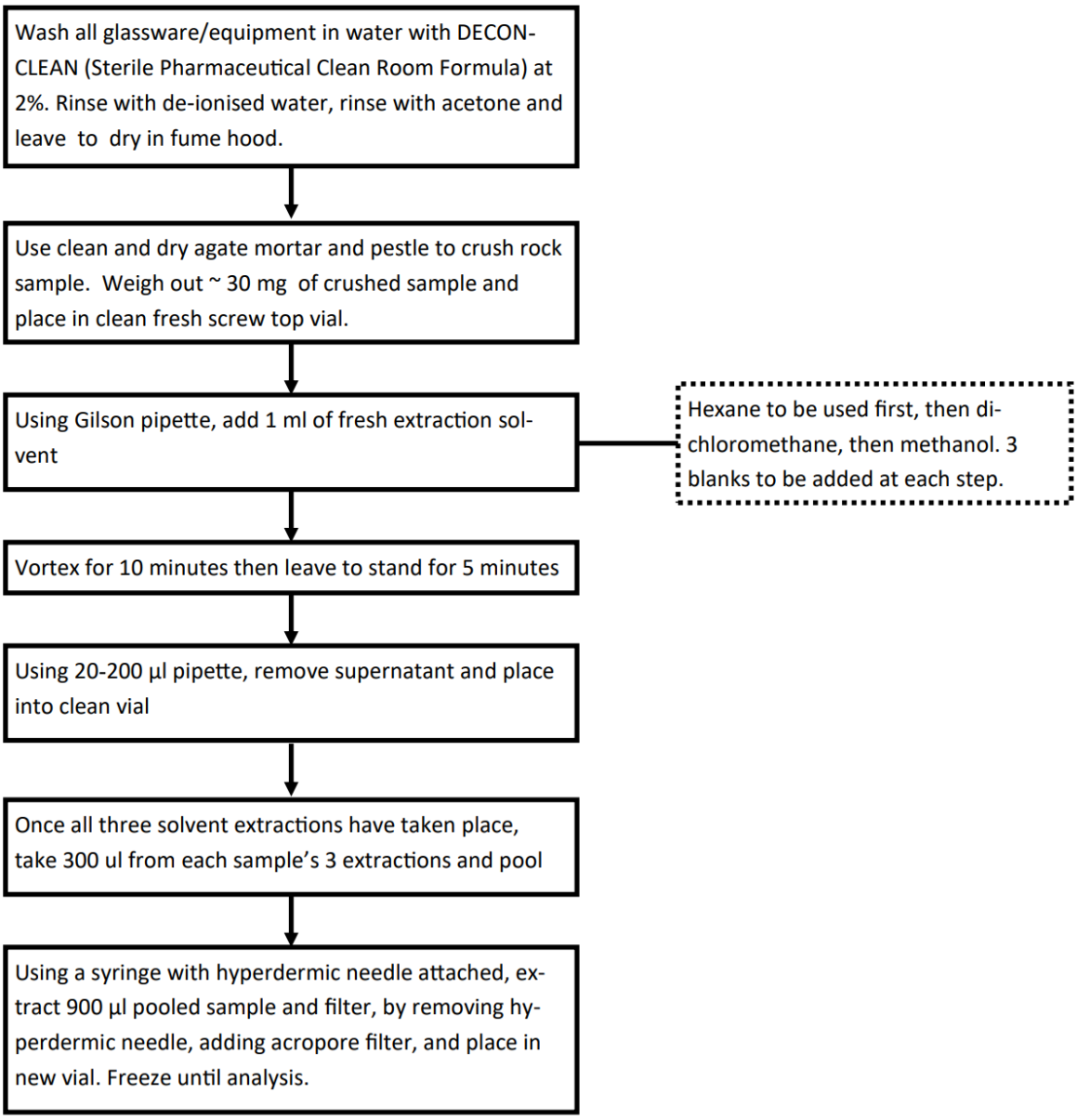

Figure 97 Outline protocol of solvent soluble organic matter extraction procedure.

Table 8 Outline of sample names and their descriptions and solvents used to extract them as used in LC-MS martian meteorite experiment

Sample Group	Description	Solvent Extractions Carried out
La 01-03	Lafayette (martian) pooled and filtered	Hexane, Dichloromethane, Methanol
Na 01-03	Nakhla (martian) pooled and filtered	Hexane, Dichloromethane, Methanol
Sv 01-03	Sverrefjellet (martian analogue) pooled and filtered	Hexane, Dichloromethane, Methanol
Si 01-03	Sigurdfjelle (martian analogue) pooled and filtered	Hexane, Dichloromethane, Methanol
Js 01-03	JSC 1(NASA Mars simulant) pooled and filtered	Hexane, Dichloromethane, Methanol
FB D1 01-03	follow through blank, started as empty vial during crushing/weighing of samples	Hexane, Dichloromethane, Methanol
FB D2 01-03	follow through blank, starting at hexane step	Hexane, Dichloromethane, Methanol
FB D3 01-03	follow through blank, starting at DCM step	Dichloromethane and Methanol
FB D3 04-06	follow through blank, starting at methanol step	Methanol
FB D4 01-03	blank made up of 1:1:1 hexane, methanol & DCM at pooling & filtering step	Hexane, Dichloromethane, Methanol

LC-MS

Once extractions had been carried out at SUERC, samples were stored at -10 °C, they were then stored on dry ice whilst transported to U of G Garscube campus for Liquid Chromatography Mass Spectrometry (LC-MS). LC-MS was used to analyse solvent extractions as a broad range of metabolite groups (ie organic molecules) can be detected without derivatisation, and using an untargeted approach. We did not know what type of organic molecules we would find, so an untargeted approach was needed for the first set of samples. 75 laboratory standards were also run on the LC-MS alongside our samples. Pooled aliquots of our samples were also created and were analysed throughout the machine's run to check for consistency. We also tested the use of gas chromatography mass spectrometry (GC-MS) with the same extractions and no derivatisation and were not able to detect any metabolites beyond the contaminants found in blanks.

LC-MS Specifications:

Hydrophilic interaction liquid chromatography (HILIC) was carried out on a Dionex UltiMate 3000 RSLC system for LC-MS, using a ZIC-pHILIC column. The column was maintained at 25°C and samples were eluted with a linear gradient (20 mM ammonium carbonate in water, A and acetonitrile, B) over 26 min at a flow rate of 0.3 ml/min. The injection volume was 10 µl and samples were maintained at 5°C prior to injection. For positive mode ionisation: source voltage +3.8 kV, S-Lens RF Level 30.00, SLens Voltage 25.00 (V), Skimmer Voltage 15.00 (V), Inject Flatopole Offset 8.00 (V), Bent Flatapole DC 6.00 (V). For negative mode ionisation: source voltage-3.8 kV

Analytical platform used

Hydrophilic interaction liquid chromatography (HILIC) was carried out on a Dionex UltiMate 3000 RSLC system (Thermo Fisher Scientific, Hemel Hempstead, UK) using a ZIC-pHILIC column (150 mm × 4.6 mm, 5 µm column, Merck Sequant)

Analytical methods used

The column was maintained at 25°C and samples were eluted with a linear gradient (20 mM ammonium carbonate in water, A and acetonitrile, B) over 26 min at a flow rate of 0.3 ml/min as follows:

Time /minutes	%A	%B
0	20	80
15	80	20
15	95	5
17	95	5
17	20	80
26	20	80

The injection volume was 10 µl and samples were maintained at 5°C prior to injection. For the MS analysis, a Thermo Orbitrap QExactive (Thermo Fisher Scientific) was operated in polarity switching mode and the MS settings were as follows:

- Resolution 70,000
- AGC 1e6

- m/z range 70–1050
- Sheath gas 40
- Auxiliary gas 5
- Sweep gas 1
- Probe temperature 150°C
- Capillary temperature 320°C

  For positive mode ionisation: source voltage +3.8 kV, S-Lens RF Level 30.00, S-Lens Voltage 25.00 (V), Skimmer Voltage 15.00 (V), Inject Flatopole Offset 8.00 (V), Bent Flatapole DC 6.00 (V). For negative mode ionisation: source voltage-3.8 kV.

The calibration mass range was extended to cover small metabolites by inclusion of low-mass calibrants with the standard Thermo calmix masses (below *m/z* 138), butylamine (C4H11N1) for positive ion electrospray ionisation (PIESI) mode (*m/z* 74.096426) and COF3 for negative ion electospray ionisation (NIESI) mode (*m/z* 84.9906726). To enhance calibration stability, lock-mass correction was also applied to each analytical run shown below:

Positive Mode Lock masses: Number of Lock Masses: 1 Lock Mass #1 (m/z): 144.9822

Negative Mode Lock masses: Number of Lock Masses: 1 Lock Mass #1 (m/z): 100.9856

Instrument .raw files were converted to positive and negative ionisation mode mzXML files. These files were processed with IDEOM (Creek et al, 2012 Jankevics, Burgess, Breitling, & Barrett, 2012) which uses the XCMS (Smith, Want, O'Maille, Abagyan, & Siuzdak, 2006) and mzMatch (Scheltema et al, 2011) software in the R environment. Briefly, this involves using the CentWave algorithm within XCMS to pick out signals based on their retention time and mass-to-charge ratio. These signals are then grouped based on sample replicates and filtered using relative standard deviation, minimum intensity, and a noise filter to produce a set of signals that are likely to be due to real metabolites.

Finally, a gap-filling step is employed to ensure that signals which may have been missed or lost from a particular group/groups while retained for another group are re-instated, to avoid erroneous identification of signals unique to a particular sample. Fragmentation data was analysed in PiMP (Gloaguen et al., 2017) with the FrAnK in-house fragmentation data

analysis software. Comparisons between the overall metabolite distributions of the samples were made using Metaboanalyst (Xia et al., 2009).

Data Reduction

Once samples were run on the LC-MS, the data were reduced by Dr Clement Regnault, Biochemical Data Analyst at the Glasgow Polyomics Facility at the U of G Garscube Campus, and funded by a grant from the Royal Astronomical Society. This initial bioinformatics processing was required to be done by a specialist in order to format the data and produce a useable database. The database produced uses IDEOM, an excel programme created using Visual Basic. IDEOM allows for detection of peaks in chromatograms and predicts the most likely isomer based on an in-house algorithm that predicts the retention time of masses of known compounds. Isomers are then listed using the KEGG database (Creek et al., 2012).

Once I was given the IDEOM file, after learning to use the interface, I focused on metabolites (detected organic molecules) that had the greatest relative intensity for the martian samples compared to blanks, analogues, and simulants for the martian meteorite experiment. I then assessed whether the peaks were real (ie some peaks were detected by IDEOM and had too much noise to distinguish them clearly from the background). Following this, I exported the chromatograms and peak intensity graphs for the detected molecules, and for those with a putative identity, their structures were exported, too. IDEOM identifies isomers with the same exact mass using the KEGG database, so I identified metabolites with no other isomers, and for those with multiple isomers, looked into potential sources, to assess whether any could be ruled out.

Martian Meteorites LC-MS Experiment Results

Bioinformatics – Initial data processing

Initial processing of the martian LC-MS data was carried out by bioinformatics specialist Dr Clement Regnault at Glasgow Polyomics, to convert the raw data produced by the OrbiTrap mass spectrometer to a database that could be used by geoscientists – IDEOM. This was funded by a successful application for the RAS Patricia Tompkins Instrumentation grant, to maximise the inferences that could be drawn from the dataset. The bioinformatical technique used to process the data is a standard procedure used by the Polyomics laboratory and is outlined in Creek et al (2012).

Principal Component Analysis

Metaboanalyst was used to carry out two-dimensional and three-dimensional principal component analysis (PCA) to determine whether the samples clustered together and in what groups. Log_{10} and glog (depending on generation of the software released when the experiment was carried out) normalisations were applied to data prior to PCA to factor in the range of intensity values of metabolites detected - due to differing interactions with the OrbiTrap - without losing patterns in the dataset so that PCA could be carried out. This data transformation is demonstrated by Figure 98, which shows how normalisation brings all data to within the same order of magnitude for PCA analyses whilst maintaining the overall patterns in the dataset. Several PCA combinations of samples were plotted using metaboanalyst (e.g., with/without blanks, different samples etc) to identify different clustering patterns and trends. A selection of these is shown below. Metaboanalyst was then used to generate a heatmap of samples, to show the distribution of metabolites in each sample (Figure 104).

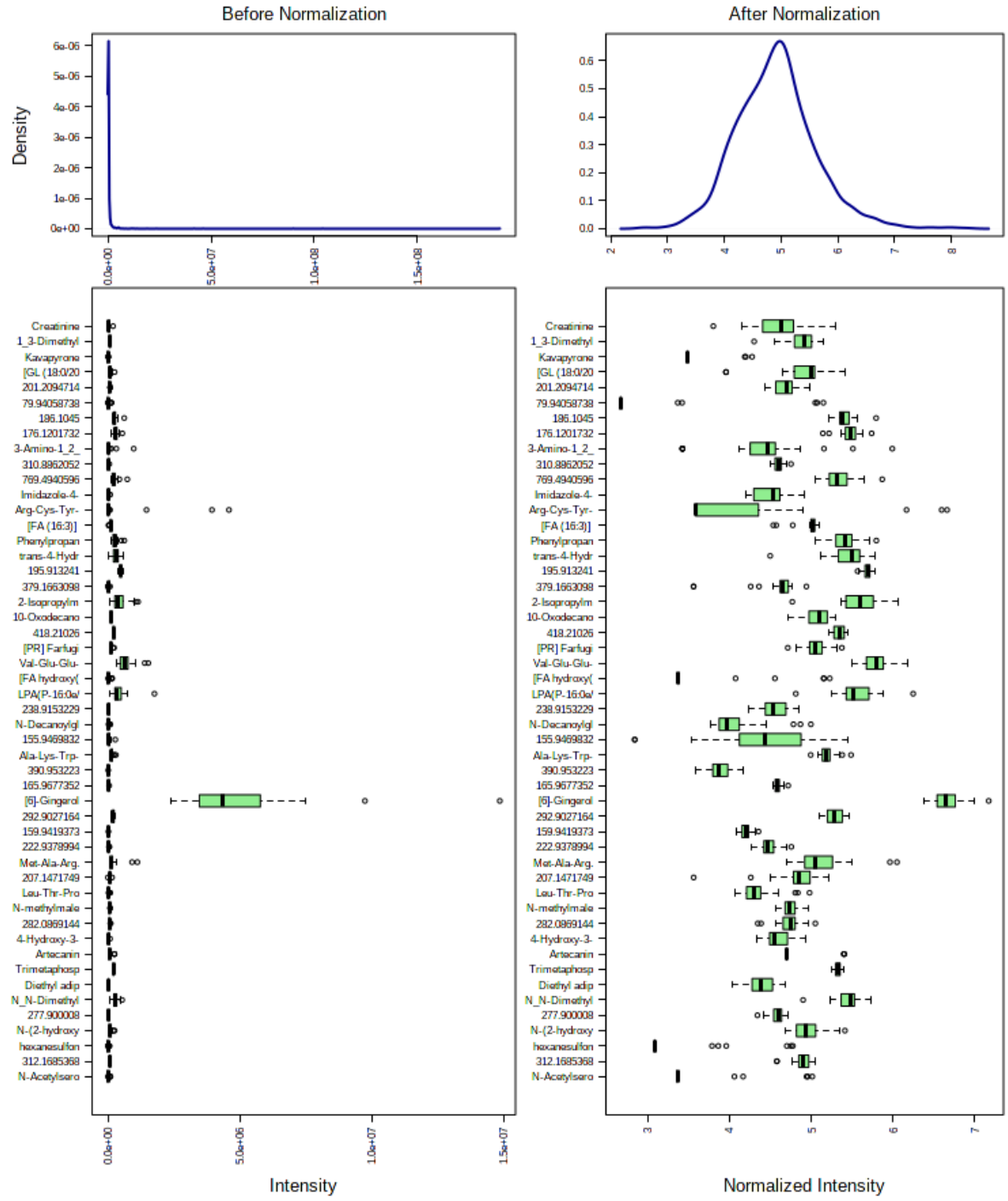

Figure 98 Plots to show effect of log_{10} normalisation on dataset when applied to intensities of LC-MS data using Metaboanalyst, only 50 features are shown for clarity. These plots demonstrate the need to normalise the dataset to create a clearer distribution which can be plotted with principal component analysis, without losing information or trends in the dataset.

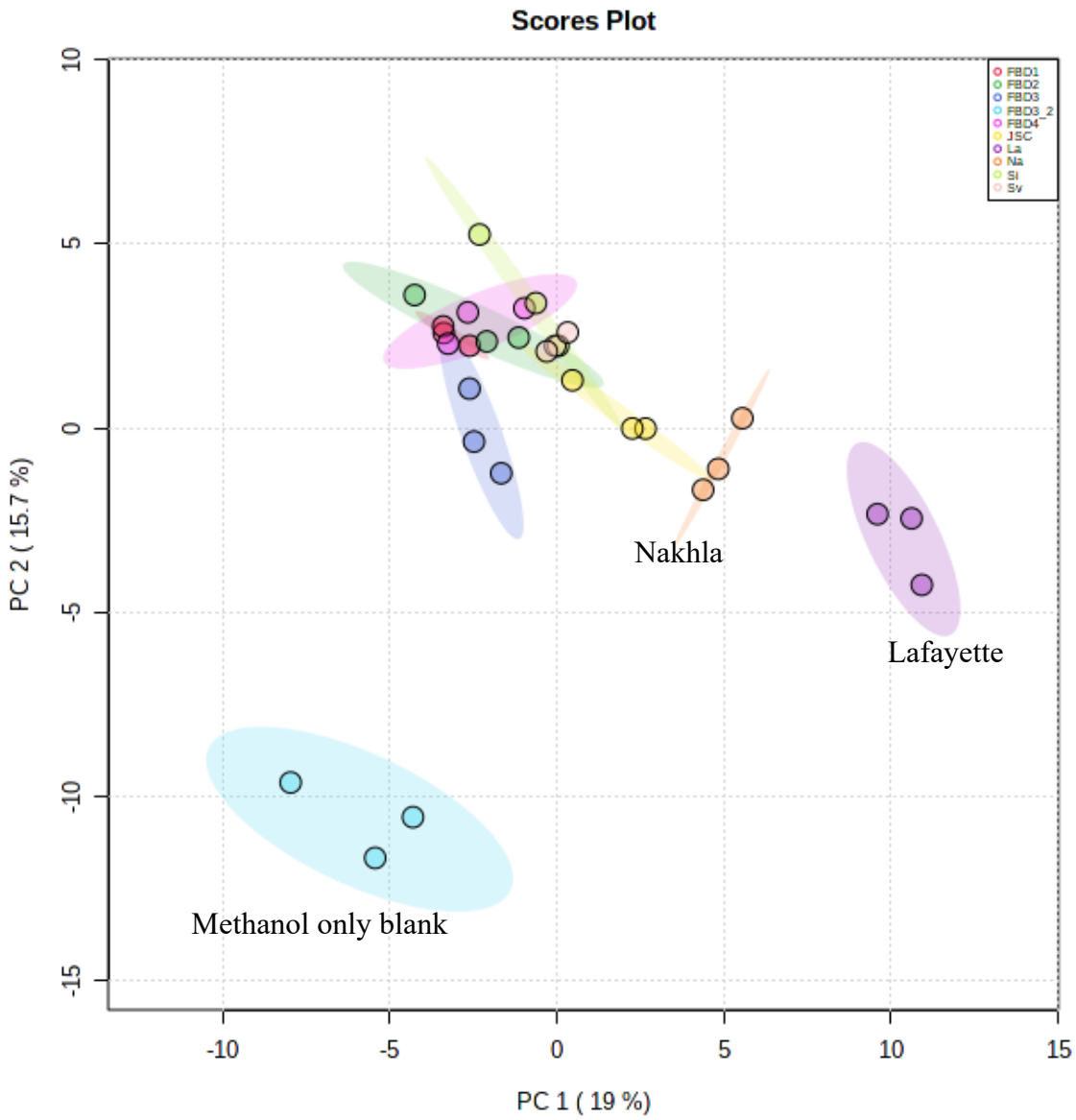

Figure 99 Plot of the first two principal components calculated for all extracts (blanks and experimental samples) for the martian meteorite LC-MS metabolomics experiment. Graph generated in MetaboAnalyst 5.0 on log_{10} transformed data obtained in IDEOM. This PCA indicates that the Lafayette samples are the most distinct from the rest in terms of the first PC, and the methanol only extract (FBD3 04-06 are the most distinct in terms of the second PC). The First PC accounts for 19 % of the variance and sets the martian samples apart from each other, as well as the other blanks, analogues, and simulant extracts. The second PC accounts for 15.7% in the metabolite distribution and primarily sets the methanol only blanks apart from the remaining samples, demonstrating the wide range of compounds detected from the solvent extraction protocol. Shaded areas represent 95% confidence regions.

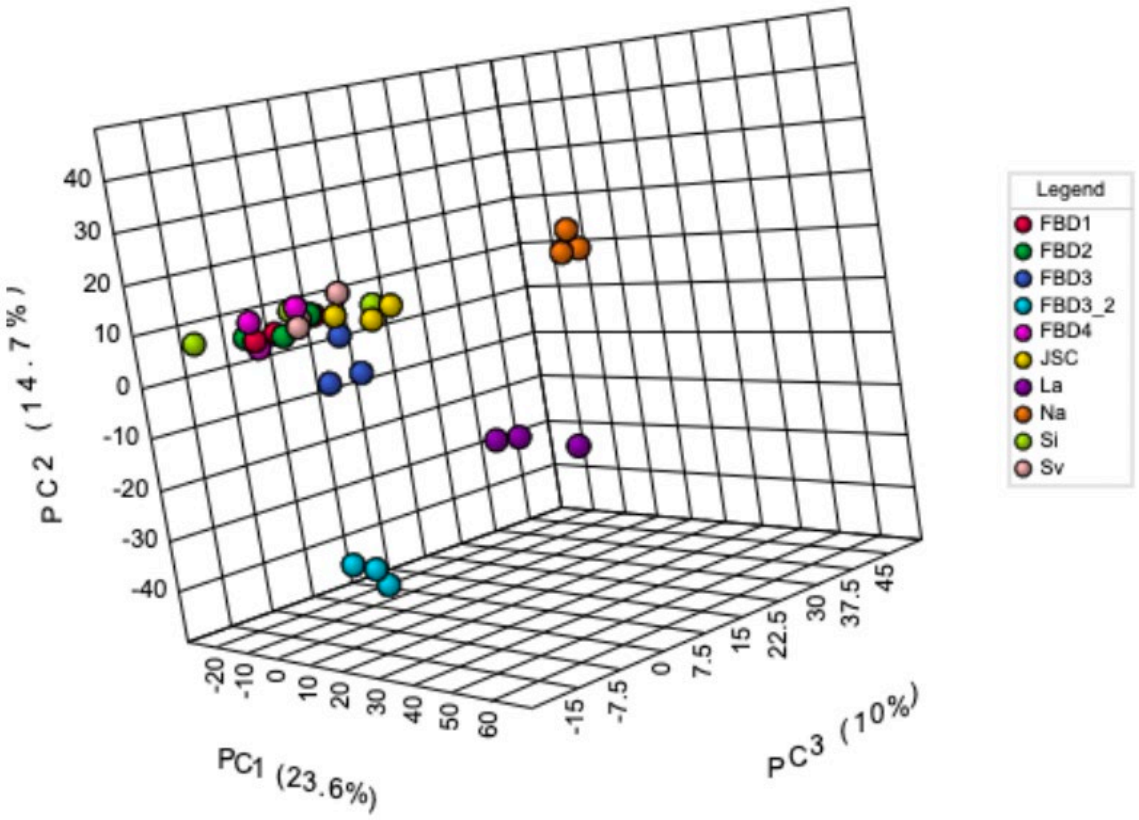

Figure 100 3D principal component analysis of all samples (experimental and procedural blanks) in LC-MS martian experiment. The additional third principal component accounts for 10% of the variance in the dataset and distinguishes Nakhla from other samples more clearly than in Figure 99.

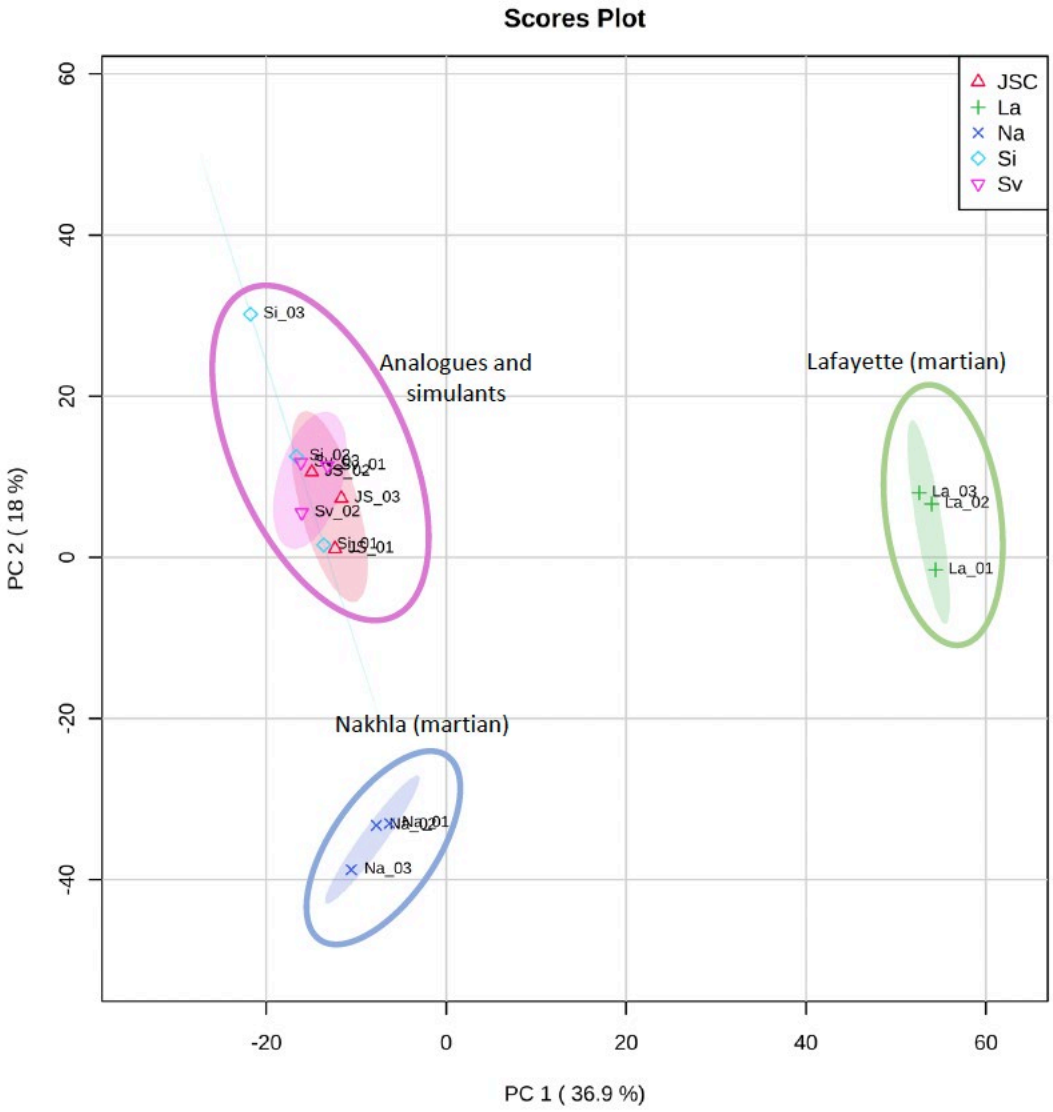

Figure 101 Plot of the first two principal components calculated for the experimental samples (ie excluding the procedural blanks)in the martian LC-MS experiment. First PC accounts for 36.9% of variance and distinguishes Lafayette (martian) sample from all other samples, whilst second principal component accounts for 18% of the variance and distinguishes Nakhla (martian) sample from the rest. Shaded area represent 95% confidence region.

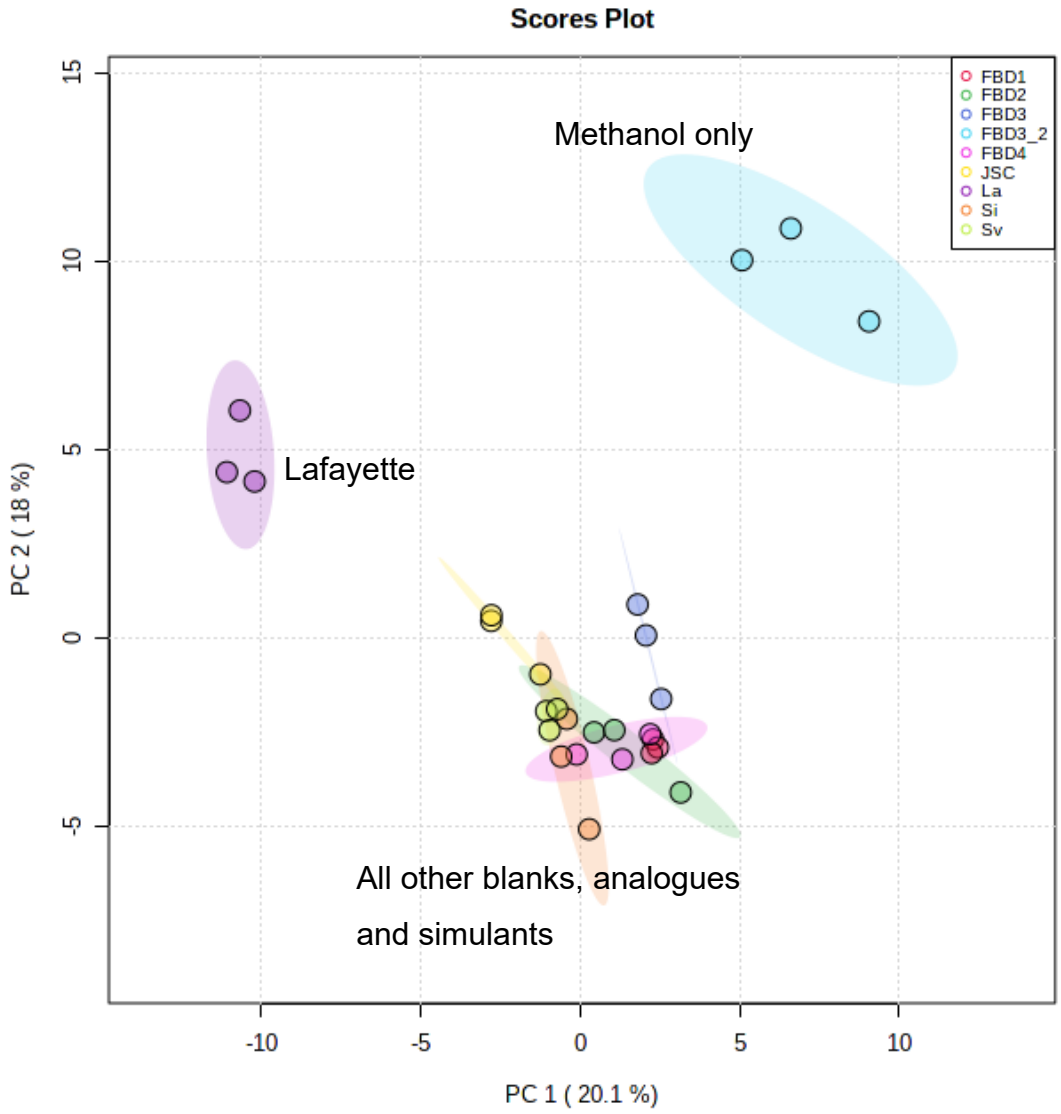

Figure 102 Two dimensional PCA displaying all martian LC-MS experiment samples except Nakhla. This was done to assess the likely contamination content in Lafayette due to its unkown terrestrial history. The first principal component accounts for 20.1% of sample variance and sets Lafayette apart from all other samples and blanks, as well as the methanol only blanks. Similarly the second principal component sets these same samples apart somewhat, and accounts for 18% of the variance.

Evaluating the effectiveness of Martian LC-MS PCA

As mentioned above, Metaboanalyst is an open-source statistical analysis software written in R for metabolomics data. In this study, the software was used to identify whether samples were distinct from one another. The heatmap (Figure 104) for example, was a useful tool in indicating that there was no accidental cross contamination or misnaming of samples during extractions. Human error such as mixing up of samples was a possibility given the hundreds of vials involved in both the martian and Winchcombe experiments, and it likely occurred during data analysis in the Jbilet Winselwan experiment as detailed in the appendix. If any replicates had been swapped by accident, this would have been visible in the heatmap, particularly as an additional version can be generated where samples are grouped by similarity in the patterns in the data, rather than by sample ID.

Principal component analysis (PCA) is a statistical method that reduces the number of dimensions in a multidimensional dataset whilst minimising the amount of information lost in the process. PCA as used in Metaboanalyst analyses the intensity distribution of the metabolites in the samples and, based on their distribution generates principal components (a group of metabolites) whose distribution is largely representative of a large proportion of the overall distribution of the sample. Two dimensional PCA as shown in Figure 99is the graphical display of the first two principal components, (i.e., the top two groups that best represent the most variance in the data set), whilst 3D PCA shows the first 3 principle components, as shown in Figure 100.

Adding further dimensions to PCA gives incrementally more detail as demonstrated by the SCREE plot displayed in Figure 103. PCA plots with more dimensions than three are difficult, if not impossible, to visualise with standard data visualisation techniques, and the plots shown in this martian project demonstrate good separation of samples, although the statistical variance does not account for more than 57% even with five principal components used. There is a significant proportion of information in the dataset which is lost from this visualisation, and it thus only used as a summary of the samples.

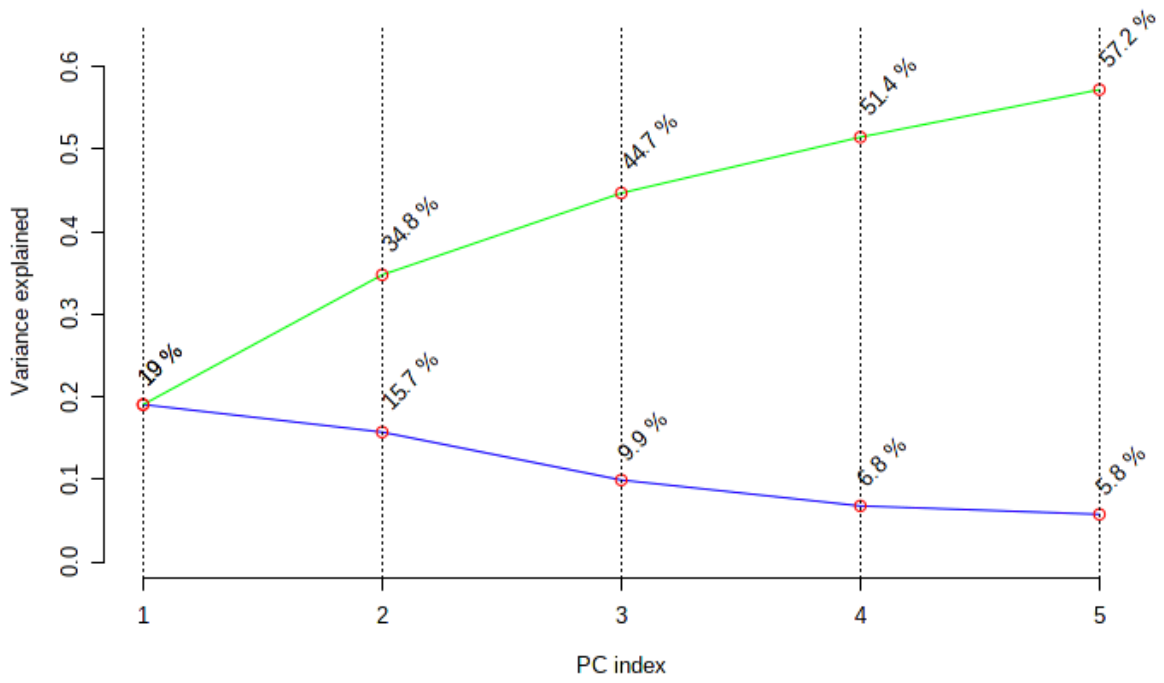

Figure 103 SCREE plot displaying the variance described by the first 5 principal components in the martian LCMS experiment (including both martian meteorites, all analogues and simulants). The upper green line shows the cumulative variance whilst the lower blue line shows the variance represented by the corresponding principal component number.

Influences on PCA in Martian LC-MS Experiment

Metaboanalyst was used to investigate the molecules which influence the first principal component the most in the martian LC-MS experiment. This PC1 (in Figure 99) shows Lafayette as the most statistically distinct sample, and the top metabolites with the highest influence on PC1 (known in metabolomics as loadings) are shown in descending order in Table 9. Table 9 shows that the molecules with the highest PC1 loadings are predominantly lipids and fatty acids, as well as the likely plant derived terrestrial contaminants discussed further below (e.g. tetraneurin E, Arnicolide A, Vomitoxin).

Table 9 Metabolites with highest influence (loading) on PC1 in Figure 99, in descending order

Metabolite	**PC1 Loadings**
[FA trihydroxy(16:0)] 2_15_16-trihydroxy-hexadecanoic acid	0.14203
Tetraneurin E	0.15073
[FA trihydroxy(18:0)] 9_10_18-trihydroxy-octadecanoic acid	0.038365
[FA hydroxy(18:1)] 9_10-dihydroxy-12Z-octadecenoic acid	0.10291
momilactone A	0.038483
Tetraneurin A	0.13696
1'-Acetoxyeugenol acetate	0.03643
[FA hydroxy(16:0/2:0)] 9-hydroxy-hexadecan-1_16-dioic acid	0.036271
Arnicolide A	0.03714
[FA oxo(4:0/4:0)] 9-oxo-12S-acetoxy-2_3_4_5-tetranor-7Z_10Z_14Z-prostatetrienaldehyde-cyclo[8_12]	0.037812
Prostaglandin A2	0.080667
Artecanin	0.035532
[FA trihydrox] 9S_11R_15S-trihydroxy-2_3-dinor-13E-prostaenoic acid-cyclo[8S_12R]	0.064276
Inulicin	0.036185
[PR] Novaxenicins A	0.036757
3-Hydroxysebacicacid	0.052919
Shiromodiol diacetate	0.11715
[FA (14:0/2:0)] Tetradecanedioic acid	0.066902
2_2-Dimethyl-8-prenylchromene 6-carboxylic acid	0.036862
[PR] Vomitoxin	0.037885
[SP] Pramanicin	0.037553
[PR] Echinenone/ (Myxoxanthin)	0.043708
Gibberellin A15	0.037496
Canin	0.038276
[FA hydroxy(14:0)] 3_11-dihydroxy-tetradecanoic acid	0.14124
Prenyl caffeate	0.13679
[FA (20:5)] 5Z_8Z_11Z_14Z_17Z-eicosapentaenoic acid	0.10009
Eriolangin	0.039151
12alpha-Hydroxyamoorstatin	0.097202

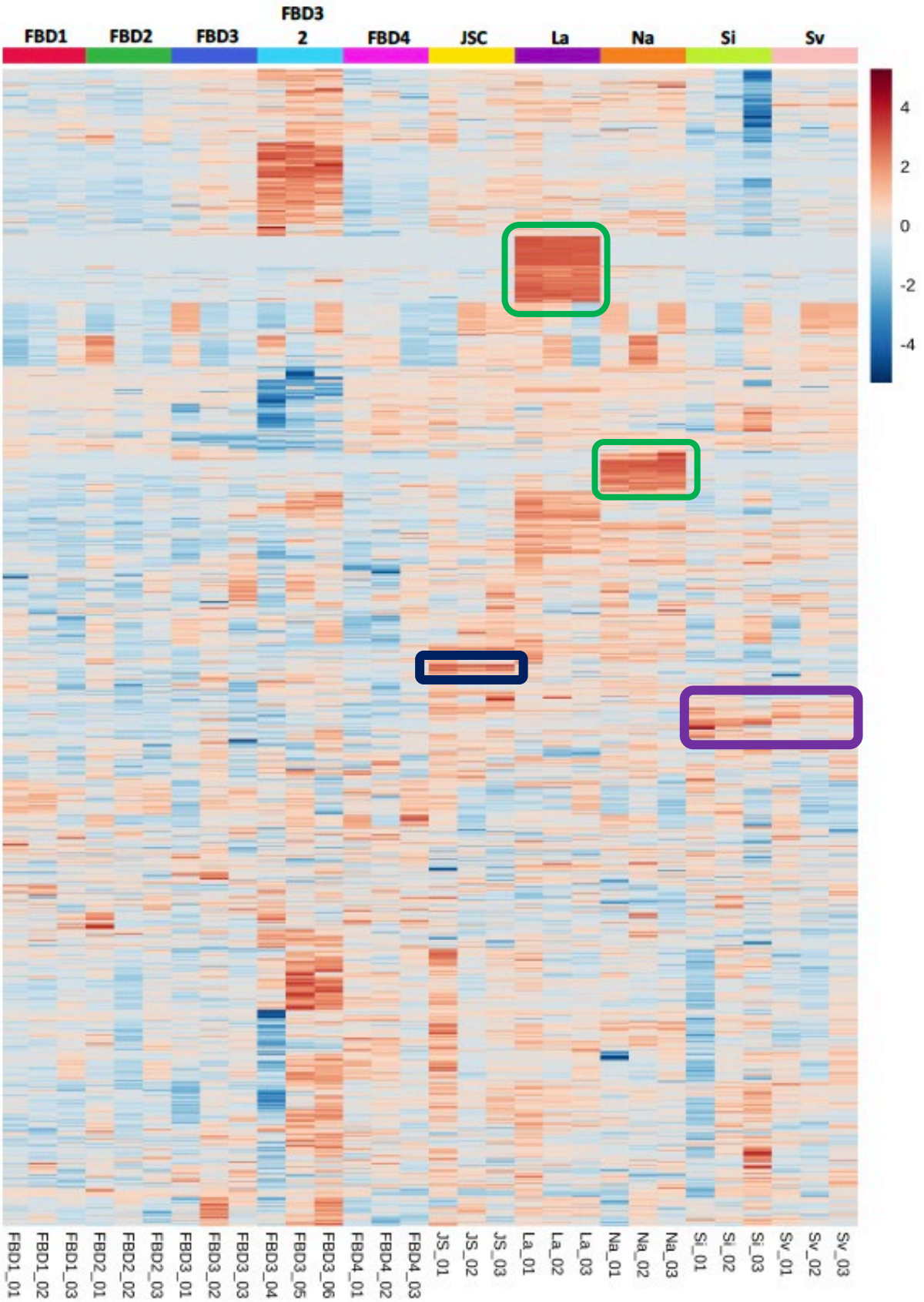

Figure 104 Heat map showing relative intensities of metabolites in samples in martian meteorite LC-MS experiment. Each individual column represents an extract, whilst each row represents an individual metabolite. Samples shown to be deepest red had the highest relative intensity (relativity based on that metabolite only, not across all metabolites) in that extract. Metabolites were clustered automatically by Metaboanalyst according to similar distribution. Distribution suggests an array of metabolites present in martian meteorite extracts not present in simulants, analogues, or blanks (as indicated by the two green boxes), as well as metabolites present only in analogues (blue and purple boxes).

Metabolites in Lafayette

The Lafayette meteorite has an unconfirmed fall record (Nininger 1935), thus extra data analysis was carried out on its likely contamination content to potentially constrain its terrestrial history.

Comparing Lafayette organic matter to that of terrestrial analogues

The solvent extraction and LC-MS protocol utilised during this study successfully detected low abundances of solvent soluble OM in the Lafayette and terrestrial martian analogue samples. Approximately 224 peaks could be annotated as likely metabolites (organic molecules detected by the OrbiTrap mass spectrometer in the experiments) in Lafayette at intensities more than twice the procedural blanks (see appendix). This number is approximate, since some peaks were low definition (denoted by an asterisk in the table in the appendix) and thus we cannot be as confident in their presence, as we can for the higher definition peaks. Many of the peaks detected in Lafayette were below detection levels in all other samples and blanks, indicating its distinct OM signature.

Two-dimensional principal component analysis (PCA) was carried out using Metaboanalyst, an open-source metabolomics data analysis tool (Xia et al., 2009). The three Lafayette replicates cluster together, separate from all other samples (see Figure 102, PCA without Nakhla included). Most procedural blanks cluster together, alongside the analogue samples. The clearest exceptions to this analogue and blanks cluster are the procedural blanks made up of methanol only. The metabolite make-up of the methanol-only blanks is distinct due to high concentrations of molecules with a similar polarity to methanol and low concentrations of less polar molecules that dissolve in hexane, for example. A similar, but less distinct, separation is observable for the blanks without hexane, which clusters slightly apart from the analogues and three-solvent blanks (see Figure 2). This finding illustrates why a three solvent extraction protocol is required to detect a wide spectrum of solvent-soluble OM within geological samples.

Metaboanalyst was also used to generate a heatmap showing the relative levels of detected metabolites in each individual sample (Figure 104). Here again, the Lafayette replicates are distinct, containing high relative abundances of numerous peaks that were not detected in any of the other samples or blanks (see the green box in the Lafayette column). The heatmap also highlights a small group of peaks that were detected in all three replicates of JSC Mars-1 in high abundance relative to the other samples (Figure 104, purple box). The

two BVC Svalbard samples contain a small group of peaks that are relatively abundant within all three replicates (mostly grouped within the blue box, Figure 104). However, none of these peaks show good reproducibility across all replicates.

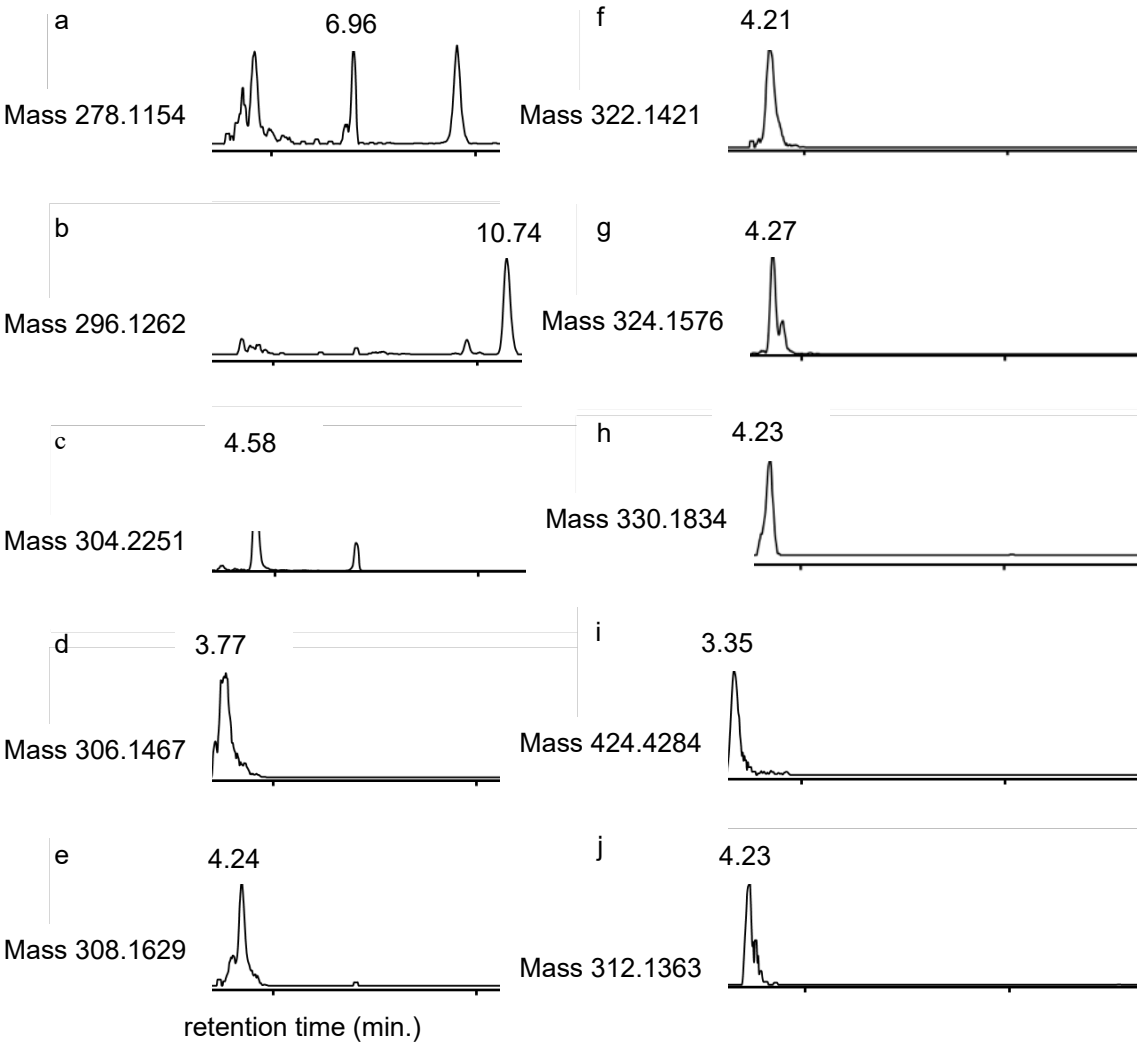

Figure 105 Extracted ion chromatograms of peaks of interest found via HILIC LC-MS in triplicate samples of Lafayette (a-h) and JSC Mars 1 (i and j). The putatively annotated peaks are: a) artecanin/canin, b) deoxynivalenol (also known as vomitoxin), c) [FA trihydroxy(16:0)] 2,15,16-trihydroxy-hexadecanoic acid, d) arnicolide A, e) inulicin, f) tetraneuin E, g) tetraneurin A, and h) gibberellin A15. The putatively annotated peaks in JSC Mars 1 are i) Octacosanoic acid and j) Desmosdumotin C.

Fatty acids

Fifty nine out of the 224 peaks detected in concentrations significantly above background in Lafayette (i.e., at least twice the levels in the procedural blanks) were putatively annotated as fatty acids, including the molecule with the highest peak intensity in Lafayette relative to the blanks [FA trihydroxy(16:0)] 2,15,16-trihydroxy-hexadecanoic acid. Fatty acids have previously been reported in other meteorite solvent extracts, for example via a GC-MS study of DCM extractions of the CM2 chondrite Tagish Lake (Hilts et al. 2014). Unlike GC-MS, this method of HILIC LC-MS is not optimised for fatty acid detection, due to the apolarity of these molecules – GC-MS would provide better separation (Schött et al. 2021). Therefore, many more fatty acids may be present in Lafayette that were not detected during this study.

Nine fatty acids were also putatively annotated within JCS Mars 1, including octacosanoic acid (see Figure 105). Only one other isomer is identified for this metabolite, which is another fatty acid (6-methyl-heptacosanoic acid).

Terrestrial metabolites within Lafayette

Without compound-specific isotope ratios, we cannot determine with certainty whether individual metabolites detected within Lafayette have a terrestrial or martian origin, and at the time of writing, we do not have the capability for this with LC-MS. However, several metabolites were detected that are known to be produced via terrestrial biological processes, thus are probable terrestrial contaminants. These metabolites can help constrain the fall scenario of this meteorite. For example, six peaks with some of the highest relative abundances in the sample were putatively annotated as sesquiterpene lactones secondary metabolites most commonly produced by plants in the *Asteracae* (also known as compositae) family.

Specifically, artecanin, canin, inulicin, arnicolide A, tetraneurin A, and tetraneurin E, were detected at high relative intensities in Lafayette only (see Figure 105). Such molecules are thought to make up to 3% of the dry mass of plants in the *Asteraceae* family (Chadwick et al. 2013), indicating that the Lafayette stone fell into an area with such plants close by. In particular, Tetraneurin E is a metabolite produced by Parthenium, a wildflower genus with one species *Parthenium integrifolium* (also known as wild quinine) native to the eastern U.S. including Indiana, where Purdue University is located (Kartesz, 2015) (see Figure

106). A standard was not run of Tetraneurin E during LC-MS analysis, but no exact mass isomer for this metabolite is present in either the HMDB or KEGG databases. Therefore, it is likely that Tetraneurin E is a terrestrial contaminant within Lafayette, the presence of which strengthens the case for its unconfirmed fall scenario.

Another putative metabolite detected in all three replicates of Lafayette, and in no other samples or blanks, was deoxynivalenol (DON), also known as vomitoxin (see Figure 105). DON is a mycotoxin (harmful fungal chemical) released by *Fusarium graminearum*, a fungal pathogen also known as *Gibberella zeae*. *F. graminearum* is a fungal pathogen which causes the crop disease fusarium head blight (FHB) of wheat and Gibberella stalk and ear rot of corn and is the dominate fungal species causing FHB in North America (Schmale and Bergstrom, 2003; McMullen et al., 2012; Munkvold and White, 2016).

There are 19 isomers (including DON) with the same m/z value as DON in the human metabolome database (HMDB), and without a DON standard we cannot be certain that DON was detected. However, the likely detection of similar plant-based metabolites, as outlined above, strengthens the case. In addition, the IDEOM algorithm developed by Glasgow Polyomics has a retention time predicting equation which picks the most likely metabolite for the given m/z and retention time value, as outlined in Creek et al. (2012), and DON was selected by the algorithm. This possibility is also reinforced by the putative detection of Gibberellin A15, a fungal terpenoid with a similar molecular structure to the sesquiterpene lactones described above (see Figure 105). Gibberellin biosynthesis was reported in the related pathogen *Fusarium fujikuroi* (Hedden and Sponsel 2015).

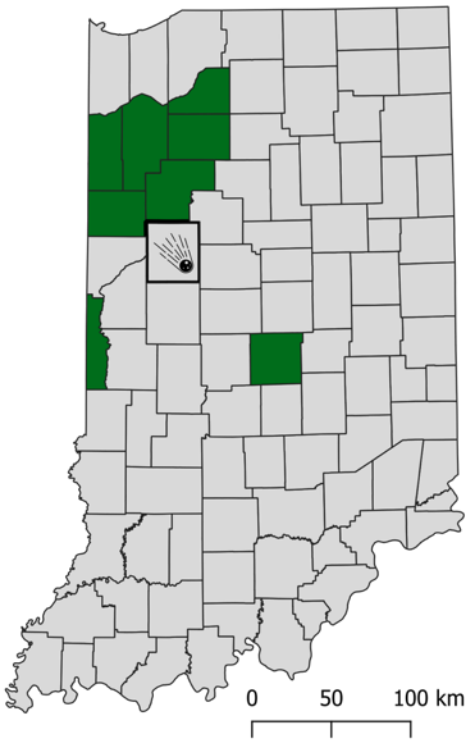

Figure 106 The reported fall location (Tippecanoe County) of Lafayette Meteorite compared to the native distribution of a plant whose derivative was found in the sample of Lafayette. Counties (in green) in Indiana with verified (pressed and location recorded specimens) native distribution of Parthenium integrifolium, the only species of parthenium genus indigenous to Indiana relative to the county (in orange) where the Lafayette meteorite was reportedly first found. Plants in the parthenium genus contain many sesquiterpene lactones, including those such as Tetraneurin E found in this experiment and in this species. Adapted from the Indiana Plant Atlas.

Organic Content of Nakhla

The extracts of Nakhla were found to contain 206 metabolites at relative abundances at least twice as high as those of the procedural blanks. Of these, 59 could not be identified from the KEGG database used by IDEOM (Creek et al. 2012), leaving 147 putatively identified metabolites. One of the unidentified metabolites was found in all replicates of both martian meteorite extracts at similar concentrations and was below detection limits in all other samples and blanks extracts, it had an m/z value of 190.1117. Further work would be required to possibly identify this molecule as there was no fragmentation data or isotope peaks in the spectrum.

Forty-three of the remaining 147 metabolites were putatively identified as fatty acids. Some of these fatty acids were found at similar high abundances in both Nakhla and Lafayette, such as [FAhydroxy(118:2)]9S-hydroxy-10E,12Z-octadecadienoic acid and (9Z)-Hexadecenoic acid, however they were also present, albeit at significantly lower concentrations, in all other samples and blanks too.

Two metabolites: orthophosphate and betaine, were detected in Nakhla only and were below detection limits in all other samples. These molecules were matched to standards, therefore their identity was confirmed.

Comparing Analogues, Simulants and Meteorites

Methionol was putatively identified in all the expermental samples at similar concentrations, and at very low concentrations in the procedural blanks. This compound was also detected in the Jbilet Winselwan experiment (see appendix) for experimental details) whereby its abundance increased as perchlorate concentration increased.

One of the sulfonates, 1-butanesulfonate, was detected in this martian experiment having been detected in all the extracts from the martian meteorites, analogues, and simulants, but was below detection limits in all of the procedural blanks. It was detected in its highest concentration in the Sverrefjellet extract, which was three times as high as that of the Lafayette extract, which had the lowest abundance of 1-butanesulfonate.

Four metabolites putatively identified as hydroxy fatty acids were found at significantly elevated levels in both Nakhla and Lafayette, compared to the rest of the samples, although they were present in all other samples.

Summary of key LC-MS Findings

- Our results demonstrate the strength of a non-targeted approach to metabolomics/LC-MS in capturing a non-biased dataset of organic compounds in a sample
- The dominant compound class present in the martian meteorite samples, and martian analogues is fatty acids, demonstrating the similarity of these analogues to martian materials
- Both Nakhla and Lafayette contain likely terrestrial contaminants, both are relatively fresh meteorite samples (ie have not experienced significant terrestrial weathering), demonstrating the need for careful curation upon Mars Sample Return
- Despite this being a non-targeted study, Nakhla contains compounds whose presence was verified with a bona fide standard: betaine and orthophosphate. Betaine is a likely contaminant, and has previously been detected in this meteorite.
- Both Lafayette and Nakhla contain a number of compounds which could not be identified using the IDEOM algorithm, ie mass and retention time not matching to KEGG database. These unknown compounds may be more likely to be indignenous to the meteorites, given they are not common biogenic molecules
- The presence of likely terrestrial plant base metabolites in Lafayette strengthens the case for the reported fall scenario that the meteorite fell in a rural location in Indiana
- These results suggest a non-targeted approach to LC-MS, followed by a subsequent targeted approach with standards to confirm compound identities, would be an excellent method for sample analyses for organics detection after Mars Sample Return

6 Bulk Techniques: HyPy

Principles of Hydrogen Pyrolysis

Hydrogen pyrolysis (HyPy) converts macromolecular refractory organic material into solvent soluble phases that allow for analysis by e.g. GC-MS (Sephton et al. 2005). HyPy uses high pressure (>10 MPa) hydrogen, with an ammonia-based catalyst, at increasing temperatures, to remove refractory organic matter from solid samples (Meredith et al. 2012). The technique converts >85% of macromolecular kerogens into solvent soluble material, and the rearrangement of product compounds is minimal, due to the continuous supply of high pressure H_2 (Sephton et al. 2005). The products are deposited onto silica beads in a cold trap. A schematic overview of this process is displayed in Figure 108.

This technique was chosen for this project since macromolecular organic material is known to be present in martian meteorites, having been detected in in-situ analyses (Steele et al. 2016). Furthermore, HyPy coupled with GC-MS had previously been applied to meteoritic macromolecular organic material in carbonaceous chondrites such as Murchison (Sephton et al. 2005) allowing a comparison to be made with such previous studies.

Sample Preparation

After solvents had been used to extract solvent-soluble OM from triplicate samples, ready for GC-MS and LC-MS, the remaining sample residues were dried overnight at 30 degrees with their vials removed. These triplicate residue samples were then pooled, and weighed, to allow for catalyst to be added for hydrogen pyryolysis (HyPy). At this stage, three additional blanks, made of pure silica beads, were added, alongside an additional sample of JSC Mars1. All four of these samples had not undergone solvent extraction treatment, so as to allow for any impurities to be identified during the HyPy process, and to identify the extent to which pyrolysable organics were removed during the solvent extraction process.

In this experiment, powdered ammonium dioxydithiomolybdate ($(NH_4)_2MoO_2S_2$) was used as

the catalyst. Approximately 5 % of the sample mass by weight of catalyst is required for optimal extraction with HyPy for samples with low carbon wt%, such as meteorites. Given that the triplicate samples used in this experiment were ~ 30 mg, it was decided that pooling samples would be the most effective method to ensure that catalyst masses were workable (ie using masses that you could weigh out in the lab) and to maximise the chance of extraction and gaining a signal when analysed with GC-MS. ~90 mg samples were therefore made by combining the 30 mg residues from LC-MS triplicates.

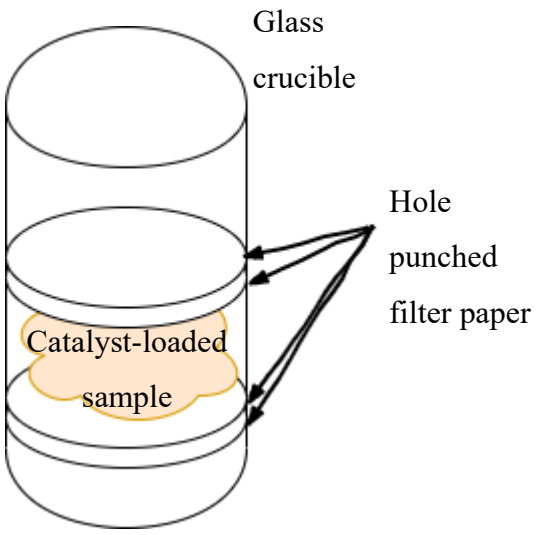

Figure 107 Schematic of the samples prepared for hydrogen pyrolysis analysis

Sample masses, along with their ideal (ie 5% by weight) and measured catalyst masses are displayed in Table 10.

Once the catalyst was added, 100 µl of 1:4 MeOH:H_20 solution was pipetted into each vial and dried down in a positive pressure fume hood overnight to mix the material. Once dry, the samples were loaded into semi-permeable small glass crucibles, with hole-punched filter paper above and below, as outlined in Figure 107. Crucibles, pre- and post- loading with sample were weighed, to calculate the mass of any sample lost. Crucibles were then frozen until they were loaded into the HyPy machine.

Table 10 Overview of samples used in hydrogen pyrolysis extraction process. Those which had previously had organic solvents passed through are detailed in column 4. 3 silica blanks were introduced to track any contamination during the process and an additional sample of JSC Mars 1, a NASA Mars simulant, to compare with the sample of JSC Mars 1 which had had solvents passed through.

Sample name	Full name	Description	Extractions Performed pre HyPy	sample mass (g)	Mass of catalyst in vial (mg)	Catalyst %
SiB 01	Silicon Beads Blank 1	Silica beads blanks introduced at HyPy stage	none	0.0362	2	5.5
SiB 02	Silicon Beads Blank 2	Silica beads blanks introduced at HyPy stage	none	0.0318	1.8	5.7
SiB 03	Silicon Beads Blank 3	Silica beads blanks introduced at HyPy stage	none	0.032	2.1	6.6
Si HyP	Sigurdfjelle	Part of a Svalbard volcanic complex that has the same macromolecular carbon as martian meteorites	hexane, DCM and methanol	0.0806	4	5.0
Sv HyP	Sverrefjellet	Part of a Svalbard volcanic complex that has the same macromolecular carbon as martian meteorites	hexane, DCM and methanol	0.0769	3.6	4.7
Js A HyP	JSC Mars 1	NASA's Mars simulant	hexane, DCM and methanol	0.0816	2.5	3.1
Na HyP	Nakhla	Martian meteorite	hexane, DCM and methanol	0.0837	4.3	5.1
JS B HyP	JSC 1 B	NASA's Mars simulant (extra sample introduced at HyPy stage)	None (added as a comparison to see if anything extra can be detected having not had solvent extraction)	0.1095	4.7	4.3
La HyP	Lafayette	Martian meteorite	hexane, DCM and methanol	0.0635	2.1	3.3

HyPy Procedure

The hydrogen pyrolysis machine at the NERC Radiocarbon facility, SUERC, was used to remove refractory organic material from the residue of samples which had previously undergone solvent extraction using hexane, dichloromethane, and methanol solvents. Following sample preparation, each individual sample was run on the HyPy (for programme, see Figure 108) with cleaning runs (full runs with no sample or silica) and blanks (collecting silica with no sample) throughout, over 5 days as outlined in Table 11.

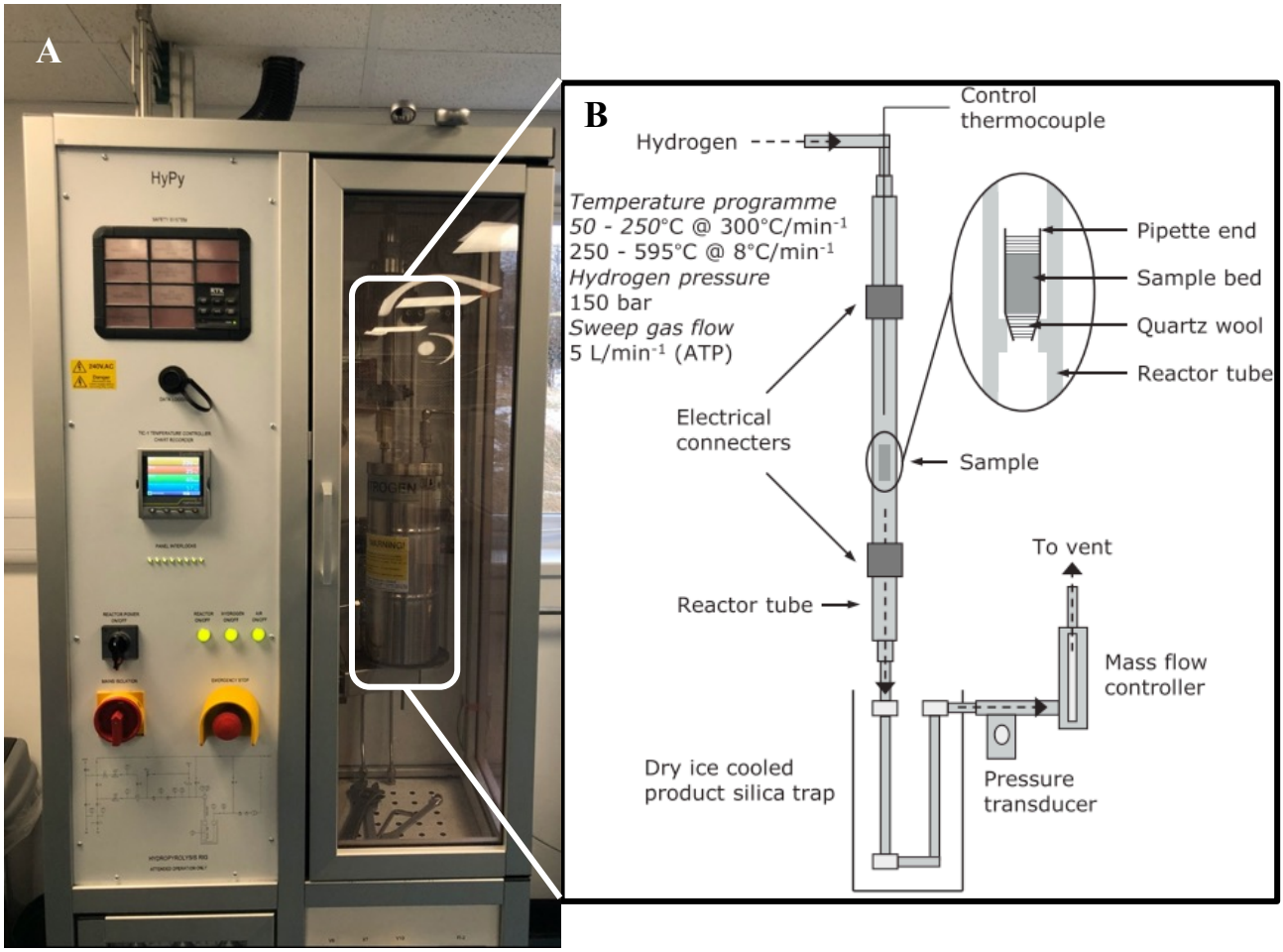

Figure 108 A Hydrogen Pyrolysis Machine at NERC Radiocarbon facility. Catalyst-bearing samples are loaded into a reactor tube insert in B. High pressure hydrogen passes through the sample, removing refractory organic material, which is then deposited onto silica beads in a dry ice cooled trap. Figure B, adapted from Meredith et al. (2012).

Prior to each HyPy sequence, the reactor tube is rinsed with dichloromethane to remove any organic residue, and electrical connectors are sanded to remove any rust to improve thermal contact to ensure required temperatures are met in the reactor. Before pyrolysis process begins, hydrogen gas is pressurised to 15 MPa, and leaks checked for. During the ~1 hour

HyPy process, temperature is gradually increased (as outlined in Figure 108), whilst high pressure (15 MPa) hydrogen continually flows through the sample, in the reactor tube, catalytically adding hydrogen to carbon in refractory material. Hydrogenated hydrocarbons are then deposited on sterile silica beads in the silica trap, which is cooled by dry ice. Once the sequence is complete, the sample is removed, and the silica beads are collected in a clean vile and frozen at -10 C until sample preparation for GC-MS begins.

Table 11 Schedule of samples run on HyPy in March 2020, demonstrating the number of cleaning runs, and blanks added, and separation of all samples by cleaning runs and blanks throughout. Following each run, samples were frozen until solvent extraction for GC-MS analysis.

Day	1	2	3	4	5	6
Date	26-Feb	27-Feb	28-Feb	02-Mar	03-Mar	04-Mar
Preparation	Solvent clean & furnace silica	In between each run- trap & reactor cleaned w/ DCM (not req for cleaning run)	In between each run- trap & reactor cleaned w/ DCM (not req for cleaning run)	In between each run- trap & reactor cleaned w/ DCM (not req for cleaning run)	In between each run- trap & reactor cleaned w/ DCM (not req for cleaning run)	In between each run- trap & reactor cleaned w/ DCM (not req for cleaning run)
	Solvent clean steel wool					
	Solvent clean Trap & Reactor (use new)					
	Prepare clean vials for silica (furnace & label)					
Samples to be run in order	1	Cleaning run (if needed)	Si Hyp	Silica only	Cleaning run	SiB 03
	2	Silica only	Cleaning run	SiB 02	Na HyP	JS B HyP
	3	SiB 01	Sv HyP	Cleaning run	Cleaning run	Cleaning run
	4	Cleaning run	Cleaning run	Js A HyP	Silica only	La HyP
	5					Cleaning run

Gas Chromatography Mass Spectrometry (GC-MS)

After hydrogen pyrolysis (which took place at SUERC in February/March 2020), GC-MS was scheduled to analyse the refractory content extracted by HyPy for late March 2020. By this time, the university had shut down leading to a ~7 month delay in the project. GC-MS was carried out finally in Autumn 2020, however it was carried out by the laboratory technician only, as social distancing rules would not allow more than one person in the lab, and I had not received sufficient prior training on the instrument pre-lockdown to carry out the experiment alone. The standard operating procedures (SOP) for extraction and GC-MS following HyPy in the BECS lab, which were carried out by the technician, Ali Salik, are found in Appendix 1.

Results

After hydrogen pyrolysis, the silicate deposited samples were extracted with hexane (to target alkanes) and dichloromethane (to target polycyclic aromatic hydrocarbons, PAHs) at the BECS lab, U of G. These were two separate extractions, run on two separate gas chromatography columns, with the hexane extract run on an RTX-1 column and the DCM extract run on the HP5-MS column purchased with a grant from the Geological Society of London, as macromolecular PAH molecules were the primary target molecules, so maximum chance of column separation for these was required.

The ASE solvent extraction, GC-FID, GC-MS, and initial data processing (see calibration curves in Appendix 1) was carried out by technician Ali Salik in October 2020, due to the pandemic as there was a one-person occupancy limit in the laboratory.

Identification of Molecules

All molecules detected in the experiment (as summarised in the tables III and IV below) had their identities confirmed via comparison with in-house standards and, when required, inspection of fragmentation spectra. All the hexane extracted samples were run on GC-FID using an RTX1 column, and a small number were also run on GC-MS to confirm the identities of detected compounds. All the DCM samples were similarly run on GC-FID using an HP5MS column, and a small number were also run on GC-MS to confirm the identities of detected compounds.

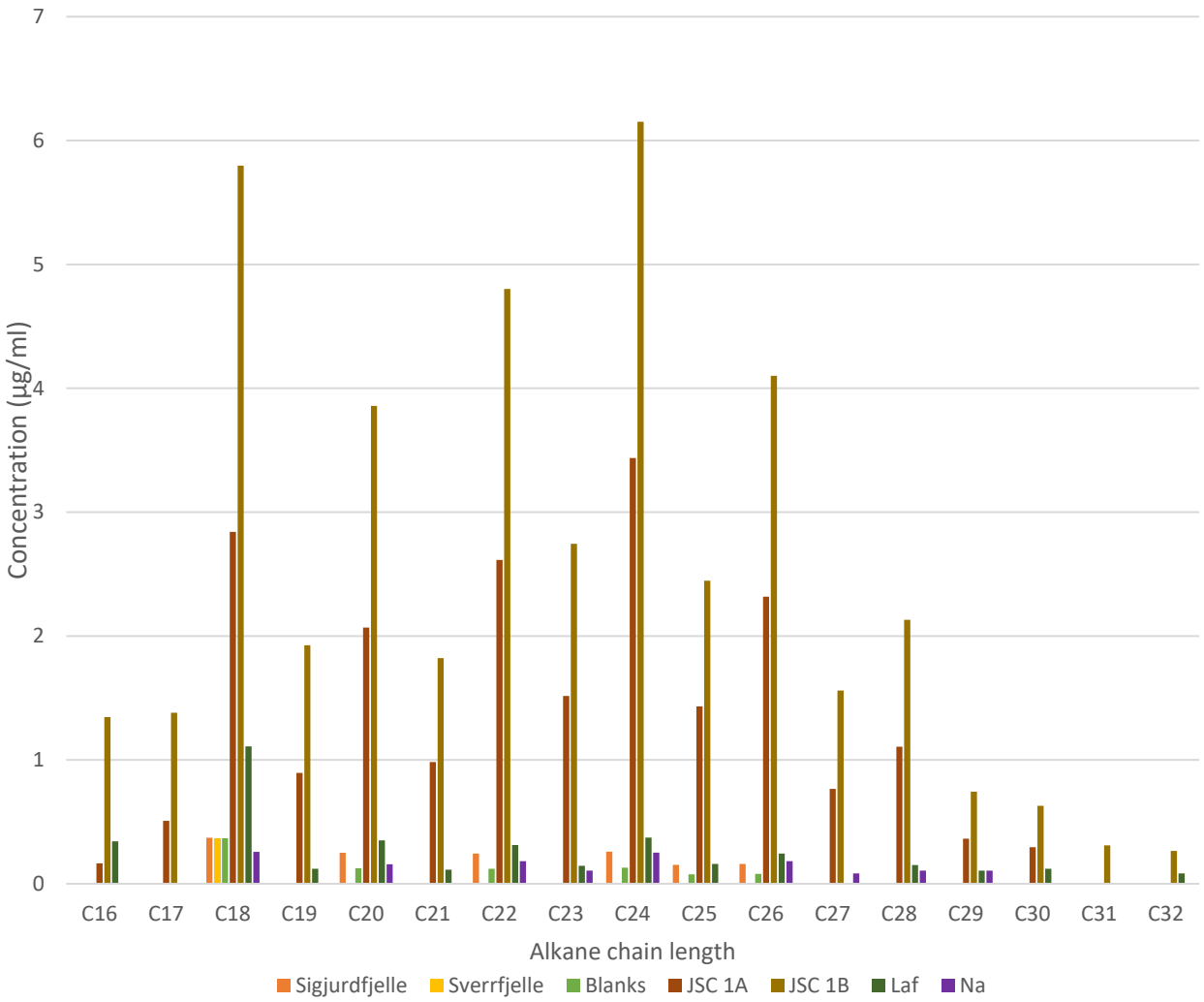

Figure 109 Alkane Results of HyPy – GC-MS experiment. Non-normalised concentrations of alkanes detected in samples that were hydrogen pyrolyzed, which deposits refractory organic material on silica, the silica was then run on the BECS auto solvent extractor to study the organic content using the BECS lab GC-MS. These concentrations are not sufficient for GC-IRMS analyses (originally planned as subsequent experiment)

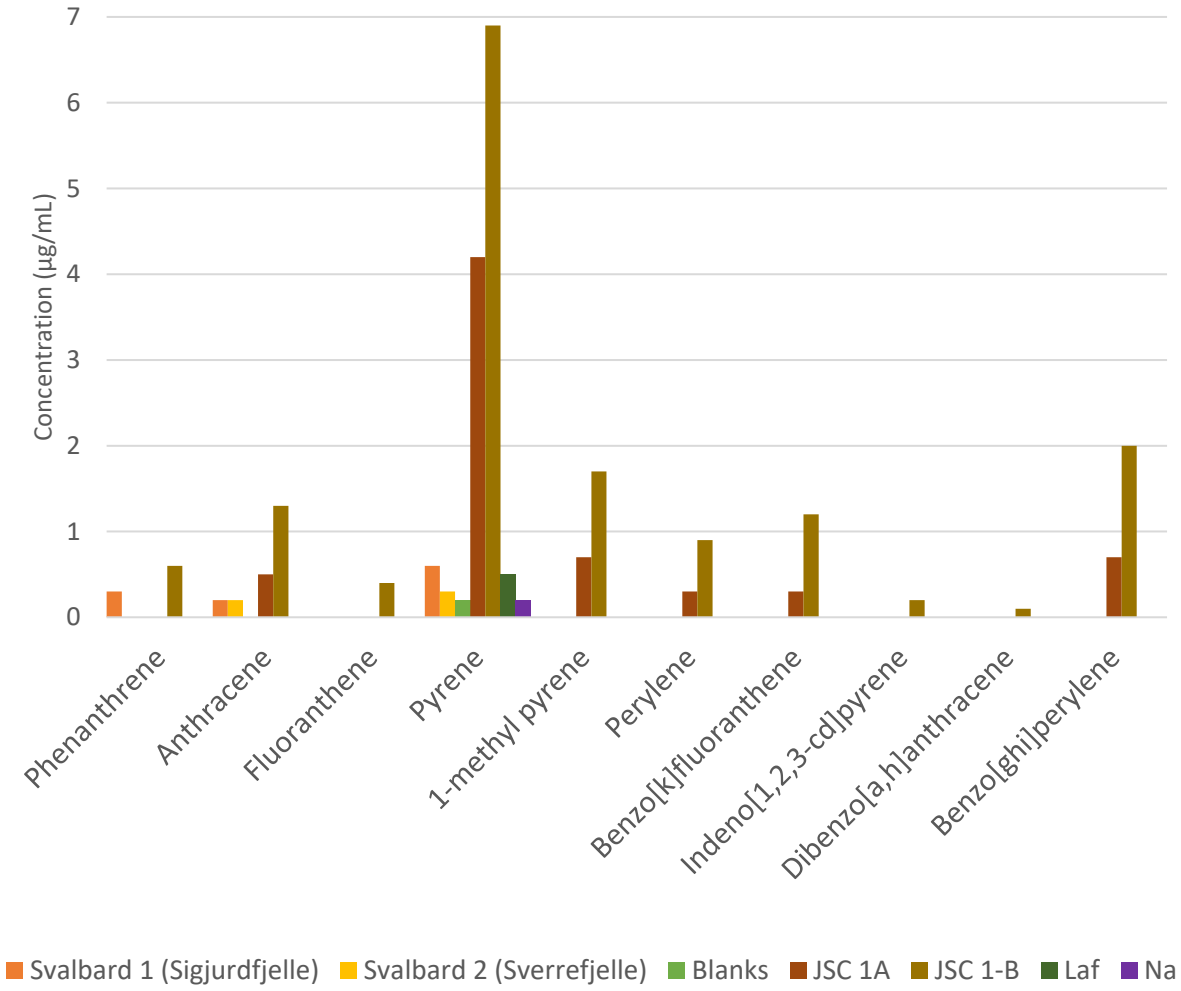

Figure 110 PAH Results of HyPy – GC-MS experiment. Non-normalised concentrations of PAH molecules detected in samples that were hydrogen pyrolyzed, which deposits refractory organic material on silica, the silica was then ran on the BECS auto solvent extractor to study the organic content using the BECS lab GC-MS. These concentrations are not sufficient for GC-IRMS analyses (originally planned as subsequent experiment)

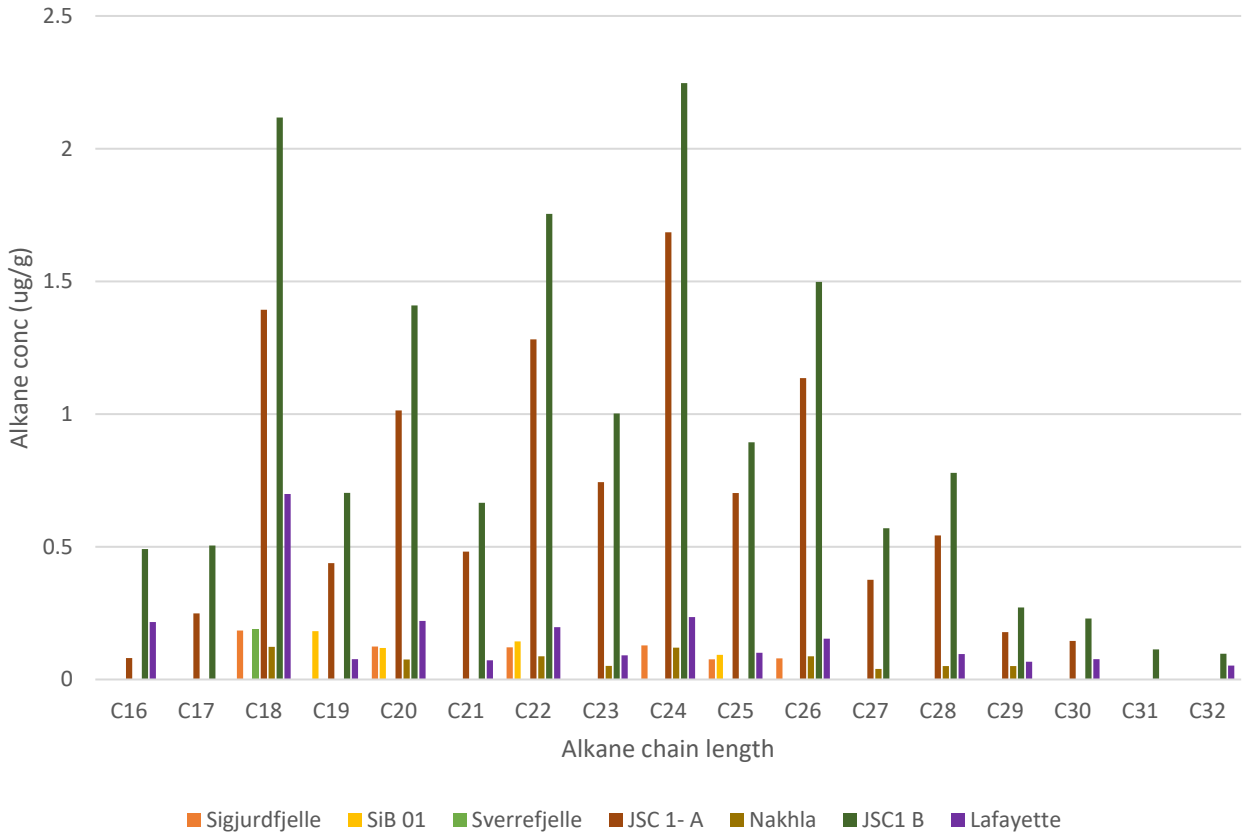

Figure 111 Normalised concentrations of alkanes detected in experimental samples and in one blank for the HyPy GC-MS experiment. Concentrations are normalised to masses of sample prior to insertion into HyPy to determine organic yield of analysis.

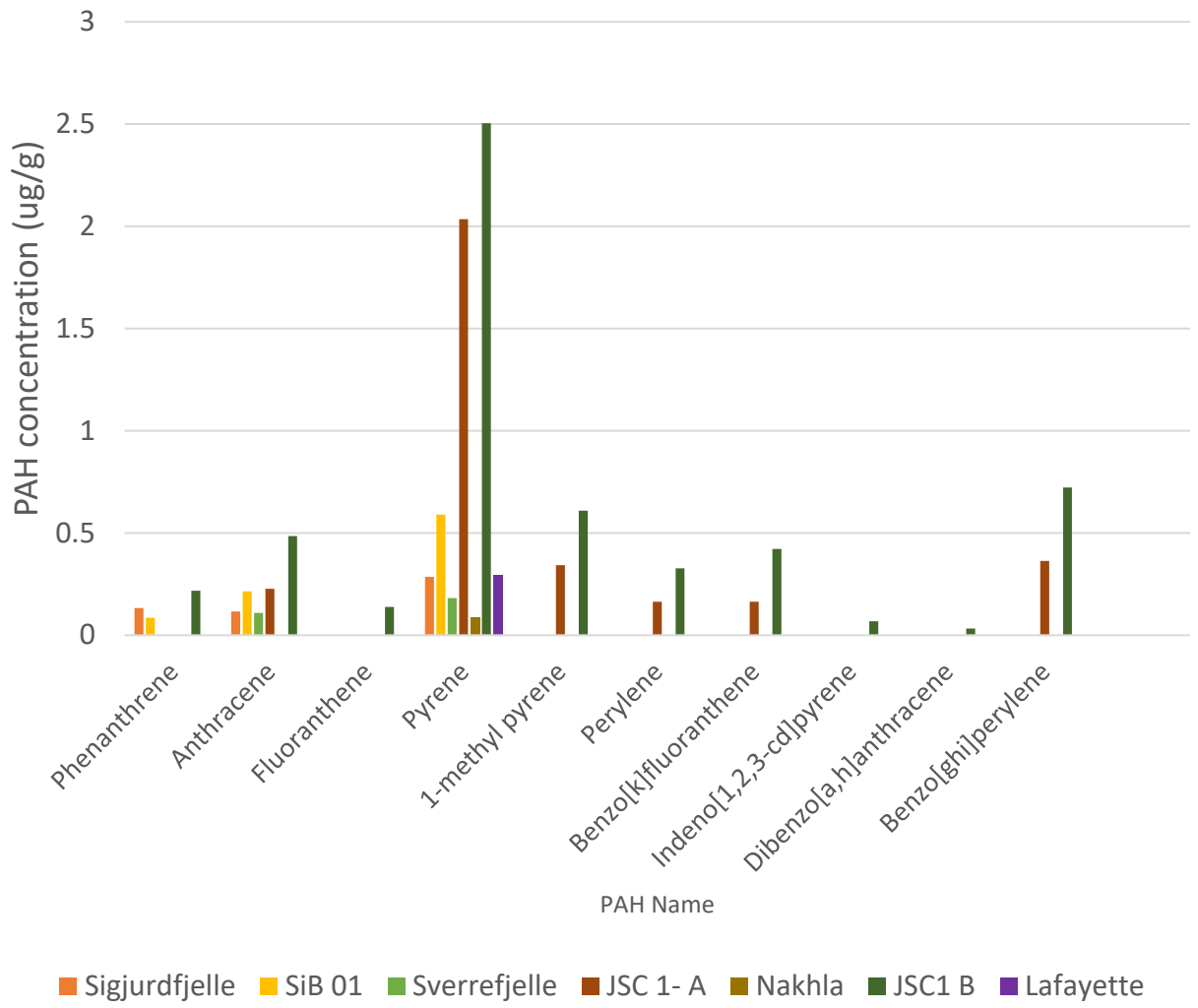

Figure 112 Normalised concentrations of PAHs detected in experimental samples and in one blank for the HyPy GC-MS experiment. Concentrations are normalised to masses of sample prior to insertion into HyPy to determine organic yield of analysis.

Table 12 Summary of alkanes detected in HyPy GC-MS experiment by GC-FID after hexane extraction and column separation using RTX-1 column, normalised concentrations are displayed in Figure 111.

Alkane Chain length	Si	Sv	Bl	JS 1A	JS 1B	Laf	Na
C16				✓	✓	✓	
C17				✓	✓		
C18	✓	✓	✓	✓	✓	✓	✓
C19				✓	✓	✓	
C20	✓		✓	✓	✓	✓	✓
C21				✓	✓	✓	
C22	✓		✓	✓	✓	✓	✓
C23				✓	✓	✓	✓
C24	✓		✓	✓	✓	✓	✓
C25	✓		✓	✓	✓	✓	
C26	✓		✓	✓	✓	✓	✓
C27				✓	✓		✓
C28				✓	✓	✓	✓
C29				✓	✓	✓	✓
C30				✓	✓	✓	
C31					✓		
C32					✓	✓	

Table 13 Summary of PAHs detected in HyPy GC-MS experiment by GC-FID after DCM extraction and column separation using HP5-MS column, concentrations are displayed in Figure 112

PAH Name	Si	Sv	Bl	JS 1A	JS 1B	Laf	Na
Phenanthrene	✓				✓		
Anthracene	✓	✓		✓	✓		
Fluoranthene					✓		
Pyrene	✓	✓	✓	✓	✓	✓	✓
1-methyl pyrene				✓	✓		
Perylene				✓	✓		
Benzo[]k]fluoranthene				✓	✓		
Indeno[1,2,3-cd]pyrene					✓		
Dibenzo[a,h]anthracene					✓		
Benzo[ghi]perylene				✓	✓		

After HyPy was carried out to liberate refractory organic molecules and deposit them on silica beads, these samples were run on the Automatic Solvent Extractor (ASE) in the BECS lab at U of G using dichloromethane and hexane to create concentrated 40ul extracts. These extracts were run on GC-FID and where necessary GC-MS targeting alkanes (as would be dissolved primarily by hexane) and polycyclic aromatic hydrocarbons (as would be dissolved primarily by DCM).

The results of this are shown in Figure 109 and Figure 110, these figures show the concentrations of the alkanes and PAHs per ml of solvent. These were then normalised (c_n) based on the detected concentration (c_d), volume (V) and mass (m) according to

$$c_n = \frac{c_d V}{m}$$

where concentration is measured in µg/ml, volume is measured in ml, and mass is measured in g. The normalised concentrations are then displayed in Figure 111 and Figure 112. The masses used were those of the samples prior to having the catalyst added during sample preparation for hydrogen pyrolysis. All identities are confirmed. Overview tables

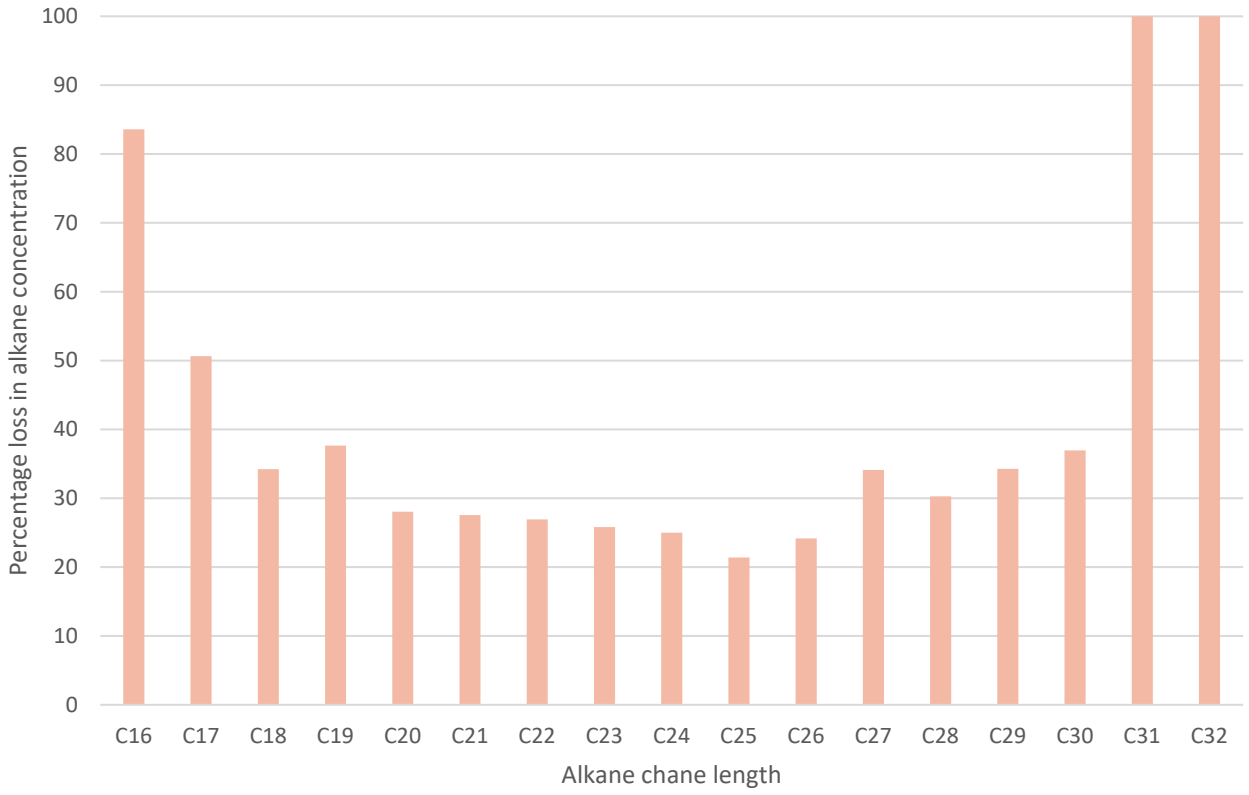

Figure 113 Percentage loss of normalised alkane concentration due to previous solvent extraction in HyPy GC-MS experiment. Calculated using the difference between concentrations in JSC1A and JSC1B (ie the sample that was solvent extracted prior to HyPy, and the sample that wasn't respectively).

which summarise the alkanes and PAHs detected in each sample are shown in Tables III and IV.

Figure 109 and Figure 110 were created using the calibration curves (see appendix) created by technician Ali Salik, due to social distancing restrictions which meant I could not work with him in the lab at the time. These figures show that a small number of polycyclic aromatic hydrocarbons (PAHs) and alkanes were above detection limits in the samples. These were at the highest concentrations in the JSC Mars 1 analogue samples. Furthermore, the additional sample of JSC Mars, 'ID= JSC 1B' which was added for this

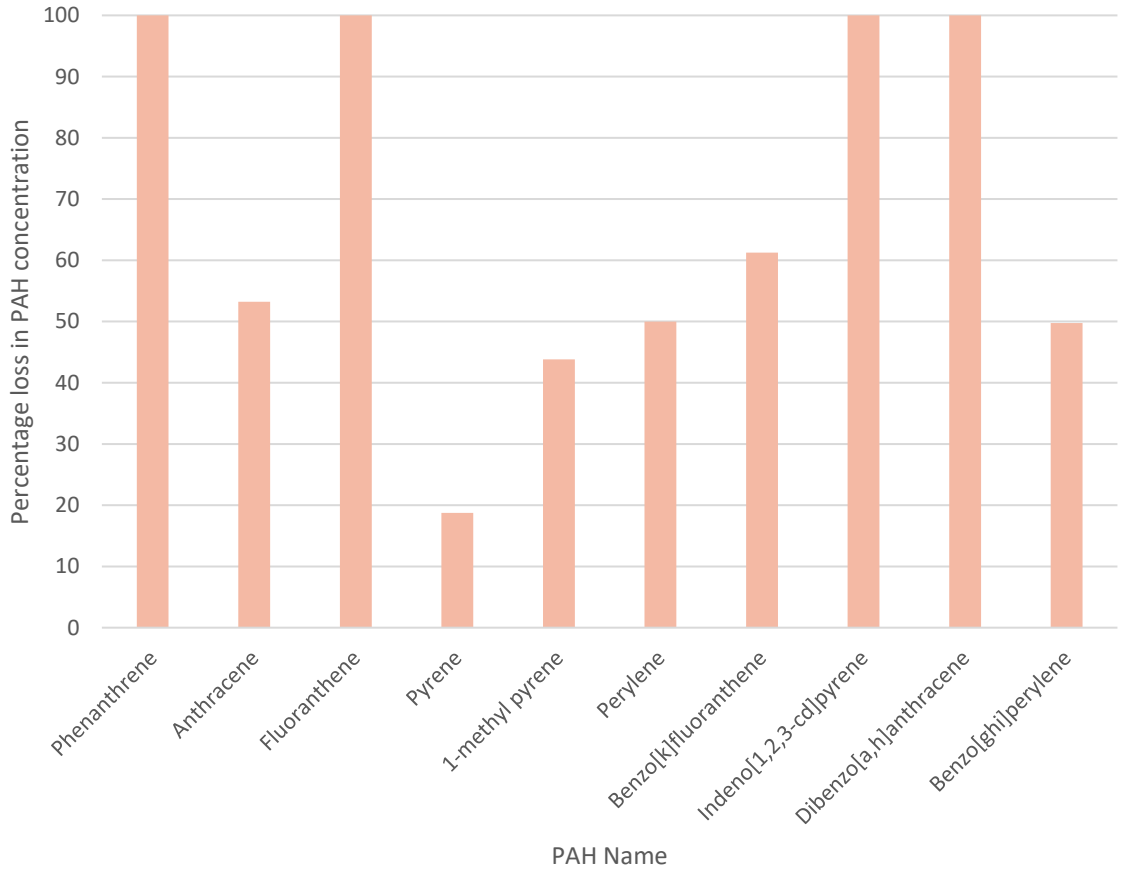

Figure 114 Percentage loss of normalised PAH concentration due to previous solvent extraction in HyPy GC-MS experiment. Calculated using the difference between concentrations in JSC1A and JSC1B (ie the sample that was solvent extracted prior to HyPy, and the sample that wasn't respectively).

experiment only and had therefore had no prior solvent extraction (for the LC-MS experiment), had higher concentrations of all molecules. Figure 113 shows the percentage loss in normalised concentration of alkanes between JSC1B and JSC1A, and Figure 114 shows the percentage loss for PAHs. These figures show significant organics loss due to primary solvent extraction when you compare JSC1A to JSC1B, both for alkanes and PAHs.

Table 12 and Table 13 show that there were no PAHs or alkanes detected only in the martian samples (Lafayette and/or Nakhla) suggesting that no indigenous martian organic material was collected above detection limits from this technique. There was very little organic material above detection limits in the procedural blanks. The concentrations in the blanks were averaged to create the blank values for the non-normalised graph, as there were six procedural blanks, but these values were very consistent (standard deviation in concentration varied from 0 to 0.08 μg/ml). For the normalised concentrations, the SiB01 blank was used, as this blank had a known mass - it had been weighed and treated with catalyst prior to HyPy (there were three such blanks in total, SiB01-03). The three additional blanks were simply empty HyPy runs and therefore were clean silica prior to HyPy, whose mass was not known, so their concentration could not be normalised.

Eleven alkanes were present at low concentrations (< 0.5 μg/g) in Lafayette that were present in much higher concentrations in both JSC Mars 1 samples. Eight alkanes were present at low concentrations (< 0.5 μg/g) in Nakhla that were present in much higher in both JSC Mars 1 samples, and not all those above detection levels Nakhla were detected in Lafayette. The only PAH detected in Nakhla or Lafayette was pyrene, which was detected in Lafayette at a similar level to the silica blank, and at a much lower abundance in Nakhla. There were also no PAHs or alkanes present in the Svalbard analogues that were not also present in the JSC Mars 1 samples; again, these concentrations were highest in the latter samples.

Summary of key HyPy Findings

- Significantly fewer compounds were detected using HyPy-GC-MS compared to LC-MS (hundreds fewer) suggesting this technique is less effective at analysing martian meteorite samples at such low masses
- More compounds were detected in the analogue samples than the meteorite samples, although still ~20 compounds per class (ie alkanes and PAHs), compared to hundreds detected using LC-MS
- JSC Mars 1 contained the highest number of compounds studied in this experiment, suggesting it is the sample riched in refractory organic content
- The sample of JSC Mars 1 which was pyrolysed after being solvent extracted had lower concentrations of, and fewer, organic compounds, than the sample which had not been previously solvent extracted. Solvent extraction therefore likely removes some pyrolysable content from the matrix.

7 Discussion

In this chapter the results from both the in-situ and bulk analyses are discussed, together with the implications of the results and evaluations of the techniques used. Included in the technique evaluations are potential future avenues of analysis. The in-situ results are considered first, with each martian meteorite studied described in turn, followed by the ureilites, then the BVC analogue materials. The bulk analyses are then evaluated in the same order. Finally, the possible origin scenarios for martian organics are outlined, contextualised using data collected in this study.

In-Situ Results

Organic Matter in Tissint

When analysed with CRIS, the macromolecular organic material detected in Tissint displayed variable G band centre positions. Its position ranged between ~1555 and ~1586 cm^{-1} within an individual MMC inclusion (see Figure 115), suggesting that MMC is heterogeneous within Tissint. This G band variation is similar to that observed within amorphous organics across interplanetary dust particles (IDPs) and carbonaceous chondrites (see Figure 2, Starkey et al. 2013). The variation measured by Starkey et al. (2013) was between ~1570 and 1605 cm^{-1} across all samples and laser wavelengths used (red: 632 nm, green: 514 nm, and blue: 473 nm). In the case of the present martian study, a green 532 nm laser was used, therefore a direct comparison between the datasets cannot be made, since Starkey et al. also showed that the G band position does vary with wavelength used. However, the same variation is observed within one individual Tissint inclusion as Starkey et al. measured across all samples (see Figure 116). This observed G band variation is unlikely to be due to laser effects. In addition, Busemann et al. (2007) observed IDP MMC G band centre position variation with a 532 nm laser and Starkey et al

(2013) attribute their G band variation to heterogeneity, which in turn they suggest may be

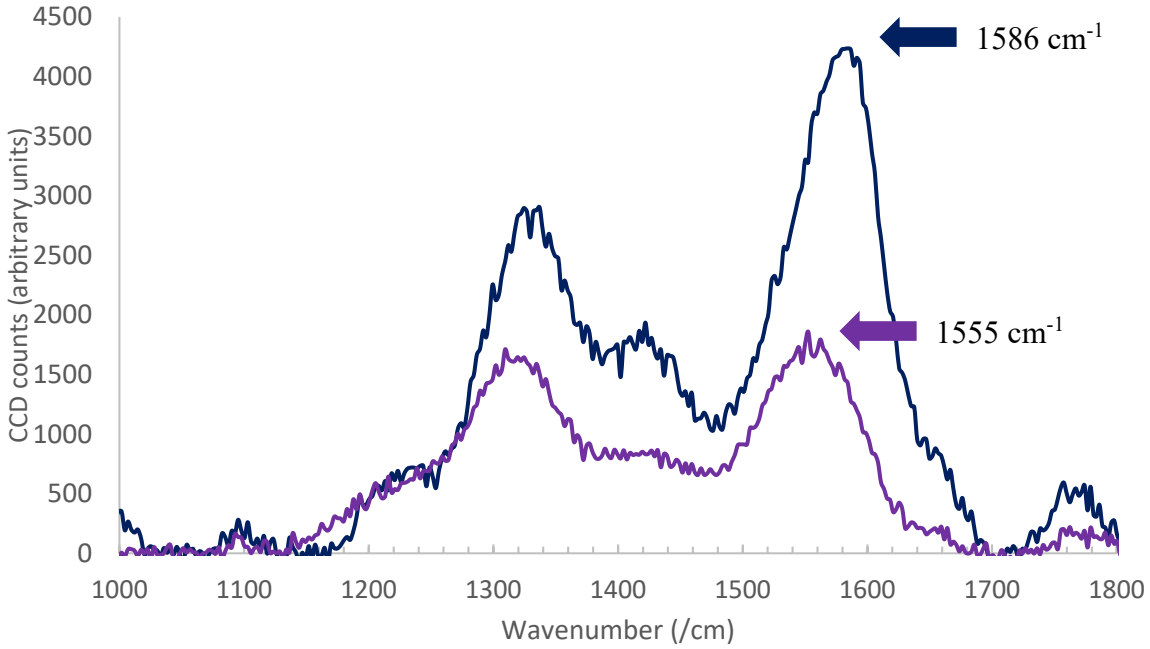

Figure 115 D and G bands for two spots within the same inclusion in Tissint A demonstrating the wide variation in G band position. G band peak centres are indicated.

related to thermal metamorphism. Tissint is a heterogeneously shocked meteorite, at a ~10 µm scale, which may cause localised heating, and therefore the observed G band variation, in the meteorite.

Our likely detection of labile carbon in Tissint pyroxene, which is spatially near to, but spectrally distinct from the epoxy thin section polymer, and only ~2 µm away from MMC, shows the heterogeneity in martian organic carbon - assuming it is indigenous material. Tissint was a recent meteoritic fall, reducing the risk of the material being terrestrially derived, however some organic contamination has been detected in this meteorite despite its short terrestrial residence (iMOST, 2018). Our detection of labile carbon is broadly consistent with the variation in organic material detected in Tissint by Lin et al. (2014), who found a range of refractory and amorphous carbon using nanoSIMS.

Labile organic material has also been previously detected in meteorites, and indeed in martian meteorites, and usually consists of 1-3 aromatic rings, as opposed to the multiple polycyclic aromatic material in macromolecular carbon (Jull et al. 2000). Jull et al. (2000) suggest that their ^{14}C and $\delta^{13}C$ measurements of Nakhla support an extra-terrestrial origin for this material, likely CM2 chondrites. It has been suggested that labile material in carbonaceous chondrites has a different origin in the Solar System to refractory organics

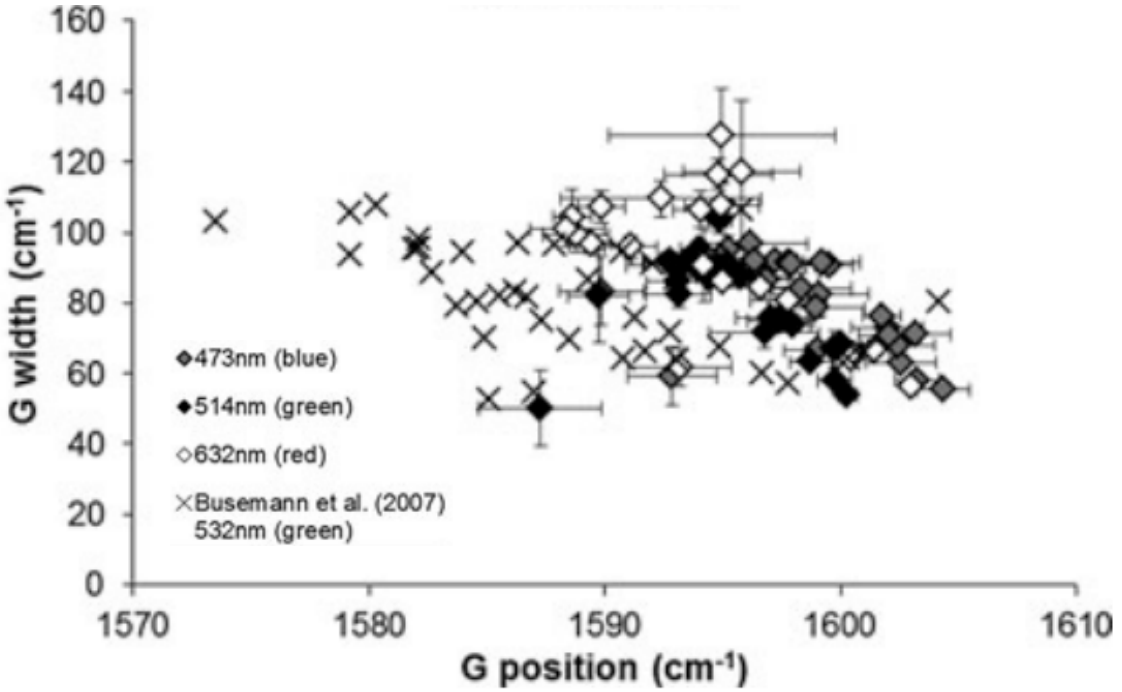

Figure 116 G band width versus G band position for the insoluble organic matter in IDPs and carbonaceous chondrites studied by Starkey et al. (2013) and Busemann et al. (2007). Adapted from Starkey et al. (2013).

(Sephton et al. 2015). The labile organics in Murchison were compared in detail to its refractory organics using hydropyrolysis coupled with mass spectrometry, liberating aromatic material, to identify molecular structures and to measure ^{13}C and ^{15}N ratios (Sephton et al. 2015). This work and previous work found that the labile organics were relatively enriched in ^{13}C and ^{15}N whilst that of the refractory organics was relatively depleted (Sephton et al. 2003; Sephton et al. 2015), thereby suggesting differing Solar System origins. Without isotopic measurements (e.g., via NanoSIMS or GC-IRMS) it would be difficult to identify whether or not the the labile material we detected in Tissint is similar to that of Nakhla and Murchison. However, the material in Tissint was found closely associated with MMC, which is also true of the Murchison material analysed by Sephton et al. (2015). These matching features between Tissint and Murchison may suggest a similar formation scenario or indeed support the suggestion of Flynn (1996) that the CM2s are the source of at least some of the martian organic material. Further confirmation via isotopic measurements would enable this idea to be tested, and indeed rule out the possibility of terrestrial contamination.

Although these results in Tissiutn show how CRIS can effectively detect likely martian organics, the structural changes made to the labile carbon by the Raman laser demonstrate

the drawbacks of Raman spectroscopy for astrobiology. Given that we have shown CRIS converts the labile carbon to MMC under a relatively short period of laser heating, our results suggest care must be taken when analysing martian organics data in the future. The confocality of this laser set up may have contributed to the formation of MMC, and thus upon Mars Sample Return, we must be careful to ensure any martian organics data acquired using such instrumentation have not been altered in this way, by keeping careful eye on time series data. Care should also be taken when probing data from the Perseverance mission, since it is equipped with a UV Raman spectrometer, as well as the RLS onboard the future ExoMars rover, should it go ahead (Rull et al. 2017; Hollis et al. 2021).

The carbon K edge and nitrogen K edge STXM XANES data from Tissint show the MMC is polyaromatic, with a large peak at 285.2 eV, and three additional organic functional groups - phenols, nitriles, and carboxyl. The large narrow aromatic peaks in all four averaged areas demonstrate the macromolecular nature of the material, in contrast to the

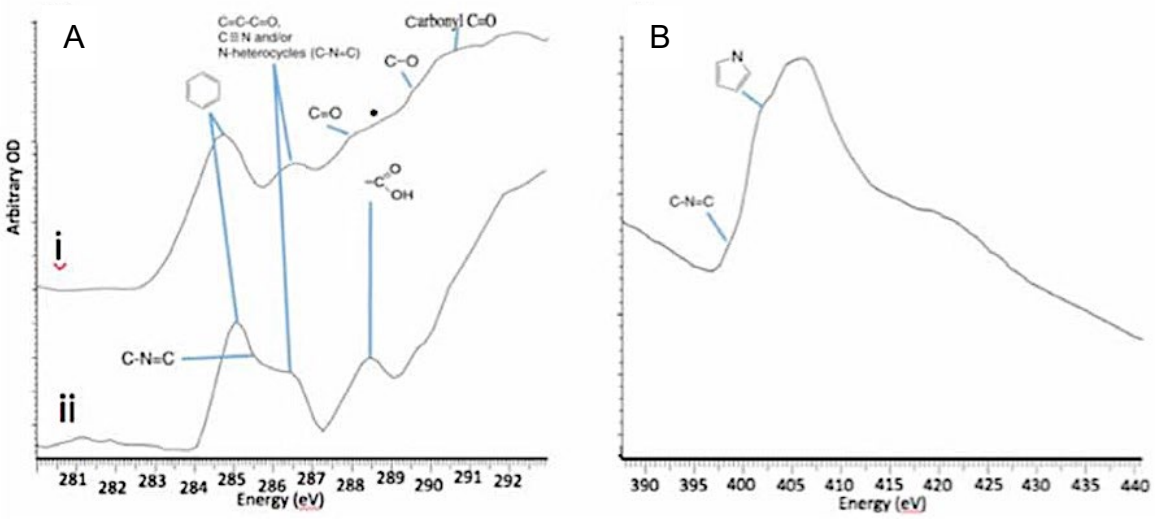

Figure 117 A Carbon K edge XANES spectra from organic rich areas in Tissint. B Nitrogen K edge XANES spectrum from organic rich area in Tissint. Adapted from Steele et al. (2018).

much smaller aromatic peaks observed in the ureilite samples studied, suggesting less refractory organic content. The presence of a nitrogen K edge jump in the MMC in Tissint suggests that this organic matter formed in a reducing environment. Results of the present study are largely consistent with the STXM XANES work on Tissint carried out by Steele et al. (2018), with many of the same peaks being detected (see Figure 117). In the study presented in Figure 117, CRIS was combined with STXM XANES and NanoSIMS analyses to demonstrate that this MMC is indigenous to Mars and formed by the

electrochemical reduction of CO_2 due to the reaction between spinels, sulfides, and brines, thanks to its association with titano-magnetite (Steele et al. 2018). This electrochemical reduction mechanism is an example of the Fischer-Tropsch Type synthesis mechanisms thought to occur widely on planetary bodies in the Solar System, explaining the origin for many extra-terrestrial organics (Treiman 2003; Mcdermott et al. 2015).

Organics in Yamato 000593 and 000749

As discussed in chapter 4, thin sections of both Y000593 and Y000749 were analysed by CRIS with limited success during the first visit to Carnegie Planets. In one CRIS map of the former, MMC was not initially found, but was successfully detected using a single spot scan with a longer retention time, albeit with very broad low intensity peaks, indicating a small amount of MMC present in the area (see Chapter 4, Figure 76). Owing to limitations on instrument availability, there was not then sufficient time to map the whole area at this longer retention time.

It is unlikely that the two Yamato samples contain a lower concentration of MMC than the other samples studied, since e.g. other nakhlites have been found to contain MMC (Steele et al. 2018). However, they were both the smallest chips of all thin sections prepared for MMC analyses, therefore very little sample area (<1 mm^2) was available to scan for MMC. For example, in contrast to the one very small chip of each meteorite, two much larger thin sections of Tissint were available. These Yamato samples were also studied with CRIS very early on (~five weeks in) in my PhD, and thus my ability to identify the most probable MMC rich inclusions was unrefined at that stage. The Yamato meteorite samples were analysed early in the research project and would not have benefitted from the later refinements in analysis and data interpretation. Future analysis of these samples would benefit from additional CRIS studies, since little time was spent scanning these thin sections. More comprehensive Raman mapping of these samples and/or additional thin sections of these meteorites would improve our understanding of the organic content of the nakhlites.

Organics in Y000593 have been previously identified in secondary iddingsite veins (alteration features) with their formation attributed to both biogenic interactions (White et al. 2014) and the exogenous deposition of organics, and subsequent impact-induced hydrothermal circulation and redistribution of the organic material (McLoughlin et al. 2019). In the former case, the morphology of the carbon-rich phases in the iddingsite veins

were found to be similar to those observed in Nakhla (Gibson et al., 2001) which is a fall of the same group as Y000593 (nakhlite). However, a morphological case alone cannot be used as evidence for extra-terrestrial life, as demonstrated by the now discredited 'martian bug' in ALH 84001 (McKay et al. 1996; Becker et al. 1999).

Organics in SaU 008

A large and fairly deep (9.5 μm below the thin section surface) MMC-rich region was found in SaU 008 using CRIS during the first trip to Carnegie Planets. The depth of the MMC was constrained by acquiring CRIS maps at 1.5 μm depth intervals through the thin section, as it was a large oxide region (see Figure 72, chapter 4). This depth scan showed how constrained the MMC was across this large inclusion. Because of the large size of this oxide inclusion, four FIB sections were extracted from this region for STXM XANES analyses, to maximise the chance of extracting the carbon, particularly given its depth. Unfortunately, one of these lamellae was lost in transit to Diamond Light source, and the other three had no carbon present when analysed at the carbon K edge. The features observable in the secondary electron images of the lost sample of SaU 008 (Chapter 4, Figure 79) appear most similar to the lamellae in other samples where carbon was detected (i.e.,rough edges, amorphous 'fuzzy' appearance, as opposed to the smoother oxide edges in the other three lamellae).

Given the primary FIB lamella was lost prior to STXM XANES analysis, care should be taken in the future, where possible, to acquire multiple lamellae. In preparation for Mars Sample Return, we suggest that FIB extraction protocols, and lamellae storage/transportation procedures are optimised to minimise the risk of any vibration etc, and thus potential sample loss.

The depth scanned region of SaU 008 was also found to contain calcite when analysed with CRIS (see Figure 72). Some of the D and G band peaks were associated with clear calcium carbonate peaks at 1082 cm^{-1}. This calcite was almost certainly produced by terrestrial weathering since it has been previously described in SaU 008 and its paired stones and attributed to weathering due to its extended period of terrestrial residence until recovery in Oman (Grossman and Zipfel, 2001). This calcite presence may suggest that the MMC present may have been altered during its terrestrial exposure, thus any STXM XANES data acquired in any case may not have had the same functional groups as it would have had as a fresh fall.

Before the second visit to Carnegie Planets, the thin sections had been carbon coated (for FIB-SEM), and then re-polished with aluminium oxide to then be studied with CRIS again. Visual inspection was carried out and no clear remnant of the carbon coat was visible, so it was hoped that the re-polishing would be sufficient to remove the carbon coat, however CRIS analyses continually detected carbon coat (large triangular peak dominating the D and G peak region) as opposed to MMC throughout the sample. Survival of the carbon coat suggests that either more thorough re-polishing was required, or that thin sections should be studied comprehensively with CRIS prior to any carbon coating. Future sample analyses should therefore avoid any CRIS after SEM where a carbon coat has been applied.

NWA 8159

The CRIS and STXM data from NWA 8159 suggest that despite the meteorite representing a unique mantle source (Herd et al. 2017b), it contains similar organic compounds to other martian meteorites (e.g., this study, Steele et al. 2016). CRIS data show calcite was detected close to, but not in association with, MMC in NWA 8159. As with SaU 008, calcite in NWA 8159 is likely a result of terrestrial alteration since the stone is highly weathered with a number of calcite veins (Herd et al. 2017b). Much like in Tissint, variable G band centre positions were observed in NWA 8159 MMC - 1551 cm^{-1} and 1583 cm^{-1}, and within the same MMC bearing region (see chapter 4, Figure 70), suggesting that the organic material is heterogeneous. NWA 8159 and Tissint are both shergottite meteorites, but Tissint is a minimally contaminated fall (iMOST 2018), whereas NWA 8159 is a terrestrially altered find (Herd et al., 2017). The similarity between the MMC in both these shergottites - those in Tissint G band centre position varies between 1555 and 1586 $cm^{-,1}$ which is also a shergottite and a minimally contaminated fall (IMOST 2018)- suggests MMC in NWA 8159 is probably not terrestrially derived. The proximity to calcite, however, suggests the structure of the MMC may have changed during terrestrial weathering, although not extensively, given the similarity of its XANES spectra to Tissint's.

Elemental sulfur was also detected in NWA 8159. There are two possibilities for the origin of this elemental sulfur. Both possibilities relate to terrestrial weathering because Herd et al. (2017) showed that the meteorite crystallised in highly oxidising conditions, but elemental sulfur is stable in reducing environments. The first possible formation scenario is via the reduction of Fe^{3+} within hematite (hematite peaks are seen alongside sulfur peaks in Figure 71, chapter 4) as outlined in the half equation below (Kumar et al. 2018):

$$Fe^{3+} + S^{2-} \rightarrow Fe^{2+} + S^{0} + e^{-}$$

Kumar et al. (2018) investigated the redox characteristics of sulfidation of hematite using STXM XANES and TEM and showed that elemental sulfur is produced when iron (iii) oxides are reduced by sulfides. Herd et al. (2017) searched for sulfides in NWA 8159 but were unsuccessful. Primary sulfide inclusions may originally have been present, then altered to elemental sulfur in the desert environment given the extensive weathering experienced by NWA 8159. Alternatively, the elemental sulfur may have been formed by the oxidation of pyrrhotite (an iron sulfide) which produces iron oxides and elemental sulfur (Buckley and Woods 1985). TEM analysis was planned to characterise this inclusion further, and possibly determine which of the two formation mechanisms occurred, but this work was cancelled due to lockdown.

STXM XANES analyses of NWA 8159 confirmed the presence of calcite, again attributed to terrestrial weathering. STXM showed that calcite and MMC are associated in the FIB lamella analysed, with a small carbonate peak visible alongside the organic aromatic, ketone, and carboxyl peaks. The aromatic peak had a much lower optical density than the carbonate peak and compared to the other martian samples in this study. This suggests that this material is less refractory. The functional groups detected, alongside the less pronounced nature of the aromatic group, are an exact match for those found in ALH 84001 (Steele et al. 2022). The organic content of ALH 84001 was also associated with carbonate, but with indigenous carbonate globules that are absent from NWA 8159. However, the consistent organic peak identities suggest that the material is indigenous to NWA 8159. This similarity in MMC suggests that organic synthesis on Mars continued from the Noachian to the Amazonian, as suggested by Steele et al. (2022), given that ALH 84001 is 4.1 Ga old, and NWA 8159 2.4 Ga old.

Organic content in the Ureilites

The EDX scans of the ureilites were sufficient to detect carbon rich areas in Goalpara and Hajmah (a), distinct from the carbon coating of the thin section. However, this technique cannot distinguish between allotropes of carbon or carbon-bearing material in these Ureilite samples. STXM XANES analyses of the three ureilite FIB lamellae detected organic carbon but no nanodiamonds. Raman spectroscopy or luminescence spectroscopy would have distinguished diamonds from graphite and other carbon polymorphs (Klinke et al. 2002; Ross et al. 2011; Lorenz et al. 2019), but these analyses could not be performed

because of the short timeline between acquiring the thin sections and the allocated synchrotron beam time.

The STXM data from the ureilites was consistent with the presence of graphite and organic carbon in both samples. The presence of the latter may constrain the heating experienced by these two meteorites, as organic compounds are unstable at higher temperatures. Temperature limitations for the ureilite parent body based on ureilite organic content are discussed by Glavin et al. (2010). Ureilites are thermally altered carbonaceous meteorites, and Almaha Sitta has been found to contain amino acids which decompose completely at ~500-600 °C (Glavin et al., 2010). However, Steele et al. (2016) suggest that both martian and ureilitic nitrogen bearing MMC may be a precursor to amino acids, as a result of thermal impact processing. These authors suggest that amino acids may have formed by the cooling of hot gases released by the degeneration of complex organics during impact both in martian meteorites and ureilites, since both are thermally altered meteorites.

The presence of organic carbon detected in this project, in addition to the previously reported detection of graphite and diamonds in the ureilites Hajmah (a) and Goalpara suggest that similar to Tissint, these meteorites experienced heterogenous shock. Shock metamorphism has been suggested to have formed diamonds in the ureilites (Nestola et al. 2020) however the detection of organic matter such as PAHs, and N-bearing organics observed with STXM-XANES suggests that if shock was the mechanism to form ureilitic diamonds from carbon, such pressures must have been heterogeneous at a ~micron scale.

C-XANES has also been carried out on the organic matter in Almaha Sitta leading to the suggestion that carbonaceous chondrites were incorporated into the Ureilite Parent Body (Kebukawa et al. 2021). The spectra that Kebukawa et al. (2021) acquired from Almaha Sitta are shown in Figure 118. Some of these spectral features are distinct from those found in the present study in Goalpara and Hajmah (a). The contrast in content between the organics detected in our samples compared to Figure 118 is consistent with previous work

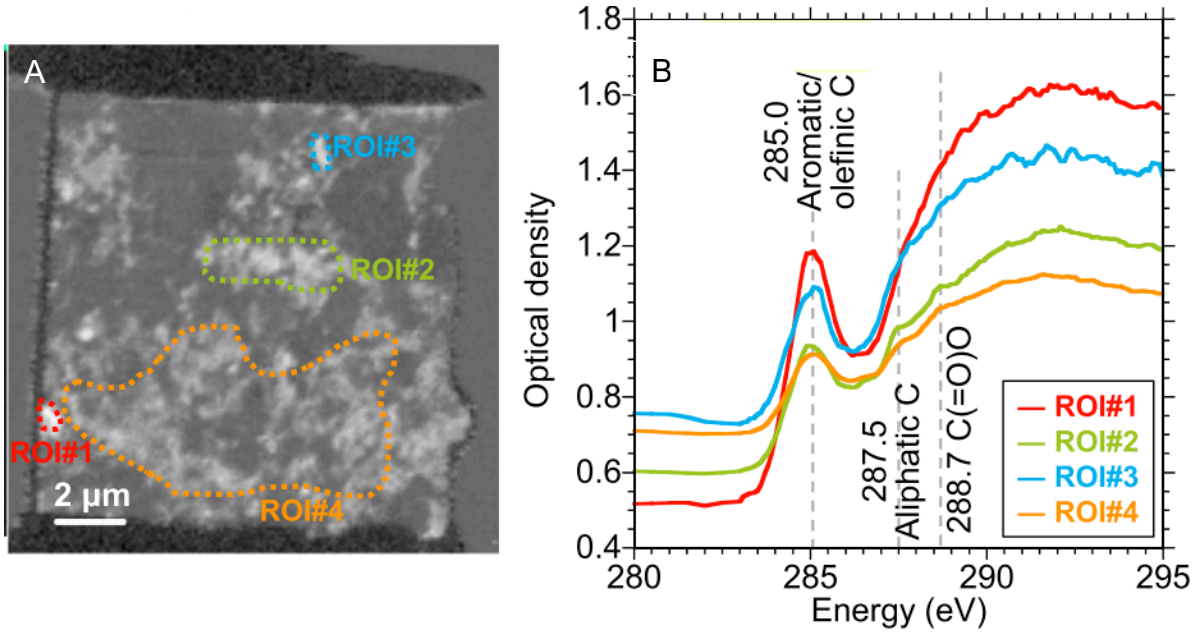

Figure 118 A- STXM XANES C K edge map of the four regions of interest in Almaha Sitta B- STXM XANES C K edge spectra of the four regions of interest. Adapted from Kebukawa et al (2021).

on ureilitic carbon, which suggests that carbon in the Ureilite Parent Body is heterogeneous (Smith et al. 2001).

Organic Content in the BVC Analogues

The STXM XANES analyses ofSigurdfjellet, one of the BVC analogues for MMC bearing organics in ALH 84001 (Steele et al. 2007), show that organic carbon is present in the outer rims of the carbonate globules. This result is consistent with previous Raman analyses of BVC carbonates (see Figure 119) (Steele et al. 2007). Figure 119, and STXM results from the present study (see Figure 92, chapter 4) show that there are two main organic rich regions in the rims of the globules, an inner rim and an outer rim. The carbonate globules are thought to have formed through the eruption of CO_2 rich volcanoes below Svalbard's permafrost and glacial ice. The MMC bearing carbonate globules formed from the rapid cooling of aqueous CO_2 bearing fluids, as the oxygen fugacity of the

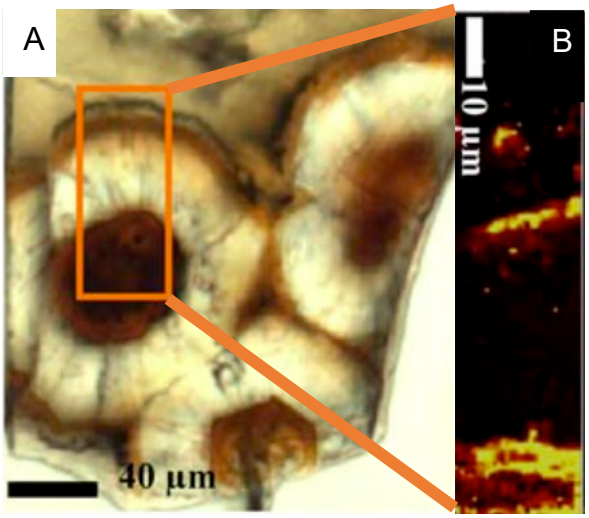

Figure 119 A transmitted light image of BVC carbonate globule B Raman map of G band in orange box region of A showing MMC is concentrated at the rims of the BVC carbonate globules. Adapted from Steele et al. (2007)

magmatic mixture decreased, producing reduced carbon (MMC) (Steele et al. 2007). The two MMC rich bands observed both in Figure 119 and in the STXM XANES analyes in this study attest to the conditions for graphite stability being met twice during crystallisation.

The aromatic, carbonyl (ketone), and inorganic carbonate peaks in our STXM analyses are consistent with the peaks observed in STXM XANES analyses of ALH 84001 carbonate globules (Steele et al. 2022), the only difference being an additional small carboxyl peak in ALH 84001. This result further confirms these samples as excellent analogues for martian meteoritic organic material.

Such analogues are vital for astrobiological investigations, since they allow for work to be done on similar samples to martian rocks, without the risk of losing precious specimens. Analogue work aids our understanding of martian geology without using samples of Mars, it also allows us to evaluate the techniques used to study martian specimens first, to ensure they are appropriate, so as not to risk wasting pieces of the red planet. The results of this study show these Svalbard samples are an excellent analogue for martian MMC, however as with all environmental samples, particularly if they are from the Arctic, unnecessary waste should be avoided.

In-Situ Techniques Protocol Evaluation and Possible Future work

The correlative in-situ protocol, from optical microscopy to STXM-XANES, was successful at detecting and characterising the organic content in the samples, although the thin sections prepared degraded over time compared to traditionally made thin sections (see Chapter 4, Figure 59). The SEM and CRIS analyses provided useful textural, mineralogical, and geochemical context for the organics detected. This context ensured the MMC-rich regions of interest were hosted in primary igneous minerals below the surface of thin sections and away from cracks, mitigating the risk of contamination. Our results suggest this protocol would be useful for Mars Sample Return, however there is a risk of structural change to any labile carbon present.

Although it was not possible to obtain D/H ratios (e.g., via NanoSIMS) to provide additional evidence for the martian origin of the analysed MMC, the functional groups detected with STXM XANES were similar to those previously reported for MMC in other martian meteorites, where NanoSIMS had been carried out (e.g. Steele et al. 2018; Steele et al. 2022). However, future work should characterise MMC inclusions of the meteorites studied in this work with NanoSIMS to provide further insight into the samples. TEM analyses of MMC would further enhance our understanding of these meteorites, too, giving more detailed textural, chemical and spatial details of the FIB lamellae prior to STXM XANES, as outlined in Steele et al. (2022).

The main purpose of the Raman analyses for this project was to identify and map the locations of MMC, as well as the surrounding mineralogy, which was successful. Possible future work could be to analyse the D and G band variations, and full width at half maximum in more detail to tease out any extra information in this dataset.

Future TEM analyses of the elemental sulfur in NWA 8159 would enable further

characterisation of the inclusion, e.g. assessing whether or not it is crystalline or amorphous and to give a deeper insight into its mineralogical associations. Additional TEM work on MMC in the martian samples would also aid understanding of the morphology and structure of the material (e.g., Steele et al., 2018; 2022). If the lamellae used in this study remain intact, this work could be carried out in the future. In the case of the elemental sulfur inclusion, the lamella was deliberately not fully thinned to electron transparency, so it is hoped that the sulfur may still be present after thinning. If this is not the case, further CRIS mapping could be carried out to identify any other possible elemental sulfur inclusions in the thin section.

The STXM XANES data can be further interrogated using other software. AXiS 2000 is a programme available in IDL (a costly programming language) which can align XANES stacks much more precisely than MANTiS (the open source software used in this study). Alignment is required due to the sample drift between energies when carrying out STXM, and the more accurate the stack alignment the less noise in the spectra generated, removing artefacts, smoothing spectra, and easing the detection of true peaks from the background. Should IDL be available, reprocessing of the data would be valuable, particularly the highly noisy nitrogen edge datasets, where peaks cannot currently be resolved. Furthermore, should the lamellae still be intact, STXM XANES at the oxygen K edge would be a useful tool to verify the presence of oxygen bearing organic functional groups, such as carboxyl.

The ureilite analyses were only partially completed, and further CRIS and/or XANES analyses could reveal, i.e., the presence of diamonds. As discussed above, this partial completion was caused by time constraints and lack of access to confocal Raman facilities at Carnegie between receiving the thin sections and synchrotron beam time at the Diamond Light Source. User feedback from the Renishaw Raman in GES shows that it can be used successfully for locating diamonds in ureilites. Future work on these samples could utilise the GES Renishaw Raman spectrometer to identify diamonds for FIB extraction and subsequent STXM-XANES analyses. The debate surrounding Ureilite Parent Body formation scenarios centres on the impurities hosted within ureilite diamonds (e.g. Lipschutz 1964; Matsuda et al. 1991; Nestola et al. 2020; Goodrich et al. 2021) (see chapter 2 for details), thus future atom probe tomography could identify and characterise any impurities hosted within these diamonds.

Bulk Results

Analysis

Martian LC-MS: Metabolites in Nakhla and Lafayette

Fatty acids are the class of metabolite that was dominantly detected via LC-MS analyses of the solvent extracts from Lafayette and Nakhla. They comprise approximately one third of the detected metabolites in Nakhla and 59/224 of those in Lafayette, (confirmed detections equal at least twice the abundance found in the procedural blanks). This detection of fatty acids is despite the fact that LC-MS is not optimised for fatty acid analysis, since they are fairly long chain nonpolar molecules, and thus GC-MS analyses would be expected to detect more of them. Future GC-MS analyses derivatising for fatty acids, targeting these molecules, to calculate concentrations would be a valuable tool to determine if more are present beyond those detected in the present study. Fatty acids have been previously detected in meteorites, such as Tagish Lake (Hilts et al. 2014), and are the most abundant water-soluble organic compounds in carbonaceous chondrites (Huang et al. 2005; Lai et al. 2019). The abundance of fatty acids in chondrite extracts, along with their abundance in both Lafayette and Nakhla, indicate these fatty acids are indigenous to Mars. Compound-specific (e.g., $\delta^{13}C$, $\Delta^{17}O$, δD) (Grady et al. 1985; Lin et al. 2014a; Hallis 2017; Steele et al. 2018; Chan et al. 2020) isotopic analysis would be needed to confirm that conclusion.

Another class of compounds found in both Nakhla and Lafayette were sulfur-bearing. 1-butanesulfonate was detected in all experimental samples (all meteorites and analogues) and was below detection limits in all procedural blanks. Another organic sulfonate, pentanesulfonate, was detected in Lafayette. An additional sulfur bearing compound, methionol, was detected in all experimental extracts, but not in any blanks. Standards were not run for any of these compounds, but ^{34}S isotope peaks were detected in the mass spectra for all three compounds, confirming that they are sulfur-bearing metabolites with the exact masses detected. In the case of Lafayette and Nakhla, they may be indigenous to the meteorite since sulfur bearing organics have been detected on Mars and within martian meteorites (Summons et al. 2011; Steele et al. 2018; Jaramillo et al. 2019).

Martian LC-MS: Organic Content in Nakhla

Betaine was detected in Nakhla and not in any of the other samples or blanks in the martian experiment. A standard of betaine was run, and therefore its presence was

confirmed. We cannot be certain that betaine is indigenous to the meteorite without compound specific isotope ratios, or amino acid enantiomeric ratios. It is also a metabolite that accumulates under environmental conditions such as drought, high salinity or low temperature, as it is produced by plants under high stress (Annunziata et al. 2019). Since Nakhla fell in Egypt in 1911, betaine is therefore likely a contaminant from this desert environment. Amino acids have previously been studied in Nakhla, including their D/L ratios, and were found to be consistent with the infiltration of biogenic matter soon after its fall to Earth (Glavin et al. 1999). Two further unconfirmed metabolites that have a similar structure to betaine, choline sulfate and D-galactosamine, were also found only in Nakhla (were below detection levels in all other samples). Choline sulfate is another plant derived metabolite, and D-galactosamine occurs naturally in humans. Detection of terrestrially derived compounds in a rapidly collected fall such as Nakhla demonstrates how easily contaminated martian samples are upon contact with the Earth.

Another compound detected in Nakhla was orthophosphate (a single phosphate unit), the presence of which was confirmed via analysis of a standard. It was below detection levels in all other samples. High abundance of phosphate (15 mg kg^{-1}) was reported in Nakhla after water-based extraction (Mautner and Sinaj 2002), at significantly higher abundances than those in analogues, blanks, and simulants. Phosphates are astrobiologically important molecules since they are key nutrients in soils, and they are often the limiting factor when evaluating biological potential (key nutrient content) of extra-terrestrial materials (Mautner et al. 1997). Thus, if orthophosphate is indigenous to Nakhla, its presence on Mars increases its habitability.

The seven metabolites with the highest relative intensity in Nakhla compared to the blanks were all compounds without names identifiable using IDEOM (Creek et al. 2012). Five of them were only present in Nakhla, and below detection levels in all other samples and blanks. This means they are compounds with exact masses that do not match any compounds found in the KEGG (Kyoto Encyclopaedia of Genes and Genomes) database, and extensive work would be required to determine their possible structure. Given that they are the molecules with the highest abundance in the sample, and poorly known biological molecules, these compounds might be indigenous to the meteorite, especially since Nakhla was a meteoritic fall. However, targeted analyses (and therefore any future D/H ratio measurement) would not be possible without knowing the molecular structures, and martian source identification would not be possible without such identification and measurements. Future calculations and measurements to determine the structure of these

compounds may be possible but are beyond the scope of this project.

Organic matter in Lafayette vs. terrestrial analogues

Principal component analysis (see chapter 4) of the LC-MS dataset suggests that much of the OM detected in the terrestrial Mars analogues and simulant in the martian LC-MS experiment was similar, and distinct from the OM of Lafayette. The metabolite detected in the highest concentrations in Sverrefjellet,Sigurdfjellet, and JSC Mars 1 was putatively annotated as Desmosdumotin C, and was below detection limits in all other samples and blanks. JSC Mars 1 and the two BVC samples were not stored together and originate from entirely different sites. However, they were stored in the same type of plastic sample bags, suggesting this metabolite may be a contaminant from sample storage. In contrast, the Lafayette chip was stored in aluminium foil, perhaps explaining the absence of this metabolite in the meteorite. The presence of a likely curation-based contaminant demonstrates the importance of accurate record keeping during sample storage during organics work. Furthermore, ideally samples would not be stored in plastic sample bags, to avoid the chance of organic contamination.

Many fatty acids were detected in Lafayette, Nakhla, and JSC Mars 1 that were not detected in the procedural blanks. Interestingly, amongst the 25 most intense peaks in JSC Mars 1, nine were tentatively annotated as fatty acids, suggesting that JSC Mars 1 is an excellent analogue material for Mars in terms of its soluble organic content.

Constraining the fall history of Lafayette

As mentioned in chapter two, detailed knowledge surrounding the fall and recovery of Lafayette is lacking. A possible but unconfirmed version of events is that a Purdue University student saw the fall in Tippecanoe County (Indiana, U.S.), and collected the stone from a muddy area near a pond (Nininger 1935). Surprisingly, our LC-MS dataset for Lafayette appears to support this story, particularly if we focus on the DON mycotoxin which was putatively detected in all three replicates of the Lafayette extract in the martian LC-MS experiment.

Fusarium head blight (FHB), or ‘scab’ is a disease on small agricultural grains caused by the fungal pathogen *F. graminearum*. This pathogen produces the DON mycotoxin, also known as vomitoxin, and typically causes disease on wheat in areas that have favourable

environmental conditions of warm temperatures and high humidity during anthesis (flowering) in the spring. FHB can cause significant yield losses and reduced grain quality. Agriculture is a major industry in Indiana and has been throughout the 19th and 20th centuries. The state's climatic and environmental conditions are ideal for *F. graminearum* to cause disease, meaning that FHB is widely recognised as a significant problem in Indiana grain. This is because the DON mycotoxin produced by *F. graminearum* is poisonous to humans in large concentrations (McMullen et al. 2012). For livestock, particularly swine, it causes sickness in much lower concentrations if infected wheat is in their feed–- many pigs will refuse feed containing ~1 ppm of DON (Schmale and Bergstrom, 2003).

Purdue University's Agronomy and Botany and Plant Pathology departments continue to monitor and research instances of FHB in the state and best management practices for this disease (Wise and Woloshuk 2010). The highest prevalence of the disease in Indiana within the 20 years prior to 1931 (when Lafayette was recognised as a meteorite) was in 1919 (Gardner, 1919). In this year FHB caused an estimated 5-10% loss in crop yield. Detailed annual records of crop diseases at the county level in the state were kept by the Indiana National Academy of Sciences from 1919 onwards as a result of this infestation. 1927 was also a significant year for the disease, although not at the same scale as 1919 (Gardner, 1927). Therefore, assuming the stone did fall as described in Nininger (1935), the LC-MS data presented here suggest 1919 or 1927 as the most likely fall years based on the annual disease records of FHB.

This fall scenario is further supported by previous liquid chromatography studies of DON infestations in soil and crops. LC-MS/MS work by Sanders et al (2014) shows that the highest concentrations of DON are found in settled infested wheat dust at five times the levels in infested grain debris. Additionally, Maiorano et al (2008) used HPLC to investigate how DON concentration in soils in regions with FHB infestation varies annually, as well as with mitigative strategies such as crop tilling. They found that minimum DON concentrations varied between a minimum of 125 $\mu g\ kg^{-1}$ in their 2004 samples, a minimum of 25 $\mu g\ kg^{-1}$ in their 2005 samples, to a minimum DON concentration of 1192 $\mu g\ kg^{-1}$ in their 2006 samples. In line with this, 2006 had a much higher FHB infestation in the wheat crops studied, and other mitigation efforts (such as tilling) had a negligible impact on DON concentration. Maiorano et al thus hypothesise that annual infestation has the biggest impact on DON concentration in their soil samples. Given that Nininger's account of the fall describes the stone as falling in the mud at the edge of a

pond, we suggest it is highly likely to have been near a field infested with FHB at the time, with a layer of infested dust at its surface, and it was likely to have been in a year of very high FHB infestation to be still detectable so many years later.

The person who saw the fall is reported to have been a student of colour registered at Purdue University prior to 1931 (Nininger 1935). During this period at Purdue in the mid-western United States, Black students were referred to as students of colour, whilst students of other non-white ethnicities were referred to as foreign students. By the time the stone was identified as a meteorite, the student's name was forgotten, and the fall scenario remained unconfirmed (Nininger 1935). Very few students of colour attended Purdue University in the late 1910s, to the point that there were no Black students known to have graduated in 1919 or 1920. However, there were three Black students were recorded to have been in the university in 1919 - two pharmaceutical students in the graduating class of 1921, and one engineering student in the graduating class of 1922. There was only one Black student known to have attended Purdue in 1927. Therefore, both years fit the reported fall scenario, however the higher prevalence of FHB in 1919 makes that year the most probable.

Intriguingly there were also well-documented fireballs in the Midwestern USA in both 1919 and 1927. A fireball event in 1927 is known to have dropped the Tilden meteorite in Illinois, a chondrite meteorite. On 26th November 1919 at 8pm, a fireball was observed primarily in Southern Michigan and northern Indiana, with additional reported sightings across the Midwest and into Canada (Hobbs, 1923). Hobbs (1923) suggests that due to the length of the fireball, the shockwave felt around Lake Michigan and into Canada, and the clear multiple paths that were observed, that a stone likely fell on land east of Lake Michigan near the town of Portage. A couple of searches took place, but a meteorite was never found. However due to extensive cloud cover in most of Michigan, the actual trajectory and fall position are unclear, although it is unlikely that this would account for the 220 km distance between the estimated fall site of Portage and Lafayette. In addition, the reported fall time of 8pm the night before Thanksgiving means it would have been dark, and therefore the student is unlikely to have been fishing at that time. The accounts of the Lafayette fall scenario imply daylight at the time, since the student was fishing, possibly explaining the absence of other fireball reports for this fall.

Regardless of the precise year of the fall (i.e., 1919 or 1927, for example), the present study supports the reported scenario of Lafayette being collected in a rural environment by

a Purdue student in the early twentieth century. It is in contrast with a calculated terrestrial age of the stone of 2.9 ± 1 Ka (Jull et al. 1999) using $^{14}C/^{10}Be$ isotopes - although this is an unpublished piece of work. Furthermore, the work of Jull et al. (1999) relies on a calculation outlined in a subsequent piece of work (Jull et al. 2004) which relates incident meteoroid sizes to $^{14}C/^{10}Be$ ratio, and in this latter paper the measured ratio of $^{14}C/^{10}Be$ is consistent with a 0 terrestrial age of Lafayette, if the stone was small (10-75 cm radius). This size range is consistent with the size of Lafayette, therefore the terrestrial age of the stone from their calculation could also be 0 Ka and so in agreement with the report by the finder of the meteorite and the present study.

Implications for MSR and curation

The detection of multiple terrestrial plant-derived secondary metabolites within an interior chip of Lafayette illustrates how easily terrestrial organic matter can contaminate martian samples. Despite the uncertainty surrounding its fall history, Lafayette's lack of terrestrial weathering features and black glassy fusion crust attest to its relatively pristine nature (Nininger 1935). The persistence of these plant-derived contaminants decades after the stone fell, and the fact that they are among the most abundant metabolites detected, indicate that the ingress of biogenic organic material into extra-terrestrial samples can easily and rapidly occur throughout an entire meteorite mass, and can be preserved for many years.

Mars Sample Return (MSR) aims to bring back soil and rock samples from the martian surface for further study here on Earth. One of the key aims of these Earth-based studies will be to catalogue the martian organic matter present within these samples (iMOST 2018). LC-MS metabolomics as described here could help with this catalogueing, with the optimal workplan including initial non-targeted analyses followed by targeted analyses alongside standards to identify specific molecular isomers (Seyler et al. 2020). However, considering that martian OM could contain some molecules with the same structure as potential terrestrial contaminants, the only way to identify the true source of these compounds would be molecule specific isotope ratio analyses, currently only available via gas chromatography isotope ratio mass spectrometry (GC-IRMS). However, as the current detection limits of this technique require sample sizes of ~1 kg for material with similar OM abundances to martian meteorites (Callahan et al. 2014), it is unfeasible for such precious samples.

The small sample sizes utilised for this study (3 x 30 mg replicates) coupled with the large number of metabolites detected – some of which are almost certainly plant-derived molecules from approximately 100 years ago - suggest that similar LC-MS protocols would be valuable during the investigation of OM in MSR.

HyPy-GC-MS: Evaluating JSC Mars 1 and BVC as Analogues for Martian Organics

Our alkane and PAH results from hydrogen pyrolysis followed by GC-MS (HyPy-GC-MS) suggest that the BVC material is a closer analogue to martian meteorite OM than JSC Mars 1, in terms of refractory organic matter. The organic content in JSC Mars 1 was much higher than that of Nakhla and Lafayette, particularly in terms of PAHs. The content inSigurdfjellet was by contrast most similar to the martian samples - although there were a number of alkanes present in both Lafayette and Nakhla absent fromSigurdfjellet. Lafayette and Nakhla also do not have the same alkane content, and the only PAH in each, pyrene, is also found in the procedural blank, and is therefore highly likely to be a contaminant.

Without compound specific isotope ratio measurements those PAHs or alkanes that are martian or terrestrial cannot be identified. As Mars is enriched in D/H, such measurements would yield definitive results (Hallis 2017). The organic concentrations in all samples were unfortunately too low to carry out compound specific analyses (GC-IRMS), although this was planned originally.

Since HyPy GC-MS analysis was undertaken on two samples of JSC Mars 1 – one that had previously been solvent extracted, and one that had not –the effect of prior solvent extraction on refractory organic removal can be determined from the percentage loss mass graphs shown in Chapter 4. These graphs show that all alkanes had at least a 20% loss in concentration, with two being lost completely after being solvent extracted, compared to having no prior solvent extraction. A similar case is true for the PAHs whereby four PAHs were lost completely from solvent extraction, and the lowest loss was 18.7 %. All other samples were solvent extracted prior to HyPy, whereas JSC1-B had not, and had the highest organic content, and therefore suggests that a substantial amount of refractory organic matter might have been lost due to solvent extraction. These results therefore indicate that solvent extraction prior to HyPy should be avoided, if there is sufficient sample available to do so.

Protocol Evaluation

Solvent Extractions

The solvent extraction protocol used in this work was adapted from the work of a previous SUERC MSc student, Jacqueline Gunn, as well as using the same solvents as Sephton et al. (2002) for the non-targeted removal of solvent soluble organics. The aim of the extraction protocol was to capture a wide range of polarities, as the extracts were initially analysed with both GC-MS and LC-MS. These data indicate that this non-targeted approach to LC-MS was successful, particularly with such a large number of blanks (> 50).

This protocol did not involve heating, hot water extraction, or acid hydrolysis, and the vortex period was 10 minutes. No heating-based steps were incorporated, to prevent any possible loss of volatile organics. Future work could incorporate heating, however, since martian organic material is likely to require temperatures of over 200 °C to be released (Lin et al. 2014) and extraction heating procedures use temperatures of up to ~ 50 °C (Simkus et al. 2019). Martian meteoritic organics would likely therefore be unaffected by gentle heating during extraction. The extractions proved successful for our non-targeted LC-MS analyses, however in future, a range of extraction protocols should be tested, including acid hydrolysis, gentle heating, and increased vortex periods (Simkus et al. 2019) to determine which protocol is the most effective to give the widest range of metabolites detected.

The martian experiment would benefit from subsequent targeted analyses, that were not possible in this work due to limited sample availability, and since extracts were used for both LC-MS and GC-MS. Such targeted analyses would assist in determining the fall scenario of Lafayette in particular. The non-targeted work in this thesis showed that the environmental conditions of the stone's fall could be constrained through the presence of terrestrial contaminants, however many of these have multiple exact mass isomers. With subsequent targeted analyses using standards, the putatively identified metabolites could be confirmed without relying on the algorithm which predicts metabolite identities based on M/Z and retention times (Creek et al. 2012). These results from Lafayette were used to improve the technique for subsequent work on the Winchcombe meteorite, during which, we were able to account for further targeted analyses when planning the extraction protocol (more sample was available, and all the solvent extracts for LC-MS were used, and no additional GC-MS was carried out). This work is available in the appendix.

Controls and Contamination

In the martian LC-MS experiment, the only blanks used were procedural blanks, to identify laboratory contaminants during the extraction protocol and in any analytical equipment. An improvement to this procedure would have been to have performed extractions from curation environment samples (e.g., sample storage bags) to identify likely contaminants, especially since in the case of the analogues and simulants that had been stored in plastic sample bags for ~1 year prior to analysis. Furthermore, much of the laboratory equipment was also plastic-based, e.g. Gilson style pipette tips, which may have led to contamination during extraction. A possible improvement to the protocol would have been to use glass pipettes instead, although the extensive procedural blanks will have captured any compounds introduced by such equipment.

In an ideal scenario, environmental controls would also be used for meteoritic falls by taking samples from the fall environment. In the case of Lafayette and Nakhla of course environmental sampling is not possible due to the amount of time passed since they fell, and with Lafayette, due to the unknown fall locality. However, one could investigate the plausibility of DON ingress into meteoritic material experimentally using analogues such as the BVC rocks, to test whether or not infested wheat debris in the locality could seep into similar material to martian meteorites and subsequently be detected.

GC-MS Analyses

The initial GC-MS work, whereby the same solvent extracts of the martian samples were analysed using GC-MS as well as LC-MS, was unsuccessful as no organic molecules were detected above the background levels with GC-MS. These extractions were carried out with hexane, dichchloromethane, and methanol, to capture a wide range of polarities for both instruments. The same extracts were highly successful when studied with LC-MS (see Chapter 5). A non-detection in these martian samples was consistent with the work of Sephton et al. (2002) who used the same three solvents to dissolve the solvent soluble portion of the organics in Nakhla, prior to hydropyrolysis, and detected no compounds above background levels. Derivatisation may have helped in this work to detect molecules successfully during GC-MS analysis. However, derivatisation requires knowledge of the type of organics within the sample. For example, for a sample with abundant amino acids the trifluoroacetic acid (TFA) derivatisation reaction is most commonly used for meteorites, undergoing esterification then alkylation (Simkus et al. 2019), and - this

process is shown in Figure 120. Derivatisation was not carried out because the organic content of the samples was unknown, therefore targeting specific compound classes and functional groups was not possible, which derivatisation requires (e.g. see Figure 120).

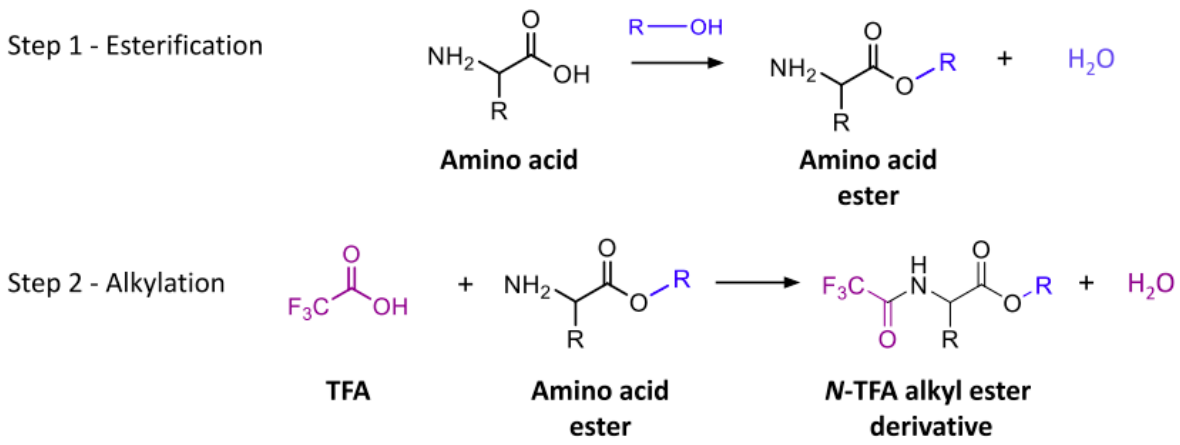

Figure 120 - TFA derivatisation for amino acids for GC analysis. Derivatisation reaction commonly used for meteoritic amino acids. Adapted from Simkus et al (2019).

Targeting amino acids (i.e., derivatising and aiming for them) with GC-MS in particular would be useful in order to determine whether detected organics are likely indigenous to the meteorites or contaminants. Amino acids are optically active and exhibit stereoisomerism/chirality., although unfortunately chirality cannot be resolved using LC-MS, but GC-MS can discern the difference between two enantiomers (Zampolli et al. 2006). Determining chirality is particularly useful in meteoritic analyses for identifying likely extra-terrestrial organics because abiogenic amino acids have no bias between e and z isomers (known as L and D for amino acids), whilst in biological amino acids we observe a clear bias towards L amino acids (Chan et al. 2020). If the ratio of L and D isomers in a mixture of amino acids could be determined, and a 1:1 ratio was found (i.e., a racemic mixture), it would be strong evidence that the material was extra-terrestrial.

Based on this work, a current masters by research student is investigating the optimum GC-MS extraction technique using the same BVC analogue material. Ms Douglas is testing sample masses, solvent combinations, and automated extraction techniques, so that future studies could incorporate GC-MS more effectively in readiness for future meteoritic analyses.

As it cannot be determined whether molecules detected with LC-MS are indigenous to the meteorites without measuring isotope ratios, and GC-IRMS analysis cannot be undertaken due to sample mass constraints, the possibility of using LC-MS to measure compound specific D/H ratios is currently being explored at U of G. It is hoped to work with collaborators at Thermo Scientific who develop the OrbiTrap MS detector to investigate this possibility in the future. This possible work, should funding be allocated, will be carried out on extracts of Winchcombe, since extra sample was allocated for targeted analyses, and because the bulk δD ratio of the water in the sample has been measured and found to be −142 ± 4 ‰ (King et al. in review). This δD value could thus be compared to compound specific values in the organic matter found in LC-MS to determine whether the compounds are likely indigenous or not, and further still, related to parent body alteration (given that the δD measurement on Winchcombe was of the water content).

In a similar vein, we can be reasonably sure that the organic content analysed in our in-situ studies is indigenous to the meteorite, but δD measurements would provide further confidence. Future work in this area could include NanoSIMS analyses, which allows the nanoscale determination of D/H ratios. This technique has been carried out on martian meteoritic organic material similar to that analysed in this project, for both $^{12}C/^{13}C$ and D/H ratios, including on Tissint (Lin et al. 2014b; Steele et al. 2022).

Future LC-MS analyses should also involve a subsequent targeted step, after non-targeted analyses, to verify presence of putatively annotated compounds. Therefore extraction should be planned with enough sample in mind to carry out at least two sets of analysis. Furthermore, LC-MS/MS analysis may also be carried out to further probe the compounds present.

Evaluation of Organic Formation Scenarios

As outlined in Chapter 2, there are multiple suggestions for the origin of martian meteoritic organics. Here these scenarios are discussed in more detail to evaluate the possible origins of the organics analysed in this project.

Indigenous Organic Martian Material

Since the misidentification of a lifeform in ALH 84001 (McKay et al. 1996) there has been

an enhanced emphasis on determining the origin of likely indigenous martian organic matter, and any possible abiotic pathways for its formation (e.g., Steele et al. 2007). The first comprehensive potential mechanism for indigenous martian MMC was described by Steele et al. (2012), who suggested that MMC is formed by a C-O-H bearing magma (for mechanism see Figure 37 in Chapter 2). They used CRIS, TEM, and laser desorption laser ionisation mass spectrometry (LD^2MS) to demonstrate that this material is likely indigenous because it is hosted entirely within primary igneous minerals. These authors report MMC in 11 martian meteorites, and LD^2MS data showed that PAHs in Da G476 were similar to the PAHs detected in ALH 84001. Analyses in the present study of Tissint, SaU 008, and NWA 8159 in particular builds on the work of Steele et al. (2012) as all MMC-rich inclusions were found in primary igneous minerals. It is therefore likely that this martian abiotic mechanism, formed the inclusions studied in this project, especially given the detection of N-bearing organics in Tissint – which require a reducing environment to form. Further analyses with TEM and NanoSIMS would give additional verification as to the exact mechanism.

Additional work has also been performed to characterise and understand the formation of organics associated with alteration products in martian meteorites. MMC inclusions were found associated with fluid mineral reactions in Tissint, Nakhla, and NWA 1950 (Steele et al. 2018) using CRIS, TEM, STXM XANES and NanoSIMS. The reaction of brine and CO_2 caused corrosion of magnetite and titanomagnetite, and the additional production of perchlorates (Steele et al. 2018), which have been detected on Mars by the SAM instrument (Glavin et al. 2013). The MMC was formed in these three martian meteorites via the electrochemical reduction of CO_2 during the interaction of spinels and/or sulfides with brines (Steele et al. 2018). NanoSIMS δD measurements of MMC in Tissint, Nakhla and NWA 1950 reveal that the brine from these meteorites originates from different reservoirs on Mars (Steele et al. 2018). In the case of Tissint, δD values of 3600 ± 1000 ‰ in the MMC are consistent with the reaction of brine which itself originated from the martian crust and had equilibrated with the martian atmosphere, thus incorporating such a high deuterium ratio, consistent with the martian atmosphere (Steele et al. 2018). δD values in the MMC of 219 ± 60 ‰ and 98 ± 20 ‰ were measured for Nakhla and NWA 1950 respectively, consistent with the brine originating from a magmatic water source (Steele et al. 2018). Additional ToFSIMS (time of flight secondary ion mass spectrometry) analyses showed that thiophenes were present, consistent with those detected by SAM at Gale Crater (Eigenbrode et al. 2018). Many of these nanoscale corrosion features were identified using TEM, thus future TEM analyses of our samples may reveal similar

features.

Pyrolysis gas chromatography mass spectrometry (Py GC-MS) data from Tissint (Jaramillo et al., 2019) supports the aqueous electrochemical reduction scenario of Steele et al. (2018). Jaramillo et al. (2019) detected N- and S-bearing aromatic hydrocarbons, as well as soluble inorganic salts such as perchlorates, also consistent with SAM analyses (Glavin et al. 2013; Eigenbrode et al. 2018). The PAHs detected were also consistent with those found in Nakhla and EETA79001 using similar techniques (Sephton et al. 2002). The nitrogen bearing organics detected using STXM XANES in Tissint in this study (see chapter 4) as well as sulfonated organic compounds detected with LC-MS in Nakhla are also consistent with the work of Jaramillo et al. (2019), suggesting these compounds are indigenous to the meteors and Mars.

The organic-bearing carbonates and iron-oxide rich veins in ALH 84001 were analysed using CRIS, TEM, NanoSIMS and STXM XANES (Steele et al., 2022). The results of this study showed that organics in ALH 84001 are associated with nanophase magnetite, silica and talc, as well as carbonates. Thus, both serpentinisation (the aqueous alteration of mafic rocks to produce serpentine minerals, magnetite, and hydrogen) and carbonation (formation of carbonates from aqueous CO_2) are likely to have generated the organic carbon in ALH 84001. The organics found associated with talc phases, as well as nanophase magnetite, are attributed to serpentinisation – whereby the hydrogen released from the processes reduces aqueous CO_2. The formation of the organics associated with amorphous silica, carbonates, and nanophase magnetite is then attributed to carbonation. STXM XANES features in both Tissint and ALH 84001 were found to be consistent (Steele et al. 2018; Steele et al. 2022), which suggests abiotic synthesis continued on Mars from the Noachian until the Amazonian, via multiple pathways.

Correlative SEM and N-XANES analyses (Koike et al., 2020) provide additional insights into the structure and possible formation mechanisms of the organics in ALH 84001. Nitrile and N-bearing aromatic functional groups were detected via N-XANES within FIB lamellae lifted out from three carbonate globules. Although it is unclear whether this material was exogenous or indigenous to Mars, these functional groups are consistent with the PAHs detected by Jaramillo et al. (2019) as well as those detected using STXM XANES in this study.

The key finding of this in-situ work is that the detection of likely indigenous martian

organic matter in the shergottites Tissint and NWA 8159, having functional group and mineralogical features in common with ALH 84001 (Steele et al. 2022) suggests that abiotic synthesis of organic carbon has continued on Mars since the Noachian until the late Amazonian.

Exogenous Delivery of Organics to Mars

The organic contribution to Mars from carbon-rich extra-terrestrial sources may be considerable. Flynn and McKay (1990) calculated that between 2700 and 59,000 tonnes of meteorites are delivered to martian soils per year, this is supported by the identification of meteorites on Mars by the Mars Exploration Rovers (e.g., Schröder et al. 2008). Therefore, is it possible that the organics detected in martian meteorites are sourced from these exogenous surface contributions.

Sephton et al. (2002) studied the insoluble organic matter (IOM) in EET A79001 (shergottite) and Nakhla (nakhlite) using Py GC-MS and GC-IRMS, finding similarities with the IOM in carbonaceous chondrites. The samples were first solvent extracted using hexane, dichloromethane, and methanol to remove the soluble organic material (judged by the authors to be likely terrestrial contaminants), and then pyrolysed the remaining meteoritic material. They found similar compounds in EET A79001 and Nakhla (but no organics in ALH 84001, which they also analysed), despite their contrasting crystallisation ages (172 ± 18 Ma and 1.3 Ga, respectively (Nyquist et al. 2001; Cohen et al. 2017b)).

NanoSIMS analyses of IOM in Tissint have produced varying results. IOM hosted in Tissint shock melt veins and fractures show elevated D/H ratios ($\delta D = +1183$ ‰), suggesting a martian origin (Lin et al., 2014). These authors suggest that Tissint contains evidence for more than one shock event, and that during hydrothermal activity resulting from the first shock event an organic rich fluid deposited the IOM, which was subsequently heterogeneously shocked by a later event (explaining the detection of nanodiamonds in addition to organic material). Based on Lin et al. (2014) and the measured $\delta^{13}C$ of Tissint IOM (Figure 120), Lin et al. (2014) suggest the aqueously altered carbonaceous chondrites could be the source of, this meteorite's organic content. However, a large proportion of the $\delta^{13}C$ values measured in Tissint lie outwith the range of values for CM and CR chondrites (Figure 121).

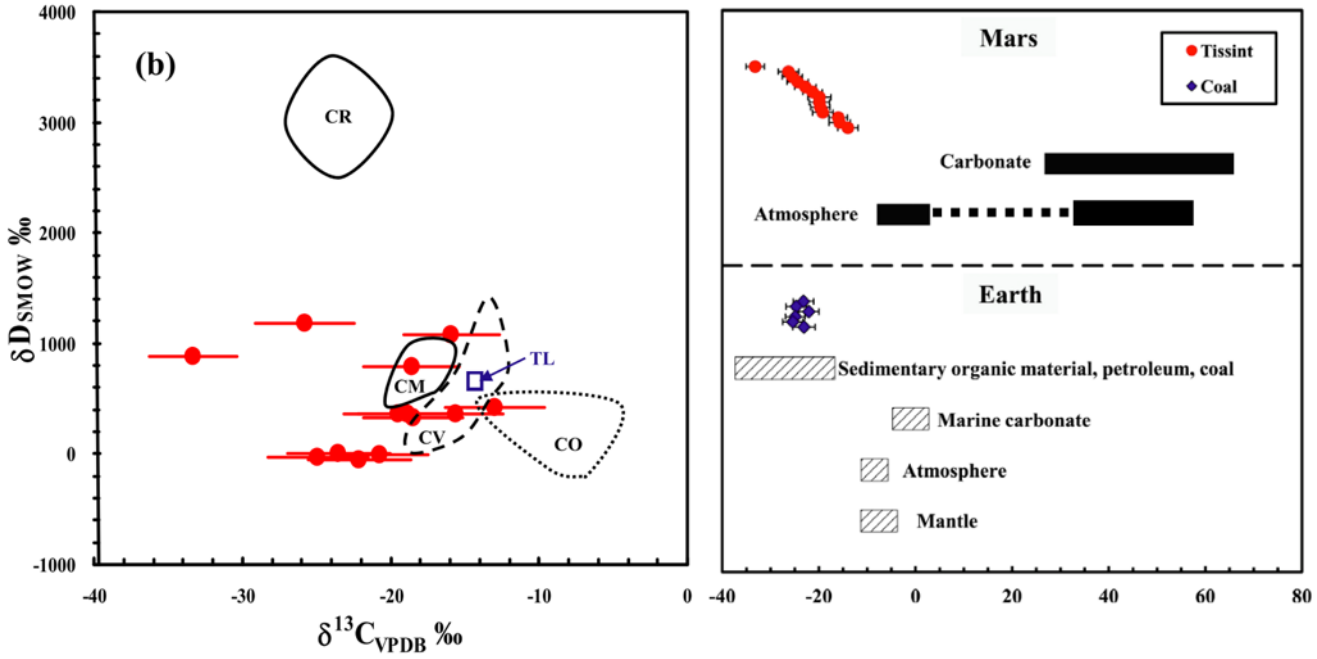

Figure 121 $\delta^{13}C$ measurements of Tissint (in red) compared to A) carbonaceous chondrites and B) martian and terrestrial sources. Adapted from Lin et al. (2014).

A similar impact-based scenario was suggested for the organics in the Y000593 nakhlite, whereby an organic-rich impactor deposited carbonaceous material on the martian surface, which the impact-generated hydrothermal activity distributed in the crater (McLoughlin et al., 2019). These authors suggest a subsequent impact ejected the nakhlites from the martian surface (see Figure 49 in Chapter 4). This double impact scenario is consistent with EBSD data from the nakhlites, indicating this group of meteorites was impacted twice, with the first impact causing heating and aqueous alteration, and the second causing the meteoritic ejection (Daly et al., 2019; see Figure 39).

Organic Contamination in Martian Meteorites

Terrestrial organic contamination in martian meteorites has been studied predominantly using bulk techniques such as stepped combustion, Py GC-MS, and LC-MS. Glavin et al. (1999) used high performance liquid chromatography (HPLC) to characterise the amino acids in Nakhla. Despite Nakhla's fall history (having fallen in the Egyptian desert), this fall was rapidly contaminated, with measured D/L ratios in the amino acids being consistent with samples taken from the river Nile nearby (Glavin et al, 1999). This contamination is consistent with results from Nakhla and Lafayette in the present study which show that both meteorites contain probable terrestrial contaminants, despite being retrieved soon after they fell (rapid recovery is suggested for Lafayette since its fusion crust is pristine).

Sephton et al. (2002) suggest that the soluble organic component of martian meteorites is likely to be predominantly terrestrial, whilst the refractory insoluble material is most likely to be indigenous. This is evidenced by the consistency of $\delta^{13}C$ measurements at high temperatures during stepped combustion (>600 °C) of different martian meteorites (Wright et al. 1992). Sephton et al (2002) removed the solvent soluble material prior to Py GC-MS using hexane, DCM and methanol and analysed it with GC-MS. Analyses of these solvent extracts via GC-MS did not detect any organic matter, consistent with the GC-MS results of the present study, using the same three solvents, whereby no compounds were detected. This non-detection again demonstrates the need for derivatisation with GC-MS due to its lower sensitivity in comparison to LC-MS (LC-MS is as much as 1000 times more sensitive than GC-MS) (Burton et al. 2012). Lin et al. (2014) suggest that the indigenous organic material detected outwith Tissint's shock features would be released at ~200-600 °C, whilst the most heavily shocked organics found in melt veins would be released at 800-1000 °C because of its increased refractory nature. However, the labile carbon detected in Tissint with CRIS is unlikely to require temperatures of >600°C for combustion because it was sensitive to laser heating (laser temperature ~50 °C), with the CRIS spectrum clearly changing over time during analysis (Figure 66, Chapter 4).

In the present study, soluble organic analyses with LC-MS detected several likely terrestrial contaminants in both Nakhla and Lafayette - particularly the plant derived metabolites in Lafayette. However, not all of these soluble organics were identified as terrestrial. For example, sulfonates were detected in Nakhla and are reported in carbonaceous chondrites (Orthous-Daunay et al. 2010) suggesting that a soluble component of martian carbon does exist and is detectable with LC-Ms.

This work demonstrates the strength of a non-targeted LC-MS approach with a broad spectrum of polarities, and a highly sensitive mass spectrometer, in order to detect likely contaminants in martian meteorites.

8 Conclusions

Here I conclude by outlining the main findings of this project, divided up into the following themes:

- Evidence for Organics Produced in a Reduced Martian Mantle;
- Evidence of Thermal Processing in Meteoritic Organics;
- The Impact of Terrestrial Weathering on Martian Organics;
- Organic Contamination and the Implications of this work for Mars Sample Return;
- Meteoritic Compounds and Martian Habitability.

Evidence for Organics Produced in a Reduced Martian Mantle

The STXM XANES and Raman data from the martian meteorites NWA 8159 and Tissint in this project support the theory that MMC was formed in a reduced magmatic environment on Mars (Steele et al. 2012).

A range of functional groups were detected in Tissint using STXM XANES including aromatic, phenolic, nitrile, and carboxyl. These functional groups were detected in MMC hosted in a primary igneous phases (maskelynite) surrounding a hematite inclusion. This MMC inclusion was below the thin section surface and no cracks were found close by. Given that this MMC was in a primary igneous phase, and nitrogen was detected in the organic matter, which requires a reducing environment to form, is the MMC is interpreted to have formed by the precipitation of reduced carbon during crystallisation of the martian mantle (Steele et al. 2012).

The detection of MMC in NWA 8159, and its STXM XANES peaks which correspond to those in ALH 84001 (Steele et al. 2022) suggest that similar abiotic synthesis forming martian MMC has continued in different environments on Mars for at least two billion years. NWA 8159 has a crystallisation age of 2.37 ± 0.25 Ga (Herd et al. 2017b) whilst ALH 84001 has a crystallisation age of 4.09 ± 0.03 Ga (Udry et al. 2020), thus their matching organic properties, despite contrasting ejection sites and eras on Mars

demonstrates that abiotic synthesis continued for an extended period on Mars. Furthermore, additional STXM XANES analyses, as well as the work in this project, of Tissint has shown that the MMC in this much more recent - crystallisation age of 664 ± 74 Ma (Schulz et al. 2020) – is also very similar to ALH 84001 and NWA 8159, suggesting that abiotic organic synthesis continued to the late Amazonian (Steele et al. 2022).

The detection of sulfonated compounds in Nakhla and Lafayette by LC-MS is also consistent with suggested abiotic mechanisms for producing martian organics. Sulfur-bearing organic compunds have been detected in martian meteorites and at Gale Crater by Curiosity's SAM instrument (Eigenbrode et al. 2018; Steele et al. 2018; Jaramillo et al. 2019). The formation mechanism of these S-bearing compounds is consistent with abiotic synthesis occurring in a range of environments on Mars.

Fatty acids are another class of compound detected at high abundance in the martian LC-MS experiment, the perchlorate Jbilet Winselwan LC-MS experiment, and the Winchcombe LC-MS experiment (see appendices for details of these). Fatty acids were the most abundant single compound class found at concentrations at least twice those above the procedural blanks in all three experiments. They are therefore unlikely to be meteorite contaminants since e.g. in Winchcombe they were found in both fall sites but absent from their corresponding environmental samples. Fatty acids have also been detected in many carbonaceous chondrites such as Murchison and Tagish Lake. Fishcher-Tropsch-Type synthesis has been suggested as the pathway for fatty acid formation in planetesimals (Lai et al. 2019), and the same mechanism class suggested for MMC production on Mars (Steele et al. 2018).

Evidence of Thermal Processing in Meteoritic Organics

The in-situ results in this thesis, both from the martian meteorite Tissint, and the ureilites Goalpara and Hajmah (a) demonstrate the sensitivity of meteoritic organic matter to heat, both from planetary processes, and analytical techniques.

The variation in the MMC G-band centre position, from ~1555 to 1585 cm^{-1}, within organic inclusions in Tissint at a micron scale is consistent with the heterogeneous shock previously reported in this meteorite (Hallis et al. 2017). The heterogeneous shock caused heterogeneous localised heating, which has been previously reported as the cause of G band variation in meteorites (Starkey et al. 2013).

The organic carbon detected in the ureilites Goalpara and Hajmah (a) with STXM XANES in this project also attests to the heterogeneously shocked nature of ureilite carbon. Given that both graphite and diamonds have previously been reported in these meteorites (e.g. Lorenz et al. 2019; Goodrich et al. 2021) the detection using STXM XANES of nitrogen-bearing organic carbon that has not been graphitised or converted to diamond, demonstrates the range in thermal metamorphism experienced by these samples at a micron scale.

The detection of labile organic carbon in Tissint, spatially related to heterogeneously shocked MMC, demonstrates the wide range of organic carbon in martian meteorites, and that martian carbon is sensitive to analysis by 'non-destructive' analytical techniques, such as Raman spectroscopy. The temperature of the part of the sample being irradiated by the laser is ~50 °C and the D and G bands were observed to form under this laser heating in < 60 seconds, thus showing that martian organics are affected by the techniques we use to characterise them. This effect of organic matter being changed by the detection technique is similar to the oxidation of organics during analysis on Mars because of the presence of perchlorates - e.g., the analyses of the SAM instrument, onboard the Curiosity rover (Sephton et al. 2014).

Overall, the in-situ organics results demonstrate that planetary processes such as impacts and thermal metamorphism, in addition to the analytical techniques used to study planetary materials, cause organic matter to change from its initial state. It is therefore crucial to bear in mind that the organic matter being studied may have different characteristics (functional groups, order, etc) compared to when it was first formed on its initial planetary body.

The Impact of Terrestrial Weathering on Martian Organics

The detection of both elemental sulfur and calcite in NWA 8159, as well as the finding of calcite in SaU 008 demonstrate the effects of terrestrial weathering on inclusions in martain meteorites.

In NWA 8159, elemental sulfur associated with hematite was detected using Raman spectroscopy. This meteorite crystallised in oxidising conditions (Herd et al. 2017b) whilst elemental sulfur requires reducing conditions to form, therefore this sulfur was likely reduced from a sulfide to sulfur during its residence in the Northwest African desert environment. Possible weathering mechanisms for the formation of elemental sulfur

include the reduction of iron (iii) oxides by sulfides (Kumar et al. 2018) or the oxidation of pyrrhotite (Buckley and Woods 1985).

MMC was detected in the vicinity of calcite (maximum ~10-20 μm apart) in NWA 8159 and SaU 008 using Raman spectroscopy and, in the case of NWA 8159, STXM XANES. Both Raman and STXM XANES data demonstrate that these carbon-bearing compounds are spectrally distinct from one another. Calcite presence in both NWA 8159 and SaU 008 was attributed to terrestrial weathering, therefore demonstrating that MMC can still be detected in weathered martian meteorites, although the organic material itself may have been altered by the prolonged period of desert exposure.

Organic Contamination and the Implications of this work for Mars Sample Return

The bulk analyses carried out in this project demonstrate that LC-MS is highly effective at carrying out a non-targeted analysis of the organic content of igneous rock samples with a low carbon content. Comparing the LC-MS to GC-MS data show that many more compounds were detected using LC-MS, consistent with the observation that LC-MS (in this case using an Orbi-Trap MS) is up to 1000 times more sensitive than GC-MS (Seyler et al. 2020).

Several likely terrestrial contaminants were found present in the LC-MS data from the nakhlites Lafayette and Nakhla. One example of such a contaminant is betaine, found in Nakhla (whose presence was confirmed by the use of a standard), which is a biological compound found in hot desert environments. A number of plant-derived metabolites were detected in Lafayette, the presence of which helps to constrain the fall scenario of this stone. Amongst these terrestrial biogenic metabolites is the toxin deoxyvalinol, (DON) which is produced by the plant disease fusarium head blight (Wegulo et al. 2008). By cross-referencing the years that this disease was at its highest with historical accounts of the meteorite's fall, as well as archival records at Purdue University, the most likely fall years of Lafayette have been constrained to either 1919 or 1927. The presence of environmental compounds in small (<40 mg) samples of meteorites which fell ~100 years ago demonstrates the longevity of contaminants in martian samples (even 'falls' such as Nakhla). In anticipation of Mars Sample Return, the curation and analysis of precious samples should be planned to minimise the potential exposure to any contaminants, given they have been shown to be detectable a century later.

The LC-MS analyses and the HyPy GC-MS analyses, also demonstrate the importance of accurate and precise curation records for interpreting results from organic analyses. There are aromatic compounds found at high abundances in the JSC Mars 1 and BVC samples, for example, which are probably derived from the plastic sample bags they were stored in for > 12 months. It is therefore crucial for meteoritic and future Mars sample return analyses, to avoid as much as possible any storage in plastic and to document all curation environments to determine any possible contamination sources for compounds detected.

Meteoritic Compounds and Martian Habitability

The detection of orthophosphate in Nakhla, as well as the detection of sulfonated compounds in Lafayette and Nakhla, and the nitrogen bearing MMC in Tissint, has positive implications on the habitability of Mars. Together these compounds cover the macronutrients (CHONPS) required for life's basic structures, such as lipids, DNA, and proteins (Domagal-Goldman et al. 2016). The small number of samples studied have therefore demonstrated that the fundamental building blocks required for life to function are present in martian samples.

The Jbilet Winselwan perchlorate experiment demonstrates the impact of perchlorates on extra-terrestrial organics. The destruction of organic compounds with increasing perchlorate concentration - and the formation of others – illustrates how organics on Mars would be affected by the strongly oxidising compounds present in the regolith. The presence of perchlorates may therefore constrain how habitable Mars may have been as biogenic compounds would be oxidised in the same way.

9 References

Abbey, W.J. et al. 2017. Deep UV Raman spectroscopy for planetary exploration: The search for in situ organics. *Icarus* 290, pp. 201–214. doi: 10.1016/j.icarus.2017.01.039.

Agee, C.B. et al. 2013. Unique meteorite from early Amazonian Mars: Water-rich basaltic breccia Northwest Africa 7034. *Science* 339(6121), pp. 780–785. doi: 10.1126/science.1228858.

Alexander, C.M.O.D., Bowden, R., Fogel, M.L., Howard, K.T., Herd, C.D.K. and Nittler, L.R. 2012. The provenances of asteroids, and their contributions to the volatile inventories of the terrestrial planets. *Science* 337(6095), pp. 721–723. doi: 10.1126/science.1223474.

Alexander, C.M.O.D., Cody, G.D., de Gregorio, B.T., Nittler, L.R. and Stroud, R.M. 2017. The nature, origin and modification of insoluble organic matter in chondrites, the major source of Earth's C and N. *Chemie der Erde* 77(2), pp. 227–256. Available at: http://dx.doi.org/10.1016/j.chemer.2017.01.007.

Alexander, C.M.O.D., Fogel, M., Yabuta, H. and Cody, G.D. 2007. The origin and evolution of chondrites recorded in the elemental and isotopic compositions of their macromolecular organic matter. *Geochimica et Cosmochimica Acta* 71(17), pp. 4380–4403. Available at: https://ac.els-cdn.com/S001670370700395X/1-s2.0-S001670370700395X-main.pdf?_tid=0d097195-0907-4f81-9cdd-dd7a665a4ec1&acdnat=1528197369_f0412af1199014c4515bd0b40d24767d [Accessed: 5 June 2018].

Allen, C.C., Morris, R. v, Karen, M.J., Golden, D.C., Lindstrom, M.M. and Lockwood, J.P. 1998. Martian Regolith Simulant Jsc Mars-1. *Lunar and planetary science conference XXIX* (Table 2), p. 1690.

Amelin, Y., Krot, A., Hutcheon, I.D. and Ulyanov, A.A. 2002. Lead isotopic ages of chondrules and calcium-aluminum-rich inclusions. *Science* 297(5587), pp. 1678–1683. doi: 10.1126/science.1073950.

Amundsen, H.E.F., Benning, L., Blake, D.F., Fogel, M. and the AMASE team 2011. *Cryogenic origin for Mars analogue carbonates in the Bockfjord volcanic complex, Svalbard (Norway)*. Available at: http://scholar.google.com/scholar?hl=en&btnG=Search&q=intitle:the+AMASE+team,+2011.+Cryogenic+origin+for+Mars+analogue+carbonates+in+the+Bockfjord+volcanic+complex,+Svalbard+(Norway)#0 [Accessed: 29 March 2019].

Annunziata, M.G., Ciarmiello, L.F., Woodrow, P., Dell'aversana, E. and Carillo, P. 2019. Spatial and temporal profile of glycine betaine accumulation in plants under abiotic stresses. *Frontiers in Plant Science* 10. doi: 10.3389/fpls.2019.00230.

Baratoux, D., Toplis, M.J., Monnereau, M. and Sautter, V. 2013. The petrological expression of early Mars volcanism. *Journal of Geophysical Research E: Planets* 118(1), pp. 59–64. doi: 10.1029/2012JE004234.

Barrat, J.A., Sansjofre, P., Yamaguchi, A., Greenwood, R.C. and Gillet, P. 2017. Carbon isotopic variation in ureilites: Evidence for an early, volatile-rich Inner Solar System. *Earth and Planetary Science Letters* 478, pp. 143–149. Available at: http://dx.doi.org/10.1016/j.epsl.2017.08.039.

Baziotis, I.P., Liu, Y., Decarli, P.S., Jay Melosh, H., McSween, H.Y., Bodnar, R.J. and Taylor, L.A. 2013. The Tissint Martian meteorite as evidence for the largest impact excavation. *Nature Communications* 4. doi: 10.1038/ncomms2414.

Becker, L., Popp, B., Rust, T. and Bada, J.L. 1999. The origin of organic matter in the Martian meteorite ALH84001. *Earth and Planetary Science Letters* 167(1–2), pp. 71–79. doi: 10.1016/S0012-821X(99)00014-X.

Becker, R.H. and Pepin, R.O. 1984. The case for a martian origin of the shergottites: nitrogen and noble gases in EETA 79001. *Earth and Planetary Science Letters* 69(2), pp. 225–242. doi: 10.1016/0012-821X(84)90183-3.

Berkley, J.L. 2006. Ureilite meteorites. *Encyclopedia of Planetary Science* , pp. 868–874. doi: 10.1007/1-4020-4520-4_430.

Bevan, A.W.R. 2006. Desert meteorites: A history. *Geological Society Special Publication* 256, pp. 325–343. doi: 10.1144/GSL.SP.2006.256.01.16.

Bottke, W.F. and Norman, M.D. 2017. The Late Heavy Bombardment. *Annual Review of Earth and Planetary Sciences* 45, pp. 619–647. doi: 10.1146/annurev-earth-063016-020131.

Bouley, S., Baratoux, D., Matsuyama, I., Forget, F., Séjourné, A., Turbet, M. and Costard, F. 2016. Late Tharsis formation and implications for early Mars. *Nature* 531(7594), pp. 344–347. doi: 10.1038/nature17171.

Bouvier, L.C. et al. 2018. Evidence for extremely rapid magma ocean crystallization and crust formation on Mars. *Nature* 558(7711), pp. 586–589. Available at: https://doi.org/10.1038/s41586-018-0222-z [Accessed: 16 May 2019].

Brandon, A.D., Walker, R.J., Morgan, J.W. and Goles, G.G. 2000. Re-Os isotopic evidence for early differentiation of the Martian mantle. *Geochimica et Cosmochimica Acta* 64(23), pp. 4083–4095. doi: 10.1016/S0016-7037(00)00482-8.

Brearley, A.J. 2006. The Action of Water. *Meteorites and the Early Solar System II* , pp. 587–624.

Buckley, A.N. and Woods, R. 1985. X-ray photoelectron spectroscopy of oxidised pyrrhotite surfaces. *Applications of Surface Science* 20(4), pp. 472–480. doi: 10.1016/0378-5963(85)90168-0.

Budde, G., Kruijer, T.S., Fischer-Gödde, M., Irving, A.J. and Kleine, T. 2015. Planetesimal differentiation revealed by the Hf-W systematics of ureilites. *Earth and Planetary Science Letters* 430, pp. 316–325. Available at: http://dx.doi.org/10.1016/j.epsl.2015.08.034.

Burton, A.S., Stern, J.C., Elsila, J.E., Glavin, D.P. and Dworkin, J.P. 2012. Understanding prebiotic chemistry through the analysis of extraterrestrial amino acids and nucleobases in meteorites. *Chemical Society Reviews* 41(16), pp. 5459–5472. doi: 10.1039/c2cs35109a.

Butcher, F.E.G., Balme, M.R., Gallagher, C., Arnold, N.S., Conway, S.J., Hagermann, A. and Lewis, S.R. 2017. Recent Basal Melting of a Mid-Latitude Glacier on Mars. *Journal of Geophysical Research: Planets* 122(12), pp. 2445–2468. doi: 10.1002/2017JE005434.

Callahan, M.P., Martin, M.G., Burton, A.S., Glavin, D.P. and Dworkin, J.P. 2014. Amino acid analysis in micrograms of meteorite sample by nanoliquid chromatography-high-

resolution mass spectrometry. *Journal of Chromatography A* 1332, pp. 30–34. Available at: http://dx.doi.org/10.1016/j.chroma.2014.01.032 [Accessed: 5 April 2021].

Carr, M.H. and Head, J.W. 2010. Geologic history of Mars. *Earth and Planetary Science Letters* 294(3–4), pp. 185–203. Available at: http://dx.doi.org/10.1016/j.epsl.2009.06.042.

Chadwick, M., Trewin, H., Gawthrop, F. and Wagstaff, C. 2013. Sesquiterpenoids lactones: Benefits to plants and people. *International Journal of Molecular Sciences* 14(6), pp. 12780–12805. Available at: /pmc/articles/PMC3709812/ [Accessed: 4 May 2021].

Chan, Q.H.S., Stroud, R., Martins, Z. and Yabuta, H. 2020. *Concerns of Organic Contamination for Sample Return Space Missions*. The Author(s). Available at: http://dx.doi.org/10.1007/s11214-020-00678-7.

Chang, G.W. and Cooper, S. 1995. Isotopic Measurements of Organic Sulfonates from the Murchison Meteorite. In: *Lunar and Planetary Science Conference 1995*., p. 281.

Chennaoui Aoudjehane, H. et al. 2012. Tissint martian meteorite: A fresh look at the interior, surface, and atmosphere of mars. *Science* 338(6108), pp. 785–788. Available at: http://science.sciencemag.org/content/sci/338/6108/785.full.pdf [Accessed: 5 June 2018].

Cockell, C.S. et al. 2019. Sample Collection and Return from Mars: Optimising Sample Collection Based on the Microbial Ecology of Terrestrial Volcanic Environments. *Space Science Reviews* 215(7). Available at: http://dx.doi.org/10.1007/s11214-019-0609-7.

Cohen, B.E., Mark, D.F., Cassata, W.S., Lee, M.R., Tomkinson, T. and Smith, C.L. 2017a. Taking the pulse of Mars via dating of a plume-fed volcano. *Nature Communications* 8(1), pp. 1–8. Available at: http://dx.doi.org/10.1038/s41467-017-00513-8.

Cohen, B.E., Mark, D.F., Cassata, W.S., Lee, M.R., Tomkinson, T. and Smith, C.L. 2017b. Taking the pulse of Mars via dating of a plume-fed volcano. *Nature Communications* 8(1), pp. 1–8. Available at: http://dx.doi.org/10.1038/s41467-017-00513-8.

Cooper, G.W., Onwo, W.M. and Cronin, J.R. 1992. Alkyl phosphonic acids and sulfonic acids in the Murchison meteorite. *Geochimica et Cosmochimica Acta* 56(11), pp. 4109–4115. Available at: https://linkinghub.elsevier.com/retrieve/pii/001670379290023C [Accessed: 5 June 2019].

Creek, D.J., Jankevics, A., Burgess, K.E.V., Breitling, R. and Barrett, M.P. 2012. IDEOM: An Excel interface for analysis of LC-MS-based metabolomics data. *Bioinformatics* 28(7), pp. 1048–1049. Available at: http://mzmatch.sourceforge.net/index.php [Accessed: 21 April 2020].

Daly, L. et al. 2019. Boom boom pow: Shock-facilitated aqueous alteration and evidence for two shock events in the Martian nakhlite meteorites. *Science Advances* 5(9). Available at: http://advances.sciencemag.org/ [Accessed: 12 April 2021].

Daly, L. et al. 2021. Solar wind contributions to Earth's oceans. *Nature Astronomy* 5(12), pp. 1275–1285. doi: 10.1038/s41550-021-01487-w.

Domagal-Goldman, S.D. et al. 2016. The astrobiology primer v2.0. *Astrobiology* 16(8), pp. 561–653. doi: 10.1089/ast.2015.1460.

Downes, H., Mittlefehldt, D.W., Kita, N.T. and Valley, J.W. 2008. Evidence from polymict ureilite meteorites for a disrupted and re-accreted single ureilite parent asteroid gardened by several distinct impactors. *Geochimica et Cosmochimica Acta* 72(19), pp. 4825–4844. Available at: http://dx.doi.org/10.1016/j.gca.2008.06.028.

Ehlmann, B.L. and Edwards, C.S. 2014. Mineralogy of the Martian Surface. *Annual Review of Earth and Planetary Sciences* 42(1), pp. 291–315. Available at: http://www.annualreviews.org/doi/10.1146/annurev-earth-060313-055024.

Ehlmann, B.L., Mustard, J.F., Murchie, S.L., Bibring, J.P., Meunier, A., Fraeman, A.A. and Langevin, Y. 2011. Subsurface water and clay mineral formation during the early history of Mars. *Nature* 479(7371), pp. 53–60. doi: 10.1038/nature10582.

Eigenbrode, J.L. et al. 2018. Organic matter preserved in 3-billion-year-old mudstones at Gale crater, Mars. *Science* 360(6393), pp. 1096–1101. Available at: http://www.ncbi.nlm.nih.gov/pubmed/29880683 [Accessed: 28 May 2019].

Flynn, G.J. 1996. The delivery of organic matter from asteroids and comets to the early surface of Mars. *Earth, Moon and Planets* 72(1–3), pp. 469–474. Available at: http://link.springer.com/10.1007/BF00117551 [Accessed: 28 May 2019].

Flynn, G.J. and McKay, D.S. 1990. An assessment of the meteoritic contribution to the

Martian soil. *Journal of Geophysical Research* 95(B9). doi: 10.1029/jb095ib09p14497.

Fukunaga, K., Matsuda, J.I., Nagao, K., Miyamoto, M. and Ito, K. 1988. Noble-gas enrichment in vapour-growth diamonds and the origin of diamonds in ureilites. *Nature* 328(6126), pp. 141–143. doi: 10.1038/328141a0.

Gibson, E.K. et al. 2001. Life on Mars: Evaluation of the evidence within Martian meteorites ALH84001, Nakhla, and Shergotty. *Precambrian Research* 106(1–2), pp. 15–34. doi: 10.1016/S0301-9268(00)00122-4.

Glavin, D.P. et al. 2013. Evidence for perchlorates and the origin of chlorinated hydrocarbons detected by SAM at the Rocknest aeolian deposit in Gale Crater. *Journal of Geophysical Research E: Planets* 118(10), pp. 1955–1973. doi: 10.1002/jgre.20144.

Glavin, D.P., Bada, J.L., Brinton, K.L.F. and Mcdonald, G.D. 1999. Amino acids in the Martian meteorite Nakhla. *Proceedings of the National Academy of Sciences of the United States of America* 96(16), pp. 8835–8838. Available at: http://www.ncbi.nlm.nih.gov/pubmed/10430856 [Accessed: 26 October 2020].

Glavin, D.P., Callahan, M.P., Dworkin, J.P. and Elsila, J.E. 2010. The effects of parent body processes on amino acids in carbonaceous chondrites. *Meteoritics and Planetary Science* 45(12), pp. 1948–1972. doi: 10.1111/j.1945-5100.2010.01132.x.

Gnos, E., Hofmann, B., Franchi, I.A., Al-Kathiri, A., Huser, M. and Moser, L. 2002. Sayh al Uhaymir 094: A new martian meteorite from the Oman desert. *Meteoritics and Planetary Science* 37(6), pp. 835–854. doi: 10.1111/j.1945-5100.2002.tb00859.x.

Goetz, W. et al. 2016. MOMA: The challenge to search for organics and biosignatures on Mars. *International Journal of Astrobiology* 15(3), pp. 239–250. doi: 10.1017/S1473550416000227.

Gomez-Lazaro, M., Freitas, A. and Ribeiro, C. 2017. Confocal Raman microscopy. *Fluorescence Imaging and Biological Quantification* (January), pp. 65–83. doi: 10.1201/9781315121017-7.

Goodrich, C.A. 1992. Ureilites : A critical review. *Meteoritics* 27, pp. 327–352. Available at: http://link.springer.com/10.1007/978-3-319-65179-8.

Goodrich, C.A., Nestola, F. and Jakubek, R.S. 2021. Diamonds in Ureilites: the Never-Ending Story. *Elements* 17(4), pp. 292–293. doi: 10.2138/gselements.17.4.292.

Goodrich, C.A., Wilson, L., van Orman, J.A. and Michel, P. 2013. Comment on "Parent body depth-pressure-temperature relationships and the style of the ureilite anatexis" by P. H. Warren (MAPS 47:209-227). *Meteoritics and Planetary Science* 48(6), pp. 1096–1106. doi: 10.1111/maps.12131.

Grady, M.M. 2020. Exploring Mars with Returned Samples. *Space Science Reviews* 216(4), pp. 1–21. Available at: https://doi.org/10.1007/s11214-020-00676-9 [Accessed: 7 July 2020].

Grady, M.M., Pratesi, G. and Moggi Cecchi, V. 2013. *Atlas of Meteorites*. First. Cambridge University Press. doi: 10.1017/9781139016308.

Grady, M.M., Wright, I.P., Swart, P.K. and Pillinger, C.T. 1985. The carbon and nitrogen isotopic composition of ureilites: Implications for their genesis. *Geochimica et Cosmochimica Acta* 49(4), pp. 903–915. doi: 10.1016/0016-7037(85)90306-0.

de Gregorio, B.T. and Stroud, R.M. 2021. INSOLUBLE ORGANIC MATTER IN RYUGU ANALOG METEORITE JBILET WINSELWAN. In: *52nd Lunar and Planetary Science Conference, held virtually, 15-19 March, 2021. LPI Contribution No. 2548, id.2059*., p. 2059. Available at: https://ui.adsabs.harvard.edu/abs/2021LPI....52.2059D.

Greshake, A. 1998. Transmission electron microscopy characterization of shock defects in minerals from the Nakhla SNC meteorite. *Meteorit. Planet. Sci.* 33, p. A63.

Grossman, J.N. and Zipfel, J. 2001. The Meteoritical Bulletin, no. 85, 2001 September. *Meteoritics and Planetary Science* 36(SUPPL TO ISSUE 9). doi: 10.1111/j.1945-5100.2001.tb01542.x.

Hallis, L.J. 2017. D / H ratios of the inner Solar System Subject Areas : *Philosophical Transactions of the Royal Society A: Mathematical, Physical and Engineering Sciences*

Hallis, L.J., Huss, G.R., Nagashima, K., Taylor, G.J., Stöffler, D., Smith, C.L. and Lee, M.R. 2017. Effects of shock and Martian alteration on Tissint hydrogen isotope ratios and water content. *Geochimica et Cosmochimica Acta* 200, pp. 280–294. doi:

10.1016/j.gca.2016.12.035.

Hamilton, V.E. et al. 2019. Evidence for widespread hydrated minerals on asteroid (101955) Bennu. *Nature Astronomy* 3(4), pp. 332–340. doi: 10.1038/s41550-019-0722-2.

Hanneman, R.E., Strong, H.M. and Bundy, F.P. 1967. Hexagonal diamonds in meteorites: Implications. *Science* 155(3765), pp. 997–999. doi: 10.1126/science.155.3765.995.

Hayatsu, R., Matsuoka, S., Scott, R.G., Studier, M.H. and Anders, E. 1977. Origin of organic matter in the early solar system-VII. The organic polymer in carbonaceous chondrites. *Geochimica et Cosmochimica Acta* 41(9), pp. 1325–1339. doi: 10.1016/0016-7037(77)90076-X.

Hedden, P. and Sponsel, V. 2015. A Century of Gibberellin Research. *Journal of Plant Growth Regulation* 34(4), pp. 740–760. doi: 10.1007/s00344-015-9546-1.

Herd, C.D.K. et al. 2017a. The Northwest Africa 8159 martian meteorite: Expanding the martian sample suite to the early Amazonian. *Geochimica et Cosmochimica Acta* 218, pp. 1–26. doi: 10.1016/j.gca.2017.08.037.

Herd, C.D.K. et al. 2017b. The Northwest Africa 8159 martian meteorite: Expanding the martian sample suite to the early Amazonian. *Geochimica et Cosmochimica Acta* 218, pp. 1–26. doi: 10.1016/j.gca.2017.08.037.

Hilts, R.W., Herd, C.D.K., Simkus, D.N. and Slater, G.F. 2014. Soluble organic compounds in the Tagish Lake meteorite. *Meteoritics and Planetary Science* 49(4), pp. 526–549. doi: 10.1111/maps.12272.

Hollis, J.R. et al. 2021. First SHERLOC Results from Mars 2020 ' s Green Zone Campaign in Jezero Crater. *Bulletin of the AAS* 53(7), pp. 2020–2022.

Horgan, B.H.N., Anderson, R.B., Dromart, G., Amador, E.S. and Rice, M.S. 2020. The mineral diversity of Jezero crater: Evidence for possible lacustrine carbonates on Mars. *Icarus* 339. doi: 10.1016/j.icarus.2019.113526.

Huang, Y., Wang, Y., Alexandre, M.R., Lee, T., Rose-Petruck, C., Fuller, M. and Pizzarello, S. 2005. Molecular and compound-specific isotopic characterization of

monocarboxylic acids in carbonaceous meteorites. *Geochimica et Cosmochimica Acta* 69(4), pp. 1073–1084. doi: 10.1016/j.gca.2004.07.030.

Hynek, B.M., Beach, M. and Hoke, M.R.T. 2010. Updated global map of Martian valley networks and implications for climate and hydrologic processes. *Journal of Geophysical Research* 115(E9), pp. 1–14. doi: 10.1029/2009je003548.

Imae, N., Ikeda, Y. and Kojima, H. 2005. Petrology of the Yamato nakhlites. *Meteoritics and Planetary Science* 40(11), pp. 1581–1598. doi: 10.1111/j.1945-5100.2005.tb00133.x.

IMOST 2018. The Potential Science and Engineering Value of Samples Delivered to Earth by Mars Sample Return, , (co-chairs D. W. Beaty, M. M. Grady, H. Y. McSween, E. Sefton-Nash; documentarian B.L. Carrier; plus 66 co-authors), 186. *White Paper* , p. 186.

Jaramillo, E.A., Royle, S.H., Claire, M.W., Kounaves, S.P. and Sephton, M.A. 2019. Indigenous Organic-Oxidized Fluid Interactions in the Tissint Mars Meteorite. *Geophysical Research Letters* 46(6), pp. 3090–3098. Available at: https://onlinelibrary.wiley.com/doi/abs/10.1029/2018GL081335 [Accessed: 30 April 2019].

Jull, A.J.T., Beck, J.W. and Burr, G.S. 2000. Isotopic evidence for extraterrestrial organic material in the Martian meteorite, Nakhla. *Geochimica et Cosmochimica Acta* 64(21), pp. 3763–3772. doi: 10.1016/S0016-7037(00)00458-0.

Jull, A.J.T., Kim, K.J., R. C. Reedy, R., M.L. and Johnson, J.A. 2004. MODELING OF 14C AND 10BE PRODUCTION RATES IN METEORITES AND LUNAR SAMPLES. In: *Lunar and Planetary Science Conference 2004*. doi: 10.7868/s0367676513050359.

Jull, A.J.T., Klandrud, S.E., Schnabel, C., Herzog, G.. F., Nishiizumi, K. and Caffee, M.W. 1999. COSMOGENIC RADIONUCLIDE STUDIES OF THE NAKHLITES. In: *Lpsc Xxix*., pp. 172–173.

Kebukawa, Y. et al. 2021. Organic matter in carbonaceous chondrite lithologies of Almahata Sitta: Incorporation of previously unsampled carbonaceous chondrite lithologies into ureilitic regolith. *Meteoritics and Planetary Science* 56(7), pp. 1311–1327. doi: 10.1111/maps.13713.

King, A.J. et al. 2019. The alteration history of the Jbilet Winselwan CM carbonaceous chondrite: An analog for C-type asteroid sample return. *Meteoritics and Planetary Science* 54(3), pp. 521–543. doi: 10.1111/maps.13224.

Kitajima, F., Nakamura, T., Takaoka, N. and Murae, T. 2002. Evaluating the thermal metamorphism of CM chondrites by using the pyrolytic behavior of carbonaceous macromolecular matter. *Geochimica et Cosmochimica Acta* 66(1), pp. 163–172. doi: 10.1016/S0016-7037(01)00758-X.

Kitazato, K. et al. 2019. The surface composition of asteroid 162173 Ryugu from Hayabusa2 near-infrared spectroscopy. *Science* 364(6437), pp. 272–275. doi: 10.1126/science.aav7432.

Klinke, C., Kurt, R., Bonard, J.M. and Kern, K. 2002. Raman spectroscopy and field emission measurements on catalytically grown carbon nanotubes. *Journal of Physical Chemistry B* 106(43), pp. 11191–11195. doi: 10.1021/jp0215217.

Koike, M., Nakada, R., Kajitani, I., Usui, T., Tamenori, Y., Sugahara, H. and Kobayashi, A. 2020. In-situ preservation of nitrogen-bearing organics in Noachian Martian carbonates. *Nature Communications* 11(1), p. 1988. Available at: http://www.nature.com/articles/s41467-020-15931-4.

Korochantseva, E.V. et al. 2011. COSMIC RAY EXPOSURE AGES OF NAKHLITES – NAKHLA, LAFAYETTE, GOVERNADOR VALADARES – AND CHASSIGNY: ONE EJECTION EVENT? In: *42nd Lunar and Planetary Science Conference*., pp. 4–5.

Kruijer, T.S., Burkhardt, C., Budde, G. and Kleine, T. 2017. Age of Jupiter inferred from the distinct genetics and formation times of meteorites. *Proceedings of the National Academy of Sciences of the United States of America* 114(26), pp. 6712–6716. doi: 10.1073/pnas.1704461114.

Kumar, N., Lezama Pacheco, J., Noël, V., Dublet, G. and Brown, G.E. 2018. Sulfidation mechanisms of Fe(iii)-(oxyhydr)oxide nanoparticles: A spectroscopic study. *Environmental Science: Nano* 5(4), pp. 1012–1026. doi: 10.1039/c7en01109a.

Kunz, G.F. 1888. Diamonds in Meteorites. *Science* ns-11(266), pp. 118–119. Available at: https://www.science.org/doi/10.1126/science.ns-11.266.118.b.

Lagain, A. et al. 2021. The Tharsis mantle source of depleted shergottites revealed by 90 million impact craters. *Nature Communications* 12(1), pp. 1–9. doi: 10.1038/s41467-021-26648-3.

Lai, J.C.Y., Pearce, B.K.D., Pudritz, R.E. and Lee, D. 2019. Meteoritic abundances of fatty acids and potential reaction pathways in planetesimals. *Icarus* 319(June 2018), pp. 685–700. Available at: https://doi.org/10.1016/j.icarus.2018.09.028.

Lammer, H., Brasser, R., Johansen, A., Scherf, M. and Leitzinger, M. 2020. Formation of Venus, Earth and Mars: Constrained by Isotopes. *Space Science Reviews* 217(1), pp. 2–12. Available at: http://dx.doi.org/10.1007/s11214-020-00778-4.

Lee, D.C. and Halliday, A.N. 1997. Core formation on Mars and differentiated asteroids. *Nature* 388(6645), pp. 854–857. doi: 10.1038/42206.

Lee, M.R., Cohen, B.E., King, A.J. and Greenwood, R.C. 2019. The diversity of CM carbonaceous chondrite parent bodies explored using Lewis Cliff 85311. *Geochimica et Cosmochimica Acta* 264, pp. 224–244. Available at: https://doi.org/10.1016/j.gca.2019.07.027.

Lee, M.R., Lindgren, P., King, A.J., Greenwood, R.C., Franchi, I.A. and Sparkes, R. 2016. Elephant Moraine 96029, a very mildly aqueously altered and heated CM carbonaceous chondrite: Implications for the drivers of parent body processing. *Geochimica et Cosmochimica Acta* 187, pp. 237–259. Available at: http://dx.doi.org/10.1016/j.gca.2016.05.008.

Leinweber, P., Kruse, J., Walley, F.L., Gillespie, A., Eckhardt, K.U., Blyth, R.I.R. and Regier, T. 2007. Nitrogen K-edge XANES - An overview of reference compounds used to identify “unknown” organic nitrogen in environmental samples. *Journal of Synchrotron Radiation* 14(6), pp. 500–511. doi: 10.1107/S0909049507042513.

Leya, I. and Stephenson, P.C. 2019. Cosmic ray exposure ages for ureilites—New data and a literature study. *Meteoritics and Planetary Science* 54(7), pp. 1512–1532. doi: 10.1111/maps.13288.

Lin, Y. et al. 2014a. NanoSIMS analysis of organic carbon from the Tissint Martian meteorite: Evidence for the past existence of subsurface organic-bearing fluids on Mars.

Meteoritics and Planetary Science 49(12), pp. 2201–2218. Available at: http://doi.wiley.com/10.1111/maps.12389 [Accessed: 4 April 2021].

Lin, Y. et al. 2014b. NanoSIMS analysis of organic carbon from the Tissint Martian meteorite: Evidence for the past existence of subsurface organic-bearing fluids on Mars. *Meteoritics and Planetary Science* 49(12), pp. 2201–2218. Available at: http://doi.wiley.com/10.1111/maps.12389 [Accessed: 30 April 2019].

Lipschutz, M.E. 1964. Origin of Diamonds in the Ureilites. *Science* 143(3613), pp. 1431–1434. doi: 10.1126/science.143.3613.1431.b.

Lorenz, C.A., Shiryaev, A.A., Vlasov, I.I. and Borisovsky, S.E. 2019. Metamorphism of four desert ureilites and luminescence spectroscopy of defects in ureilitic diamonds. *Meteoritics and Planetary Science* 54(6), pp. 1197–1214. doi: 10.1111/maps.13274.

MacArthur, J.L. et al. 2019. Mineralogical constraints on the thermal history of martian regolith breccia Northwest Africa 8114. *Geochimica et Cosmochimica Acta* 246, pp. 267–298. Available at: https://doi.org/10.1016/j.gca.2018.11.026.

Mason, B., Nelon, J.A., Muir, P. and Taylor, S.R. 1976. the Composition of the Chassigny Meteorite. *Meteoritics* 11(1), pp. 21–27. doi: 10.1111/j.1945-5100.1976.tb00311.x.

Matsuda, J. ichi, Fukunaga, K. and Ito, K. 1991. Noble gas studies in vapor-growth diamonds: Comparison with shock-produced diamonds and the origin of diamonds in ureilites. *Geochimica et Cosmochimica Acta* 55(7), pp. 2011–2023. doi: 10.1016/0016-7037(91)90039-8.

Mautner, M.N., Conner, A.J., Killham, K. and Deamer, D.W. 1997. Biological potential of extraterrestrial materials. *Icarus* 129(1), pp. 245–253. doi: 10.1006/icar.1997.5786.

Mautner, M.N. and Sinaj, S. 2002. Water-extractable and exchangeable phosphate in Martian and carbonaceous chondrite meteorites and in planetary soil analogs. *Geochimica et Cosmochimica Acta* 66(17), pp. 3161–3174. doi: 10.1016/S0016-7037(02)00910-9.

Mcdermott, J.M., Seewald, J.S., German, C.R., Sylva, S.P. and Canfield, D.E. 2015. Pathways for abiotic organic synthesis at submarine hydrothermal fields. 112(25). doi: 10.1073/pnas.1506295112.

McKay, D.S. et al. 1996. Search for past life on Mars: Possible relic biogenic activity in martian meteorite ALH84001. *Science* 273(5277), pp. 924–930. Available at: http://science.sciencemag.org/ [Accessed: 4 April 2021].

McLoughlin, N., Grosch, E.G., Vullum, P.E., Guagliardo, P., Saunders, M. and Wacey, D. 2019. Critically testing olivine-hosted putative martian biosignatures in the Yamato 000593 meteorite—Geobiological implications. *Geobiology* 17(6), pp. 691–707. doi: 10.1111/gbi.12361.

Meredith, W., Ascough, P.L., Bird, M.I., Large, D.J., Snape, C.E., Sun, Y. and Tilston, E.L. 2012. Assessment of hydropyrolysis as a method for the quantification of black carbon using standard reference materials. *Geochimica et Cosmochimica Acta* 97, pp. 131–147. doi: 10.1016/j.gca.2012.08.037.

Mikouchi, T. and Kurihara, T. 2008. Mineralogy and petrology of paired lherzolitic shergottites Yamato 000027, Yamato 000047, and Yamato 000097: Another fragment from a Martian "lherzolite" block. *Polar Science* 2(3), pp. 175–194. Available at: http://dx.doi.org/10.1016/j.polar.2008.06.003.

Miyahara, M. et al. 2015. Unique large diamonds in a ureilite from Almahata Sitta 2008 TC3 asteroid. *Geochimica et Cosmochimica Acta* 163, pp. 14–26. Available at: http://dx.doi.org/10.1016/j.gca.2015.04.035.

Morris, R. v., Golden, D.C., Bell, J.F., Lauer, H. v. and Adams, J.B. 1993. Pigmenting agents in martian soils: Inferences from spectral, Mössbauer, and magnetic properties of nanophase and other iron oxides in Hawaiian palagonitic soil PN-9. *Geochimica et Cosmochimica Acta* 57(19), pp. 4597–4609. doi: 10.1016/0016-7037(93)90185-Y.

Nabiei, F. et al. 2018. A large planetary body inferred from diamond inclusions in a ureilite meteorite. *Nature Communications* 9(1), pp. 6–11. Available at: http://dx.doi.org/10.1038/s41467-018-03808-6.

Nakamura, T. 2005. Post-hydration thermal metamorphism of carbonaceous chondrites. *Mineralogical and Petrological Sciences* 100, pp. 260–272.

Nakamuta, Y. and Toh, S. 2013. Transformation of graphite to lonsdaleite and diamond in the Goalpara ureilite directly observed by TEM. *American Mineralogist* 98(4), pp. 574–

581. doi: 10.2138/am.2013.4341.

Needham, A.W., Abel, R.L., Tomkinson, T. and Grady, M.M. 2013. Martian subsurface fluid pathways and 3D mineralogy of the Nakhla meteorite. *Geochimica et Cosmochimica Acta* 116, pp. 96–110. Available at: http://dx.doi.org/10.1016/j.gca.2012.07.004.

Nestola, F. et al. 2020. Impact shock origin of diamonds in ureilite meteorites. *Proceedings of the National Academy of Sciences of the United States of America* 117(41), pp. 25310–25318. doi: 10.1073/pnas.1919067117.

Nichols, R.H. 2006. Chronological Constraints on Planetesimal Accretion. *Meteorites and the Early Solar System II* , pp. 463–472. doi: 10.2307/j.ctv1v7zdmm.28.

Nininger, H. 1935. The Lafayette Meteorite. *Popular Astronomy* (XLIII), pp. 404–408. Available at: http://articles.adsabs.harvard.edu/pdf/1935PA.....43..404N.

Nyquist, L.E., Bogard, D.D., Shih, C.-Y., Greshake, A., Stöffler, D. and Eugster, O. 2001. Ages and Geologic Histories of Martian Meteorites. *Space Science Reviews* , pp. 105–164. doi: 10.1007/978-94-017-1035-0_5.

O'Brien, Á.C. et al. 2022. The Winchcombe Meteorite: one year on. *Astronomy & Geophysics* 63(1), pp. 1.21-1.23. doi: 10.1093/astrogeo/atac009.

Orthous-Daunay, F.R., Quirico, E., Lemelle, L., Beck, P., deAndrade, V., Simionovici, A. and Derenne, S. 2010. Speciation of sulfur in the insoluble organic matter from carbonaceous chondrites by XANES spectroscopy. *Earth and Planetary Science Letters* 300(3–4), pp. 321–328. Available at: https://ac-els-cdn-com.ezproxy.lib.gla.ac.uk/S0012821X10006461/1-s2.0-S0012821X10006461-main.pdf?_tid=5d477c71-64d2-4dee-a914-5566c00b178d&acdnat=1526653973_a9b3335dcf8535868efff8c2560ec75e [Accessed: 18 May 2018].

Papike, J.J., Karner, J.M., Shearer, C.K. and Burger, P. v. 2009. Silicate mineralogy of martian meteorites. *Geochimica et Cosmochimica Acta* 73(24), pp. 7443–7485. Available at: http://dx.doi.org/10.1016/j.gca.2009.09.008.

Pitt, J.J. 2009. Principles and applications of liquid chromatography-mass spectrometry in

clinical biochemistry. *The Clinical biochemist. Reviews* 30(1), pp. 19–34. Available at: http://www.ncbi.nlm.nih.gov/pubmed/19224008.

Quantin-Nataf, C. et al. 2021. Oxia Planum: The Landing Site for the ExoMars "rosalind Franklin" Rover Mission: Geological Context and Prelanding Interpretation. *Astrobiology* 21(3), pp. 345–366. doi: 10.1089/ast.2019.2191.

Rai, N., Downes, H. and Smith, C. 2020. Ureilite meteorites provide a new model of early planetesimal formation and destruction. *Geochemical Perspectives Letters* , pp. 20–25. doi: 10.7185/geochemlet.2018.

Raymond, S.N. and Izidoro, A. 2017. Origin of water in the inner Solar System: Planetesimals scattered inward during Jupiter and Saturn's rapid gas accretion. *Icarus* 297, pp. 134–148. doi: 10.1016/j.icarus.2017.06.030.

Ross, A.J. et al. 2011. MicroRaman spectroscopy of diamond and graphite in Almahata Sitta and comparison with other ureilites. *Meteoritics and Planetary Science* 46(3), pp. 364–378. doi: 10.1111/j.1945-5100.2010.01157.x.

Royle, S.H., Oberlin, E., Watson, J.S., Montgomery, W., Kounaves, S.P. and Sephton, M.A. 2018. Perchlorate-Driven Combustion of Organic Matter During Pyrolysis-Gas Chromatography-Mass Spectrometry: Implications for Organic Matter Detection on Earth and Mars. *Journal of Geophysical Research: Planets* 123(7), pp. 1901–1909. doi: 10.1029/2018JE005615.

Rull, F. et al. 2017. The Raman Laser Spectrometer for the ExoMars Rover Mission to Mars. *Astrobiology* 17(6–7), pp. 627–654. Available at: www.liebertpub.com [Accessed: 10 May 2019].

Saikia, B.J., Parthasarathy, G. and Borah, R.R. 2017. Mineralogy of Meteorites from the North-Eastern India: A Brief Review. *Geomaterials* 07(03), pp. 83–95. doi: 10.4236/gm.2017.73007.

Salvatore, M.R., Mustard, J.F., Wyatt, M.B. and Murchie, S.L. 2010. Definitive evidence of Hesperian basalt in Acidalia and Chryse planitiae. *Journal of Geophysical Research* 115(E7), pp. 1–16. doi: 10.1029/2009je003519.

Schött, H.F., Konings, M.C.J.M., Schrauwen-Hinderling, V.B., Mensink, R.P. and Plat, J. 2021. A Validated Method for Quantification of Fatty Acids Incorporated in Human Plasma Phospholipids by Gas Chromatography-Triple Quadrupole Mass Spectrometry. *ACS Omega* 6(2), pp. 1129–1137. doi: 10.1021/acsomega.0c03874.

Schröder, C. et al. 2008. Meteorites on Mars observed with Mars Exploration Rovers. *Journal of Geophysical Research E: Planets* 113(6), pp. 1–19. doi: 10.1029/2007JE002990.

Schulz, T. et al. 2020. The history of the Tissint meteorite, from its crystallization on Mars to its exposure in space: New geochemical, isotopic, and cosmogenic nuclide data. *Meteoritics and Planetary Science* 55(2), pp. 294–311. doi: 10.1111/maps.13435.

Sephton, M.A. 2013. Aromatic units from the macromolecular material in meteorites: Molecular probes of cosmic environments. *Geochimica et Cosmochimica Acta* 107, pp. 231–241. Available at: http://dx.doi.org/10.1016/j.gca.2012.12.042.

Sephton, M.A., Lewis, J.M.T., Watson, J.S., Montgomery, W. and Garnier, C. 2014. Perchlorate-induced combustion of organic matter with variable molecular weights: Implications for Mars missions. *Geophysical Research Letters* 41(21), pp. 7453–7460. Available at: http://doi.wiley.com/10.1002/2014GL062109.

Sephton, M.A., Love, G.D., Meredith, W., Snape, C.E., Sun, C.G. and Watson, J.S. 2005. Hydropyrolysis: A new technique for the analysis of macromolecular material in meteorites. *Planetary and Space Science* 53(12), pp. 1280–1286. Available at: www.elsevier.com/locate/pss [Accessed: 30 April 2019].

Sephton, M.A., Verchovsky, A.B., Bland, P.A., Gilmour, I., Grady, M.M. and Wright, I.P. 2003. Investigating the variations in carbon and nitrogen isotopes in carbonaceous chondrites. *Geochimica et Cosmochimica Acta* 67(11), pp. 2093–2108. doi: 10.1016/S0016-7037(02)01320-0.

Sephton, M.A., Watson, J.S., Meredith, W., Love, G.D., Gilmour, I. and Snape, C.E. 2015. Multiple Cosmic Sources for Meteorite Macromolecules? *Astrobiology* 15(10), pp. 779–786. Available at: http://www.liebertpub.com/doi/10.1089/ast.2015.1331 [Accessed: 23 June 2019].

Sephton, M.A., Wright, I.P., Gilmour, I., de Leeuw, J.W., Grady, M.M. and Pillinger, C.T. 2002. High molecular weight organic matter in martian meteorites. *Planetary and Space Science* 50(7–8), pp. 711–716. Available at: https://linkinghub.elsevier.com/retrieve/pii/S0032063302000533 [Accessed: 5 June 2019].

Seyler, L., Kujawinski, E.B., Azua-Bustos, A., Lee, M.D., Marlow, J., Perl, S.M. and Cleaves II, H.J. 2020. Metabolomics as an Emerging Tool in the Search for Astrobiologically Relevant Biomarkers. *Astrobiology* 20(10), pp. 1251–1261. doi: 10.1089/ast.2019.2135.

Sharp, T.G., Walton, E.L., Hu, J. and Agee, C. 2019. Shock conditions recorded in NWA 8159 martian augite basalt with implications for the impact cratering history on Mars. *Geochimica et Cosmochimica Acta* 246, pp. 197–212. Available at: https://doi.org/10.1016/j.gca.2018.11.014.

Siljeström, S., Freissinet, C., Goesmann, F., Steininger, H., Goetz, W., Steele, A. and Amundsen, H. 2014. Comparison of prototype and laboratory experiments on MOMA GCMS: Results from the AMASE11 campaign. *Astrobiology* 14(9), pp. 780–797. Available at: www.liebertpub.com [Accessed: 22 March 2020].

Simkus, D.N., Aponte, J.C., Elsila, J.E., Parker, E.T., Glavin, D.P. and Dworkin, J.P. 2019. Methodologies for analyzing soluble organic compounds in extraterrestrial samples: Amino Acids, Amines, Monocarboxylic Acids, Aldehydes, and Ketones. *Life* 9(2). doi: 10.3390/life9020047.

Smith, C.L., Franchi, I.A., Wright, I.P., Grady, M.M. and Pillinger, C.T. 2001. New Data on Carbon Isotopic Compositions of Some Ureilites. *32nd Lunar and Planetary Science Conference* , p. Abstract #1878. Available at: http://www.lpi.usra.edu/meetings/lpsc2001/pdf/1878.pdf.

Starkey, N.A., Franchi, I.A. and Alexander, C.M.O. 2013. A Raman spectroscopic study of organic matter in interplanetary dust particles and meteorites using multiple wavelength laser excitation. *Meteoritics and Planetary Science* 48(10), pp. 1800–1822. doi: 10.1111/maps.12196.

Steele, A. et al. 2012. A reduced organic carbon component in martian basalts. *Science*

337(6091), pp. 212–215. doi: 10.1126/science.1220715.

Steele, A. et al. 2018. *Organic synthesis on Mars by electrochemical reduction of CO2*. Available at: http://advances.sciencemag.org/ [Accessed: 1 February 2019].

Steele, A. et al. 2022. Organic synthesis associated with serpentinization and carbonation on early Mars. *Science* 375(6577), pp. 172–177. doi: 10.1126/science.abg7905.

Steele, A., Fries, M.D., Amundsen, H.E.F., Mysen, B.O., Fogel, M.L., Schweizer, M. and Boctor, N.Z. 2007. Comprehensive imaging and Raman spectroscopy of carbonate globules from Martian meteorite ALH 84001 and a terrestrial analogue from Svalbard. *Meteoritics and Planetary Science* 42(9), pp. 1549–1566. doi: 10.1111/j.1945-5100.2007.tb00590.x.

Steele, A., Fries, M.D. and Pasteris, J.D. 2020. Geoscience Meets Biology: Raman Spectroscopy in Geobiology and Biomineralization. *Elements* 16(2), pp. 111–116. doi: 10.2138/gselements.16.2.111.

Steele, A., McCubbin, F.M. and Fries, M.D. 2016. The provenance, formation, and implications of reduced carbon phases in Martian meteorites. *Meteoritics and Planetary Science* 51(11), pp. 2203–2225. doi: 10.1111/maps.12670.

Summons, R.E. et al. 2011. Preservation of Martian Organic and Environmental Records: Final Report of the Mars Biosignature Working Group. *Astrobiology* 11(2), pp. 157–181. Available at: www.liebertpub.com [Accessed: 7 January 2019].

Tonui, E., Zolensky, M., Hiroi, T., Nakamura, T., Lipschutz, M.E., Wang, M.-S. and Okudaira, K. 2014. Petrographic, chemical and spectroscopic evidence for thermal metamorphism in carbonaceous chondrites I: CI and CM chondrites. *Geochimica et Cosmochimica Acta* 126, pp. 284–306. Available at: www.elsevier.com/locate/gcaAvailableonlineatwww.sciencedirect.com.

Treiman, A.H. 2003. Submicron magnetite grains and carbon compounds in martian meteorite ALH84001: Inorganic, abiotic formation by shock and thermal metamorphism. *Astrobiology* 3(2), pp. 369–392. doi: 10.1089/153110703769016451.

Udry, A., Howarth, G.H., Herd, C.D.K., Day, J.M.D., Lapen, T.J. and Filiberto, J. 2020.

What Martian Meteorites Reveal About the Interior and Surface of Mars. *Journal of Geophysical Research: Planets* 125(12), pp. 1–34. doi: 10.1029/2020JE006523.

Urey, H.C. 1956. Diamonds, Meteorites, and the Origin of the Solar System. *The Astrophysical Journal* 124, p. 623. doi: 10.1086/146269.

Váci, Z. and Agee, C. 2020. Constraints on martian chronology from meteorites. *Geosciences (Switzerland)* 10(11), pp. 1–15. doi: 10.3390/geosciences10110455.

Warren, P.H. 2011. Stable-isotopic anomalies and the accretionary assemblage of the Earth and Mars: A subordinate role for carbonaceous chondrites. *Earth and Planetary Science Letters* 311(1–2), pp. 93–100. Available at: http://dx.doi.org/10.1016/j.epsl.2011.08.047.

Wegulo, S.N., Pathologist, E.P., Jackson, T. a, Baenziger, P.S., Carlson, M.P. and Nopsa, J.H. 2008. Fusarium Head Blight of Wheat. *University of Nebraska–Lincoln Extension* EC1896(The Board of Regents of the University of Nebraska), pp. 1–8.

Westall, F. et al. 2015. Biosignatures on Mars: What, Where, and How? Implications for the Search for Martian Life. *Astrobiology* 15(11), pp. 998–1029. Available at: http://online.liebertpub.com/doi/10.1089/ast.2015.1374.

White, L.M., Gibson, E.K., Thomas-Keprta, K.L., Clemett, S.J. and McKay, D.S. 2014. Putative indigenous carbon-bearing alteration features in martian meteorite yamato 000593. *Astrobiology* 14(2), pp. 170–181. doi: 10.1089/ast.2011.0733.

Wise, K. and Woloshuk, C. 2010. Fusarium Head Blight (Head Scab). Purdue Ext, pp. 1–4. Available at: www.agry.purdue.edu/ext/smgrain.

Wright, I.P., Grady, M.M. and Pillinger, C.T. 1992. Chassigny and the nakhlites: Carbon-bearing components and their relationship to martian environmental conditions. *Geochimica et Cosmochimica Acta* 56(2), pp. 817–826. doi: 10.1016/0016-7037(92)90100-W.

Zampolli, M., Meunier, D., Sternberg, R., Raulin, F., Szopa, C., Pietrogrande, M.C. and Dondi, F. 2006. GC-MS analysis of amino acid enantiomers as their N(O,S)-perfluoroacyl perfluoroalkyl esters: Application to space analysis. *Chirality* 18(4), pp. 279–295. doi: 10.1002/chir.20241.

Zipfel, J. 2000. Sayh al uhaymir 005/008 and its relationship to Dar al Gani 476/489. In: *Meteoritics & Planetary Science*., p. 178. Available at: https://articles.adsabs.harvard.edu/cgi-bin/nph-iarticle_query?db_key=AST&bibcode=2000M%26PSA..35Q.178Z&letter=0&classic=YES&defaultprint=YES&whole_paper=YES&page=178&epage=178&send=Send+PDF&filetype=.pdf.

Appendix 1: Supplementary Bulk Experimental Materials

Appendix 1 contains supplementary information from the bulk experiments carried out on martian meteorites and martian analogues.

Firstly, the standard operational procedures for extraction and GC-MS in the BECS lab in GES are given (as carried out by Ali Salik in Autumn 2020, due to social distancing requirements). Additional information on metabolites of interest putatively identified in the martian LC-MS experiment are then shown in Table 15, displaying their molecular structures, spectra, and sample distribution, as well as any information on standards run or isomers. Table 16 focuses on the metabolites detected in Lafayette at highest intensity relative to the first procedural blank (FBD1). Table 17 does the same for Nakhla.

Automatic Solvent Extraction (ASE) Operation Procedure (SOP)

Below is the SOP for the use of the ASE in BECS, as created by Professor Jaime Toney. The ASE was used to solvent extract the hydrogen pyrolysed martian and Mars analogue samples prior to GC-MS analyses.

Operating Procedures for ASE 350

Loading the ASE cells for a run:

1. We have 24 10ml cells. On average, a 10ml cell can hold ~3g of sediment (depending on its properties). Make sure you extract a sufficient amount of sample for your analyses.

2. Use 60ml collection vials for 10ml cells.

3. In general, end-caps of cells should remain assembled during the wash process,unless particularly dirty samples were extracted

4. Put a glass fiber filter onto the top of the cell body. Make sure the filter does not overlap the ridge at the edge of the cell; this will prevent the end-cap from making an appropriate

seal.

5. Place the cell on the balance and zero it. Load freeze-dried sample into the cell using the specialized funnel. Weigh the samples directly in the cell. Keep the threads on the cell body and cap free of dust particles to prevent thread fouling and extend the life of the cell.

6. Fill any void volume in the cell with combusted sand; this reduces the amount of solvent used during the extraction.

7. Place a filter on the top of the cell body and screw the end-cap onto the top of the cell body. Hand-tighten only – do not use excessive force. Do not attach any labels to the cell. For sample identification, write on the top cap with a marking pen.

8. Place the loaded cells into the tray slots on ASE 350 in numerical order. Hang the cells vertically in the tray slots. Make sure the marked side is on top. Load the labelled collection vials in the corresponding vial tray slots. The vials should be capped with the open-hole-screw-thread caps with either Teflon septa or aluminium foil.

9. Make sure that a 250ml collection bottle is in the R1 rinse slot. Empty rinse vials and the waste vial after each run.

Operating the ASE 350:

10. Check the level of N2 gas in the cylinder in the cage outside. Make sure that the residual pressure is above 200psi before starting a new sequence. Check the air pressure to make sure it ~100psi.

11. Turn the flow ‘on’ in the lab with the valve on the wall.

12. Make sure the clear protective shield on the ASE’s lower carousel is closed.

13. Perform the “rinse” function on the ASE, at least three times prior to extracting your samples

14. Check that the amount of solvent in the solvent bottles. Add more solvent if needed, then hand-tighten the cap. Press the trays button on the keypad to engage or disengage the tray.

15. Use Method Control to run all extractions. Press menu to display the MENU OF SCREENS, and press Enter (or 1) to display the LOAD METHOD OR SEQUENCE screen. If you are extracting traditional lake, bog, or sediment samples - input METHOD 1 and press the ENTER again.

a. The LOAD METHOD OR SEQUENCE screen closes and the CURRENT STATUS screen displays, showing the method number loaded and the status of the ASE 350 with various operating parameters.

b. The oven will begin heating from room temperature to 120°C. Each sample takes about 60min and consumes about 30ml solvent.

16. Most runs will not need this!! [Compress the cells (if needed). Get to the mainmenu, press 7 (Diagnostic menu), press ". . ." (3 dots). Then put in 9137 and press enter. Press 8 (Manual control). Make sure the ASE has control of the trays (you won't be able to turn the trays, if you can, press trays button once). Go to the right hand column, and put in cell 1. Press ASE arm (out). Press ASE arm (up). Press ASE arm (in). Press Oven compression (yes). After 10 seconds, press oven compression (no). After 5 seconds. Press ASE arm (out). Press ASE arm (down). Move onto cell 2, and repeat.]

17. Press START to run a sequence of samples. There are seven main steps in the extraction process: (1) Loading the cell; (2) Filling the cell; (3) Heating the cell (equilibration); (4) Static extraction; (5) Flushing with fresh solvent; (6) Purging solvent from the system; (7) Unloading the cell.

18. After the extraction, uncap the cells. Residual sample can be discarded or stored in corresponding labeled whirlpak bags. Disassemble the cell bodies from the end-caps. Note: end-caps should not be taken apart unless particularly dirty samples were extracted.

19. Clean all the parts according to the Cleanup Procedure. This should be done immediately after use to make the instrument ready for the next person to use.

20. The composition of the extracts generated by the ASE 350 is very similar to that generated by Soxhlet or other liquid extraction techniques using the same solvent system.

Evaporation of the samples by Techne Evaporation or Turbovap:

21. Remove the solvent with Nitrogen using the Techne evaporator if you are using 60ml vials. Simply select the correct aluminium block, place them in the heating block and blow down with nitrogen. (If quick turn around time is important samples can be transferred to combusted 40ml vials and evaporated by following step #22.)

22. Remove the solvent with Nitrogen using the Turbo Evaporator. Use a water bath temperature of 35°C for ca. 30min. Monitor the solvent evaporation progress. Do not let the samples remain without solvent – volatile compounds can be lost.

Carry out further chromatographic clean-up procedures before GC-FID analysis.

Cleanup Procedures for ASE Cells:

23. Note: careful cleaning of the cells is very important to avoid contamination of your samples and to prolong the lifetime of the static valves, which are expensive.

Follow the steps carefully. GC grade and HPLC grade solvents are expensive. Initial cleaning should use the general grade solvents available from chemistry department.

24. Disassemble the ASE bodies from the end-caps. If you have run particularly dirty samples, then completely disassemble the end-caps (removing the retaining rings with the ring tool).

25. Put any sand in a beaker labeled “dirty ASE sand” and discard in the trash or save your sediments in whirlpak bags. If disassembling the end-caps, separate the small parts (filters, o-rings, retaining rings) from the big parts (cell caps, bodies, and inner rings).

26. Rinse and scrub all parts with water to remove any sediment, sand, and hydrophilic compounds. Let the parts dry in the oven for a few hours before proceeding.

27. We have one small Teflon jar and two big Teflon jars. The small stainless steel filters should be cleaned in the small jar, while all other cell parts should be cleaned in big jars. It is very important that the filters are cleaned very well, otherwise small sample particles in the filter will block the static valve (£400 each).

28. Put half of the end-caps into a Teflon jar #1 and fill the remaining space with cell bodies. (Note: small parts should go in the small Teflon jar.) Fill with ‘Rinse 2 Acetone’

and sonicate for 30 minutes – this is Rinse 1*.

*Note that ‘Rinse 1 Acetone’ should be ‘Rinse 2 Acetone’ from previous cleaning process.

29. Move the parts into Teflon jar #2 and fill with fresh acetone – this is Rinse 2. (For the small parts, strain the old acetone out and fill with fresh acetone.) Dispose of the acetone used as Rinse 1 and load the remaining half of the big parts into that jar. Fill with fresh acetone. Sonicate all 3 jars for 30 minutes. Note that you have now staggered the cleaning procedure such that half of the big parts are one step behind the other half.

30. Move the big parts that have undergone Rinse 2 into the empty Teflon jar. Fill with DCM:MeOH 2:1. This is Rinse 3. (For the small parts, strain out the acetone and fill with DCM:MeOH 2:1, as well.) Dispose of the acetone in the big jar, and then move the other half of the big parts into it. Fill with fresh acetone. Sonicate everything for another 30 minutes.

31. Line a steel tray that the cells are stored in with a fresh piece of aluminum foil. Remove the small parts and big parts (keeping the cell bodies and end-caps in separate trays) that have gone through all three rinses and let the parts dry in the tray in the fume hood loosely covered in foil. Do not dump out the DCM:MeOH in the big jar – instead, move the last half of the big parts into it and return this jar to the sonicator for Rinse 3. You can reuse the DCM:MeOH Rinse 3 up to three times. When the last jar is done, remove the parts and let them dry in the tray.

32. When the cells are dry, cover the tray more tightly with aluminum foil and place the tray on the shelf above the ASE cell prep area. Label the foil with your name, the date, and “clean.”

Further GC-MS Sample Preparation

Acid/Neutral Separation Procedure:

1. Use the column stand to hold six short, glass pipettes

2. Using tweezers pull a small, fluffy wad of glass wool out and twist into a ball. Push the quartz wool into the top of the short pipette.

3. Use the long pipette to gently push the wool into the tip of the short pipette. The wool should fit snuggly enough to prevent Si-gel beads from passing, but should not be so tight that it restricts the flow of solvent.

4. Use the modified funnel to put ~4cm of dry, LC-NH2 SPE Si-gel into the short pipette.

5. Tap on the side of the pipette gently until the Si-gel settles.

6. Add a small amount of combusted sand to the top of the column to help prevent drying of the upper layer of silica gel.

7. Clean the LC-NH2 SPE column with 3 bed-volumes (5 to 10 ml) of 1:1 DCM:isopropyl alcohol (ISO).

8. Re-dissolve and transfer the aliquot of TLE with a small amount of 1:1 DCM:ISO (x3) onto the LC-NH2 SPE column. Allow the sample to seep into the silica gel.

9. Elute the Total Neutral Fraction (TNF) with 4ml of 1:1 DCM:ISO and collect the TNF into an 8ml sample vial.

10. Elute the Total Acid Fraction (TAF) with 4ml of ether with 4% acetic acid. Collect the TAF into an 8ml sample vial.

11. Dry the TNF and TAF gently under N2.

12. The TAF needs methylation (see Section 6), while the TNF needs further separation through Si-gel (see Section 7).

Clean up and further Separation of the Total Neutral Fraction (TNF)

1. The mass of TNF that is added to a silica gel column should not exceed 10mg, because the ratio of the weight of the TLE to the weight of the silica in the column should not exceed 1:100. (e.g., we use ~1g (1000mg) of silica so the maximum TNF weight is 10mg.)

2. Prepare 230-400 mesh/35-70 micron silica powder (stored under the hood. Note: this is different from the specialized LC-NH2 Si-gel used in the Acid:Neutral separations).

3. Use the column stand to hold six short, glass pipettes

4. Using tweezers pull a small, fluffy wad of glass wool out and twist into a ball. Push the quartz wool into the top of the short pipette.

5. Use the long pipette to gently push the wool into the tip of the short pipette. The wool should fit snuggly enough to prevent Si-gel beads from passing, but should not be so tight that it restricts the flow of solvent.

6. Use the modified funnel to put ~5cm of dry, Si-gel into the short pipette.

7. Tap on the side of the pipette gently until the Si-gel settles.

8. Add a small amount of combusted sand to the top of the column to help prevent drying of the upper layer of silica gel.

9. Prepare your workstation. Make sure your 8ml vials are labelled and you have enough of the solvent mixtures shown in Table 14

10. In this section you will separate the TNF into the four fractions (N1, N2, N3 & N4) by eluting with the volume of solvents listed in Table 1. The solvents will be loaded onto the column using a syringe. The individual fractions will be collected into 8ml vials.

11. Clean the Si-gel by eluting with 4ml of hexane. (Note: it is important to use the full 4ml of hexane)

12. Re-dissolve the TNF in as little hexane as possible (~200ul, x3) with sonication, if necessary, and load onto the column using a pipette.

13. Collect the N1 to N4 fractions in 8ml vials using solvents as shown in Table 1.

Table 14 The solvents and solvent volumes used in Si-gel chromatography for separation of the TNF into four fractions

Fraction	Solvent	Volume ml (Solvent)	Organic Content
N1	Hexane	4	Aliphatic hydrocarbons
N2	DCM	4	Ketone/Ester/Aromatics
N3	Ethyl acetate:hexane (25:75)	4	Alcohols
N4	Methanol	4	Polar

NB: in this project, N1 and N2 only were extracted and analysed.

14. Blow down the solvent in all four fractions under N2. Both the aliphatic and aromatic fractions are ready for GC-FID analysis. All four fractions can be transferred to a GC-vial (2-ml) using DCM (x3).

15. The N1 & N2 fractions can be dried down under N2 and store in labeled cryoboxes until they are ready to run.

16. The ethyl acetate:hexane and methanol fractions need BSTFA derivitisation before GC analysis (see Section 8). (Note: If you plan to measure GDGTs, weigh the N4 GC vials before transfer and record the N4 mass after the transfer and drying.)

Preparing to run samples on the GC-FID and GC-MS

First, do a pilot run:

1. All samples should be dry and in GC vials.

2. Before running a full set of samples from a batch/project, run a few pilot samples to get an idea of concentration.

3. Dilute and only use an aliquot of the sample. This applies to TNF and TAF.

4. Dissolve your sample in 500µl of n-Hexane, take an appropriate aliquot (i.e. 100 ul) and transfer that into a vial with an insert. You can then dilute/concentrate in the insert without messing about with the original sample.

5. Run on the GC-FID. Use the BECS standard mix as an external standard to quantify the concentration of your samples. (If you are running three pilots, run the standard before and after the three samples.)

6. Once you work out the amount of sample aliquot and concentration to run onthe GC-FID from the pilot samples, prepare the rest of your samples for a GCFID.

7. An internal standard should be used to quantify your compounds. If the concentration of your pilot samples is consistent, you can use Section 10 to determine the amount of

internal standard to add. If your pilot samples are highly variable in concentration, then you will have to run all samples once before determining the correct amount of standard to add.

Adding GC Standards to Determine Concentration

1. Add standards to fractions that you are analyzing. (Make sure that you are certain about your calculations before adding anything to your samples!!)

2. Use the results from the pilot samples in Section 9 to see which standards and how much should be added.

3. The sample should not have a concentration higher than 10000 ng/□ (10µg/ml). (If your sample is strongly colored, use caution with analysis. First dilute it until coloration is weak. Organic/pigment-rich samples can contaminate the injector and destroy the column.)

4. As above, you will dissolve your sample in 500µl of n-hexane, take an appropriate aliquot and transfer that into an insert. You can then dilute or concentrate in the insert without messing about with the original sample.

5. Prepare a GC standard that will be ~10µg of standard per 1mg of your compound. This will be dependent on the concentration of your pilot samples. For example, if you plan to dissolve your sample in 50µl of solvent for the GC-FID run, then your GC standard should be 10µg/ml in 50µl. This way, you can transfer your sample, dry it under N2, then add 50µl of your GC standard mixture to the sample, cap and are ready to run. (See notes below on creating a 'mother solution')

6. Note: Trial run your prepared GC standard on the GC-FID before adding it to your samples… be sure that you have calculated the correct concentration!! After your trial runs, check:

a. That the standard is not co-eluting with any of the natural compounds in your sample.

b. If needed adjust your GC-standard concentration, so that in your GC runs the standard peak height is about twice that of your compounds of interest.

7. Typically, BAME (C23 FAME) is a good GC standard for the neutral fractions. An

alkane or ketone is good for the TAF.

Supplementary LC-MS Data

Additional data from the martian LC-MS experiment, specifically the chromatograms, masses, sample distributions, and details of any isomers of compounds of interest detected, are given in Table 15. Compounds are arranged in alphabetical order.

Table 16 Displays details of all metabolites detected in Lafayette at levels at least twice those detected in the procedural blanks. Table 17 displays details of compounds detected in Nakhla at least twice the levels of the procedural blanks.

Table 15 Molecules of note found in martian LC-MS experiment. Metabolite's putative IDs are given where possible, alongside isomers according to the KEGG database, their mass and retention time (RT, in minutes), their chemical structure, and their spectra and distribution in the samples

Adenine	Standard run (thus presence confirmed)
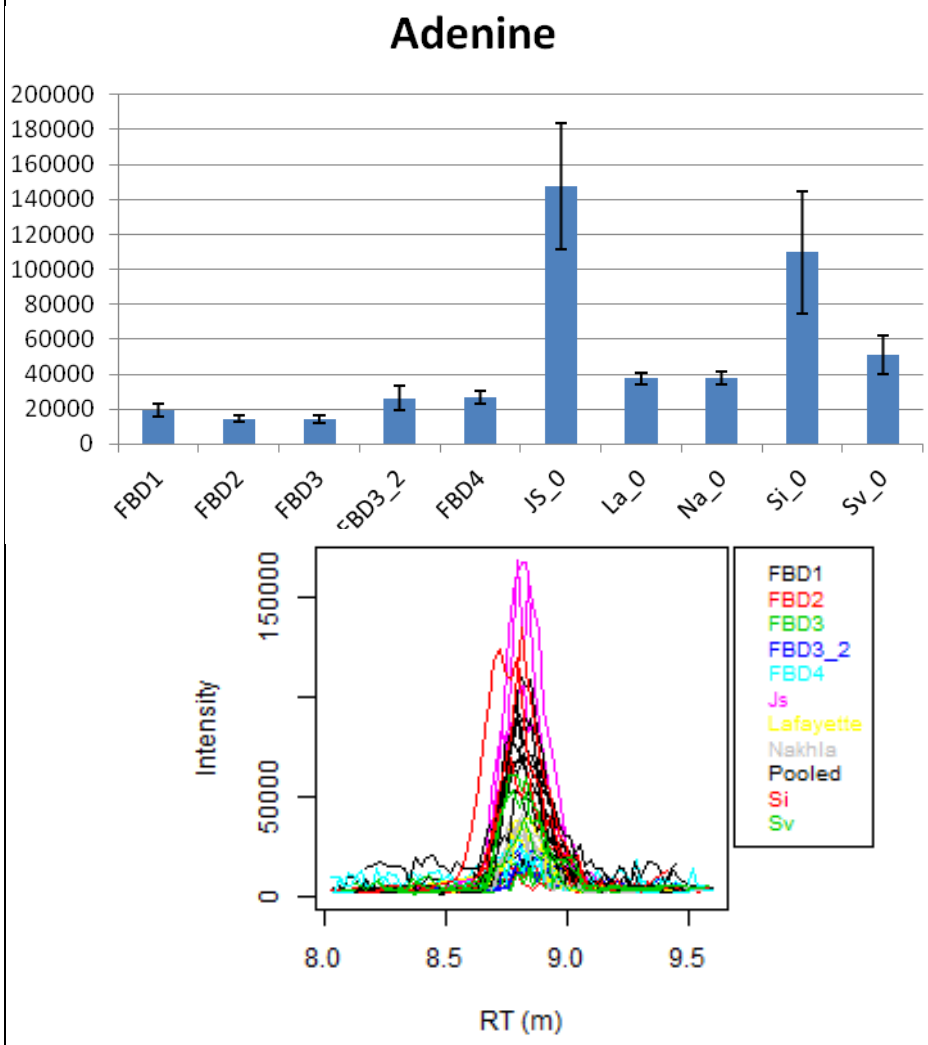	Mass 135.05 RT 8.808 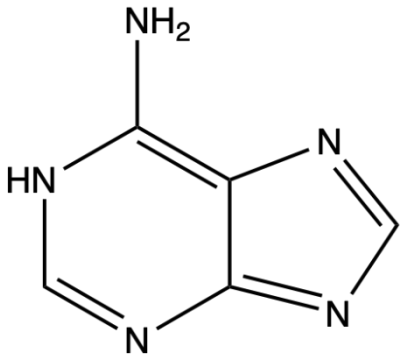

Arnicolide A

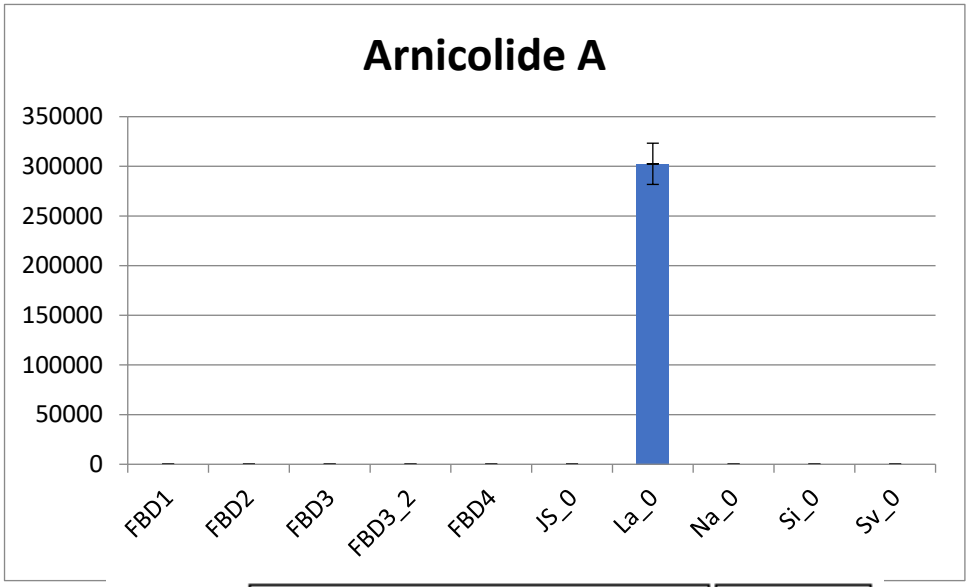

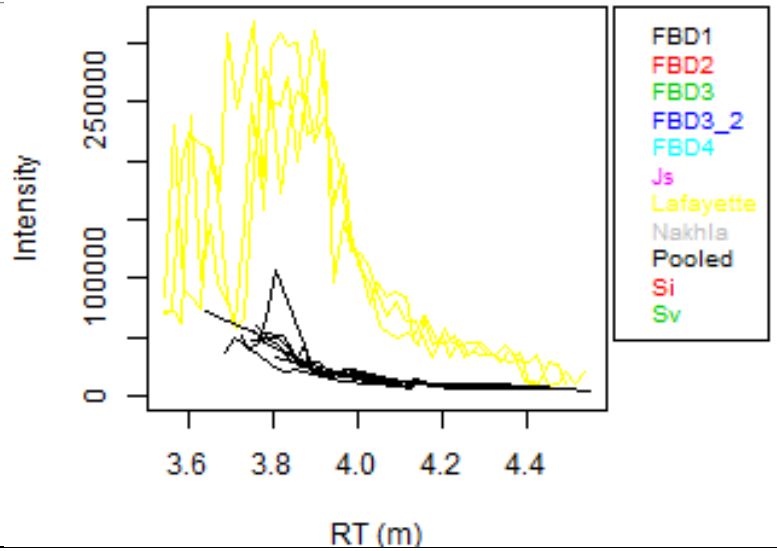

Mass 306.15

RT 3.774

14 isomers

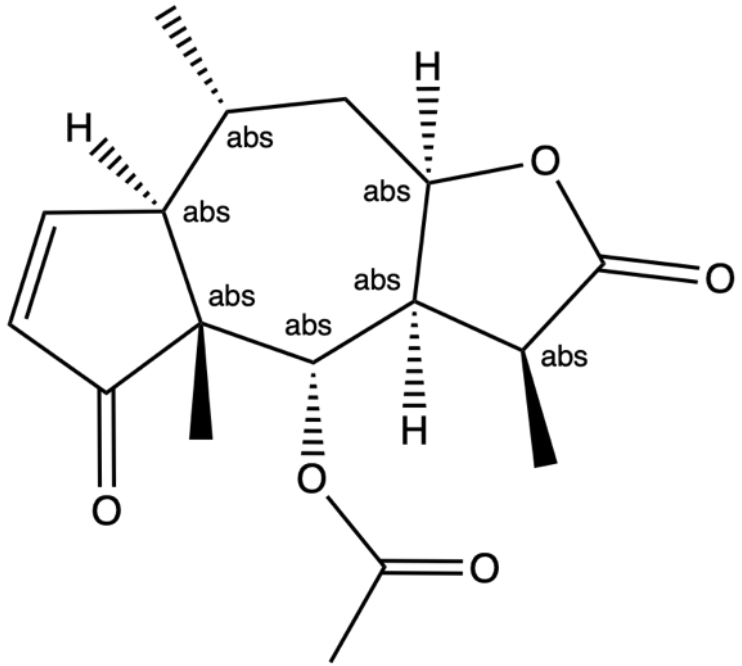

Artecanin

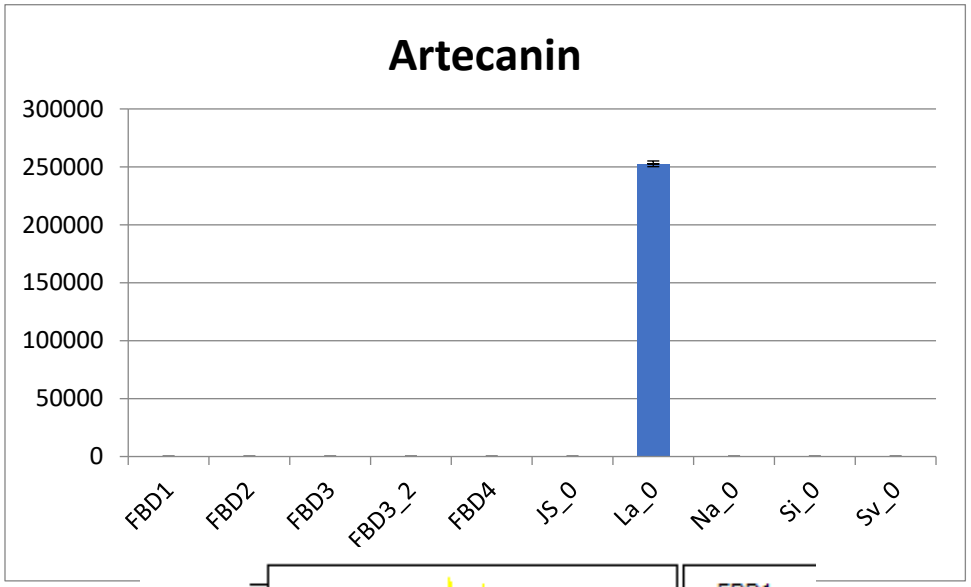

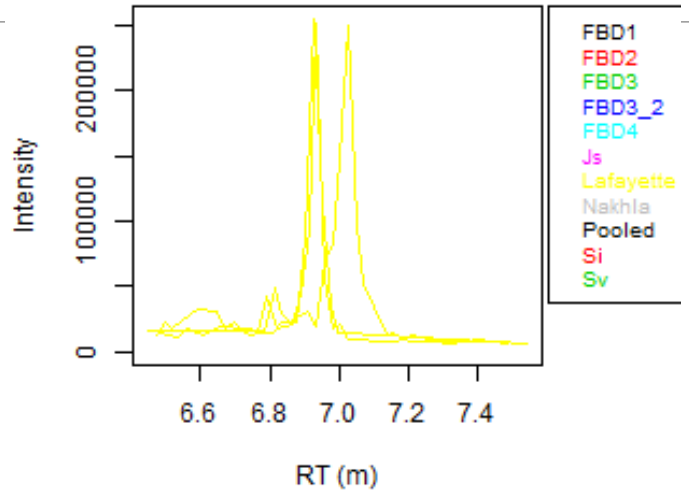

Mass 278.12, RT 6.962

6 isomers

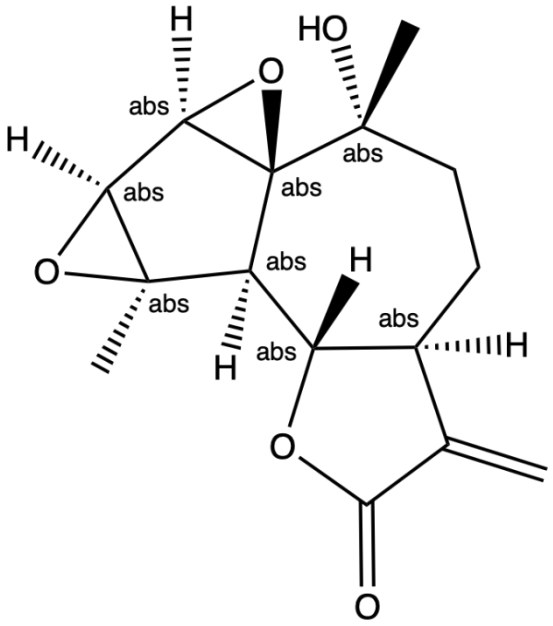

Betaine

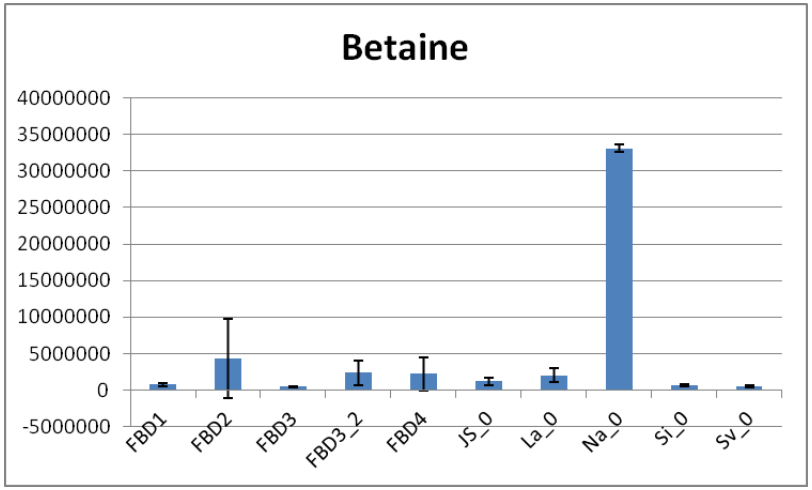

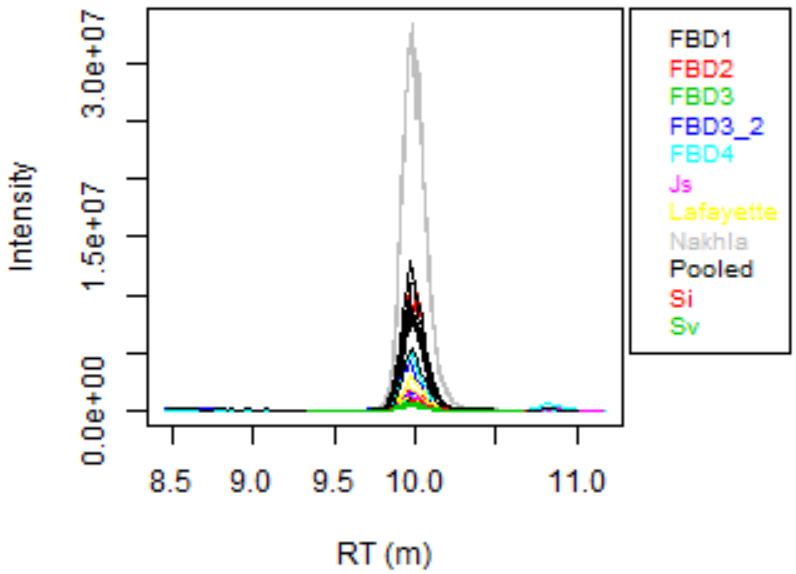

mass 117.08

RT 9.9777

Standard run, thus presence confirmed

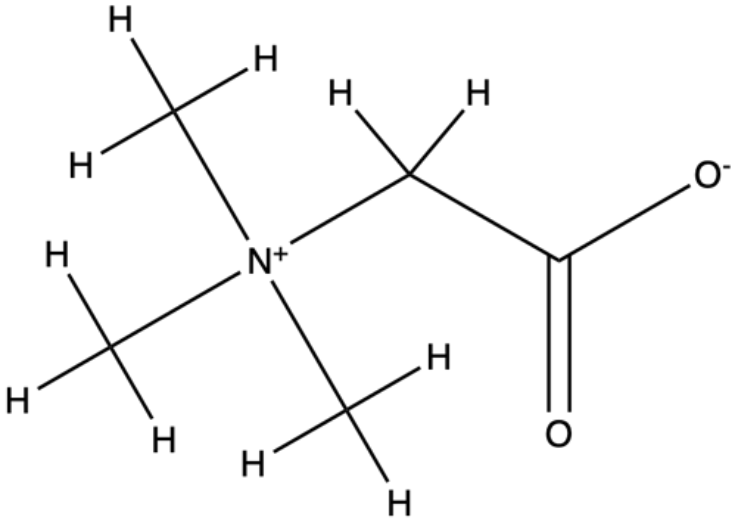

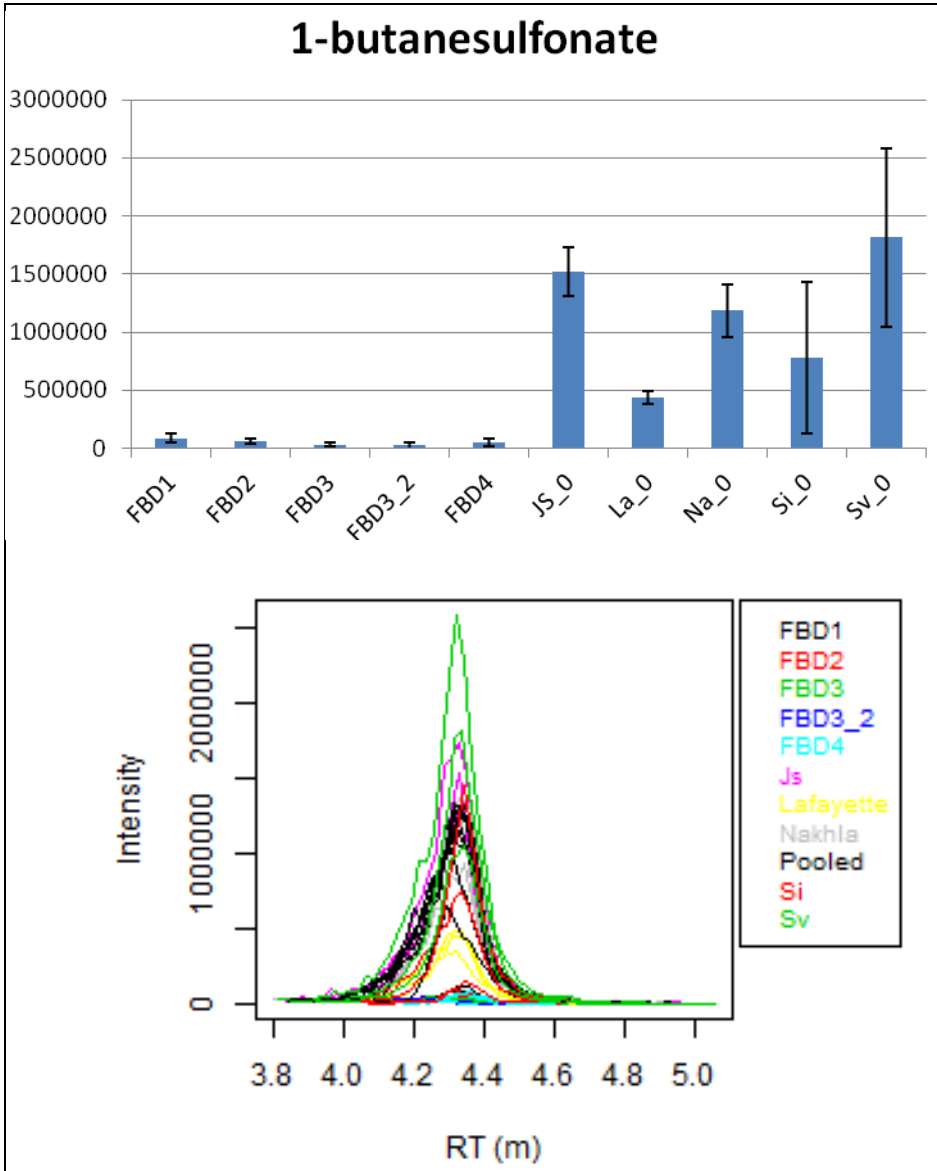

- 2 isomers with this mass found in the system. This isomer found in negative mode.
- Mass 138.03, Ret Time 4.311 (other isomer 138.04, 8.883 ret time)
- No other exact mass isomers in KEGG database

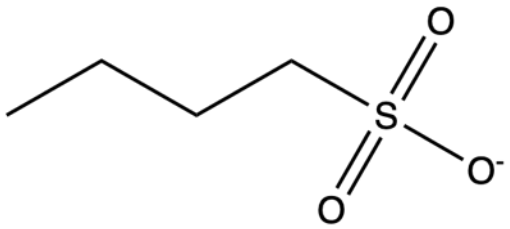

Canin

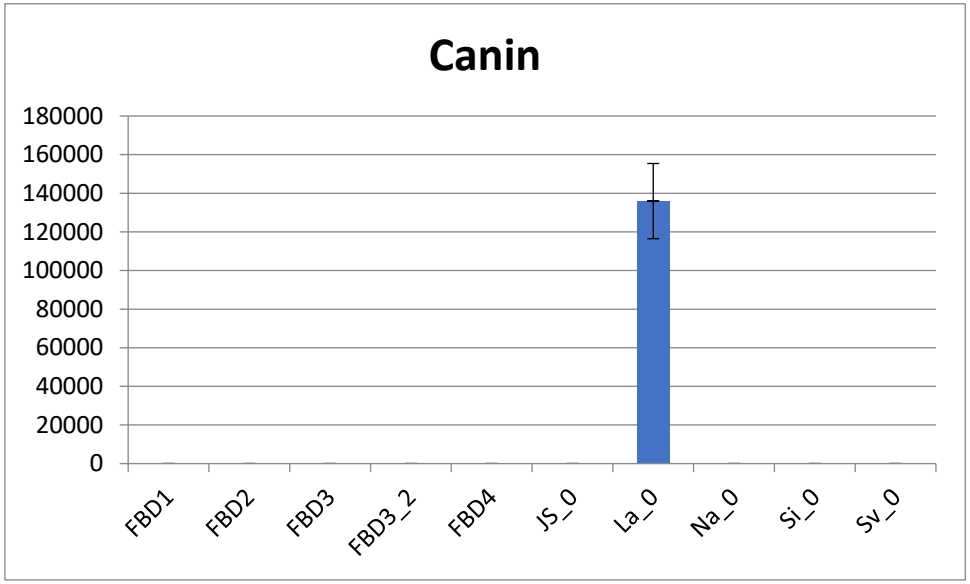

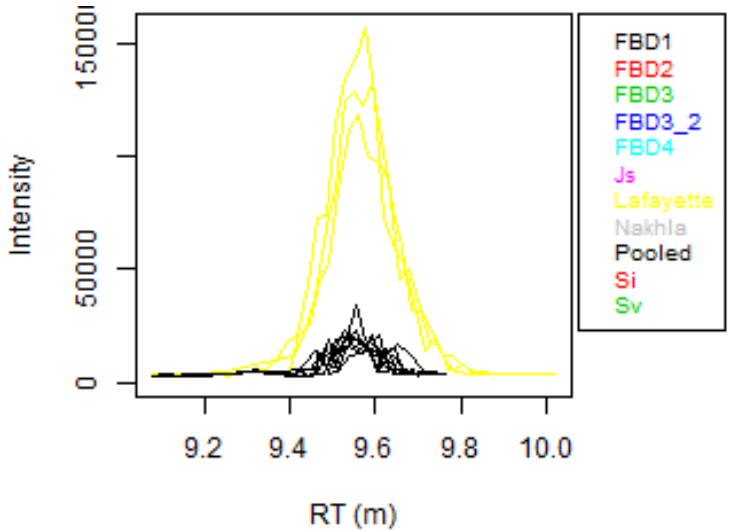

mass 278.12

RT 9.562

6 isomers

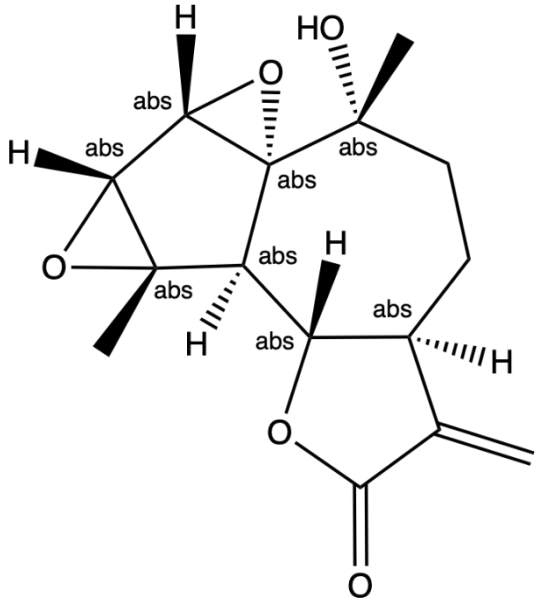

D-Galactosamine

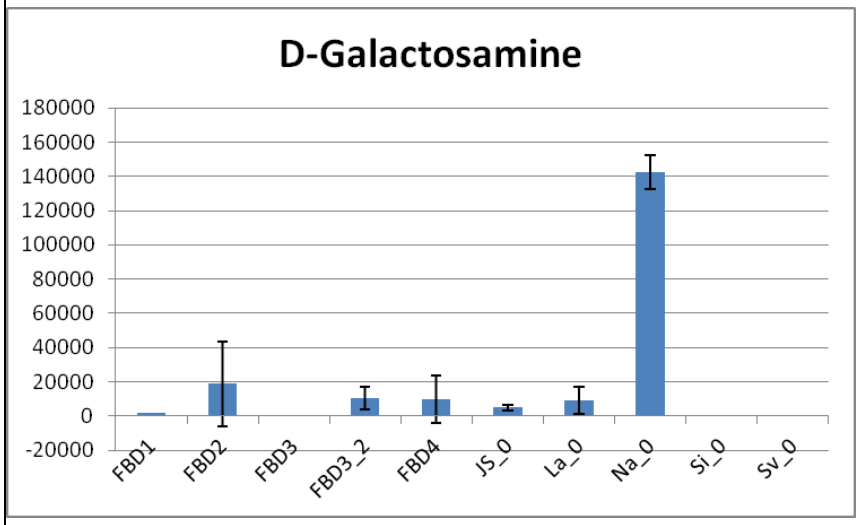

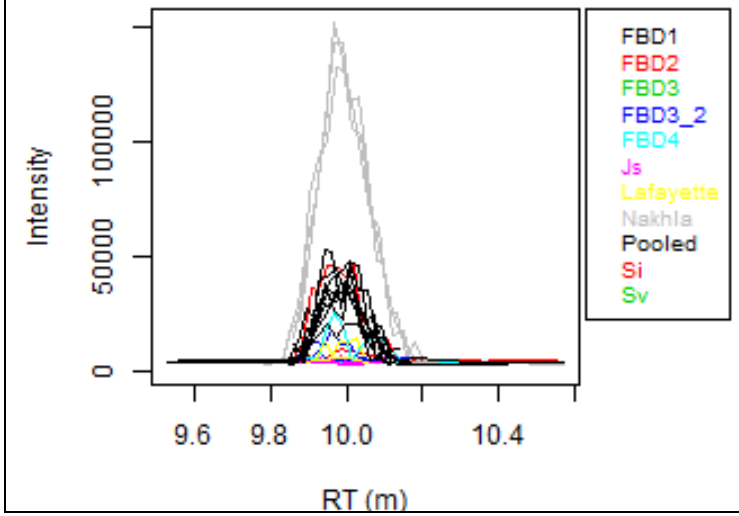

mass 179.08

ret time 9.985 mins

10 isomers

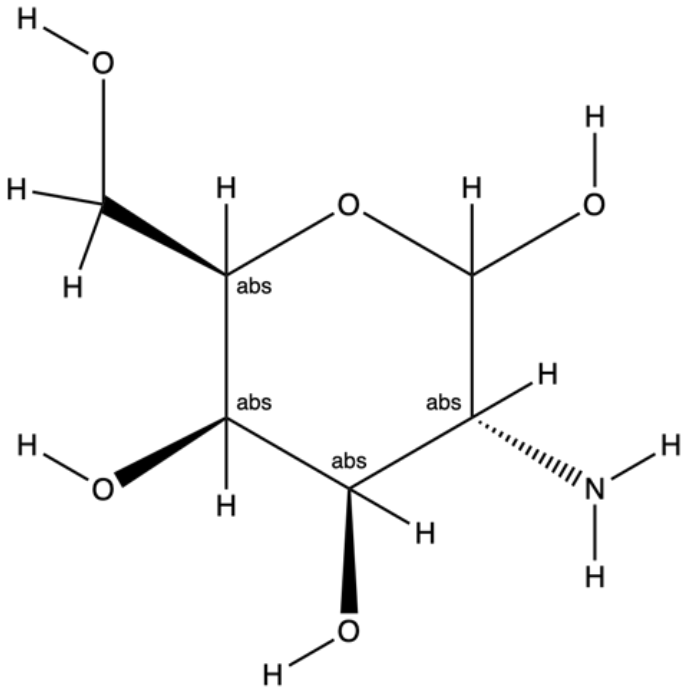

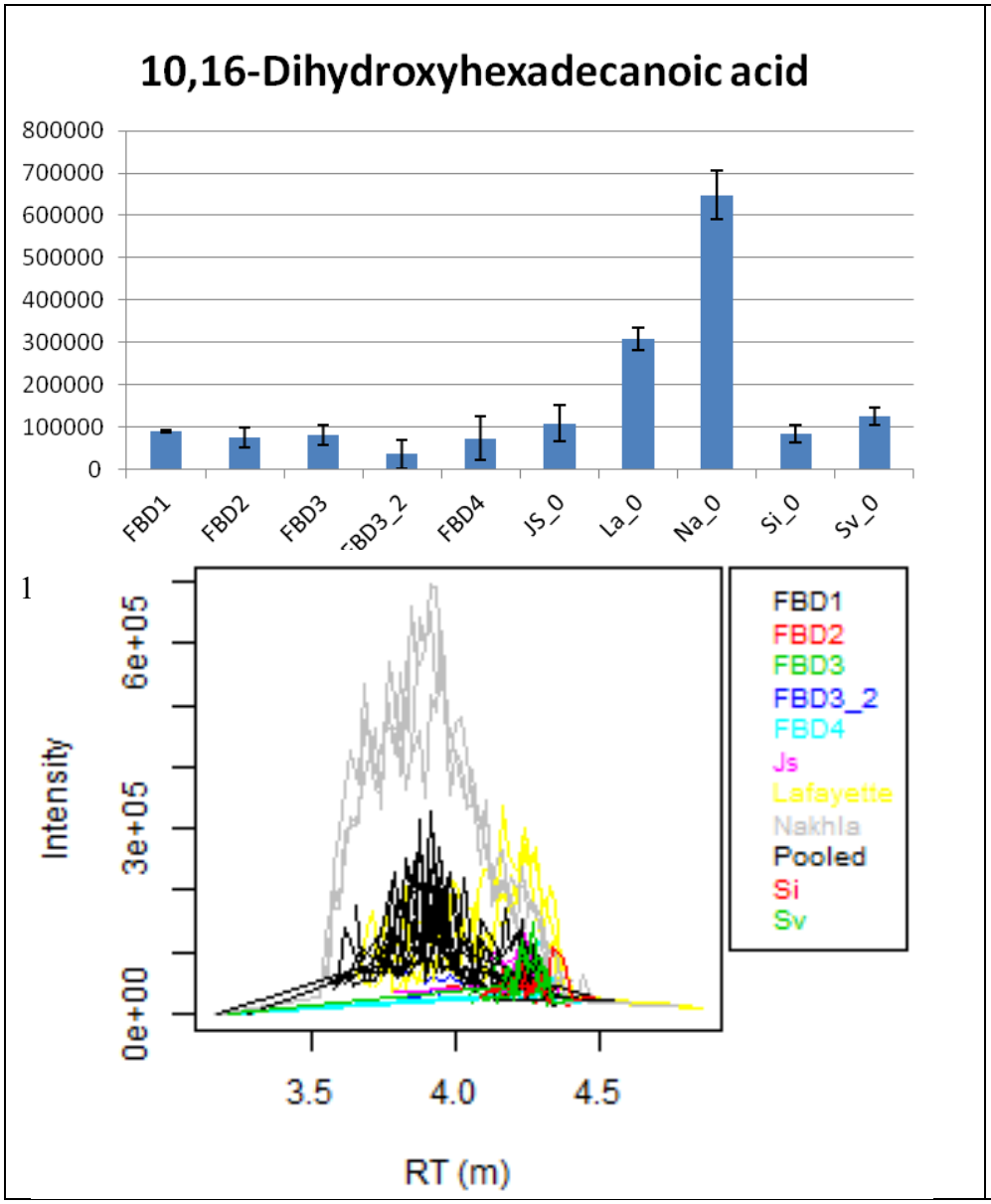

mass 288.23, RT 4.112

(low def peak)

6 isomers

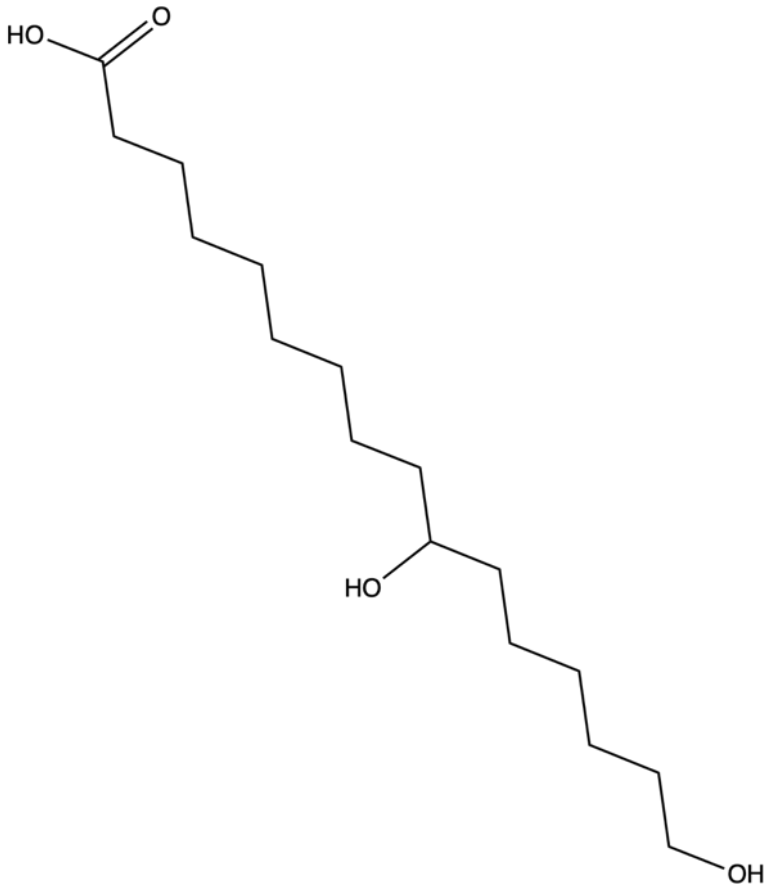

Ethyl(R)-3-hydroxyhexanoate

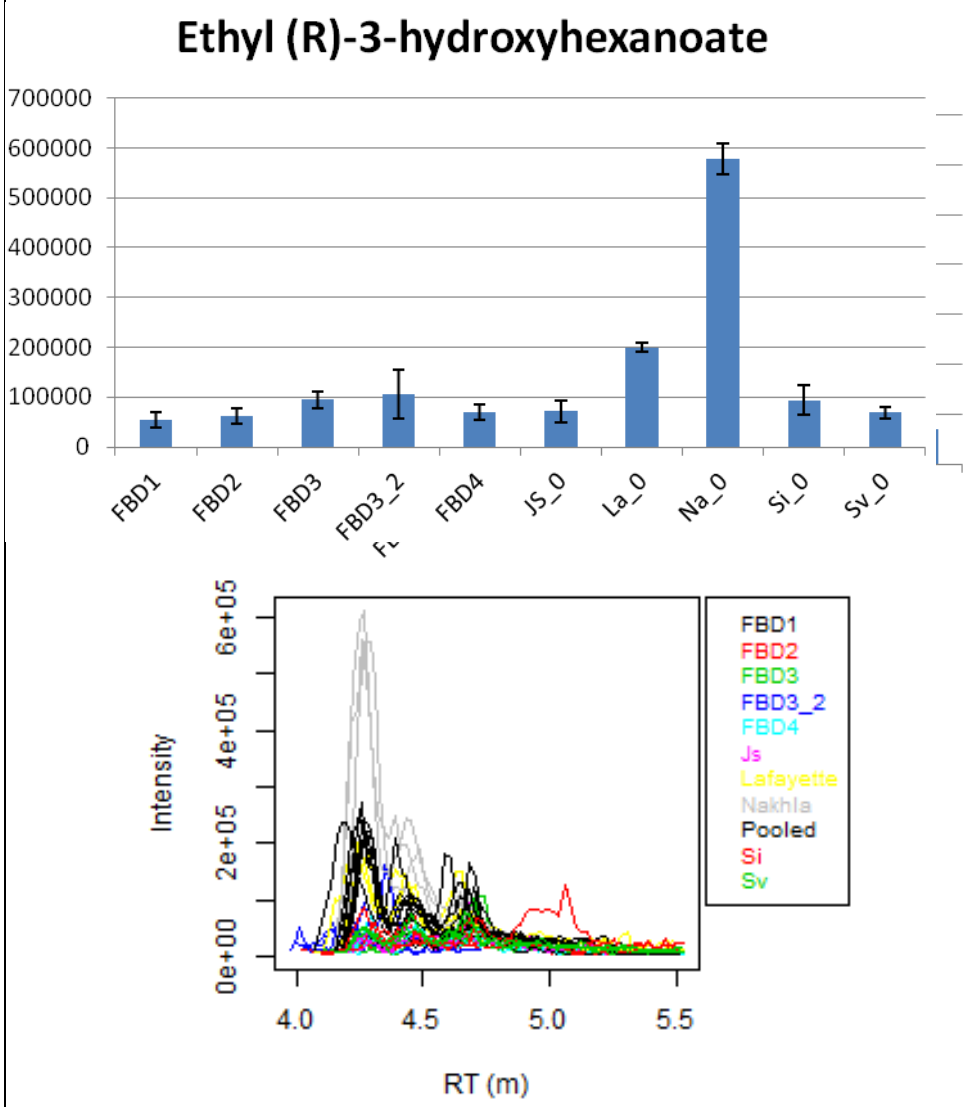

mass 160.11, RT 4.46

14 isomers

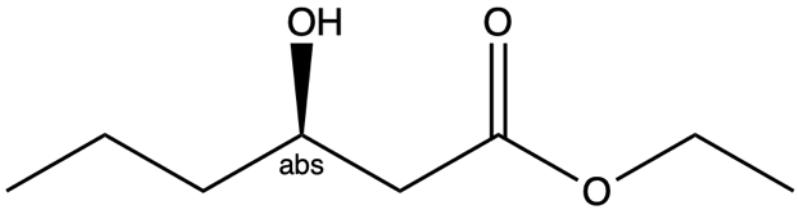

ethyl-(2R)-methyl-(3S)-hydroxybutanoate

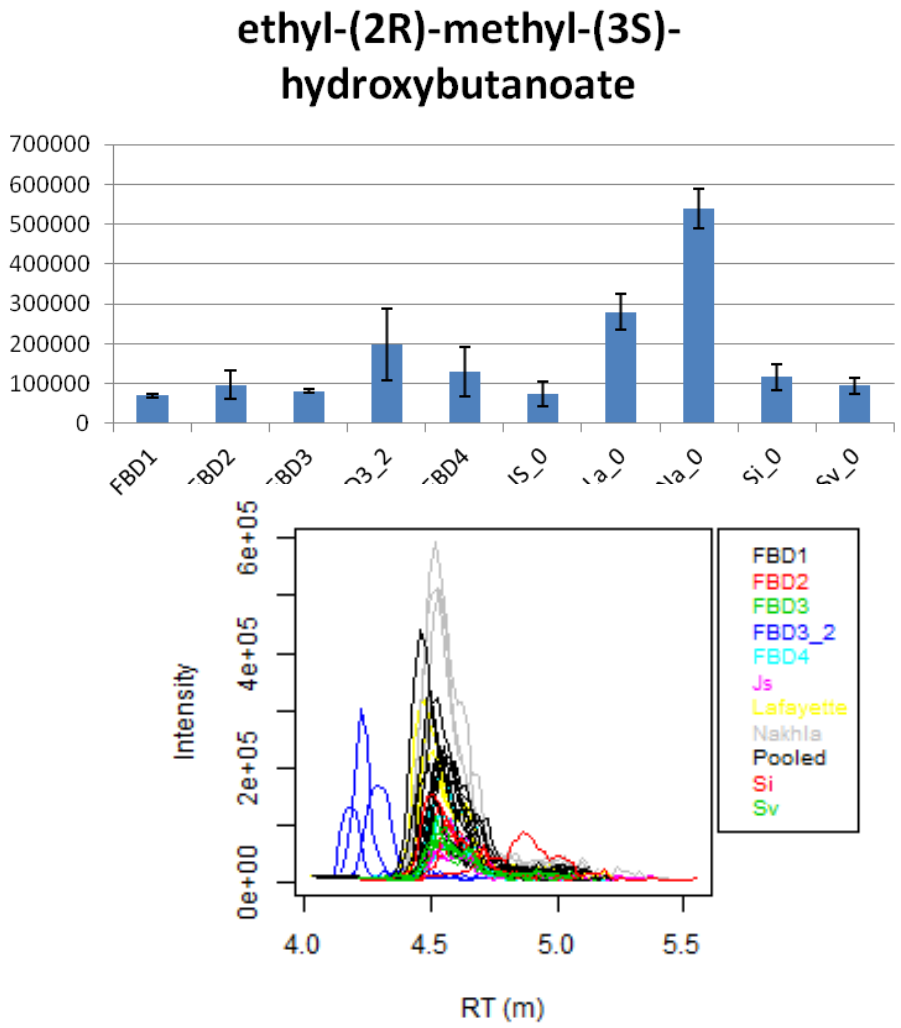

mass 146.09, RT 4.522

8 isomers

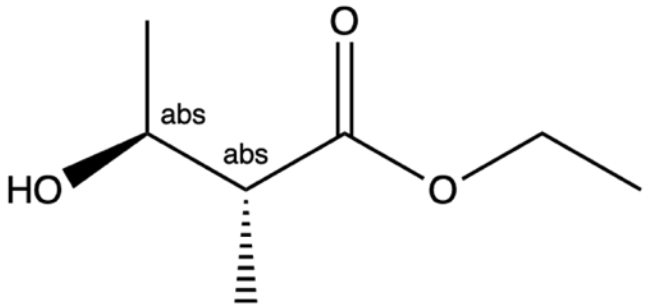

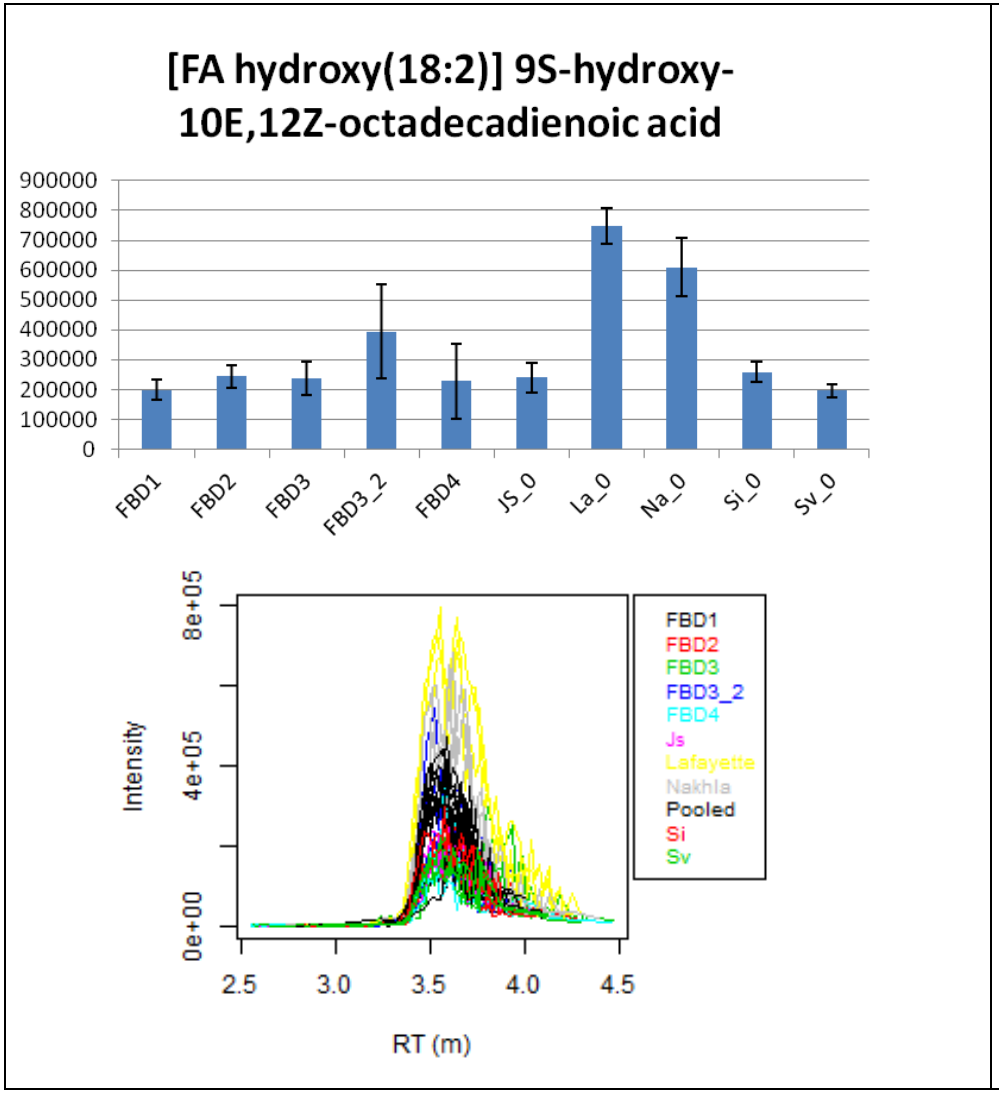

296.24 mass, RT 3.599

33 isomers

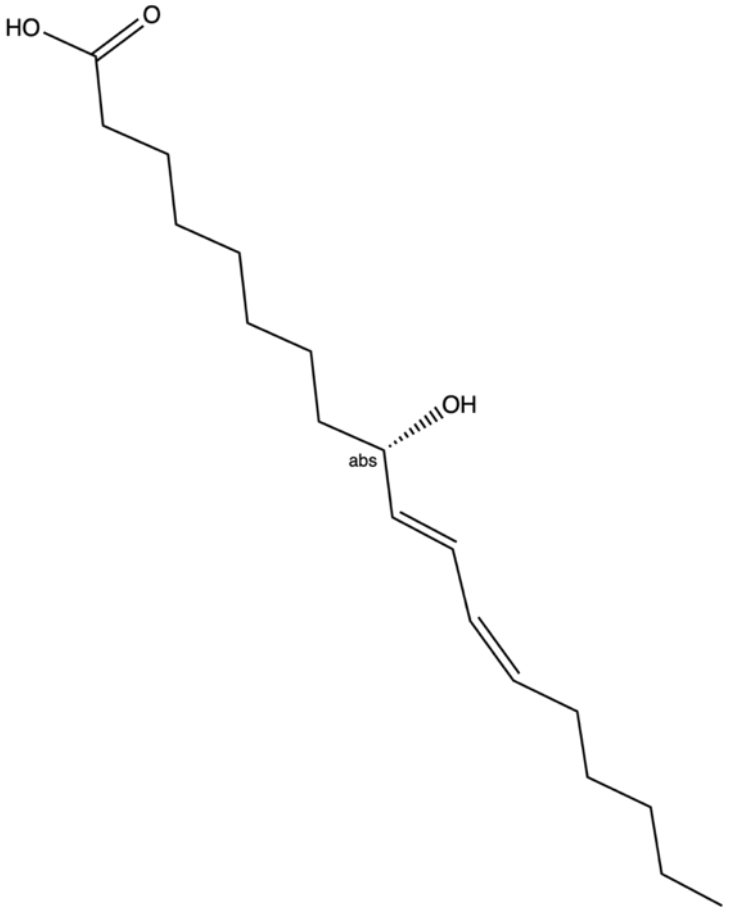

[FA methyl(14:0)] 12-methyl-tetradecanoic acid

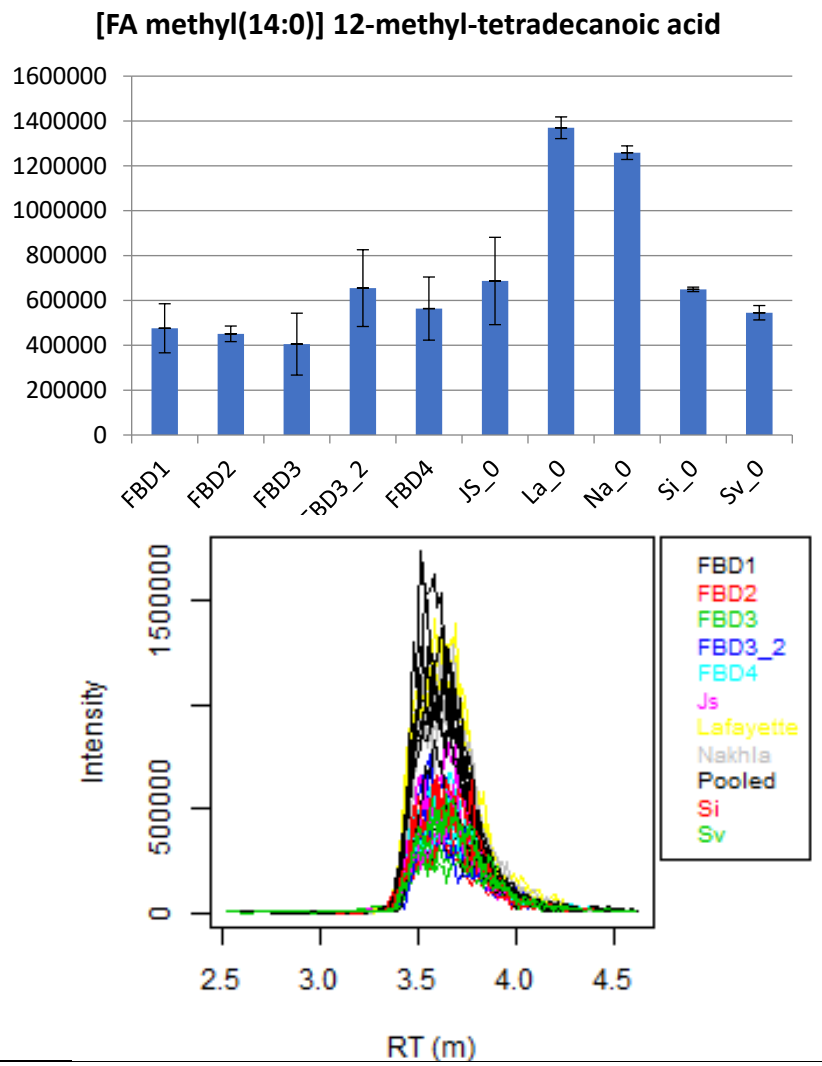

242.22 mass, RT 3.619

9 isomers

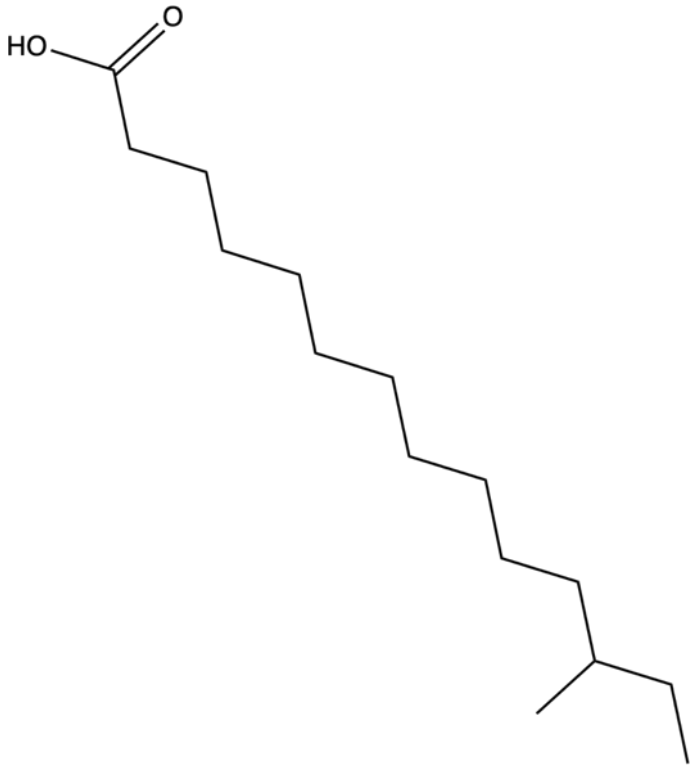

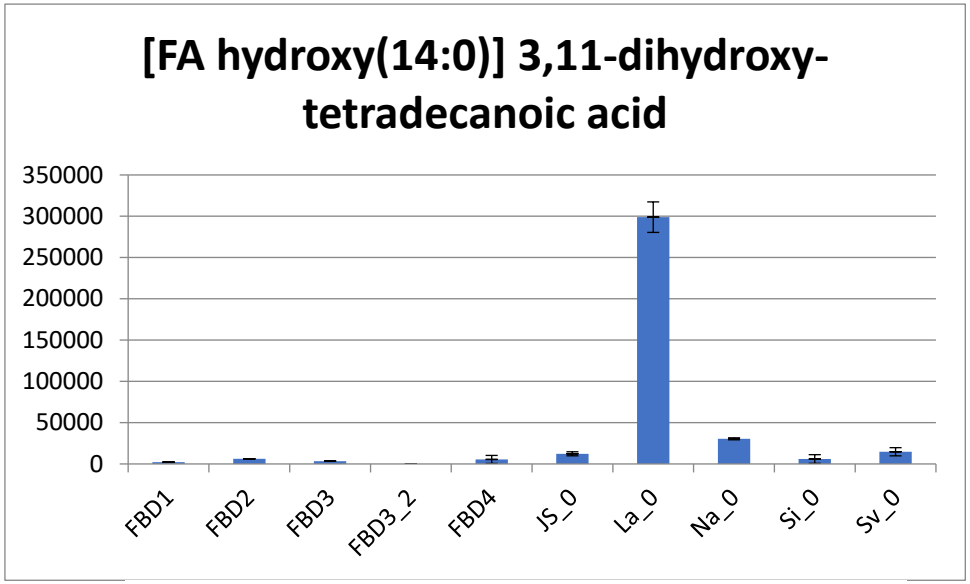

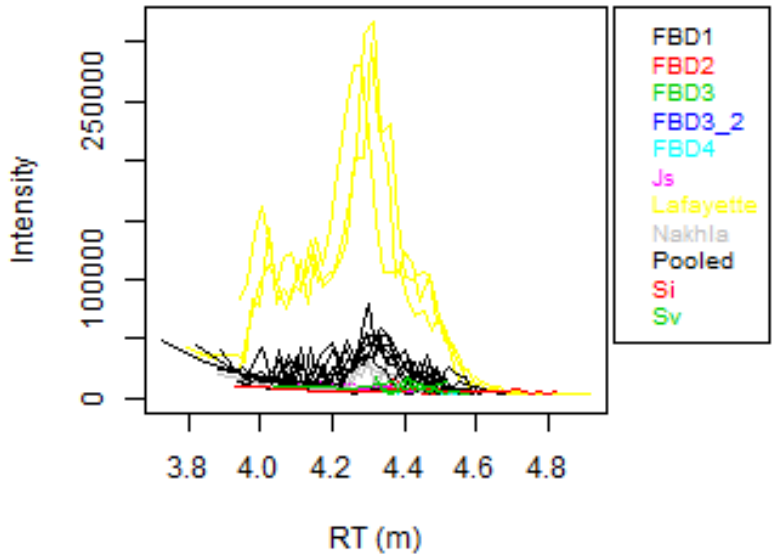

mass 260.2 RT 4.297 **found in negative mode**

no other isomers

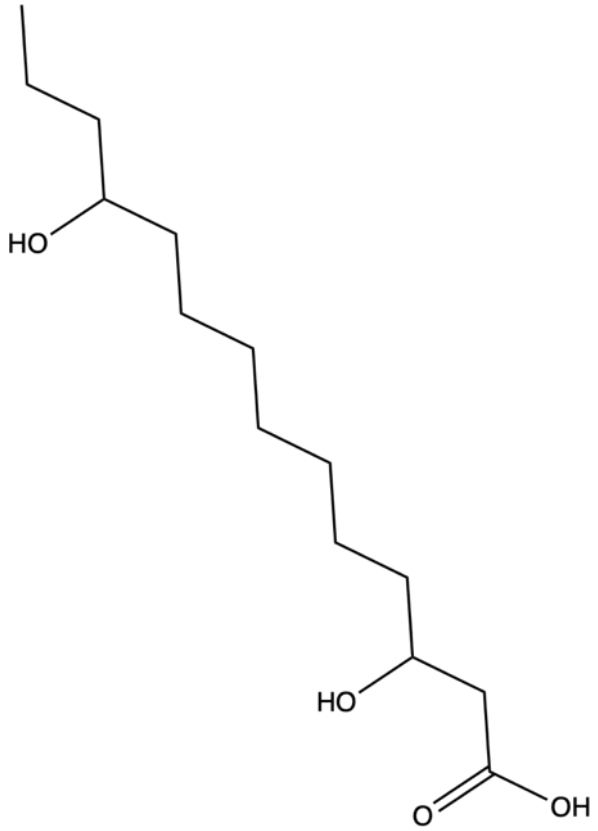

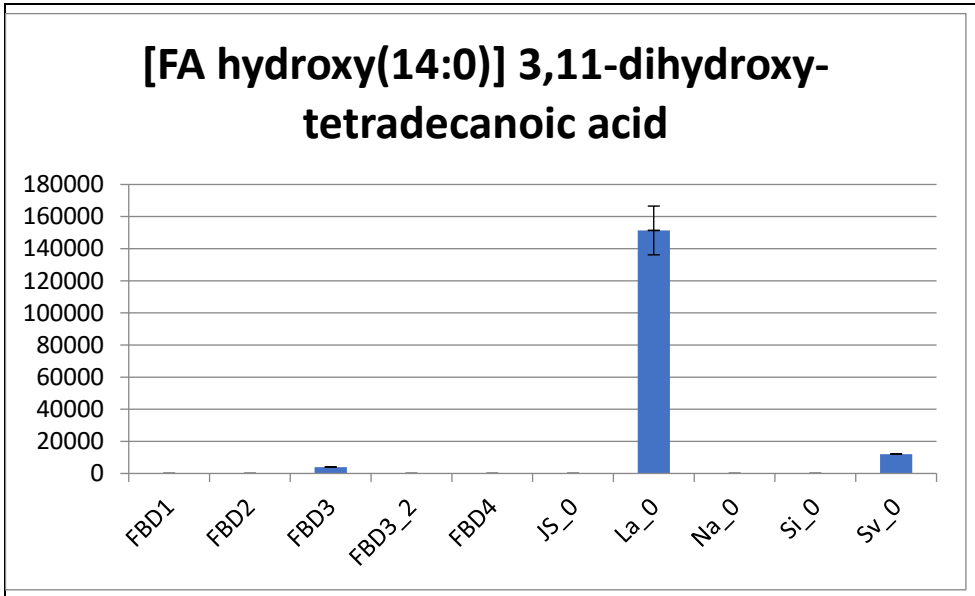

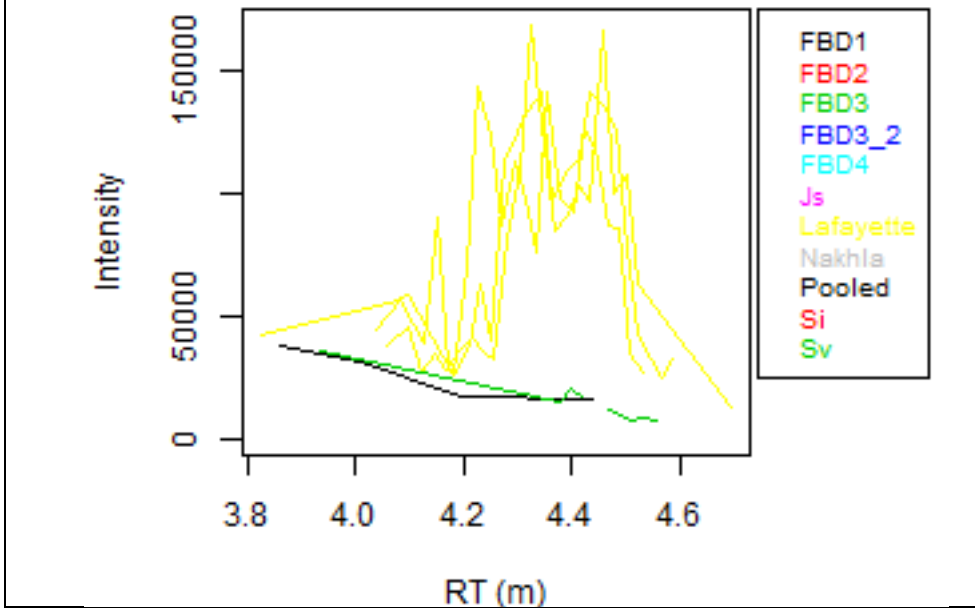

mass 260.2 RT 4.208 **Found in positive mode**

no other isomers

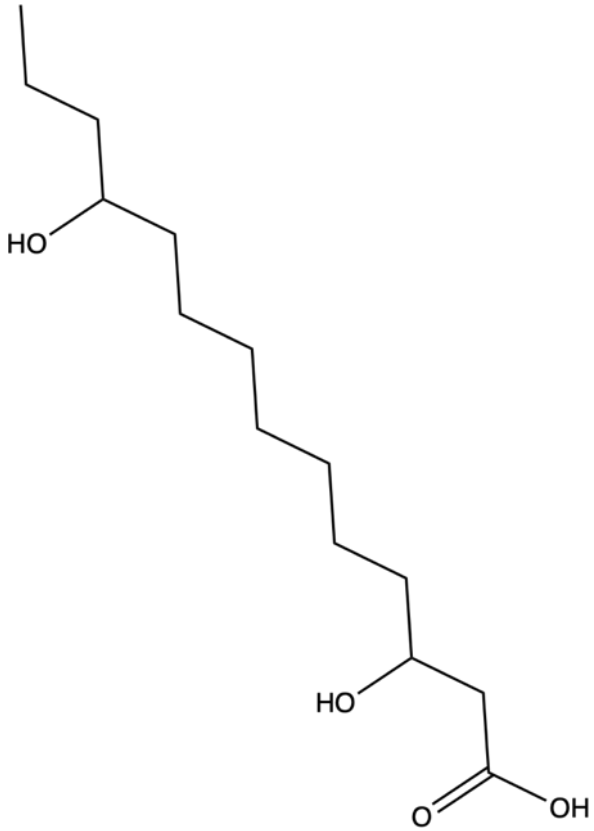

[FA trihydroxy(16:0)] 2,15,16-trihydroxy-hexadecanoic acid

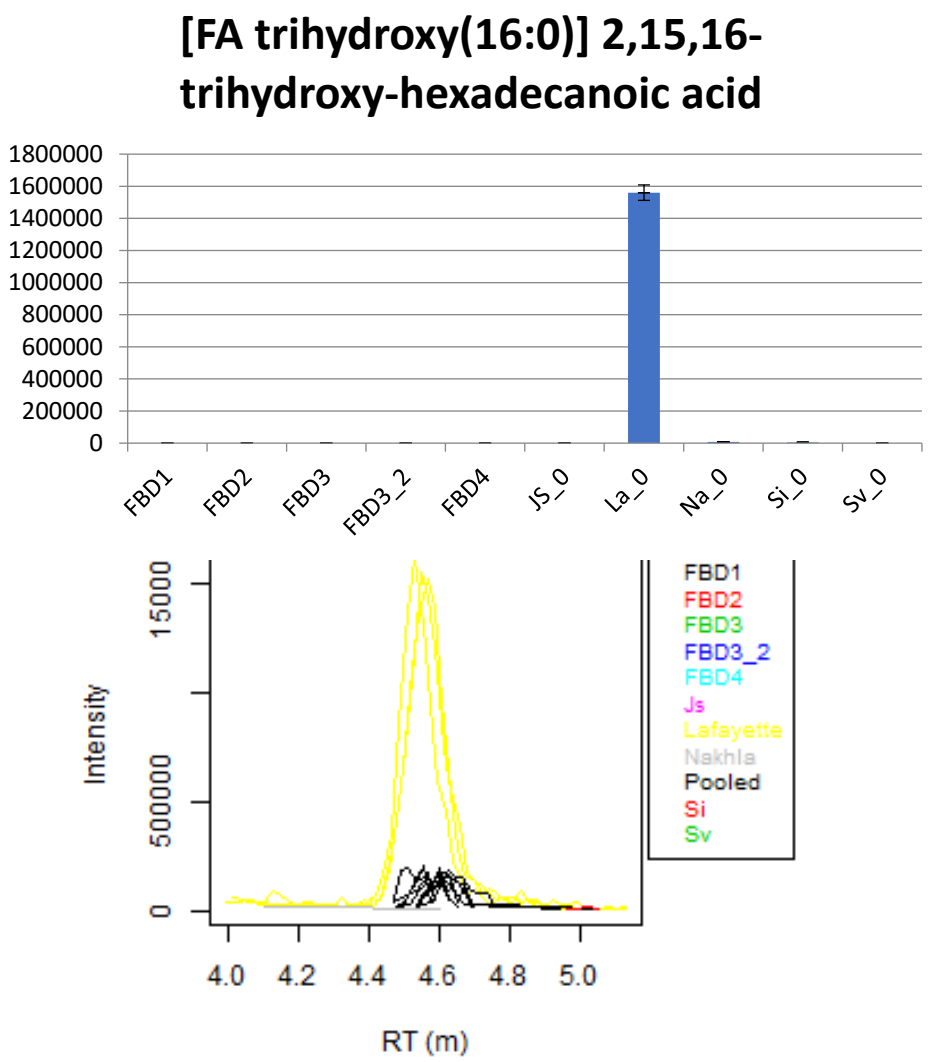

mass 304.23 RT 4.024

4 isomers

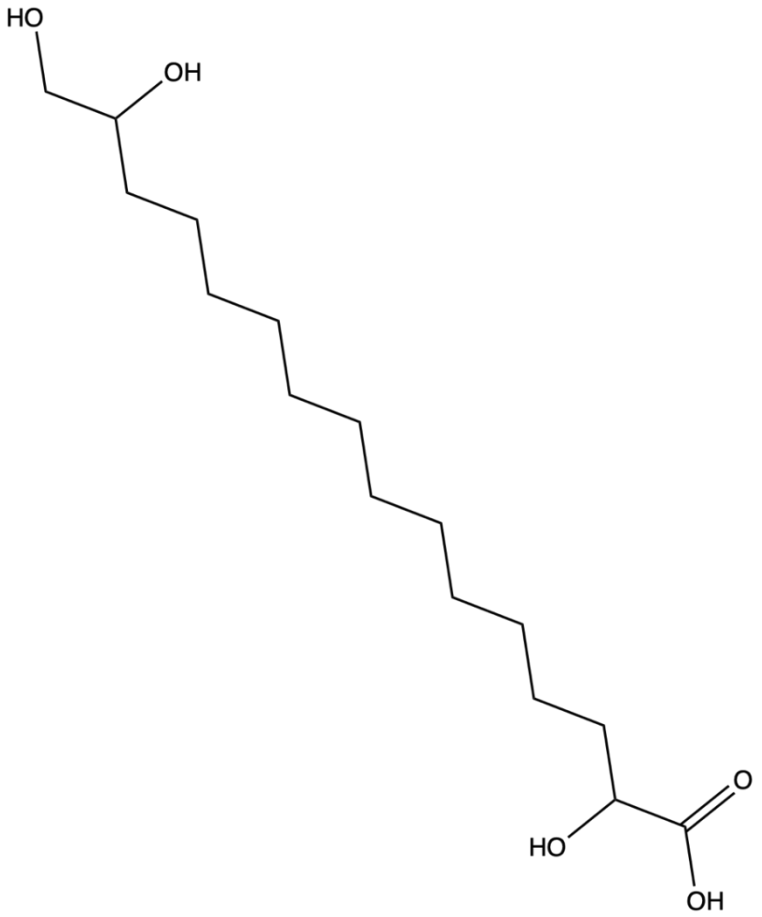

[FA oxo(4:0/4:0)] 9-oxo-12S-acetoxy-2,3,4,5-tetranor-7Z,10Z,14Z-prostatetrienaldehyde-cyclo[8,12]

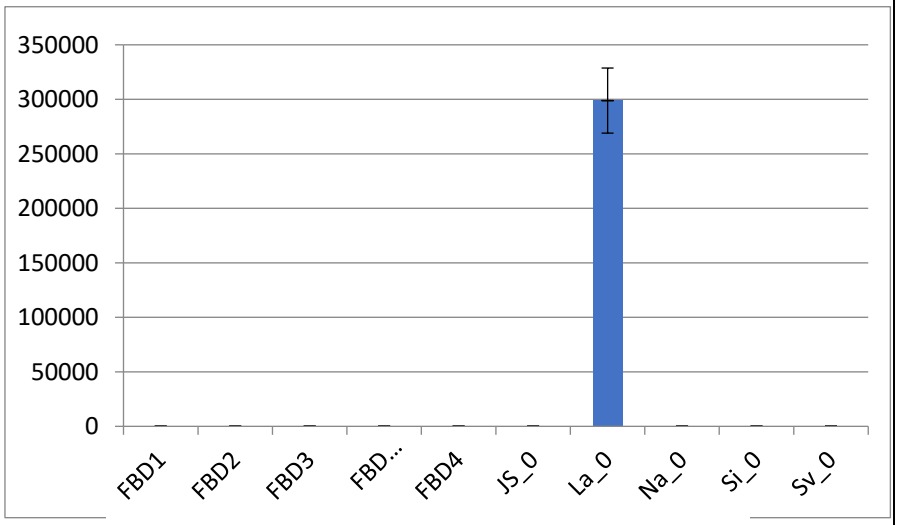

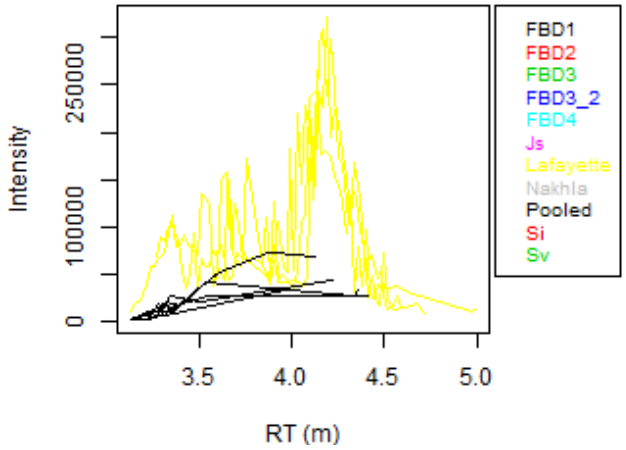

Mass 290.15, RT 3.77

5 isomers

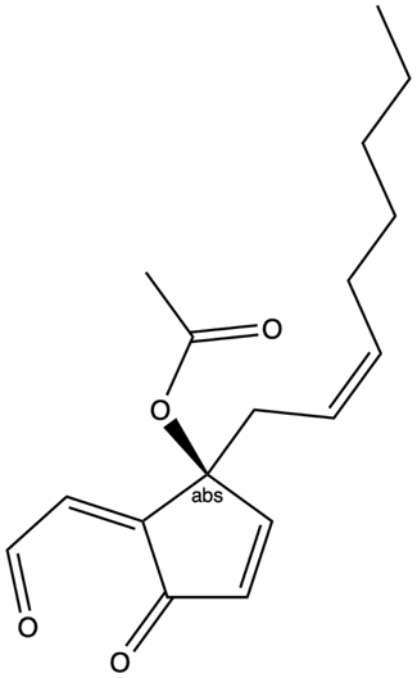

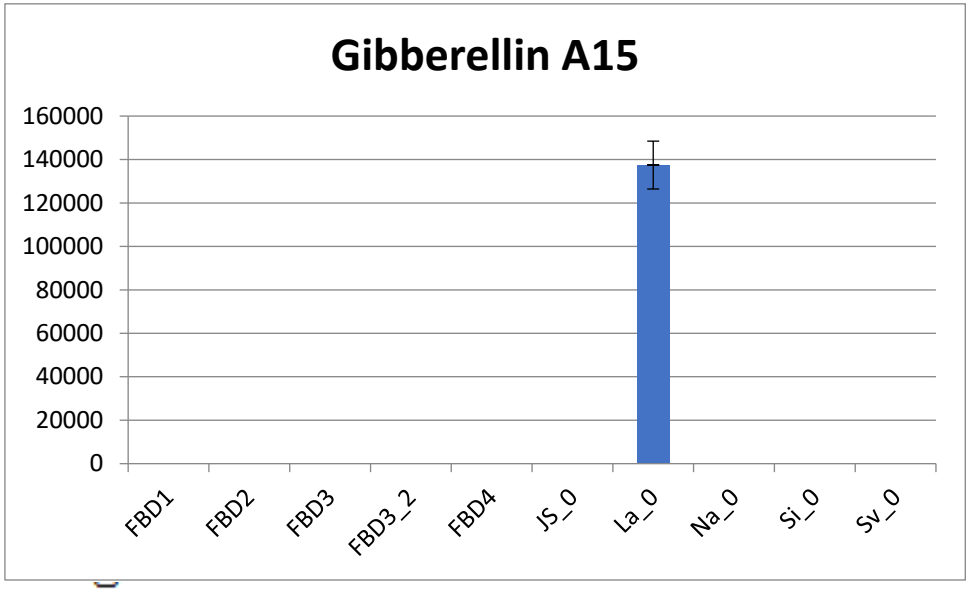

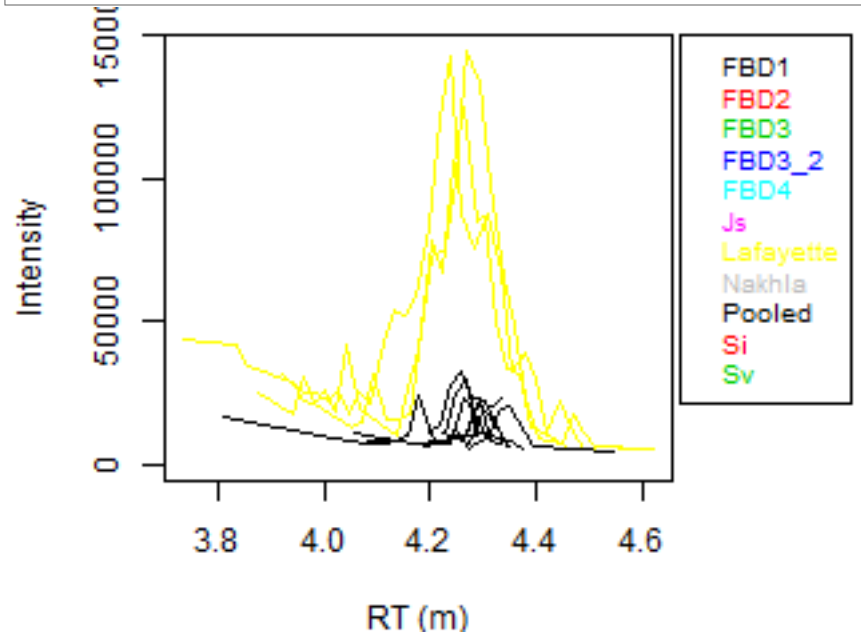

Mass 330.18 RT 4.226

4 isomers

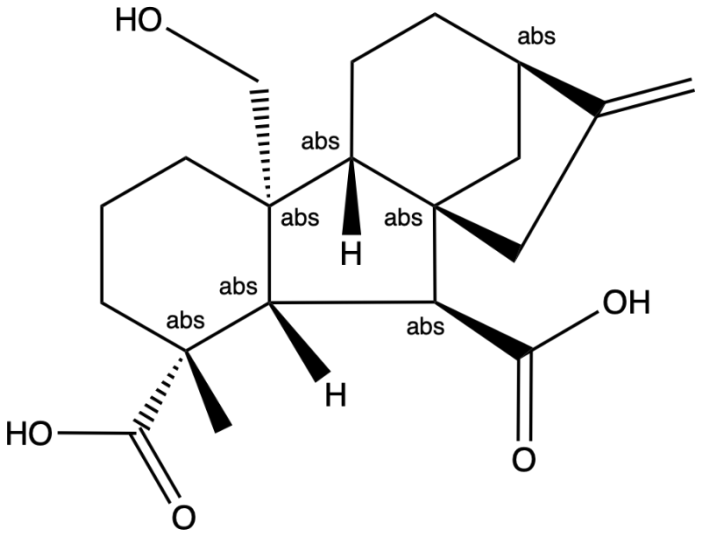

(9Z)-Hexadecenoic acid

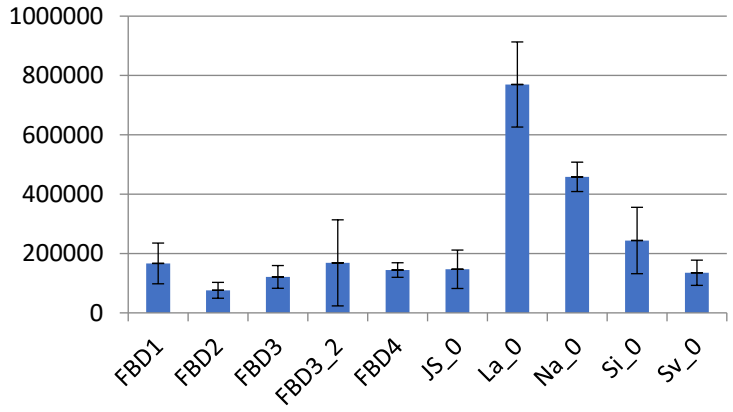

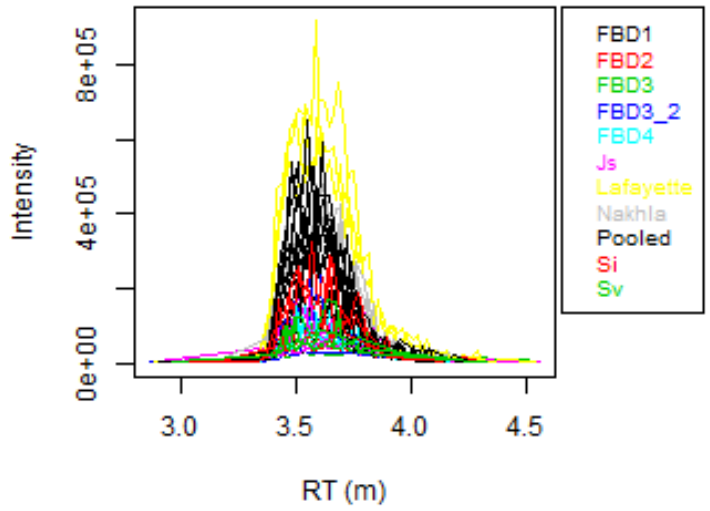

254.22 Mass, 3.574 RT

19 isomers

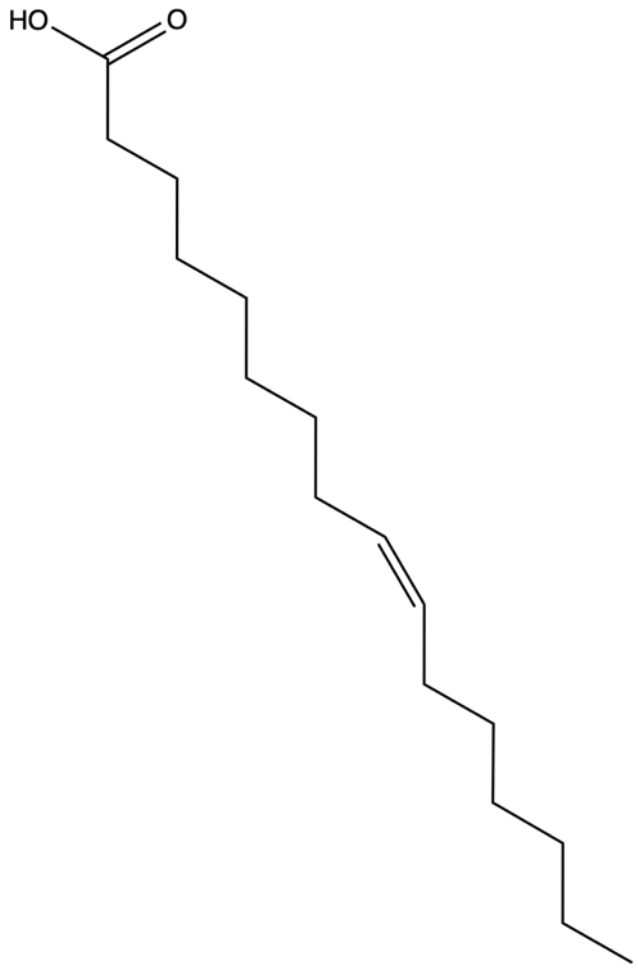

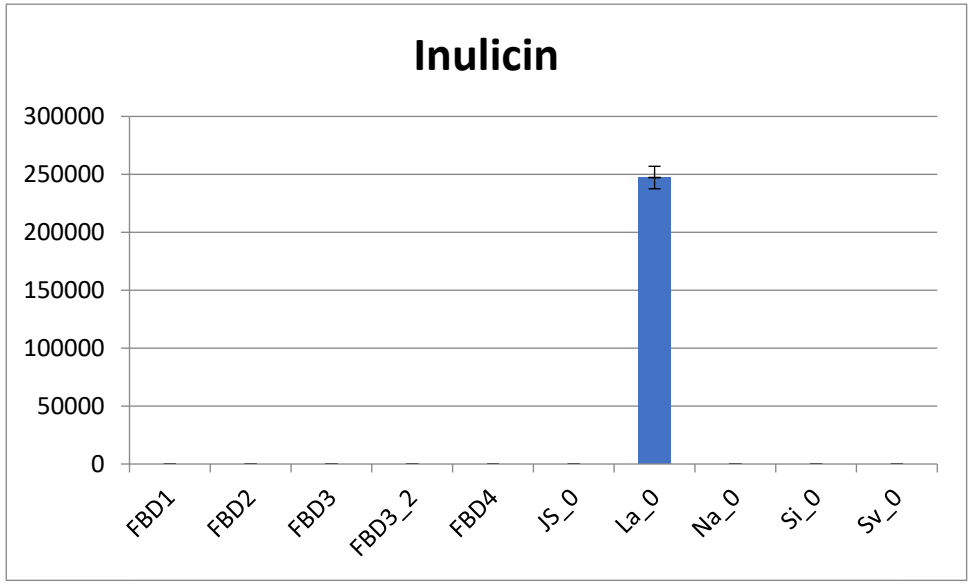

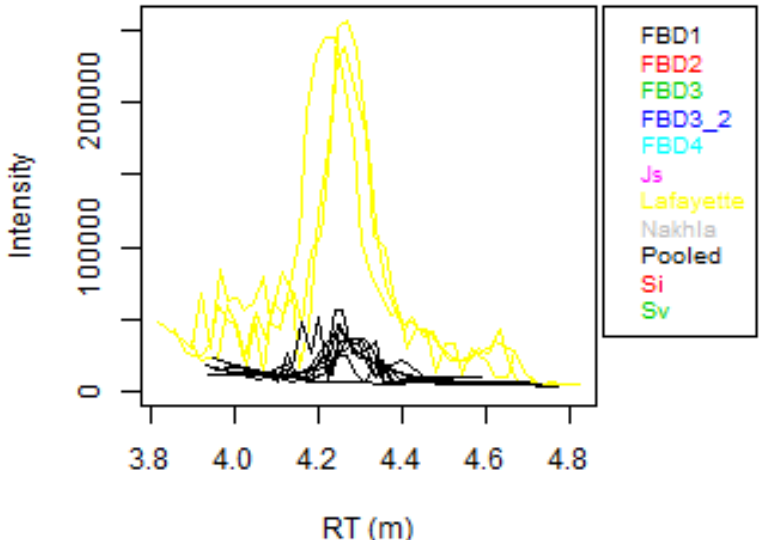

mass 308.16 RT 4.244

2 isomers

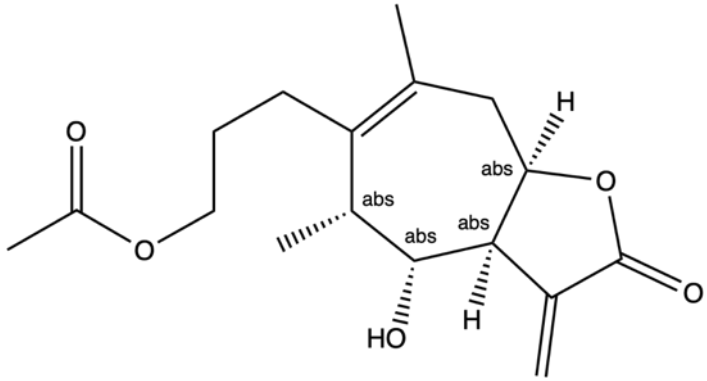

4-Maleylacetoacetate

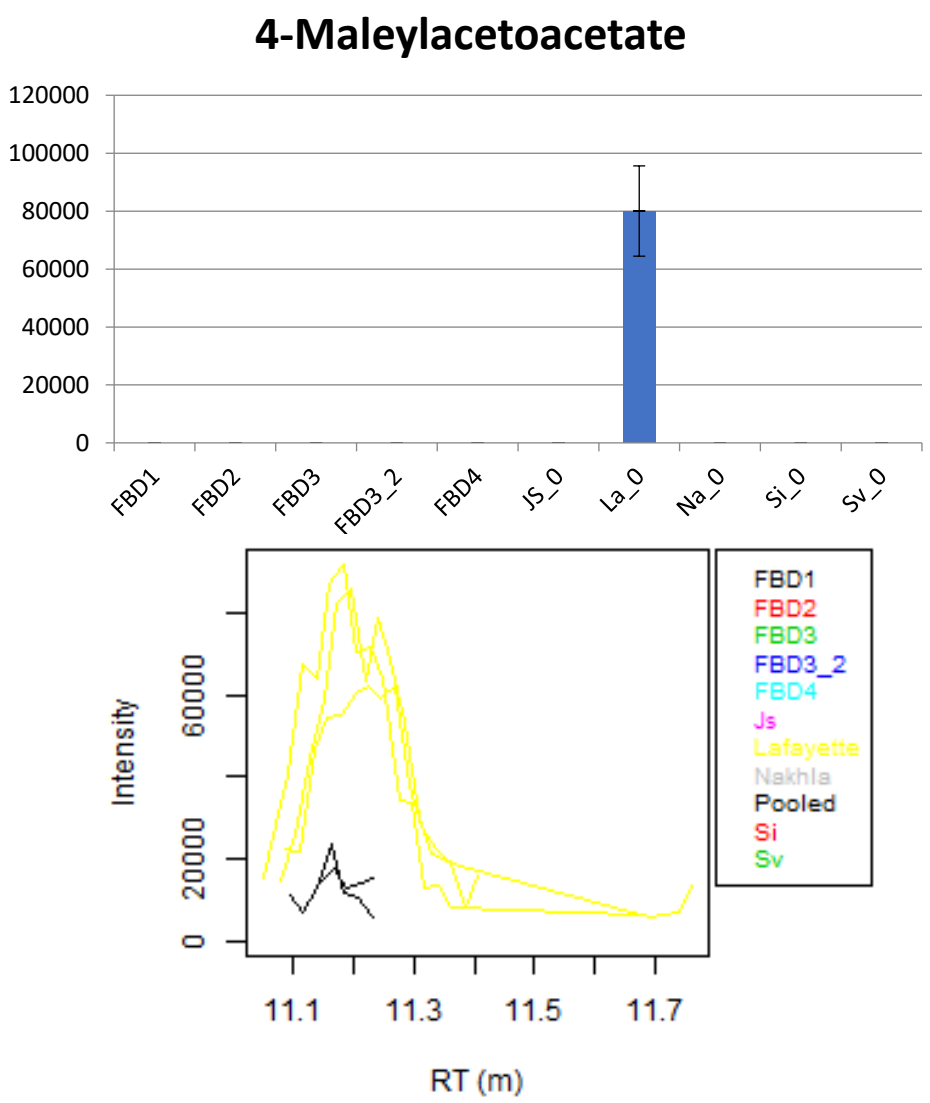

mass 200.03

RT 11.2

8 isomers

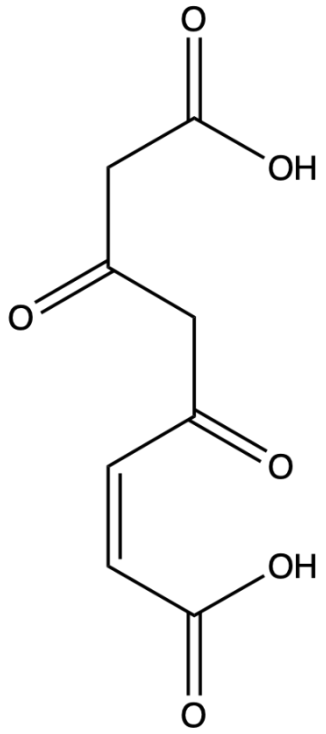

Methionol

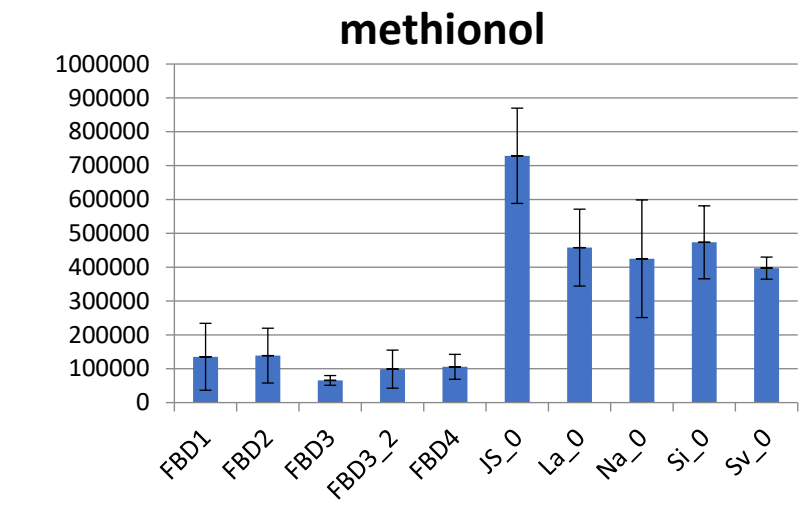

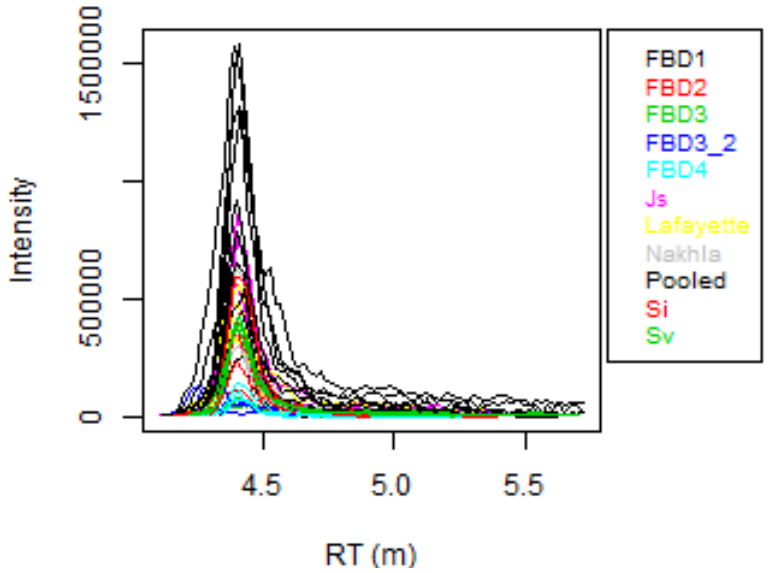

106.05 mass, 4.396 RT

no other isomers

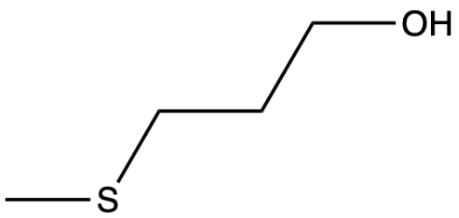

2-(5'-methylthio)pentylmalate

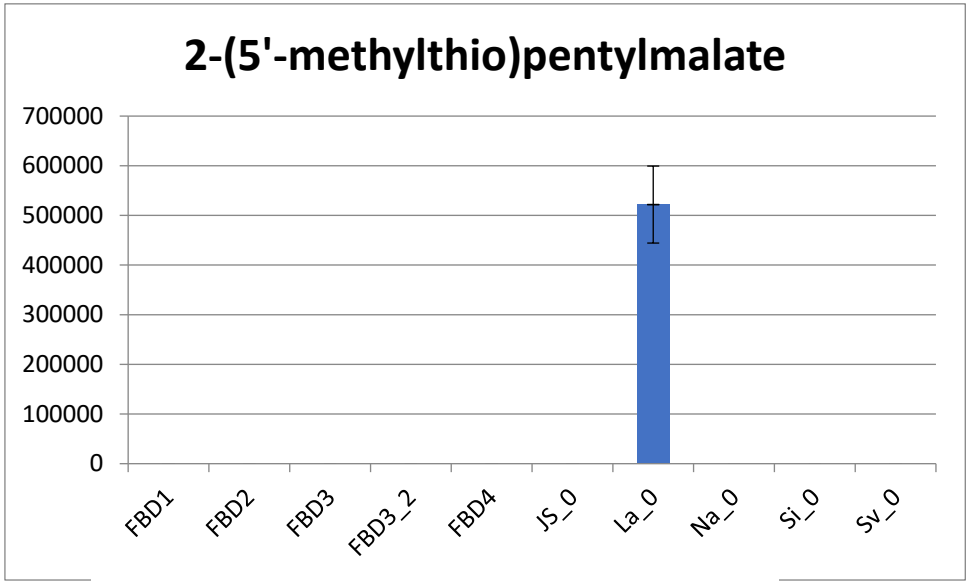

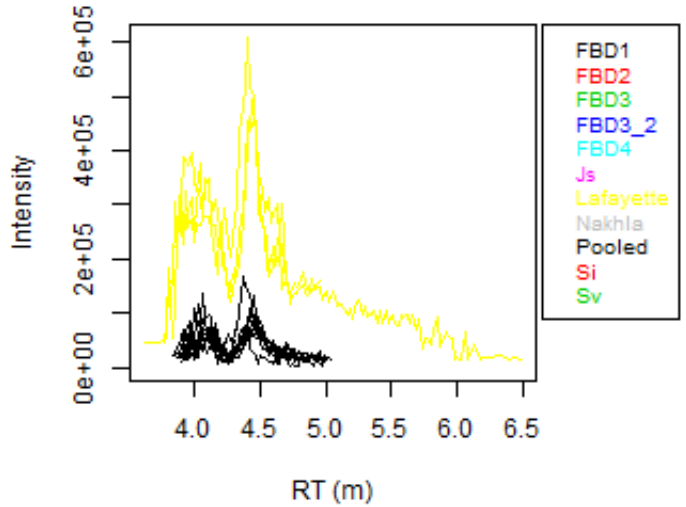

Mass 250.09 RT 4.4

2 isomers

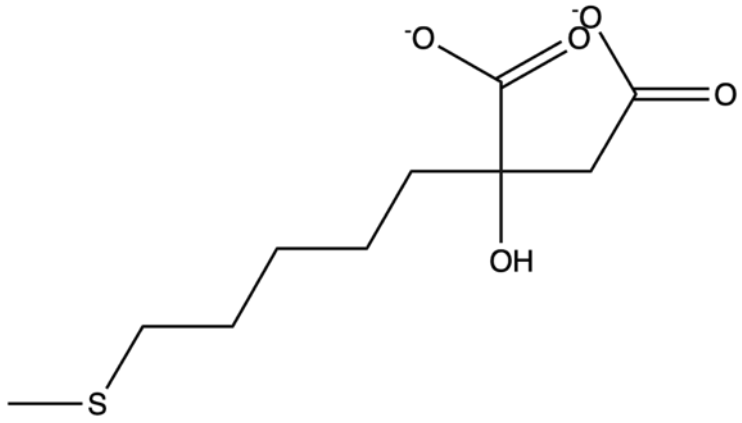

N-Acetylserotonin

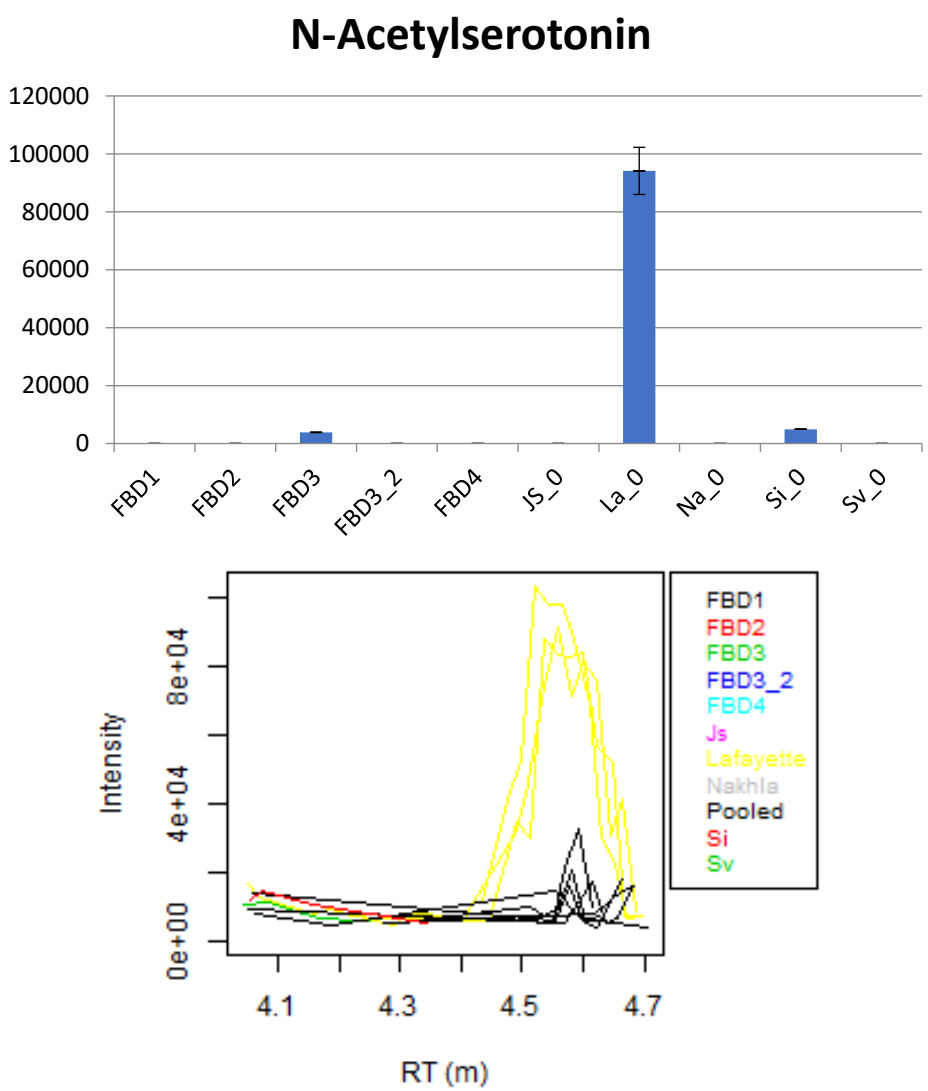

Mass 218.11

RT 4.497

7 isomers

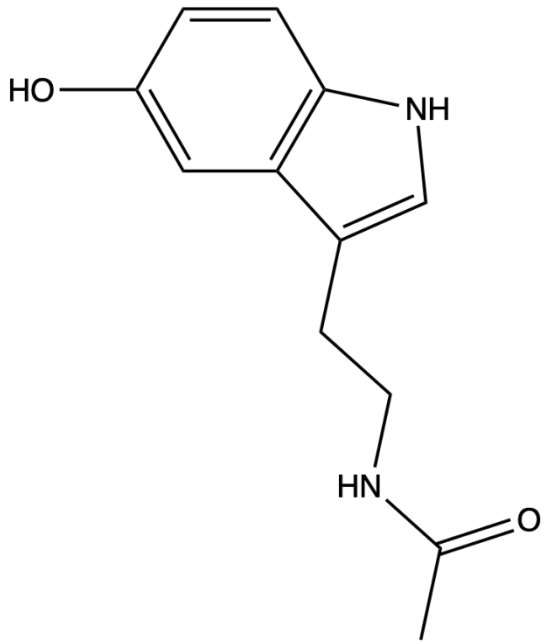

N-propyl gallate

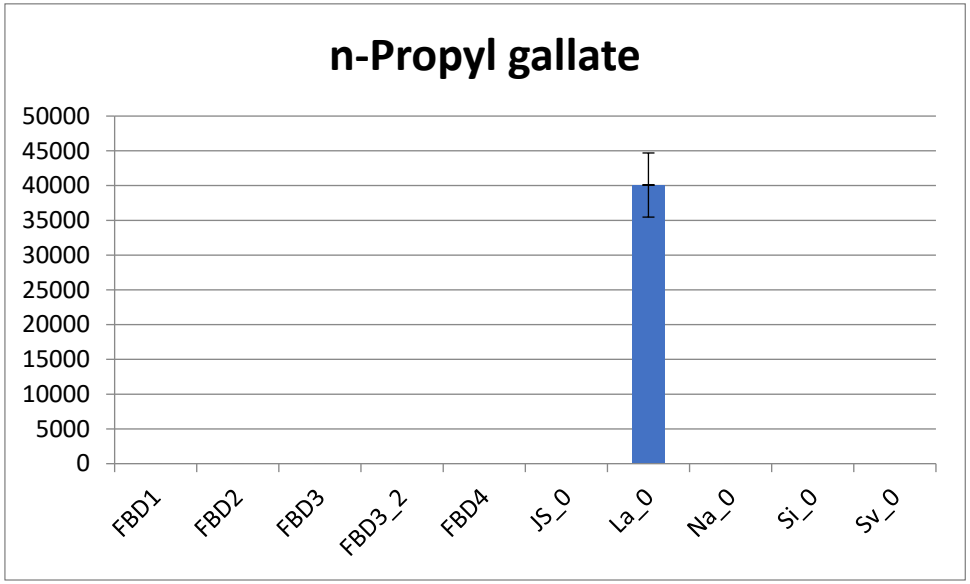

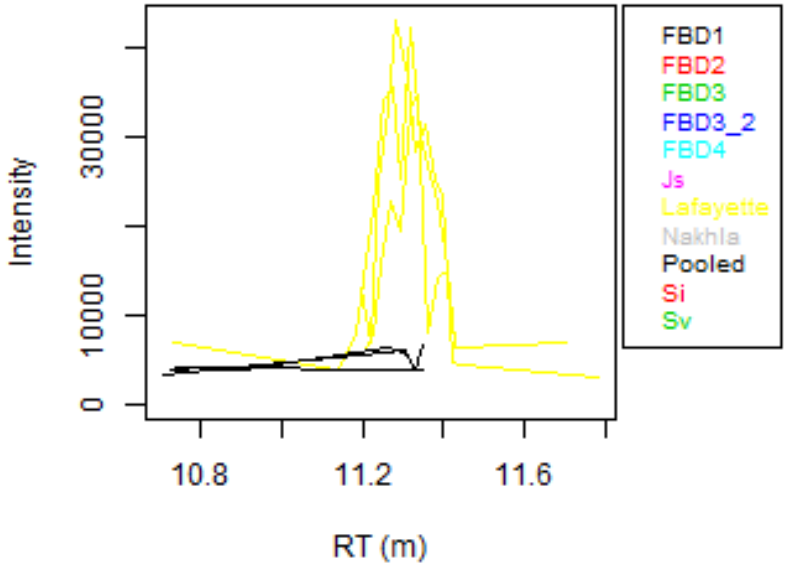

Mass 212.07 RT 11.23

4 isomers

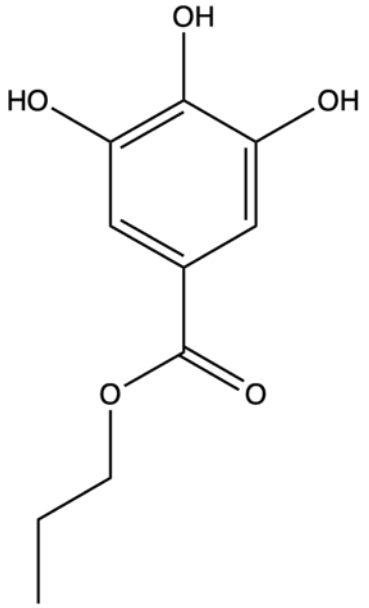

Orthophosphate

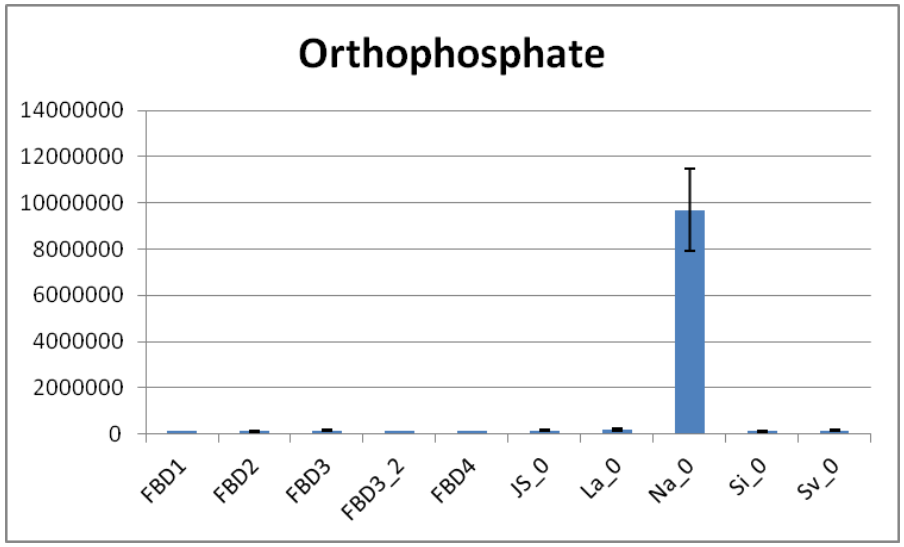

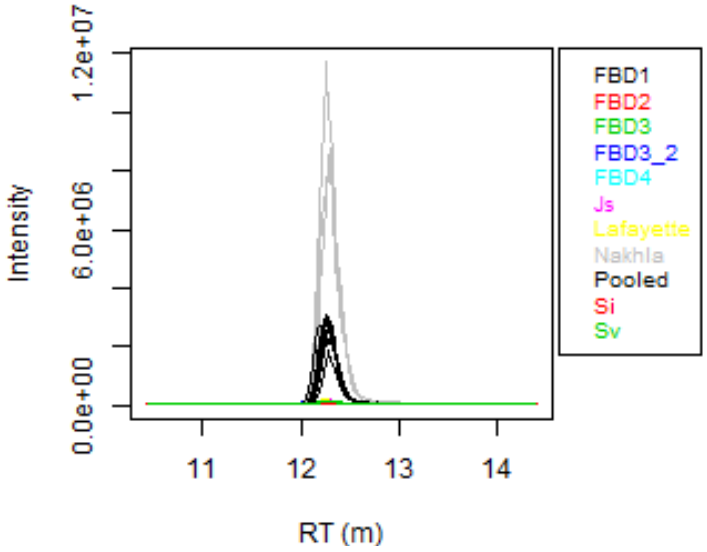

mass 97.977, RT 12.27

Standard run (therefore presence confirmed)

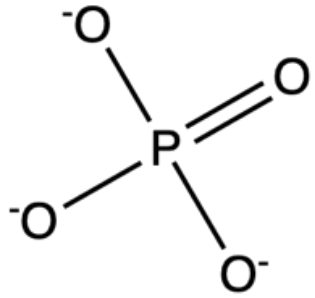

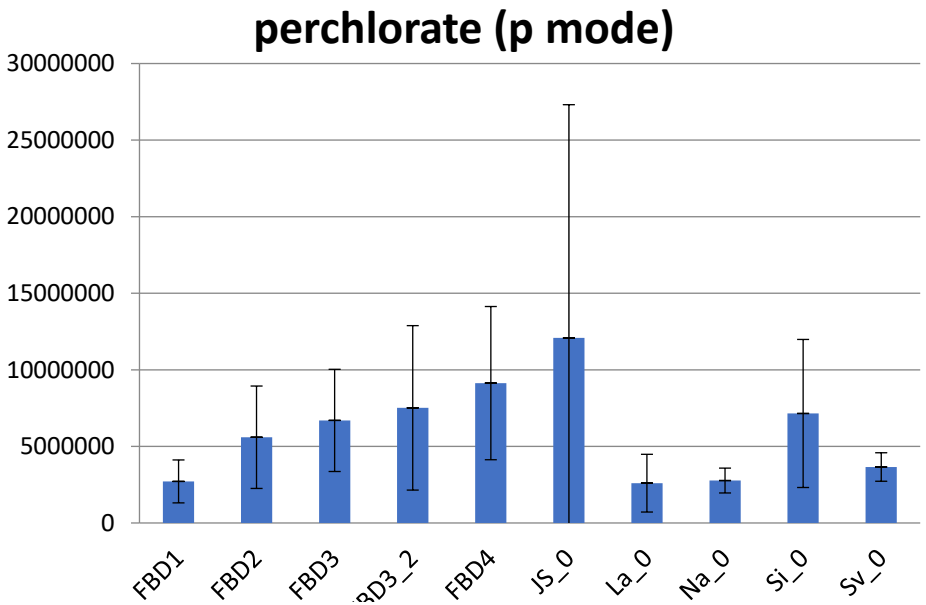

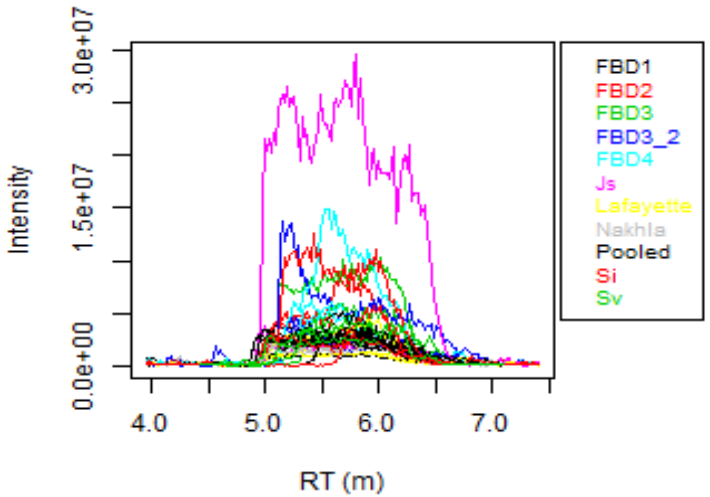

Perchlorate RT 5.602, no other isomers

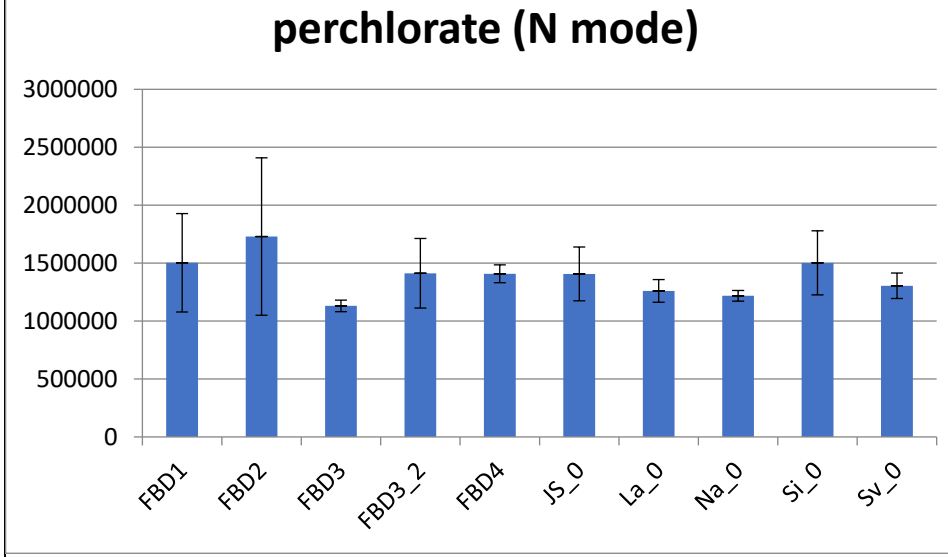

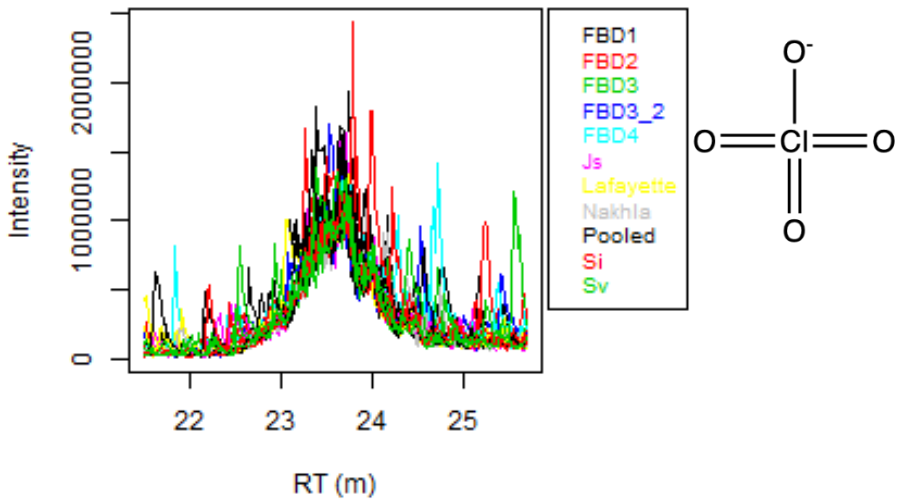

mass 99.956 RT 23.7, no other isomers

Pentanesulfonate

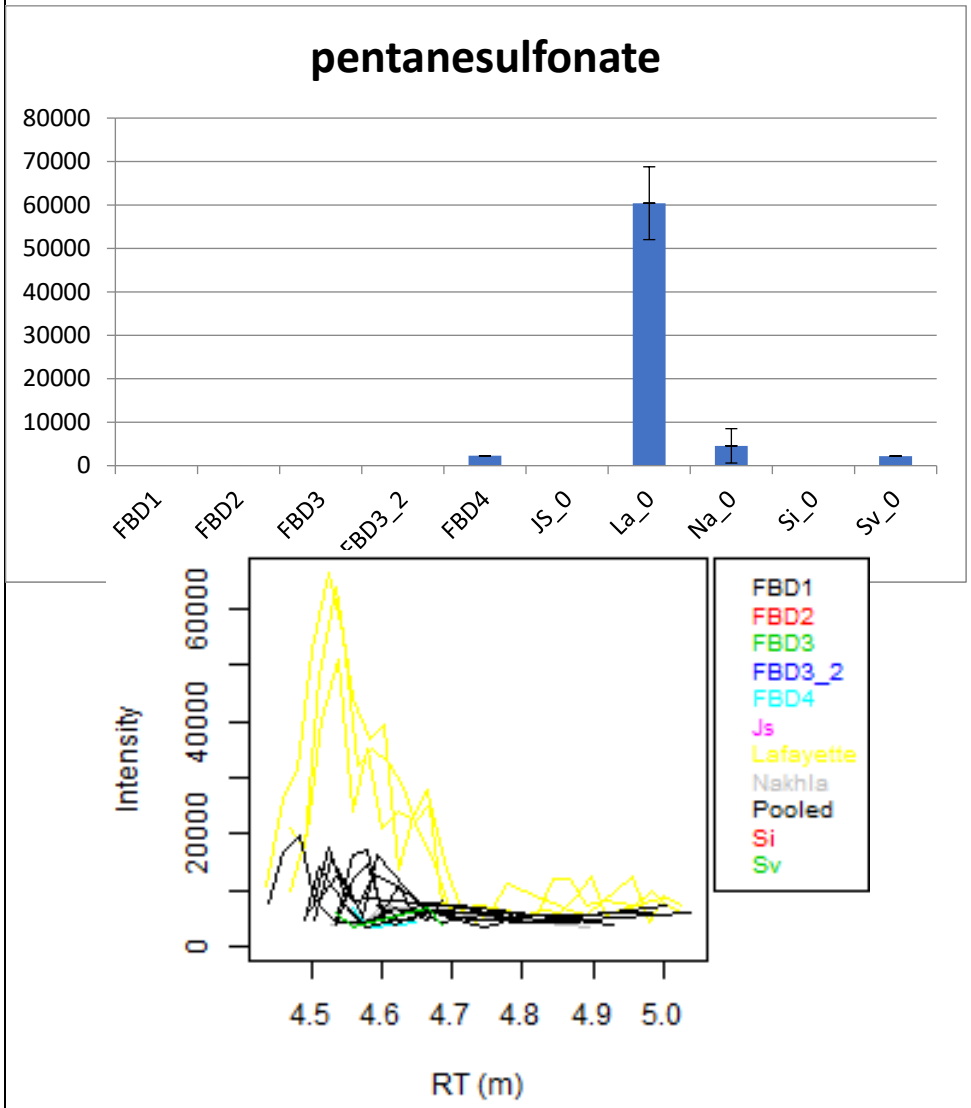

mass 152.0506 RT 4.569

no other isomers

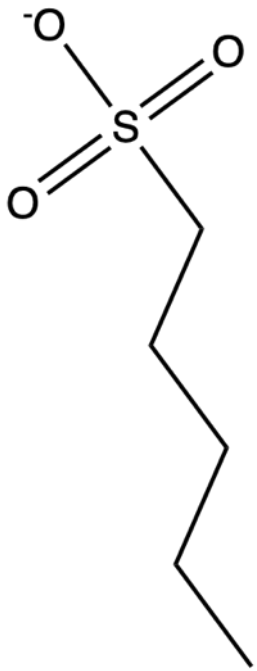

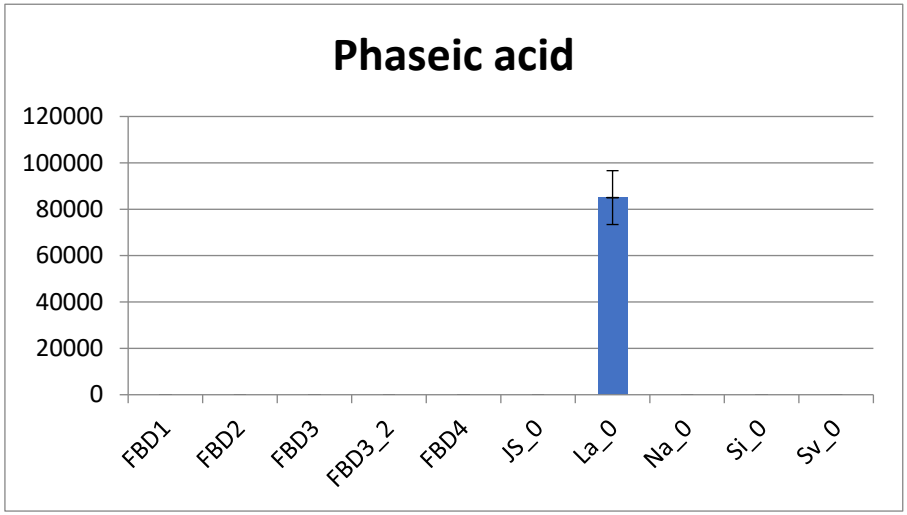

Phaseic Acid

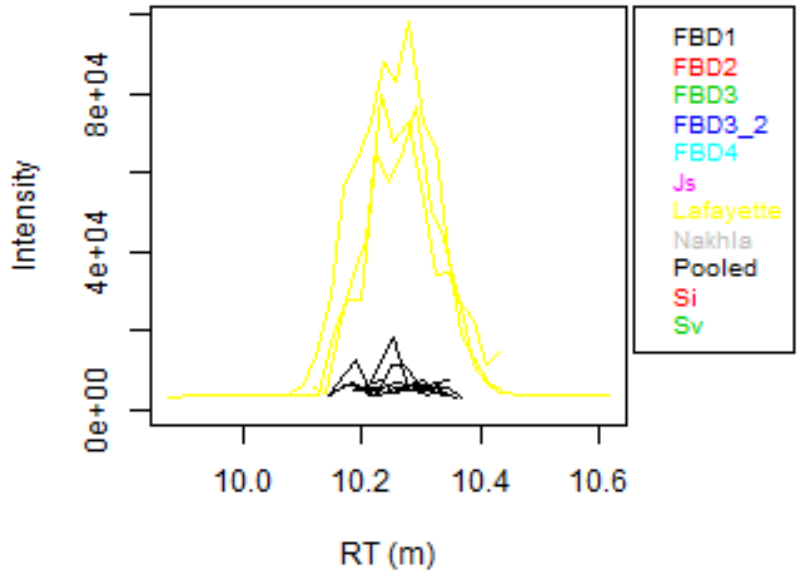

mass 280.131 RT10.26

6 isomers

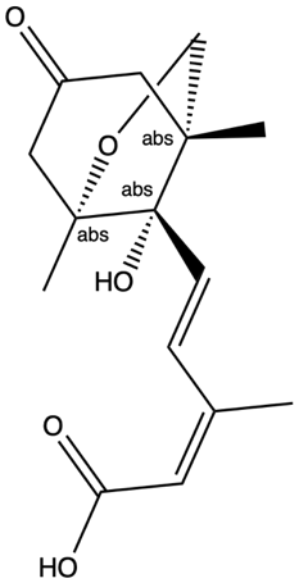

Pramanicin

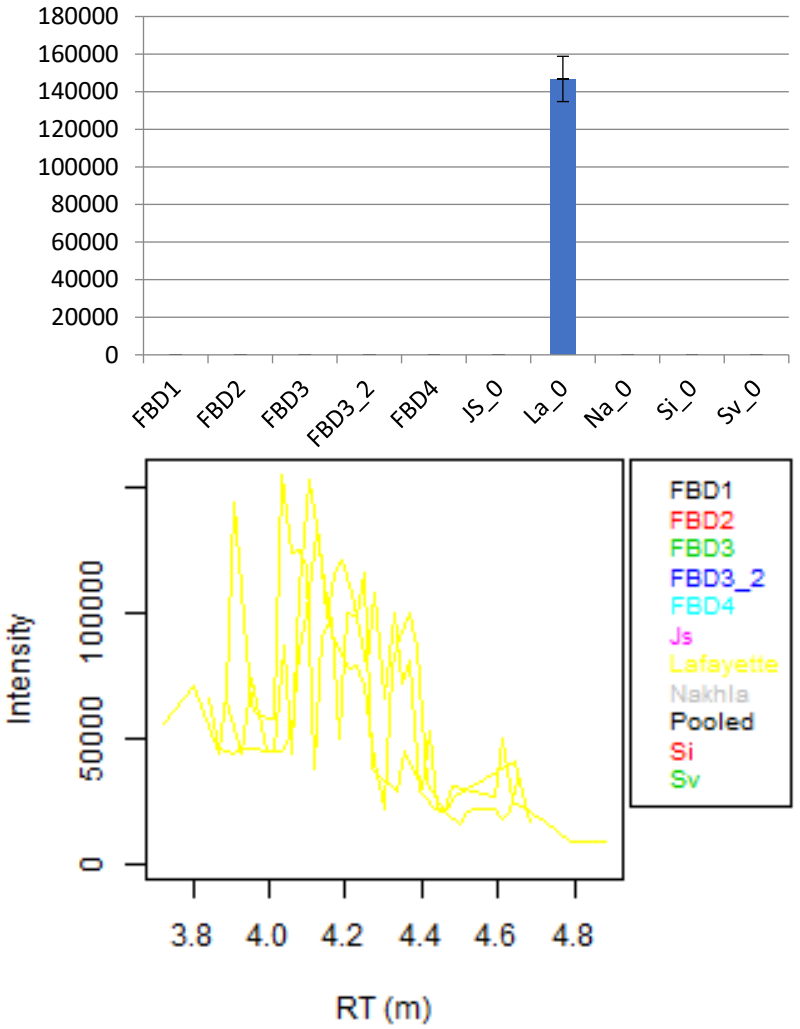

Mass 369.22 RT 4.087

No other isomers

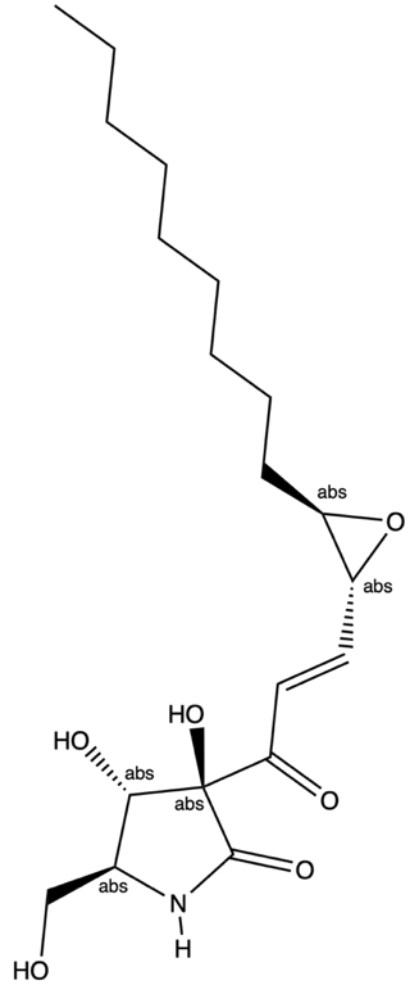

Shiromodiol diacetate

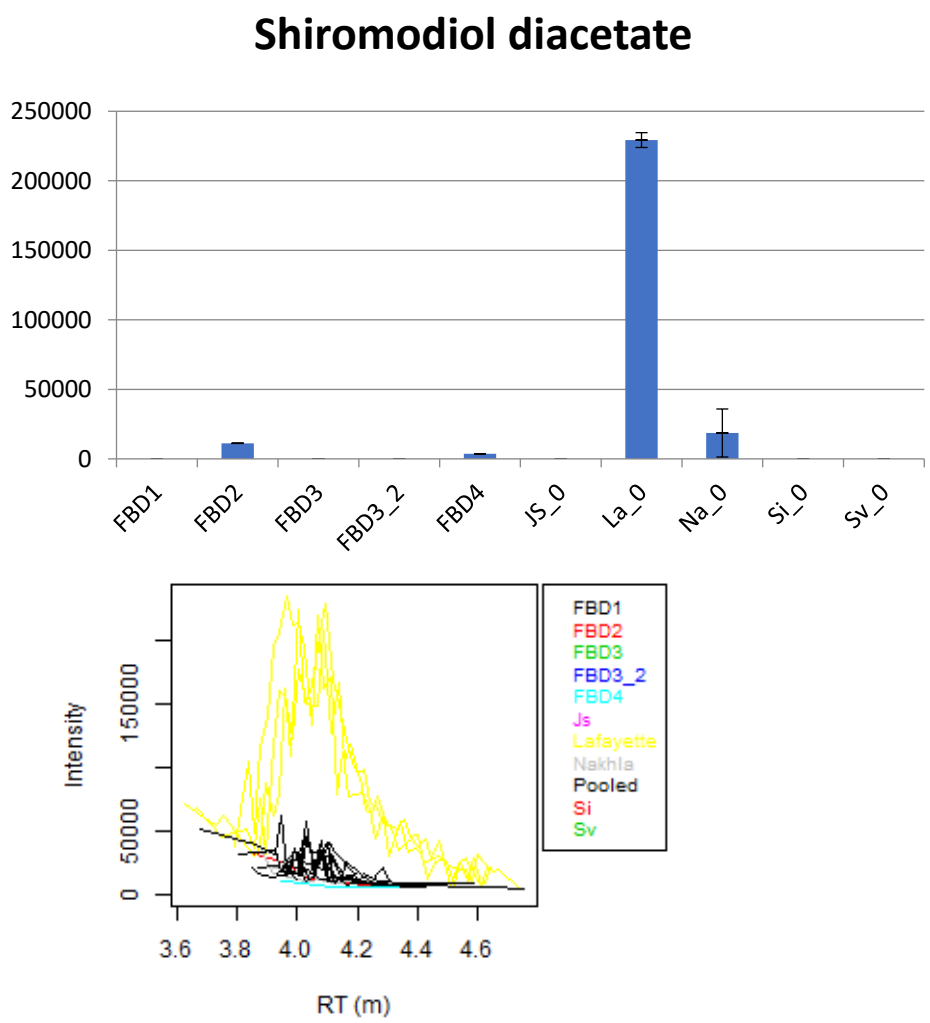

Mass 338.21 RT 3.987

No other isomers

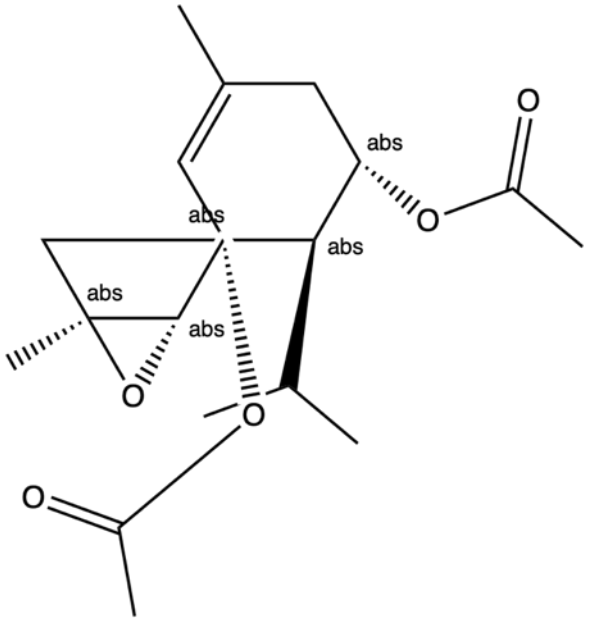

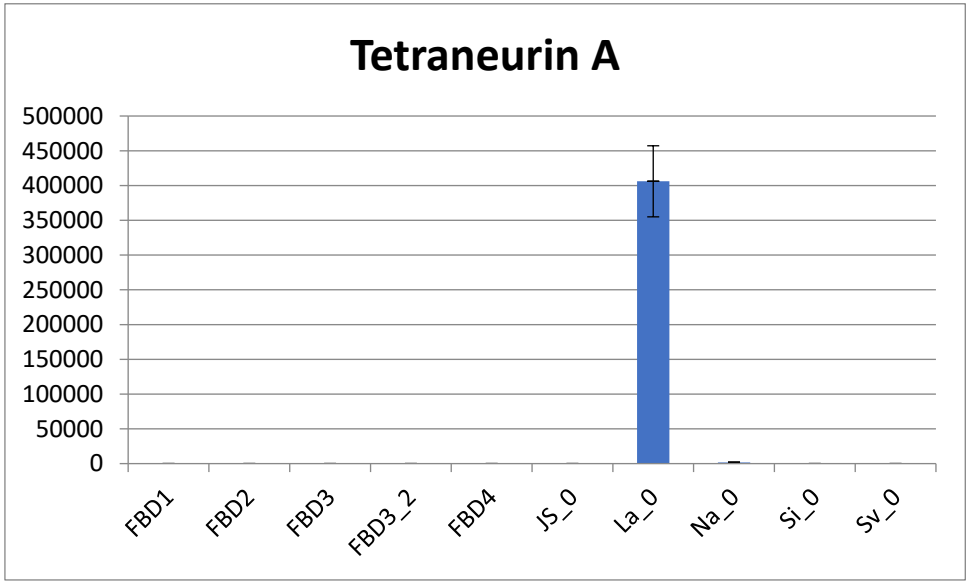

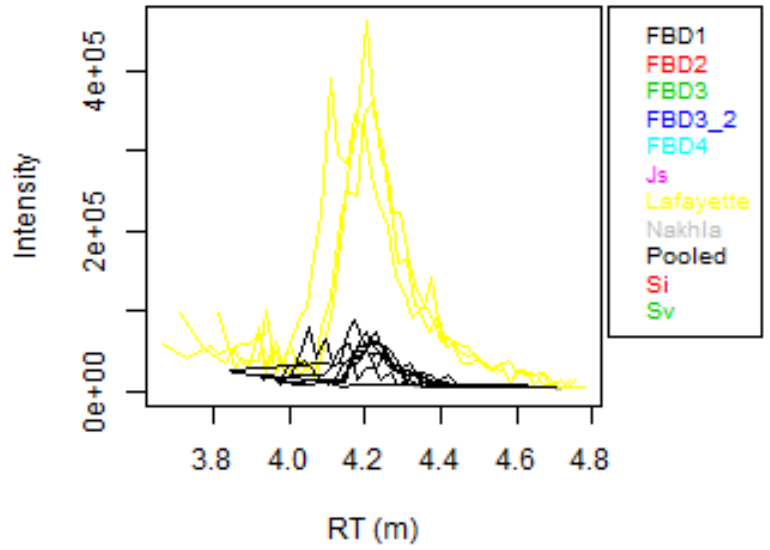

Mass 322.14 RT 4.214

2 isomers

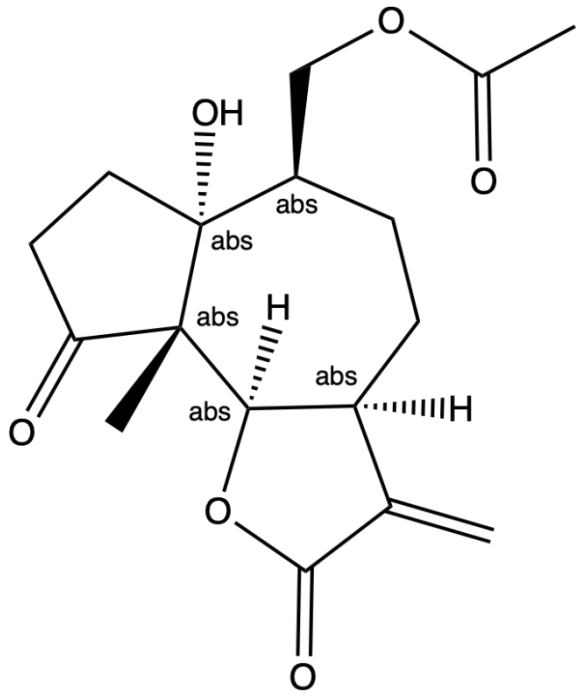

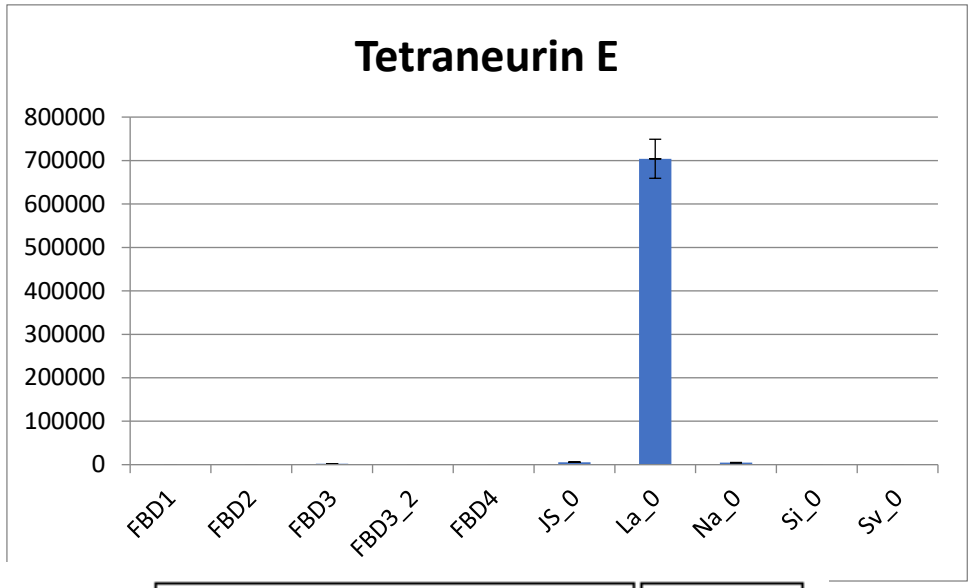

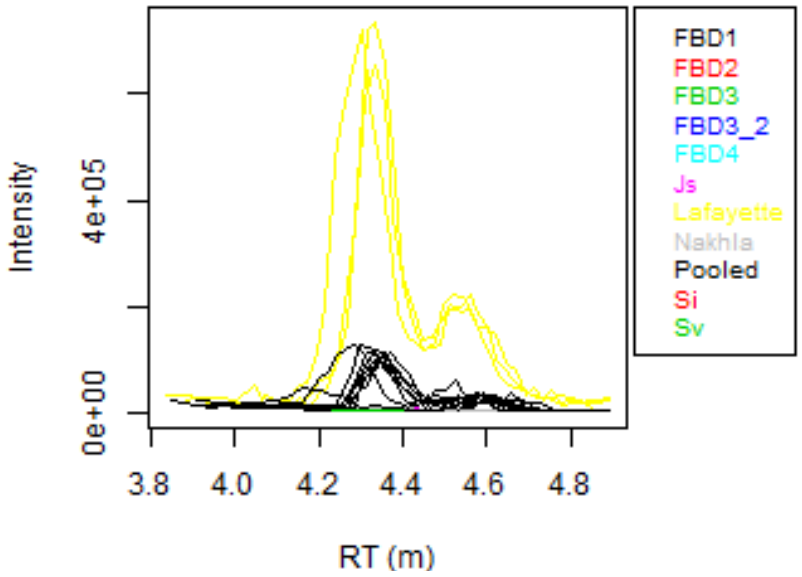

Mass 324.1576 RT 4.27

No other isomers

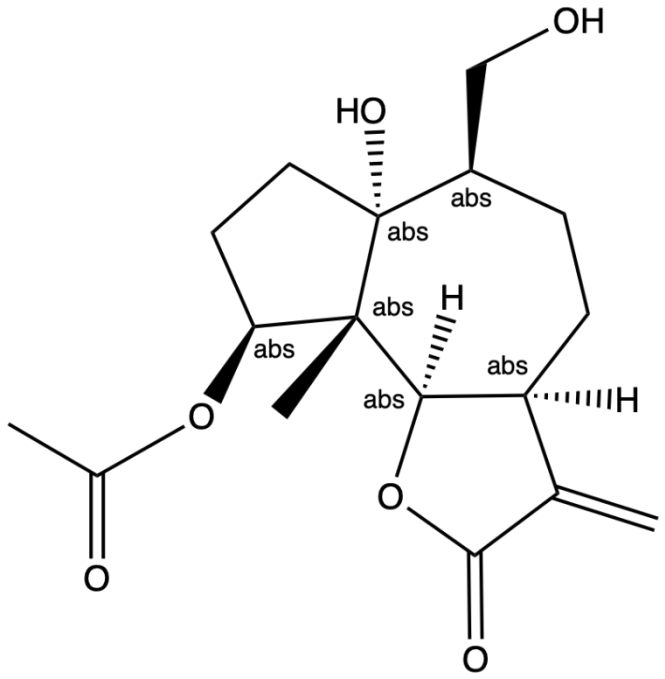

Tutin

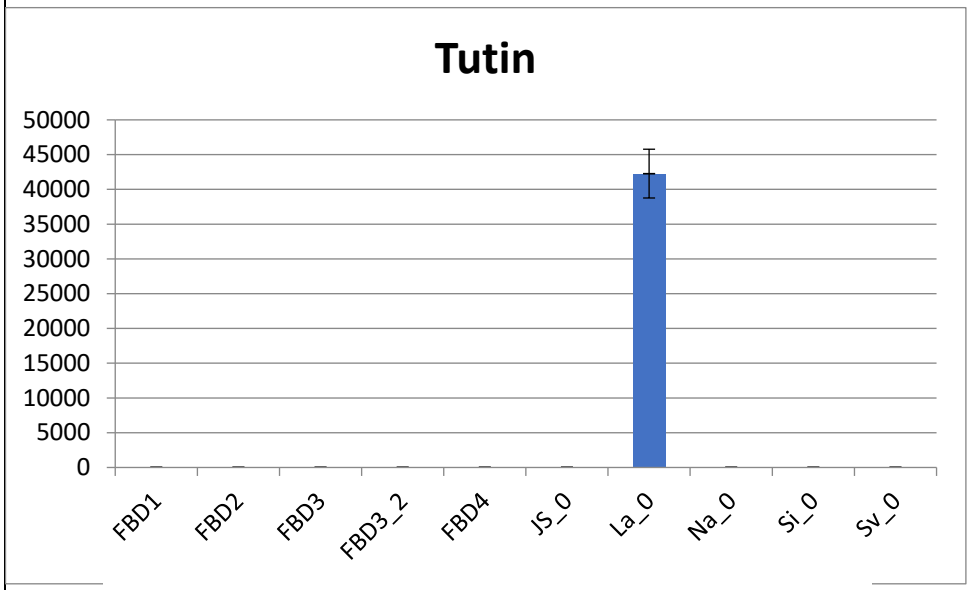

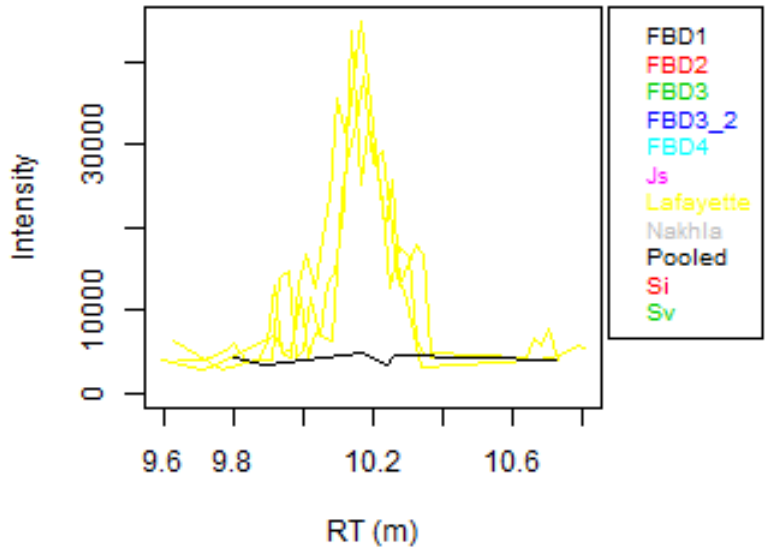

mass 294.11 RT 10.16

1 isomer

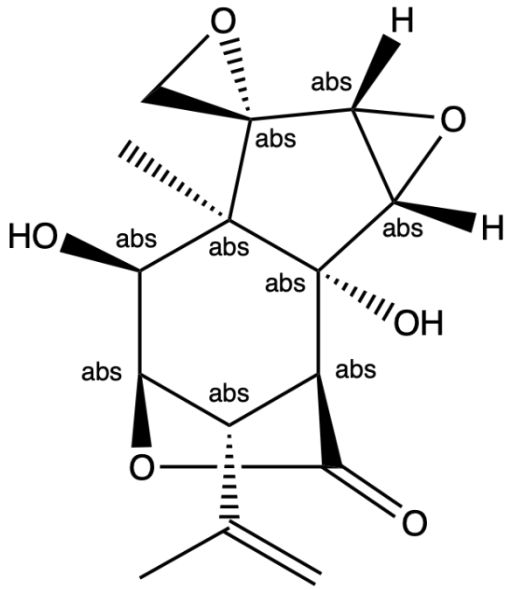

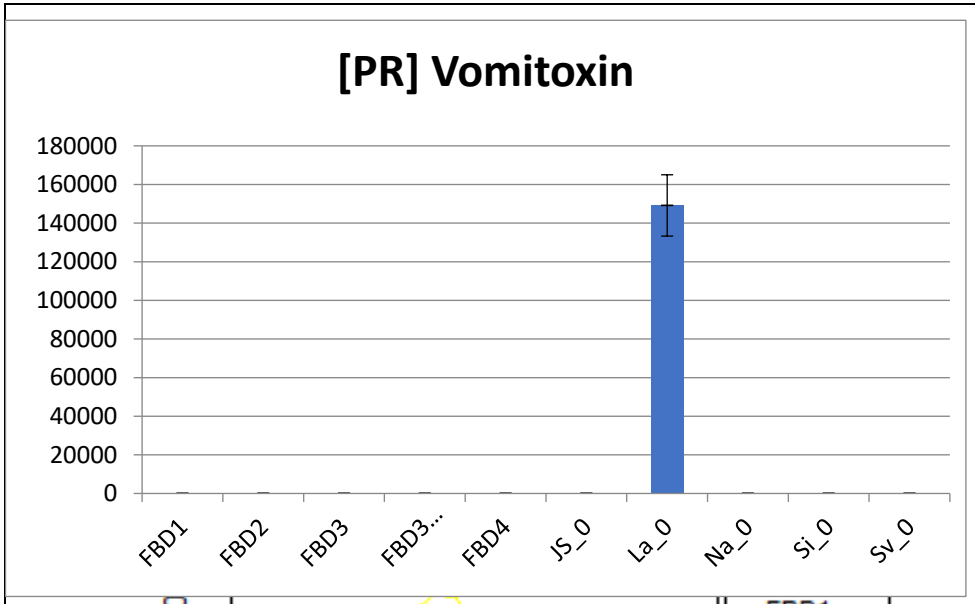

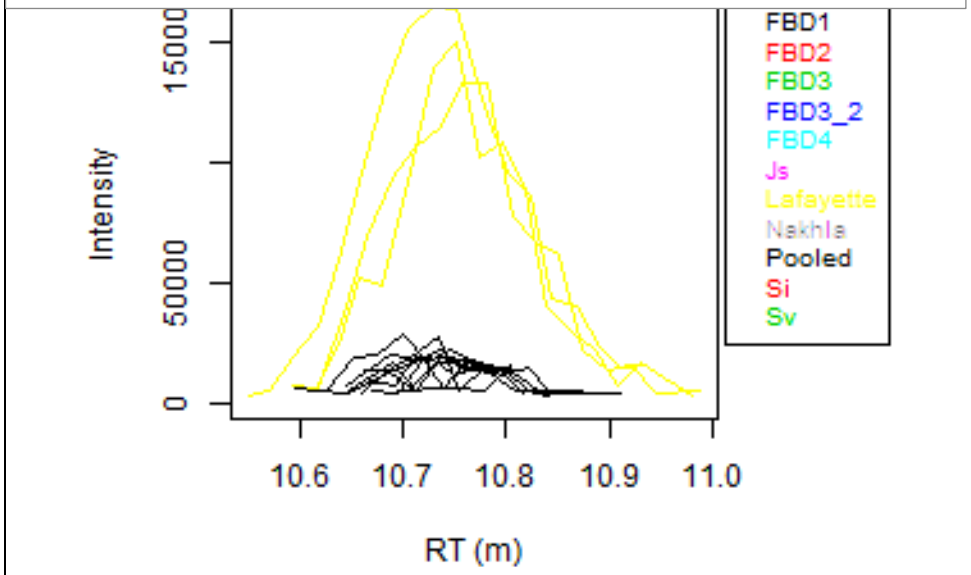

Vomitoxin

Mass 296.13 RT 10.74

2 isomers (more in HMDB)

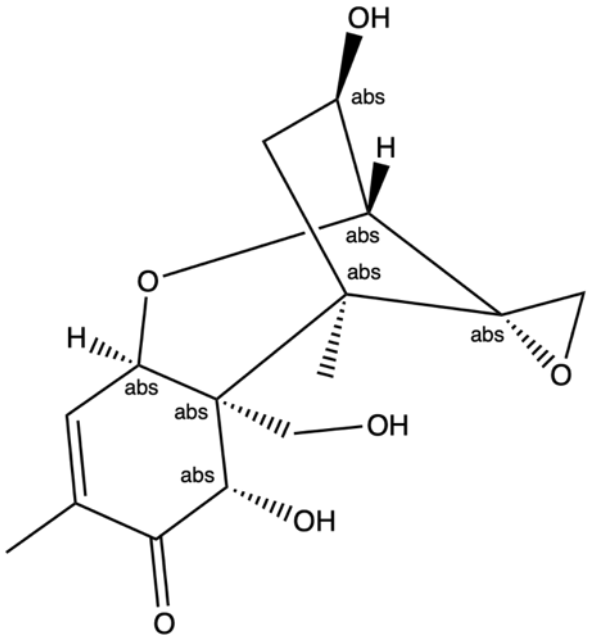

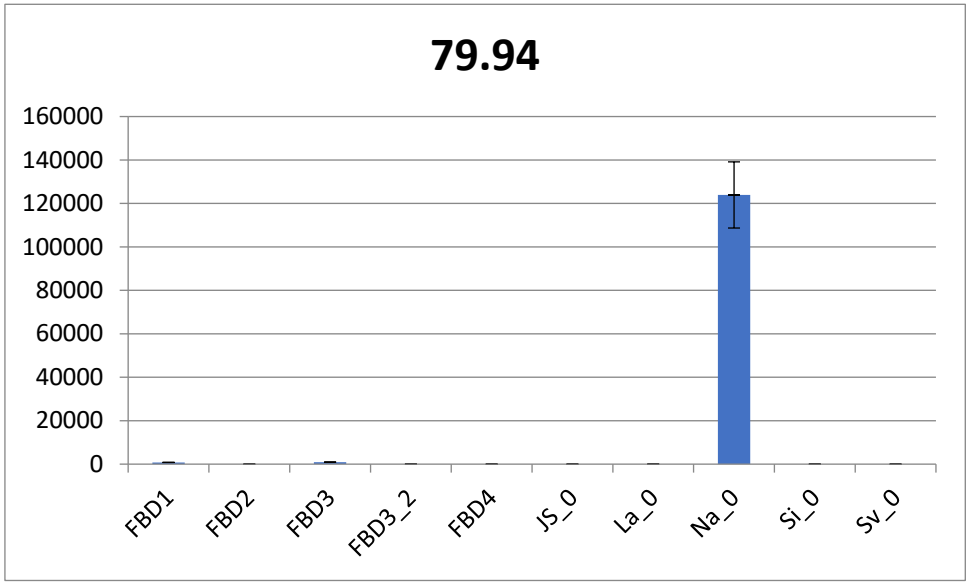
79.94
160000
140000
120000
100000
80000
60000
40000
20000
0
FBD1
FBD2
FBD3
FBD3_2
FBD4
JS_0
La_0
Na_0
Si_0
Sv_0

RT 12.28

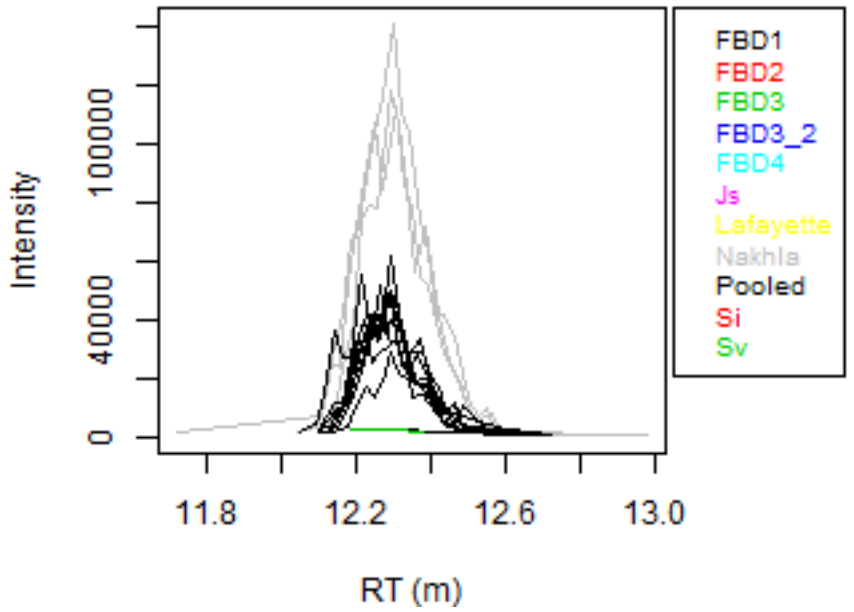
Intensity
0
40000
100000
11.8
12.2
12.6
13.0
RT (m)
FBD1
FBD2
FBD3
FBD3_2
FBD4
Js
Lafayette
Nakhla
Pooled
Si
Sv

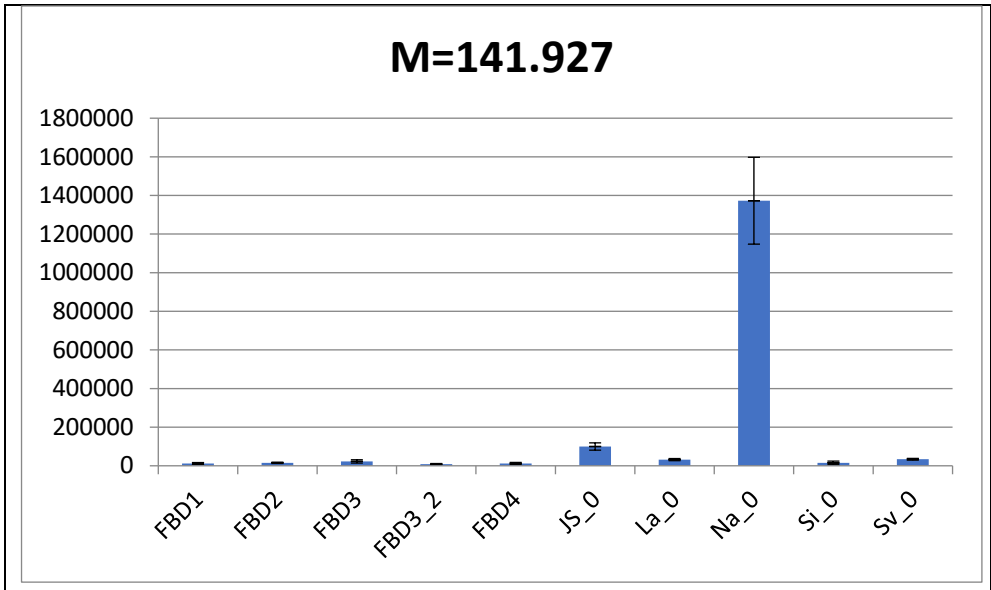
M=141.927
1800000
1600000
1400000
1200000
1000000
800000
600000
400000
200000
0
FBD1
FBD2
FBD3
FBD3_2
FBD4
JS_0
La_0
Na_0
Si_0
Sv_0

RT 12.91

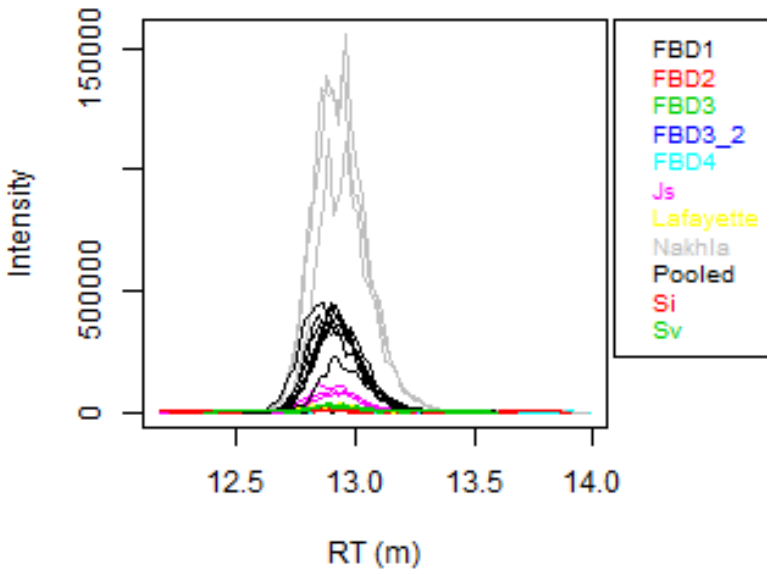
Intensity
150000
500000
0
12.5
13.0
13.5
14.0
RT (m)
FBD1
FBD2
FBD3
FBD3_2
FBD4
Js
Lafayette
Nakhla
Pooled
Si
Sv

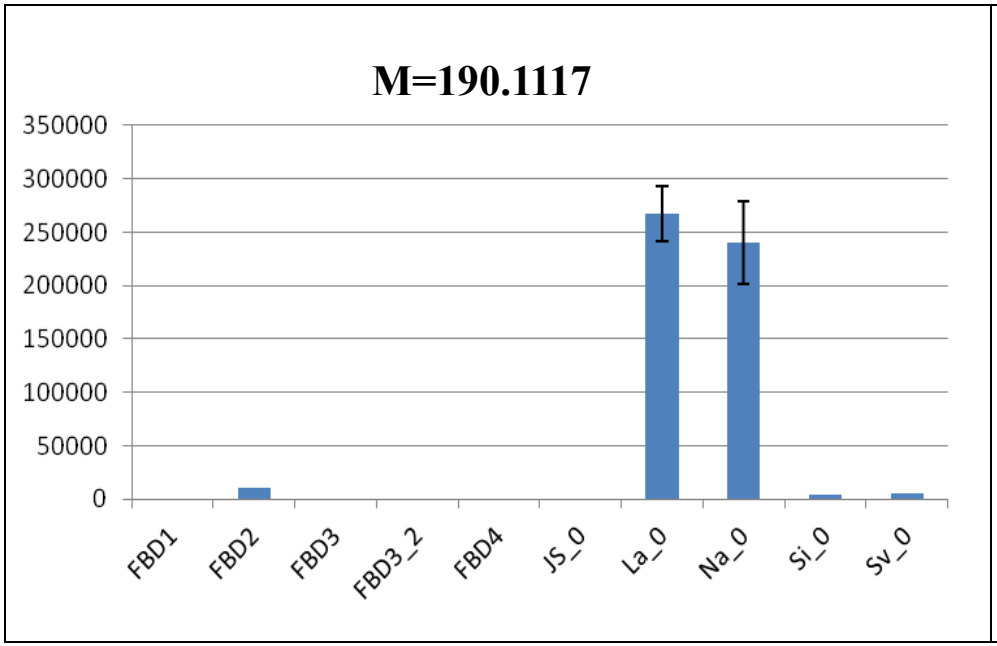
M=190.1117
350000
300000
250000
200000
150000
100000
50000
0
FBD1
FBD2
FBD3
FBD3_2
FBD4
JS_0
La_0
Na_0
Si_0
Sv_0

RT 4.071

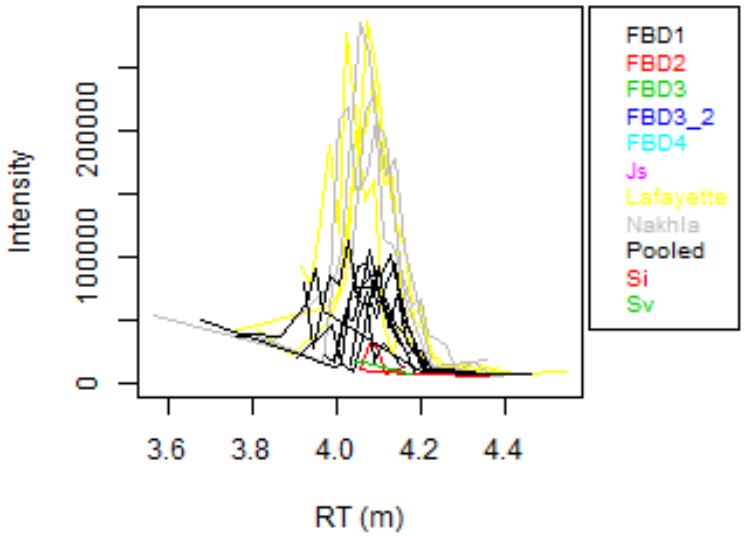
Intensity
0
100000
200000
3.6
3.8
4.0
4.2
4.4
RT (m)
FBD1
FBD2
FBD3
FBD3_2
FBD4
Js
Lafayette
Nakhla
Pooled
Si
Sv

234.18

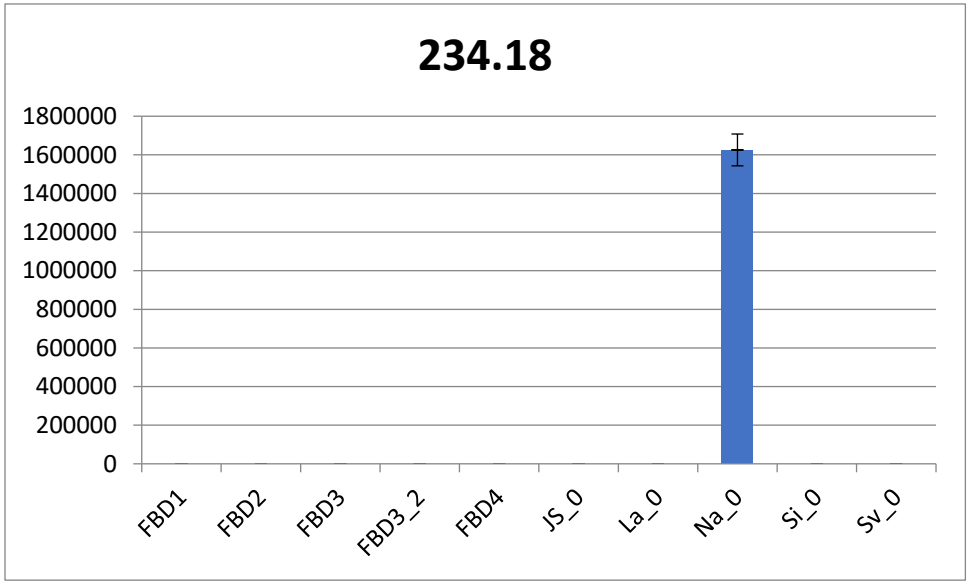
234.18
1800000
1600000
1400000
1200000
1000000
800000
600000
400000
200000
0
FBD1
FBD2
FBD3
FBD3_2
FBD4
JS_0
La_0
Na_0
Si_0
Sv_0

RT 4.36

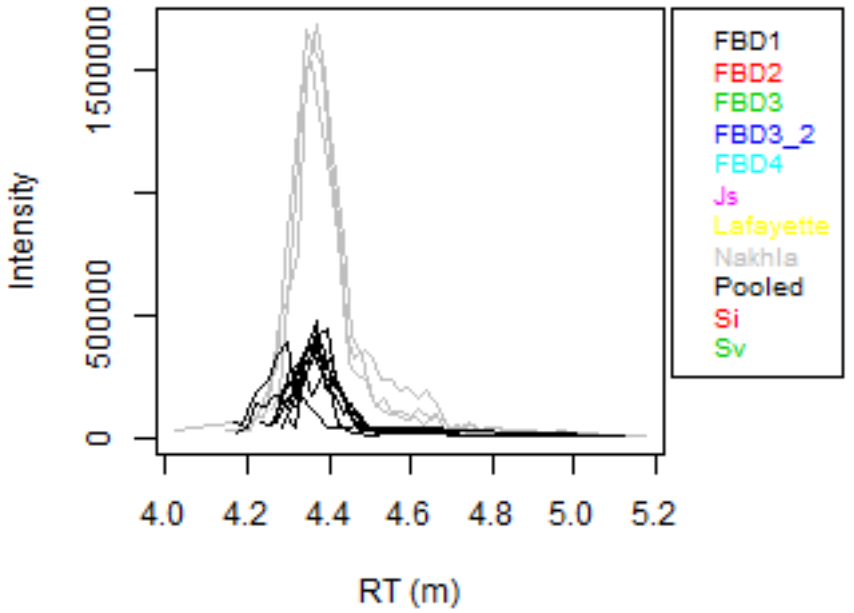
Intensity
1500000
500000
0
4.0
4.2
4.4
4.6
4.8
5.0
5.2
RT (m)
FBD1
FBD2
FBD3
FBD3_2
FBD4
Js
Lafayette
Nakhla
Pooled
Si
Sv

268.13

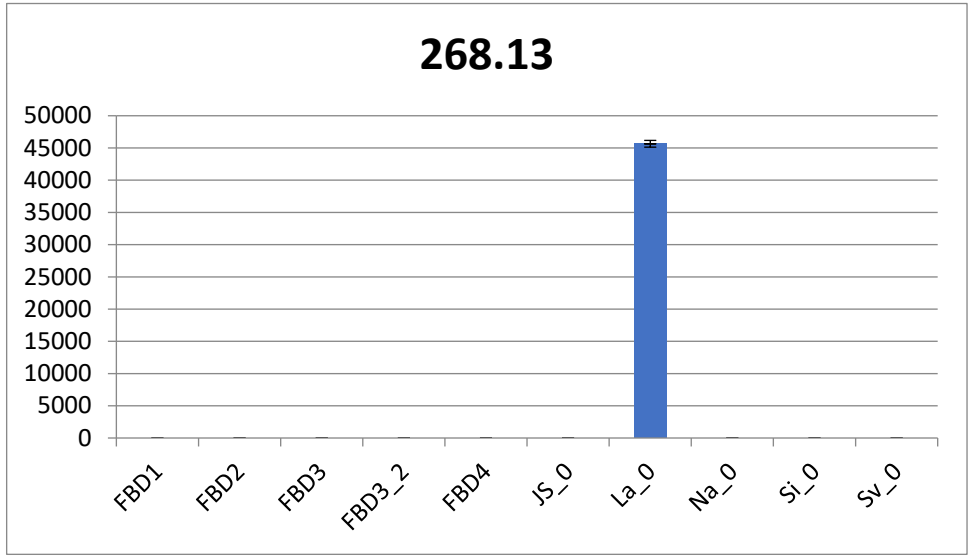

Mass 268.13 RT 8.204

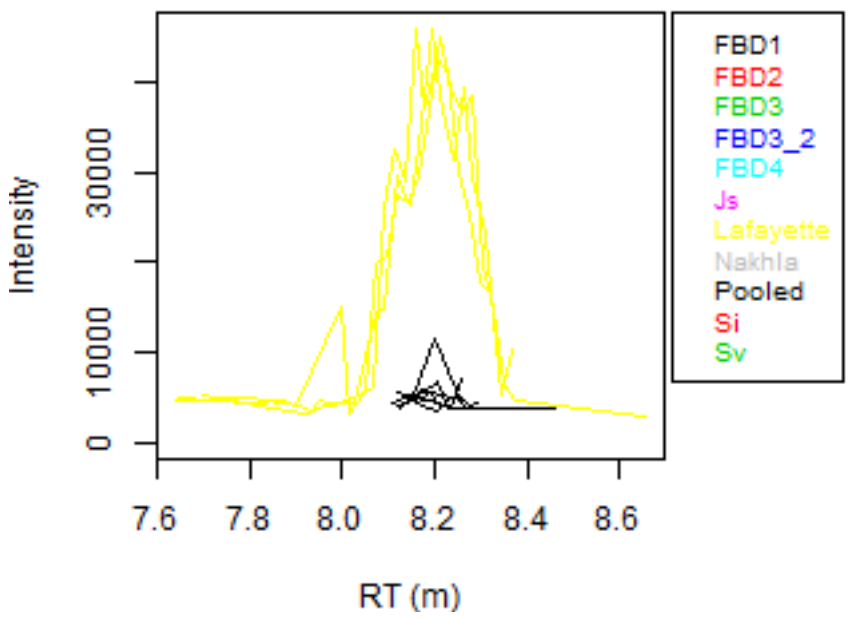

Table 16 Metabolites detected in Lafayette at levels at least twice those detected in the blanks, table shows mass, retention time, characteristics of putatively identified metabolite, and the relative abundance of the metabolite in Lafayette compared to the day 1 blank (FBD1) and the same for those in Nakhla. Metabolites are arranged in descending order of levels in Lafayette relative to the procedural blanks. Some metabolites present in the list were also present in other samples, others were also identified by Polyomics as lower definition peaks (denoted by an asterisk in the final column)

Mass (Da)	Retention time (min)	Formula	Putative metabolite	Number of isomers	Map	Pathway	Fold-change La vs FBD1	Fold-change Na vs FBD1	Low definition peak
304.2250566	4.580775016	C16H32O5	[FA trihydroxy(16:0)] 2,15,16-trihydroxy-hexadecanoic acid	4	Lipids: Fatty Acyls	Fatty Acids and Conjugates	1560.24	8.00	
324.1575623	4.266622179	C17H24O6	Tetraneurin E	1	0	0	704.04	4.75	
332.2564063	3.901616669	C18H36O5	[FA trihydroxy(18:0)] 9,10,18-trihydroxy-octadecanoic acid	4	Lipids: Fatty Acyls	Fatty Acids and Conjugates	586.55	0.00	
250.0877564	4.400387531	C10H18O5S	2-(5'-methylthio)pentylmalate	2	0	0	521.83	0.00	
314.2458477	3.753200001	C18H34O4	[FA hydroxy(18:1)] 9,10-dihydroxy-12Z-octadecenoic acid	12	Lipids: Fatty Acyls	Fatty Acids and Conjugates	465.05	78.94	
314.1883712	3.729172219	C20H26O3	momilactone A	12	0	0	420.60	0.00	
322.1420652	4.214212819	C17H22O6	Tetraneurin A	2	0	0	406.08	1.76	
250.1605347	3.540233273						343.32	0.00	
264.0997959	4.675634681	C14H16O5	1'-Acetoxyeugenol acetate	1	0	0	341.33	0.00	*
302.2091932	4.42762502	C16H30O5	[FA hydroxy(16:0/2:0)] 9-hydroxy-hexadecan-1,16-dioic acid	2	Lipids: Fatty Acyls	Fatty Acids and Conjugates	314.82	0.00	

306.1470453	3.77446946	C17H22O5	Arnicolide A	14	0	0	302.53	0.00	
290.1516066	3.770437495	C17H22O4	[FA oxo(4:0/4:0)] 9-oxo-12S-acetoxy-2,3,4,5-tetranor-7Z,10Z,14Z-prostatetrienaldehyde-cyclo[8,12]	5	Lipids: Fatty Acyls	Eicosanoids	298.84	0.00	
334.2144589	3.847200012	C20H30O4	Prostaglandin A2	32	Lipids: Fatty Acyls	Arachidonic acid metabolism	272.23	20.20	*
306.1467922	4.055404154	C17H22O5	Matricin	14	Lipids: Prenols	Isoprenoids	269.65	0.00	*
190.1117183	4.071398043						266.94	239.93	
278.1154345	6.96248898	C15H18O5	Artecanin	6	0	0	252.64	0.00	*
328.2249753	4.070579147	C18H32O5	[FA 308rihydroxy] 9S,11R,15S-trihydroxy-2,3-dinor-13E-prostaenoic acid-cyclo[8S,12R]	6	Lipids: Fatty Acyls	Eicosanoids	252.08	0.00	*
308.1628615	4.24361941	C17H24O5	Inulicin	2	0	0	247.25	0.00	
264.1758231	3.561533356						245.73	0.00	*
348.1937149	4.195994398	C20H28O5	[PR] Novaxenicins A	8	Lipids: Prenols	Isoprenoids	243.86	0.00	*
218.115536	7.014432469	C10H18O5	3-Hydroxysebacicacid	2	Lipids: Fatty Acyls	0	241.43	51.39	*
338.2098075	3.987374973	C19H30O5	Shiromodiol diacetate	1	0	0	229.30	18.61	
258.1831483	3.969324523	C14H26O4	[FA (14:0/2:0)] Tetradecanedioic acid	6	Lipids: Fatty Acyls	Fatty Acids and Conjugates	218.63	31.59	
272.1411289	4.062729136	C17H20O3	2,2-Dimethyl-8-prenylchromene 6-carboxylic acid	4	0	0	205.89	0.00	*
230.0614551	4.185018031						155.67	0.00	

548.3353077	3.60321668						152.74	0.00	*
260.1986559	4.208372158	C14H28O4	[FA hydroxy(14:0)] 3,11-dihydroxy-tetradecanoic acid	1	Lipids: Fatty Acyls	Fatty Acids and Conjugates	151.37	0.00	*
296.126183	10.74094721	C15H20O6	[PR] Vomitoxin	2	Lipids: Prenols	Isoprenoids	149.15	0.00	
369.2150645	4.08737225	C19H31NO6	[SP] Pramanicin	1	Lipids: Sphingolipids	Sphingoid bases	146.79	0.00	*
275.2095577	4.15806661	C40H54O	[PR] Echinenone/ (Myxoxanthin)	6	Lipids: Prenols	Isoprenoids	143.54	0.00	
330.1834197	4.225925001	C20H26O4	Gibberellin A15	4	Lipids: Prenols	Isoprenoids	137.44	0.00	
278.1154777	9.562366825	C15H18O5	Canin	6	0	0	135.95	0.00	
260.1988943	4.297238068	C14H28O4	[FA hydroxy(14:0)] 3,11-dihydroxy-tetradecanoic acid	1	Lipids: Fatty Acyls	Fatty Acids and Conjugates	133.89	13.62	
248.1049891	4.320286788	C14H16O4	Prenyl caffeate	2	0	0	131.23	2.32	
314.093078	4.476783316						129.26	0.00	
208.1076324	5.016112125						124.24	3.15	*
302.2246569	3.528523531	C20H30O2	[FA (20:5)] 5Z,8Z,11Z,14Z,17Z-eicosapentaenoic acid	43	Lipids: Fatty Acyls	Biosynthesis of unsaturated fatty acids	118.18	2.76	*
364.1891863	4.024943936	C20H28O6	Eriolangin	10	0	0	114.32	0.00	*
323.1733221	3.820323835						110.04	0.00	*
266.115596	4.166475817	C28H36O10	12alpha-Hydroxyamoorstatin	1	0	0	109.05	6.52	*
530.324767	3.49427621						105.55	0.00	*

320.1988525	3.563151798	C19H28O4	ubiquinol-2	4	Metabolism of Cofactors and Vitamins	Oxidative phosphorylation	101.68	11.57	*
218.1051696	4.496937862	C12H14N2O2	N-Acetylserotonin	7	Amino Acid Metabolism	Tryptophan metabolism	94.12	0.00	
280.1310852	10.26431986	C15H20O5	Phaseic acid	6	Biosynthesis of Secondary Metabolites	Carotenoid biosynthesis	85.02	0.00	
312.0768074	4.133783298						81.14	0.00	
200.0323422	11.1958433	C8H8O6	4-Maleylacetoacetate	8	Amino Acid Metabolism	Tyrosine metabolism__Styrene degradation	80.03	0.00	
180.0788166	4.255351714	C10H12O3	Coniferyl alcohol	7	Biosynthesis of Secondary Metabolites	Phenylpropanoid biosynthesis	76.78	1.37	
216.0998841	10.91075628	C21H28N4O6	Leu-Trp-Asp	4	Peptide(tri-)	Hydrophobic peptide	71.10	1.73	
152.0506308	4.569143772	C5H12O3S	pentanesulfonate	1	0	0	60.41	4.56	
218.0978756	4.112261115	C10H18O3S	DMB-S-MMP	2	0	0	58.93	0.00	*
166.0664077	4.250626678	C6H14O3S	hexanesulfonate	1	0	0	55.57	5.49	*
214.1030472	4.695038859						54.91	0.00	*
308.1263967	4.292469406	C16H20O6	14-Dihydroxycornestin	2	0	0	53.65	0.00	*
328.1676429	3.807155524	C20H24O4	Crocetin	4	Lipids: Prenols	crocetin biosynthesis __ crocetin esters biosynthesis	51.32	0.00	*
260.1047367	10.75724453	C15H16O4	8-Deoxylactucin	5	0	0	51.28	0.00	*
384.2152249	4.354942437						48.76	0.00	*
268.1311267	8.203500084						45.65	0.00	

294.1106333	10.16392924	C15H18O6	Tutin	1	0	0	42.27	0.00	
212.0688117	11.22862786	C10H12O5	n-Propyl gallate	4	Xenobiotics Drugs etc	0	40.08	0.00	
172.0372833	4.410162481	C7H8O5	2,4,6-trioxoheptanoate	9	0	orcinol degradation	36.66	0.00	*
593.3933762	3.369411045						34.51	0.00	*
307.1783576	3.051102532						34.37	3.32	
424.4284168	3.349989466	C28H56O2	[FA (28:0)] octacosanoic acid	2	Lipids: Fatty Acyls	Fatty Acids and Conjugates	33.63	21.94	*
244.2039482	3.923733324	C14H28O3	2S-Hydroxytetradecanoic acid	12	Lipids: Fatty Acyls	Fatty Acids and Conjugates	33.51	1.87	
298.1418731	7.006884609	C24H40N10O6S	Arg-Cys-Tyr-Arg	1	Peptide(tetra-)	Basic peptide	33.21	0.00	*
265.1314302	4.208394646	C14H19NO4	N(alpha)-Benzyloxycarbonyl-L-leucine	2	0	0	32.86	3.04	
427.4025923	3.41772186						26.36	15.63	*
242.1883417	3.753603349	C14H26O3	[FA oxo(14:0)] 3-oxo-tetradecanoic acid	11	Lipids: Fatty Acyls	Fatty Acids and Conjugates	24.14	4.66	
270.1704404	4.528166644						22.97	320.44	*
300.2089168	3.817577452	C20H28O2	[PR] Tretinoin/All-Trans Retinoic Acid	25	Lipids: Prenols	Retinol metabolism	21.11	0.00	*
130.074264	6.964017976	C5H10N2O2	Casein K	4	0	0	20.72	28.86	*
170.0944525	6.96370675	C9H14O3	Furfural diethyl acetal	2	0	0	20.26	3.24	*
395.3246907	3.682024344						19.77	16.84	*

151.0494985	11.02043641	C5H5N5O	Guanine	3	Nucleotide Metabolism	Purine metabolism	19.08	2.93	*
161.1133661	4.353980737						18.58	53.32	*
303.2926138	7.054758499						17.15	3.01	
212.1049938	4.362779034	C22H32O8	Didrovaltratum	2	Lipids: Prenols	Isoprenoids	16.98	1.06	
331.3238586	6.94392142						16.78	3.77	*
232.109964	8.182427639	C14H16O3	Kavapyrone	3	0	0	16.75	0.00	*
325.3708868	6.792449573	C22H47N	di-n-Undecylamine	1	0	0	16.40	3.46	*
200.0685345	11.70831361						16.01	1.10	
116.0585985	9.16511027	C4H8N2O2	Diacetylhydrazine	2	Xenobiotics Biodegradation and Metabolism	Drug metabolism – other enzymes	15.86	1.64	
410.4125984	3.360706245	C27H54O2	[FA (27:0)] heptacosanoic acid	2	Lipids: Fatty Acyls	Fatty Acids and Conjugates	15.78	8.29	*
264.1362327	4.454322394	C15H20O4	Abscisate	29	Biosynthesis of Secondary Metabolites	Carotenoid biosynthesis	15.69	2.99	
185.1415882	7.037002172						15.37	1.77	*
282.1469085	4.225293207	C15H22O5	[PR] Artemisin	6	Xenobiotics Drugs etc	artemisinin biosynthesis	14.94	7.83	*
182.0579275	4.544541653	C9H10O4	3-Methoxy-4-hydroxyphenylglycolaldehyde	13	Amino Acid Metabolism	Tyrosine metabolism	13.57	5.37	*

346.235929	3.887603091	C18H34O6	[FA hydroxy(18:0)] 9-hydroperoxy-12,13-dihydroxy-10-octadecenoic acid	3	Lipids: Fatty Acyls	Fatty Acids and Conjugates	11.74	3.31	
184.1099982	4.638226944	C10H16O3	1,6,6-Trimethyl-2,7-dioxabicyclo[3.2.2]nonan-3-one	9	Biosynthesis of Secondary Metabolites	Terpenoid biosynthesis	10.71	1.54	
191.0582217	3.232389933	C10H9NO3	5-Hydroxyindoleacetate	5	Amino Acid Metabolism	Tryptophan metabolism	10.67	0.00	*
145.0528119	6.895302981	C9H7NO	3-Methyleneoxindole	7	0	0	9.44	7.66	*
202.0843005	4.662166198	C9H14O5	Diethyl 2-methyl-3-oxosuccinate	1	0	0	9.32	1.33	
281.1260944	6.932001834	C14H19NO5	Harzianopyridone	1	0	0	9.11	1.13	*
332.198823	3.508922224	C20H28O4	[FA oxo,hydroxy(4:0)] 9-oxo-15S-hydroxy-5Z,10Z,13E,17Z-prostatetraenoic acid	20	Lipids: Fatty Acyls	Eicosanoids	8.86	2.17	*
182.0943963	4.631094015	C10H14O3	[PR] Iridotrial	8	Lipids: Prenols	Isoprenoids	8.81	1.40	*
200.104915	6.939687628	C10H16O4	[FA dioxo(10:0)] 3,6-dioxo-decanoic acid	7	Lipids: Fatty Acyls	Fatty Acids and Conjugates	8.72	1.03	*
701.2061276	3.43418838						8.45	3.94	*
286.2146106	3.99054859	C16H30O4	[FA (16:0/2:0)] Hexadecanedioic acid	5	Lipids: Fatty Acyls	Fatty Acids and Conjugates	8.28	1.80	

284.1986681	3.870148588	C16H28O4	(10S)-Juvenile hormone III diol	1	Biosynthesis of Secondary Metabolites	Insect hormone biosynthesis	8.24	4.08	*
146.0943797	7.139044855	C7H14O3	[FA hydroxy(7:0)] 2-hydroxy-heptanoic acid	8	Lipids: Fatty Acyls	Fatty Acids and Conjugates	8.24	1.67	
172.073701	6.903263685	C8H12O4	[FA dioxo(8:0)] 4,7-dioxo-octanoic acid	4	Lipids: Fatty Acyls	Fatty Acids and Conjugates	7.81	1.80	*
250.1569295	3.783328645	C15H22O3	Xanthoxin	9	Biosynthesis of Secondary Metabolites	Carotenoid biosynthesis	7.39	1.86	*
262.1203876	6.796308765	C15H18O4	[PR] Parthenin	10	Lipids: Prenols	Isoprenoids	7.14	1.18	
216.1362727	4.134480801	C11H20O4	[FA (11:0/2:0)] Undecanedioic acid	1	Lipids: Fatty Acyls	Fatty Acids and Conjugates	7.05	1.38	
455.4338668	3.426883305						6.95	1.51	*
326.3297013	6.214689728						6.93	8.17	
283.3237577	6.962160303	C19H41N	CTAB	1	0	0	6.86	3.53	*
319.2360078	3.758826137						6.83	16.18	*
110.0367606	7.23290254	C6H6O2	p-Benzenediol	5	Amino Acid Metabolism	Tyrosine metabolism__gamma-Hexachlorocyclohexane degradation__Bisphenol A degradation__2,4-Dichlorobenzoate degradation__Riboflavin metabolism	6.81	2.19	*
198.1089731	4.127518824						6.72	1.38	*

182.0943883	6.920541017	C10H14O3	5-Oxo-1,2-campholide	8	0	D-camphor degradation	6.55	1.65	*
166.0994489	6.964163704	C10H14O2	[PR] (+)-Bornane-2,5-dione	17	Lipids: Prenols	D-camphor degradation	6.50	1.43	*
165.079077	4.724369642	C9H11NO2	Benzocaine	7	Xenobiotics Drugs etc	0	6.49	2.21	*
240.0671811	3.776267529						6.37	2.27	*
164.0685807	6.953694175	C6H12O5	L-Rhamnulose	25	Carbohydrate Metabolism	Fructose and mannose metabolism	6.17	2.67	*
179.8228841	12.84772793						6.16	14.98	*
170.0944874	4.593531623	C9H14O3	2-butyl-4-hydroxy-5-methyl-3(2H)-furanone	2	0	furaneol biosynthesis	5.96	1.52	*
370.3084258	3.467135533	C22H42O4	2-monooleoylglycerol	3	Lipids: Glycerolipids	Monoradylglycerols	5.69	1.08	*
279.1470611	6.997991513	C15H21NO4	Metalaxyl	1	0	0	5.55	1.45	*
233.1991583	4.678735686						5.49	2.15	*
314.2462057	3.748673079	C18H34O4	[FA hydroxy(18:1)] 9,10-dihydroxy-12Z-octadecenoic acid	12	Lipids: Fatty Acyls	Fatty Acids and Conjugates	5.45	3.37	*
187.193533	11.4674037						5.40	178.34	
233.1627061	4.014616648	C28H44F2O3	[ST (3:0/3:0/3:0)] (5Z,7E)-(1S,3R)-24,24-difluoro-24a-homo-9,10-seco-5,7,10(19)-cholestatrien-1,3,25-triol	1	Lipids: Sterol lipids	Secosteroids	5.25	1.63	*
120.0939027	8.24470089	C9H12	1,2,4-Trimethylbenzene	6	0	0	5.10	0.93	

138.034873	4.310593421	C4H10O3S	1-butanesulfonate	1	0	0	5.02	13.59	
192.1152043	4.079255976	C12H16O2	[FA (12:4)] 2E,4E,8Z,10E-dodecatetraenoic acid	5	Lipids: Fatty Acyls	Fatty Acids and Conjugates	5.00	2.52	
179.0793399	9.985170044	C6H13NO5	D-Galactosamine	10	Carbohydrate Metabolism	Galactose metabolism	4.94	76.65	
316.2615676	3.798168815	C18H36O4	[FA hydroxy(18:0)] 9,10-dihydroxy-octadecanoic acid	19	Lipids: Fatty Acyls	Fatty Acids and Conjugates	4.65	2.36	
254.224894	3.574449575	C16H30O2	(9Z)-Hexadecenoic acid	19	Lipid Metabolism	Fatty acid biosynthesis	4.62	2.75	
162.0804012	4.345691081						4.59	1.69	*
166.0482438	4.018409423	C14H21N2O3ClS	Tos-Lys-CH2Cl	1	0	0	4.56	2.14	
165.0790719	6.935176517	C9H11NO2	D-Phenylalanine	7	Amino Acid Metabolism	Phenylalanine metabolism	4.55	2.47	*
228.09998	7.041807282	C11H16O5	[FA hydroxy(11:2/11:2)] 2R,9R-dihydroxy-3S,4S,7S,8S-diepoxy-5E,10-undecadien-1-ol	1	Lipids: Fatty Acyls	Fatty alcohols	4.52	2.32	*
188.0687172	4.908344432	C8H12O5	2-oxosuberate	1	0	0	4.48	1.25	*
232.1465445	3.998211533	C15H20O2	Costunolide	10	Biosynthesis of Secondary Metabolites	costunolide biosynthesis	4.47	1.08	*
330.2409753	4.240916683	C18H34O5	[FA trihydroxy(18:1)] 9S,12S,13S-trihydroxy-10E-octadecenoic acid	10	Lipids: Fatty Acyls	Octadecanoids	4.39	3.72	*
180.042562	10.46532978	C9H8O4	2-Hydroxy-3-(4-hydroxyphenyl)propenoate	11	Amino Acid Metabolism	Tyrosine metabolism	4.36	2.71	*

196.0737778	4.408795701	C10H12O4	phlorisobutyrophenone	9	Biosynthesis of Secondary Metabolites	cohumulone biosynthesis __ hyperforin biosynthesis __ bitter acids biosynthesis	4.34	1.31	*
134.1095411	4.328189315	C10H14	p-Cymene	5	Xenobiotics Biodegradation and Metabolism	Biphenyl degradation	4.27	1.03	*
354.3499976	3.372432788	C23H46O2	[FA (23:0)] tricosanoic acid	3	Lipids: Fatty Acyls	Fatty Acids and Conjugates	4.21	2.48	*
136.0994823	4.540200568	C15H28O4	[FA methyl(14:0/2:0)] 3-methyl-tetradecanedioic acid	3	Lipids: Fatty Acyls	Fatty Acids and Conjugates	4.12	4.03	*
202.0843009	6.948588053	C9H14O5	Diethyl 2-methyl-3-oxosuccinate	1	0	0	4.10	1.60	*
172.1101463	6.799671806	C9H16O3	[FA hydroxy(9:1)] 9-hydroxy-5Z-nonenoic acid	12	Lipids: Fatty Acyls	Fatty Acids and Conjugates	4.09	1.64	*
230.0557063	10.60153453	C15H21N6O9P	β-ketophosphonate	1	0	0	4.04	4.66	*
146.0943484	4.522466265	C7H14O3	ethyl-(2R)-methyl-(3S)-hydroxybutanoate	8	0	0	4.02	7.72	
294.2194175	3.557722054	C18H30O3	[FA oxo(5:1/5:0/8:0)] (1S,2S)-3-oxo-2-(2'Z-pentenyl)-cyclopentaneoctanoic acid	38	Lipids: Fatty Acyls	Octadecanoids	3.98	2.96	*
136.038579	9.428998403	C5H4N4O	Hypoxanthine	3	Nucleotide Metabolism	Purine metabolism	3.94	2.97	*
479.1499246	3.514378788						3.85	2.67	*
214.0856722	11.12541707						3.83	1.30	
124.0195041	7.561144459	C3H8O3S	propanesulfonate	1	0	0	3.80	1.04	

296.2351998	3.598732047	C18H32O3	[FA hydroxy(18:2)] 9S-hydroxy-10E,12Z-octadecadienoic acid	33	Lipids: Fatty Acyls	Linoleic acid metabolism	3.76	3.06	
268.1673607	3.989323338	C15H24O4	dihydroartemisinic acid hydroperoxide	1	Biosynthesis of Secondary Metabolites	artemisinin biosynthesis	3.71	3.82	*
394.1459801	6.798783927						3.69	2.85	*
160.1099854	4.459589262	C8H16O3	Ethyl ®-3-hydroxyhexanoate	14	0	0	3.66	10.60	
132.0938932	4.090048733	C10H12	Tetralin	2	Xenobiotics Biodegradation and Metabolism	1- and 2-Methylnaphthalene degradation	3.65	1.15	*
197.178059	3.847105558						3.64	1.42	*
286.2142948	7.181606847	C16H30O4	[FA (16:0/2:0)] Hexadecanedioic acid	5	Lipids: Fatty Acyls	Fatty Acids and Conjugates	3.63	1.06	*
203.1158977	4.663244407	C9H17NO4	O-Acetylcarnitine	1	Amino Acid Metabolism	Alanine and aspartate metabolism	3.59	2.06	*
219.110719	4.748501261	C9H17NO5	Pantothenate	1	Amino Acid Metabolism	beta-Alanine metabolism__Pantothenate and CoA biosynthesis	3.56	1.44	*
188.1050824	6.941415014	C9H16O4	Azelaic acid	2	Xenobiotics Drugs etc	Fatty Acids and Conjugates	3.52	2.08	*
186.0352438	4.558547419						3.47	2.18	*
162.1044632	4.331065234	C11H14O	[FA (11:2)] 4,10-undecadiynal	1	Lipids: Fatty Acyls	Fatty aldehydes	3.46	1.12	
188.0686933	7.167972245	C8H12O5	2-oxosuberate	1	0	0	3.45	1.72	*

202.0842663	11.35380382	C9H14O5	Diethyl 2-methyl-3-oxosuccinate	1	0	0	3.45	0.66	
288.2299748	4.112163135	C16H32O4	10,16-Dihydroxyhexadecanoic acid	6	Lipids: Fatty Acyls	cutin biosynthesis	3.44	7.24	*
181.074035	6.951596187	C9H11NO3	3-Amino-3-(4-hydroxyphenyl)propanoate	11	Amino Acid Metabolism	Tyrosine metabolism	3.40	2.58	*
106.0450029	4.395785001	C4H10OS	methionol	1	0	methionine degradation III	3.38	3.14	
184.1100472	6.933967982	C10H16O3	4,5-dihydro-5,5-dimethyl-4-(3-oxobutyl)furan-2(3H)-one	9	0	Terpenoid biosynthesis	3.34	1.53	*
126.0317039	5.142552141	C6H6O3	Phloroglucinol	8	Xenobiotics Biodegradation and Metabolism	Benzoate degradation via CoA ligation	3.31	0.00	*
219.1106994	7.012182943	C9H17NO5	Pantothenate	1	Amino Acid Metabolism	beta-Alanine metabolism__Pantothenate and CoA biosynthesis	3.31	2.77	*
396.3968879	3.368324122	C26H52O2	[FA (26:0)] hexacosanoic acid	3	Lipids: Fatty Acyls	Fatty Acids and Conjugates	3.29	3.08	*

137.0477109	7.476102102	C7H7NO2	Anthranilate	14	Xenobiotics Biodegradation and Metabolism	Benzoate degradation via hydroxylation__Tryptophan metabolism__Phenylalanine, tyrosine and tryptophan biosynthesis__Carbazole degradation__Benzoate degradation via CoA ligation__Acridone alkaloid biosynthesis	3.27	1.57	*
214.085092	4.667974762						3.27	1.35	*
176.0474139	6.988642714	C10H8O3	4-Methylumbelliferone	4	Xenobiotics Drugs etc	0	3.26	2.34	*
187.1208564	6.959383777	C9H17NO3	8-Amino-7-oxononanoate	3	Metabolism of Cofactors and Vitamins	Biotin metabolism	3.22	3.82	*
226.1680508	6.805338033	C12H22N2O2	1,8-Diazacyclotetradecane-2,9-dione	1	0	nylon-6 oligomer degradation	3.22	2.00	*
149.1052796	13.26189231	C6H15NO3	Triethanolamine	1	Lipid Metabolism	Glycerophospholipid metabolism	3.19	5.80	
118.0630419	6.96879189	C5H10O3	5-Hydroxypentanoate	12	Lipids: Fatty Acyls	Fatty Acids and Conjugates	3.17	4.72	*
229.1678443	4.312458925	C12H23NO3	N-Decanoylglycine	1	0	0	3.16	1.85	*
156.0423281	7.583351709	C7H8O4	2,3-Dihydro-2,3-dihydroxybenzoate	12	Biosynthesis of Polyketides and Nonribosomal Peptides	Biosynthesis of siderophore group nonribosomal peptides	3.12	1.74	

284.2350376	3.680870095	C17H32O3	[FA methoxy(16:1)] 2-methoxy-5Z-hexadecenoic acid	7	Lipids: Fatty Acyls	Fatty Acids and Conjugates	3.12	2.74	*
126.0654364	10.4881615	C3H6N6	Melamine	1	Xenobiotics Biodegradation and Metabolism	Atrazine degradation	3.10	2.70	*
342.2882521	4.514639302						3.03	1.20	*
382.381425	3.365633868	C25H50O2	[FA (25:0)] pentacosanoic acid	2	Lipids: Fatty Acyls	Fatty Acids and Conjugates	3.02	2.73	*
226.1571386	3.944150844						3.01	1.87	*
189.1728508	7.013453834						3.00	3.18	*
184.073623	4.665504684	C9H12O4	3-Methoxy-4-hydroxyphenylethyleneglycol	6	Amino Acid Metabolism	Tyrosine metabolism	2.99	1.34	*
132.0786855	7.178649172	C6H12O3	6-Hydroxyhexanoic acid	14	Xenobiotics Biodegradation and Metabolism	Caprolactam degradation	2.98	3.96	*
176.0837781	4.356874371	C11H12O2	Ethyl cinnamate	8	0	0	2.96	1.23	*
158.0579881	6.926834224	C7H10O4	2-Isopropylmaleate	5	Amino Acid Metabolism	Valine, leucine and isoleucine biosynthesis	2.94	1.53	*
252.1363759	4.238833755	C14H20O4	ubiquinol-1	1	0	0	2.92	1.44	*
433.7727695	3.432337223						2.92	3.72	*
242.2247014	3.618899138	C15H30O2	[FA methyl(14:0)] 12-methyl-tetradecanoic acid	9	Lipids: Fatty Acyls	Fatty Acids and Conjugates	2.88	2.65	
158.0943483	6.924590621	C8H14O3	[FA oxo(8:0)] 3-oxo-octanoic acid	9	Lipids: Fatty Acyls	Fatty Acids and Conjugates	2.87	2.20	*

130.0630654	6.964324808	C6H10O3	(S)-3-Methyl-2-oxopentanoic acid	17	Amino Acid Metabolism	Valine, leucine and isoleucine degradation__Valine, leucine and isoleucine biosynthesis	2.87	2.81	*
167.0218876	12.53279956	C7H5NO4	Pyridine-2,3-dicarboxylate	7	Amino Acid Metabolism	Tryptophan metabolism__beta-Alanine metabolism__Nicotinate and nicotinamide metabolism	2.85	2.45	*
170.0068214	7.548581624						2.83	1.78	
262.1416808	4.618622204	C21H36N10O6	Arg-Val-Asn-His	1	Peptide(tetra-)	Basic peptide	2.83	1.83	*
250.193143	7.197347814	C16H26O2	Methyl farnesoate	9	Biosynthesis of Secondary Metabolites	Insect hormone biosynthesis	2.83	1.12	*
160.0736387	6.948365001	C7H12O4	[FA (7:0/2:0)] Heptanedioic acid	4	Lipids: Fatty Acyls	Biotin metabolism	2.82	2.52	*
140.0838217	4.553757255	C8H12O2	2-Methyl-6-oxohepta-2,4-dienal	10	0	0	2.79	1.24	*
243.1834414	4.346888889	C13H25NO3	N-Undecanoylglycine	1	0	0	2.75	2.12	*
100.0160723	6.983032931	C4H4O3	2-oxobut-3-enanoate	1	0	3-methylquinoline degradation	2.70	2.31	*
226.0150546	4.49829871						2.68	1.85	
196.1101245	6.964266694	C22H32O6	Isodomedin	1	0	0	2.67	1.35	*
117.0789898	9.976705124	C5H11NO2	Betaine	16	Amino Acid Metabolism	Glycine, serine and threonine metabolism	2.66	43.26	
141.9267153	12.90692564						2.62	112.58	
236.1049527	4.63649485	C13H16O4	3-Dimethylallyl-4-hydroxymandelic acid	1	Biosynthesis of Secondary Metabolites	Novobiocin biosynthesis	2.62	2.93	

188.141433	4.355662406	C10H20O3	10-Hydroxydecanoic acid	13	Lipids: Fatty Acyls	Fatty Acids and Conjugates	2.62	3.50	*
132.0422887	6.987879057	C5H8O4	2-Acetolactate	16	Carbohydrate Metabolism	Butanoate metabolism__Pantothenate and CoA biosynthesis	2.60	2.10	*
132.0647213	10.44963373	C3H8N4O2	Methylenediurea	1	0	0	2.60	1.36	*
166.0994437	4.629462811	C10H14O2	Perillic acid	17	Biosynthesis of Secondary Metabolites	Limonene and pinene degradation	2.59	1.32	*
279.147599	4.249415135	C15H21NO4	Metalaxyl	1	0	0	2.54	0.77	*
242.1756667	3.937028833						2.53	13.07	*
224.1050611	4.16768463	C12H16O4	Aspidinol	3	0	0	2.52	1.41	*
162.0894716	8.431464523	C7H14O4	beta-Cymaropyranose	2	0	0	2.51	1.80	*
250.193168	3.87739831	C16H26O2	Triton X-100	9	0	0	2.50	1.79	*
176.0687313	11.345106	C7H12O5	(2R,3S)-3-Isopropylmalate	7	Amino Acid Metabolism	Valine, leucine and isoleucine biosynthesis	2.50	1.45	*
226.1932925	3.796716237	C14H26O2	(9Z)-Tetradecenoic acid	12	Lipids: Fatty Acyls	Fatty Acids and Conjugates	2.48	1.68	*
270.2194047	3.586544024	C16H30O3	[FA oxo(16:0)] 3-oxo-hexadecanoic acid	19	Lipids: Fatty Acyls	Fatty Acids and Conjugates	2.48	1.74	
350.3299093	7.083662281						2.48	0.90	*
198.0889976	10.97660729	C10H14O4	cis-2,3-Dihydroxy-2,3-dihydro-p-cumate	5	Xenobiotics Biodegradation and Metabolism	Biphenyl degradation	2.47	0.88	*
153.9936822	6.940412838	C3H6O5S	3-sulfopropanoate	1	0	0	2.47	1.97	*

214.1571247	3.994022663	C12H22O3	3-Oxododecanoic acid	10	Lipids: Fatty Acyls	Fatty Acids and Conjugates	2.43	2.48	*
272.2351531	3.652083757	C16H32O3	16-hydroxypalmitate	18	0	cutin biosynthesis	2.43	1.70	
132.0786756	4.663409789	C6H12O3	[FA hydroxy(6:0)] 4-hydroxy-hexanoic acid	14	Lipids: Fatty Acyls	Fatty Acids and Conjugates	2.42	5.13	*
174.0528197	11.63002737	C7H10O5	2-oxopimelate	6	0	0	2.42	1.13	
144.1150609	4.22273675	C8H16O2	[FA (8:0)] octanoic acid	11	Lipids: Fatty Acyls	Fatty acid biosynthesis	2.42	2.65	
340.3344535	3.432481202	C22H44O2	Docosanoic acid	4	Lipid Metabolism	Biosynthesis of unsaturated fatty acids	2.42	1.97	*
261.2303321	4.534357224						2.41	1.15	*
323.1367699	6.95870557	C16H21NO6	Acremoauxin A	1	0	0	2.41	1.53	
370.31946	4.39911797						2.40	1.25	*
234.0891971	3.866670836	C13H14O4	1’-Acetoxychavicol acetate	1	0	0	2.40	1.35	*
226.0843587	7.129955181	C11H14O5	Genipin	1	0	0	2.39	1.41	*
215.152245	4.600996542	C11H21NO3	N-Nonanoylglycine	1	0	0	2.37	1.99	*
144.0786759	4.67018503	C7H12O3	7-oxoheptanoate	8	Metabolism of Cofactors and Vitamins	coenzyme B biosynthesis	2.35	1.69	*
130.0994459	4.407070062	C7H14O2	[FA (7:0)] heptanoic acid	14	Lipids: Fatty Acyls	Fatty Acids and Conjugates	2.34	2.04	
223.1208861	4.271329826	C12H17NO3	Cerulenin	2	0	0	2.34	1.33	*
289.2615705	4.333706835						2.34	1.15	*
221.1862031	3.980520082						2.30	1.26	*

122.036811	6.929763703	C7H6O2	Benzoate	6	Amino Acid Metabolism	Phenylalanine metabolism__Benzoate degradation via hydroxylation__Biphenyl degradation__Toluene and xylene degradation__Benzoate degradation via CoA ligation__Alkaloid biosynthesis II	2.28	1.34	*
285.3030004	7.173186721	C18H39NO	[SP] 1-deoxy-sphinganine	1	Lipids: Sphingolipids	Sphingoid bases	2.27	2.14	*
99.06840489	4.97611024	C5H9NO	2-hydroxy-2-methylbutyronitrile	3	0	lotaustralin degradation __ lotaustralin biosynthesis __ superpathway of linamarin and lotaustralin biosynthesis	2.26	1.36	*
202.1570242	4.298520934	C11H22O3	[FA hydroxy(11:0)] 2-hydroxy-undecanoic acid	6	Lipids: Fatty Acyls	Fatty Acids and Conjugates	2.25	1.70	*
259.1419177	6.947968377	C12H21NO5	N-(3-oxooctanoyl)-L-homoserine	1	0	0	2.24	1.55	*
355.3085939	6.951700913	C21H41NO3	Pristanoylglycine	1	0	0	2.23	2.79	*
261.1938856	8.491615699						2.20	2.62	*
259.1207933	6.906615363	C15H17NO3	Norsanguinine	1	0	0	2.20	2.14	*
214.1934377	3.660561097	C13H26O2	CAI-1	15	0	0	2.20	1.98	*
105.0790067	15.71720344	C4H11NO2	Diethanolamine	2	Lipid Metabolism	Glycerophospholipid metabolism	2.19	8.89	
300.033801	3.883011142						2.18	1.35	*
144.0786991	6.928550016	C7H12O3	trans-4-Hydroxycyclohexanecarboxylate	8	0	0	2.18	2.10	*
186.1620441	3.754217934	C11H22O2	[FA (11:0)] undecanoic acid	12	Lipids: Fatty Acyls	Fatty Acids and Conjugates	2.17	2.27	

139.0633421	6.943404734	C7H9NO2	3,4-dihydroxybenzylamine	3	0	0	2.17	1.44	*
200.0685894	6.960238504						2.17	1.23	*
313.3343715	6.986810707	C20H43NO	[SP amino,dimethyl(18:0)] 2-amino-14,16-dimethyloctadecan-3-ol	1	Lipids: Sphingolipids	Sphingoid bases	2.15	2.21	*
154.0994695	4.299231172	C9H14O2	[FA (9:2)] 2,6-nonadienoic acid	11	Lipids: Fatty Acyls	Fatty Acids and Conjugates	2.15	1.16	*
375.1749437	6.897616668	C14H25N5O7	Thr-Gln-Gln	7	Peptide(tri-)	Polar peptide	2.14	2.78	*
219.1471471	4.504506012						2.13	1.60	*
230.1518634	4.095008544	C12H22O4	Dodecanedioic acid	2	Lipids: Fatty Acyls	Fatty Acids and Conjugates	2.10	1.72	*
327.1931595	3.323379908						2.09	1.89	
188.0686979	8.198771354	C8H12O5	2-oxosuberate	1	0	0	2.08	1.16	*
177.1365522	7.363797897						2.08	1.81	*
202.1205572	4.168702143	C10H18O4	Diethyl adipate	2	0	0	2.08	1.39	*
69.2790471	4.705598368						2.08	1.99	*
178.1205684	4.674535429						2.08	1.64	*
255.1680695	4.675243528						2.07	1.29	*
186.1257293	4.359490602	C10H18O3	10-Oxodecanoate	19	Lipids: Fatty Acyls	Fatty Acids and Conjugates	2.06	2.10	*
168.0786953	6.951743571	C9H12O3	1,3,5-trimethoxybenzene	3	Biosynthesis of Secondary Metabolites	1,3,5-trimethoxybenzene biosynthesis	2.06	1.46	*
110.0480259	7.504378673	C5H6N2O	Imidazole-4-acetaldehyde	2	Amino Acid Metabolism	Histidine metabolism	2.05	2.10	*

178.1105591	8.409124782	C10H14N2O	(S)-6-Hydroxynicotine	7	Metabolism of Cofactors and Vitamins	Nicotinate and nicotinamide metabolism	2.04	1.68	*
120.0575019	4.45589357	C8H8O	Phenylacetaldehyde	8	Amino Acid Metabolism	Phenylalanine metabolism__Styrene degradation	2.04	1.10	*
283.2873884	6.942941467	C18H37NO	Octadecanamide	1	Lipids: Fatty Acyls	Fatty amides	2.04	1.77	*
147.06843	4.900126961	C9H9NO	3-Methyloxindole	3	0	0	2.03	1.49	*
240.067164	6.102532907						2.03	1.26	*
110.0037677	8.627635049	C2H6O3S	ethanesulfonate	2	0	0	2.03	0.92	*
389.1905061	6.824683765	C15H27N5O7	Ala-Thr-Ala-Gln	10	Peptide(tetra-)	Polar peptide	2.03	1.67	*
176.1049737	8.805242333	C8H16O4	[FA hydroxy(8:0)] 6,8-dihydroxy-octanoic acid	2	Lipids: Fatty Acyls	Fatty Acids and Conjugates	2.02	1.59	*
256.2037125	3.710852142	C15H28O3	[FA oxo(15:0)] 4-oxo-pentadecanoic acid	5	Lipids: Fatty Acyls	Fatty Acids and Conjugates	2.02	2.40	*
138.0106291	13.45512776						2.02	2.56	*
204.0610521	11.81977568						2.01	1.69	
190.0630153	4.554757422	C11H10O3	7-Ethoxycoumarin	3	0	0	2.01	1.71	*
122.0401658	6.910169832	C8H12N4O5	5-Azacytidine	1	Xenobiotics Drugs etc	0	2.01	1.58	*
240.0999164	4.36168162	C25H28N4O6	Glu-Phe-Trp	1	Peptide(tri-)	Hydrophobic peptide	2.01	1.52	*

205.131605	6.933815837	C9H19NO4	Pantothenol	1	Metabolism of Cofactors and Vitamins	Pantothenate and CoA biosynthesis	2.01	2.43	*
214.0994806	3.922274279	C14H14O2	(+)-(1R,2R)-1,2-Diphenylethane-1,2-diol	7	0	0	2.00	1.33	*
368.3656593	3.398343169	C24H48O2	Tetracosanoic acid	5	Lipid Metabolism	Biosynthesis of unsaturated fatty acids	2.00	1.92	*
282.2559773	3.501008117	C18H34O2	[FA (18:1)] 9Z-octadecenoic acid	29	Lipids: Fatty Acyls	Fatty acid biosynthesis__Biosynthesis of unsaturated fatty acids	2.00	1.55	

Table 17 Metabolites detected in Nakhla at levels at least twice those detected in the blanks, table shows mass, retention time, characteristics of putatively identified metabolite, and the relative abundance of the metabolite in Nakhla compared to the day 1 blank (FBD1) and the same for those in Lafayette. Metabolites are arranged in descending order of levels in Nakhla relative to the procedural blanks. Some metabolites present in the list were also present in other samples, others were also identified by Polyomics as lower definition peaks (denoted by an asterisk in the final column).

Mass (Da)	Retention time (min)	Formula	Putative metabolite	Number of isomers	Map	Pathway	Fold-change Na vs FBD1	Fold-change La vs FBD1	Low definition peak
234.1831067	4.35775138						1625.42	0.00	
270.1704404	4.528166644						320.44	22.97	*
306.2407481	4.024225778						286.87	0.00	
190.1117183	4.071398043						239.93	266.94	*
248.1623186	4.640255398						208.68	0.00	*
163.0125941	3.920350011	C5H9NOS2	S-allylmercapto-L-cysteine	2	0	0	181.65	0.00	*
347.2307864	8.756649984						180.98	0.00	*
187.193533	11.4674037						178.34	5.40	*
163.1209635	17.86669225	C20H32F2O	3,3-Difluoro-17-methyl-5alpha-androstan-17beta-ol	1	0	0	167.02	1.52	*
79.94058738	12.27585464						158.95	0.00	
141.9267153	12.90692564						112.58	2.62	
314.2458477	3.753200001	C18H34O4	[FA hydroxy(18:1)] 9,10-dihydroxy-12Z-	12	Lipids: Fatty Acyls	Fatty Acids and Conjugates	78.94	465.05	*

			octadecenoic acid						
97.97707409	12.27227822	H3O4P	Orthophosphate	1	Energy Metabolism	Oxidative phosphorylation__Photosynthesis__Peptidoglycan biosynthesis	78.87	1.46	
323.1861615	9.859244453	C36H54O10	Abrusoside A	1	0	0	77.29	0.00	*
179.0793399	9.985170044	C6H13NO5	D-Galactosamine	10	Carbohydrate Metabolism	Galactose metabolism	76.65	4.94	
225.0904512	4.019998593						72.04	0.00	*
333.2151109	9.211503046	C16H31NO6	octyl 2-acetamido-2-deoxy-α-D-glucopyranoside	1	0	0	71.52	0.85	*
161.1133661	4.353980737						53.32	18.58	*
218.115536	7.014432469	C10H18O5	3-Hydroxysebacica cid	2	Lipids: Fatty Acyls	0	51.39	241.43	*
443.3609682	6.973075705	C25H49NO5	12-Hydroxy-12-octadecanoylcarnitine	1	0	0	45.40	1.52	*
117.0789898	9.976705124	C5H11NO2	Betaine	16	Amino Acid Metabolism	Glycine, serine and threonine metabolism	43.26	2.66	

177.1365418	15.29984879						36.11	0.95	*
129.9492101	8.154869588						33.71	0.00	*
258.1831483	3.969324523	C14H26O4	[FA (14:0/2:0)] Tetradecanedioic acid	6	Lipids: Fatty Acyls	Fatty Acids and Conjugates	31.59	218.63	*
373.3191249	7.49435779						30.83	1.08	*
130.074264	6.964017976	C5H10N2O2	Casein K	4	0	0	28.86	20.72	*
140.0222264	9.855500081	C5H4N2O3	2-hydroxy-4-carboxypyrimidine	1	0	lathyrine biosynthesis	25.04	0.00	*
427.3661555	6.954590861	C25H49NO4	Stearoylcarnitine	1	0	0	24.83	0.87	*
212.0951717	4.181002231	C13H12N2O	Harmine	2	0	beta-carboline biosynthesis	24.22	0.00	*
175.8967495	8.254216766						23.16	0.00	*
397.8332497	12.30424873						21.98	0.95	*
424.4284168	3.349989466	C28H56O2	[FA (28:0)] octacosanoic acid	2	Lipids: Fatty Acyls	Fatty Acids and Conjugates	21.94	33.63	*
667.0677537	3.234492348						20.95	0.88	*
334.2144589	3.847200012	C20H30O4	Prostaglandin A2	32	Lipids: Fatty Acyls	Arachidonic acid metabolism	20.20	272.23	*
338.2098075	3.987374973	C19H30O5	Shiromodiol diacetate	1	0	0	18.61	229.30	*
395.3246907	3.682024344						16.84	19.77	*
319.2360078	3.758826137						16.18	6.83	*
427.4025923	3.41772186						15.63	26.36	*

159.9515238	12.62386999						15.03	0.89	
179.8228841	12.84772793						14.98	6.16	*
123.8901189	12.91635691						14.82	0.00	*
260.1988943	4.297238068	C14H28O4	[FA hydroxy(14:0)] 3,11-dihydroxy-tetradecanoic acid	1	Lipids: Fatty Acyls	Fatty Acids and Conjugates	13.62	133.89	
138.034873	4.310593421	C4H10O3S	1-butanesulfonate	1	0	0	13.59	5.02	*
209.9422545	12.47618338						13.34	1.26	
242.1756667	3.937028833						13.07	2.53	
387.334676	7.242897008	C56H86O	2-decaprenylphenol	1	Metabolism of Cofactors and Vitamins	ubiquinone-10 biosynthesis (prokaryotic)	11.58	0.91	
320.1988525	3.563151798	C19H28O4	ubiquinol-2	4	Metabolism of Cofactors and Vitamins	Oxidative phosphorylation	11.57	101.68	
183.056567	10.19431763	C5H13NO4S	Choline sulfate	1	0	choline-O-sulfate degradation	11.18	0.86	
160.1099854	4.459589262	C8H16O3	Ethyl (R)-3-hydroxyhexanoate	14	0	0	10.60	3.66	
449.371686	3.69379667						10.39	1.07	
225.8974484	12.4088671						9.25	1.09	

105.0790067	15.71720344	C4H11NO2	Diethanolamine	2	Lipid Metabolism	Glycerophospholipid metabolism	8.89	2.19	
139.9518441	12.40683607						8.84	1.29	
410.4125984	3.360706245	C27H54O2	[FA (27:0)] heptacosanoic acid	2	Lipids: Fatty Acyls	Fatty Acids and Conjugates	8.29	15.78	*
326.3297013	6.214689728						8.17	6.93	*
304.2250566	4.580775016	C16H32O5	[FA trihydroxy(16:0)] 2,15,16-trihydroxy-hexadecanoic acid	4	Lipids: Fatty Acyls	Fatty Acids and Conjugates	8.00	1560.24	*
282.1469085	4.225293207	C15H22O5	[PR] Artemisin	6	Xenobiotics Drugs etc	artemisinin biosynthesis	7.83	14.94	*
146.0943484	4.522466265	C7H14O3	ethyl-(2R)-methyl-(3S)-hydroxybutanoate	8	0	0	7.72	4.02	
145.0528119	6.895302981	C9H7NO	3-Methyleneoxindole	7	0	0	7.66	9.44	*
288.2299748	4.112163135	C16H32O4	10,16-Dihydroxyhexadecanoic acid	6	Lipids: Fatty Acyls	cutin biosynthesis	7.24	3.44	
83.96143352	12.3525846	HO3Cl	Chlorate	1	0	0	7.19	1.23	*

149.1052525	8.639501379	C6H15NO3	Triethanolamine	1	Lipid Metabolism	Glycerophospholipid metabolism	7.14	1.51	*
266.115596	4.166475817	C28H36O10	12alpha-Hydroxyamoorstatin	1	0	0	6.52	109.05	
216.1474162	4.916623525	C10H20N2O3	Val-Val	1	Peptide(di-)	Hydrophobic peptide	6.30	1.38	*
174.1077343	4.03204274						6.29	1.99	*
72.05748245	4.323762395	C4H8O	Butanal	4	Carbohydrate Metabolism	Butanoate metabolism	6.06	1.19	*
127.1361244	18.50782069	C8H17N	Coniine	1	0	gamma-coniciene and coniine biosynthesis	5.98	1.62	*
149.1052796	13.26189231	C6H15NO3	Triethanolamine	1	Lipid Metabolism	Glycerophospholipid metabolism	5.80	3.19	
166.0664077	4.250626678	C6H14O3S	hexanesulfonate	1	0	0	5.49	55.57	*
182.0579275	4.544541653	C9H10O4	3-Methoxy-4-hydroxyphenylglycolaldehyde	13	Amino Acid Metabolism	Tyrosine metabolism	5.37	13.57	*
132.0786756	4.663409789	C6H12O3	[FA hydroxy(6:0)] 4-hydroxy-hexanoic acid	14	Lipids: Fatty Acyls	Fatty Acids and Conjugates	5.13	2.42	*
324.1575623	4.266622179	C17H24O6	Tetraneurin E	1	0	0	4.75	704.04	*

118.0630419	6.96879189	C5H10O3	5-Hydroxypentanoate	12	Lipids: Fatty Acyls	Fatty Acids and Conjugates	4.72	3.17	*
230.0557063	10.60153453	C15H21N6O9P	β-ketophosphonate	1	0	0	4.66	4.04	*
242.1883417	3.753603349	C14H26O3	[FA oxo(14:0)] 3-oxo-tetradecanoic acid	11	Lipids: Fatty Acyls	Fatty Acids and Conjugates	4.66	24.14	*
243.077462	11.33612322						4.56	0.34	*
152.0506308	4.569143772	C5H12O3S	pentanesulfonate	1	0	0	4.56	60.41	*
172.0737131	9.975112446	C8H12O4	2-Octenedioicacid	4	0	0	4.32	1.20	
119.0946764	11.90443553	C5H13NO2	betaine aldehyde hydrate	1	0	glycine betaine biosynthesis III (plants)	4.09	0.94	
284.1986681	3.870148588	C16H28O4	(10S)-Juvenile hormone III diol	1	Biosynthesis of Secondary Metabolites	Insect hormone biosynthesis	4.08	8.24	*
136.0994823	4.540200568	C15H28O4	[FA methyl(14:0/2:0)] 3-methyl-tetradecanedioic acid	3	Lipids: Fatty Acyls	Fatty Acids and Conjugates	4.03	4.12	*

132.0786855	7.178649172	C6H12O3	6-Hydroxyhexanoic acid	14	Xenobiotics Biodegradation and Metabolism	Caprolactam degradation	3.96	2.98	*
701.2061276	3.43418838						3.94	8.45	*
268.1673607	3.989323338	C15H24O4	dihydroartemisinic acid hydroperoxide	1	Biosynthesis of Secondary Metabolites	artemisinin biosynthesis	3.82	3.71	*
187.1208564	6.959383777	C9H17NO3	8-Amino-7-oxononanoate	3	Metabolism of Cofactors and Vitamins	Biotin metabolism	3.82	3.22	*
331.3238586	6.94392142						3.77	16.78	*
330.2409753	4.240916683	C18H34O5	[FA trihydroxy(18:1)] 9S,12S,13S-trihydroxy-10E-octadecenoic acid	10	Lipids: Fatty Acyls	Octadecanoids	3.72	4.39	*
433.7727695	3.432337223						3.72	2.92	*
202.1319217	7.997385922	C9H18N2O3	Leu-Ala	3	Peptide(di-)	Hydrophobic peptide	3.56	0.94	
283.3237577	6.962160303	C19H41N	CTAB	1	0	0	3.53	6.86	*
188.141433	4.355662406	C10H20O3	10-Hydroxydecanoic acid	13	Lipids: Fatty Acyls	Fatty Acids and Conjugates	3.50	2.62	*
325.3708868	6.792449573	C22H47N	di-n-Undecylamine	1	0	0	3.46	16.40	*

314.2462057	3.748673079	C18H34O4	[FA hydroxy(18:1)] 9,10-dihydroxy-12Z-octadecenoic acid	12	Lipids: Fatty Acyls	Fatty Acids and Conjugates	3.37	5.45	*
299.2461027	3.627046151	C17H33NO3	Pentadecanoylglycine	1	0	0	3.35	1.33	*
307.1783576	3.051102532						3.32	34.37	*
346.235929	3.887603091	C18H34O6	[FA hydroxy(18:0)] 9-hydroperoxy-12,13-dihydroxy-10-octadecenoic acid	3	Lipids: Fatty Acyls	Fatty Acids and Conjugates	3.31	11.74	*
170.0944525	6.96370675	C9H14O3	Furfural diethyl acetal	2	0	0	3.24	20.26	*
148.1252587	3.720875442						3.21	1.57	*
189.1728508	7.013453834						3.18	3.00	*
208.1076324	5.016112125						3.15	124.24	*
106.0450029	4.395785001	C4H10OS	methionol	1	0	methionine degradation III	3.14	3.38	
396.3968879	3.368324122	C26H52O2	[FA (26:0)] hexacosanoic acid	3	Lipids: Fatty Acyls	Fatty Acids and Conjugates	3.08	3.29	*

296.2351998	3.598732047	C18H32O3	[FA hydroxy(18:2)] 9S-hydroxy-10E,12Z-octadecadienoic acid	33	Lipids: Fatty Acyls	Linoleic acid metabolism	3.06	3.76	
265.1314302	4.208394646	C14H19NO4	N(alpha)-Benzyloxycarbonyl-L-leucine	2	0	0	3.04	32.86	*
303.2926138	7.054758499						3.01	17.15	*
133.8752051	12.082647						3.00	1.12	
264.1362327	4.454322394	C15H20O4	Abscisate	29	Biosynthesis of Secondary Metabolites	Carotenoid biosynthesis	2.99	15.69	*
136.1082023	6.912257724						2.98	1.29	*
282.2559151	6.747641017	C18H34O2	(6Z)-Octadecenoic acid	29	Lipids: Fatty Acyls	Fatty Acids and Conjugates	2.97	0.98	*
136.038579	9.428998403	C5H4N4O	Hypoxanthine	3	Nucleotide Metabolism	Purine metabolism	2.97	3.94	*
294.2194175	3.557722054	C18H30O3	[FA oxo(5:1/5:0/8:0)] (1S,2S)-3-oxo-2-(2'Z-pentenyl)-cyclopentaneoctanoic acid	38	Lipids: Fatty Acyls	Octadecanoids	2.96	3.98	*

236.1049527	4.63649485	C13H16O4	3-Dimethylallyl-4-hydroxymandelic acid	1	Biosynthesis of Secondary Metabolites	Novobiocin biosynthesis	2.93	2.62	*
151.0494985	11.02043641	C5H5N5O	Guanine	3	Nucleotide Metabolism	Purine metabolism	2.93	19.08	*
394.1459801	6.798783927						2.85	3.69	*
130.0630554	4.737645285	C6H10O3	3-Oxo-4-methylpentanoic acid	17	Amino Acid Metabolism	Valine, leucine and isoleucine degradation	2.83	1.28	*
111.9830478	8.656507313	CH4O4S	Monomethyl sulfate	2	0	0	2.82	0.45	
130.0630654	6.964324808	C6H10O3	(S)-3-Methyl-2-oxopentanoic acid	17	Amino Acid Metabolism	Valine, leucine and isoleucine degradation__Valine, leucine and isoleucine biosynthesis	2.81	2.87	*
171.1259391	4.414911091	C9H17NO2	Gabapentin	1	Xenobiotics Drugs etc	0	2.80	1.31	
355.3085939	6.951700913	C21H41NO3	Pristanoylglycine	1	0	0	2.79	2.23	*
375.1749437	6.897616668	C14H25N5O7	Thr-Gln-Gln	7	Peptide(tri-)	Polar peptide	2.78	2.14	*
219.1106994	7.012182943	C9H17NO5	Pantothenate	1	Amino Acid Metabolism	beta-Alanine metabolism__Pantothenate and CoA biosynthesis	2.77	3.31	*

302.2246569	3.528523531	C20H30O2	[FA (20:5)] 5Z,8Z,11Z,14Z,17Z-eicosapentaenoic acid	43	Lipids: Fatty Acyls	Biosynthesis of unsaturated fatty acids	2.76	118.18	*
254.224894	3.574449575	C16H30O2	(9Z)-Hexadecenoic acid	19	Lipid Metabolism	Fatty acid biosynthesis	2.75	4.62	
210.016693	15.30791373						2.74	1.02	*
284.2350376	3.680870095	C17H32O3	[FA methoxy(16:1)] 2-methoxy-5Z-hexadecenoic acid	7	Lipids: Fatty Acyls	Fatty Acids and Conjugates	2.74	3.12	*
382.381425	3.365633868	C25H50O2	[FA (25:0)] pentacosanoic acid	2	Lipids: Fatty Acyls	Fatty Acids and Conjugates	2.73	3.02	*
180.042562	10.46532978	C9H8O4	2-Hydroxy-3-(4-hydroxyphenyl)propenoate	11	Amino Acid Metabolism	Tyrosine metabolism	2.71	4.36	*
126.0654364	10.4881615	C3H6N6	Melamine	1	Xenobiotics Biodegradation and Metabolism	Atrazine degradation	2.70	3.10	
364.0981476	12.42192977						2.68	1.93	

164.0685807	6.953694175	C6H12O5	L-Rhamnulose	25	Carbohydrate Metabolism	Fructose and mannose metabolism	2.67	6.17	*
479.1499246	3.514378788						2.67	3.85	*
144.1150609	4.22273675	C8H16O2	[FA (8:0)] octanoic acid	11	Lipids: Fatty Acyls	Fatty acid biosynthesis	2.65	2.42	
242.2247014	3.618899138	C15H30O2	[FA methyl(14:0)] 12-methyl-tetradecanoic acid	9	Lipids: Fatty Acyls	Fatty Acids and Conjugates	2.65	2.88	
281.2716868	3.727217096	C18H35NO	[FA (18:1)] 9Z-octadecenamide	1	Lipids: Fatty Acyls	Fatty amides	2.63	1.65	
261.1938856	8.491615699						2.62	2.20	*
181.074035	6.951596187	C9H11NO3	3-Amino-3-(4-hydroxyphenyl)propanoate	11	Amino Acid Metabolism	Tyrosine metabolism	2.58	3.40	*
139.9779627	14.47042137	C2H4O5S	Sulfoacetate	1	Amino Acid Metabolism	Taurine and hypotaurine metabolism	2.57	1.71	
155.9469832	8.661650457						2.57	0.43	
138.0106291	13.45512776						2.56	2.02	*
257.1626829	8.99923933	C13H23NO4	2-Hexenoylcarnitine	1	0	0	2.55	1.68	
160.0736387	6.948365001	C7H12O4	[FA (7:0/2:0)]	4	Lipids: Fatty	Biotin	2.52	2.82	*

			Heptanedioic acid		Acyls	metabolism			
192.1152043	4.079255976	C12H16O2	[FA (12:4)] 2E,4E,8Z,10E-dodecatetraenoic acid	5	Lipids: Fatty Acyls	Fatty Acids and Conjugates	2.52	5.00	*
199.1572446	9.893680253	C11H21NO2	2-Hexenoylcholine	1	0	0	2.50	1.28	*
214.1571247	3.994022663	C12H22O3	3-Oxododecanoic acid	10	Lipids: Fatty Acyls	Fatty Acids and Conjugates	2.48	2.43	*
354.3499976	3.372432788	C23H46O2	[FA (23:0)] tricosanoic acid	3	Lipids: Fatty Acyls	Fatty Acids and Conjugates	2.48	4.21	*
165.0790719	6.935176517	C9H11NO2	D-Phenylalanine	7	Amino Acid Metabolism	Phenylalanine metabolism	2.47	4.55	*
135.104858	6.925193591	C9H13N	Amphetamine	2	Xenobiotics Drugs etc	0	2.45	1.60	*
167.0218876	12.53279956	C7H5NO4	Pyridine-2,3-dicarboxylate	7	Amino Acid Metabolism	Tryptophan metabolism__beta-Alanine metabolism__Nicotinate and nicotinamide metabolism	2.45	2.85	*
201.1729197	7.528871376	C11H23NO2	[FA amino(11:0)] 11-amino-	2	Lipids: Fatty Acyls	Amino Fatty Acids	2.44	1.33	*

			undecanoic acid						
205.131605	6.933815837	C9H19NO4	Pantothenol	1	Metabolism of Cofactors and Vitamins	Pantothenate and CoA biosynthesis	2.43	2.01	*
361.2904712	3.460699128						2.41	1.67	
256.2037125	3.710852142	C15H28O3	[FA oxo(15:0)] 4-oxo-pentadecanoic acid	5	Lipids: Fatty Acyls	Fatty Acids and Conjugates	2.40	2.02	*
134.0579507	9.487412073	C5H10O4	Deoxyribose	8	Carbohydrate Metabolism	Pentose phosphate pathway	2.39	1.17	*
316.2615676	3.798168815	C18H36O4	[FA hydroxy(18:0)] 9,10-dihydroxy-octadecanoic acid	19	Lipids: Fatty Acyls	Fatty Acids and Conjugates	2.36	4.65	*
114.031724	6.95000704	C5H6O3	2-Hydroxy-2,4-pentadienoate	6	Amino Acid Metabolism	Phenylalanine metabolism__Benzoate degradation via hydroxylation__Biphenyl degradation__Toluene and xylene	2.35	1.91	*

						degradation__1,4-Dichlorobenzene degradation__Fluorene degradation__Carbazole degradation__Ethylbenzene degradation__Styrene degradation			
176.0474139	6.988642714	C10H8O3	4-Methylumbelliferone	4	Xenobiotics Drugs etc	0	2.34	3.26	*
248.1049891	4.320286788	C14H16O4	Prenyl caffeate	2	0	0	2.32	131.23	*
228.09998	7.041807282	C11H16O5	[FA hydroxy(11:2/11:2)] 2R,9R-dihydroxy-3S,4S,7S,8S-diepoxy-5E,10-undecadien-1-ol	1	Lipids: Fatty Acyls	Fatty alcohols	2.32	4.52	*
100.0160723	6.983032931	C4H4O3	2-oxobut-3-enanoate	1	0	3-methylquinoline degradation	2.31	2.70	*

201.2094714	11.36344615						2.30	1.66	*
186.1620441	3.754217934	C11H22O2	[FA (11:0)] undecanoic acid	12	Lipids: Fatty Acyls	Fatty Acids and Conjugates	2.27	2.17	
240.0671811	3.776267529						2.27	6.37	
521.2310848	3.599835789	C24H35N5O6S	Cys-Leu-Thr-Trp	4	Peptide(tetra-)	Hydrophobic peptide	2.24	1.24	*
229.240634	9.731849162	C14H31NO	[SP (14:0)] 1-deoxy-tetradecasphinganine	1	Lipids: Sphingolipids	Sphingoid bases	2.21	1.80	
165.079077	4.724369642	C9H11NO2	Benzocaine	7	Xenobiotics Drugs etc	0	2.21	6.49	*
313.3343715	6.986810707	C20H43NO	[SP amino,dimethyl(18:0)] 2-amino-14,16-dimethyloctadecan-3-ol	1	Lipids: Sphingolipids	Sphingoid bases	2.21	2.15	*
193.0737168	6.957841896	C10H11NO3	5,6-Dihydroxy-3-methyl-2-oxo-1,2,5,6-tetrahydroquinoline	10	0	3-methylquinoline degradation	2.21	1.32	*
172.1464749	3.920466255	C10H20O2	Decanoic acid	9	Lipid Metabolism	Fatty acid biosynthesis	2.20	1.88	

158.0943483	6.924590621	C8H14O3	[FA oxo(8:0)] 3-oxo-octanoic acid	9	Lipids: Fatty Acyls	Fatty Acids and Conjugates	2.20	2.87	*
108.093909	4.101982469	C16H24	[PR] (+)-3-longipinen-5-one	1	Lipids: Prenols	Isoprenoids	2.19	1.80	*
110.0367606	7.23290254	C6H6O2	p-Benzenediol	5	Amino Acid Metabolism	Tyrosine metabolism__gamma-Hexachlorocyclohexane degradation__Bisphenol A degradation__2,4-Dichlorobenzoate degradation__Riboflavin metabolism	2.19	6.81	*
186.0352438	4.558547419						2.18	3.47	*
174.1256621	4.286600005	C9H18O3	[FA hydroxy(9:0)] 2-hydroxy-nonanoic acid	8	Lipids: Fatty Acyls	Fatty Acids and Conjugates	2.18	1.29	

332.198823	3.508922224	C20H28O4	[FA oxo,hydroxy(4:0)] 9-oxo-15S-hydroxy-5Z,10Z,13E,17Z-prostatetraenoic acid	20	Lipids: Fatty Acyls	Eicosanoids	2.17	8.86	*
233.1991583	4.678735686						2.15	5.49	*
166.0482438	4.018409423	C14H21N2O3ClS	Tos-Lys-CH2Cl	1	0	0	2.14	4.56	
259.1207933	6.906615363	C15H17NO3	Norsanguinine	1	0	0	2.14	2.20	*
285.3030004	7.173186721	C18H39NO	[SP] 1-deoxy-sphinganine	1	Lipids: Sphingolipids	Sphingoid bases	2.14	2.27	*
351.313709	3.670498722	C22H41NO2	[FA (20:2)] N-(11Z,14Z-eicosadienoyl)-ethanolamine	1	Lipids: Fatty Acyls	Fatty amides	2.12	1.45	
243.1834414	4.346888889	C13H25NO3	N-Undecanoylglycine	1	0	0	2.12	2.75	
184.1575367	13.90943549						2.11	1.01	*
255.2560945	6.958207233	C16H33NO	Palmiticamide	1	0	0	2.11	1.61	*
145.0851616	12.38762979	C5H11N3O2	4-Guanidinobutanoate	3	Amino Acid Metabolism	Arginine and proline metabolism	2.11	1.21	
144.0786991	6.928550016	C7H12O3	trans-4-Hydroxycyclohex	8	0	0	2.10	2.18	*

			anecarboxylate						
143.1674673	10.48267608						2.10	1.33	
110.0480259	7.504378673	C5H6N2O	Imidazole-4-acetaldehyde	2	Amino Acid Metabolism	Histidine metabolism	2.10	2.05	*
132.0422887	6.987879057	C5H8O4	2-Acetolactate	16	Carbohydrate Metabolism	Butanoate metabolism__Pantothenate and CoA biosynthesis	2.10	2.60	*
186.1257293	4.359490602	C10H18O3	10-Oxodecanoate	19	Lipids: Fatty Acyls	Fatty Acids and Conjugates	2.10	2.06	*
188.1050824	6.941415014	C9H16O4	Azelaic acid	2	Xenobiotics Drugs etc	Fatty Acids and Conjugates	2.08	3.52	*
698.2996149	3.440973931						2.08	1.36	
104.0110026	12.84009519	C3H4O4	Malonate	3	Nucleotide Metabolism	Pyrimidine metabolism__beta-Alanine metabolism	2.07	1.59	
158.0691834	12.30165731	C6H10N2O3	4-Methylene-L-glutamine	2	Carbohydrate Metabolism	C5-Branched dibasic acid metabolism	2.07	0.63	
158.1501003	15.82638159						2.06	1.61	*
203.1158977	4.663244407	C9H17NO4	O-Acetylcarnitine	1	Amino Acid Metabolism	Alanine and aspartate metabolism	2.06	3.59	*

222.1256548	4.371281185	C13H18O3	(+/-)-6-Hydroxy-3-oxo-alpha-ionone	2	0	0	2.05	1.92	*
130.0994459	4.407070062	C7H14O2	[FA (7:0)] heptanoic acid	14	Lipids: Fatty Acyls	Fatty Acids and Conjugates	2.04	2.34	
722.5807971	3.562332386						2.04	1.82	*
129.1518015	14.8491705	C8H19N	Tetraethylammonium	2	0	0	2.04	1.35	
184.1657622	5.854394844						2.03	1.26	*
125.0476864	6.993184199	C6H7NO2	N-Ethylmaleimide	4	0	0	2.02	1.12	*
151.0633756	6.937380812	C8H9NO2	(Z)-4-Hydroxyphenylacetaldehyde-oxime	17	Amino Acid Metabolism	Tyrosine metabolism	2.01	1.58	*
147.0532858	9.842048319	C5H9NO4	D-Glutamate	14	Amino Acid Metabolism	Glutamate metabolism__D-Glutamine and D-glutamate metabolism__Vitamin B6 metabolism	2.01	1.37	*
148.073632	7.18697095	C6H12O4	[FA methyl,hydroxy(5:0)] 3R-methyl-3,5-dihydroxy-	14	Lipids: Fatty Acyls	Fatty Acids and Conjugates	2.01	1.31	*

			pentanoic acid						
124.019407	4.185543562	C3H8O3S	propanesulfonate	1	0	0	2.00	1.25	*
198.1621075	3.811155551	C12H22O2	[PR] Citronellyl acetate	17	Lipids: Prenols	Isoprenoids	2.00	1.71	*
226.1680508	6.805338033	C12H22N2O2	1,8-Diazacyclotetradecane-2,9-dione	1	0	nylon-6 oligomer degradation	2.00	3.22	*

HyPy GC-MS Calibration Curves

In order to convert peak area values into concentrations of organics in the solvent extracts (as shown in Chapter 4) calibration curves using in house standards were created. These standards were created by Ali Salik in the BECS lab with known concentrations. Three calibration curves were created for each extract (DCM and hexane). The same standard was used for calibration an n-alkane calibration standard (predominantly alkane) which is custom made and produced by LGC Solutions in a UKAS accredited lab. This solvent is dissolved in hexane and all peaks had a concentration of 10 μg/ml. The standard contains 11 compounds: n-hexadecane $C_{16}H_{34}$, n-octadecane $C_{18}H_{38}$, n-nonadecane $C_{19}H_{40}$, n-tricosane $C_{23}H_{48}$, n-pentacosane $C_{25}H_{52}$, n-hexacosane $C_{26}H_{54}$, squalene $C_{30}H_{62}$, n-octacosane $C_{28}H_{58}$, n-triacontane $C_{30}H_{62}$, n-dotriacontane $C_{32}H_{66}$ and n-heptatriacontane $C_{37}H_{76}$. Curves were then created using these peaks with their known concentrations to determine the relationship between peak area and concentration for unknown peaks in the samples, as shown in the calibration curves. The curves, equation and relationships calculated, and corresponding peaks, are shown below in Figure 122 and Figure 123.

Identification of Molecules

All molecules detected in the experiment (as summarised in Table 18 and Table 19 below) had their identities confirmed via comparison with in-house standards and, when required, inspection of fragmentation spectra. All the hexane extracted samples were run on GC-FID using an RTX1 column, and a small number were also analysed with GC-MS to confirm the identities of detected compounds. All the DCM samples were similarly analysed with GC-FID using an HP5MS column, and a small number were also run on GC-MS to confirm the identities of detected compounds.

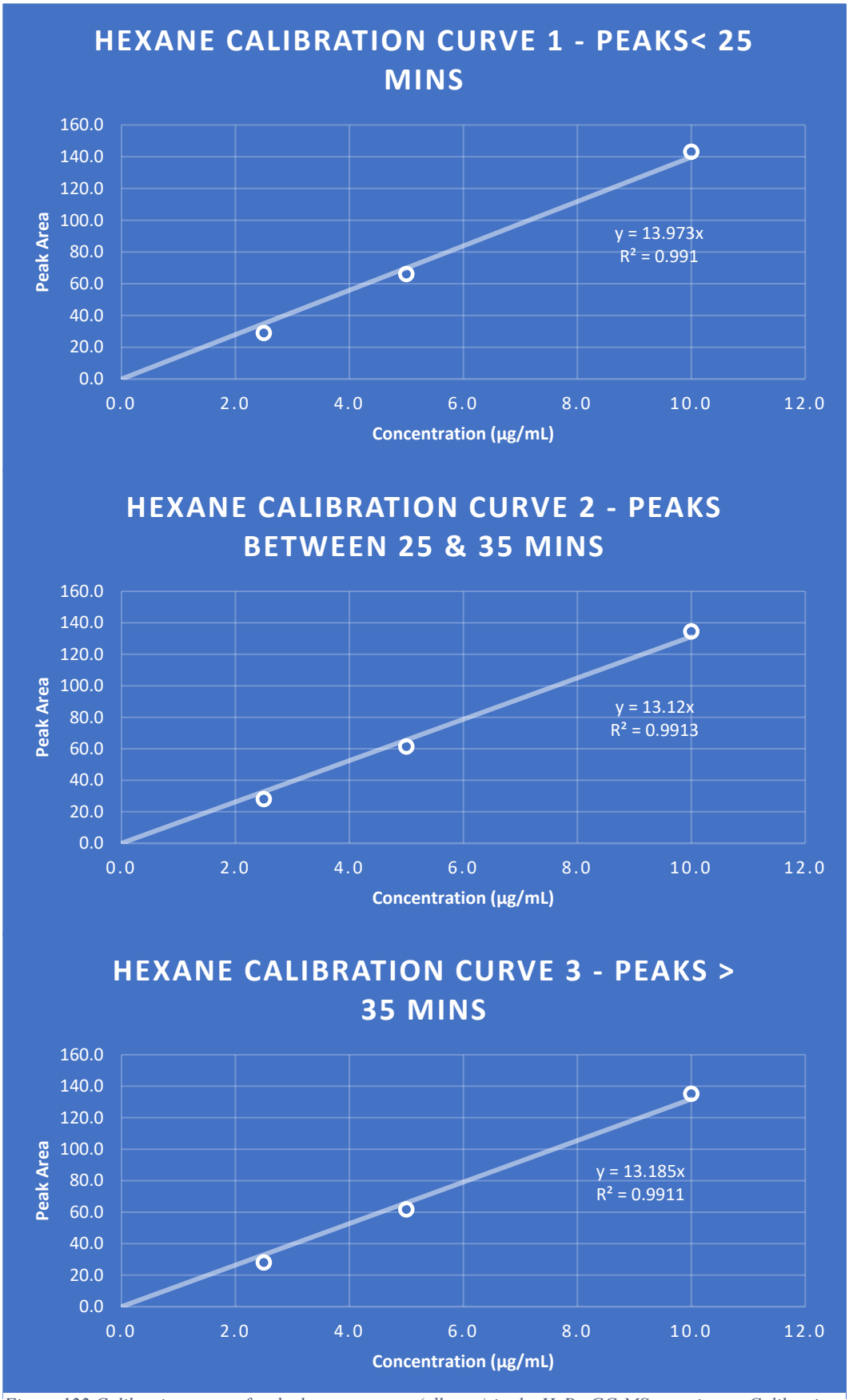

Figure 122 Calibration curves for the hexane extract (alkanes) in the HyPy-GC-MS experiment. Calibration curves are distributed according to peak retention time (< 25 minutes in CC 1, between 25 and 35 minutes in CC 2, and <35 minutes in CC 3)

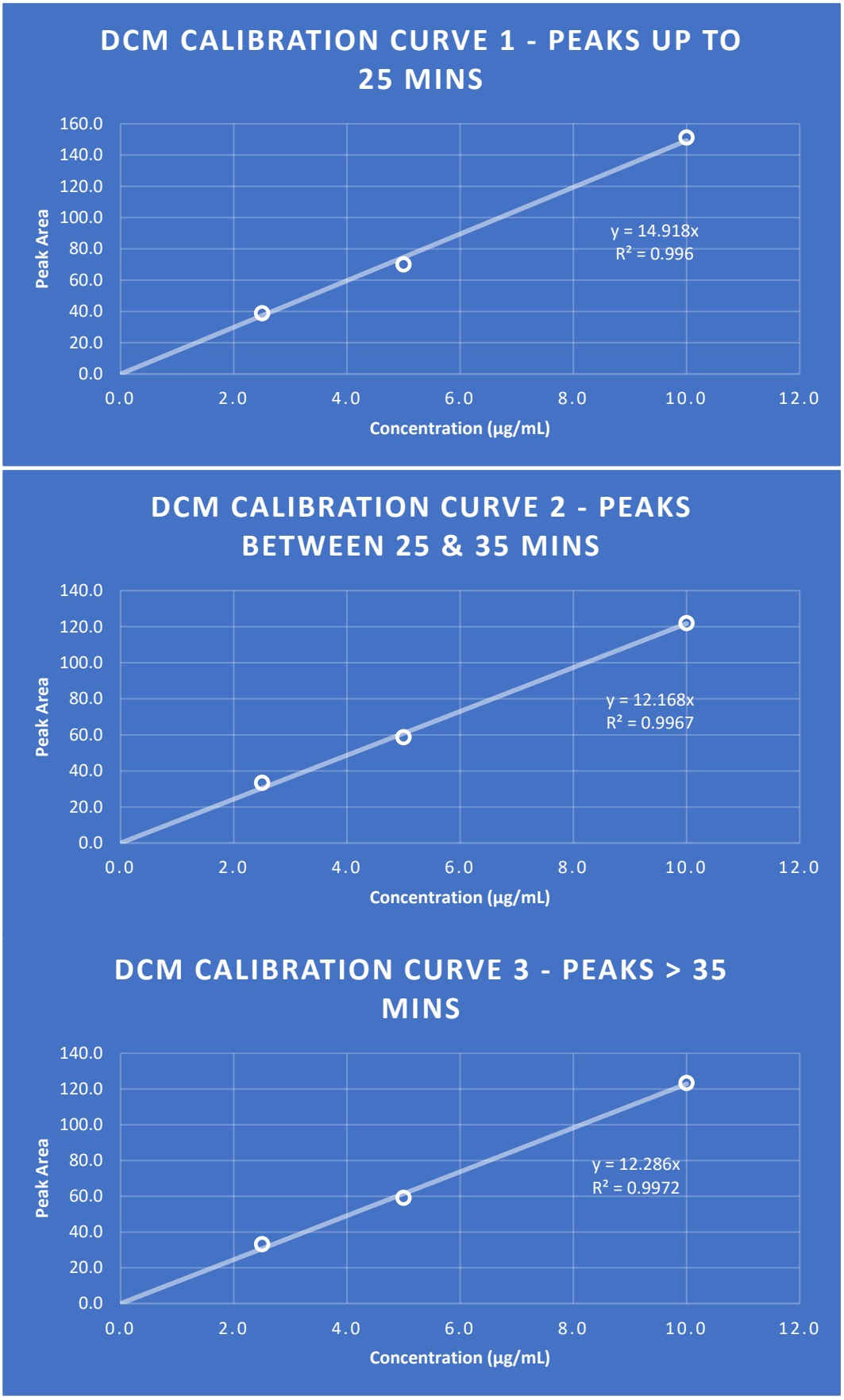

Figure 123 Calibration curves for the DCM extract (PAHs) in the HyPy-GC-MS experiment. Calibration curves are distributed according to peak retention time (< 25 minutes in CC 1, between 25 and 35 minutes in CC 2, and <35 minutes in CC 3)

DCM Calibration Curve Calculations

Peaks detected in DCM fraction

Table 18 Peak table for PAHs detected in DCM fraction

Peak Table for N2/DCM - PAHs	
Compound	Retention Time (mins)
Naphthalene	8.59
Acenaphthylene	14.03
Acenaphthene	14.87
Fluorene	17.28
Phenanthrene	22.23
Anthracene	22.47
Fluoranthene	28.90
Pyrene	30.10
1-methyl pyrene	32.75
Benz[a]anthracene	37.14
Chrysene	37.36
Perylene	41.47
Benzo[b]fluoranthene	43.04
Benzo[k]fluoranthene	43.17
Benzo[a]pyrene	44.59
Indeno[1,2,3-cd]pyrene	49.74
Dibenzo[a,h]anthracene	49.92
Benzo[ghi]perylene	50.77

Calibration # 1	
Concentration (µg/mL)	Peak Area
2.5	38.8
5.0	70.0
10.0	151.1

Equation obtained	y = 14.918x

Calibration # 2	
Concentration (µg/mL)	Peak Area
2.5	33.4
5.0	58.7
10.0	122.0

Equation obtained	y = 12.168x

Calibration # 3	
Concentration (µg/mL)	Peak Area
2.5	33.2
5.0	59.1
10.0	123.4

Equation obtained	y = 12.286x

Hexane Calibration Curve Calcuations

Table 19 Peak table for compounds detected in hexane fraction

Peak Table for N1/Hex - n-alkanes	
Compound	Retention Time (mins)
C16	16.727
C17	18.751
C18	20.742
C19	22.67
C20	24.535
C21	26.327
C22	28.053
C23	29.709
C24	31.306
C25	32.837
C26	34.317
C27	35.739
C28	37.117
C29	38.45
C30	39.732
C31	40.979
C32	42.187

Calibration # 1	
Concentration (µg/mL)	Peak Area
2.5	29.0
5.0	66.1
10.0	143.1

Equation obtained	y = 13.973x

Calibration # 2	
Concentration (µg/mL)	Peak Area
2.5	28.0
5.0	61.4
10.0	134.5

Equation obtained	y = 13.12x

Calibration # 3	
Concentration (µg/mL)	Peak Area
2.5	28.0
5.0	61.7
10.0	135.2

Equation obtained	y = 13.185x

Appendix 2: Jbilet Winselwan Experiment

Carbonaceous Chondrites – an Introduction

In this project two carbonaceous chondrites were studied, Jbilet Winselwan and the recent UK fall, Winchcombe. Jbilet Winselwan was studied as part of a collaboration with Stirling University investigating the effect of perchlorates on organics in meteorites, and Winchcombe was analysed rapidly (solvent extracted ~three weeks after the fall) in order to characterise its organic content after minimal interaction with the terrestrial environment.

Carbonaceous chondrites are primitive, organic- and water-rich meteorites originating from asteroids from the outer solar system which migrated to ~2.5-2.8 AU (Alexander et al. 2012). They are critical for our understanding of the early solar system, and in particular for how volatiles and prebiotic material was delivered to the terrestrial planets (Lee et al. 2019). Studying fragments of these primitive planetesimals also provides a window into the early Solar System, as they have remained unchanged for billions of years until they underwent atmospheric re-entry when they reached Earth (Sephton et al. 2015). Spectroscopic studies also indicate that the JAXA and NASA sample return missions of Hayabusa 2 and OSIRIS Rex to asteroids Bennu and Ryugu, respectively, both most closely resemble carbonaceous chondrites (Hamilton et al. 2019; Kitazato et al. 2019).

Both Jbilet Winselwan and Winchcombe are CM2 chondrites, a sub-class of the 'Mighei-like' class of carbonaceous chondrites. CMs' parent bodies are thought to have experienced low temperature (< 150 ºC) alteration and contain ~10% water in the form of ~70% phyllosilicates (Brearley 2006). The parent bodies of some CMs also experienced significant heating which dehydrated the alteration products and graphitised/carbonised some of the organic matter (Kitajima et al. 2002; Nakamura 2005; Tonui et al. 2014; Lee et al. 2016). Spectroscopic studies of Ryugu also indicate that it has experienced similar shock/heating thereby resembling such CMs.

Methods

In addition to the primary LC-MS experiment detecting and analysing organics in martian

meteorites, I also worked in collaboration with Dr Alastair Tait of Stirling and Monash Universities to evaluate carbonaceous chondrite meteorites as a source of martian organics. This work is included as an appendix as it was an additional unplanned collaboration added to my PhD halfway through. It is, however included in my thesis since the results are highly relevant.

As discussed in Chapter 2, martian soil is thought to be rich in oxidising perchlorate salts, which oxidise organic matter and inhibit their detection in rover instruments (Goetz et al. 2016; Royle et al. 2018). By treating crushed samples of Jbilet Winselwan (an organic rich CM2 carbonaceous chondrite meteorite) with varying concentrations of perchlorate salts (carried out by Dr Tait at Stirling), prior to solvent extraction (as outlined in Chapter 5) the effect of perchlorates on the organic contents of meteorites was investigated. Perchlorate treatment was carried out by Dr Tait at Stirling University, whilst solvent extractions were planned and mostly (>80%) carried out by me at SUERC. After perchlorate treatment (and a subsequent rinse with deionised water to remove the perchlorate residue) all steps carried out were the same. We then plan to compare detected organics to those found by the Curiosity Sample Analyser on Mars (SAM) instrument.

The samples used in this experiment are summarised in Table 20.

Table 20 Overview of samples used in the Jbilet Winselwan perchlorate experiment

Sample ID	Sample Name	Description
A_control	Analogue Control	Roasted basalt sample, heated at ~600 ^{o}C overnight to sterilise
E_control	Environmental Control	Nullarbor sand sample, to provide an environmental analogue for desert environment meteorite fell
U_Blank	Untreated Blank	Sterile silica beads to act as a follow through procedural blank, ie added at the Glasgow stage
T_Blank	Treated Blank	Silica beads blank treated with perchlorate, ie added at the Stirling stage
Met	Meteorite	Untreated meteorite sample of Jbilet Winselwan
Met_1x	Meteorite 1 x perchlorate	Jbilet Winselwan sample with 1 x perchlorate concentration
Met_20x	Meteorite 20 x perchlorate	Jbilet Winselwan sample with 20 x perchlorate concentration
Met_100x	Meteorite 100 x perchlorate	Jbilet Winselwan sample with 100 x perchlorate concentration

Results

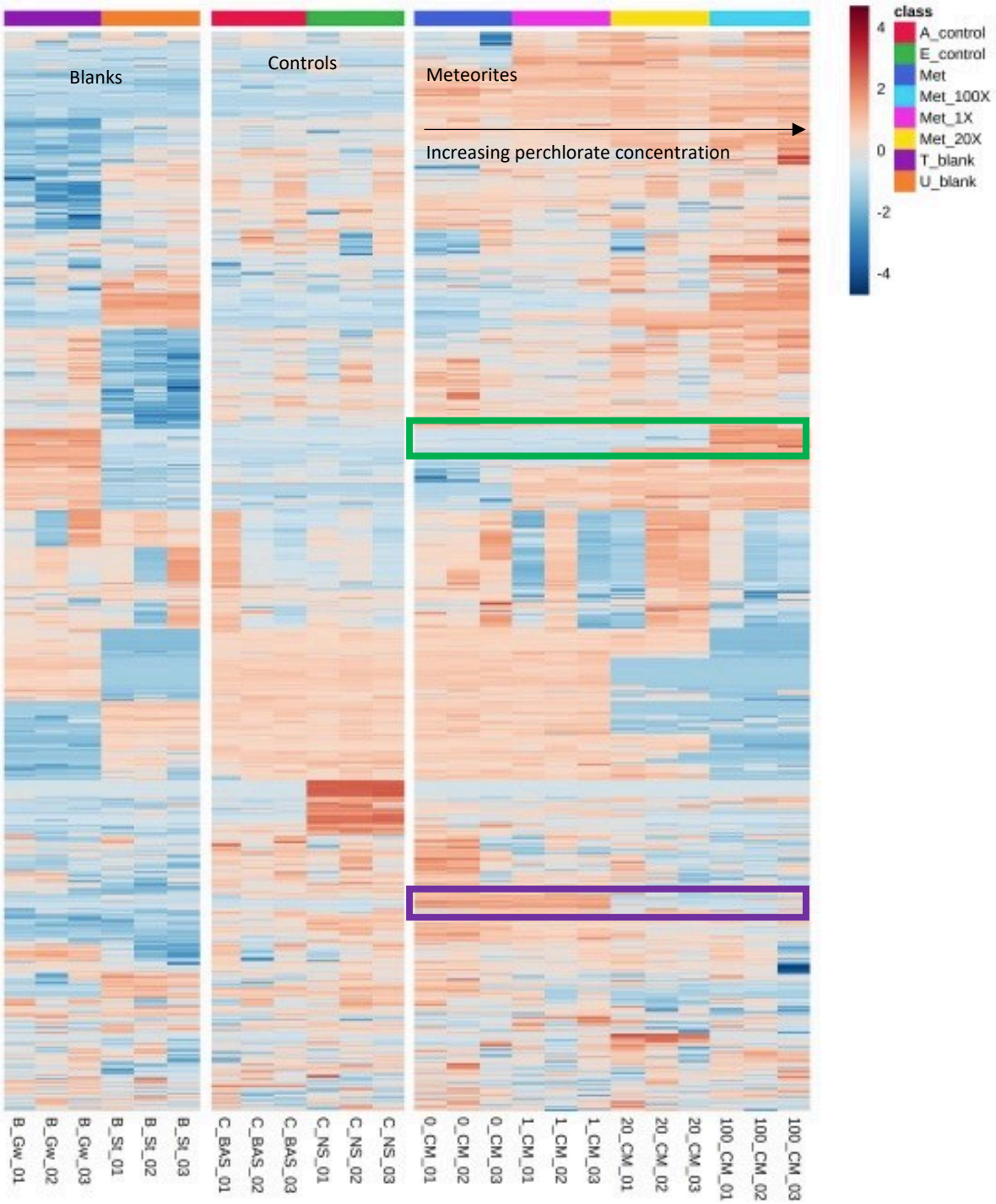

Figure 124 Heat map generated in Metaboanalyst displaying samples in Jbilet Winselwan experiment, where increasing perchlorate concentration indicates a change in metabolite distribution. Each horizontal line represents one metabolite, whilst each vertical line represents one sample. Brightness represents relative intensity, relative only to each metabolite, not across all metabolites, with brightest red being the highest intensity peak signal. Some metabolites are not detected with any perchlorate treatment, and are then detected when perchlorate treatment increases (green box), whilst others are present at low perchlorate concentrates, and are not detected at higher perchlorate concentrations (purple box).

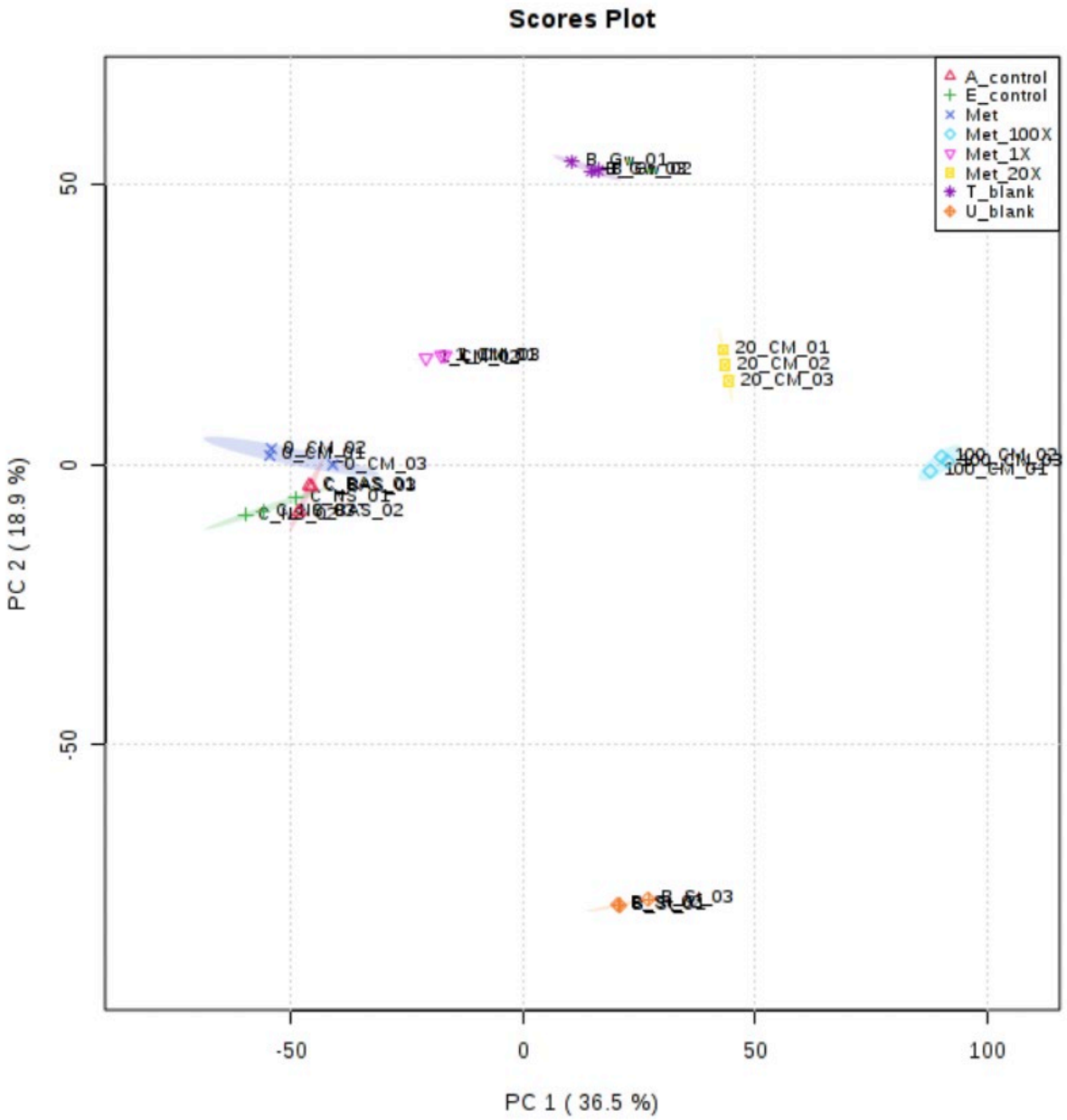

Figure 125 Plot of the first two principal components calculated for the samples from the Jbilet Winselwan experiment. First PC accounts for 36.5% of variance and separates samples with increasing perchlorate concentration from 0 to 100 x concentration. Sample IDs are outlined in Table 20

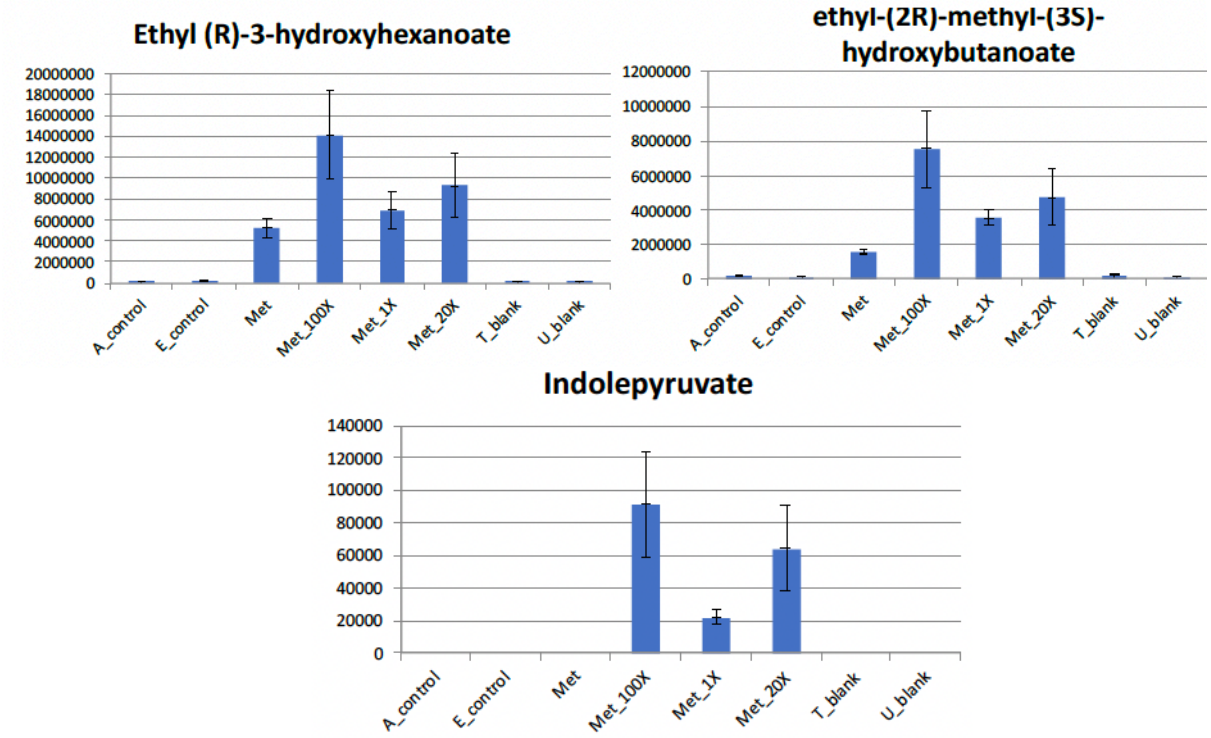

Figure 126 A selection of putatively detected metabolites from the Jbilet Winselwan experiment that demonstrate the trend of increasing in intensity (and therefore abundance) as perchlorate concentration increased (ie from 0 to 100X treatment). Error bars are standard deviations.

As this was an additional experiment carried out in collaboration with Dr Alastair Tait, these data have not been processed to the same degree as the martian experiment. The aim was to carry out the two projects (this and the martian LC-MS project) in parallel to produce complementary datasets. Dr Tait was unable to acquire funding to continue this work. As this was a supplementary project to this PhD, the work had to be deprioritised. Below is a summary of the initial data processed with Dr Tait.

Principal component analysis was carried out using Metaboanalyst to produce Figure 125, and shows that the experimental samples cluster apart from one another in their sample

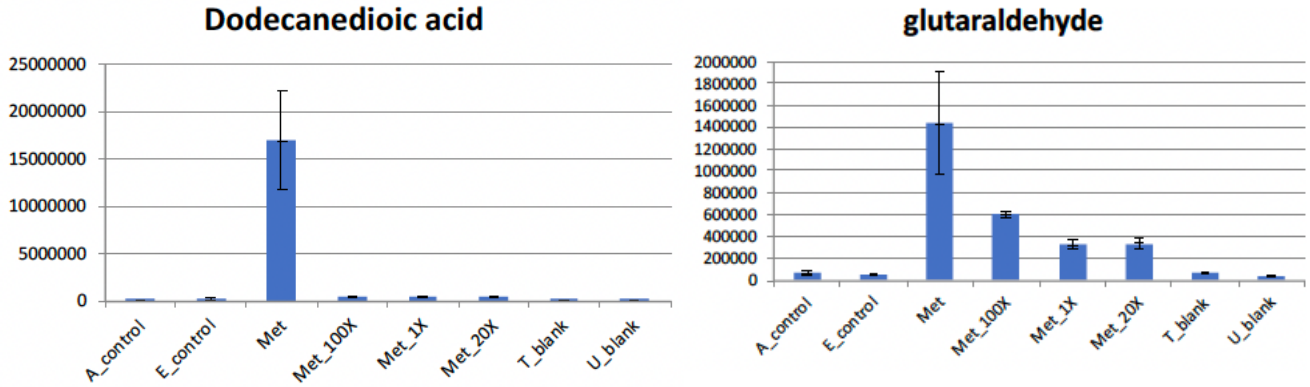

Figure 127 A selection of putatively detected metabolites from the Jbilet Winselwan experiment that demonstrate the trend of decreasing in intensity (and therefore concentration) as their perchlorate treatment concentration increased. Error bars are standard deviations.

groups (ie each treatment concentration clusters together, and is separated from others). The first principal component accounts for 36.5% of the variance in the samples and shows a trend where the untreated sample of Jbilet Winselwan clusters with the control samples, and the experimental samples separate in order of perchlorate treatment from untreated to 100 x. The second principal component accounts for 18.9% of the variance and shows that the untreated blanks (B_St_01-03) are distinct from the treated blanks (B_Gw_01-03) and the experimental samples and controls.

There may have been some confusion, however, as to the naming of these sample IDs, as the untreated blanks were those introduced at the Glasgow step, rather than the Stirling step. The naming appears to have been reversed in the PCA diagrams. This would make sense since the B_Gw samples have a more similar distribution in the heat map to the untreated meteorite samples. If the B_Gw samples are indeed the untreated samples, then the error lies in the key on the PCA generated by Polyomics in Metaboanalyst (identifying B_Gw as treated, rather than treated). However this does not have any implications on the results of the experiment.

The heat map produced in Metaboanalyst from the Jbilet Winselwan experiment shows that the metabolites detected and their relative intensities change as the concentration of perchlorate treatment increases (Figure 124). Some metabolites which are not present at 0 x concentration (ie sample ID 0_CM_01-03) are present as the perchlorate treatment increases (e.g. sample 100_CM_01-03), an example of this is shown in the green box. Three such examples of this are shown in Figure 126, whereby the average intensity distributions as calculated by IDEOM (Creek et al. 2012) are plotted for putatively identified metabolites. For example, indolepyruvate was below detection levels with no perchlorate treatment, 20,000 arbitrary units for 1 x concentration, and 90,000 for 100 x concentration – i.e., a 4.5 fold increase in metabolite concentration, for a 100 fold increase in perchlorate treatment. This metabolite was also detected at very low levels in all the blanks and controls.

Some metabolites which were detected at low perchlorate concentrations were then not detected at the highest perchlorate concentrations, examples of these are highlighted in the purple box of the heat map (Figure 124). The intensity distributions of two putatively detected metabolites which demonstrate this trend are shown in Figure 127. Dodecanedioic acid, a fatty acid, is present only in the 0x sample of Jbilet Winselwan, and below detection levels in all other samples, including blanks. For glutaraldehyde, the untreated sample of

Jbilet Winselwan has an intensity of 1,400,000 arbitrary units, and the 100 x treated sample an intensity of 600,000 arbitrary units, a 67% decrease in concentration. For this sample, the intensities were even lower for the 20x and 1x samples, than the 100 x however.

Discussion

In this perchlorate experiment with Jbilet Winselwan, as perchlorate concentration increased, the metabolite profile detected changed. Some molecules were detected at high abundances in samples of Jbilet Winselwan prior to perchlorate treatment, and were not detected at high concentrations of perchlorate treatment. Other molecules were not detected prior to perchlorate treatment, and were then detected at increasing abundances with increasing perchlorate treatment. This suggests that the presence of perchlorates is altering the organic profile of the samples, destroying some of the material, and perhaps altering some of the other molecules which were previously undetectable. This is perhaps due to their mass or polarity, such that after being oxidised by perchlorates, their mass is reduced to within the limits of the OrbiTrap^{TM}. Regardless of the reasoning, the results are consistent with previous work showing the effects of perchlorates oxidising meteoritic and martian organics (Glavin et al. 2013; Steele et al. 2018; Jaramillo et al. 2019).

Appendix 3: Organic Analysis of the Winchcombe Meteorite

This appendix outlines the successful retrieval and subsequent analysis of the Winchcombe CM2 meteorite. This work is included as an appendix as it was an unplanned piece of work (it literally fell out of the sky in my fourth year), but highly relevant. It appears in the appendix in part due to funding requirements by the funder, STFC.

Field Search

A bright ~7 second fireball event was observed across the UK and Northern/Western Europe at ~9:50 pm on Sunday 28th February 2021. Thanks to favourable climactic conditions, numerous camera networks and citizen scientists were able to capture the flight of the fireball which allowed for calculations of the approximate mass, size, and triangulation of the fireball's flight. Colleagues at the Desert Fireball network (DFN), and the UK Fireball Alliance (UKFAll) collaborated and quickly determined that a meteorite had likely fallen in the Gloucestershire countryside.

On the morning of 1st March 2021, a ~300 g shattered piece of the meteorite was found in the village of Winchcombe by Rob Wilcock, member of the public on their driveway (see Figure 128). This piece was soon identified by Dr Richard Greenwood (The Open University) as a carbonaceous chondrite and thus a rare and precious sample which

Figure 128 The main mass of the Winchcombe meteorite found on the Wilcock family driveway in Winchcombe, Gloucestershire.. Credit: Rob Wilcock

required urgent curation due to potential contamination risks associated with the rich organic content.

Calculations by colleagues at the DFN after observations of the fireball event determined the original meteoroid was approximately 100 kg when it reached the Earth's atmosphere,

Figure 129 Modelled strewn field of the Winchcombe meteorite, overlaid with locations of the sites of the finds of the meteorite (red stars with their masses shown). Image credit: UKFAll.

and ~ 1 kg would have reached Earth, and it had likely fragmented during its fall to the Earth's surface. They determined other pieces visible to the naked eye would be found close by. Models were refined by the DFN team and a strewn field (likely fall zone) of ~ 4 km x 400 m was constrained, which generated a distribution of masses across the most probable fall line (see Figure 129).

Given the precious nature of the sample, and the high potential scientific return due to its apparent classification it was necessary to arrange a search team to collect any additional pieces of the Winchcombe meteorite in the field. Two years previously, the UK Fireball Alliance had set up a mailing list for members of the public to assist in the event of such fireball observations. Given Winchcombe fell at the highest level of COVID lockdown restrictions, this list could unfortunately not be mobilised. A team of ~15 planetary scientists therefore assembled to cover as much ground as possible as quickly as possible before any rain, and before any press coverage that might draw attention to the area and any samples removed by non-specialists.

The strewn field made up an area of ~ 1,600,000 m^2. Most of this terrain was privately owned farmland with a mixture of terrain types. Other areas in the strewn field were housing, public bridleways, parks, gardens, and roads. As can be seen in Figure 129, modelling of the strewn field by the DFN indicated that the distribution of masses would vary depending on location. The higher the mass the sample, the easier it would be to spot in the field, and therefore searches were prioritised in areas with high probabilities of higher mass fragments. Of course, this had to be combined with suitable, accessible terrain, e.g a field with short grass and little else would be much easier to search than a river, or a forest. Permission also had to be granted from all landowners of private lands searched.

Systematic searches for the stone were carried out in socially distanced (2-3 m apart) straight lines moving up and down fields staying in line with one another. Each person was to stay in line with the person on their left, whilst scanning the ground in an arc ~120 cm in front of them, rather than the ground immediately at their feet, as this gives them a larger field of view (see Figure 130). Looking any further than ~120 cm would mean a greater scanning zone but risk missing any potential finds as meteorites in the field were expected to be 0.5-100 g in size, and indistinct from environmental samples, given the number of faeces in the field that resembled meteorites.

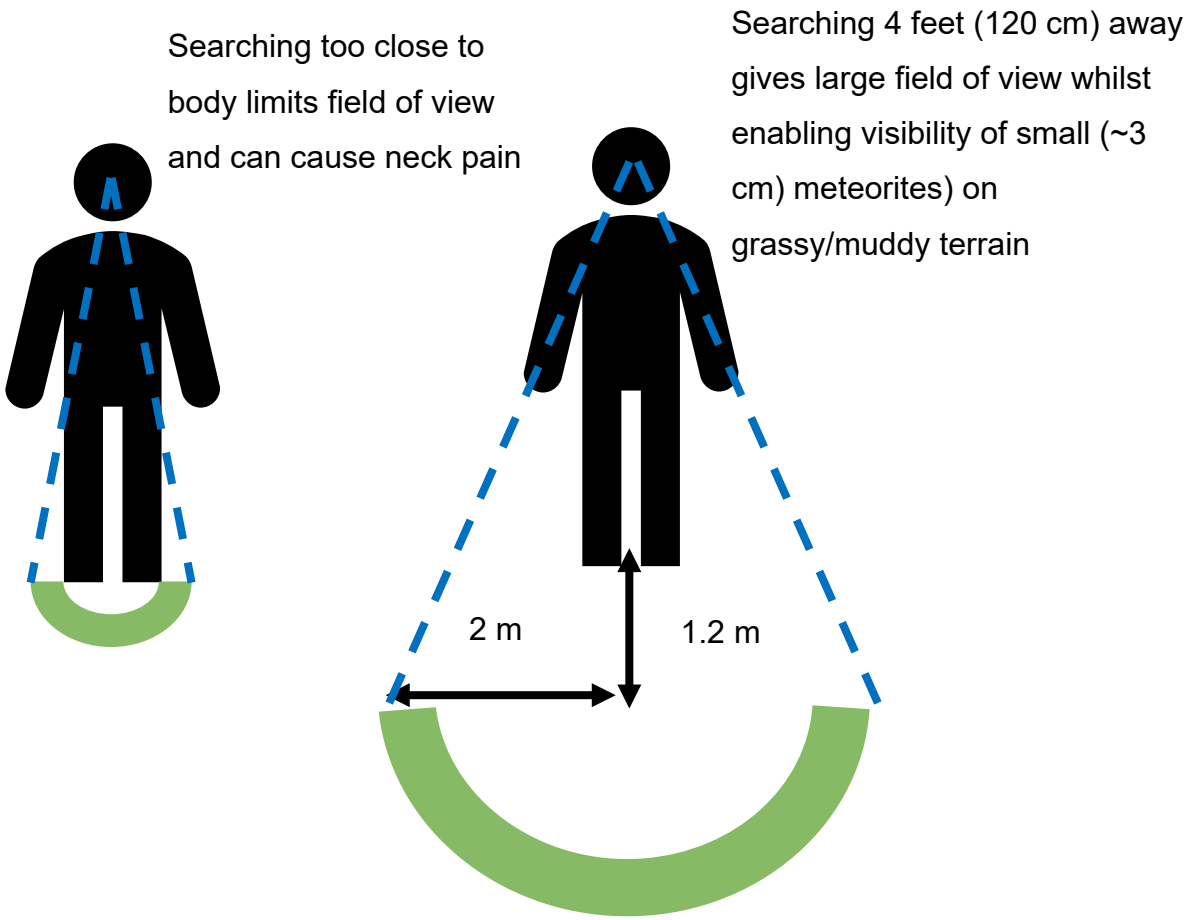

Figure 130 Schematic diagram to outline scanning technique for meteorite search in the field. Search team should scan the area ~120 cm ahead to maximise amount of ground covered versus size of stone visible. Care should be taken so that gaps do not form between area scanned by members of the search team, to do this, the team should stay in a straight line, approximately 2 m apart.

The first search took place with the full group of ~15 on Cleeve Hill. This was hilly rugged terrain, any meteorites exposed on the grass would have been fairly easy to see. It was found, however, that it was very difficult to maintain a straight line with such a large group of people, particularly with uneven terrain. Figure 131 illustrates this, where in both pictures, the group is very spread out. After the first morning, searches took places in groups of no larger than ~7 people.

Figure 131 Photographs taken during first morning of the search for Winchcombe meteorite. Search party is part of greater group of ~15 people and is not in a straight line.

Systematic searches of fields took place as shown in Figure 131 and Figure 132, where the team walked in straight lines up and down fields. Ideally someone at each end would have a GPS recording device to ensure that the team kept in line; the team would then pivot around the end person as they reach one end of the field to continue searching back down it. The GPS device was also required to keep record of areas searched and any potential finds. Landmarks on the horizon and/or team kit such as ruck sacks were used to mark the ends of the line when in large fields to aid the team in keeping straight as shown in Figure 132.

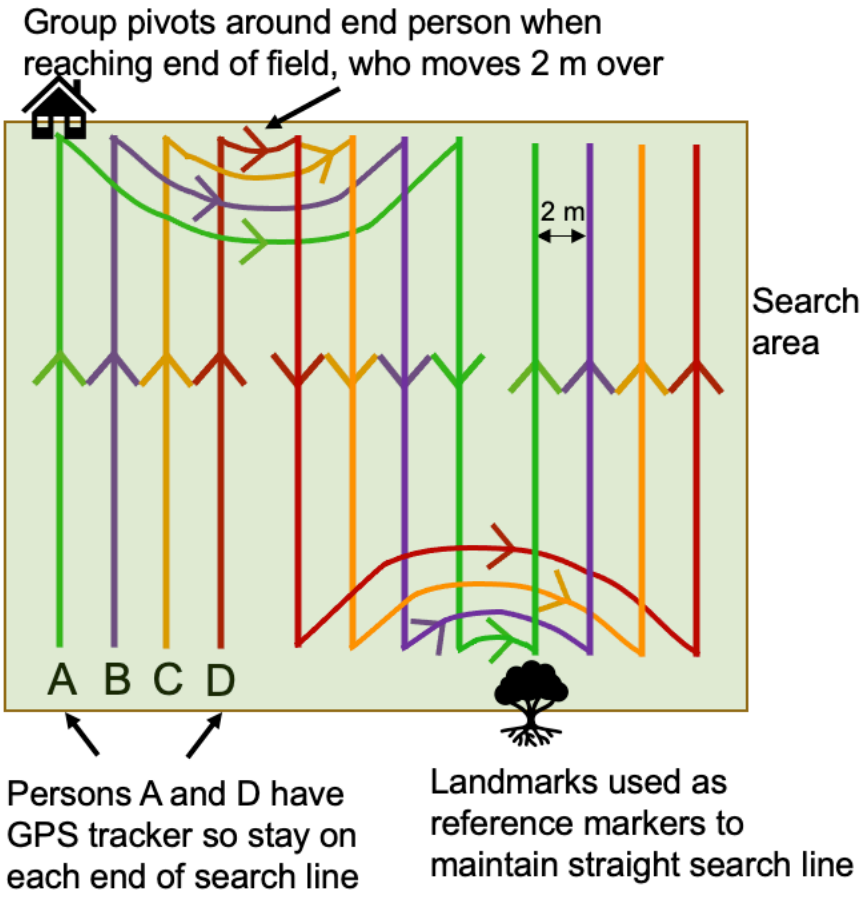

Figure 132 Schematic representation of the strategy deployed for the search for fragments of the Winchcombe Meteorite. Teams of ~4-7 stood in a straight line ~2 m apart walking forwards at the same speed. Ideally the persons at each end of the line would have a GPS recording device to track area covered. Any local landmarks are used to help team to stay on track, or team's kit items, such as rucksacks, can be placed at the end of fields to use instead.

5 days of field searching were carried out between 4th March and 8th March 2021, with one successful find in the field on 6th March 2021. Figure 133 shows the GPS records of the areas searched by the members of the University of Glasgow team across those five days, with the approximate location of the find indicated and fall line shown in grey. As can be

seen in Figure 131, whilst the team attempted to walk in a straight line when searching in the field, this was challenging, particularly in large irregularly shaped fields with few landmarks. The team found a ~200 g piece of Winchcombe embedded ~5 cm into the ground on 6th March, 6 days after the meteorite fell. This piece is shown in Figure 134. The proximity of sheep wool to the sample, and the similarity of the sample to sheep faeces indicates the difficulties had during the fieldwork in distinguishing meteorites from 'meteorwrongs' successfully leading to a number of false alarms.

In the time since the fireball it had not rained in Gloucestershire, which was promising for limiting weathering to this sample, however there was significant dew on the grass on the field that morning meaning some weathering may be present. The GPS coordinates of the

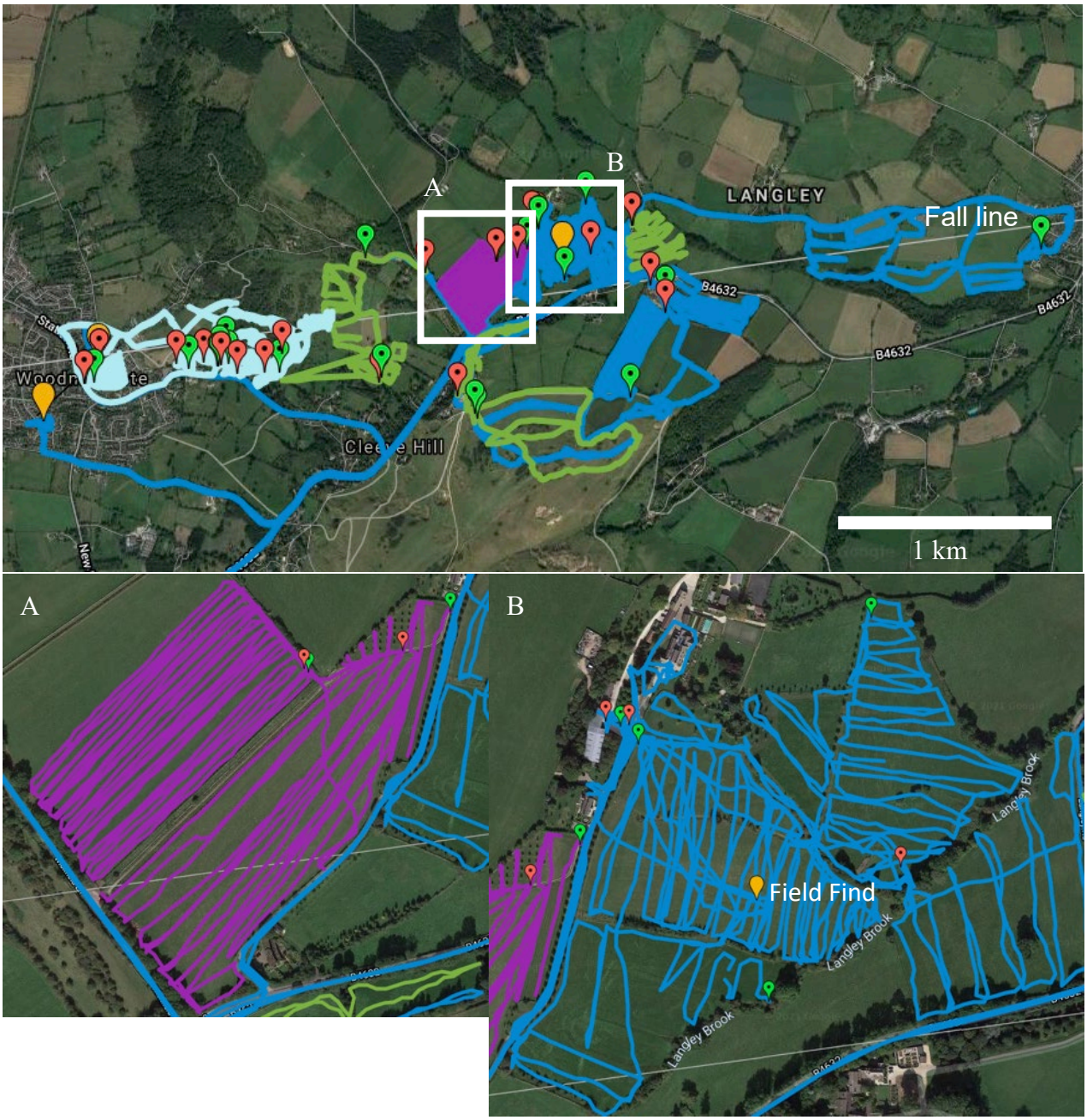

Figure 133 A selection of the field sites from the search for fragments of the Winchcombe meteorite. Coloured search lines are from the GPS trackers belonging to the search party members showing the ground covered. The search party systematically covered as much of a ~ 4km x 400 m area over 5 days as they could gain access to to search for fragments. The approximate calculation of the most likely fall line is shown in grey, with A and B displaying zoomed in maps to demonstrate the search pattern carried out. The location of the successful field find at Rushbury farm is shown in B.

find were recorded, and gloves were used to extract the sample from the soil and place into a sample bag, minimising human contamination. During excavation, the meteorite fragment split into 2 pieces. Environmental samples of soil from the fall site were also collected using gloves, in separate sample bags, to allow for detection of terrestrial

contaminants at the fall site.

Figure 134 The Winchcombe meteorite field find as observed in situ, and during extraction from its impact site. The approximate location of the find is shown above in Figure 129

Solvent Extractions

Following the successful retrieval of the Winchcombe Meteorite in March 2021, an additional metabolomics study was planned. In this study, two sets of analyses were planned, whereby the first was a non-targeted metabolomics approach, and the second a

targeted approach. To achieve this, six extracts (using the same protocol as outlined in Chapter 5) were acquired for each sample, so that three could be analysed in the initial untargeted study, and 3 in the targeted study. The solvent extractions and LC-MS specifications were carried out as outlined in Chapter 5, with the only exceptions to this being in the overall experimental design. This was an urgent additional project that could not wait until I had finished my thesis, to limit the interaction of the meteorite with the Earth's atmosphere. A workflow for the meteorites and their environmental samples is given in Figure 135, whilst the blanks protocol is shown in Figure 136. Table 21 shows all sample IDs, their descriptions, and the analyses carried out/planned. The targeted analyses is not complete due to unplanned instrument down time.

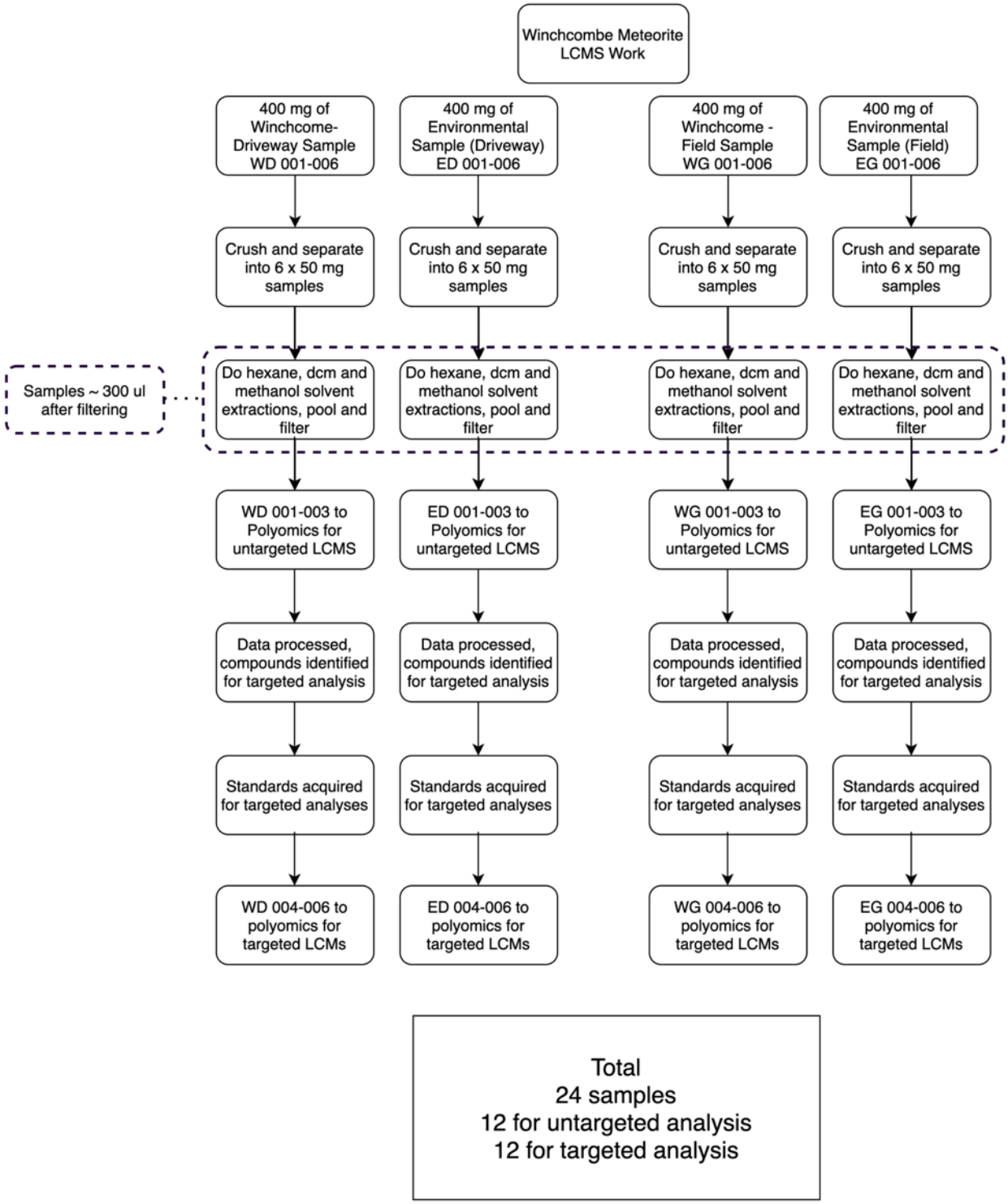

Figure 135 Experimental overview for Winchcombe metabolomics analyses. An outline of the samples used and at what stage is shown.

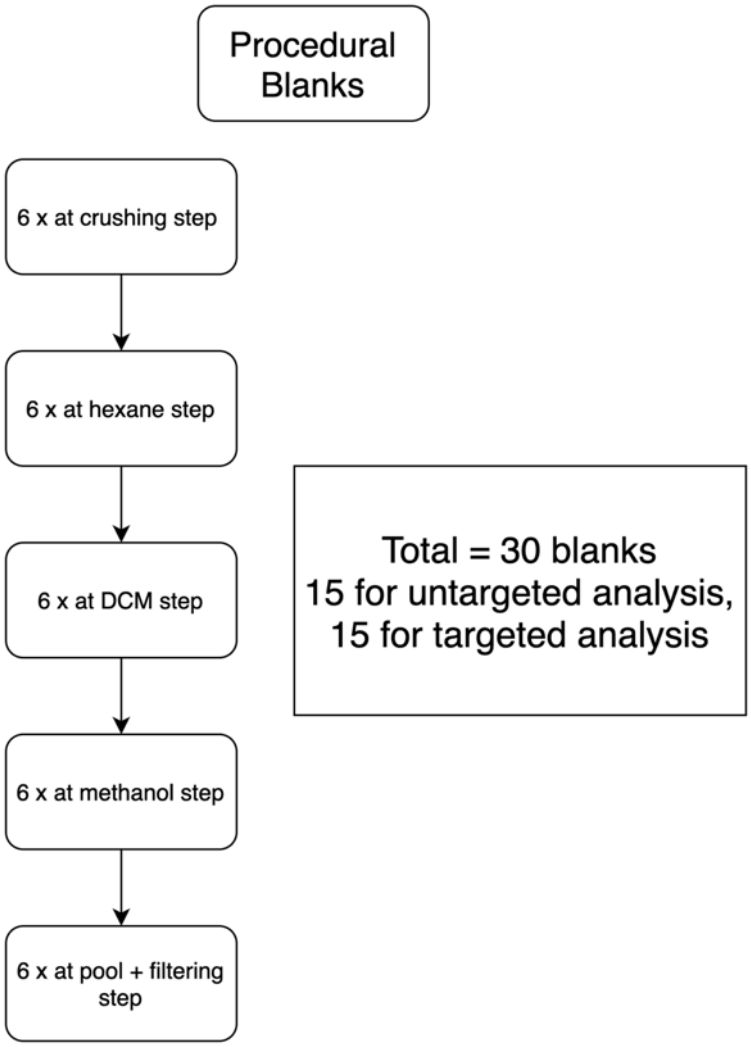

Figure 136 Procedural blanks introduced during Winchcombe metabolomics experiment. Procedural blanks were introduced for each step of the solvent extractions to identify any laboratory contaminants.

Table 21 Description of samples used in Winchcombe LCMS experiment

Vial IDs	Description	Targeted or non-targeted LCMS?	Solvents in solution
WD 01-03	Winchcombe driveway (meteorite piece that fell onto driveway and was collected ~ 12 hours later	Non-targeted	Hexane, Dichloromethane and methanol
WD 04-06	Winchcombe driveway (meteorite piece that fell onto driveway and was collected ~ 12 hours later	Targeted	Hexane, Dichloromethane and methanol
ED 01-03	Environmental sample - soil from driveway piece	Non-targeted	Hexane, Dichloromethane and methanol
ED 04-06	Environmental sample - soil from driveway piece	Targeted	Hexane, Dichloromethane and methanol
WG 01-03	Winchcombe field (meteorite piece that fell and landed at Rushbury House farm on the Sunday and was collected the subsequent Saturday)	Non-targeted	Hexane, Dichloromethane and methanol
WG 04-06	Winchcombe field (meteorite piece that fell and landed at Rushbury House farm on the Sunday and was collected the subsequent Saturday)	Targeted	Hexane, Dichloromethane and methanol
EG 01-03	Environmental sample - soil from field piece	Non-targeted	Hexane, Dichloromethane and methanol
EG 04-06	Environmental sample - soil from field piece	Targeted	Hexane, Dichloromethane and methanol
BCr 01-03	Procedural blank introduced at crushing step	Non-targeted	Hexane, Dichloromethane and methanol
BCr 04-06	Procedural blank introduced at crushing step	Targeted	Hexane, Dichloromethane and methanol
BHx 01-03	Procedural blank introduced at hexane step	Non-targeted	Hexane, Dichloromethane and methanol
BHx 04-06	Procedural blank introduced at hexane step	Targeted	Hexane, Dichloromethane and methanol
BDC 01-03	Procedural blank introduced at DCM step	Non-targeted	Dichloromethane and methanol
BDC 04-06	Procedural blank introduced at DCM step	Targeted	Dichloromethane and methanol
BMe 01-03	Procedural blank introduced at methanol step	Non-targeted	Methanol

BMe 04-06	Procedural blank introduced at methanol step	Targeted	Methanol
BPo 01-03	Procedural blank introduced at pooling step	Non-targeted	Hexane, Dichloromethane and methanol
BPo 04-06	Procedural blank introduced at pooling step	Targeted	Hexane, Dichloromethane and methanol

Results

All the metabolites found in the experimental samples from the Winchcombe LC-MS experiment (i.e., the meteorite extracts and the environmental controls) and not detected in the procedural blanks were first analysed in IDEOM (Creek et al. 2012) to remove any laboratory contaminants from the dataset. Metaboanalyst was used to carry out principal component analysis of the non-targeted samples to assess whether the metabolite make up in the meteorite extracts were distinct from their corresponding environment controls, this two dimensional PCA is shown in Figure 137. A heat map was also generated using the same software – see Figure 138 to further assess contamination levels and trends.

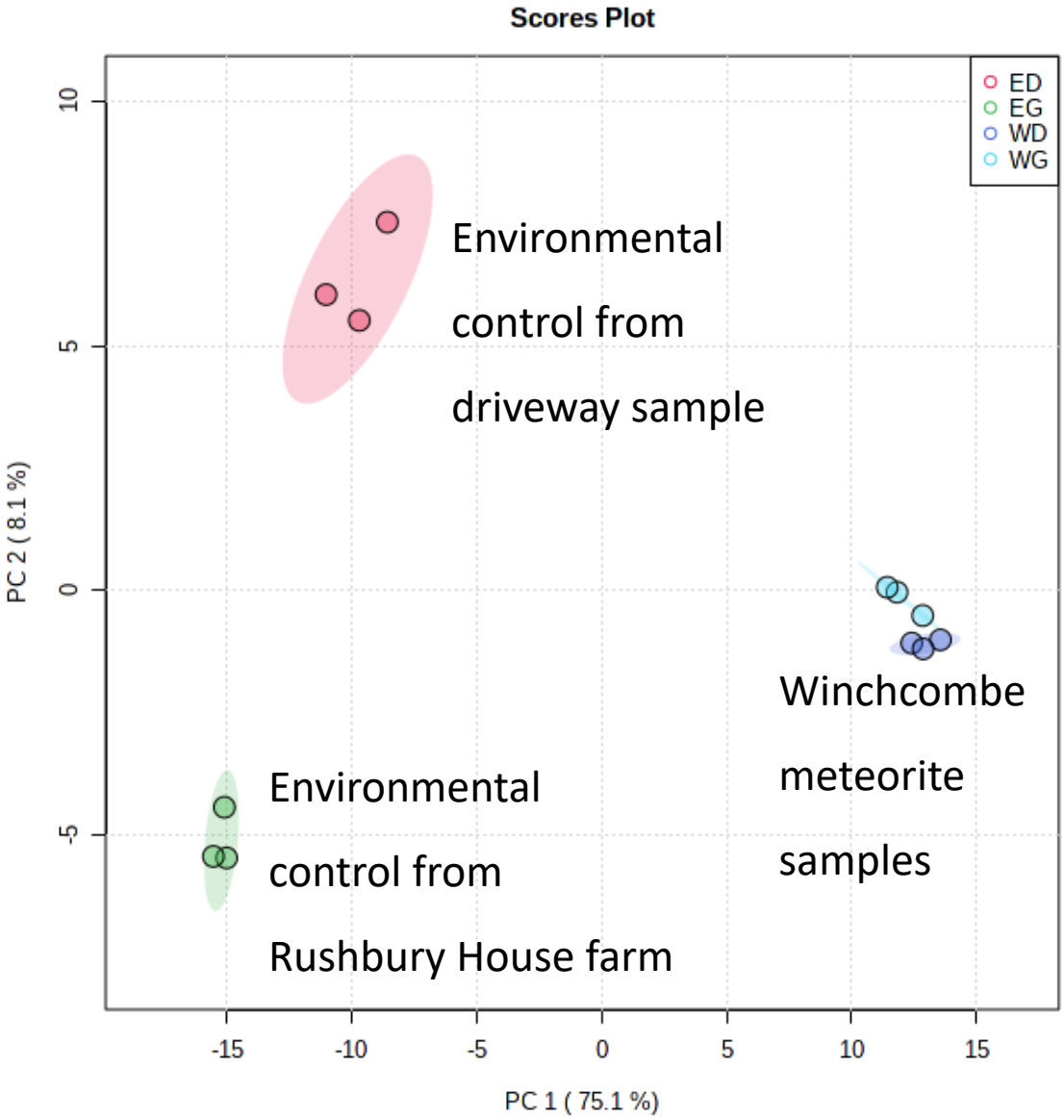

Figure 137 Two dimensional principal component analysis from the experimental samples studied in the Winchcombe LC-MS experiment. The first principal component accounts for 75.1% of the variance, and clearly distinguishes the meteorite samples from the environmental controls collected at the fall sites, whilst the second principal component accounts for 8.1% of the variance, and distinguishes the environmental controls from one another. Shaded areas represent 95% confidence region.

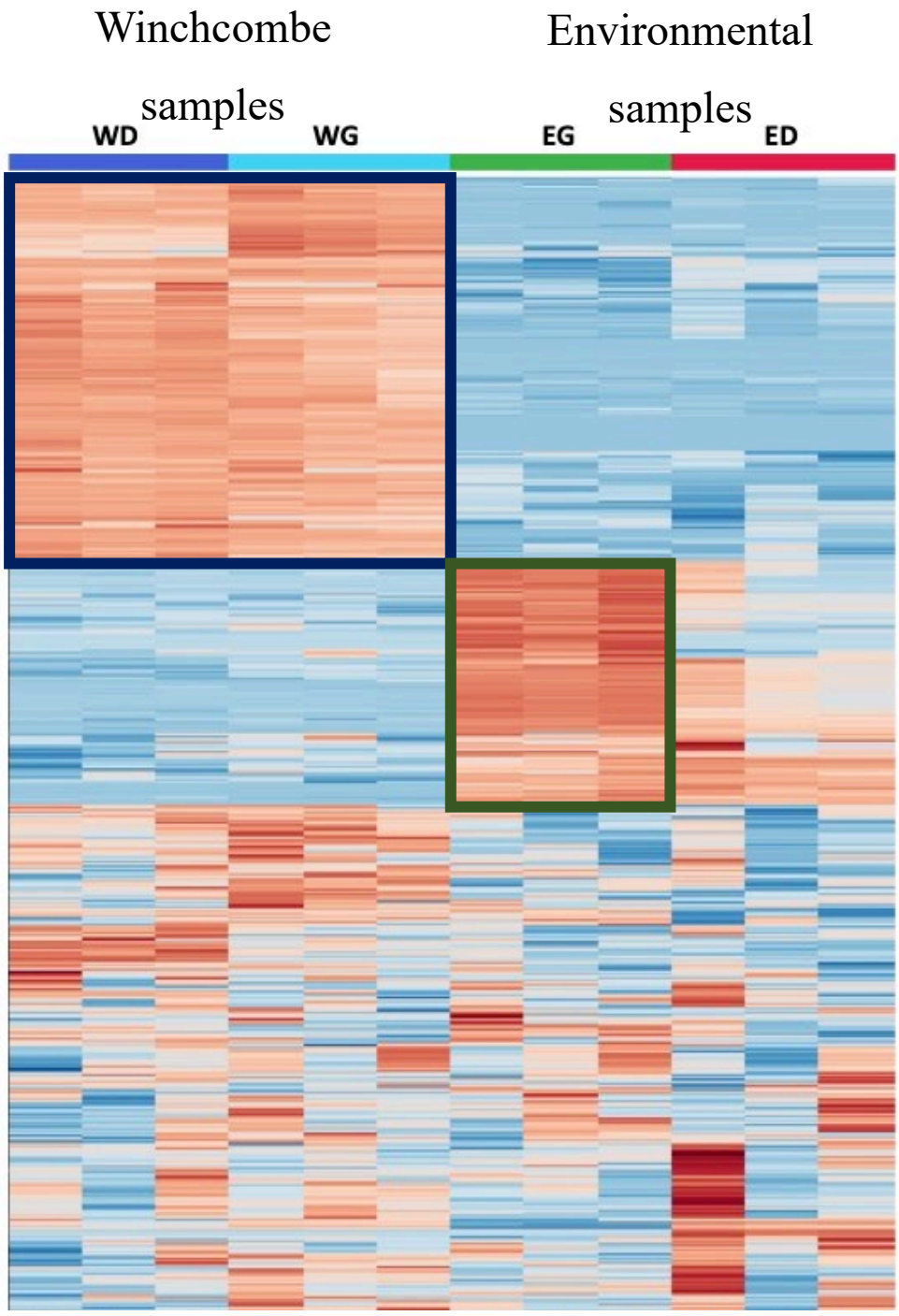

Figure 138 Heat map of metabolites detected in the experimental samples from Winchcombe LC-MS. Each row represents one metabolite whilst colour represents relative intensity of that metabolite's peak (bright red = highest relative intensity). Blue box indicates set of metabolites detected in all six Winchcombe extracts and below detection limits in their corresponding environmental controls. Green box represents set of metabolites detected in the environmental control from Rushbury House Farm and not in its corresponding meteorite extracts.

Table 22 List of top 22 putatively identified metabolites in descending order of influence (loading) on the first principal component in the Winchcombe LC-MS experiment. Identification of metabolites was carried out using IDEOM (Creek et al, 2012) however upon further investigation, 1-hydroxychlordene appears to be a sulfonated compound, due to presence of sulfonate fragment in spectrum, and lack of Cl-37 peak in spectrum. All other sulfonates have had similar verification completed, by presence of S-36 isotope peak in spectrum and in some cases additional presence of sulfonate fragment in fragmentation spectra.

Metabolite ID	Loading on PC1
1-Hydroxychlordene*	0.11427
345.767645	0.11375
2-Mercaptoethanesulfonate	0.10963
Thiosulfate	0.10642
343.771899	0.10431
113.936137	0.10276
2-oxo-8-methylthiooctanoate	0.10231
96.9834365	0.10226
2-(Methylthio)ethanesulfonate	0.10201
127.960239	0.095037
[FA methyl(20:4)] N-methyl-5Z_8Z_11Z_14Z-eicosatetraenoyl amine	0.092622
N-(Cyclohexylmethyl)-N-methylbenzenamine	0.092566
159.93233	0.091207
166.147054	0.087082
hexanesulfonate	0.085852
259.926453	0.082436
propanesulfonate	0.082189
2-oxo-10-methylthiodecanoate	0.079291
pentanesulfonate	0.078958
[SP (4:0)] 1-deoxy-sphinga-6Z_9Z_12Z_15Z-tetraenine	0.077713
(-)-Pellotine	0.076738
ethanesulfonate	0.072118

The 2D PCA (Figure 137) shows us that the meteorite extracts have detected metabolite signatures similar to one another, and distinct from their corresponding environmental controls. The first principal component (PC1) accounts for 75.1% of the variance in the dataset and shows the six Winchcombe replicates clustering close together, with their controls at the other end of this PC1 axis. The second principal component (PC2) accounts for 8.1% of the variance in the dataset and shows that the two environmental controls are distinct from one another, with them clustering separately. The cumulative variance (83.2%) accounted for by this PCA is sufficiently high to suggest this trend is representative for the dataset.

The heat map (Figure 138) shows the relative intensities of metabolites that were detected in the extracts from the experimental samples, but were below detection levels in the

procedural blanks. The heat map shows that there is a large number of metabolites which were detected in all six of the Winchcombe meteorite extracts (i.e., from both the Rushbury House farm and Wilcocks driveway sample) and were at low intensities/below detection limits in the environmental controls, these are outlined in the blue box. The heat map also shows that there was a number of metabolites detected in the environmental control extracts that were below detection limits in the meteorite extracts (green box).

Since PC1 shows how the Winchcombe samples are distinct from their controls, and a future targeted study was planned, we used Metaboanalyst to investigate the metabolites which influence PC1 the most. These are the metabolites which, after $\log_{10}$ normalisation due to differing intensity ranges, have the highest loadings on PC1, and therefore have the highest relative concentration in both the meteorite samples compared to the environmental controls. It was hoped that these would therefore most likely be the organics indigenous to the meteorites and the best molecules for targeted analysis. These are displayed in Table 22.

Of the putatively identified molecules in Table 22, there are some whose identification could be more confidently stated thanks to further analyses of their spectra. All sulfonates had their sulfur presence confirmed by the presence of a ^{36}S isotope peak in their spectra, confirming that they are sulfur-bearing organics. Some of the sulfonates in the table were also found to have additional sulfonate fragments associated with their spectra, whereby their fragmentation spectra were consistent with the mass loss of their alkyl group, confirming their mass. Fragmentation data was obtained for 2-Mercaptoethanesulfonate (third in Table 22 above) for example, which consisted of a single peak with an m/z=79.9573, matching the mass of an SO_3^- ion. This means that after untargeted analyses, we can be confident of the presence of organic sulfonates, though the exact structure of the organic component may be different – so long as its mass matches that of the molecule's total mass minus that of a sulfonate ion.

The spectrum of the metabolite first in Table 22 was inspected further since targeted analyses were planned, and because 1-hydroxychlordene contains 6 chlorine atoms, additional ^{37}Cl peaks would be observed in this metabolite's spectrum if it were present. There were no such ^{37}Cl peaks in the spectrum, however, but, upon further analysis the MS2 (fragmentation) spectrum contains a fragment with an m/z of 79.9572 which is the mass of a sulfonate group, suggesting it is an organic sulfonate. However there is no corresponding match in databases with this m/z so further work is required to identify the

exact metabolite, but it is a likely organic sulfonate.

Similar to the martian experiment, a number of metabolites putatively annotated as lipids were found to have high levels in the Winchcombe samples. In particular, several detected signals presenting well-defined, reproducible peaks with high intensities in both the WD and WG groups were putatively annotated as fatty acids and their derivatives:

-Octadecatrienenitrile
-[FA (19:0/3:0)]-nonadecatrienenitrile
-[FA (11:1)] 10-undecenoic acid
-[FA (11:2)] undecadienoic acid
-[FA methyl(12:1)] 2-methyl-2-dodecenoic acid
-[FA (13:2)] tridecadienoic acid
-10-Oxodecanoate
-[FA (8:1)] octenoic acid
-[FA (11:0)] undecanoic acid
[FA hydroxy(9:1)] 4-hydroxy-2-nonenal.

Discussion

The cumulative variance of 83.2% accounted for by the 2D PCA of the Winchcombe LC-MS experiment shows that very little information in the dataset is lost from this data visualisation. We can therefore be confident this is an accurate representation of the distribution of metabolites in the samples.

Although the six Winchcombe meteorite extracts cluster together, and apart from their corresponding environmental controls along the PC1 axis, there is a slight separation between them vertically along the PC2 axis. The samples do not separate toward their corresponding environmental control (ie the WD meteorite sample from the Wilcocks' driveway is clusters slightly toward the Rushbury House farm EG sample, whilst the WG meteorite from the from Rushbury House farm clusters slightly toward the ED environmental sample from the Wilcocks' home). The two samples represent the two main lithologies found in Winchcombe (King et al. in review). One would expect that if terrestrial contamination were the reason for the separation along the PC2 axis, that they would cluster toward their host environment, thus this opposite separation may be due to a variation in organic content in the two lithologies. Future targeted work could probe these differences and assess any variation between samples, distinct from the environmental controls.

For the targeted analyses (currently postponed due to unplanned instrument downtime), the

organic sulfonates are being prioritised. This is because they have some of the highest statistical loadings on PC1 (see Table 22), therefore are most abundant in the meteorite samples, and not in the environmental controls. We are also confident that organic sulfonates are present, due to their fragmentation patterns (consistent with a sulfonate ion mass) and secondary ^{34}S peaks present, so the targeted analyses seeks to verify their exact structures. Organic sulfonates have also previously been detected in Murchison, another CM2 meteorite, specifically ethane sulfonate, isopropanesulfonate and n-propanesulfonate (Cooper et al. 1992). Subsequently $\delta^{13}C$ measurements were carried out on the sulfonates in Murchison, which found that the $\delta^{13}C$ ratios became increasingly depleted with carbon chain length from -4.9 ‰ for methyl sulfonate, to -19.8 ‰ in n-propyl sulfonate (Chang and Cooper 1995).

Another class of metabolite that dominates Table 22 are the fatty acids. These are the most common water-soluble water-soluble organic compounds found in carbonaceous chondrites (Lai et al. 2019). Meteoritic fatty acids are thought to originate from planetesimals, forming through Fischer-Tropsch-Type (FTT) mechanisms (Lai et al. 2019). FTT mechanisms are also suggested to have been the class of abiotic synthesis for MMC in martian meteorites (Steele et al. 2018). In the martian LC-MS experiment, fatty acids were also found amongst the martian meteorites Nakhla and Lafayette, in common with the work of Steele et al (2018). This demonstrates common organic formation mechanisms in the Solar System. Targeted LC-MS analyses to probe the fatty acids and confirm the structure in this work were not possible, as LC-MS is not optimised for fatty acid detection, due to chain length and apolarity, and associated peak coelution. Future work using GC-MS, derivatising for lipids would elucidate further information about the structure and formation of these molecules in Winchcombe.